VOLUME
76

Advances in Inorganic Chemistry

Nanoscale Coordination Chemistry

Volume Editors
Daniel Ruiz-Molina
Rudi van Eldik

Advances in Inorganic Chemistry
Volume 76: Nanoscale Coordination Chemistry

ADVISORY BOARD

Advances in
INORGANIC CHEMISTRY

EDITED BY

Rudi van Eldik

University of Erlangen-Nürnberg
Erlangen
Germany

Daniel Ruiz-Molina

Institut Catala de Nanociencia i
Nanotecnologia (ICN2)
Barcelona
Spain

VOLUME 76: Nanoscale Coordination Chemistry

ELSEVIER

Amsterdam • Boston • Heidelberg • London • New York • Oxford
Paris • San Diego • San Francisco • Singapore • Sydney • Tokyo
Academic Press is an imprint of Elsevier

ACADEMIC
PRESS

Academic Press is an imprint of Elsevier
50 Hampshire Street, 5th Floor, Cambridge, MA 02139, United States
525 B Street, Suite 1650, San Diego, CA 92101, United States
The Boulevard, Langford Lane, Kidlington, Oxford, OX5 1GB, United Kingdom
125 London Wall, London, EC2Y 5AS, United Kingdom

First edition 2020

Notices

Knowledge and best practice in this field are constantly changing. As new research and experience broaden our understanding, changes in research methods, professional practices, or medical treatment may become necessary.

Practitioners and researchers must always rely on their own experience and knowledge in evaluating and using any information, methods, compounds, or experiments described herein. In using such information or methods they should be mindful of their own safety and the safety of others, including parties for whom they have a professional responsibility.

To the fullest extent of the law, neither the Publisher nor the authors, contributors, or editors, assume any liability for any injury and/or damage to persons or property as a matter of products liability, negligence or otherwise, or from any use or operation of any methods, products, instructions, or ideas contained in the material herein.

ISBN: 978-0-12-820252-4
ISSN: 0898-8838

Publisher: Zoe Kruze
Acquisitions Editor: Sam Mahfoudh
Editorial Project Manager: Shellie Bryant
Production Project Manager: Denny Mansingh
Cover Designer: Alan Studholme

Typeset by SPi Global, India

Contents

Contributors

Ramon Alibes
Departament de Química, Universitat Autònoma de Barcelona (UAB), Barcelona, Spain

Pilar Amo-Ochoa
Departamento de Química Inorgánica, Facultad de Ciencias, Universidad Autónoma de Madrid, Madrid, Spain

Pablo Ares
Department of Physics & Astronomy and National Graphene Institute, University of Manchester, Manchester, United Kingdom

Katsuhiko Ariga
WPI-MANA, National Institute for Materials Science, Tsukuba, Ibaraki; Department of Advanced Materials Science, Graduate School of Frontier Sciences, The University of Tokyo, Kashiwa, Chiba, Japan

Henrik Birkedal
Department of Chemistry & iNANO, Aarhus University, Aarhus, Denmark

Felix Busque
Departament de Química, Universitat Autònoma de Barcelona (UAB), Barcelona, Spain

Celia Castillo-Blas
Departamento de Química Inorgánica, Facultad de Ciencias, Universidad Autónoma de Madrid, Madrid, Spain

Maria Cazacu
Department of Inorganic Polymers, "Petru Poni" Institute of Macromolecular Chemistry, Iasi, Romania

Yaqing Chen
Department of Chemistry & iNANO, Aarhus University, Aarhus, Denmark

Javier Conesa
Departamento de Química Inorgánica, Facultad de Ciencias, Universidad Autónoma de Madrid, Madrid, Spain

Yann Garcia
Institute of Condensed Matter and Nanosciences, Molecular Chemistry, Materials and Catalysis Division (IMCN/MOST), Universite catholique de Louvain, Louvain-La-Neuve, Belgium

Younes Hanifehpour
Sayyed Jamaleddin Asadabadi University, Asadabad, Iran

Lida Hashemi
Department of Chemistry, Tarbiat Modares University, Tehran, Islamic Republic of Iran

Sang Woo Joo
School of Mechanical Engineering, WCU Nano Research Center, Yeungnam University, Gyeongsan, South Korea

Julia Lorenzo
Institut de Biotecnologia i de Biomedicina and Departament de Bioquímica i Biologia Molecular, Universitat Autónoma de Barcelona, Barcelona, Spain

Babak Mirtamizdoust
Department of Chemistry, Faculty of Science, University of Qom, Qom, Iran

Carmen Montoro
Departamento de Química Inorgánica, Facultad de Ciencias, Universidad Autónoma de Madrid, Madrid, Spain

Ali Morsali
Department of Chemistry, Tarbiat Modares University, Tehran, Islamic Republic of Iran

Fernando Novio
Catalan Institute of Nanoscience and Nanotechnology (ICN2), CSIC and BIST; Departament de Química, Universitat Autònoma de Barcelona (UAB), Barcelona, Spain

Ana E. Platero-Prats
Departamento de Química Inorgánica, Facultad de Ciencias, Universidad Autónoma de Madrid, Madrid, Spain

Daniel Ruiz-Molina
Catalan Institute of Nanoscience and Nanotechnology (ICN2), CSIC and BIST, Barcelona, Spain

Ruben Solórzano
Catalan Institute of Nanoscience and Nanotechnology (ICN2), CSIC and BIST; Departament de Química, Universitat Autònoma de Barcelona (UAB), Barcelona, Spain

Salvio Suárez-García
Catalan Institute of Nanoscience and Nanotechnology (ICN2), CSIC and BIST, Barcelona, Spain

Mirela-Fernanda Zaltariov
Department of Inorganic Polymers, "Petru Poni" Institute of Macromolecular Chemistry, Iasi, Romania

Felix Zamora
Departamento de Química Inorgánica, Facultad de Ciencias, Universidad Autónoma de Madrid, Madrid, Spain

Preface

As Editor of *Advances in Inorganic Chemistry* since Vol. 54 of the series, I was fortunate to convince Daniel Ruiz-Molina to join me as Co-Editor of Vol. 76 because of his expert knowledge on Nanoscale Coordination Chemistry, the theme of this volume. Over the past few years, I became aware of the exciting inorganic chemistry that was being done all over the world in the area of *Nanoscale Coordination Chemistry*. We were fortunate to be able to select a group of international and well-established practitioners to contribute to this thematic issue.

The feature article of this volume (Chapter 1) was written by Daniel Ruiz-Molina and coworkers from the Catalan Institute of Nanoscience and Nanotechnology, Barcelona, Spain on the subject: Nanoscale coordination polymers for medicine and sensors. The group presents an excellent coverage of the topic which is of vital information to new comers to the field. The next contribution (Chapter 2) comes from Ali Morsali and coworker, Department of Chemistry, Tarbiat Modares University, Tehran, Iran, with the title: Nanoscale coordination polymers: Preparation, function and application. The authors present an account on effective factors in the synthesis and application of nanocoordination polymers. Chapter 3 coming from the Departamento de Química Inorgánica, Universidad Autónoma de Madrid, Spain, was written by Felix Zamora and coworkers. It deals with the role of defects on the properties of functional coordination polymers and shows how the relevance of confinement effects and the presence of defects can be controlled during the preparation process. The next contribution (Chapter 4) comes from Yann Garcia, Institute of Condensed Matter and Nanosciences, Molecular Chemistry, Materials and Catalysis, Universite catholique de Louvain, Belgium with the theme: Selected polyazole based coordination polymers displaying functional properties. The author focuses on the design and synthesis of transition metal coordination networks built from 1,2,4-triazole, tetrazole, benzimidazole, or pyrazole building blocks. The authors of Chapter 5, Maria Cazacu and coworker, Department of Inorganic Polymers, "Petru Poni" Institute of Macromolecular Chemistry, Lasi, Romania, prepared a manuscript entitled: Coordination compounds with siloxane/silane-containing ligands capable of self-assembly at nano/micro scale in solid state and in solution. In this report carboxylic or azomethine ligands containing tetramethyldisiloxane spacers or trimethylsilane tails, were prepared and used to build 0D, 1D, 2D, or 3D metal complexes. The following Chapter 6 comes from Younes

Hanifehpour and coworkers, School of Mechanical Engineering, WCU Nano Research Center, Yeungnam University, South Korea, and is entitled: Nanoscale coordination compounds. The authors present a review on the area of coordination-driven self-assembly, which can be divided into solution and solid-state based area of molecular architecture and the more materials oriented discipline of coordination polymers and network solids. In Chapter 7, Katsuhiko Ariga from the WPI-MANA, National Institute for Materials Science, Ibaraki, Japan, reports on Nano-architectonics for coordination assemblies at interfacial media. The author reviews the fabrication and properties of metal complexes and coordination compounds, focusing on their interfacial effects especially in interfacial thin films. The final Chapter 8 of this volume comes from Henrik Birkedal and coworker, Department of Chemistry & iNANO, Aarhus University, Denmark, and reports on Mussel inspired self-healing materials: Coordination chemistry of polyphenols. The authors discuss polyphenols such as the catechol group of the amino acid DOPA used in mussel byssal threads to form a self-healing coating for adhesion and are excellent coordinators of metal ions.

The Editors are most appreciative of the efforts of the principal authors in generating lucid accounts of their own research, set in the context of the overall field. The accompanying figures and schemes and references provide excellent support for each contribution. The coauthors of each chapter are also gratefully acknowledged, as each one has had a significant input toward the success of this volume. This volume will be of value to early stage research students, and early career investigators in acquainting themselves with this timely account of Nanoscale Coordination Chemistry. Well-established investigators in the field may also benefit from having up to date reviews of various aspects of the subject in one source. We invite inorganic and other chemists, as well as multi-disciplinary researchers in wider fields, to avail themselves of the opportunity to become familiar with the remarkable recent research achievements.

Daniel Ruiz-Molina
Co-Editor,
Catalan Institute of Nanoscience and Nanotechnology (ICN2)
Barcelona, Spain

Rudi van Eldik
Editor of Advances in Inorganic Chemistry
Emeritus Professor of Inorganic Chemistry
University of Erlangen–Nuremberg, Germany

Professor of Inorganic Chemistry
Jagiellonian University, Krakow, Poland

Professor of Inorganic Chemistry
N. Copernicus University, Torun, Poland

The Advances in Inorganic Chemistry series, presents timely and informative summaries on current progress in a variety of subject areas. This acclaimed serial features reviews written by experts in the field, serving as an indispensable reference to advanced researchers that empowers readers to pursue new developments in each field. Users will find this to be a comprehensive overview of recent findings and trends from the last decade that covers various kinds of inorganic topics, from theoretical oriented supramolecular chemistry, to the quest for accurate calculations of spin states in transition metals.

CHAPTER ONE

Nanoscale coordination polymers for medicine and sensors

Rubén Solórzano[a,b], Salvio Suárez-García[a], Fernando Novio[a,b], Julia Lorenzo[c], Ramon Alibés[b], Félix Busqué[b], Daniel Ruiz-Molina[a,*]

[a]Catalan Institute of Nanoscience and Nanotechnology (ICN2), CSIC and BIST, Barcelona, Spain
[b]Departament de Química, Universitat Autònoma de Barcelona (UAB), Barcelona, Spain
[c]Institut de Biotecnologia i de Biomedicina and Departament de Bioquímica i Biologia Molecular, Universitat Autónoma de Barcelona, Barcelona, Spain
*Corresponding author e-mail address: dani.ruiz@icn2.cat

Contents

Abstract

Miniaturization of coordination polymers to the nanoscale represents a unique opportunity to assemble a novel class of highly customizable functional materials that marry the rich diversity, chemistry and properties of coordination complexes to the advantages of nanomaterials. The new structures, which exhibit well-defined and dispersed morphologies, can allow for a proper correlation with their functionality, and therefore, enable the rational design of new generations of these nanostructures targeting specific desired properties.

In this chapter we will give a brief introduction to the rational fabrication of such functional nanostructures following different coordination polymerization mechanisms. The novel "smart" nanoscale coordination polymer particles (NCPs) exhibit interesting properties of relevance for different fields and applications, worth to mention nanomedicine and sensors.

Herein we make a summary of the main results obtained in both areas that evidence the significance of this novel family of materials. For this, the review has been divided into two main sections. In the first part we revise general methodologies for cargo loading and delivery, including the design of stimuli-responsive systems.

Advances in Inorganic Chemistry, Volume 76
ISSN 0898-8838
https://doi.org/10.1016/bs.adioch.2020.03.001

In the second section we will review the latest advances in the use of NCPs as chemical sensing platforms. These results open new avenues for all the possible applications that can be derived from the implications of CPPs on surfaces. Finally, a brief introduction to the new research line on 2D-coordination polymers will be outlined.

1. Introduction

The self-assembly of coordination polymers (CPs) at the nanoscale represents a novel opportunity to develop a unique class of highly tailorable functional materials that combines the rich diversity of CPs with the advantages of nanomaterials. The synthetic flexibility of directional metal-ligand bonds is used to systematically control and tune the chemical topology, nano-dimensions and morphologies of the corresponding materials. The limitless choice of metallic elements ensures a broad range of interesting magnetic, electronic, optical, and catalytic properties. And finally, miniaturization to the nanometer scale improves their colloidal stability, increases the surface area (and therefore the catalytic, sensing or storage capabilities) and is used to systematically fine-tune the physical properties of the materials. All of these advantages are highly required for most envisioned applications.[1]

So far, two main families of CPs at the nanoscale have been described:

- Amorphous coordination polymer nanoparticles, referred from now on as nanoscale coordination polymers (NCPs),[2] also called infinite coordination polymers (ICPs)[3] or coordination polymer particles (CPPs).[4]
- Nanoscale crystalline and porous coordination polymer structures, from now on NMOFs.

NMOFs exhibit exceptionally high surface areas and loading capacities while allow for control over the release of cargo via modification of tunable pores. The crystalline nature of MOFs also facilitates analyses of host-guest interactions and therefore, a systematic design and optimization of drug encapsulation and release studies. As a result of these interests, several comprehensive reviews summarizing progress in MOFs for applications are available elsewhere,[5] being the nanomedicine of the emerging areas of interest over the last years.[6] On the other hand, NCPs have emerged as an alternative to NMOFs. This new family of nanoparticles are amorphous with spherical morphologies ranging from a few to hundreds of nanometers in size. The most common synthetic approach to obtain NCPs is mixing metal ions and the corresponding organic ligands in the presence of a poor solvent that induces a fast precipitation, i.e., using out-of-equilibrium conditions.[7]

To minimize the interfacial free energy between the surface of the NCPs and the solvent during the reaction, the nanoparticles acquire the spherical shape. Other approaches to obtain NCPs have been described:[8] worth to mention are reverse micro-emulsions,[9] lab-on-a-chip implementation[10] and dip-pen nanolithography (DPN).[11]

Since first reported in 2005 by Mirkin[12] and Wang,[13] the number of publications related with NCPs is growing exponentially along with the variety of applications exemplified, including heterogeneous catalysis,[14] spin-crossover,[10,15] separation of oils from water,[16] bio-sensing,[17] pH sensors,[18] gas absorption systems,[19] hybrid nanoparticle-based devices,[20] fluorescent sensors,[21] precursors for inorganic particles[22] and thermochromic nanostructures.[23] Especial mention deserves the application of NCPs in medicine. With this aim, drugs can be trapped as constitutive building blocks of the polymeric unit (chemical entrapment) or through the physical encapsulation inside the nanoparticle.[24] Physical encapsulation of active substances such as organic dyes, magnetic nanoparticles, or luminescent quantum dots was already reported back in 2009.[25] One year later, the same authors showed that these capsules not only can encapsulate but also can release active principles as polymeric nanoparticles do.[25] On the other side, chemical entrapment allows for a better fine-tuning of the release kinetics (up to many hours) as well as a better formulation with increased encapsulation yields. The use of active metal drugs, such as Pt(IV),[26] as polymeric nodes of coordination polymers represents the most successful example of chemical entrapment. Less explored has been the chemical entrapment through tethering of active drugs as chelating ligands, in spite of the fact that its efficiency has already been reported.[27] Moreover, the chemical flexibility of organic synthesis may allow for the design of drugs (ligands) cleaved under physiological conditions.[28] Together, encapsulation capabilities, nanodimensions and excellent colloidal and chemical stabilities have allowed for their use in medical applications.

Beyond their use in Nanomedicine, the scope of application of NCPs nanoparticles as platforms for chemical sensing has also grown exponentially in the last years.[28] Lanthanide-based NCPs nanoparticles constitute the main class of these nanostructures used as sensors for different chemical species, based on its performance in enhancing or quenching the fluorescence of a sample in the presence of a certain analyte.

Herein we make a summary of the main results obtained in both areas that evidence the significance of this novel family of materials. For this, the review has been divided into two main sections. In the first part,

we revise general methodologies for cargo loading and delivery, including the design of stimuli-responsive systems. In the second section, we will review the latest advances in the use of NCPs as chemical sensing platforms. Rather than a detailed list of examples and specific cases reported so far, it is our aim to go deeper into the mechanistic details of their behavior.

2. Nanoscale coordination polymers for drug delivery

2.1 Encapsulation and release approaches

As mentioned above, cargo loading is accomplished either via direct incorporation of active drugs as NCPs building blocks (metal ions or organic ligands) or via guest encapsulation during NCPs synthesis or in a post-synthetic step. Following this approach, we can achieve high drug loadings, although the morphology and physicochemical properties are difficult to control. Using the second approach, we have more control over the morphology but overall the active drugs are incorporated in lower amounts and their loading strongly depends on the physicochemical properties of each drug (leakage can occur). Amorín-Ferré et al. illustrated the differences between both encapsulation approaches and their drug release kinetics (Fig. 1).[24] NCPs composed by Co(II), 1,4-bis(imidazol-1-ylmethyl)benzene (bix) and 3,5-di-*tert*-butylcatechol, were formed in the presence of fluorescent compounds, either containing a free chelating catechol (coordination to the main backbone takes place) or a protected one (physical entrapment). Cargo loading via direct attachment to the NCPs framework was slowly released only upon particle degradation, whereas the encapsulated one was easily released through a diffusion mechanism. On the other hand, Novio et al. reported the formation of catechol-iron based NCPs containing carboxylic groups as platforms for further functionalization via condensation reactions.[29] As a proof-of-concept, the particles were covalently labeled with bioactive functional moieties as a fluorescent dye or polyethylene glycol (PEG). The particles showed efficient cellular uptake and no significant cytotoxicity. Their use as drug delivery platforms was then modeled by encapsulating the anticancer drug camptothecin, showing an improvement in IC_{50} values as compared with the free drug.[29]

Liang et al. synthesized nanowire coils of organometallic coordination polymers by using the emulsion polymerization technique.[30] The nanowires were formed by the self-assembly of a triblock copolymer terminated with a complex of β-cyclodextrin and 4,4′-bipyridine and their subsequent polymerization using Ni(II). The resulting material was able to incorporate

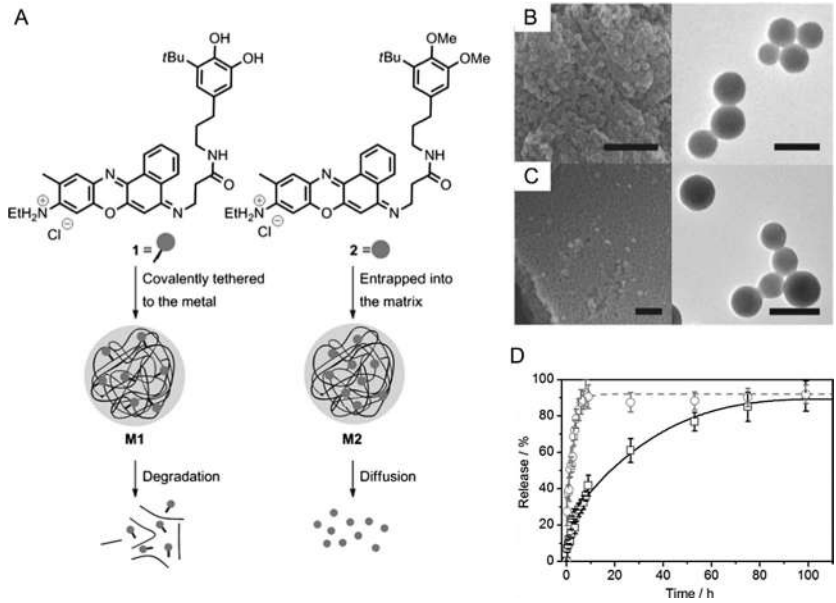

Fig. 1 (A) Chemical structures of fluorescent guest compounds **1** and **2** used in the formation of structural-analogous of **M1** and **M2** particles, used to investigate degradation and diffusion-controlled release in NCPs. (B) and (C) SEM (left) and TEM (right) images of **M1** (B) and **M2** (C) particles. Scale bars for SEM are 1 μm and 200 nm for TEM. (D) Release profiles of fluorescent guest molecules from **M1** (□) and **M2** (○) at 37°C, averaged over four independent experiments. *Reproduced from reference Amorín-Ferré, L.; Busqué, F.; Bourdelande, J. L.; Ruiz-Molina, D.; Hernando, J.; Novio, F. Chem. A Eur. J. 2013, 19, 17508–17516 with permission of the copyright holder.*

hydrophobic organic cargoes, as showed by the encapsulation of model hydrophobic dye Nile red. Li et al. reported nanostructures made by the self-assembly of curcumin, amino acids and Zn(II).[31] The nanostructuration of the curcumin molecule helped to overcome its quick degradation in physiological media. Additionally, tumor accumulation and inhibition were enhanced when curcumin was delivered as NCPs. Li et al. illustrated the feasibility of NCPs for macromolecule delivery with the report of iron-induced DNA self-assemblies.[32] The resulting nanostructures could be fine-tuned by modifying the Fe/nucleotide ratio or their concentration during the reaction mixture. Although DNA is unable to penetrate cell membranes, its nanoassembly allowed an efficient cellular uptake, reported mainly in endosomes or lysosomes. In vitro and in vivo studies showed the potentiality for DNA delivery using CpG, an immune stimulatory DNA.

Fan et al. developed an interesting strategy for monitoring drug release in real-time based on the self-assembly of a tryptophan-phenylalanine dipeptide with Zn(II) ions to form dipeptide nanoparticles (DNPs).[33] DNPs were found to display fluorescence in the visible range and possessed advantages over organic fluorophores, quantum dots or green fluorescent proteins like photo- and thermal stability, biocompatibility and narrower emission bandwidth. Conjugation of the chemotherapeutic drug dioxorubicin through π-π stacking, afforded DNPs able to experience release (50% in 24 h, pH 6.0), which could be then monitored in vitro due to their fluorescent properties. Bertleff-Zieschang et al. described an approach for the coordination-driven assembly of different flavonoids and Fe(III) ions, which could be either used for the preparation of films or microcapsules after template removal.[34] The resulting structured flavonoids displayed higher antioxidant activity than in the free form and was preserved over multiple scavenging cycles.

2.2 Stimuli-responsive delivery platforms

The high degree of tuneability in the design of NCPs allows the fabrication of materials with responsive properties. Several examples have been reported in which an external stimulus is able to trigger a more controlled drug delivery. Probably the most relevant stimulus is pH, because of both the pH-dependence nature of coordination bonds and the relevance of pH variations within intra- and extracellular environments. Other potential stimuli for cargo release might include redox- or light-responsive materials.

2.2.1 pH-responsive

Gao et al. reported nanoparticles composed by the self-assembly of iron ions and 1,1′-(1,4-butanediyl)bis(imidazole) and the subsequent encapsulation of dioxorubicin hydrochloride (40% drug loading content) followed by silica coating.[35] Interestingly, these particles exhibited sustainable drug release for several days, which was significantly faster at pH 5.0 than under physiological conditions. Another example of pH-dependent dioxorubicin delivery using NCPs was reported by Bai et al.[36] In this work, a triblock copolymer composed by poly(ethylene glycol)-b-poly(2-hydroxyethyl methacrylate-Boc-histidine)-b-poly(styrene) (PEG-PBHE-PS) was prepared and self-assembled into micelles. Further polymerization of histidine moieties, dioxorubicin and Cu(II) allowed the formation of micelles with a drug loading as high as 26.1%. Due to the pH-dependence of the stability of the coordination bonds between copper, histidine and dioxorubicin, drug leakage was strongly suppressed at physiological pH but drug release was

drastically increased at pH 5.0. Further studies using dioxorubicin included NCPs composed by an iron(III)-gallic acid network that could potentially encapsulate dioxorubicin up to 93.5% drug loading content by its coordination with the Fe(III) centers.[37] In this work, Han et al. showed that these acid-sensitive NCPs allowed a real-time drug release monitoring into lysosomes, as dioxorubicin inherent fluorescence was quenched when the polymer was nanostructured but recovered as dioxorubicin was released due to the acidity in lysosomes. Moreover, in vivo evaluation showed significant tumor growth inhibition with minimal heart toxicity.

Xu et al. proposed a strategy for releasing Fe-salphen complexes using core-shell nanoparticles composed by a Fe_3O_4 core and a salphen-In(III) coordination polymer shell.[38] Using this approach, the polymeric shell was observed to rapidly hydrolyze at pH 5.0, while the Fe_3O_4 core slowly collapsed to release iron ions chelated by salphen and form the active therapeutic species. In vitro studies determined significant selectivity for cancer cells and IC_{50} values comparable to those of pharmaceutically-active Mn(II)-salen complexes.

Wang et al. exploited the lability of metal-ligand bonds to cap titanium nanotubes (TNTs) containing antibacterial agents using coordination polymers.[39] In this work, TNTs were loaded with model drugs ibuprofen, vancomycin or Ag nanoparticles and then capped by the bix ligand and Zn(II) or Ag(I) ions. At physiological pH, drug release was found to be blocked; however, it increased as pH decreased, due to the degradation of the coordination polymer. In addition, metal ions could offer favorable biological functions: Zn(II) could promote the proliferation of osteoblastic cells while Ag^+ exhibited antibacterial properties.

Ejima et al. took advantage of the pH dependency in Fe(III)-catechol coordination by preparing coatings based on the polymerization of tannic acid with iron(III) ions.[40] The authors reported a general approach for the one-step formation of films in a wide variety of substrates, including inorganic, organic and biological templates. The capsules formed were observed to disassemble in acidic pH due to protonation of catechol moieties and therefore destabilization of crosslinks. In addition, cytotoxicity was not observed in any iron-tannic acid coating tested. In a follow-up study, the authors also described a multistep assembly of iron(III)-tannic acid, which exhibited different properties than the ones made by one-step deposition, e.g. permeability, stiffness or degradability.[41] Their pH-responsiveness was further exploited in the formation of dioxorubicin-loaded metal-phenolic microcapsules using mesoporous $CaCO_3$ particles as sacrificial templates.[42]

Capsules were prepared by the polymerization of tannic acid with Al(III), although Mn(II) and Gd(III) were also used for potential theranostic applications. As expected, their disassembly was observed to be pH-dependent, being relatively stable at pH 7.4 but degraded in a significant amount (80%) during 48 h at pH 5.0. In vitro assays also showed efficient capsule internalization and intracellular drug release, as well as comparable or even improved, in some cases, therapeutic effects. The same strategy was followed by Ju et al. using a mixture of catechol-functionalized hyaluronic acid and polyethyleneglycol instead of tannic acid.[43] The resulting dioxorubicin-loaded material showed an acid-triggered drug release along with enhanced targeting for CD44+ cancer cell line instead of CD44- cells due to the presence of hyaluronic acid and polyethyleneglycol. A further study showed the benefits of protein corona in such systems, improving target specificity.[44] In a subsequent study, Park et al. used the previous approach to coat individual yeast cells.[45] Coated cells were found to retain their metabolic activities and viability, as well as an enhanced protection against binding of *E. coli*, UV-C irradiation, lyticase and silver nanoparticles. Due to the pH-sensitive nature of their coating, cells could also be both preserved and exposed on-demand. Catechol-iron coordination was also used by Besford et al. to coat oleic acid nanoemulsions with a crosslinking of catechol-containing polyethyleneglycol and Fe(III) ions.[46] The resulting dioxorubicin-loaded nanostructures displayed an acid-induced drug release behavior. In vivo assays showed a stealth-like response with regards to cell association and a blood circulation half-life of 50 min. In vitro tests revealed significant cytotoxicity against human breast cancer cells, demonstrating successful cell internalization and intracellular release of the drug.

Huang et al. recently reported the synthesis of Zn-based hexahistidine-metal nanoassemblies (HmA) for drug encapsulation.[47] Such assemblies exhibited interesting properties such as an average size of 60 nm, the possibility of encapsulating from small molecules (fluorescein) to polymers (dextran-40 k) and a loading capacity of up to 53%. Moreover, a pH dependence was reported, with a burst release at pH 4.5 in minutes and a slow release at neutral pH. Minimal cytotoxicity and fast internalization were also reported for the HmA. In addition, encapsulation of the chemotherapeutic drug camptothecin improved the antitumor activity compared to the free drug.

Not only coordination bonds within NCPs can trigger a pH-dependent response, but also the NCPs ligand design. As a proof-of-concept, Nador et al. compared the pH-responsiveness of two structurally analogous bis(catechol)-based cobalt NCPs, containing either an imine functionality

or an alkyl chain.[18] Notably, NCPs composed by the imine-containing linker showed a loss of their spherical shape and aggregation at pH 5.0, in addition to the disappearance of the characteristic imine infrared bands. However, NCPs treated at neutral pH preserved their morphology and chemical composition. Likewise, NCPs composed by the alkyl chain based linker confirmed the role of the imine moiety in the nanostructure disassembly, as they displayed great stability independent of the pH value used. Further examples include the nanostructures designed by Liu et al. based on Hf(IV) and an imine-based acid sensitive linker that were used for the encapsulation of the chemotherapeutic drug chloro(triphenylphosphine)gold(I) (TPPGC).[48] These particles exhibited excellent stability at physiological pH but rapidly collapsed in mild acidic environments to release their cargo. In vitro and in vivo studies examined the feasibility of this system as combinational chemo-radiotherapy, due to the mixture of the encapsulated chemotherapeutic drug and hafnium ions that act as radio-sensitizers, showing an improvement as compared with conventional chemotherapy or radiotherapy. In addition, these nanostructures displayed no significant toxicity and their biodegradability could potentially avoid long-term toxicity concerns. In another study, Liu et al. further exploited this idea by encapsulating collagenase using a self-assembly between the previous imine-based acid sensitive linker and Mn(II) ions.[49] After its PEGylation, these NCPs showed a similar pH-dependence than those of the previous work, being stable at neutral pH to degrade under acidic environments. In vivo studies demonstrated efficient accumulation within tumors. In addition, the released collagenase would allow an enhanced retention and permeation of a second wave of therapeutic nanoparticles (chlorin e6 (Ce6)-loaded liposomes) which lead to an improved photodynamic therapeutic effect.

Yang et al. described a series of nano-constructs formed by a dicarboxylic cisplatin (IV) prodrug, poly-L-histidine-PEG and a metal cation (Ca(II), Co(II), Ni(II), Hf(IV), Tb(III)).[50] In this case, the NCPs experimented a charge conversion from slightly negative to positive upon a pH decrease from physiological to pH 5.5. Thus, these nanoparticles were stable under pH 7.4 but experimented a rather fast drug release at acidic pH. Such behavior was rationalized by the weakening of the histidine-metal bond by protonation of imidazole groups and further network collapse. Therapeutic efficacy of these NCPs was tested in vitro and in vivo, showing tumor suppression efficacy under relatively low drug doses.

Wang et al. reported a concept of pH-responsive NCPs based on the coordination of Cu(II) and an organic linker containing the macrocycle dioxocyclam.[51] In this approach, particles were formed by solvent-assisted

precipitation of the corresponding soluble Cu(II)-linker. Upon a pH decrease, the dioxocyclam-Cu(II) complex was dissociated as the macrocycle was protonated, leading to the disassembly of the nanostructure. Interestingly, this work also demonstrated polymer collapse upon the addition of a competitive copper chelator (EDTA) at neutral pH.

2.3 Other stimuli

Concerning the use of other stimuli in NCPs, several examples have been recently reported. For instance, Zhang et al. developed a simple method for the fabrication of photodegradable nanostructures based on the self-assembly of Zn(II) and a bis(imidazole) ligand containing a photocleavable *o*-nitrobenzyl unit.[52] These structures exhibited the capability to physically encapsulate different cargoes. Specifically, fluorescein, the antibiotic agent tetracycline or the chemotherapeutic drug dioxorubicin, were separately encapsulated within the polymer network. Interestingly, their release in aqueous solution was significantly increased upon UV light irradiation when compared with no irradiated samples. In addition, in vitro experiments using HeLa cells showed no significant cytotoxicity for the non-loaded NCPs, while dioxorubicin-loaded NCPs retained a cytotoxic effect which became more evident upon irradiation, suggesting an enhanced drug release into the cells under these conditions. Liu et al. reported a strategy for light-controlled drug release based on Hf(IV) following an analogous approach to that used in the fabrication of a pH-sensitive NCPs for combinational chemo-radiotherapy.[53] In this case, nanostructures were formed by the polymerization of a bis-(alkylthio) alkene linker (BATA), a singlet-oxygen sensitive ligand, and Hf(IV) cations. After loading with both photosensitizer chlorin e6 and chemotherapeutic drug dioxorubicin, these NCPs were able to produce singlet oxygen upon red light irradiation, thus inducing drug release due to BATA cleavage and collapse of the nanoparticle. Notably, CT imaging and biodistribution measurements showed efficient tumor accumulation, while presenting an improvement for combined chemo-photodynamic therapy and reduced toxicity when compared with the free drugs (Fig. 2). Hu et al. synthesized novel NCPs based on photochromic ligands for the potential encapsulation/release of cargoes upon light irradiation.[54] In this study, microparticles formed by Zn(II) and a carboxylic-functionalized diarylethene photoswitch exhibited reversible photochromic behavior in the solid state and in solution. Remarkably,

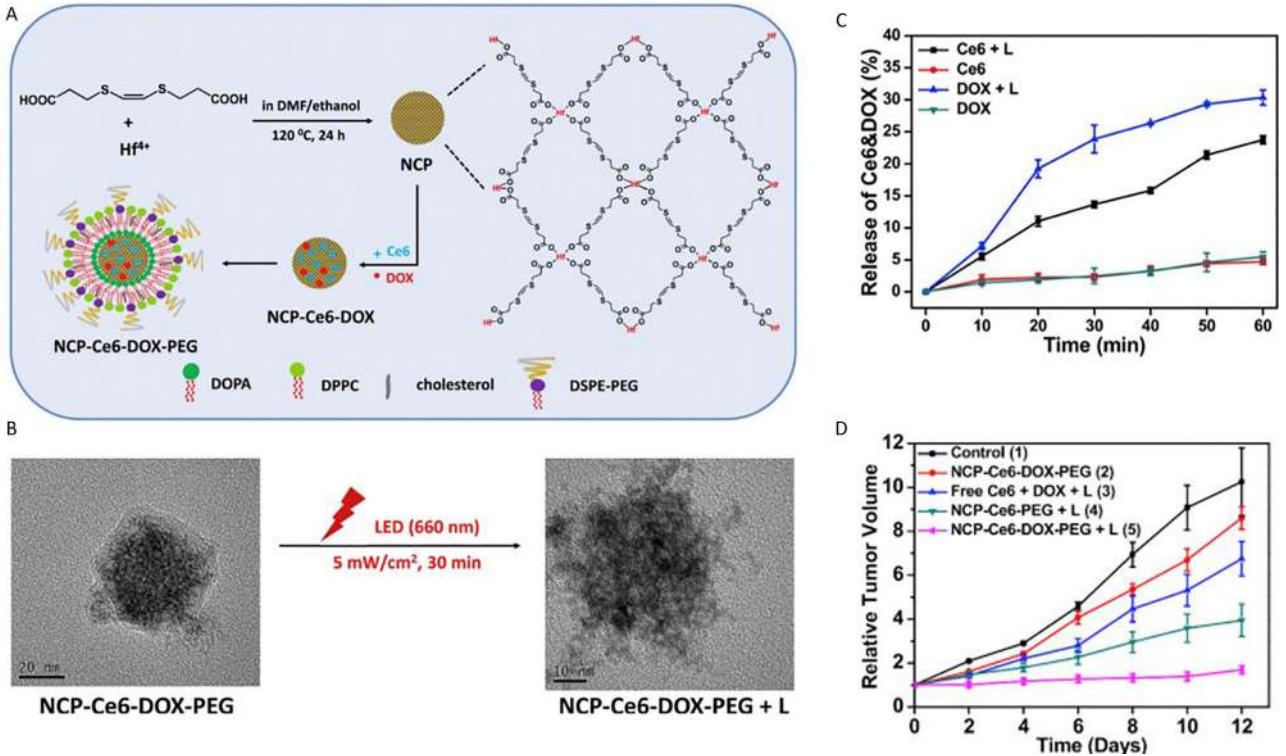

Fig. 2 (A) Schematic illustration for the synthesis of NCP-Ce6-DOX-PEG nanoparticles (B) TEM images of NCP-Ce6-DOX-PEG before and after light irradiation. (C) Sustained release of Ce6 and DOX from NCP-Ce6-DOX-PEG with or without 660 nm LED light exposure at the power density of 5 mW cm^{-2}. (D) Tumor growth curves of mice in different groups after receiving various treatments. *Reproduced from reference Liu, J.; Yang, G.; Zhu, W.; Dong, Z.; Yang, Y.; Chao, Y.; Liu, Z. Biomaterials 2017, 146, 40–48 with permission of the copyright holder.*

their change in surface area, pore shape and size upon interconversion by UV or visible light could provide a novel approach for light-triggered cargo release.

Cherepanov et al. reported the redox-dependent disassembly of gallic acid-Fe(III) networks.[55] The authors evaluated the electrochemical reversibility of the system, identified the oxidation state of the redox-active species and showed that release of Fe(III) could be achieved, additionally identifying the specific conditions for "on-off" or continuous disassembly of the networks. Concerning redox-induced disassembly of nanostructures, Buywalda et al. developed micelles based on poly(ethylene glycol)-poly (N(2-hydroxypropyl)methacrylamide (PEG-P(HPMA)) including hydrophobic 4-(methylthio)benzoyl side groups that could be crosslinked using the metal-organic linker [ethylenediamineplatinum(II)]$^{2+}$.[56] As a proof-of-concept, curcumin was encapsulated in such micelles with and without crosslinking. When compared to the free micelles, the crosslinking resulted in a smaller size, a lower critical micellar concentration and a better retention of the encapsulated drug. Drug release was found to be lower in the crosslinked micelles; however, it was increased in the presence of dithioerythritol, which mimicked the presence of glutathione in the intracellular environment.

2.4 Multi stimuli-responsive systems

Li et al. reported a simultaneously pH- and glutathione-responsive nanoparticles composed by the self-assembly of Zn(II) and a histidine containing dipeptide or a amphiphilic histidine derivative (Fig. 3).[57] Moreover, the model drug chlorin e6 could be incorporated in loading capacities higher than 50% through cooperative coordination with the peptide and Zn(II). Importantly, the nanostructures displayed robust stability in physiological conditions but experimented a burst release upon either a pH decrease or a glutathione concentration increase. Owing to these features, these NCPs presented prolonged blood circulation lifetime, enhanced accumulation in tumors, improved antitumor efficacy compared to non-encapsulated photosensitizers and negligible in vitro or in vivo toxicities.

Another example of multistage responsiveness was reported by Liu et al.[58] In this work, MnO_2 nanoparticles stabilized by bovine serum albumin were prepared and coated with a shell composed by the polymerization of Hf(IV) and c,c,t-(diamminedichlorodisuccinato)Pt(IV) (DSP), a cisplatin prodrug. After a PEGylation step, the formed nanocomposite could act as a

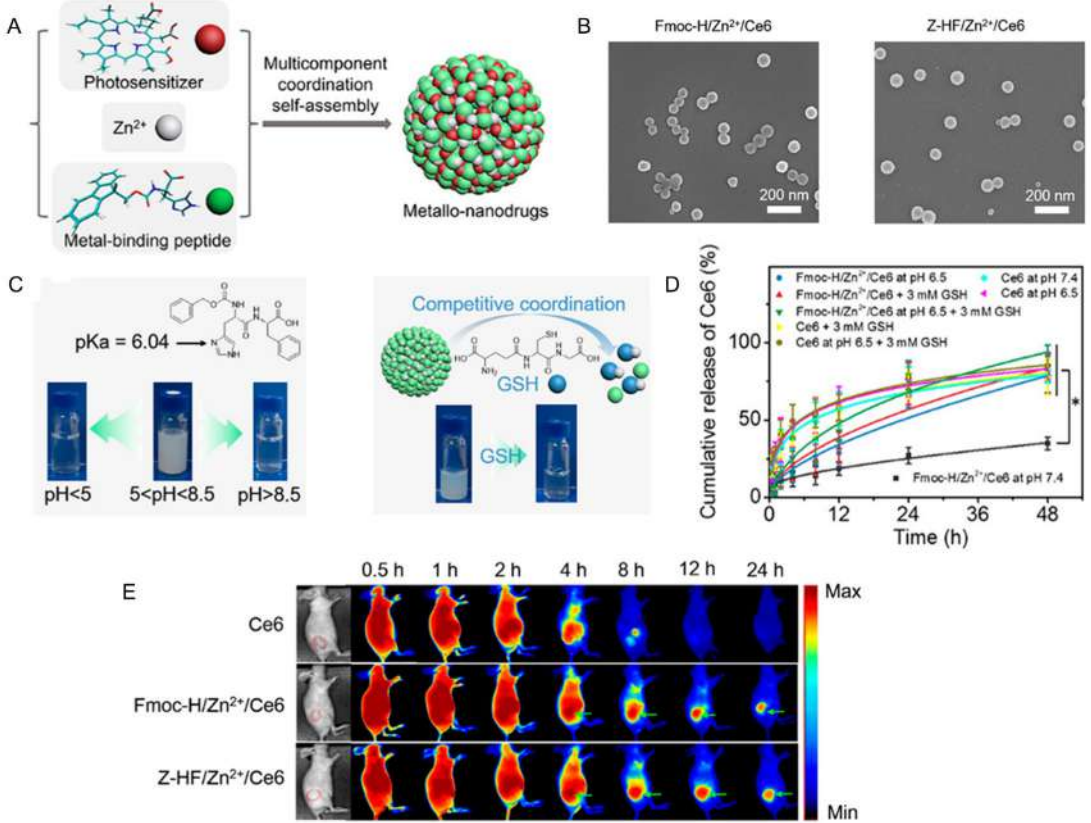

Fig. 3 (A) Construction of metallo-nanodrugs through cooperative coordination of small peptides and photosensitizers (Ce6) in the presence of zinc ions. (B) SEM images of the metallo-nanodrugs. (C) Schematic illustration and pictures showing the ultrasensitive response of Fmoc-H/Zn^{2+} to pH and GSH changes. (D) Ce6 release profiles from Fmoc-H/Zn^{2+}/Ce6 in different release buffers. Unencapsulated Ce6 was used as a control group. The lines are the fitted results according to the Gompertz kinetic release model. Error bars denote the standard deviation ($n = 3$). $^{*}P < 0.05$ (one-way ANOVA). (E) Fluorescence images showing that Fmoc-H/Zn2+/Ce6 and *Z*-HF/Zn2+/Ce6 allow better accumulation of Ce6 in tumor sites than unencapsulated Ce6. *Reproduced from reference Li, S.; Zou, Q.; Li, Y.; Yuan, C.; Xing, R.; Yan, X. J. Am. Chem. Soc. 2018, 140, 10794–10802 with permission of the copyright holder.*

radio-sensitizer due to the presence of hafnium ions, as chemotherapeutic agent resulting from cisplatin release under reductive environments upon cell uptake or as magnetic resonance imaging contrast owing to the decomposition of MnO_2 in the acidic tumor environment. In addition, MnO_2 could trigger decomposition of tumor endogenous H_2O_2 improving hypoxia-associated radiotherapy resistance. As a result of these factors, an efficient in vivo chemo-radiotherapy was observed while the inherent biodegradability of NCPs and MnO_2 lead to efficient excretion the nanocomposites with no appreciable toxicity.

Wang et al. described an interesting example of drug release triggered by cellular endogenous species.[59] Specifically, the authors designed a folic acid-PEG-poly(4-vinylpyridine)-Ir(III)-2-phenylquinoline complex that self-assembled in water to form core-shell spherical nanoparticles with an average radius of 25 nm. Within this nanostructure, the Ir(III)-containing moiety acted as the core, whereas PEG remained in the shell. Remarkably, in vitro experiments revealed the interaction of intracellular histidine with the nanoparticles in order to release the iridium complex $[Ir(pq)_2]^+$ (pq = 2-phenylquinoline), which served both as drug and as precursor of a phosphorescent emitter, thus enabling not only intracellular drug release but also phosphorescent tracking of its cellular internalization.

The possibility of fine-tuning and rationalize NCPs composition also allows the formation of multi-responsive systems that act as molecular logic gates. Pu et al. illustrated such behavior in nanostructures composed by the self-assembly of Tb(III) or Eu(III) ions and the nucleotide guanosine 5′-monophosphate (GMP).[60,61] These nanoparticles, after the encapsulation of *N*-methyl mesoporphyrin IX (NMM), exhibited fluorescence emission that could be described as the output of different binary logic gates when two or three distinct stimuli (inputs) were applied. Therefore, this input-dependent encapsulation could be used for controlled release and, simultaneously, cellular imaging. Gao et al. also reported GMP-lanthanide assemblies that could respond to several external stimuli such as dipicolinic acid, ethylene diamine tetraacetic acid, pH and Cu(II) or Hg(II) ions.[62] In a similar way, Bai et al. described the core-cross-linking of a disulfide-containing dioxorubicin prodrug with Cu(II) to form nanoparticles that acted as an AND logic gate, i.e., the output is released only if both inputs are present.[63] In this example, inputs corresponded to acidic and reductive conditions, commonly found in cancer cells. Thus, premature drug release was observed to be suppressed under neutral and non-reductive environments, but enhanced when both conditions, low pH and reducing agents, were accomplished.

3. Nanoscale coordination polymers for chemical sensing

The scope of application of NCPs as platforms for chemical sensing has also grown exponentially in the last years. Lanthanide-based NCPs nanoparticles constitute the main class of these nanostructures used as sensors for different chemical species, resting its performance in enhancing or quenching the fluorescence of a sample, in the presence of a certain analyte. In turn, Terbium(III) is the most common lanthanide ion used.[64–78]

Tb(III) nanosensors, based on an enhancement of the fluorescence, can operate following three different mechanisms: (i) by suppression of the inhibition of Tb(III)-ligand network fluorescence;[64,65] (ii) by sensitization of Tb(III) fluorescence;[66,67] and (iii) through the releasing of a fluorescent dye.[68–70] Among the examples working by suppression of the inhibition of Tb(III)-ligand network fluorescence, Chen and coworkers demonstrated the utility of NCPs composed of Tb(III), adenine (Ad) as the main constitutive ligand, and dipicolinic acid (DPA) as an auxiliary ligand sensitizer of the fluorescence of the metal, as a fluorescence nanosensor for Hg(II) (Fig. 4).[64] The fluorescence of the NCP network is very low due to a photoinduced electron transfer (PET) from adenine to DPA which avoids the expected intramolecular energy transfer from this molecule to Tb(III) that otherwise sensitizes the fluorescence of this atom. In the presence of Hg(II), a significant enhancement of fluorescence takes place due to the disappearance of the PET process as a consequence of the coordination of this metal to adenine. As nanosensor for Hg(II), it presents a remarkable sensitivity and range of application between 0.2 and 100 nM.

A similar strategy based on the enhancement of fluorescence of NCPs composed of Tb(III) ions has been described by Shi and coworkers for the selective sensing of biothiols, hydrogen peroxide or glucose in solution.[65] The nanoparticles are made with Tb(III), the nucleotide guanosine monophosphate (GMP) as bridging ligand and Hg(II) which interacts with GMP and quenches the fluorescence of the Tb-GMP network. The as-prepared Tb–GMP–Hg nanoprobe can be used for the "turn on" fluorescent determination of several biothiols (Cys: cysteine, Hcys: homocystine, GSH: glutathione), through their high affinity for Hg(II), in a range between 10 and 1000 μM. Moreover, the addition of H_2O_2 reverses the Cys-mediated luminescence increase in the Tb–GMP–Hg probe, originating a "turn off" luminescent assay for H_2O_2 in concentrations

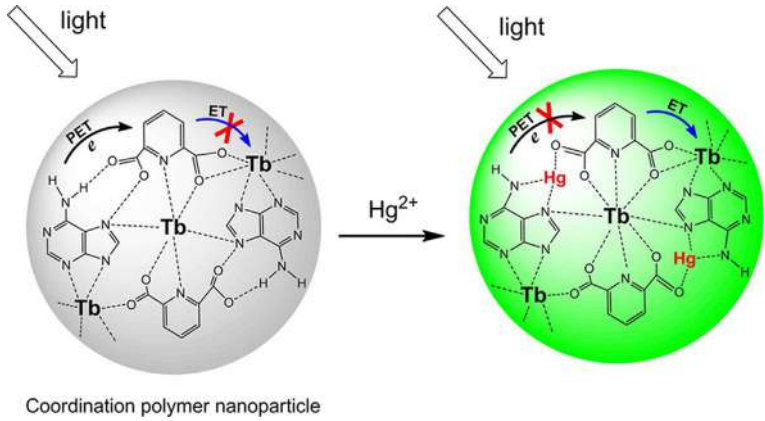

Fig. 4 The use of Tb(III) Coordination Polymer Nanoparticles for mercury(II) sensing constitutes a paradigmatic example of using the enhancement of fluorescence in presence of an analyte for sensing purposes. In this case, a suppression of the inhibition of Tb(III)-ligand network fluorescence in the presence of Hg (II) takes place. The fluorescence of the NCP network is very low due to a photoinduced electron transfer (PET) from adenine to DPA which avoids the expected intramolecular energy transfer from this molecule to Tb(III) that otherwise sensitizes the fluorescence of this atom. In the presence of Hg(II) a significant enhancement of fluorescence takes place due to the disappearance of the PET process as a consequence of the coordination of this metal to adenine. *Reproduced from reference Tan, H.; Liu, B.; Chen, Y. ACS Nano 2012, 6, 10505–10511 with permission of the copyright holder.*

between 1 and 200 μM. The Tb–GMP–Hg- Cys material is also suitable for the detection of glucose, through the generation of H_2O_2, if the enzyme glucose oxidase (GOx) is incorporated in the system.

An additional example of enhancing the fluorescence of Tb(III)-based NCPs to constitute an efficient nanoprobe is the reported by Tan et al. for the detection of antibiotic Ciprofloxacin.[66] In this case, the NCP network is formed with Tb(III) and adenine as bridging ligand. A fluorescent emission of Tb(III) occurs in the presence of ciprofloxacin, due to the formation of a complex between this molecule with Tb(III) atoms on the surface on the NCPs. The thus obtained nanosensor presents a range of applications with linear enhancement of fluorescence between 60 nM to 14 μM. In the example presented by Cao and coworkers, the enhancement of fluorescence of NCPs composed of Tb(III) ions and the bis hydrazine of 4-formyl-3-hidroxybenzoic acid (HDBB) as fluorescent bridging ligand, allowed the development of a fluorescent probe for zinc.[67] The Tb-HDBB network emits fluorescence at 590 nm when excited at 365 nm. Upon the addition of Zn(II),

some carboxylic acid groups on the surface of the Tb-HDBB nanoparticles bind to this cation, resulting in the formation of new Tb-HDBB-Zn nanoparticles that present an additional increase in fluorescence emission at 470 nm with a concomitant decrease at 590 nm, providing a probe for the ratiometric assay for Zn(II) in a remarkable wide range from 100 nM to 60 μM.

The last strategy for enhancing the fluorescence of a sample in the presence of an analyte consists of the encapsulation of an adequate dye in the NCPs. Thus, in the work reported by Mao and coworkers, NCPs composed of Tb(III) ions, GMP as constitutive ligand and the encapsulated fluorescent dye 7-amino-4-methyl coumarin, are used as a fluorescent probe for alkaline phosphatase (ALP) activity.[68] The coumarin dye itself emits weak fluorescence while encapsulated, but upon the presence of ALP, the phosphate group in the GMP ligand is cleaved, resulting in the destruction of the Tb-GMP network and the release of encapsulated coumarin dye into solution, causing the decrease in the fluorescence intensity emitted from the Tb-GMP network itself and the increase in the fluorescence intensity emitted from coumarin, providing a probe for the ratiometric assay for ALP in a range from 0.025 U/mL to 0.2 U/mL. Similarly, in a work reported by Ye and coworkers, heterobinuclear NCPs composed of Ce(III) and Tb(III) ions and the nucleotide AMP as constitutive ligand, provided a fluorescent probe for Hg(II).[69] In this case, a fluorescent dye (coumarin) was encapsulated to form nanoparticles which emit characteristic luminescence of Tb(III) at 548 nm after excitation, whereas coumarin itself emits weak fluorescence at 445 nm. In the presence of Hg(II), a strong coordination between AMP and Hg(II) occurs, resulting in the destruction of the Ce-Tb-AMP nanoparticles and the release of encapsulated coumarin dye into solution. As a result of this process, a quenching of the fluorescence intensity emitted from the Ce-Tb-GMP network takes place while increasing the fluorescence intensity emitted from coumarin, providing a double signal based nanoprobe for the ratiometric assay for Hg(II) in a wide range from 0.08 to 1000 nM. Following a closely related strategy, Li and coworkers reported NCPs composed of Tb(III) ions, GMP as binding ligand and an encapsulated NIR fluorescent hemicyanine dye (CyOH) as a fluorescent probe for alkaline phosphatase (ALP) endogenous activity in biological samples, along with satisfactory tissue imaging capability at the depths of 40–120 μm.[70] In the presence of ALP, phosphate bonds in the Tb-GMP network are cleaved, resulting in the destruction of the nanoparticles and the release of encapsulated CyOH into solution, originating from an increase of

fluorescence intensity emitted by this dye that provides a NIR fluorescent nanoprobe for ALP activity in cells, tissues and mice.

On the other hand, the quenching of fluorescence of different atoms in NCPs has also been a recurrent strategy for the development on nanosensors of different chemical species. Thus, Liu and coworkers described the use of NCPs nanoparticles as a tool for selective DNA homopolymers sensing and adsorption.[71] Thus, a series of diverse NCPs between a nucleobase (adenine) or different nucleotides and various metal ions (Au(III) and Tb(III) among others) was prepared and tested for sensing of complementary DNA homopolymers. In the case of using Au(III) and adenine, the corresponding fluorescent NCPs can be used as a sensor for complementary DNA homopolymers due to a linear quenching of the fluorescence of the nanoparticles in a range of DNA concentrations between 5 and 20 nM. A similar strategy based on the quenching of fluorescence of NCPs composed of Tb(III) ions has been described by Song and coworkers for the selective sensing of hydrogen peroxide in biological fluids.[72] The NCP network is formed with Tb(III) phenylalanine as structural ligand and carboxyphenylboronic acid (CPBA) as guest ligand and sensitizer of the Tb(III) fluorescence. In the presence of H_2O_2 the fluorescence of the NPs is quenched as a consequence of oxidative deboronation of CPBA molecules and the corresponding intramolecular charge transfer (ICT) process from the formed 4-oxo anions to the emissive state of lanthanide ions. The fluorescence of the nanosensor decreases linearly with the increase of H_2O_2 concentration from 6 μM to 1 mM and can be used in urine samples. In another example, Wu and coworkers reported the implementation of NCPs of Tb(III) as a selective fluorescent method for the sensing of Cu(II) in rat brain. The NCPs is composed of terbium ion, adenosine monophosphate (AMP) as main constitutive ligand and 5-sulfosalicylic acid (SSA) as an auxiliary ligand sensitizer of the fluorescence of Tb(III).[73] The addition of Cu(II) into a solution of SSA/AMP-Tb nanoparticles strongly quenches the fluorescence because the specific coordination interaction between SSA and Cu(II) makes the energy transfer from SSA to Tb(III) inefficient. The decrease in ratio of the fluorescence intensity of SSA/AMP-Tb shows a linear relationship for Cu(II) within a concentration range between 1.5 and 24 μM. Eventually, by combining with micro-dialysis techniques, the method resulted successfully in the detection of cerebral Cu(II) in rat brain. Similarly, Chen and coworkers described the quenching of fluorescence of NCPs composed of Tb(III) ions for the selective sensing of nitrite ion (NO_2^-).[74] In this case, the NCP network is formed with Tb(III) 5-fluorouracil as structural ligand and

4,4-oxybis(benzoic acid) (OBBA) as guest ligand and sensitizer of the Tb(III) fluorescence. In the presence of NO_2^- the florescence of the NPs is quenched as a consequence of an energy transfer from Tb(III) to NO_2^-. The response of the nanoprobe decreases linearly with the increase of NO_2^- concentration from 0.3 to 470 μM. In a study described by Qiu and coworkers, bimetal NCPs of Tb(III) and Ce(III) acted as a selective fluorescent probe for sensing of H_2O_2.[75] The NCP network is formed using Tb(III) and Ce(III) and adenosine triphosphate (ATP) as the bridging ligand. The suitable emission energy of Ce(III) matching to the adsorption energy of Tb(III) allows an efficient energy transfer from Ce(III) to Tb(III), resulting in the characteristic fluorescent emission of Tb(III). This fluorescence can be switched off by oxidation of Ce(III) to Ce(IV) in the presence of H_2O_2, as a consequence of interrupting the energy transfer from Ce(III) to Tb(III). On the basis of this quenching mechanism, these nanoparticles are used to detect H_2O_2 in a wide range from 5 nM to 50 μM. If glucose oxidase is present in the system, glucose can be determined using this nanosensor. Similarly, Xiao and coworkers reported the use of bimetal NCPs of Tb(III) and Ce(III) as a selective fluorescent probe for ALP activity.[76] The NCP network is generated using Tb(III) and Ce(III) and nucleotide GMP as the bridging ligand. As previously disclosed, an efficient energy transfer from Ce(III) to Tb(III) causes the characteristic fluorescent emission of Tb(III). This luminescence can be quenched by destruction of the Tb-GMP bonds by a dephosphorylation process in the presence of ALP, interrupting the energy transfer from Ce(III) to Tb(III). Based on this quenching of fluorescence, these nanoparticles are used to detect ALP in serum samples in a remarkable range from 0.05 to 20 U/mL.

In a study reported by Ye and coworkers, a combined strategy of sensitizing, quenching and enhancement of the fluorescence of Tb(III) (on-off-on switch) in NCPs is applied for the selective sensing of histidine and cysteine.[77] Thus, the nanoparticles were formed by self-assembly of AMP with Tb(III), and 5-sulfosalicylic acid (SSA) as an auxiliary ligand sensitizer of the fluorescence of Tb(III). The fluorescence of the AMP-Tb-SSA network is quenched by Cu(II), but is significantly enhanced by His and Cys, leading to a specific fluorescence "turn-on" assay for these amino acids by using Cu/SSA/AMP-Tb as a sensing nanoplatform. The enhancement of fluorescence resulted proportional to concentrations of His and Cys in the range from 0.2 to 150 μM and 0.5 to 200 μM, respectively. A similar strategy based on sensitizing, quenching and enhancement of the fluorescence of Eu(III) and Tb(III) in binuclear NCPs nanoparticles was applied

by Wu and coworkers for the selective sensing of the anthrax biomarker dipicolinic acid (DPA).[78] The nanoparticles are made with Tb(III) and Eu(III) and the nucleotide GMP as bridging ligand and sensitizer to promote the Tb(III) luminescence at 549 nm without affecting Eu(III). Interestingly, the fluorescent emission of Eu(III) also appears at 620 nm because an effective energy transfer from Tb(III) to Eu(III) takes place. Upon the addition of DPA, a robust coordination with Tb(III) occurs, blocking this energy transfer between metals, causing the emission intensity of Tb(III) to increase during which a gradual decrease in the corresponding emission of Eu(III) is observed. The relative emission intensity (I549/I620) showed a linear response toward DPA within a concentration range from 2 to 16 μM, thus originating in a dual emission luminescent nanoprobe for DPA. Remarkably, this sensor allowed for the real-time monitoring of DPA release from noninfectious spores of simulant bacteria for *B. anthracis*, *B. subtilis*.

Besides Tb(III), other lanthanide ions such as Eu(III) and Ce(III) have been used to generate nanoprobes based on NCPs. Among the Eu(III)-based examples, Qu and coworkers reported the use of NCPs composed of Eu(III) ions, GMP as constitutive ligand and four different encapsulated fluorescent dyes, for the construction of an artificial tongue (Fig. 5).[79] Different metal ions interact distinctively with GMP, affecting in turn the fluorescence of the dyes, providing a fluorescent probe for the simultaneous sensing of several ions. In particular, Ag(I) and Cu(II) concentrations can be univocally determined in a range from 0.1 to 50 μM.

Shi and coworkers described how NCPs composed of Eu(III) ions and fluorochrome riboflavin-5′-phosphate (RiP) as constitutive bridging ligand can act as a nanosensor for anthrax biomarker DPA.[80] RiP in solution has a strong fluorescence at 536 nm, but in the NCPs network, this fluorescent emission decreases. Upon addition of DPA, the NCPs are broken, as a consequence of the strong interaction Eu(III) and DPA, resulting in the release of RiP and a concomitant enhancement of fluorescence, thus generating a nanosensor of DPA with a range of application between 0.04 and 1 μM.

Following another strategy, Chen and coworkers described how NCPs composed of Eu(III), and isophthalic acid (IPA) as main constitutive ligand and sensitizer of the fluorescence of Eu(III), constitute a switch-on fluorescence nanosensor for Hg(II).[81] The fluorescence of the NCP network is quenched in the presence of imidazole-4,5-dicarboxylic acid (Im) due to an inner filter effect (iFE) of this compound that absorbs part of the emission luminescence of Eu(III). Upon the addition of Hg(II), a significant

Fig. 5 Example of Eu(III)-based NCPs for chemical sensing. NCPs composed of Eu(III) ions, GMP as constitutive ligand and four different encapsulated fluorescent dyes, constitute an artificial tongue. *Reproduced from reference Pu, F.; Ran, X.; Ren, J.; Qu, X. Chem. Commun. 2016, 52, 3410–3413 with permission of the copyright holder.*

enhancement of fluorescence takes place due to the disappearance of the iFE process as a consequence of the coordination of Hg(II) to Im. As nanosensor for Hg(II), it presents a remarkable range of application between 2 nM to 2 μM, including applications in biological fluids. Similarly, Xu and coworkers reported an example of Eu(III)-based NCPs nanoparticles acting as an efficient turn-on fluorescent nanoprobe for the detection of antibiotic ciprofloxacin.[82] In this case, the NCP network is formed with Eu(III) and GMP as bridging ligand. A fluorescent emission of Tb(III) occurs in the presence of ciprofloxacin, due to the formation of a complex between this compound and Eu(III) atoms. The thus obtained nanosensor presents a range of applications with linear enhancement of fluorescence between 1 and 40 μM. As previously referred, the anthrax biomarker DPA,[78] and alkaline phosphatase activity,[76] have also been the target of sensing by NCPs based on Eu(III) along with Tb(III). There are also several reported examples of using Ce(III)-based NCPs for chemical sensing. Thus, Qiu and coworkers described the use of fluorescent NCPs nanoparticles constructed by Ce(III), ATP as bridging ligand and units of tris(hydroxymethyl)aminomethane hydrochloric salt (Tris), for hydrogen peroxide detection.[83] ATP sensitizes

the fluorescence of Ce(III) but upon the addition of H_2O_2, part of Ce(III) atoms in the ATP-Ce-Tris network are oxidized to the Ce(IV) state, by which a quenching of the fluorescence occurs. The decrease of emission intensity showed a linear response toward H_2O_2 within a remarkable concentration range from 0.6 nM to 80 μM, thus originating a switch-off luminescent nanoprobe for H_2O_2. If coupled with the GOx enzyme, the sensor probed to be also effective for glucose sensing in a range between 0.1 and 100 μM.

Similarly, Lu and coworkers reported another switch-off fluorescent nanoprobe based on NCPs made of Ce(III), ATP as bridging ligand and Tris, for alkaline phosphatase activity sensing.[84] In this case, in the presence of the ALP enzyme, the ATP phosphate bonds are hydrolyzed, leading to the dissociation of the NCPs network and eventually to a decrease of the fluorescence. The fluorescence quenching efficiency shows a linear relationship for ALP in a range from 0.1 to 10 mU mL^{-1} and can be used in human serum samples. Other nanoprobes made of NCPs based on Ce(III) have previously been reported in this section for the sensing of DNA,[71] H_2O_2,[75] and Hg(II),[69] in relation with Tb(III)-based nanosensors.

NCPs based on other ions different from lanthanide metals have also been described as sensors. Thus, NCPs with useful sensing properties based on Fe(III) originated in situ from the decomposition of Fe(II) present in the compound ferrocenedicarboxylic acid (FcDA) has been reported by Mao and coworkers. These authors described that the photodecomposition of FcDC in methanol produces electroactive NCPs particles.[85] Under exposition to natural light, partial decomposition of ferrocene dicarboxylate takes place, generating Fe(II) which is oxidized to give Fe(III) that in turn, coordinates with carboxylic acids present in the FcDA units, thus generating the NCPs network. The resulting nanoparticles showed interesting properties in the presence of O_2, as redox mediator in the reduction of O_2 to H_2O by the enzyme laccase. Tang and coworkers reported the use of bimetal Pt-Fe(III) NCPs for the sensing of the prostate-specific antigen (PSA) used for prostate cancer prognosis.[86] In this case, previously formed Pt NPs are encapsulated in the process of formation of the NCPs network between molecules of ferrocene dicarboxylate and Fe(III) generated by partial photodecomposition of the FcDA. Next, these nanoparticles are conjugated to anti-PSAantibody (Ab2) and deposited on an electrode surface functionalized with anti-PSAantibody (Ab1), generating a sandwich-type electrochemical immune sensor based on the capacity of the platinum particles for catalytic H_2O_2 reduction. Upon addition of H_2O_2 to the solution, a current resulted

proportional to the logarithm of PSA concentration in a remarkable range from 0.001 to 60 ng/mL. Cu(II) has also been used as constitutive metal in several NCPs applied for sensing purposes. Thus, Zhou and coworkers described the use of NCPs nanorods made of Cu(II) and tyrosine or aspartic acid as bridging ligands as enzyme-free electrochemical biosensor for H_2O_2.[87] The material deposited on an electrode surface showed fast amperometric response in the presence of H_2O_2 in the range between 0.04 and 6.3 mM. Gai and coworkers reported NCPs, constructed by Cu(II) and GMP as bridging ligand, for H_2O_2 detection.[88] In solution, the particles were able to oxidize 3,3′,5,5′-tetramethylbenzidine (TMB) to a blue colored product in the presence of H_2O_2, generating a colorimetric H_2O_2 assay based on the absorbance at 652 nm, in the range between 20 and 160 μM. If coupled with the GOx enzyme, the sensor probed to be also effective for glucose sensing ranging from 25 to 100 μM. In the case of Zn(II), Mao and coworkers described the use of NCPs made of Zn(II), 1,4-bis (imidazole-1-ylmethyl)benzene (bix) as bridging ligand, and the encapsulated dye Rhodamine B (RhB), as a colorimetric and fluorescent dual-mode sensor to measure the alcohol content in spirit samples.[21] In this case, the RhB-Zn(bix) nanoparticles are stable in pure alcohol, but upon the progressive addition of water the Zn(bix) network is destroyed, resulting in the release of RhB which confers color and fluorescent properties to the solution, constituting a colorimetric and fluorescent dual-mode sensing of the alcohol strength, in a range between 20 and 100% where the values of real samples fall. Following a similar strategy, Cao and coworkers demonstrated the utility of NCPs composed of Zn(II), biphenyl-4,4′-dicarboxylic acid (BDA) as main constitutive ligand, and encapsulated fluorophore rhodamine B and quencher methylene blue, as a turn-on fluorescent nanosensor for phosphate in human serum.[89] The nanoparticles are disassembled in the presence of phosphate owing to the strong coordination between zinc and phosphate, liberating RhB into solution and triggering the corresponding fluorescence response, thus generating a switch-on fluorescent probe for PO_4^{3-} in a range between 0.5 and 50 μM in human serum samples.

Other metals have been used as constitutive part of NCPs, but only in single examples. Co(II) in combination with 3,5-diterbutylcatechol and bix as constitutive ligands, was reported by Zhou and coworkers to form NCPs used as a colorimetric and fluorescence dual sensor for hypochlorite ions.[90] Similarly to other studies using different metals, the liberation of encapsulated RhB upon the degradation of the nanoparticles by the

influence of an analyte, generates a switch-on probe of it. In this case, ClO^- destroys the NCPs network, liberating RhB and enhancing both color and fluorescence of the solution in a linear range from 1 to 400 μM of ClO^-. Ye and coworkers described the use of nickel-based NCPs as sacrificial template for the synthesis of nickel oxide nanostructures used as part of an urease-based bio-electrode for urea sensing.[91] The NCPs are made with Ni(II) and benzene-1,4-dicarboxylic acid as constitutive bridging ligand. The prepared bio-electrode showed a linear response over the physiological range of urea concentration from 1.33 to 3.33 mM. Shen and coworkers reported the construction of a biosensor for glucose, using a modified electrode with glucose oxidase immobilized in a layer of Au-Ag-Pt core-shell nanoparticles, previously coated with a NCPs network formed between the Ag of the nanoparticles, H_2PtCl_6 and the ligand 2,5-dimercapto-1,3,4-thiadiazole.[92] The obtained biosensor showed a remarkable range for glucose sensing from 0.5 μM to 3.33 mM.

4. Perspectives

In spite of being at relative early stages of development (this novel family of nanoparticles was described for the first time 15 years ago), the results so far obtained in areas such as nanomedicine and sensors are really exciting. These nanoparticles do not exhibit an open-framework structure, but they can encapsulate different drugs with very high yields through both chemical and physical entrapment. Accordingly, different release routes have been explored such that the drugs have IC_{50} values similar to those of the free drug, even higher, while minimizing side effects. Moreover, it has already been shown that the coordination framework does not exhibit any toxicity (whenever the proper choice of metal ions and ligands are made). The chemical flexibility of these nanoparticles also allows for the fabrication of smart nanoparticles that respond to different external stimuli. Upon exposure to a given physiological media, the active units are released to the media showing suitable efficiencies. This is one of the challenges followed nowadays in the field of drug release as ON/OFF systems are expected to significantly decrease undesired toxicities. The use of NCPs as platforms for chemical sensing has also grown exponentially over the last years. Lanthanide-based NCPs nanoparticles constitute without any doubt the main family of NCPs used as sensors for different chemical species; mainly, the fluorescence of a sample is enhanced or quenched in the absence/presence of a certain analyte. Therefore, NCPs offer a significant versatility

and variety to develop new materials with ever-improved properties thanks to the countless combinations provided by coordination chemistry.

Even though successful, there are still a lot of issues to be addressed, among them:

- To understand the mechanisms that control the release of the drugs. For this, it is required to gain more control over the kinetics of: (i) diffusion, (ii) degradation of the nanostructure (which does not necessarily involve chemical degradation) or (iii) a combination of both. Diffusion-induced delivery is modulated mainly by host-guest interactions, whereas degradation-induced diffusion through nanoparticle-body fluid interactions.
- Another challenge to be faced in the near future is the fabrication of stable and monodisperse colloidal solutions by controlling the nature of the metal ions and ligands (though this approach could be limited by the need to incorporate active drugs) or surface modification. This last approach is expected to be more successful thanks to its inherent chemical flexibility and the surface modification of the nanoparticles with other active units such as fluorophores, PEG or even antibodies.
- Finally, further studies yielding insight into their bio-distribution and bio-degradation mechanisms are required. Development of proper pharmacokinetic profiles will be another major step. If successful, NCPs perform both detection and efficacy of a given therapy, foundational perspectives for "theranostics" or personalized therapy.

Acknowledgments

This work was supported by grants RTI2018-098027-B-C21 and CTQ2016-75363-R from the Spanish Government funds and by the European Regional Development Fund (ERDF). The ICN2 is funded by the CERCA programme/Generalitat de Catalunya. The ICN2 is supported by the Severo Ochoa Centres of Excellence programme, funded by the Spanish Research Agency (AEI, grant no. SEV-2017-0706). R.S. thanks the Ministerio de Educación, Cultura y Deporte for the predoctoral grant FPU14/ 03170. S.S.-G. acknowledges the support from MINECO BES-2015-071492 grant. The authors acknowledge the support from the Cost ENBA CA15216.

References

1. Chen, L. J.; Yang, H. B. *Acc. Chem. Res.* **2018**, *51*, 2699–2710.
2. Lin, W.; Rieter, W. J.; Taylor, K. M. L. *Angew. Chem. Int. Ed.* **2009**, *48*, 650–658.
3. Spokoyny, A. M.; Kim, D.; Sumrein, A.; Mirkin, C. A. *Chem. Soc. Rev.* **2009**, *38*, 1218–1227.
4. Lee, H. J.; Cho, Y. J.; Cho, W.; Oh, M. *ACS Nano* **2013**, 7, 491–499.
5. Dang, S.; Zhu, Q. L.; Xu, Q. *Nat. Rev. Mater.* **2017**, *3*, 17075.

6. (a) Lan, G.; Ni, K.; Lin, W. *Coord. Chem. Rev.* **2019**, *379*, 65–81; (b) Lu, K.; Aung, T.; Guo, N.; Weichselbaum, R.; Lin, W. *Adv. Mater.* **2018**, *30*, 1–20.
7. Adarsh, N. N.; Novio, F.; Ruiz-Molina, D. *Dalton Trans.* **2016**, *45*, 11233–11255.
8. Guardingo, M.; Busqué, F.; Ruiz-Molina, D. *Chem. Commun.* **2016**, *52*, 11617–11626.
9. Bousseksou, A.; Molnár, G.; Salmon, L.; Nicolazzi, W. *Chem. Soc. Rev.* **2011**, *40*, 3313–3335.
10. Puigmartí-Luis, J. *Chem. Soc. Rev.* **2014**, *43*, 2253–2271.
11. (a) Guardingo, M.; González-Monje, P.; Novio, F.; Bellido, E.; Busqué, F.; Molnár, G.; Bousseksou, A.; Ruiz-Molina, D. *ACS Nano* **2016**, *10*, 3206–3213; (b) Bellido, E.; González-Monje, P.; Guardingo, M.; Novio, F.; Sánchez, A.; Montero, M.; Molnar, G.; Bousseksou, A.; Ruiz-Molina, D. *RSC Adv.* **2016**, *6*, 76666–76672.
12. Oh, M.; Mirkin, C. A. *Nature* **2005**, *438*, 651–654.
13. Sun, X.; Dong, S.; Wang, E. *J. Am. Chem. Soc.* **2005**, *127*, 13102–13103.
14. Park, K. H.; Jang, K.; Son, S. U.; Sweigart, D. A. *J. Am. Chem. Soc.* **2006**, *128*, 8740–8741.
15. (a) Forestier, T.; Mornet, S.; Daro, N.; Nishihara, T.; Mouri, S.; Tanaka, K.; Fouché, O.; Freysz, E.; Létard, J.-F. *Chem. Commun.* **2008**, *36*, 4327–4329; (b) Volatron, F.; Catala, L.; Rivière, E.; Gloter, A.; Stéphan, O.; Mallah, T. *Inorg. Chem.* **2008**, *47*, 6584–6586; (c) Boldog, I.; Gaspar, A. B.; Martínez, V.; Pardo-Ibañez, P.; Ksenofontov, V.; Bhattacharjee, A.; Gütlich, P.; Real, J. A. *Angew. Chem. Int. Ed.* **2008**, *47*, 6433–6437; (d) Coronado, E.; Galán-Mascarós, J. R.; Monrabal-Capilla, M.; García-Martínez, J.; Pardo-Ibáñez, P. *Adv. Mater.* **2007**, *19*, 1359–1361; (e) Galán-Mascarós, J. R.; Coronado, E.; Forment-Aliaga, A.; Monrabal-Capilla, M.; Pinilla-Cienfuegos, E.; Ceolin, M. *Inorg. Chem.* **2010**, *49*, 5706–5714.
16. Novio, F.; Ruiz-Molina, D. *RSC Adv.* **2014**, *4*, 15293–15296.
17. (a) Rieter, W. J.; Taylor, K. M. L.; An, H.; Lin, W.; Lin, W. *J. Am. Chem. Soc.* **2006**, *128*, 9024–9025; (b) Taylor, K. M. L.; Rieter, W. J.; Lin, W. *J. Am. Chem. Soc.* **2008**, *130*, 14358–14359.
18. Nador, F.; Novio, F.; Ruiz-Molina, D. *Chem. Commun.* **2014**, *50*, 14570–14572.
19. Jeon, Y. M.; Armatas, G. S.; Heo, J.; Kanatzidis, M. G.; Mirkin, C. A. *Adv. Mater.* **2008**, *20*, 2105–2110.
20. González-Monje, P.; Novio, F.; Ruiz-Molina, D. *Chem. A Eur. J.* **2015**, *21*, 10094–10099.
21. Deng, J.; Ma, W.; Yu, P.; Mao, L. *Anal. Chem.* **2015**, *87*, 6958–6965.
22. (a) Hu, M.; Belik, A. A.; Imura, M.; Mibu, K.; Tsujimoto, Y.; Yamauchi, Y. *Chem. Mater.* **2012**, *24*, 2698–2707; (b) Wang, K.; Geng, Z.; Zheng, M.; Ma, L.; Ma, X.; Wang, Z. *Cryst. Growth Des.* **2012**, *12*, 5606–5614; (c) Shahverdizadeh, G. H.; Masoudian, S.; Soudi, A. A.; Bigdeli, F.; Monfared, H. H.; Morsali, A.; Khavasi, H. R. *J. Inorg. Organomet. Polym.* **2011**, *21*, 171–174.
23. (a) Guardingo, M.; Busqué, F.; Novio, F.; Ruiz-Molina, D. *Inorg. Chem.* **2015**, *54*, 6776–6781; (b) Imaz, I.; Maspoch, D.; Rodríguez-Blanco, C.; Pérez-Falcón, J. M.; Campo, J.; Ruiz-Molina, D. *Angew. Chem. Int. Ed.* **2008**, *47*, 1857–1860.
24. Amorín-Ferré, L.; Busqué, F.; Bourdelande, J. L.; Ruiz-Molina, D.; Hernando, J.; Novio, F. *Chem. A Eur. J.* **2013**, *19*, 17508–17516.
25. (a) Imaz, I.; Hernando, J.; Ruiz-Molina, D.; Maspoch, D. *Angew. Chem. Int. Ed.* **2009**, *48*, 2325–2329; (b) Imaz, I.; Rubio-Martínez, M.; García-Fernández, L.; García, F.; Ruiz-Molina, D.; Hernando, J.; Puntes, V.; Maspoch, D. *Chem. Commun.* **2010**, *46*, 4737–4739.
26. Rieter, W. J.; Pott, K. M.; Taylor, K. M. L.; Lin, W. *J. Am. Chem. Soc.* **2008**, *130*, 11584–11585.
27. Solórzano, R.; Tort, O.; García-Pardo, J.; Escribà, T.; Lorenzo, J.; Arnedo, M.; Ruiz-Molina, D.; Alibés, R.; Busqué, F.; Novio, F. *Biomater. Sci.* **2019**, *7*, 178–186.

28. Novio, F.; Simmchen, J.; Vázquez-Mera, N.; Amorín-Ferré, L.; Ruiz-Molina, D. *Coord. Chem. Rev.* **2013**, *257*, 2839–2847.
29. Novio, F.; Lorenzo, J.; Nador, F.; Wnuk, K.; Ruiz-Molina, D. *Chem. A Eur. J.* **2014**, *20*, 15443–15450.
30. Liang, G.; Ni, H.; Bao, S.; Zhu, F.; Gao, H.; Wu, Q. *J. Phys. Chem. B* **2014**, *118*, 6339–6345.
31. Yan, X.; Li, Y.; Zou, Q.; Yuan, C.; Li, S.; Xing, R. *Angew. Chem. Int. Ed.* **2018**, *57*, 17084–17088.
32. Li, M.; Wang, C.; Di, Z.; Li, H.; Zhang, J.; Xue, W.; Zhao, M.; Zhang, K.; Zhao, Y.; Li, L. *Angew. Chem. Int. Ed.* **2019**, *58*, 1350–1354.
33. Fan, Z.; Sun, L.; Huang, Y.; Wang, Y.; Zhang, M. *Nat. Nanotechnol.* **2016**, *11*, 388–394.
34. Bertleff-Zieschang, N.; Rahim, M. A.; Ju, Y.; Braunger, J. A.; Suma, T.; Dai, Y.; Pan, S.; Cavalieri, F.; Caruso, F. *Chem. Commun.* **2017**, *53*, 1068–1071.
35. Gao, P. F.; Zheng, L. L.; Liang, L. J.; Yang, X. X.; Li, Y. F.; Huang, C. Z. *J. Mater. Chem. B* **2013**, *1*, 3202–3208.
36. Bai, L.; Song, F.; Wang, X. H.; Cao, J. Y. Q.; Han, X.; Wang, X. L.; Wang, Y. Z. *RSC Adv.* **2015**, *5*, 47629–47639.
37. Han, K.; Zhang, W. Y.; Zhang, J.; Ma, Z. Y.; Han, H. Y. *Adv. Healthc. Mater.* **2017**, *6*, 1–9.
38. Xu, S.; Liu, J.; Li, D.; Wang, L.; Guo, J.; Wang, C.; Chen, C. *Biomaterials* **2014**, *35*, 1676–1685.
39. Wang, T.; Liu, X.; Zhu, Y.; Cui, Z. D.; Yang, X. J.; Pan, H.; Yeung, K. W. K.; Wu, S. *ACS Biomater Sci. Eng.* **2017**, *3*, 816–825.
40. Ejima, H.; Richardson, J. J.; Liang, K.; Best, J. P.; Van Koeverden, M. P.; Such, G. K.; Cui, J.; Caruso, F. *Science* **2013**, *341*(6142), 154–157.
41. Rahim, M. A.; Ejima, H.; Cho, K. L.; Kempe, K.; Müllner, M.; Best, J. P.; Caruso, F. *Chem. Mater.* **2014**, *26*, 1645–1653.
42. Ping, Y.; Guo, J.; Ejima, H.; Chen, X.; Richardson, J. J.; Sun, H.; Caruso, F. *Small* **2015**, *11*, 2032–2036.
43. Ju, Y.; Cui, J.; Sun, H.; Müllner, M.; Dai, Y.; Guo, J.; Bertleff-Zieschang, N.; Suma, T.; Richardson, J. J.; Caruso, F. *Biomacromolecules* **2016**, *17*, 2268–2276.
44. Ju, Y.; Dai, Q.; Cui, J.; Dai, Y.; Suma, T.; Richardson, J. J.; Caruso, F. *ACS Appl. Mater. Interfaces* **2016**, *8*, 22914–22922.
45. Park, J. H.; Kim, K.; Lee, J.; Choi, J. Y.; Hong, D.; Yang, S. H.; Caruso, F.; Lee, Y.; Choi, I. S. *Angew. Chem. Int. Ed.* **2014**, *53*, 12420–12425.
46. Besford, Q. A.; Ju, Y.; Wang, T. Y.; Yun, G.; Cherepanov, P. V.; Hagemeyer, C. E.; Cavalieri, F.; Caruso, F. *Small* **2018**, *14*, 1–9.
47. Huang, W.; Hao, P.; Qin, J.; Luo, S.; Zhang, T.; Peng, B.; Chen, H.; Zan, X. *Acta Biomater.* **2019**, *90*, 441–452.
48. Liu, J.; Wang, H.; Yi, X.; Chao, Y.; Geng, Y.; Xu, L.; Yang, K.; Liu, Z. *Adv. Funct. Mater.* **2017**, *27*, 1–10.
49. Liu, J.; Tian, L.; Zhang, R.; Dong, Z.; Wang, H.; Liu, Z. *ACS Appl. Mater. Interfaces* **2018**, *10*, 43493–43502.
50. Yang, Y.; Xu, L.; Zhu, W.; Feng, L.; Liu, J.; Chen, Q.; Dong, Z.; Zhao, J.; Liu, Z.; Chen, M. *Biomaterials* **2018**, *156*, 121–133.
51. Wang, B.; Jacquet, M.; Wang, K.; Xiong, K.; Yan, M.; Courtois, J.; Royal, G. *New J. Chem.* **2018**, *42*, 7823–7829.
52. Zhang, Y.; Guo, Y.; Wu, S.; Liang, H.; Xu, H. *ACS Omega* **2017**, *2*, 2536–2543.
53. Liu, J.; Yang, G.; Zhu, W.; Dong, Z.; Yang, Y.; Chao, Y.; Liu, Z. *Biomaterials* **2017**, *146*, 40–48.
54. Hu, X. G.; Li, X.; Yang, S. I. *Chem. Commun.* **2015**, *51*, 10636–10639.

55. Cherepanov, P. V.; Rahim, M. A.; Bertleff-Zieschang, N.; Sayeed, M. A.; O'Mullane, A. P.; Moulton, S. E.; Caruso, F. *ACS Appl. Mater. Interfaces* **2018**, *10*, 5828–5834.
56. Buwalda, S.; Nottelet, B.; Bethry, A.; Kok, R. J.; Sijbrandi, N.; Coudane, J. *J. Colloid Interface Sci.* **2019**, *535*, 505–515.
57. Li, S.; Zou, Q.; Li, Y.; Yuan, C.; Xing, R.; Yan, X. *J. Am. Chem. Soc.* **2018**, *140*, 10794–10802.
58. Liu, J.; Chen, Q.; Zhu, W.; Yi, X.; Yang, Y.; Dong, Z.; Liu, Z. *Adv. Funct. Mater.* **2017**, *27*, 10.
59. Wang, Y.; Wu, Y.; Li, F.; Chen, D. *Inorg. Chem. Commun.* **2014**, *40*, 143–147.
60. Pu, F.; Ju, E.; Ren, J.; Qu, X. *Adv. Mater.* **2014**, *26*, 1111–1117.
61. Pu, F.; Ren, J.; Qu, X. *ACS Appl. Mater. Interfaces* **2014**, *6*, 9557–9562.
62. Gao, R.-R.; Shi, S.; Li, Y.-J.; Wumaier, M.; Hu, X.-C.; Yao, T.-M. *Nanoscale* **2017**, *9*, 9589–9597.
63. Bai, L.; Wang, X. H.; Song, F.; Wang, X. L.; Wang, Y. Z. *Chem. Commun.* **2015**, *51*, 93–96.
64. Tan, H.; Liu, B.; Chen, Y. *ACS Nano* **2012**, *6*, 10505–10511.
65. Zhang, M.; Qu, Z.-B.; Han, C.-M.; Lu, L.-F.; Li, Y.-Y.; Zhou, T.; Shi, G. *Chem. Commun.* **2014**, *50*, 12855–12858.
66. Tan, H.; Zhang, L.; Ma, C.; Song, Y.; Xu, F.; Chen, S.; Wang, L. *ACS Appl. Mater. Interfaces* **2013**, *5*, 11791–11796.
67. Lin, N.; Zhang, Q.; Xia, X.; Liang, M.; Zhang, S.; Cao, Q.; Ding, Z. *RSC Adv.* **2017**, *7*, 21446–21451.
68. Deng, J.; Yu, P.; Wang, Y.; Mao, L. *Anal. Chem.* **2015**, *87*, 3080–3086.
69. Zhang, Z.; Wu, Y.; He, S.; Mao, L.; Xu, Y.; Li, G.; Ye, B. *Anal. Chim. Acta* **2018**, *1014*, 85–90.
70. Ou-Yang, J.; Li, C.-Y.; Li, Y.-F.; Yang, B.; Li, S.-J. *Sens. Actuators B* **2018**, *255*, 3355–3363.
71. Wang, F.; Liu, B.; Huang, P. J.; Liu, J. *Anal. Chem.* **2013**, *85*, 12144–12155.
72. Tan, H.; Ma, C.; Li, Q.; Wang, L.; Xu, F.; Chen, S.; Song, Y. *Analyst* **2014**, *139*, 5516–5522.
73. Huang, P.; Wu, F.; Mao, L. *Anal. Chem.* **2015**, *87*, 6834–6841.
74. Qi, Z.; You, Q.; Chen, Y. *Anal. Chim. Acta* **2016**, *902*, 168–173.
75. Zeng, H.-H.; Zhang, L.; Rong, L.-Q.; Liang, R.-P.; Qiu, J.-D. *Biosens. Bioelectron.* **2017**, *89*, 721–727.
76. Wang, F.; Hu, X.; Hu, J.; Peng, Q.; Zheng, B.; Du, J.; Xiao, D. *J. Mater. Chem. B* **2018**, *6*, 6008–6015.
77. Zhang, Z.; Wang, L.; Li, G.; Ye, B. *Analyst* **2017**, *142*, 1821–1826.
78. Gao, N.; Zhang, Y.; Huang, P.; Xiang, Z.; Wu, F.-Y.; Mao, L. *Anal. Chem.* **2018**, *90*, 7004–7011.
79. Pu, F.; Ran, X.; Ren, J.; Qu, X. *Chem. Commun.* **2016**, *52*, 3410–3413.
80. Xue, S.-F.; Zhang, J.-F.; Chen, Z.-H.; Han, X.-Y.; Zhang, M.; Shi, G. *Anal. Chim. Acta* **2018**, *1012*, 74–81.
81. Li, Q.; Wang, C.; Tan, H.; Tang, G.; Gao, J.; Chen, C.-H. *RSC Adv.* **2016**, *6*, 17811–17817.
82. Liu, B.; Huang, Y.; Shen, Q.; Zhu, X.; Hao, Y.; Qu, P.; Xu, M. *RSC Adv.* **2016**, *6*, 100743–100747.
83. Zeng, H.-H.; Qiu, W.-B.; Zhang, L.; Liang, R.-P.; Qiu, J.-D. *Anal. Chem.* **2016**, *88*, 6342–6348.
84. Chen, C.; Yuan, Q.; Ni, P.; Jiang, Y.; Zhao, Z.; Lu, Y. *Analyst* **2018**, *143*, 3821–3828.
85. Zhang, L.; Gao, X.; Yang, L.; Yu, P.; Mao, L. *ACS Appl. Mater. Interfaces* **2013**, *5*, 8120–8124.

86. Zhang, B.; Liu, B.; Chen, G.; Tang, D. *Biosens. Bioelectron.* **2015**, *64*, 6–12.
87. Zhou, B.; Xu, F.-C.; Yang, J.; Yao, J.; Xiao, Y.-H. *Mater. Lett.* **2013**, *107*, 206–209.
88. Hou, T.; Zhao, T.; Li, W.; Li, F.; Gai, P. *J. Mater. Chem. B* **2017**, *5*, 4607–4613.
89. Lin, N.; Li, J.; Lu, Z.; Bian, L.; Zheng, L.; Cao, Q.; Ding, Z. *Nanoscale* **2015**, *7*, 4971–4977.
90. Zhang, X.; Deng, J.; Shi, G.; Zhou, T. *RSC Adv.* **2015**, *5*, 107964–107969.
91. Mai, H. D.; Sung, G. Y.; Yoo, H. *RSC Adv.* **2015**, *5*, 78807–78814.
92. Wang, L.; Zeng, Y.; Shen, A.; Fu, Y.; Zeng, L.; Hu, J. *RSC Adv.* **2016**, *6*, 86025–86033.

CHAPTER TWO

Nanoscale coordination polymers: Preparation, function and application

Ali Morsali*, Lida Hashemi
Department of Chemistry, Tarbiat Modares University, Tehran, Islamic Republic of Iran
*Corresponding author: e-mail address: morsali_a@modares.ac.ir

Contents

Abstract

The synthesis of nanostructured material is importance for the step from fundamental science to potential applications. This is true for coordination polymers and (porous) coordination networks particular. They are discussed for their high potential in drug

Advances in Inorganic Chemistry, Volume 76
ISSN 0898-8838
https://doi.org/10.1016/bs.adioch.2020.03.007

delivery, chemical sensing, catalysis, as well as contrast agents, battery electrodes or solid electrolytes. Such applications are difficult to visualize for bulk materials, but need nano-size and incorporation into composite materials or functional devices. Advantages in processing and device construction are one further motivation for the nanostructures of such materials. In other hand, the nucleation and growth are two important processes for nanocrystal formation in a liquid medium. Synthesis methods are available for the synthesis of nanostructures of coordination polymers such as controlled precipitation (solvent-induced precipitation, ultrasonic, microwave, capping ligands, modulators, etc.) micro-emulsion as micro-reactors for size control and electrostatic stabilization. Among the various synthetic routes, ultrasound-assisted method is applicable for nanoscaled coordination polymer preparation as their reaction conditions can be easily adapted from conventional approaches, and is now positioned as one of the most powerful tools. In this chapter, the focus has been more on this method and various factors have been studied on the size and morphology of the nanostructures. Finally application of nano coordination polymers in field of adsorption removal, photocatalytic degradation, use as templates in order to obtain the desired nanomaterials, anti-cancer drugs, supercapacitors and catalytic activities has been investigated.

1. Introduction to coordination polymers

Coordination polymers are a general term used to indicate an infinite array composed of metal ions bridged by certain ligands. This is a general term that incorporates a wide range of architectures, including one-dimensional chains to large mesoporous frameworks.[1–3] Generally, the formation process proceeds automatically and, therefore, is called a self-assembly process. In general, the type and topology of the product generated from the self-assembly of inorganic metal nodes and organic spacers, depend on the functionality of the ligand and valences, and geometric needs of the metal ions used. Organic ligands are very important in the design and construction of desirable frameworks, since changes in flexibility, length, and symmetry of organic ligands can lead to the formation of a class of materials with diverse architectures and functions.[4]

Depending on the metal element that is used in the polymer, and its valency, different geometries may be created, e.g., linear, trigonal-planar, T-shaped, tetrahedral, square-planar, square-pyramidal, trigonal-bipyramidal, octahedral, trigonal-prismatic, pentagonal-bipyramidal, and their distorted forms.[5] Organization of building blocks can lead to the formation of metal coordination polymers of various dimensions: one-, two- or three-dimensional architectures. Dimension is usually determined through the nodes (metal centers) and the coordination mode of the

ligand.[6] Metal coordination polymers have been studied widely as they represent an important interface between synthetic chemistry and materials science, and they have specific structures, properties, and reactivity's that are not found in mononuclear compounds. In the last two decades, rapid developments in the crystal engineering of metal-organic coordination polymers have produced many novel materials with various structural features and properties.

1.1 Development of coordination polymers

The development of coordination polymer research was reinforced by the growth of two other closely related areas: crystal engineering and supramolecular chemistry. Crystal Engineering seeks to understand why molecules are packaged in the ways they do and use that knowledge to consciously engineer the order of molecules in new materials. This is important because the properties of materials are often controlled by the way in which their constituent molecules are arranged.[7,8] A coordination polymer contains metal ions linked by coordinated ligands into an infinite array. Since coordination polymers constitute one of the most important classes of organic–inorganic hybrid materials,[9–11] the rational design via self-assembly depends on a variety of parameters, basically including the suitable pre-designed organic ligands and metal centers with versatile coordination geometries.[12] Design and synthesis of novel discrete and polymeric metal-organic complexes are attracting more attention, not only for their interesting molecular topologies, but also for their potential applications as functional materials,[13] ion exchange, catalysis, molecular recognition, nonlinear optics,[14,15] molecular magnetic materials, electrical conductivity,[16,17] separation and gas storage.[18,19] The structure and properties of coordination polymers depend on the coordination habits and geometries of both metal ions and connecting ligands, as well as on the influence of secondary interactions such as hydrogen bonding, π–π stacking interactions and so on.[20] Several factors, including coordination bonds and secondary interactions, metal-to-ligand molar ratio, coordinative function of the ligands, type of metal ions, presence of solvent molecules, counter ions and organic guest molecules should be taken into account in the process of the design and synthesis of metal coordination polymers.[21,22]

In molecular crystal engineering, the interactions are weaker than in coordination bonds and can range in strength from very strong hydrogen bonding to weak C—H ··· A hydrogen bonds, halogen bonds, π interactions and, ultimately, van der Waals forces. The crystal engineer seeks to

understand and harness all these interactions. However, despite the differences in the interactions, there is much that is common in these two areas. Indeed, coordination polymers, which essentially exist only in the solid state, should be considered as subtopics of crystal engineering. Furthermore, the *net*-based approach for coordination polymers is equally valid for molecular species connected by well-defined interactions.

Many of the concepts and terminology in molecular crystal engineering also apply to coordination polymers. Interactions between molecules that direct their packing arrangements are known as supramolecular synthons; in coordination polymers, the main synthons are coordination bonds (although weaker synthons can also be important). The building blocks are used to form the structure and in coordination polymers, are included metal ions and ligands. The aim of supramolecular chemistry is similar: to create assemblies of molecules, i.e., not to create structures through an atom at a time, but to design molecules that when combined, they spontaneously self-assemble in a predetermined fashion into larger architectures. Thus crystal engineering can, in fact, be considered to be the supramolecular chemistry of the solid state.

1.2 Design of coordination polymers

One of the most powerful techniques in crystal engineering for both the analysis and design of solids is to reduce their crystal structures to networks (or nets). Networks can aid the description and understanding of complicated structures or provide a blueprint for the targeting of particular packing arrangements and their associated properties. An early leading figure in this approach was A. F. Wells, who, in a series of seminal books,[23] described a number of molecular and polymeric structures in terms of networks and delineated a large number of possible networks, some already seen in real structures and others that, remarkably, were still theoretical at the time. A good understanding of networks is therefore vital to the crystal engineer. But what is a network? For our purposes, a network is a polymeric collection of interlinked nodes; each link connects two nodes and each node is linked to three or more other nodes. A node cannot be connected to only two nodes; in this case it then becomes a link. Similarly, a link can only connect two nodes; if it connects more than two it is a node. And finally, since we are talking about crystal structures here, the network must also have a repeating pattern and thus a finite number of unique nodes and links.

1.3 Synthetic methods of coordination polymers

Several different synthetic approaches have been offered for the preparation of coordination polymers. Some of them are; (1) slow diffusion of the reactants into a polymeric matrix, (2) layering technique, (3) evaporation of the solvent at ambient or reduced temperatures, (4) precipitation or recrystallization from a mixture of solvents, (5) temperature-controlled cooling, (6) hydrothermal synthesis, (7) gel growth crystallization technique (8) sonochemical synthesis and (9) microwave technique.[23,24] We have shown another new and simple method for the construction of multi-dimensional coordination polymers, the branched tube method. The new method is straight forward, cheap and trouble-free and can be used for the preparation of other types of coordination polymers. In this method, as shown in Scheme 1, ligand was placed in one arm of the branched tube and the mixture of salts in the other. Solvent was carefully added to fill the arms. The tube was sealed and the arm containing the ligands was immersed in a bath at 60 °C, while the other was kept at ambient temperature. After some days, crystals have been found in the cooler arm; the crystals were filtered off, washed with acetone and ether, and air dried.

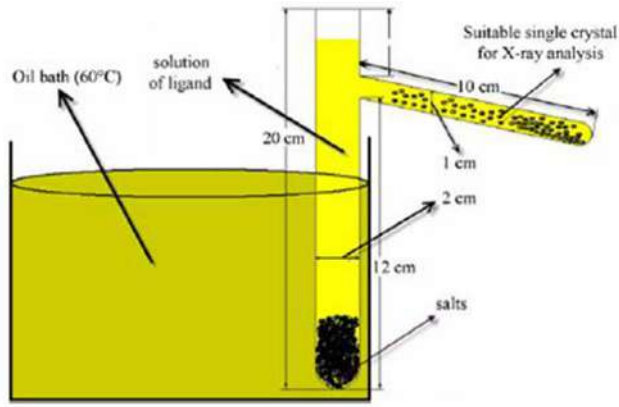

Scheme 1 Depiction of the branched tube for syntheses and isolation of single crystals of multi-dimensional coordination polymers.

2. Introduction to nano coordination polymers (NCPs)

At the end of the last century, chemists focused on supramolecular frameworks composed of molecules, whereas in the 21st century a new area

of nano-sized space chemistry. We have to develop new synthetic routes to form the desired nanosized coordination polymers effectively and on a large scale, and this is a basic methodology required for nanotechnologies. The most practical methods to build nano-sized spaces are chemical self-assembly and self-organization and coordination bonds are the key to the development of the required new synthetic technologies. Coordination bonds are not as strong as covalent bonds and not as weak as hydrogen bonds. Constituent organic molecules and metal ions are assembled into a variety of spatial structures under mild conditions. In this area the molecules were designed to build spaces that gives an opportunity to find new phenomena based on molecular coagulation, molecular stress, and activation of molecules. For this purpose, a new chemistry that allows us to control structures and functionality of spaces was needed. Motifs built by molecular blocks are: (1) reactions of metal ions (connector) with organic ligands (linker) to give coordination crystals with infinite structures. We can build coordination polymers with different sizes composed of several or tens of molecules. (2) Surfaces of bulk material and nanoparticles can be recognized as coordination polymer. Control over nano-sized building blocks is crucial for future success of science and technology in the nanoscale realm. Bearing these facts in mind, several different morphologies offering wide industrial applications could be synthesized by precise control over particle sizes.

2.1 Development of nano coordination polymers (NCPs)

The synthesis of nanostructured materials is importance not only from a fundamental point of view but also because of all potential applications. This is especially true for coordination polymers and (porous) coordination networks. They are discussed in term of their high potential in drug delivery, chemical sensing, catalysis, as well as contrast agents, battery electrodes or solid electrolytes. Such applications are difficult to envision for bulk materials, but require a nano-size and incorporation into composite materials or functional devices. Advantages in processing and device construction are further motivations for the nano-structuring of such materials. For example, colloidal suspensions of MOF nanoparticles (NPs) were already used for self-assembly of the NPs directly on a substrate surface, but until now it has been difficult to achieve order over a large area. In the other hand, nucleation and growth are two important processes for nanocrystal formation in a liquid medium. To describe the changes in particles size, LaMer nucleation followed by Ostwald ripening is often used. In LaMer burst nucleation,

the individual nucleation events happen en masse, quasi-simultaneously, and at nearly identical homogeneous conditions. These properties make LaMer burst nucleation important for applications that require monodispersed particles and also for theoretical analyses. At first chemists predicted that the number of nuclei generated during a LaMer burst depends only on the solute supply rate and the growth rate, independent of the nucleation kinetics. Some experiments confirm that solute supply kinetics control the number of nuclei, but flaws in the original theoretical analysis raise questions about the predicted roles of growth and nucleation kinetics. Next has been provided a rigorous analysis of the coupled equations that govern concentrations of nuclei and solutes. Results confirm that the number of nuclei is largely determined by the solute supply and growth rates. Finally has been found that additional nucleus size dependent corrections should emerge in systems with slow growth kinetics and has been shown that nucleation kinetics determine the particle size distribution. They suggest that measured particle size distributions might therefore provide ways to test theoretical models of homogeneous nucleation kinetics. Nucleation, the formation of seeds or nuclei, is the first stage of crystallization processes. The short nucleation period of the LaMer mechanism is critical for the synthesis of uniform nanoparticles (NPs). It is mandatory to generate a large number of seeds to obtain nano-sized uniform, 10–100 nm, nano coordination polymers. According to the Ostwald ripening mechanism, particle growth is based on the changes of nanocrystal solubility as a function of their size. During particle growth, seeds with high surface energy may re-dissolve and release their ligands into solution. Therefore, it is important to generate a large number of seeds and prevent them from dissolving to synthesize nano-sized uniform metal coordination polymers.

2.2 Synthetic methods for nano coordination polymers (NCPs)

Synthetic methods are available for the synthesis of nanoparticles (NPs) of inorganic solids. Examples are the controlled decomposition of complexes, the reduction of metal salts or the application of the micro-emulsion technique. In contrast to this, the number of methods for the synthesis of nanostructure coordination polymers is restricted and furthermore depends strongly on the used system. Controlled precipitation (solvent-induced precipitation, ultrasonic, microwave, capping ligands, modulators, etc.),[25,26] micro-emulsion as micro-reactors for size control,[25,26] electrostatic stabilization, solvo-thermal synthesis, spray techniques and synthesis on patterned

sacrificial templates, for example, polymer are some of the nano coordination polymer synthetic methods.[24–26]

The first successful approach for the synthesis of NPs of coordination polymers and networks was independently developed by the groups of Mirkin[27] and Wang[28] in 2005. Spherical NPs were obtained through solvent-induced precipitation. For this, the synthesis of the coordination polymer was done in a solvent, in which the starting materials and product are soluble. Addition of an "anti-solvent" induces precipitation, allowing a control over size and morphology through subtle changes in reaction conditions. This approach was successfully used for a variety of different systems. Its major limitation is that little information is available on how and why a particular particle morphology or shape is obtained vs another. There are even examples for reversible morphological changes upon change of solvent, counter ion or ancillary ligand.[29] In addition to the controlled (fast) precipitation, micro-emulsions have been successfully used to synthesize nanostructured coordination polymers.[24–26] However, not in all cases surfactants are necessary to achieve nanostructures. Nano- or mesostructured Prussian blue analogues are highly interesting coordination networks due to the application potential in the field of coatings, photo-magnetic switches, electro catalysts, or as sensors.[30] Nanoparticles of the Prussian blue analogue $Cs_xNi[Cr(CN)_6]_y$ were obtained by Mallah and co-workers through spontaneous electrostatic stabilization as dispersion in water.[31] The 6.5 nm bimetallic NPs can be recovered from solution using different coating agents, whereby the coating agent influences the magnetic properties, showing either a superparamagnetic or a spin-glass-like behavior. The electrostatic stabilization of surfactant-free particles enabled in subsequent study the design of core-multishell nanocrystals. This was done by epitaxial growth of different shells on various charged cores. The shell growth is controlled on the nanometer scale and can be repeated with different metal ions.[32] The (photo-) magnetic properties of such multilayer composites are influenced by interface-induced interactions.[33] In an alternative route, Prussian blue meso-structures were obtained through the use of amphiphilic ligands, applying a similar approach as the aqueous liquid-crystal-templating route used for the synthesis of oxides and chalkogenides.[34] The mesostructure of the material can be modified through variation of the chain length of the amphiphilic ligand. Another family of responsive materials is valence tautomers. Solvent-induced precipitation was used to synthesize spherical nanoparticles of a valence tautomeric coordination polymer built from cobalt (II) acetate, 3,5-di-tert-butyl-1,2-catechol, and 1,4-bis(imidazole-1-ylmethyl)benzene as the bridging ligand.[35] The size of the NPs was controlled

through the rate of addition of anti-solvent. By this method, NPs with sizes ranging between 75 and 200 nm were obtained with a valence tautomeric conversion around room temperature. As previously described, coordination polymers offer a high synthetic flexibility and modulation of the properties due to the wide variety of different ligands and metal centers that can be used. In bulk materials, these properties furthermore depend on chain length, mono-dispersity, the packing (crystallinity vs amorphous materials), and the chain end, allowing a further fine-tuning of the properties. However, there is still a wide range of coordination polymers and networks in which the different approaches mentioned above fail or show limitations in the possibility to control size, shape, and morphology of the nanomaterial. Consequently, there is a high demand for the development of new methods for the nanostructuring of these materials.

2.2.1 Ultrasound (US) assisted synthetic method

Over the past decade, high intensity ultrasound (US)-assisted synthesis of nanomaterials has been widely used as it offers a rapid, mild, cost-effective, reproducible, and environmentally friendly methodology for the preparation of nano/microscale coordination compounds with novel morphologies and unique properties.

Sono-chemical methods via homogeneous and accelerated nucleation can also achieve a reduction in crystallization time and significantly smaller particles size than those produced by the conventional solvo-thermal synthesis. As shown in Scheme 2, a substrate solution mixture for a given MOF structure is introduced to a horn-type Pyrex reactor fitted to a sonicator bar with an adjustable power output without external cooling.

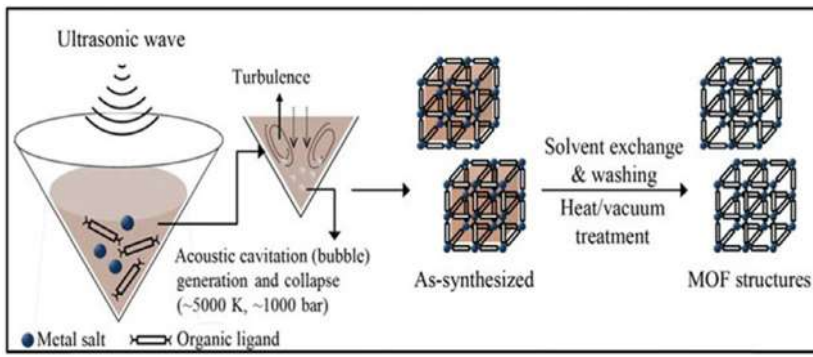

Scheme 2 Sono-chemical synthesis of nano metal coordination polymers.

Formation and collapse of bubbles formed in the solution after sonication, termed acoustic cavitation, produces very high local temperatures (~5000 K) and pressures (~1000 bar), and results in extremely fast heating and cooling rates (>1010 K/s) producing fine crystallites.

High-quality MOF-5 crystals in the 5–25 μm range were obtained within 30 min by sono-chemical synthesis using NMP (1-methyl-2-pyrrolidone) as the solvent.[36] Detailed characterization and comparison with a conventionally synthesized sample showed almost identical physical properties. HKUST-1 (Hong Kong University of Science and Technology) is a metal-organic coordination polymer that made up of copper nodes with 1,3,5-benzenetricarboxylic acid struts between them that also prepared using DMF/EtOH/H_2O mixed-solution in an ultrasonic bath.[37] The product formed after 5 min as a nano-crystalline powder (10–40 nm), on increasing the reaction time led to larger crystals (50–200 nm) and higher yields, but further reaction resulted in their partial decomposition. High-quality Mg-MOF-74 crystals (1640 m^2/g BET surface area) with particle size of ca. 0.6 μm were successfully synthesized in 1 h by a sono-chemical method after addition of triethylamine (TEA) as a deprotonating agent.[37] Recent articles have also focused on the synthesis of metal coordination polymers following this route.[38–41]

2.2.2 Self-assembled block copolymers as template

There are only few examples for the use of block copolymers to obtain coordination polymers or network nanostructures. Tang et al. used amphiphilic block copolymers for a polymer-directed self-assembly to produce uniform NPs of iron(III) with tannic acid through flash nanoprecipitation.[42] Soluble Prussian blue nano-worms were synthesized by the MacLachlan group from the assembly of metal-organic block ionomers.[43] A diblock copolymer (PS-b-PHEMA) was used, in which the hydroxyethylmethylacrylate (HEMA) units were functionalized to obtain monoquaternized 4,4′-biypridine. The corresponding block ionomer forms reverse micelles in less polar solvents through self-assembly with the ionic block in the rigid core. A dynamic equilibrium between micelles and single chains was observed and investigated with ^{1}H NMR spectroscopy. The addition of the iron(II) precursor $Na_3[Fe(CN)_5NH_3]$ lead to a replacement of NH_3 through coordination to the block ionomer, which can be followed by UV/vis spectroscopy. Crosslinking of this metal-organic block ionomer to a Prussian

blue-type network was possible through addition of a second metal salt (e.g., iron(III), zinc(II) or cobalt(II) nitrate). EDX analysis and TEM showed worm-like nanostructures with an inner diameter of approximately 20 nm that are highly reproducible and monodisperse. Variation of block lengths and reaction conditions allowed the synthesis of hollow nanocontainers for encapsulation through emulsion-induced assembly of the metal containing amphiphilic block ionomers.[44] The size of the capsules can be tuned through variation of the reaction conditions and they are selectively permeable toward the encapsulation of methylene blue.

2.2.3 Micro-emulsion technique

Micro-emulsions of the starting materials dissolved in a polar phase (water or ethanol/methanol) are prepared by the use of surfactants (e.g., NaAOT = sodium bis(2-ethylhexyl)sulfosuccinate) and an unpolar phase (e.g., n-octane). In the next step the micro-emulsions are mixed allowing micellar exchange (e.g., initiated through the application of ultrasound) that leads to the formation of the desired coordination polymer or network. The particle size can be controlled through variation of the solvent:surfactant concentration ratio and the concentration of the starting materials.[45] Triazole-based 1D coordination polymers are extremely well suited for NP synthesis using this method.[46–48] The cooperative spin transition with hysteresis observed in the bulk material is maintained down to very small particle sizes. This allows, for example, investigations on the conductivity of NPs as a function of the spin state. Furthermore the spin state of the NPs deposited on graphene influences the graphene conductivity and allows an indirect read out of the spin state.

For Hofmann clathrate based 2D and 3D networks, NPs can also be prepared using the micro-emulsions approach. In some cases the hysteresis disappears upon size reduction.[49] However, as pointed out before it can reappear below a critical size[46] or if a rigid matrix is used to coat the particles.[48] Another approach to achieve nanostructures of Hofmann clathrate based systems is the layer by layer technique.[50] For those examples hysteresis is maintained. The reason for this is still under debate as the SCO properties of nano-sized systems are influenced by many different parameters. Matrix effects, differences in crystalline quality of the differently sized nanoparticles, or even different polymorphs could be responsible for this (Scheme 3).[51]

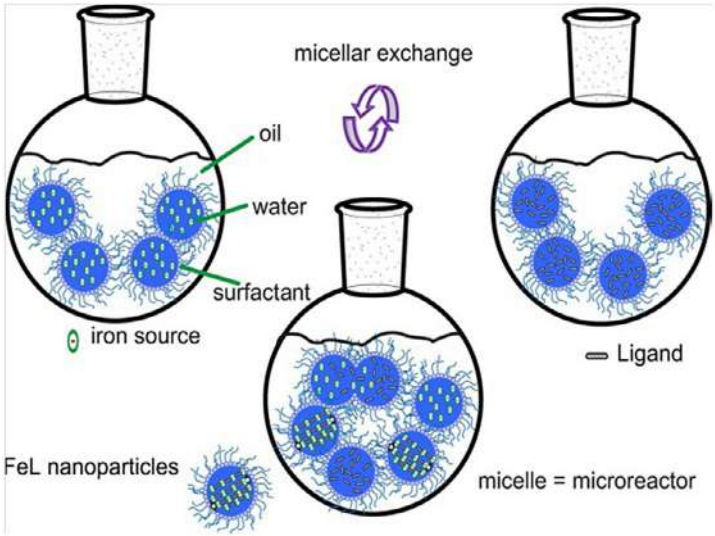

Scheme 3 Principles of the micro-emulsion technique for nano metal coordination polymer synthesis.[51]

2.2.4 Microwave assisted synthesis

Microwave (MW) assisted synthesis is based on the interaction of electromagnetic waves with polar solvent molecules and/or ions in solution. The direct interaction of electromagnetic waves with the solution/reactants results in high heating rates and homogeneous heating with high-energy efficiency and shorter synthesis time.[52a] Smaller crystals can be obtained by MW heating since fast formation of many seeds occurs by local superheating.

Microwave (MW) and ultrasound synthetic routes have drawn attention due to homogeneous heating, fast kinetics, high phase purity, and high yield rate of products in relatively short time.[52b] MW and US techniques have significant advantages such as fast crystallization, uniform nucleation, easy control of morphology, phase selectivity, decrease in particle size and rapid warming.

In addition, controlling the particle size distribution is one advantage of MW since shorter reaction times tend to have a narrower particle size distribution. Previously, MOF-5 was produced in larger amounts by using the microwave irradiation process, and various synthetic parameters such as the effects of the microwave power level, irradiation time, temperature, solvent concentration, and substrate composition on the product crystallinity and morphology were investigated in detail.[53] MW irradiation time and power

level are also important factors in the synthesis of MOFs with smaller sizes. The increase of MW irradiation time and power level results in larger crystals (20–25 μm).[54]

In order to obtain monodisperse NPs of coordination polymers with a high yield and scale-up, a suitable synthetic method must be used. Although many different synthetic routes for MOFs have been reported in the literature, scale-up synthesis of MOFs is rare. Since the starting materials (availability and cost), synthetic conditions (low temperature, ambient pressure), high yields, low impurities, and the amounts of solvents are critical parameters for scale-up, the synthetic procedures for MOFs must be chosen to comply with industrial-scale synthetic requests. Since fast reactions can allow for scale-up of MOFs, MW and US methods are suitable for mass production.[52] For example, by using consecutive combination of US and MW uniform MOF-5 micro crystals (5–15 μm) were synthesized.[52a] In contrast to traditional energy sources, ultrasonic irradiation is regarded as a facile and environmentally friendly energy source, which could provide rather unusual reaction conditions (a short duration of extremely high temperatures and pressures within liquids). These extreme conditions can drive chemical reactions and then promote the formation of nanostructured materials.

2.3 Size and morphology of nano coordination polymers

Nucleation and growth are two important processes for nanocrystal formation in a liquid medium. To describe the changes in particles size, LaMer nucleation followed by the Ostwald ripening is often used. Nucleation and the formation of seeds or nuclei, is the first stage of the crystallization processes. The short nucleation period of the LaMer mechanism is critical for the synthesis of uniform nanoparticles that has been discussed before. It is mandatory to generate large number of seeds to obtain nano-sized uniform, 10–100 nm, nano coordination polymers. According to the Ostwald ripening mechanism, the particle growth is based on the changes of nanocrystal solubility as a function of their size. During particle growth, seeds with high surface energy may re-dissolve and release their ligands into solution. Therefore, it is important to generate large numbers of seeds and prevent them from dissolving to synthesize nano-sized uniform metal coordination polymers. The *presence of TEA* in precursor solutions during the secondary growth step was found to be critical to prevent the seed crystals from dissolving.[55] The concentration of TEA used in the synthesis of metal coordination polymers is also important. For example, as TEA

concentration are increased from 0.75 to 1.3 mM, the average size of MOF-5 decreased from 2534 to 1499 nm, but the particle size distribution became wider.[56] Besides, higher TEA concentrations would also induce the formation of unknown crystals.[57] Mixing speed of TEA into precursor solutions is also important for fast generation of a large number of seeds at the early stage of crystallization.

Coordination modulation is also effective in nano-sized MOF synthesis by employing surfactant, blocking or capping agents. The size and morphology of MOFs can be effectively controlled by addition of surfactants as capping agents. The present strategy (the coordination modulation method) for the fabrication of NMOFs involves the utilization of modulators in modulating the coordination equilibrium by adding capping agents with the same chemical functionality as the linkers to adjust the coordination interactions between metal ions and organic linkers; and thus control the rate of framework extension and crystal growth, and finally allows tailoring over the size and morphology of the resulting crystals.[58] Fig. 1 has been shown the mechanism of coordination modulation method too.

For example, the use of CTAB and C12E4 along with TEA leads to the synthesis of nano-sized MOF-5.[59]

The type of metal salt (nitrate, acetate, etc.) *and its concentration* in a starting solution are two important parameters in obtaining smaller particles. For example, in the synthesis of MOF-5, the dilution of terephthalic acid from 50 to 0.2 mM (the metal/ligand molar ratio remained 4:3) resulted in particles with a size of <1 μm.

The effect of synthetic routes on nano-sized coordination polymers has also been explored.[52] MOFs with different particle sizes and size distributions can be obtained by different synthetic routes.[53] RT (room temperature), ST (solvo-thermal), MW (microwave), EC (electrochemical), US (ultrasound)

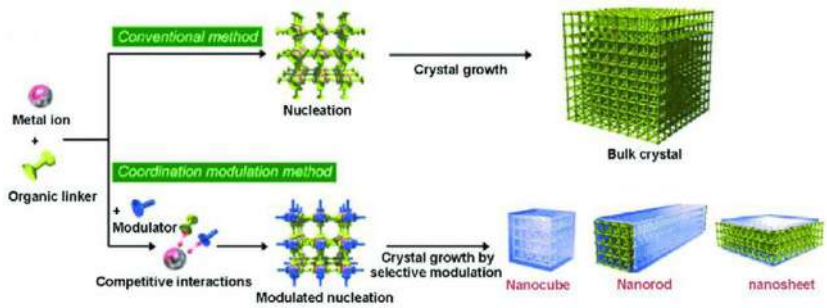

Fig. 1 Mechanism of coordination modulation method.[58]

and MC synthetic routes are being used for nano/micron-sized MOF synthesis.[60] Although nano-sized MOFs can be obtained by room temperature and solvo-thermal synthetic routes with the aid of coordination modulation, they are relatively slow. RT synthetic methods with TEA were used to produce well-known and new MOFs such as MOF-5, MOF-74, MOF-177, MOF-199 and IRMOF-0 having the same cubic topology of MOF-5. These well-known MOFs have high storage capacities for hydrogen and methane due to ultrahigh porosity of MOF-5 and MOF-177, one-dimensional pore structure of MOF-74 and open metal sites of MOF-74 and MOF-199. It was also proposed that these room temperature synthetic methods can be successfully used to prepare Cu(II) and Zn(II) containing MOFs. Huang et al. used the RT direct mixing method with the help of TEA to produce a highly porous nanometer-sized MOF-5, and showed that thermally stable and highly porous MOF-5 nanocrystals (30–150 nm diameter) at RT with high yield (~90%) can be synthesized in short reaction times (~0.5 h).[59] It was possible to synthesize nano-sized, 20–30 nm, MOF-5 with the aid of TEA by the RT route.

The use of the US in the synthesis of nano/microscale MOF particles has become increasingly of interest.[60,61] Since the wavelength of US is much larger than molecular dimensions, US and molecules cannot interact in chemical reactions. However, high-energy US can interact with liquids. The result is that liquids exposed to high-energy US can undergo acoustic cavitation (bubble formation, growth, and collapse). Cavitation causes regional hot points (temperatures of ~5000 K and pressures of ~1000 bar and liquid jets of up to 1000 km/h), and results in physical and chemical changes. High temperature and pressure, micro-flow, micro-turbulence, shock waves and micro-jets can speed up the chemical treatment and improve the composition of nanoscale structures because it increases crystallization.[60,61] Chemical reactions become faster and homogeneous nucleation can be obtained by US.[60–62]

3. Effective factors in synthetic of nano coordination polymers

Chemical and physical properties of solid materials strongly depend on the shape and size of the microscopic particles they are made up from. This is especially valid for materials with morphological features smaller than a micron in at least one dimension, which is generally referred to as nanoscale materials, or simply just nanomaterials. In these materials the ratio of surface area to volume is vastly increased compared to compounds with larger grain

sizes and quantum mechanical effects including "quantum size effect" begin to play a substantial role. These effects only play a minor role when transferring from macro to micro dimensions, yet become of prime importance when reaching the nanometer size range. Controlling the growth of materials in the submicron scale is extremely important. In the emerging field of nanotechnology, nanometer-sized particles of metal coordination polymers are fascinating to explore, since their unique properties are controlled by the large number of surface molecules, which experience a completely different environment than those inside a bulk crystal. Although considerable effort has been dedicated toward the controlled synthesis of nanoscale particles of metals, oxides, sulfides, and ceramic materials, little attention has been focused up to now on nanostructures of coordination polymers.

Over the past decade, the use of ultrasound for the synthesis of nanomaterials has been growing at an enormous rate, and is now positioned as one of the most powerful tools in metal-organic coordination compounds. Ultrasound leads to high-energy chemistry. It does so through the process of acoustic cavitation, which includes formation, growth, and explosive collapse of bubbles in the liquid medium. A bubble can overgrow and subsequently collapse within very short lifetime (>1010 K/s). A large energy release is achieved throughout the collapse, resulting in a local temperature of $\sim$5000 K and a pressure of $\sim$1000 bar. Consequently, various kinds of chemical reactions can proceed using ultrasonic irradiation.

Reaction time, temperature, ultrasound irradiation power, concentration of initial reagent, whether or not to use surfactants and solvents, play an important role in the size and morphology of products (nano coordination polymers), which we will briefly discussed here.

Sono-chemical systems are generally multi-bubble environments where in practically all cases the chemical reactions occur in association with the powerful and rapid compressed and heated interior of collapsing bubbles. Consequently, nanoscale materials with various sizes, shape, structure either as amorphous or crystalline forms, could be perpetually prepared using sonochemical reactions. The main advantages of applying ultrasound radiation are that it does not produce high temperature during the reactions, does not require surfactants, and also yields smaller particles. The consequences of ultrasonic irradiation are acceleration and initiation of new reactions which are difficult to obtain under normal conditions. Control over nano-sized building blocks is crucial for the future success of science and technology in the nanoscale realm. Bearing these facts in mind, several different morphologies offering wide industrial applications could be synthesized by precise control over particle sizes.

3.1 Effects of ultrasound radiation, temperature and time

The effects of ultrasound radiation on chemical reactions were reported in recent studies.[63–65] In one of them, Morsali and co-workers have developed a simple sono-chemical technique to prepare nanostructures of $[K(H_3L)(H_2L)(H_2O)]_n \cdot H_2O$ (**1**) and $[K(H_2L')(HL')(H_2O)_2] \cdot H_2O$ (**2**). The ultrasonic power, sonicating time and temperature of the reaction were the parameters that were varied to reach the optimized condition.

Various conditions for the preparation of compounds **1** and **2** nanostructures are summarized in Tables 1–3. In these tables, sample 1-1 and 2-1 were studied without power ultrasound and the other samples were studied under variable temperature, power ultrasound and time. In order to find out the role of power ultrasound irradiation on the nature of the product, reactions were performed under completely different ultrasound irradiation conditions. Results show a decrease in the particle size on increasing the power of ultrasound irradiation. In sample 1-1, the reactions were

Table 1 Influence of temperature, on the size of compound **1** and **2** particles.

Compound 1 samples	T (°C)[a]	T (min)[b]	Sonication (input power) (W)	SEM[c]
1-2	50	60	60	71
1-5	70	60	60	41
Compound 2 samples	**T (°C)[a]**	**T (min)[b]**	**Sonication (input power) (W)**	**SEM[c]**
2-2	50	60	60	83
2-5	70	60	60	63

[a]Reaction temperature.
[b]Reaction time.
[c]Average diameter (nm).

Table 2 The influence of sonication power, on the size of compound **1** and **2** particles.

Compound 1 samples	T (°C)[a]	T (min)[b]	Sonication (input power) (W)	SEM[c]
1-1	50	60	0	365
1-2	50	60	60	71
Compound 2 samples	**T (°C)[a]**	**T (min)[b]**	**Sonication (input power) (W)**	**SEM[c]**
2-1	50	60	0	230
2-2	50	60	60	83

[a]Reaction temperature.
[b]Reaction time.
[c]Average diameter (nm).

Table 3 The influence of reaction time, on the size of compound **1** and **2** particles.

Compound 1 samples	T (°C)[a]	T (min)[b]	Sonication (input power) (W)	SEM[c]
1-2	50	60	60	71
1-3	50	30	60	48
Compound 2 samples	**T (°C)[a]**	**T (min)[b]**	**Sonication (input power) (W)**	**SEM[c]**
2-2	50	60	60	83
2-3	50	30	60	53

[a]Reaction temperature.
[b]Reaction time.
[c]Average diameter (nm).

studied without power ultrasound. Results show that the particle size of sample 1-1 (Fig. 2A) is larger than of 1-2 (Fig. 2B), similar to that for samples 2-1 and 2-2 (Fig. 3A, B). Tables 1–3 show the average diameter of the prepared samples measured with field emission scanning electron microscope (FE-SEM) and scanning electron micrographs (SEM). Results show that high power ultrasound irradiation decreased agglomeration, and thus led to a decrease in particle size. Comparison between samples 1-2 and 1-3 shows a decrease in nanoparticle size. Thus, the particle size of sample 1-3 is smaller than 1-2 (Fig. 2B, C). These observations are repeated in samples 2-2 and 2-3 (Fig. 3B, C). However, reduction of the reaction time led to a decrease in particle size of sample 1-3. Particle size and morphology of nanoparticles also depend on temperature. A higher temperature (70 °C) results in an increased solubility, and a reduced supersaturation of growth species in solution, thus the particle size of sample 1-4 is smaller than the particle size of sample 1-2 (Fig. 2B, D). These facts are repeated in samples 2-2 and 2-4 (Fig. 3B, D). Tables 1–3 show the average diameter of particles from FE-SEM and SEM images of the prepared samples.[66]

In other work by Morsali's research group, two new Hg(I) coordination supramolecular compounds $[Hg_2(L)_2(Br)_4]_n$ (**3**) and $[Hg(L')(SCN)_2]$ (**4**), (L = 2-amino-4-methylpyridine, L′ = 2,6-pyridinedicarboxlic acid), have been synthesized by sono-chemical irradiation.[67]

Influence of temperature, power ultrasound and reaction time on the morphological properties of the two compounds was also studied. These parameters have noticeable influences on the morphology of the nanoparticles. These systems depicted a decrease in the particle size on increasing the temperature, and the power ultrasound as well as reducing the reaction time. Furthermore, the best conditions for obtaining smaller

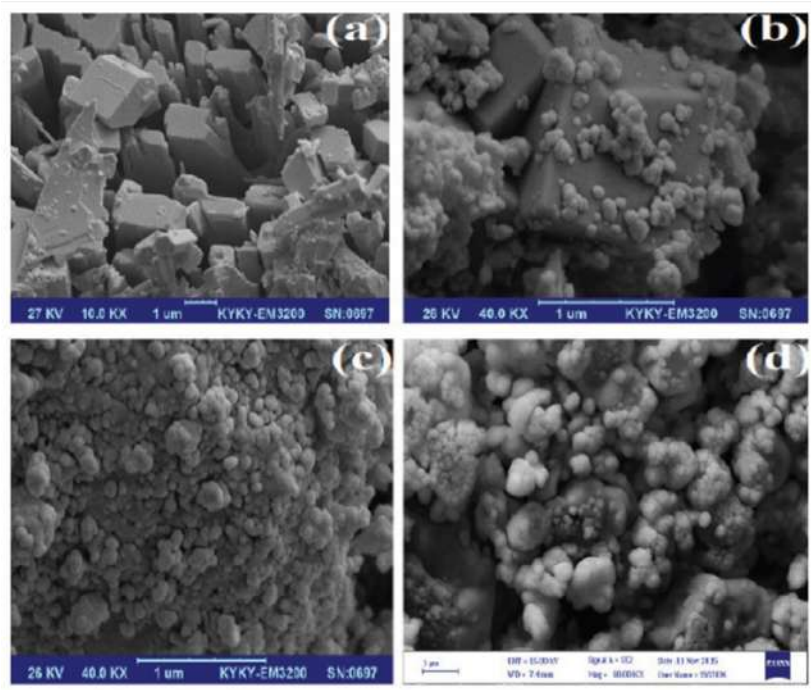

Fig. 2 SEM image of nano particles **1**, (A) without sono-chemical reaction, (B) by sono-chemical reaction at a temperature of 50 °C, time of 60 min and power of 60 W, (C) by sono-chemical reaction at a temperature of 50 °C, time of 30 min and power of 60 W, (D) by sono-chemical reaction at a temperature of 70 °C, time of 60 min and power of 60 W.[66]

size and less agglomerated nanostructure materials for these two mercury supramolecular coordination compounds, are temperature, reaction time and power of the ultrasonic irradiation, viz. 70 °C, 60 min and 60 W, respectively, as shown in Table 4.[67]

In other related work from this group, two new nano Hg(II) coordination supramolecular compounds $[Hg(L)(I)_2]_n$ (**5**) and $[Hg_2(L')_2(SCN)_2]\cdot 2H_2O$ (**6**), (L = 2-amino-4-methylpyridine and L′ = 2,6-pyridinedicarboxlic acid), were synthesized by sono-chemical irradiation. The influence of temperature, power ultrasound and reaction time on the morphological properties of the two compounds was studied and these parameters have significant influences on the size and morphology of the nanostructures described. Differences in the size and shape of the micro/nanostructures of compounds **5** and **6** were observed by changing parameters such as temperature, ultrasound power and reaction time. The optimized parameters to obtain well-defined and

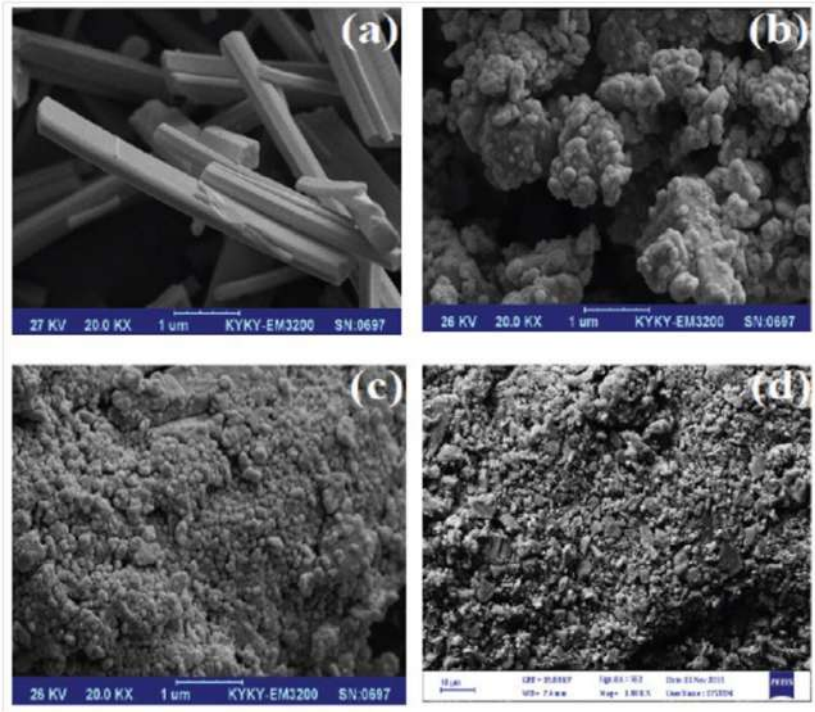

Fig. 3 SEM image of nano particles **2**, (A) without sono-chemical reaction, (B) by sono-chemical reaction at a temperature of 50 °C, time of 60 min and power of 60 W, (C) by sono-chemical reaction at a temperature of 50 °C, time of 30 min and power of 60 W, (D) by sono-chemical reaction at a temperature of 70 °C, time of 60 min and power of 60 W.[66]

Table 4 The influence of temperature, reaction time and sonication power on the size of compound **3** and **4** particles.

Compound 1 samples	T (°C)[a]	T (min)[b]	Sonication (input power) (W)	SEM[c]
1-1	50	60	0	617
1-2	50	60	60	79
1-3	50	30	60	55
1-4	70	60	60	42
Compound 2 samples	**T (°C)[a]**	**T (min)[b]**	**Sonication (input power) (W)**	**SEM[c]**
2-1	50	60	0	590
2-2	50	60	60	85
2-3	50	30	60	57
2-4	70	60	60	53

[a]Reaction temperature.
[b]Reaction time.
[c]Average diameter (nm).

Table 5 The influence of temperature, reaction time and sonication power on the size of compound **5** and **6** particles.

Compound 1 samples	T (°C)[a]	T (min)[b]	Sonication (input power) (W)	SEM[c]
1-1	50	60	0	820
1-2	50	60	60	122
1-3	50	30	60	108
1-4	70	60	60	85
Compound 2 samples	**T (°C)[a]**	**T (min)[b]**	**Sonication (input power) (W)**	**SEM[c]**
2-s1	50	60	0	530
2-2	50	60	60	78
2-3	50	30	60	64
2-4	70	60	60	47

[a]Reaction temperature.
[b]Reaction time.
[c]Average diameter (nm).

homogeneous nanotructures for these two mercury coordination supramolecular compounds are 70 °C, 60 min and 60 W, respectively, as shown in Table 5.[68]

3.2 Effect of solvents

The effect of solvent is a fundamental issue in the area of supramolecular networks. The role of solvents has been studied in reaction kinetics and thermodynamics during coordination processes as well as in crystal growth, crystalline morphology, and lattice structure of the final solid.[69] There are some examples that show size and morphological changes by using different solvents via the US route. By using horn-type US operating at 20 kHz (600 W), nano-sized particles of the 3D lead(II) CP, $[Pb(\mu_6\text{-Fum})]_n$, were obtained in methanol, whereas the particles obtained in water were aggregated and their morphology was not uniform. Interestingly, sheet-like plate morphology was obtained in the mixture of water and methanol solution.[70]

3.3 Effect of additives

Nair and his co-workers reported a systematic study on US synthesis of a Cu-MOCP, and described the effects of important synthetic parameters such as temperature, sonication power, and solvent composition on the

resulting size, structure, yield, and CO_2 uptake of the product.[71] Sub-micron particles of nanoporous Cu[(hfipbb)(H_2hfipbb)$_{0.5}$] (Cu-hfipbb) was prepared in a horn-type US operating at 20 kHz at temperatures as low as 0 °C. The particle geometry of crystals of Cu-hfipbb was influenced by the presence of 2-propanol, which acts as a "crystal-shape-directing" agent. In the absence of 2-propanol, Cu-hfipbb grows as long needle-like particles, but more isotropic particles are formed upon addition of 1.2% 2-propanol.

This change in morphology is caused by competition for the apical site on Cu(II) between the —OH group of 2-propanol and the protonated carboxylic acid group on H_2hfipbb. The yield of the synthesis performed at 0 °C was lower (~11%) in comparison to other reports of US synthesized MOFs and of CE (conventional electric) synthesized Cu-hfipbb,[72] related to the lack of solubility of H_2hfipbb in water. Further increase of temperature up to 90 °C lead to an increase in yield to 40% comparable to that of the CE synthesis. Moreover, the CO_2 uptake isotherms demonstrated that rather than sacrificing performance for a reduction in particle size, the use of US methods produced a material with slightly enhanced CO_2 adsorption, from 1.0 mol of CO_2 per unit cell (0.76 mmol/g) for the CE synthesized sample to 1.1 mol per unit cell (0.87 mmol/g) for the sonicated sample, at 10 bar.

Recently, Zhou et al. reached slightly different conclusions by studying the surfactant-assisted US synthesis of amino acid-based nanoscale CP, $[Cu(tyr)_2]_n$.[73] Ultrasonication accelerated the synthesis and completed it in only 10 min, whereas the synthesis under magnetic stirring required 3 h. The US route also resulted in somewhat smaller particles. However, a too long sonication time (30 min) produced larger blocks. Moreover, increasing the pH improved the solubility and coordination ability of the ligand, resulting in faster homogeneous nucleation, and a smaller particle size. In contrast to the previously mentioned report, the authors revealed that PVP greatly reduced the size of the CP obtained. As the concentration of PVP was increased from 0.05 to 0.1 and 0.2 mol dm^{-3}, the size of products decreased from ~500 to 200–300 and ~200 nm, respectively. Furthermore, nano-crystallization of CP improved their performance in enzyme-free electrochemical biosensors for H_2O_2.

3.4 Effect of concentration of initial reagents

The concentration of initial reagents has important effects on the morphology, particle size, and nature of the products.[74–76]

Recently, Morsali and his research group have reported the role of the initial reagent concentrations, power level of US irradiation and reaction time, on the size and morphology of the nanostructures of TMU-16-NH_2.

Nanostructures of TMU-16-NH_2 were synthesized using the US method by the reaction of zinc(II) acetate dehydrate, linear amino-1,4--benzenedicarboxylate (NH_2-BDC) and a long, rigid bipyridyl-based ligand, 2,5-bis(4-pyridyl)-3,4-diaza-2,4-hexadiene (4-bpdh) in N,N-dimethylformamide (DMF) as solvent using a horn-type sonicator at three different concentrations of initial reagents (0.01, 0.02 and 0.04 M) and three different US powers (6, 12 and 18 W) at two different reaction times of 5 and 15 min. In order to investigate the role of these parameters on the morphology and size of the TMU-16-NH_2 samples, the effects were characterized by FE-SEM. Fig. 4 shows the FE-SEM of the MOF prepared in different concentrations of initial reagents of 0.01, 0.02 and 0.04 M using constant US generator power of 12 W for 15 min irradiation time. Comparison between the samples of different concentrations shows that high concentrations of the initial reagents increased the particle size. Thus, nanoparticles produced using lower concentrations of initial reagents (0.01 M, Fig. 4A, B) are smaller and more uniform than particles produced using higher concentrations (0.02 and 0.04 M, Fig. 4C–F).

Moreover, in order to investigate the role of power on the US irradiation on the nature of products, reactions were performed under different US generator powers of 6, 12 and 18 W at constant concentration of initial reagents and irradiation time of 0.02 M and 15 min, respectively. Comparison between the samples with different power of US irradiation shows that high power US irradiation (18 W) leads to the smallest and most uniform nano-cubes when compared to lower powers (6 and 12 W). Increasing the power of the US level led to an increase in heating rate that consecutively decreases the initial crystal formation time. Increasing the reaction time from 5 to 15 min causes a specific morphological transformation from microspheres to uniform nano-cubes of TMU-16-NH_2.[77]

In other work from this research group, two porous Zn(II)-based metal-organic frameworks $[Zn(oba)(4\text{-bpdh})_{0.5}]_n.(DMF)_{1.5}$ (TMU-5) and $[Zn(oba)(4\text{-bpmb})_{0.5}]_n.(DMF)_{1.5}$ (TMU-6) were prepared by the sonochemical process and characterized. Sonication time and concentration of initial reagents affect the size and morphology of nanostructured MOFs. Various sonication times and concentrations of initial reagents were evaluated to prepare the nanostructure of these MOFs. The results show that the best uniform distribution of nano-rods and plates of TMU-5 and TMU-6

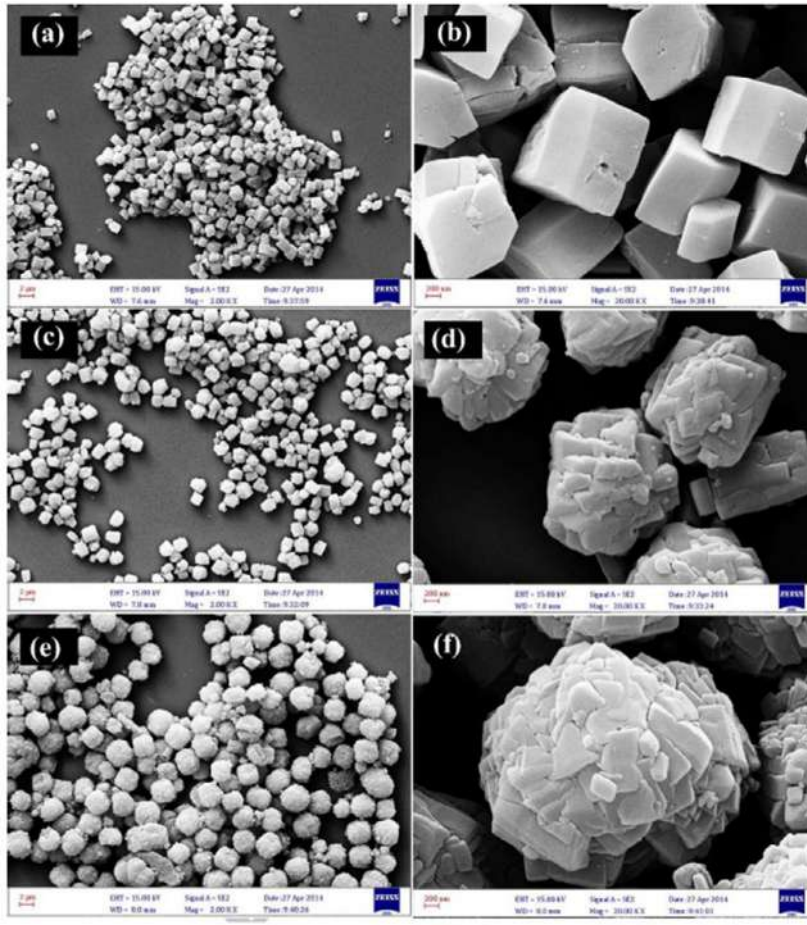

Fig. 4 SEM images of S-TMU-16-NH_2 nanostructures prepared by US generator power of 12 W at 15 min irradiation time at different concentrations of initial reagents (A,B) 0.01 M, (C,D) 0.02 M and (E,F) 0.04 M.[77]

were obtained at lower concentrations of the initial reagents, whereas, by increasing the rate of nucleation, the sizes of the obtained MOFs were reduced. These results show that the sono-chemical process is an effective method for fast and simple preparation of nano-MOFs.[41]

4. Application of nano coordination polymers

Metal coordination polymers and especially nano metal coordination polymers due to the high number of vacancies in the structure and the high

surface area have the potential of playing many roles which has led to many applications. These include; adsorption removal (adsorbent application to removal of pollutants), photo-catalytic degradation, the use as templates in order to obtain desired nanomaterials, anti-cancer drugs, supercapacitors and catalytic activities which is briefly illustrated with the various examples below.[40,41,78–112]

4.1 Adsorption removal

The global warming effect is believed to be associated with increasing concentrations of hazardous materials in water and in the atmosphere. Among pollutants, industrial dyes can lead to serious and devastating environmental and health problems. Several advanced technologies for the removal of various pollutants have been studied, among which adsorption byr nano structured materials appears to be very attractive and to extend nanoscale adsorbent application to the removal of pollutants from water.[41,78–80]

Recently Morsali and his co-workers[41] reported the adsorption capacity of two Zn(II) metal-organic frameworks {$[Zn(oba)(4\text{-bpdh})_{0.5}]_n$ $(DMF)_{1.5}$ (TMU-5) and $[Zn(oba)(4\text{-bpmb})_{0.5}]_n$ $(DMF)_{1.5}$ (TMU-6)} in the presence of the rhodamine B dyeRhodamine B (RhB) was chosen as a model pollutant to evaluate adsorption capacity of the MOF nanostructures. An aqueous stock solution of RhB was prepared by dissolving RhB in deionized water. Aqueous solutions with the desired concentration of RhB were obtained by dilution of the stock solution with water. Adsorption experiments of RhB were carried out on stirred aqueous solutions in a cylindrical quartz UV-reactor containing about 50 mL of 100 ppm RhB aqueous solution in the presence of about 25 mg of MOF nanostructures. The suspension was sonicated for 5 min. The temperature of the solutions did not exceed 20 °C using a tap water circulation in the jacket of the reactor. Samples for analyses were taken from the reaction suspension at specified reaction times and immediately centrifuged at 6000 rpm for 10 min to remove the particles. The solutions were analyzed by monitoring the absorbance at 553 nm using an UV–vis spectrophotometer. The concentration of the dye in each sample was determined at $\lambda_{max} = 553$ nm, using a calibration curve. By this method, the degree of removal (percentage) of RhB may be obtained at different intervals. The percent removal was calculated by the equation $\{\%\ \text{Removal} = (C_i - C_t)/C_i \times 100\}$, where, C_i is the initial concentration of dye and C_t is the concentration of dye at any specified time.

The adsorption capacity of TMU-5 and TMU-6 nanostructures with different morphologies and ZnO nanoparticles obtained from the thermolysis of them (TMU-5 and TMU-6) in the presence of 100 ppm RhB aqueous solution after 90 min was investigated. The maximum percent adsorption of RhB was roughly 96.2% and 92.8% after 90 min in the presence of 5F and 6F, respectively. A decrease in particle size together with uniform morphology can cause more adsorption of the target pollutant. On the other hand, there is a large change in the RhB concentration in a shorter time with the nano-rod morphology in both MOFs (5F and 6F).[41]

In similar work by this group, a new 3D Zn(II) based MOF of $[Zn_4(oba)_3(DMF)_2]$ (TMU-39) was synthesized using the nonlinear dicarboxylate ligand, 4,4′-oxybis(benzoic acid) (H_2oba) via sono-chemical and solvo-thermal methods. Congo red and Sudan-red dyes were employed to explore the efficiency of this MOF in removal of the dye pollutants. The percentage removal was computed by the equation given in the previous section. Removal efficiency of TMU-39 crystals and powder obtained from the sono-chemical process after 60 min in the presence of 50 ppm CR and SR aqueous solution was investigated. The removal efficiency in the presence of CR is almost 53% for the sono-chemical synthesized sample and 27% with the solvo-thermal synthesized crystals, and the removal efficiency of SR is 87% and 10% for powder and crystals, respectively. The higher percentage of removal efficiency for SR compared to CR can be attributed to the smaller size of Sudan-red dye which enables it to enter the TMU-39 cavities. Also, higher adsorption in the sono-chemical synthesized sample may be attributed to smaller particle size and higher BET surface area of the sample compared to the crystals.[78]

In another study,[79] a magnetic infinite coordination polymer with the morphology of a nano-capsule, as an efficient adsorbent for the removal of mercury(II) ions has been introduced. This infinite coordination polymer was synthesized from Zinc(II) ions and a ditopic organic ligand (1,3-bis(-tetrazol-5-ylmethyl)benzene (btb)), and its efficiency as an adsorbent was studied in view of adsorption isotherms, kinetics and thermodynamics. The adsorption capacity of mercury(II) ions was affected by the pH and adsorption time, and the optimal adsorption conditions were reported as a pH value of 8 and an adsorption time of 75 min. Results indicated that the adsorption was an endothermic process. Moreover, this adsorption process was fitted with a pseudo-second order kinetic model. Finally, the magnetic properties of the nano-capsules synthesized for high and low concentrations of the initial reagents were investigated. Studies showed that

the saturation magnetization of nano-capsules synthesized for a low concentration of initial reagents was higher.[79]

Zheng and his co-workers[80] reported a facile electrochemical synthesis of nano iron porous coordination polymers using scrap iron for simultaneous and cost-effective removal of organic and inorganic arsenic. Besides the universal features of conventional porous coordination polymers (PCPs) including 3D-ordered porous structure and high surface areas, these prepared Fe-PCPs can not only form Fe—O—As bonds with arsenic species, but also produce hydrophobic and π–π conjugation through the aromatic rings of organic arsenics and Fe-PCPs, allowing it to have high adsorption capacity for both inorganic and organic arsenic species. The performance of Fe-PCPs on arsenic removal was validated by using three contaminated water samples. One of these samples was groundwater collected from a well and the other two were surface water collected from a river of the Datong Basin, Shanxi province, China. The concentrations of arsenic species in these water samples before and after treatment with Fe-PCPs were analyzed by HPLC-ICPMS, as shown in Fig. 5A–C. The results showed that only

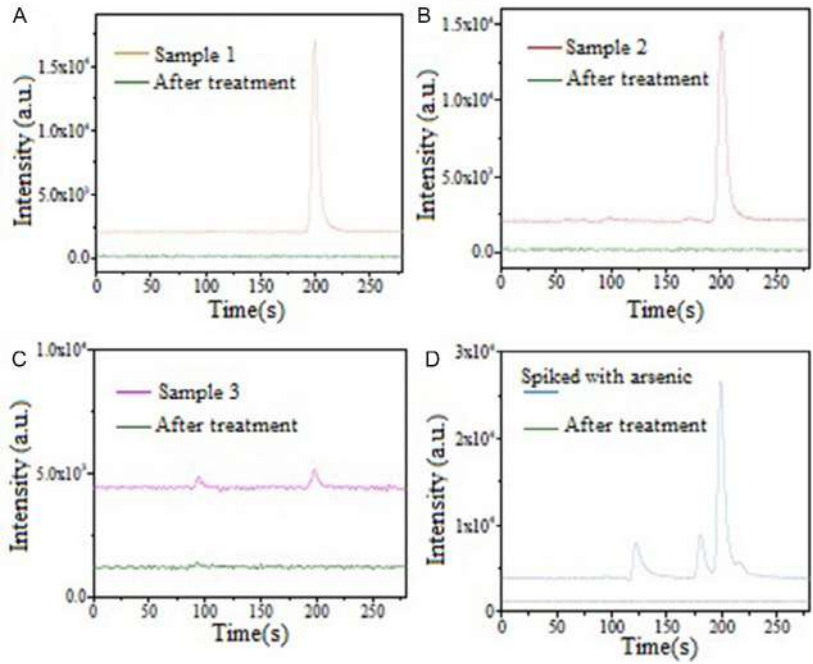

Fig. 5 The concentrations of inorganic and organic arsenic species measured by HPLC-ICP-MS.[80]

As(V) was found in the surface water samples. The original concentrations of As(V) in these two samples were higher than 300 μg/L, which are much higher than that permitted by the WHO guideline (10 μg/L). Although As(III) was observed in the groundwater sample, the concentrations of both As(III) and As(V) in this sample were much lower than those of surface water samples. In order to demonstrate that Fe-PCPs can simultaneously remove inorganic and organic arsenics from water, a certain amount of As(V), MMA, DMA and ASA was added to one of the surface water samples. The concentrations of the inorganic and organic arsenics before and after treatment were also analyzed by HPLC-ICP-MS, as shown in Fig. 5D. The results show that all the inorganic and organic arsenic were efficiently removed and their concentrations in the treated water was much lower than their LODs obtained by HPLC-ICP-MS (ranging from 0.5 to 2 μg/L on sampling 20 μL of sample).[80]

4.2 Precursors for preparation of nanomaterials

MOCPs can be used as templates in order to obtain the desired nanomaterials. By choosing appropriate MOCP precursors with special morphologies and under suitable experimental conditions, obtaining the desired morphologies will become possible. Nano MOCP precursors may also be used to obtain nanomaterials with better and more useful properties. Depending on the conditions, MOCP precursors may lead to the preparation of metals, metal oxides, metal sulfides or other nano-sized materials. With this method, nanomaterials can be obtained in different morphologies from different MOCP precursors. Similar to other solid-phase production approaches, metal-organic frameworks can be easily transformed into metal oxides via simple calcination at high temperature in air, which is an effective method to synthesize metal oxides with controlled sizes, morphologies, structures, and properties. The distinct advantages of using MOF templates are correlated to their structural and functional tailor ability at the molecular level that are rarely acquired in any other conventional template/precursor.[81]

Recently Morsali's research group[82] reported the synthesis of ZnO nanostructures from a 3D porous Zn(II)-based metal-organic framework $\{[Zn_2(oba)_2(4\text{-bpmn})]\ (DMF)_{1.5}\}_n$ (TMU-21), (4-bpmn = N,N′-Bis-pyridin-4-ylmethylene-naphtalene-1,5-diamine, H_2oba = 4,4′-oxybis(benzoic acid)) with nano-rod morphology. Synthesis of nanostructures of zinc(II) oxide with controlled sizes and morphologies was studied in detail. It is a well-known semiconductor with a wide band gap (3.37 eV) and a large exciton

binding energy of 60 meV at room temperature. It has many applications such as in solar cells, acoustic devices, gas and chemical sensors, catalysts, micro lasers, memory arrays and biomedical.[82] In addition, ZnO has advantages such as non-toxicity and a low price. Nanostructures of ZnO have been produced by calcination of the four samples (TMU-6, activated TMU-6, TMU-21 and activated TMU-21) {[Zn_2(oba)$_2$(4 bpmn)] (TMU-21) and {[Zn_2(oba)$_2$(4-bpmb)] (TMU-6) at 550 °C for 3 h. Based on their IR and XRD patterns, analyses in four cases indicated ZnO formation. Also X-ray diffraction (XRD) was used to study the structure of ZnO. Sharp diffraction peaks revealed the crystalline character of the ZnO powder, showing broad diffraction peaks (XRD) that are in agreement with nano-crystalline materials (hexagonal phase, space group *P63mc*, with lattice constants a = 3.2530 Å, b = 3.2530 Å, c = 5.2130 Å, Z = 2). The morphology and size of the particles are different in the two samples obtained from TMU-21 and activated TMU-21, also from TMU-6 and activated TMU-6. This aspect shows the influence of precursors with and without solvent molecules, on the morphology and size of ZnO nanostructures.[82]

In other studies by this group, two coordination polymers were used as precursors for the preparation of ZnO and CdO nanostructures by calcination at 550 °C. CdO, an n-type semiconductor with a narrow band gap (2.2 eV), can couple with ZnO for modification of the band gap. ZnO–CdO composites have been used for various applications such as photo-catalysis, gas sensing and optoelectronic devices.[83,84]

Two compounds {[Zn_3(Oba)$_4$][Me_2NH_2)$_2$] 6DMF·3H_2O (**7**) and [Cd_3(Oba)$_4$][Me_2NH_2)$_2$] 2DMF·2H_2O (**8**)} were used as precursors for preparation of metal oxides. ZnO and CdO nanostructures were obtained upon calcination of **7** and **8** at 550 °C for 2 h, respectively. The XRD pattern of calcined **7** exhibits the typical patterns of a hexagonal wurtzite structure of ZnO (JCPDS No. 36-1451, $a = 3.25$ and $c = 5.20$ Å). For the sample obtained from the calcination of **8**, a cubic monteponite structure of CdO (JCPDS No. 05-0640, $a = 4.69$ Å) was observed.[85]

In similar work,[86] CdO nanoparticles were prepared by thermolysis of the compound [Cd(p-2yeinh)(NO_2)]$_n$ (p-2yeinh = pyridin-2-yl ethylidene-isonicotinohydrazide) at 180 °C with oleic acid as a surfactant. The average diameter of the nanoparticles was estimated by XPRD to be 23 nm. The morphology and size of the prepared CdO nanoparticles were further studied using SEM (Fig. 6).[86]

RuO_2 is a suitable metal oxide candidate for organic electronics, stable anodes, field emission displays, thin film resistors, catalysis, fuel cells and

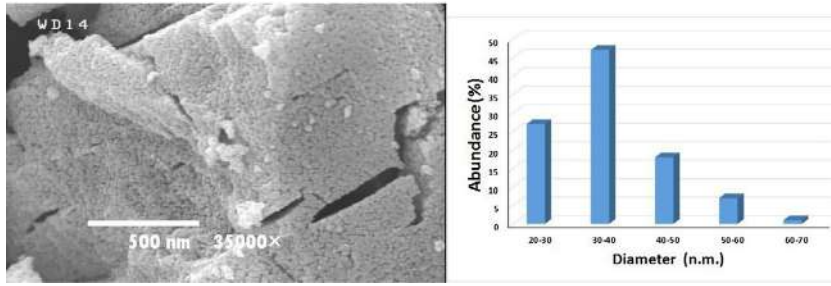

Fig. 6 SEM photograph of CdO nano-powder (produced by the thermolysis of nanostructures of $[Cd(p\text{-}2yeinh)(NO_2)]_n$ at 180 °C) and particle size histogram.[86]

capacitors.[113] Many methods have been used in the preparation of nano RuO_2 such as wet chemical, biological, sol-gel process, thermal deposition and thin film-based techniques. In addition, the preparation of nanoscale coordination supramolecular compounds by ultrasonic irradiation is a valuable method because of the eco-friendly source, short reaction time, low cost and ease of synthesis in comparison with prevalent thermal synthetic techniques. Recently, two new Ru(II) complexes, $[(\mu^6\text{-}p\text{-cymene})RuCl(L1)]PF_6$ and $[(\mu^6\text{-}C_6H_6)RuCl(L1)]PF_6$ with the ligand (E)-4-(methylthio)-N-((quinolin-2-yl)methylene)benzenamine (L1), were synthesized by Morsali's research group. Calcination after treating these complexes by the ultrasonic method produces RuO_2 nanoparticles. It was shown that ultrasound waves affected the characteristics of the nanoparticles. In this work, nanoparticles of small size and uniform morphology were obtained. So Ru(II) coordination polymers are suitable precursors for the synthesis of nanostructures.[113]

Synthesis of other metal oxides such as NiO, PbO, CuO or mixed metal oxides with or without using surfactants has also been reported.[87–91,114]

4.3 Photo-catalytic degradation

Since Garcia first reported the photo-catalytic degradation of phenol in 2007 with MOF-5 as photo-catalyst,[92] many coordination polymers (CPs) as photo-catalysts for the photo-catalytic degradation of organic dyes under UV or visible light irradiation have been synthesized and reported. However, relative few coordination polymers performed good photo-catalytic activities when they were under visible light irradiation because CPs are usually poor photo-responders in the visible range.[93,94] The MOF based composites were also developed for visible light catalytic

degradation.[95] In the photo-catalytic degradation processes, the electrons of semiconductor photo-catalysts such as coordination polymers can be excited from the valence band (VB) to the conduction band (CB) when the photo-catalysts are irradiated by light with energy equal to or larger than the energy band gap between the VB and CB of the photo-catalysts. The electrons in the CB could combine with H_2O_2, O_2 or H_2O to produce hydroxyl radicals (·OH). The hydroxyl radicals ($^{\bullet}OH$) can oxidize the dye and decompose the organic dyes into small molecules, H_2O and CO_2.

Recently Li′s research group[96] has reported the synthesis of four structurally diverse nickel coordination polymers $\{[Ni(ttpa)(1,4\text{-ndc})(H_2O)_2]\cdot 2H_2O\}_n$ (**9**), $\{[Ni(ttpa)(1,3\text{-bda})]\cdot 2H_2O\cdot DMF\}_n$ (**10.2H$_2$O.DMF**), $\{[Ni(ttpa)(1,4\text{-bdc})]\cdot H_2O\}_n$ (**11**) and $\{[Ni(ttpa)(aip)(H_2O)]\cdot 3H_2O\}_n$ (**12.3H$_2$O**) (ttpa = tris(4-(1,2,4-triazol-1-yl)phenyl)amine, 1,4-ndc = 1,4-naphthalenedicarboxylate, 1,3-bda = 1,3-benzenediacetate, 1,4-bdc = 1,4-benzenedicarboxylate, aip = 5-aminoisophthalate) by using hydrothermal and sono-chemical methods. The organic dye methylene blue (MB) was selected as the model dye to observe the photo-catalytic properties under visible light irradiation. The photo-catalytic properties of crystalline solid and nano-sized **9**–**12** were studied. The catalytic efficiencies of **9**–**12** were also compared with the well-known commercial TiO_2. Results showed that **9**–**12** are good catalysts for the degradation of MB. The catalytic efficiencies are **9** > **11** > **10** > **12** > TiO_2 (20 nm) > TiO_2 (60 nm). The effects of the sonication synthetic conditions and morphology of nano-sized **9**–**12** on the photo-catalytic efficiencies were also studied. The higher sonication frequency resulted in the formation of uniform and smaller nano-sized coordination polymers which have higher catalytic efficiency.[96]

In other work by Cui and his research group,[97] a new Co(II) coordination polymer, $[Co(Hbibp)(nbta)]_n$, (bibp = 4,4′-bis(1-imidazolyl)biphenyl, H_3nbta = 5-nitro-1,2,3-benzenetricarboxylic acid) was synthesized and showed high photo-catalytic activities for the degradation of MB under UV irradiation. The photo-degradation process was mainly caused by $^{\bullet}$OH radicals. It can be seen that the photo-catalytic efficiency reached approximately 90.2% in the presence of nano-sized listed CP after 120 min under UV light irradiation. However, only 11.9% of MB was decomposed without any catalyst. The increased photo-catalytic degradation efficiency indicates that nano-sized CP is an excellent candidate as photo-catalyst in decomposing MB under UV light irradiation. Furthermore, when nano-sized CP was placed into an aqueous solution of the MB in a dark environment for half an hour, there is no obvious

decrease in the absorbance value, which may avoid the possibility of adsorbing such a dye molecule into the framework.[97] Similar articles have recently been published in this field (photo-degradation process of Methyl Blue by use of nano coordination polymers) which has been referenced here and details are given in the literature.[98–101]

4.4 Catalytic activity

Coordination polymers have good thermal stability so they can be employed in catalytic reactions, such as oxidation of inert C—H bonds of hydrocarbons, hydrogenation of olefins, Knoevenagel condensation reaction, etc. The Knoevenagel condensation of aromatic ketons with active methylene compounds is an important carbon–carbon bond coupling reaction in the synthesis of several fine chemicals and pharmaceuticals. The discovery of MOFs and coordination polymer catalysts for the Knoevenagel condensation has become a matter of increasing interest in recent years. There have been many reports that already displayed that MOFs and coordination polymers that can be superior heterogeneous catalysts for Knoevenagel condensation. One of them is from a recent study by Morsali and his co-workers.[40] They synthesized and characterized a new mixed-ligand Co(II)-based two-dimensional coordination polymer, $[Co_2(ppda)(4\text{-bpdh})_2(NO_3)_2]_n$, (ppda = pphenylenediacrylic acid, 4-bpdh = 2,5-bis(4-pyridyl)-3,4-diaza-2,4-hexadiene). This compound was synthesized in three different concentrations of initial reagents (0.005, 0.01 and 0.05 M), two different ultrasound powers (12 and 24 W) and three different reaction times of 30, 45 and 60 min. The results have shown that the higher concentrations of reagents lead to increase in thickness and particle size. Also increasing the power of ultrasonic irradiation led to nanoparticle morphology. These results reveal that the sono-chemical method is an effective approach for quick and simple preparation of nanostructures and a very promising method for the synthesis of nanoscale coordination polymers. Moreover, the nanostructure of the CP showed better catalytic activity in the Knoevenagel condensation reactions compared to a bulk sample of the CP.[40]

In another study by this group,[102] the ability of two new three-dimensional isoreticular F-MOFs nanostructures $[Zn_2(hfipbb)_2(4\text{-bpdh})]$. $(DMF)_{0.5}$ (TMU-55) and $[Zn_2(hfipbb)_2(4\text{-bpdb})]$. $(DMF)_2$ (HTMU-55) with a smaller size and higher surface area as the heterogeneous catalysts for the catalytic reaction in comparison to bulk samples, the Henry reaction was selected. Results are summarized in Table 6.

The better catalytic activity of TMU-55 is attributed to the presence of the methyl groups on the N basic centers in 4-bpdh that enhance the basicity

Table 6 Henry reaction performed in the presence of the two isoreticular F-MOFs catalysts (TMU-55, HTMU-55, and nanostructures of them) and in their absence.

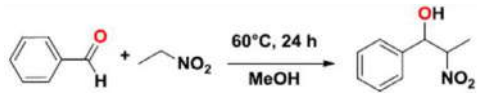

Entry	catalyst	Conversion (%)
1	TMU-55	71
	TMU-55 nanostructure	97
2	HTMU-55	68
	HTMU-55 nanostructure	87
3	–	6

GC yield, reaction conditions: benzaldehyde (0.2 mmol), nitromethane (0.5 mmol), 15 mg (3 mol%) catalyst, solvent: methanol (3 mL), 60 °C, 24 h.

of the nitrogen active centers. This study demonstrates the important role of the basicity of azine functionalized frameworks, as well as that of the high surface area of the frameworks on the catalytic performance.[102]

Another application of coordination polymers as heterogeneous catalyst has been reported by Soleimannejad's group in the production of biodiesel. The nano-sized compound $\{(bipyH)[Ba_2(pydc)_2(Hpydc)(H_2O)_2]\}_n \cdot nH_2O$, (bipy = 4,4′-bipyridine and H_2pydc = pyridine-2,6-dicarboxylic acid) was shown to be a promising nano-catalyst for the synthesis of biodiesel with an excellent yield in a relatively short time (150 min) in the presence of ultrasonic irradiation. Furthermore, the barium based nano-CP was found to be a stable and recyclable catalyst with no loss of catalytic activity during the course of reactions.[103]

4.5 Electrochemical behavior; high-performance electrode for flexible supercapacitor

Electrochemical capacitors, also known as supercapacitors, have attracted considerable attention because of their fast charge/discharge ability, good cycling performance and high power density. As known, the characteristics of electrode materials have a huge impact on the performance of supercapacitors. 2D nanomaterials have been full of surprises since their emergence and are intensively investigated as active materials for energy storage/transformation in recent years, because of their unique physical and chemical properties, as well as a great variety.[104,105] During the past decade, promising research on graphene and other graphene-like 2D

nanomaterials such as transition metal dichalcogenides (TMDs) and, layered metal oxide/hydroxide, further stimulated the exploration of new 2D nanomaterials, transition metal nitrides, coordination polymers (CPs), covalent-−organic frameworks (COFs) and polymers. Among them, 2D CPs, as an importance member of the 2D family, are attracting increasing attention due to their functional diversity achievement by judicious selection of the metal ions and organic linkers.[106,107] Recently, it was proposed that hybridization of CPs and polymers is an effective strategy to obtain new and versatile materials that exhibit peculiar properties hard to realize with individual components. For instance, incorporation of a conductive polymer in CPs can efficiently improve the conductivity, and thus may give rise to enhanced electrochemical performance of the composites. Polypyrrole (PPy), as a typical conducting polymer, is extensively used as capacitive material because of its easy synthesis, relatively high capacitance and intrinsic flexible property.[108]

Recently Yang's research group[109] has reported a strategy of growth of conductive polymers (PPy) on 2D CPs nano-sheets to enhance their capacitive performance. They choose a typical 2D CP (Cu-TCPP, TCPP = 5, 10, 15, 20-tetrakis (4-carboxyphenyl)porphyrin) as the 2D platform, onto which PPy was grown by a simple in situ chemical oxidation method. In this kind of 2D CPs nano-sheets, one TCPP ligand is linked by four Cu paddlewheel metal nodes, i.e., $Cu_2(COO)_4$, to form a 2D layered sheet. The strong π-stacked conjugation and the heteroatom of the TCPP may enhance both the electron transport and the interaction with conductive polymers. Morphologies of the PPy, Cu-TCPP and Cu-TCPP@PPy hybrids have been studied by SEM. The pristine Cu-TCPP is a well dispersed nano-flate. After growth of PPy, the entire Cu-TCPP sheets are covered with PPy nanoparticles to form the Cu-TCPP@PPy nanocomposites. The nanocomposite coated with PPy nanoparticles has shown to have a rough surface, which may promise enhanced ion diffusion because of the increased interface areas between the electrode material and electrolyte when compared with that of the pure material. With increase of PPy loading, the thickness of the Cu-TCPP@PPy nano-flates increases and the shape of the composites tend to become sphere-like shapes. The presence of Cu-TCPP nano-sheets not only act as a polymerization substrate in the polymerization system to modify the morphology of PPy, but also provide a path for the insertion and extraction of ions within the PPy, hence ensure a high specific capacitance. For viewing voltammetric diagrams [cyclic voltammetry (CV), galvanostatic charge/discharge (GCD) and electrochemical impedance spectroscopy (EIS)] and other details, see reference 109.

4.6 Anti-cancer drug

Nanotechnology has provided new tools for addressing unmet clinical situations, especially in the oncology field. The development of smart nanocarriers able to deliver chemotherapeutic agents specifically to the diseased cells and to release them in a controlled way has offered a paramount advantage over conventional therapy. Among the different types of nanoparticle that can be employed for this purpose, inorganic porous materials have received significant attention in the last decade due to their unique properties such as high loading capacity, chemical and physical robustness, low toxicity and easy and cheap production in the laboratory The use of porous inorganic nanoparticles as drug carriers for cancer therapy has the potential to improve the life expectancy of the patients affected by this disease. However, much work is needed to overcome their drawbacks, which are aggravated by their hard nature, exploiting the advantages offered by highly the ordered pore network of these materials.[110] Although great success has been achieved in the field of biological medicine, cancer is still the leading disease which causes the death of millions of people each year. Coordination compounds are of essence as they could act as anti-cancer agents.[111] Numerous Cu(II)-related compounds have been found to be potential anti-tumor agents and some of them have been reported to be so active in vitro and in vivo as in the case of platinum drugs. On the other hand, the metal cadmium has been shown to be of none-medicinal value in chemistry because of their well-known toxicity. However, Cd(II)-related coordination polymers have been reported to be much less poisonous than the Cd(II) ions and they can cause apoptosis by inhibiting the tumor cellular proteasome.

Recently, You's research group has reported the fabrication of two new coordination complexes $[Cu_3(\mu_3\text{-}O)(pz)_3(Hpz)(Hpdc)(H_2O)_2](H_2O)_4$ (**11**, H_2pdc = pyridine-3,5-dicarboxylic acid, Hpz = pyrazol) and $[Cd(phen)(bdc)](H_2O)$ (**12**, phen = 1,10-phenanthroline, H_2bdc = 1,2-benzenedicarboxylic acid) through the application of carboxylic acid and the N-containing linkers as co-ligands. Furthermore, an ultrasonic treatment method was used to produce the nano particles of CPs 1-2 with good water dispersibility and framework integrality. Moreover, the in vitro 3-(4,5-dimethylthiazol-2-yl)-2,5-diphenyltetrazolium bromide (MTT) method was administered on the breast cancer cell line BT474 with rising aggregations of the nanostructures 1-2, indicating that both these two nanostructures have anti-tumor activity in vitro. In addition to this, the

apoptosis and ROS detection results indicated the anti-cancer activity of nanostructures 1-2 due to the cancer cell apoptosis mediated by increasing ROS accumulation.[112]

In other work by Delavar and his co-workers, the activity and efficiency of nano CdO (which was made through the direct a calcination process of $[Cd(NO_3)(bipy)(pzca)]_n$ at 500 °C) as an anti-cancer drug has been studied on cancer cells for different concentrations. The results showed that the viability of cancer cells reduced above a 2 μg/mL of CdO-NPs concentration.[115] Refer to the following references for further discussion of this broad application.[116–119]

5. Conclusions and future perspectives

The synthesis of nanostructured material is important for the step from fundamental science to potential applications. This is true for coordination polymers and (porous) coordination networks in particular. Preparation of nanoscale coordination polymers involves self- assembly of organic ligands and metal ions. They have many promising characteristics including structural adaptivity and flexibility, multiple coordination sites, and various functions. Among the various synthetic routes, ultrasound-assisted method is applicable for nanoscale coordination polymer preparation as their reaction conditions can be easily adapted from conventional approaches. Accelerated nucleation and short crystallization time in sono-chemical synthesis, especially with low reaction temperature and ambient pressure, make particles more uniform and smaller. According to the results for reaction time, temperature, ultrasound irradiation power, concentration of initial reagent, whether or not to use surfactants and solvents, play an important role in the size and morphology of products (nano coordination polymers). Increase of temperature, sonication power and decrease in reaction time, lead to a decrease in particle size. As can be seen from the results presented in this chapter, a wide range of nanoscale coordination polymers can be produced using the ultrasound assistant technique, featuring diverse structures, metal ions, ligand types, and dimensionalities.

Acknowledgments

Support of this investigation by Tarbiat Modares University of I.R. Iran is gratefully acknowledged.

References

1. Lehn, J.-M. *Supramolecular Chemistry: Concepts and Perspectives*. VCH, 1995.
2. James, S. L. *Chem. Soc. Rev.* **2003**, *32*(5), 276–288.
3. Robson, R. *Dalton Trans.* **2000**, *21*, 3735–3744.
4. Wu, A. Q.; et al. *Cryst. Growth Des.* **2006**, *6*(2), 444–450.
5. Kitagawa, S.; Noro, S. *Comprehensive Coordination Chemistry*. Vol. 7, **2004**, 231.
6. Robin, A. Y.; Fromm, K. M. *Coord. Chem. Rev.* **2006**, *250*, 2127–2157.
7. Batten, S. R.; Neville, S. M.; Turner, D. R. *Angew. Chem. Int. Ed.* **2009**, *48*, 4890–4891.
8. Abrahams, B. F.; et al. *Angew. Chem. Int. Ed.* **1996**, *35*(15), 1690–1692.
9. Zhao, Y.-H.; et al. *Inorg. Chem. Commun.* **2007**, *10*(4), 410–414.
10. Blake, A. J.; et al. *Coord. Chem. Rev.* **1999**, *183*(1), 117–138.
11. Wu, C.-D.; et al. *Inorg. Chem.* **2002**, *41*(12), 3302–3307.
12. Du, M.; Cai, H.; Zhao, X.-J. *Inorg. Chim. Acta* **2005**, *358*(13), 4034–4038.
13. Xue, L.; et al. *J. Mol. Struct.* **2007**, *832*(1–3), 132–137.
14. Youm, K.-T.; et al. *Angew. Chem. Int. Ed.* **2006**, *45*(24), 4003–4007.
15. Chae, H. K.; et al. *Nature* **2004**, *427*(6974), 523–527.
16. Li, G.; et al. *Inorg. Chem.* **2003**, *42*(16), 4995–5004.
17. Hoskins, B. F.; Robson, R. *J. Am. Chem. Soc.* **1990**, *112*(4), 1546–1554.
18. Liu, Y.-H.; et al. *Inorg. Chem.* **2002**, *41*(9), 2592–2597.
19. Mao, J.-G.; Wang, Z.; Clearfield, A. *Inorg. Chem.* **2002**, *41*(23), 6106–6111.
20. Zhang, X.-F.; et al. *Acta Crystallogr., Sect. C: Cryst. Struct. Commun.* **2006**, *62*(12), m617–m619.
21. Yang, J.; et al. *Inorg. Chem.* **2007**, *46*(16), 6542–6555.
22. Fan, S.-R.; Zhu, L.-G. *Inorg. Chem.* **2007**, *46*(16), 6785–6793.
23. Batten, S. R.; Neville, S. M.; Turner, D. R. *Coordination Polymers Design, Analysis and Application*. Royal Society of Chemistry, **2009**.
24. Kawaguchi, S. *Coord. Chem. Rev.* **1986**, *70*, 51.
25. (a) Flegel, E. A.; Ranft, A.; Haase, F.; Lotsch, B. V. *J. Mater. Chem.* **2012**, *22*, 10119–10133; (b) Sindoro, M.; Yanai, N.; Jee, A.-Y.; Granick, S. *Acc. Chem. Res.* **2014**, *47*, 459–469.
26. Catala, L.; Mallah, T. *Coord. Chem. Rev.* **2017**, *346*, 32–61.
27. Oh, M.; Mirkin, C. A. *Nature* **2005**, *438*, 651–654.
28. Sun, X.; Dong, S.; Wang, E. *J. Am. Chem. Soc.* **2005**, *127*, 13102–13103.
29. Spokoyny, A. M.; Kim, D.; Sumrein, A.; Mirkin, C. A. *Chem. Soc. Rev.* **2009**, *38*, 1218–1227.
30. (a) Ohkoshi, S.; Tokoro, H. *Acc. Chem. Res.* **2012**, *45*, 1749–1758; (b) Vaucher, S.; Li, M.; Mann, S. *Angew. Chem. Int. Ed.* **2000**, *39*, 1793–1796, Angew. Chem. **2000**, 112, 1863–1866.
31. Brinzei, D.; Catala, L.; Louvain, N.; Rogez, G.; Stephan, O.; Gloter, A.; Mallah, T. *J. Mater. Chem.* **2006**, *16*, 2593–2599.
32. Catala, L.; Brinzei, D.; Prado, Y.; Gloter, A.; Stephan, O.; Rogez, G.; Mallah, T. *Angew. Chem. Int. Ed.* **2009**, *48*, 183–187, Angew. Chem. **2009**, 121, 189–193.
33. Dumont, M. F.; Knowles, E. S.; Guiet, A.; Pajerowski, D. M.; Gomez, A.; Kycia, S. W.; Meisel, M. W.; Talham, D. R. *Inorg. Chem.* **2011**, *50*, 4295–4300.
34. Roy, X.; Thompson, L. K.; Coombs, N.; MacLachlan, M. J. *Angew. Chem. Int. Ed.* **2008**, *47*, 511–514, Angew. Chem. **2008**, 120, 521–524.
35. Imaz, I.; Maspoch, D.; Rodríguez-Blanco, C.; Perez-Falcón, J. M.; Campo, J.; Ruiz-Molina, D. *Angew. Chem. Int. Ed.* **2008**, *47*, 1857–1860, Angew. Chem. **2008**, 120, 1883–1886.
36. Son, W. J.; Kim, J.; Ahn, W. S. *Chem. Commun.* **2008**, *47*, 6336–6338.

37. Li, Z. Q.; Qiu, L. G.; Su, T.; Wu, Y.; Wang, W.; Wu, Z. Y.; Jiang, X. *Mater. Lett.* **2009**, *63*, 78–80.
38. Hashemi, L.; et al. *J. Mol. Struct.* **2014**, *1072*, 260–266.
39. Gharib, M.; Safarifard, V.; Morsali, A. *Ultrason. Sonochem.* **2018**, *42*, 112–118.
40. Joharian, M.; Abedi, S.; Morsali, A. *Ultrason. Sonochem.* **2017**, *39*, 897–907.
41. Masoomi, M. Y.; Bagheri, M.; Morsali, A. *Ultrason. Sonochem.* **2016**, *33*, 54–60.
42. Tang, C.; Amin, D.; Messersmith, P. B.; Anthony, J. E.; Prud'homme, R. K. *Langmuir* **2015**, *31*, 3612–3620.
43. Roy, X.; Hui, J. K.-H.; Rabnawaz, M.; Liu, G.; MacLachlan, M. J. *Angew. Chem. Int. Ed.* **2011**, *50*, 1597–1602, Angew. Chem. **2011**, 123, 1635–1640.
44. Roy, X.; Hui, J. K.-H.; Rabnawaz, M.; Liu, G.; MacLachlan, M. J. *J. Am. Chem. Soc.* **2011**, *133*, 8420–8423.
45. Gimenez-Marques, M.; Luisa Garcia-Sanz de Larrea, M.; Coronado, E. *J. Mater. Chem. C* **2015**, *3*, 7946–7953.
46. Felix, G.; Nicolazzi, W.; Salmon, L.; Molnor, G.; Perrier, M.; Maurin, G.; Larionova, J.; Long, J.; Guari, Y.; Bousseksou, A. *Phys. Rev. Lett.* **2013**, *110*, 235701.
47. Galon-Mascarjs, J. R.; Coronado, E.; Forment-Aliaga, A.; Monrabal-Capilla, M.; Pinilla-Cienfuegos, E.; Ceolin, M. *Inorg. Chem.* **2010**, *49*, 5706–5714.
48. Raza, Y.; Volatron, F.; Moldovan, S.; Ersen, O.; Huc, V.; Martini, C.; Brisset, F.; Gloter, A.; Stephan, O.; Bousseksou, A.; Catala, L.; Mallah, T. *Chem. Commun.* **2011**, *47*, 11501–11503.
49. Volatron, F.; Catala, L.; RiviHre, E.; Gloter, A.; Stephan, O.; Mallah, T. *Inorg. Chem.* **2008**, *47*, 6584–6586.
50. Cobo, S.; Molnor, G.; Real, J. A.; Bousseksou, A. *Angew. Chem. Int. Ed.* **2006**, *45*, 5786–5789, *Angew. Chem.* **2006**, 118, 5918–5921.
51. Weber, B. *Chem. Eur. J.* **2017**, *23*, 18093–18100.
52. (a) Stock, N.; Biswas, S. *Chem. Rev.* **2012**, *112*, 933–969; (b) Cheong, V. F.; Moh, P. Y. *Mater. Sci. Technol.* **2018**, *34*, 1025–1045.
53. Blăniță, G.; et al. *Rev. Roum. Chim.* **2011**, *56*, 583–588.
54. Hayati, P.; Suárez-García, S.; Gutierrez, A.; Ruiz Molina, D.; Morsali, A.; Rezvani, A. R. *Ultrason. Sonochem.* **2018**, *42*, 320–326.
55. Yoo, Y.; Lai, Z.; Jeong, H. K. *Microporous Mesoporous Mater.* **2009**, *123*, 100–106.
56. Wang, S.; Lv, Y.; Yao, Y.; Yu, H.; Lu, G. *Inorg. Chem. Commun.* **2018**, *93*, 56–60.
57. Nordin, N. A. H. M.; Ismail, A. F.; Mustafa, A.; Goh, P. S.; Rana, D.; Matsuura, T. *RSC Adv.* **2014**, *4*, 33292–33300.
58. (a) Wang, S.; McGuirk, C. M.; Aquino, A.; Mason, J. A.; Mirkin, C. A. *Adv. Mater.* **2018**, *30*, 1800202; (b) Cravillon, J.; Nayuk, R.; Springer, S.; Feldhoff, A.; Huber, K.; Wiebcke, M. *Chem. Mater.* **2011**, *23*, 2130–2141.
59. Huang, L.; Wang, H.; Chen, J.; Wang, Z.; Sun, J.; Zhao, D.; Yan, Y. *Microporous Mesoporous Mater.* **2003**, *58*, 105–114.
60. Azad, F. N.; Ghaedi, M.; Dashtian, K.; Hajati, S.; Pezeshkpour, V. *Ultrason. Sonochem.* **2016**, *31*, 383–393.
61. Masoomi, M. Y.; Morsali, A.; Junk, P. C. *RSC Adv.* **2014**, *4*, 47894–47898.
62. Burgaz, E.; Erciyes, A.; Andac, M.; Andac, O. *Inorg. Chim. Acta* **2019**, *485*, 118–124.
63. Soofivand, F.; Mohandes, F.; Salavati-Niasari, M. *Mater. Res. Bull.* **2013**, *48*, 2084–2094.
64. Soofivand, F.; Salavati-Niasari, M.; Mohandes, F. *J. Ind. Eng. Chem.* **2014**, *20*, 3780–3788.
65. Noori, E.; Bazarganipour, M.; Salavati-Niasari, M.; Gholami, T. *J. Cluster Sci.* **2013**, *24*, 1171–1180.
66. Hayati, P.; Rezvani, A. R.; Morsali, A.; Retailleau, P. *Ultrason. Sonochem.* **2017**, *34*, 195–205.

67. Hayati, P.; Rezvani, A. R.; Morsali, A.; Retailleau, P.; García Granda, S. *Ultrason. Sonochem.* **2017**, *34*, 968–977.
68. Hayati, P.; et al. *Ultrason. Sonochem.* **2017**, *37*, 382–393.
69. Li, C. P.; Du, M. *Chem. Commun.* **2011**, *47*, 5958–5972.
70. Aboutorabi, L.; Morsali, A. *Ultrason. Sonochem.* **2011**, *18*, 407–411.
71. Carson, C. G.; Brown, A. J.; Sholl, D. S.; Nair, S. *Cryst. Growth Des.* **2011**, *11*, 4505–4510.
72. Pan, L.; Sander, M. B.; Huang, X.; Li, J.; Smith, M.; Bittner, E.; Bockrath, B.; Johnson, J. K. *J. Am. Chem. Soc.* **2004**, *126*, 1308–1309.
73. Zhou, B.; Xu, F.-C.; Yang, J.; Yao, J.; Xiao, Y.-H. *Mater. Lett.* **2013**, *107*, 206–209.
74. Marandi, F.; Hashemi, L.; Morsali, A.; Krautscheid, H. *Ultrason. Sonochem.* **2016**, *32*, 86–94.
75. Tahmasian, A.; Safarifard, V.; Morsali, A.; Joo, S. W. *Polyhedron* **2014**, *67*, 81–88.
76. Hashemi, L.; Morsali, A. *Ultrason. Sonochem.* **2015**, *24*, 146–149.
77. Safarifard, V.; Morsali, A. *Ultrason. Sonochem.* **2018**, *40*, 921–928.
78. Abdollahi, N.; Masoomi, M. Y.; Morsali, A.; Junk, P. C.; Wang, J. *Ultrason. Sonochem.* **2018**, *45*, 50–56.
79. Nouri, R.; Tahmasebi, E.; Morsali, A. *Mater. Chem. Phys.* **2017**, *198*, 310–316.
80. (a) Zhang, M.; Jia, J.; Huang, K.; Hou, X.; Zheng, C. *Chin. Chem. Lett.* **2018**, *29*, 456–460; (b) Novio, F.; Ruiz-Molina, D. *RSC Adv.* **2014**, *4*(29), 15293–15296.
81. Masoomi, M. Y.; Morsali, A. *Coord. Chem. Rev.* **2012**, *256*, 2921–2943.
82. Bigdeli, F.; Ghasempour, H.; Azhdari Tehrani, A.; Morsali, A.; Hosseini-Monfared, H. *Ultrason. Sonochem.* **2017**, *37*, 29–36.
83. Zhou, L.-J.; et al. *Sens. Actuators B* **2014**, *197*, 370–375.
84. Zou, X.; Wang, P.-P.; Li, C.; Zhao, J.; Wang, D.; Asefa, T.; Li, G.-D. *J. Mater. Chem. A* **2014**, *2*, 4682–4689.
85. Masoomi, M. Y.; Morsali, A.; Junk, P. C. *Ultrason. Sonochem.* **2017**, *34*, 984–992.
86. Mojtabazade, F.; Mirtamizdoust, B.; Morsali, A.; Talemi, P. *Ultrason. Sonochem.* **2018**, *42*, 134–140.
87. Hayati, P.; Suárez-García, S.; Gutierrez, A.; Şahin, E.; Ruiz Molina, D.; Morsali, A.; Rezvani, A. R. *Ultrason. Sonochem.* **2018**, *42*, 310–319.
88. Zare Karizi, F.; Beheshti, S.; Morsali, A. *Ultrason. Sonochem.* **2018**, *97*, 144–148.
89. Souri, B.; Hayati, P.; Rezvani, A. R.; Janczak, J. *Inorg. Chim. Acta* **2018**, *483*, 516–526.
90. Mirtamizdoust, B.; Trávníček, Z.; Hanifehpour, Y.; Talemi, P.; Hammud, H.; Joo, S. W. *Ultrason. Sonochem.* **2017**, *34*, 255–261.
91. Mohammadikish, M.; Ghanbari, S. *J. Solid State Chem.* **2018**, *264*, 86–90.
92. Alvaro, M.; Carbonell, E.; Ferrer, B.; Xamena, F. X. L.; Carcia, H. *Chem. Eur. J.* **2007**, *13*, 5106–5112.
93. Wang, C. K.; Xing, F. F.; Bai, Y. L.; Zhao, Y. M.; Li, M. X.; Zhu, S. R. *Cryst. Growth Des.* **2016**, *16*, 2277–2288.
94. Zhang, M.; Wang, L. W.; Zeng, T. Y.; Shang, Q. G.; Zhou, H.; Pan, Z. Q.; Cheng, Q. R. *Dalton Trans.* **2018**, *47*, 4251–4258.
95. Tabatabaei, N.; Dashtian, K.; Ghaedi, M.; Sabzehmeidani, M. M.; Ameri, E. *New J. Chem.* **2018**, *42*, 9720–9734.
96. Qian, L.-L.; et al. *Ultrason. Sonochem.* **2019**, *56*, 213–228.
97. Cui, J.-W.; Li, Y.-H.; Zhao, L.-Y.; Cui, G.-H. *Ultrason. Sonochem.* **2017**, *39*, 837–844.
98. Hao, S. Y.; Li, Y. H.; Zhu, J.; Cui, G. H. *Ultrason. Sonochem.* **2017**, *37*, 414–423.
99. Said, M. I.; Ibrahim, M. *Mater. Chem. Phys.* **2019**, *233*, 329–338.
100. Li, J.-X.; Qin, Z.-B.; Li, Y.-H.; Cui, G.-H. *Ultrason. Sonochem.* **2018**, *48*, 127–135.
101. Said, M. I.; El-Said, A. I.; Aly, A. A. M.; Abou-Taleb, A. *Ultrason. Sonochem.* **2018**, *46*, 68–78.
102. Joharian, M.; Morsali, A. *J. Solid State Chem.* **2019**, *270*, 135–146.

103. Moghzi, F.; Soleimannejad, J. *Ultrason. Sonochem.* **2018**, *42*, 193–200.
104. Zhang, X.; Hou, L.; Ciesielski, A.; Samorì, P. *Adv. Energy Mater.* **2016**, *6*, 1600671–1600691.
105. Mendoza-Sanchez, B.; Gogotsi, Y. *Adv. Mater.* **2016**, *28*, 6104–6135.
106. Li, W.; Sun, L.; Qi, J.; Jarillo-Herrero, P.; Dincă, M.; Li, J. *Chem. Sci.* **2017**, *8*, 2859–2867.
107. Clough, A. J.; Skelton, J. M.; Downes, C. A.; De la Rosa, A.; Yoo, J. W.; Walsh, A.; Melot, B. C.; Marinescu, S. C. *J. Am. Chem. Soc.* **2017**, *139*, 10863–10867.
108. Meng, Q.; Cai, K.; Chen, Y.; Chen, L. *Nano Energy* **2017**, *36*, 268–285.
109. Yao, H.; Zhang, F.; Zhang, G.; Luo, H.; Liu, L.; Shen, M.; Yang, Y. *Chem. Eng. J.* **2018**, *334*, 2547–2557.
110. Baeza, A.; Ruiz-Molina, D.; Vallet-Regí, M. *Expert Opin. Drug Deliv.* **2017**, *14*(6), 783–796.
111. Guo, M. Y.; Zhang, X.; Zhao, L.; Li, Y. K.; Chen, D. Y.; Yang, G. W.; Li, Q. Y. *J. Solid State Chem.* **2018**, *259*, 104.
112. Wang, P.; Hou, Q.-Q.; Cui, X.-L.; You, G.-D. *J. Mol. Struct.* **2019**, *1193*, 62–68.
113. Jin, C.; Bigdeli, F.; Jin, Z.-M.; Xie, Y.-R.; Hu, M.-L.; Morsali, A. *Ultrason. Sonochem.* **2017**, *39*, 420–429.
114. Hanifehpour, Y.; Morsali, A.; Mirtamizdoust, B.; Joo, S. W.; Soltani, B. *Ultrason. Sonochem.* **2017**, *37*, 430–435.
115. Afzalian Mend, B.; Delavar, M.; Darroudi, M. *J. Mol. Struct.* **2017**, *1134*, 599–605.
116. Suárez-García, S.; et al. *ACS Appl. Mater. Interfaces* **2018**, *10*(45), 38819–38832.
117. Adarsh, N. N.; et al. *Chem. Eng. J.* **2018**, *340*, 94–102.
118. Hu, Y.; et al. *Nano Lett.* **2019**, *19*(4), 2731–2738.
119. Ni, K.; et al. *Angew. Chem. Int. Ed.* **2020**, *59*(3), 1108–1112.

CHAPTER THREE

The role of defects in the properties of functional coordination polymers

Celia Castillo-Blas[a], Carmen Montoro[a], Ana E. Platero-Prats[a], Pablo Ares[b], Pilar Amo-Ochoa[a], Javier Conesa[a], Félix Zamora[a,*]

[a]Departamento de Química Inorgánica, Facultad de Ciencias, Universidad Autónoma de Madrid, Madrid, Spain
[b]Department of Physics & Astronomy and National Graphene Institute, University of Manchester, Manchester, United Kingdom
*Corresponding author: e-mail address: felix.zamora@uam.es

Contents

Abstract

Coordination Polymers (CPs) are periodic architectures defined by the assembly of metal entities and ligands through coordination bonds. They can be designed to present porous architectures, known as Metal-Organic Frameworks (MOFs). They can be prepared as bulk materials and at the nanoscale using bottom-up synthesis or top-down approaches.

Nanoscale CPs are a subject of high current interest due to the new physico-chemical properties that they can show because of confinement effects as well as their material process-ability. We present several selected CP samples with different electronic properties, electrical conductivity and/or emission, as well as ways to down-size their scale to obtain CP nanostructures. Studies on their physical properties at the nanoscale show the relevance of the confinement effects and the presence of defects, which can

Advances in Inorganic Chemistry, Volume 76
ISSN 0898-8838
https://doi.org/10.1016/bs.adioch.2020.03.002

be controlled during the preparation process. Indeed, defect engineering is an extremely relevant tool to manipulate the material crystal quality and its specific properties. Therefore, engineered defects are gaining attention in both CPs and their porous version, MOFs, because of their implications for both physical properties and properties affecting catalysis and sorption. However, this is still a very poorly developed field.

The main scope of this chapter is to provide a general overview of the impact that defects may have on the chemical, physical, electrical and/or optical properties, as well as in catalysis and sorption capabilities of some CPs, and the way to gain control of the defect production. We have selected two relevant types of 1D CP families, MMX and Cu_2I_2 double chains, to discuss their electronic properties and the influence that the incorporation of defects has on them.

MMX chains based on the assembly of two dimetallic entities: $[Pt_2(dta)_4]$ (*dta* = ditiocarboxylate) and $[Pt_2(dta)_4I_2]$, behave as metallic conductors at room temperature in bulk and at the nanoscale, but the weakness of the Pt—I coordination bonds facilitates the occurrence of defects such as iodine vacancies, which significantly alter their conductivity. Their preparation at the nanoscale is feasible based on the reversible process between $[Pt_2(dta)_4]$ and $[Pt_2(dta)_4I_2]$. Thus, the polymer $[Pt_2(dta)_4I_2]_n$ can be solubilized or sublimated to produce $[Pt_2(dta)_4]$ and $[Pt_2(dta)_4I_2]$ and rearrange back to $[Pt_2(dta)_4I_2]_n$ even on-surfaces. The exquisite control of the assembling process gives rise to a number of structural defects present along the MMX chains. In any case, electrical measurements in single chains of $[Pt_2(dta)_4I_2]_n$ currently postulated these CPs among the best molecular wires.

We also describe several examples of Cu_2I_2 double chains grafted with N-aromatic terminal ligands. They show interesting electronic properties as emission and semiconductivity. The general structural core of these 1D-CPs is based on a Cu_2I_2 double chain which is very sensitive to chemical and physical stimuli. We discuss the use of these CPs as stimuli-response materials, their bottom-up preparation using fast precipitation and the use of these nanostructures to prepare novel composites as multifunctional ultra-thin films. Moreover, we also show the possibility of modulating their physical properties upon the creation of structural defects.

Finally, we describe different synthetic pathways (pre- and post-synthesis) to harness the incorporation of both local- and long-range defects in MOFs, resulting in altered chemistry and structures without compromising the porous scaffold. The role of defects in MOF properties related to catalysis, sorption and conductivity is widely discussed in this chapter, highlighting the importance of using advanced scanning probe microscopy, synchrotron X-rays and neutron techniques to achieve a better understanding of these functional nanomaterials.

1. Introduction

Whenever we initially attempt to perform a new preparation of a novel coordination polymer (CP), we try to find the suitable experimental conditions to get a single crystal in order to obtain (*i*) a highly crystalline

material with the designed properties that we expect based on its structure, and (*ii*) to solve its atomic structure by X-ray diffraction techniques. In that way we try to gain knowledge to establish a relationship between the material structure and their properties. However, despite this is a rational strategy, this scenario can become more complex when some structural defects are present in the material. Indeed, it is well-known that structural defects can play a fundamental role in determining the physical properties, such as luminescence, magnetism or conductivity,[1] but also catalysis and adsorption.[2] The variety of defects is large in nature and length scales, but they can be classified according to their dimensionality in different groups.

Point defects involve single atoms and are the most common defects. Vacancies (Fig. 1A) are the most frequent, since they are present in all solids. They are produced when an atom is absent from its periodic position. According to thermodynamics, the presence of vacancies in a solid increases its entropy, therefore improving its stability.

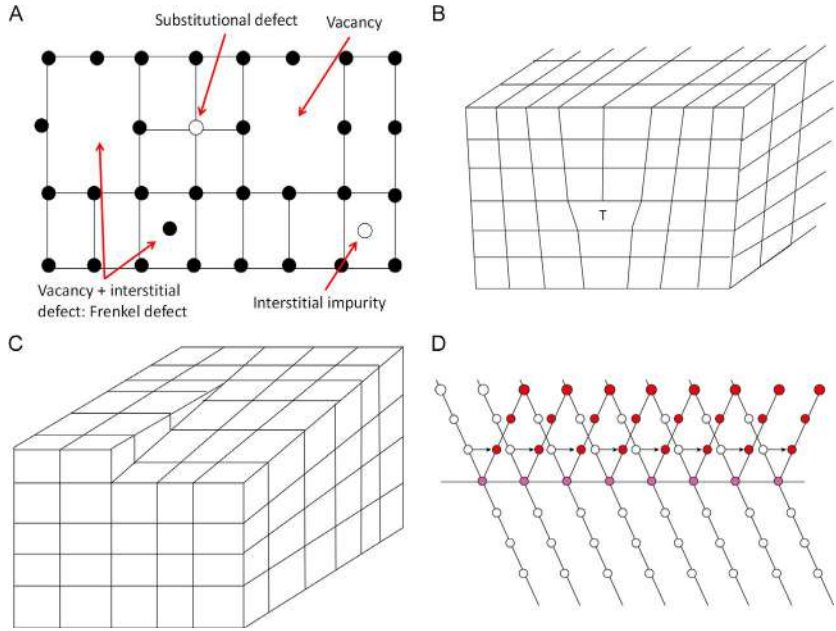

Fig. 1 Summary of structural defects present in a material. (A) Schematic representation of point defects. (B) Schematic representation of an edge dislocation. The "T" marks the spot where this defect takes its origin. (C) Schematic representation of a screw dislocation. (D) Schematic representation of a twin defect. The twin plane is depicted as the horizontal line.

Interstitial defects (Fig. 1A) involve the presence of an atom in a hole or interstitial position of the crystal lattice. Since the atom located at the interstice can be substantially larger than the site, it generates important distortions in the surrounding lattice. Consequently, interstitial defects are less common than vacancies. A Frenkel defect (Fig. 1A), the displacement of an atom from its periodic position to the interstitial site is also feasible, therefore generating a vacancy as well. This combination of an interstitial defect and a vacancy is predominant in ionic materials.

Substitutions (Fig. 1A) are produced when an atom in the crystal lattice is substituted by a different one, frequently named as an impurity. In ionic materials, the electric charge of the impurity can modify the structure of the material in different ways. If its charge is equivalent to that of the ion replaced, the lattice remains unaltered, unless the size of the impurity is 15% higher or lower (this would produce distortions in the lattice similarly as interstitial defects).

Together with point defects, dislocations (Fig. 1B and C) are an important subgroup of defects. They are produced when a row of atoms in the crystal lattice is missing, producing a lack of stacking which originates a misalignment of the adjacent atoms. This defect produces significant distortions in the periodicity of the crystal close to the dislocation line. Depending on the nature of the dislocations, they can be divided into two groups: edge dislocations and screw dislocations. But in some cases, they can be found together within the structure of a material. Edge dislocations are characterized to be centered around the dislocation line. Then, away from the place where the dislocation is created, the crystal lattice structure becomes periodic again (Fig. 1B). Screw dislocations are formed by the effect of shear stresses such as those generated by grinding processes. These defects cause the dislocation of a row of atoms from one position to the adjacent site, giving rise to a helical path around the dislocation line (Fig. 1C).

Another important group of defects are named as two-dimensional defects or surface defects or interfacial defects. They produce the separation of different regions of a material with different crystal structures or orientations, the so-called domains. They are sub-divided in two important groups: (*i*) twin planes which are formed at the frontier of two crystalline domains through a mirror symmetry plane (Fig. 1D). However, due to their nature, they can be considered as a special case of grain boundary. Typically, twin defects are produced by shear forces or during annealing processes; and (*ii*) grain boundaries are two-dimensional limits, which separate two crystalline

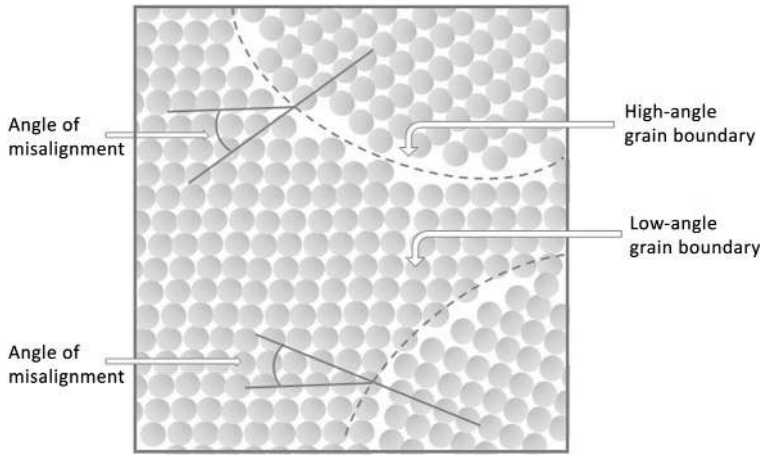

Fig. 2 Schematic representation of grain boundaries.

domains of a material, independent of their orientation. The difference in orientation of the crystal structure between the two domains produces an atomic mismatch (Fig. 2).

Apart from surface defects, twin planes and grain boundaries, external surfaces, where the atoms at those edges have some unoccupied bonding sites, also called "unsaturation" are another type of defect to be considered, mainly when the material reduces its size entering the nanoscale, where these defects are located.

Finally, bulk defects are also found in solid materials. Typically, they are present in a much larger amount than those discussed above. Bulk defects involve cracks, pores, foreign inclusions, and the presence of different phases in the same material. They are produced during material fabrication and/or processing steps.

As we have already mentioned, the presence of defects in a solid material can be very relevant in defining its physico-chemical properties. Therefore, the production of specific defects is a field of high research interest. Thus, for instance, controlled doping of a material using different synthetic conditions has been explored to modify its optical properties.[3,4] Typically, the dopant species represent between 1% and 20%, giving rise to significant changes in the material structure and morphology. This amount of defects is considered high and can be studied by using conventional structural characterization techniques.[5]

Currently, defect engineering is extremely relevant to manipulate crystal quality and the specific properties of a material. However, the study of

structural defects still remains very intricate, in particular for low dimensional defects present in low concentrations, where the usual spectroscopic and diffractometric techniques do not provide information.[6]

Therefore, engineered defects are gaining attention in both CPs and their porous version, MOFs, because of their implications in both physical properties modification and properties affecting catalysis and sorption.[7] However, this is still a very poorly developed field. The main scope of this chapter is to provide a general overview of the impact that defects may have on the chemical, physical, electrical and/or optical properties, as well as catalysis and sorption capabilities, of some CPs and the way to gain control of defect production.

2. Low dimensional nanoscale coordination polymers

2.1 Introduction

One-dimensional (1D) nanostructures are those with a dimension within the range between 1 and 100 nm. The morphologies, composition and structures cover a large variety including wires, rods, tubes, ribbons of metal/semimetals, oxides, sulfides, halides, *etc.* The physical properties of one-dimensional structures have pointed these materials toward many potential applications from ultrasensitive sensors to nano-(opto)-electronics, as well as nanomaterials useful in drug-delivery or biological systems.[8] During the last decade, CPs have become a new source of 1D nanomaterials.

The incorporation of CPs to generate nanostructures is of high interest because: (*i*) these materials are chemically designable based on the selection of their building blocks, which allows a great structural variety; and (*ii*) their physico-chemical properties are tunable based on their structure and composition.

As for the rest of nanomaterials, the general approaches for 1D nanostructure preparation follow two main routes: *top-down* and *bottom-up* strategies.

Top-down approaches are based on the use of different external sources of energy to break-down the initial macro-scale morphology of a given material to get into the nanoscale. This miniaturization process can involve expensive photolithography, as in the well-known case of silicon transistor fabrication, or less expensive methods such as ultra-sonication or ball-milling. On the other hand, *bottom-up* approaches are based on the self-assembly of molecules using either chemical bonds or molecular interactions. Therefore, the concept of *bottom-up* methods comes from the ability of specific

molecules to self-organize and generate larger entities such as supramolecules or polymers, this idea resembles the way nucleic acids work in nature. However, the predictable self-assembly of molecular subunits to produce specific architectures is still a major challenge for chemists.[9] Indeed, CPs are infinite aggregates of metal ions or fragments linked by ligands, where they self-assemble in one, two or three dimensions, producing a large variety of structures.[10,11] Selection of the molecular building blocks is the fundamental key to design a specific architecture of a CP and also largely determines its physico-chemical properties.[12,13] Research on CPs has increased exponentially because their functional properties including magnetism, chromism, non-linear optical, redox and electrical conduction,[10,14] among porous CPs and MOFs, which in addition incorporate gas/molecule storage and separation. Nevertheless, despite the huge number of CPs that have been studied in the bulk, the amount of studies focused on CPs at the nanoscale is still limited.[15–17] The key limitation is possibly a consequence of their limited process ability, because of their lack of solubility, rapid degradation in solution as well as decomposition upon heating. But in recent years, reports on 1D and 2D CPs at the nanoscale are increasing as new preparation methods have been incorporated.[17]

2.2 Electrically conductive MMX chains: The influence of structural defects

There is an intense research activity focused on the miniaturization of electrical circuits. This has pushed in recent years the field of molecular electronics, where molecular building blocks are used to fabricate electronic components. Beyond miniaturization, this approach takes advantage of the molecular self-assembly capabilities, allowing the fabrication of complex architectures from a bottom-up strategy. Electronic devices are made up of different components, namely resistors, diodes, transistors, *etc.* Their functioning is essential for the optimization of such devices, including faster and lower power consumption performances, which has countless implications for both fundamental research and everyday life. Currently, there are high expectations for the incorporation of new nanomaterials with promising applications and novel circuit architectures,[18] thus work in understanding their properties is among the most active research areas.

Among the essential components in an electronic device are the wires that interconnect the rest of the device elements. A molecular wire must fulfill two main requirements: it should allow currents with a reasonably low resistance and it should have structuring capabilities. For instance, carbon

nanotubes and DNA chains are examples of molecular wire candidates that just fulfill one of the conditions: on the one hand, while carbon nanotubes are excellent conductors, they lack self-assembly capabilities. The opposite is true of DNA chains, which can easily form complex structures, but their electrical conductivity is not high enough. Up to date, there are few molecular systems that fulfill both requirements.[19–22] These compounds comprise a particular type of CPs based on coordinate bonds between metal ions and organic ligands. In particular, MMX metal–organic polymers, which are those with quasi-1D sequences of single halide atoms (X) bridging subunits with two metal ions (MM) connected by organic ligands (Fig. 3), have been predicted by density functional theory (DFT) to have a metallic band structure,[23] with a spin-degenerate half-filled band crossing the Fermi level along the chain axis. They have shown indeed excellent experimental electrical transport properties both in terms of current densities and long distances.[19,20,22] Nevertheless, the experimental results always present higher resistances than those predicted by theory. This is not surprising, as the single-particle DFT description does not take into account effects such as the electrode-chain contact resistance, scattering with the substrate, electron–phonon interactions, or, importantly, the presence of defects along the chains.

Highly conductive Pt-based MMX nanostructures of the CPs $[Pt_2(dta)_4I]_n$ (*dta* = dithiocarboxylate, alkyl groups) have been produced on insulating substrates thanks to their exceptional reversible depolymerization/repolymerization following two different strategies: (*i*) direct sublimation of polymer crystals, which has been shown to be a suitable procedure to obtain robust CP nanoribbons 5–25 nm high, 100–200 nm wide and several μm long;[20,22] (Fig. 4A) and (*ii*) drop-casting a solution of CP monocrystals, obtaining MMX fibers from 20 to 100 nm high and μm long, down to the single molecule regime with lengths of hundreds of nm[19,24] (Fig. 4B).

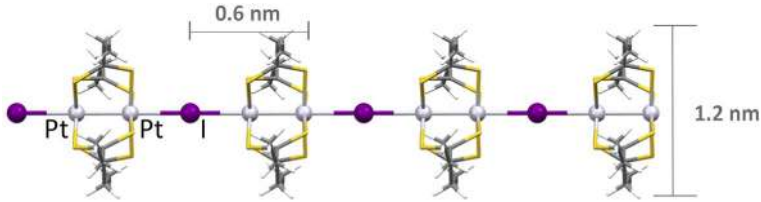

Fig. 3 Schematic representation of the crystal structure of a $[Pt_2(EtCS_2)_4I]_n$ (Et = CH_2—CH_3) chain. *Adapted from Ares, P.; Amo-Ochoa, P.; Soler, J. M.; Palacios, J. J.; Gomez-Herrero, J.; Zamora, F.* Adv. Mater. ***2018,*** 30 *(21), 1705645 © 2018 John Wiley and Sons.*

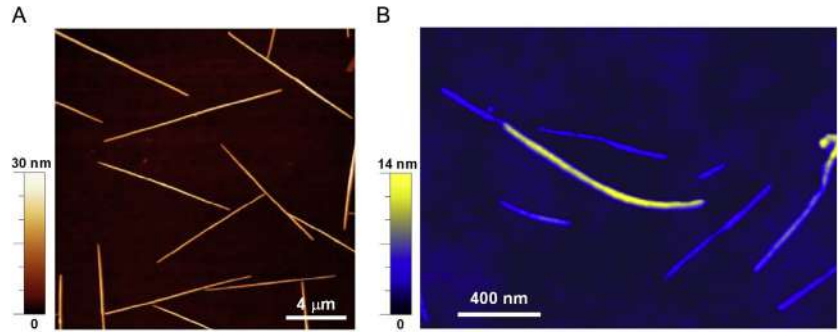

Fig. 4 AFM images of CP nanoribbons and fibers of Pt-based MMX polymers. (A) Nanoribbons obtained by direct crystal sublimation. (B) Fibers obtained from drop-casting a dichloromethane solution of MMX crystals. *Adapted from Ares, P.; Amo-Ochoa, P.; Soler, J. M.; Palacios, J. J.; Gomez-Herrero, J.; Zamora, F.* Adv. Mater. ***2018,*** 30 *(21), 1705645 © 2018 John Wiley and Sons and Hermosa, C.; Vicente Alvarez, J.; Azani, M.-R.; Gomez-Garcia, C. J.; Fritz, M.; Soler, J. M.; Gomez-Herrero, J.; Gomez-Navarro, C.; Zamora, F.* Nat. Commun. ***2013,*** 4, *1709 © 2013 Springer Nature.*

The electrical transport properties of these nanoribbons and fibers were characterized using conductive atomic force microscopy (C-AFM). A macroscopic metal electrode is deposited on the substrate with the nanostructures and AFM was used to find nanoribbons and fibers partially covered by this electrode. Then, a conductive AFM tip was used as a second mobile electrode to contact the uncovered part of the MMX nanostructures (Fig. 5A).

In the case of the sublimated nanoribbons, metallic current *vs.* voltage (*IV*) curves have been observed (Fig. 5B), with current densities up to $\sim 10^4$ A cm^{-2}.[20,22] However, a non-linear dependence of the resistance *vs.* length *R(L)* was observed (Fig. 5C), suggesting that the presence of defects is the main source of resistance. A simple model of CP chains connected in parallel with a random configuration of defects (vacancies of either iodine atoms or dimetallic subunits[25]) interrupting the current through a single molecular chain, explains the observed behavior, and yields a concentration of defects up to ~1% with a characteristic length of ~200 nm (mean distance between defects). For distances higher than this characteristic length, the CP chains have at least one defect. Thus, electrical transport perpendicular to the CP chains becomes determinant, leading to diffusive transport.

In the case of the drop-casted fibers, it has been possible to probe the electrical transport properties at the single molecule level (from one/two individual CP chains).[19] On the one hand, the drop-casting approach

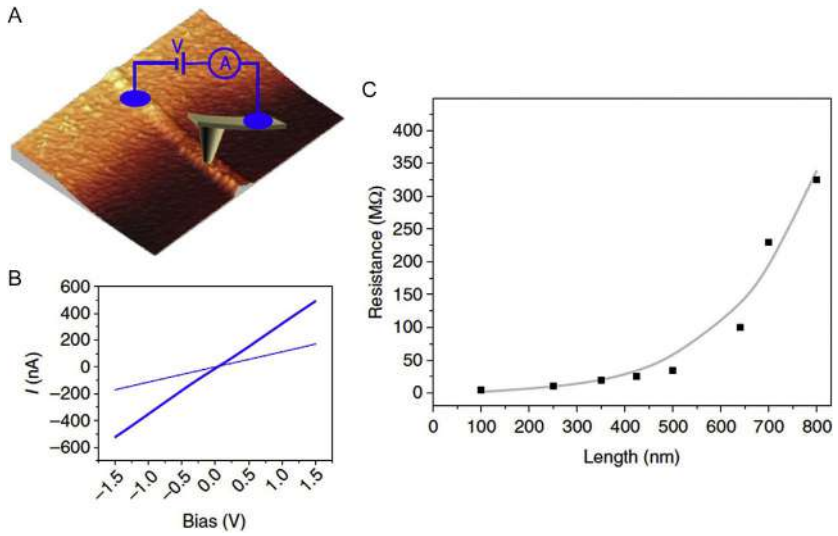

Fig. 5 Electrical characterization of sublimated MMX nanoribbons by C-AFM. (A) Schematic of the setup used to probe the electrical properties of the nanoribbons. (B) *IV* curves on the same nanoribbon at different distances from the fixed gold electrode. (C) *R(L)* for the same nanoribbon as in (B). The black dots correspond to experimental measurements and the gray line is a fit to an exponential function. *Adapted from Hermosa, C.; Vicente Alvarez, J.; Azani, M.-R.; Gomez-Garcia, C. J.; Fritz, M.; Soler, J. M.; Gomez-Herrero, J.; Gomez-Navarro, C.; Zamora, F.* Nat. Commun. ***2013,*** 4, *1709 © 2013 Springer Nature.*

presents some advantages over sublimation, such as better process ability and chemical functionalization, but on the other hand, chains assembled this way might be more prone to the presence of defects. C-AFM characterization of one/two individual CP chains (Fig. 6A) showed a current density of $\sim 10^5$ A cm^{-2} and a characteristic length of ~20 nm, with remarkable currents up to distances beyond 250 nm, surpassing that of all other molecular wires reported so far. The *R(L)* (Fig. 6B) presents again an exponential dependence, pointing to defects as the main source of resistance. This similar behavior has been observed in carbon nanotubes,[26] and was attributed to Anderson localization caused by the interaction of electrons with structural defects. To verify this conjecture, quantum transport calculations were carried out at two levels of sophistication. First the quantum conductance for a single defect in an otherwise perfect MMX wire was computed, considering the most feasible defects (a kink, an OH molecule substituting an iodine atom and an iodine vacancy, Fig. 6C). It was observed that the iodine vacancy was the defect having the largest electron transmission reduction.

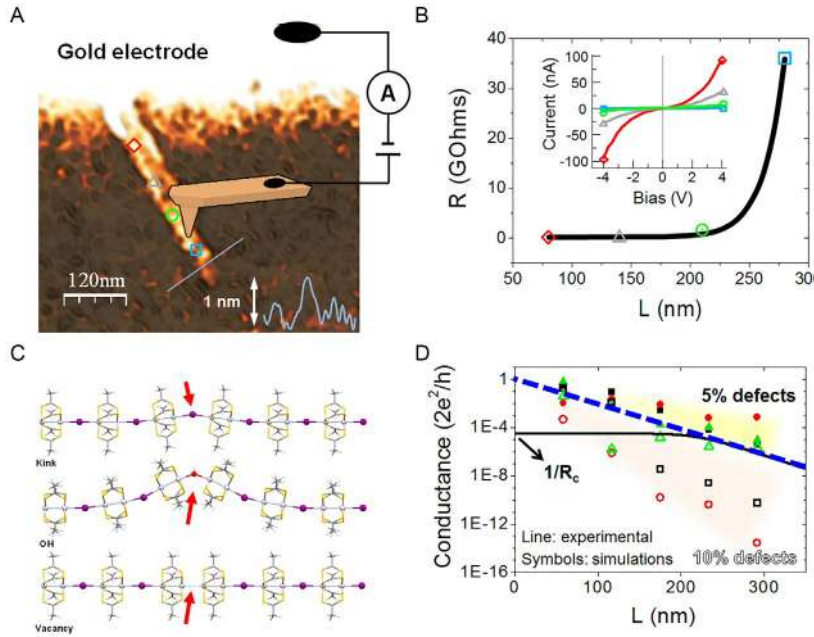

Fig. 6 Electrical characterization of drop-casted MMX fibers down to the single molecule regime by C-AFM. (A) Schematic of the setup used to probe the electrical properties of the fibers. The inset shows the height profile along the solid blue line. (B) *R(L)* for the same one/two fibers shown in (A). The black line is a fit to an exponential function. The inset shows the *IV* curves acquired at different distances from the fixed gold electrode according to the colored symbols along the chains marked in (A). (C) Schematic relaxed structures of three types of defects considered for DFT simulations (red arrows indicate the structural defect). (D) Conductance obtained for different disorder realizations at a 5% (filled symbols) and 10% (empty symbols) concentration of vacancies (black squares, red circles, and green triangles correspond to each of these realizations) in a single-orbital tight-binding model. The black line corresponds to the experimental result and the blue dashed line to an extrapolation of the measured conductance assuming absence of experimental contact resistance. *Reprinted with permission from Ares, P.; Amo-Ochoa, P.; Soler, J. M.; Palacios, J. J.; Gomez-Herrero, J.; Zamora, F.* Adv. Mater. ***2018,*** 30 *(21), 1705645 © 2018 John Wiley and Sons.*

Thus, the conductance for hundreds of nm MMX chains with many vacancy defects was calculated using a single-orbital tight-binding model. Fig. 6D shows the results for two different concentrations of defects at random positions along different chains. The conductance follows an exponential decay with wire length, in agreement with the experiments, yielding a percentage of vacancies in the range 6–8%, compatible with the results observed in the sublimated nanoribbons.

These studies have shown the influence of defects in molecular electronics and that, despite their effect on the electrical conductance, CPs are one of the best options for long distance molecular wires, as they present a good balance between possible functionalization and long-range transport.

2.3 Multi-stimuli-response copper(I)-halide chains

Among CPs a sub-family integrated by compounds formed by a common structural motif arises: the copper(I)-halide chain. These CPs, with general formula $[CuXL]_n$ (where X^- is an halide and L is an organic ligand, usually N-donor or S-donor), were discovered about a century ago,[27] but in the last 40 years they have attracted the attention of the scientific community due to their interest from the point of view of crystal engineering[28–34] and their outstanding optical properties.[35–39] In fact, thanks to these optical properties, some Cu(I)-I clusters have been proposed to act as OLEDs (Organic Light-Emitting Diodes).[40,41]

Cu(I)-X CPs are mostly recognized by the great flexibility of their chains, which makes them very sensitive to physical stimuli, such as temperature or pressure,[37,42–46] or chemical ones, meaning vapors of certain molecules.[47–50] Therefore, these CPs have been proposed to act as sensors, thus reaching fields such as aerospace[51,52] or food and packaging industries.[53–55] This, apart from the advances in nano-processing methods,[56] is why the preparation of nanostructures of these compounds has started to draw attention.

2.3.1 Nanoscale Cu(I)-I CPs

Most Cu(I)-I CPs present a feature which involves a crucial difference with respect to other coordination polymers: their reversibility in solution, with the concomitant facility to process them in this state.[57] With this in mind, it is not preposterous to think that these CPs will be excellent candidates to be subjected to nano-processing procedures. However, the first studies on the nano-processing of Cu(I)-X CPs arose in 2008 and the following years. These studies were focused on CPs with high insolubility, and therefore the nanostructures had to be obtained *via* top-down strategies such as liquid-phase exfoliation.[58,59] However, the discovery of reversible CPs changed the way to obtain these CPs, switching to bottom-up processes starting from an acetonitrile solution of the initial building blocks.

These studies started in 2016, when Troyano *et al.*[60] discovered CPs with Cu(I) or Ag(I) centers and thiobenzoate (TB) as linker. The Ag(I) CP, namely $[AgTB]_n$, was subjected to a liquid-liquid interface synthesis starting

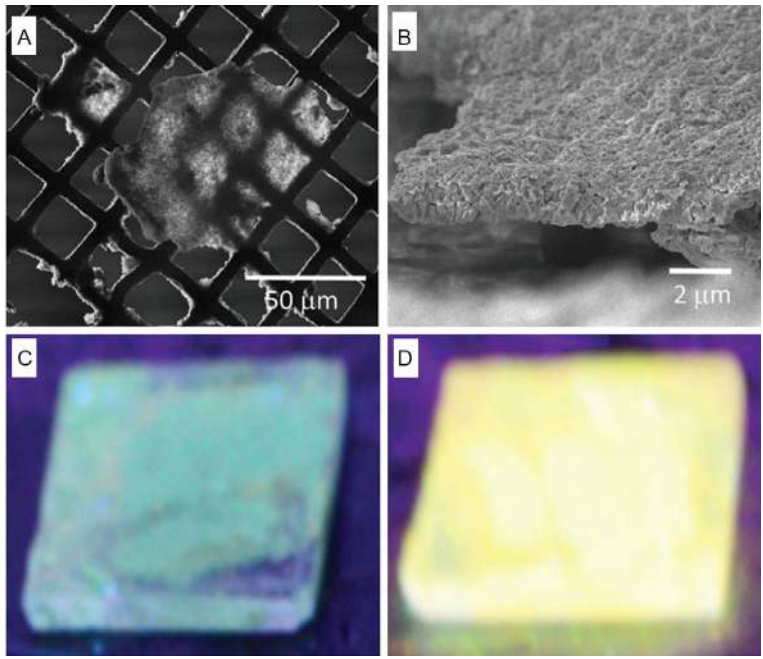

Fig. 7 (A and B) FE-SEM images of $[AgTB]_n$ (TB = thiobenzoate) films: (A) upper view of a thin film deposited on a copper TEM grid; (B) lateral view of the same thin film. (C and D) Luminescent properties of free-standing $[AgTB]_n$ thin films: emission at 298 K (C) and at 77 K (D). *Adapted from Troyano, J.; Castillo, Ó.; Amo-Ochoa, P.; Fernández-Moreira, V.; Gómez-García, C. J.; Zamora, F.; Delgado, S.* J. Mater. Chem. C ***2016,*** 4 *(36), 8545-8551 with permission from Royal Society of Chemistry.*

from a solution of thiobenzoic acid in *n*-pentane and an aqueous solution of $AgNO_3$. After 10 min of slow diffusion of the reactants, a free-standing film was collected by the Langmuir-Schaeffer process. SEM images of these films (Fig. 7A and B) show how they are formed by aggregates of disc-shaped crystalline particles of $[AgTB]_n$, reaching thicknesses of 1–2 μm. These films also proved to show a luminescent thermochromic behavior, identical to that of the bulk compound: at room temperature, they display a weak blue luminescence, whereas at 77 K the emission changes to a bright yellow color reversibly, returning to the original emission as the temperature increases.

More recently, in 2017, similar studies performed on CPs based on double *zig-zag* Cu(I)-I chains arose. In these cases, the insolubility of the CPs in the reaction medium and their extreme facility to crystallize allow the immediate formation of nanostructures which can be easily isolated by simple centrifugation processes.

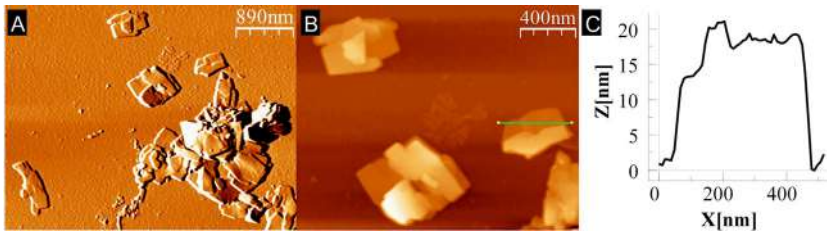

Fig. 8 (A) AFM image of $[Cu_2I_2(Apyz)]_n$ nanosheets on SiO_2. (B) A zoomed area of (A), the upper central part. (C) A typical height profile of a nanosheet across the green line represented in (B). *Reprinted with permission from Conesa-Egea, J.; Gallardo-Martinez, J.; Delgado, S.; Martinez, J. I.; Gonzalez-Platas, J.; Fernandez-Moreira, V.; Rodriguez-Mendoza, U. R.; Ocon, P.; Zamora, F.; Amo-Ochoa, P.* Small ***2017,*** 13*(33), 1700965–1700976 © 2017 John Wiley and Sons.*

The first of these CPs to be nano-processed was a 2D CP with aminopyrazine (Apyz) as linker between the Cu_2I_2 chains, namely $[Cu_2I_2(Apyz)]_n$.[61] A simple magnetic stirring process during the synthesis of the CP allowed the immediate formation of nanosheets with thicknesses of 20 nm (Fig. 8). The thermochromic properties of these nanosheets were evaluated on aggregates with thicknesses above 100 nm by confocal microscopy (Fig. 9). Herein we could observe how the nanosheets experienced a reversible increase in their luminescence intensity in the region between 550 and 600 nm (their emission maximum is 560 nm) at 77 K.

Following this basis, the 1D compounds $[Cu(MeIN)I]_n$ and $[Cu(NH_2\text{-}MeIN)I]_n$, where MeIN is methyl isonicotinate and NH_2-MeIN is methyl 2-aminoisonicotinate, were subjected to the same synthetic method (room temperature and magnetic stirring), obtaining nanofibers of these CPs. These fibers showed thicknesses of 50–500 nm in the case of $[Cu(MeIN)I]_n$, and down to 5 nm for $[Cu(NH_2\text{-}MeIN)I]_n$ (Fig. 10). These CPs also showed a luminescent thermochromic behavior, but this property suffers slight variations when it is measured in microcrystals or nanofibers (Fig. 11).[62]

2.3.2 Cu(I)-I CPs as dopants in composite thin films

Nanoscale Cu(I)-I CPs present one disadvantage although they can be used as-synthesized, they do not present good mechanical properties, so this hampers their use. In order to solve this problem, they can be used as dopants in composite materials, in a way that they can keep the properties which make them functional, and at the same time take advantage of the mechanical resistance of the matrix.

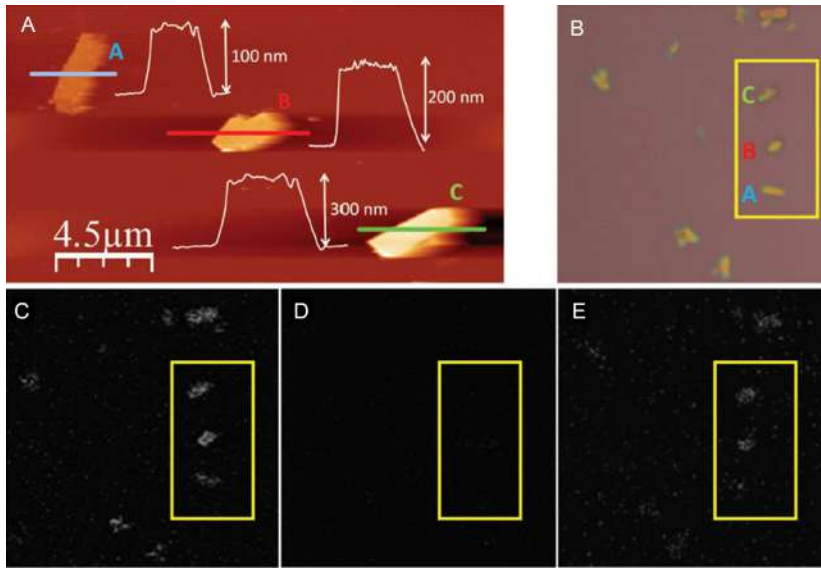

Fig. 9 (A) Topographic AFM image of $[Cu_2I_2(Apyz)]_n$ nanosheets deposited on an SiO_2 substrate and their height profiles, named as A–C. (B) Optical microscope image of the $[Cu_2I_2(Apyz)]_n$ nanosheets (A–C) in (a) at 298 K. (C) Confocal microscopy image of $[Cu_2I_2(Apyz)]_n$ nanosheets (A–C) at 80 K. (D) Confocal microscopy image of $[Cu_2I_2(Apyz)]_n$ nanosheets (A–C) at 300 K (same area as in C). (E) Confocal microscopy image of $[Cu_2I_2(Apyz)]_n$ nanosheets (A–C) 7 min after being at 80 K (same area as in D). *Reprinted with permission from Conesa-Egea, J.; Gallardo-Martinez, J.; Delgado, S.; Martinez, J. I.; Gonzalez-Platas, J.; Fernandez-Moreira, V.; Rodriguez-Mendoza, U. R.; Ocon, P.; Zamora, F.; Amo-Ochoa, P.* Small ***2017,*** 13*(33), 1700965–1700976 © 2017 John Wiley and Sons.*

Organic polymers such as polymethyl methacrylate (PMMA), polyvinylidene difluoride (PVDF) or polylactic acid (PLA), with good flexibility and transparency, are preferred to act as matrices in composites containing CPs, known as mixed-matrix membranes (MMMs). The former two are typically used with MOFs.[29,63–65] But recent studies carried out in 2018 and 2019 showed that non-porous CPs with copper(I) as metal center could easily be combined with these organic matrices.

Examples of these MMMs are micro-sheets made from PVDF and CPs with S-donor ligands,[66] originating from a mixture of a PVDF solution and nanostructures of these CPs (Fig. 12). Similar results were obtained by mixing a PVDF solution with $[Cu(NH_2\text{-MeIN})I]_n$ nanofibers, but this time the use of dip-coating or spin-coating deposition methods led to the formation of composite thin films with nanometer dimensions.[62] Similar results were obtained by mixing PLA with $[Cu_2I_2(Apyz)]_n$ (Fig. 13).[67]

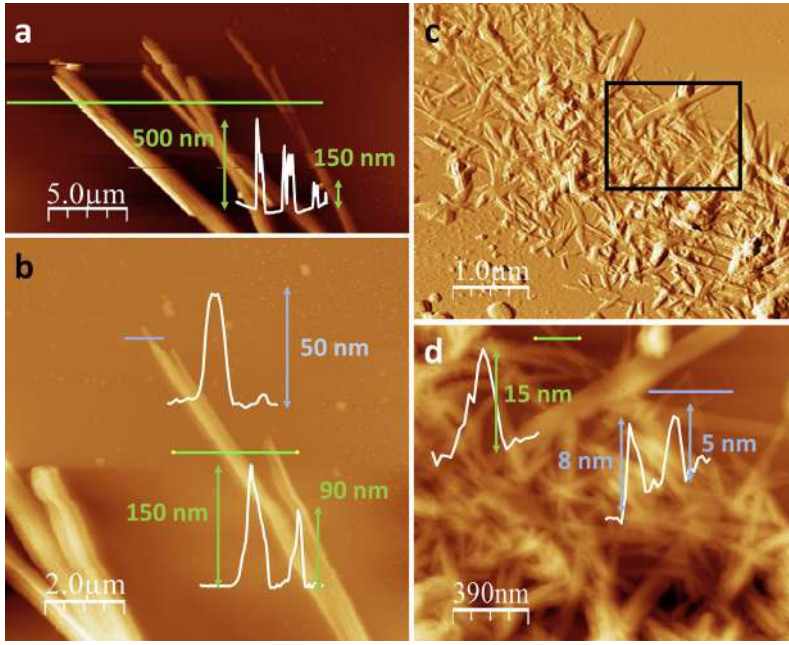

Fig. 10 (A) AFM image of $[Cu(MeIN)I]_n$ nano- and sub-microfibers on SiO_2 prepared by drop casting, with their height profile across the green line. (B) A zoomed area of (A), with its height profiles across the blue and green lines. (C) AFM image of $[Cu(NH_2\text{-}MeIN)I]_n$ nanofibers on SiO_2 prepared by dip-coating. (D) A zoomed area of (C), the black rectangle, with height profiles across the green and blue lines. *Reprinted from Conesa-Egea, J.; Nogal, N.; Martinez, J. I.; Fernandez-Moreira, V.; Rodriguez-Mendoza, U. R.; Gonzalez-Platas, J.; Gomez-Garcia, C. J.; Delgado, S.; Zamora, F.; Amo-Ochoa, P.* Chem. Sci. ***2018,*** 9 *(41), 8000–8010 with permission from Royal Society of Chemistry.*

2.3.3 Point defects and its effect in the optical properties of Cu(I)-I chains

As mentioned in the introduction, many properties of the materials are determined by the presence of defects. In fact, there are studies showing that volume, surface and point defects dramatically modify the physical and chemical properties of materials.[2,6,68]

Thus, the generation of specific defects through controlled doping has already been reported. In most of these investigations, the dopant species represent *ca.* 1–20%, this defect content provokes significant changes in the structure and morphology of the materials that can be studied by conventional characterization techniques. Despite the enormous interest in studying and controlling the generation of defects in order to have control over the properties of materials, these types of studies are still rare due to the

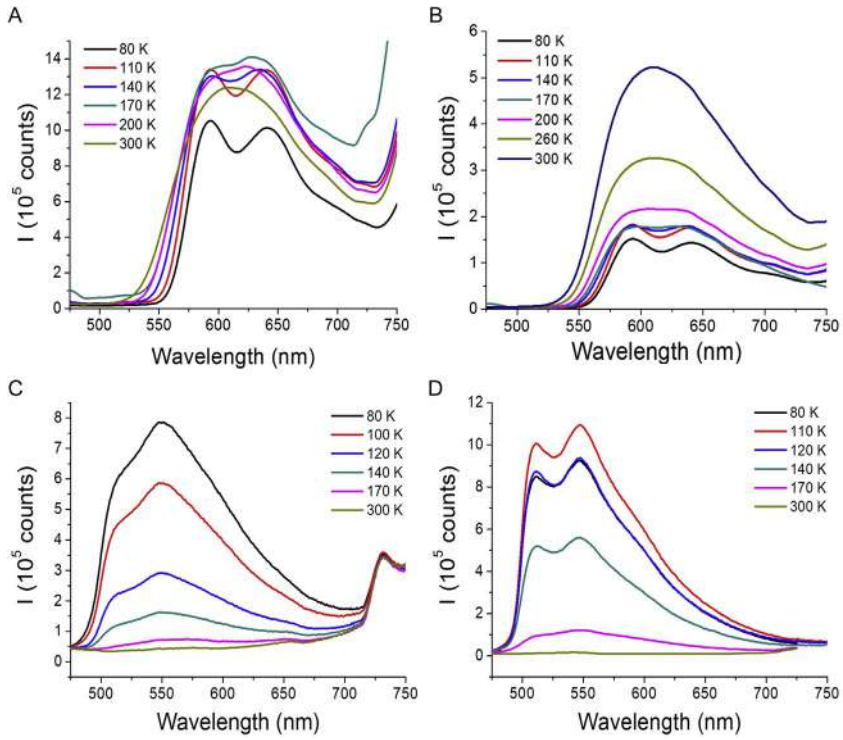

Fig. 11 (A and B) Thermal dependence of the luminescence spectra of $[Cu(MeIN)I]_n$ in the shape of nanofibers (A) and microcrystals (B). (C and D) Thermal dependence of the luminescence spectra of $[Cu(NH_2\text{-}MeIN)I]_n$ in the shape of nanofibers (C) and microcrystals (D). *Reprinted from Conesa-Egea, J.; Nogal, N.; Martinez, J. I.; Fernandez-Moreira, V.; Rodriguez-Mendoza, U. R.; Gonzalez-Platas, J.; Gomez-Garcia, C. J.; Delgado, S.; Zamora, F.; Amo-Ochoa, P.* Chem. Sci. ***2018,*** 9 *(41), 8000–8010 with permission from Royal Society of Chemistry.*

difficulty of both their well-controlled preparation and full characterization. An extreme case is the presence of point defects, since below a certain concentration the material can show substantial changes in the optical and electrical properties, but the presence of defects is almost undetectable by most of the common structural, analytical and spectroscopic characterization techniques (FTIR, X-ray single crystal diffraction, NMR, *etc.*).

An excellent example of the effects caused by a low concentration of structural defects in a Cu(I)-I CP has been recently reported.[69] In this study, it has been observed that a simple modification of the synthetic conditions in the reaction carried out between $CuCl_2$ and 3,5-dichloropyridine modulates the structural defect concentration in the so-formed crystals of

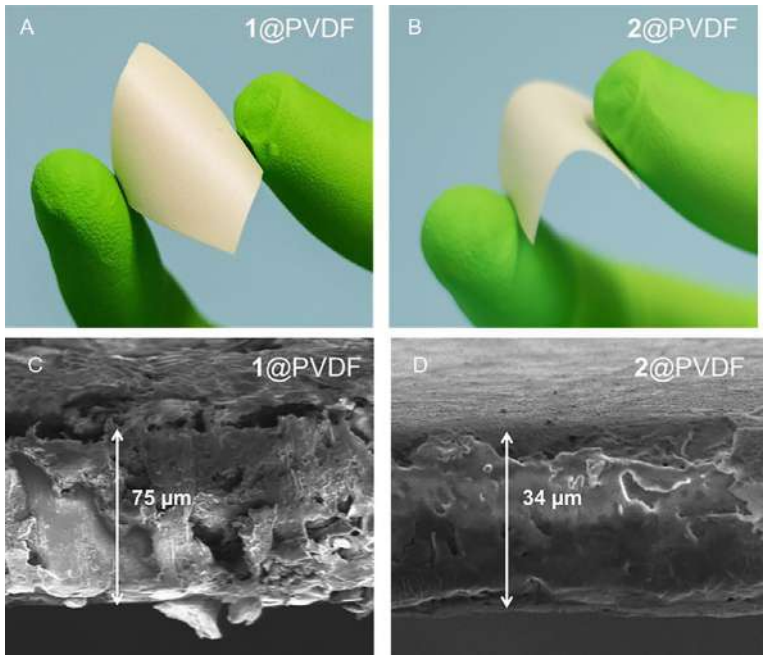

Fig. 12 (A and B) Photographs of the flexibility of the composites 1@PVDF (A) and 2@PVDF (B). (C and D) FE-SEM images of 1@PVDF (C) and 2@PVDF (D), showing their thicknesses. 1 = $[Cu(CT)]_n$, where CT = 4-carboxylthiophenolate; 2 = $[Cu(MCT)]_n$, where MCT = 4-methoxycarbonylthiophenolate. *Adapted from Troyano, J.; Castillo, O.; Martinez, J. I.; Fernandez-Moreira, V.; Ballesteros, Y.; Maspoch, D.; Zamora, F.; Delgado, S.* Adv. Funct. Mater. ***2018,*** 28 *(5), 1704040 © 2018 John Wiley and Sons.*

$[Cu(Cl_2\text{-py})I]_n$ (Cl_2-py = 3,5-dichloropyridine). Indeed, the only synthetic difference in the formation of the most thermodynamic stable species of $[Cu(Cl_2\text{-py})I]_n$, named ***A***, and the kinetical intermediate species named ***B***, is the solvothermal treatment of the initial CuI and 3,5-dicloropyridine acetonitrile solution, that seems to produce a defective composition of one of the reactants producing a more defective structure, ***B***. Interestingly, ***B*** is transformed into ***A*** upon slow recrystallization in acetonitrile. Additionally, when the reaction conditions were adjusted to produce an equimolecular mixture of ***A*** and ***B***, recrystallization also led to the isolation of only ***A***. These reactions confirm that the thermodynamic, and therefore the least defective material, corresponds to ***A***. All the analyses carried out with the two compounds ***A*** and ***B***, show identical spectroscopic features, chemical composition and X-ray diffraction patterns. The structure of ***A*** and ***B*** corresponds to the formula $[Cu(Cl_2\text{-py})I]_n$, which is similar to that found in many other reported Cu(I)-I CPs,[29,70] and consists of a polymeric staircase

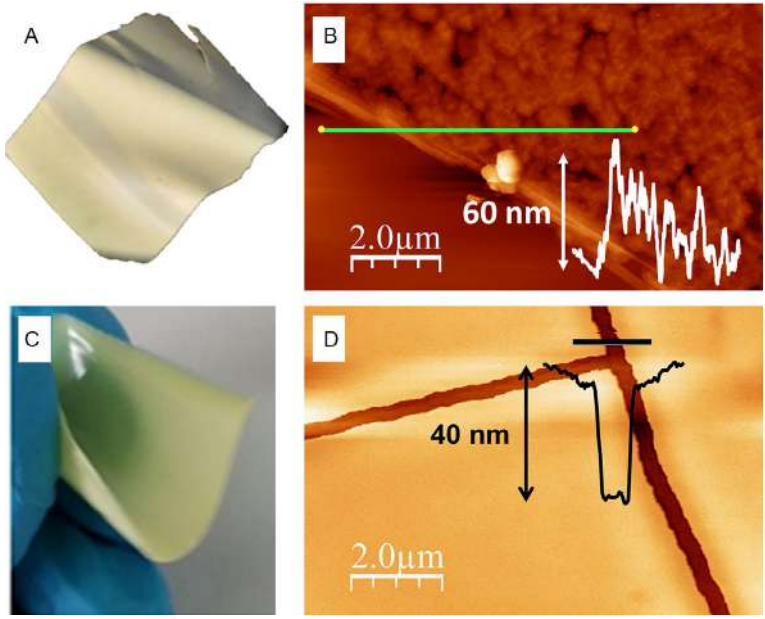

Fig. 13 (A and C) Photographs of the flexibility of $[Cu(NH_2\text{-MeIN})I]_n$@PVDF (A) and $[Cu_2I_2(Apyz)]_n$@PLA (C). (B and D) AFM images of $[Cu(NH_2\text{-MeIN})I]_n$@PVDF (B) and $[Cu_2I_2(Apyz)]_n$@PLA (D), with their height profiles across the lines. *Panels (A and B): adapted from Conesa-Egea, J.; Nogal, N.; Martinez, J. I.; Fernandez-Moreira, V.; Rodriguez-Mendoza, U. R.; Gonzalez-Platas, J.; Gomez-Garcia, C. J.; Delgado, S.; Zamora, F.; Amo-Ochoa, P.* Chem. Sci. ***2018,*** 9 *(41), 8000–8010 with permission from Royal Society of Chemistry. Panels (C and D): adapted from Conesa-Egea, J.; Moreno-Vazquez, A.; Fernandez-Moreira, V.; Ballesteros, Y.; Castellanos, M.; Zamora, F.; Amo-Ochoa, P.* Polymers ***2019,*** 11, *1047–1061 with permission, copyright 2019 MDPI.*

motif of edge-sharing Cu_2I_2 rhomboids. In this case, the polymeric chain runs parallel to the *b* axis, and is decorated with 3,5-dichloropyridine acting as a N-donor terminal ligand. However, they display remarkable differences in their luminescence ($\lambda_{exc} = 375$ nm), featuring broad emission bands centered at 515 and 670 nm for ***A*** and ***B***, respectively (Fig. 14).

Theoretical calculations have rationalized the nature of this unexpected behavior which is attributed to structural defects related to the weaker coordination bonds present in the structure. A theoretical study of the effect in their electronic structures *vs.* the presence of structural defects in the Cu_2I_2 double chains using first-principles calculations was carried out.[69] Three different point defects were considered (Fig. 15): two structures with defects for representative chain fragments of three lengths: 3, 5 and 9-units chain fragments, and another structure for a defective infinite chain. The first

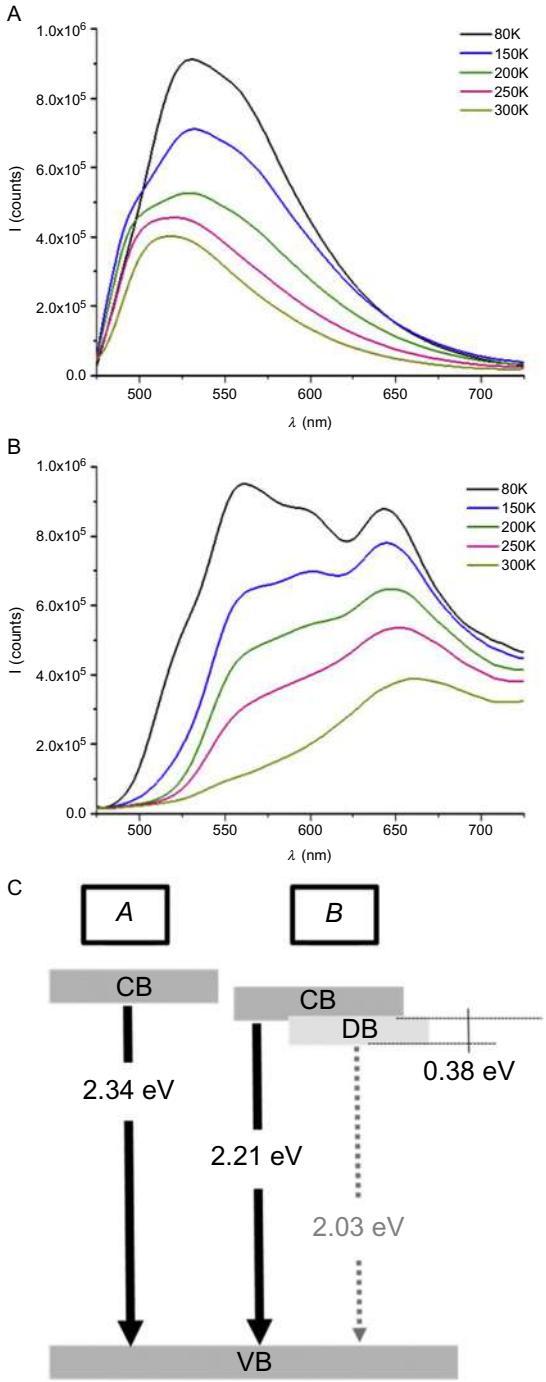

Fig. 14 Thermal dependence of the luminescence spectra of ***A*** (A) and ***B*** (B). $\lambda_{exc} = 375$ nm. (C) Emitting excited state scenario ruled by the structural defects. *Reprinted from Egea, J. C.; Gonzalez-Platas, J.; Rodriguez-Mendoza, U. R.; Martínez, J. I.; Pilar, O.; Fernandez, V.; Costa, R. D.; Fernandez.Cestay, J.; Zamora, F.; Amo-Ochoa, P.* J. Mater. Chem. C ***2020***, 8, *1448–1458 with permission, copyright 2020 Royal Society of Chemistry.*

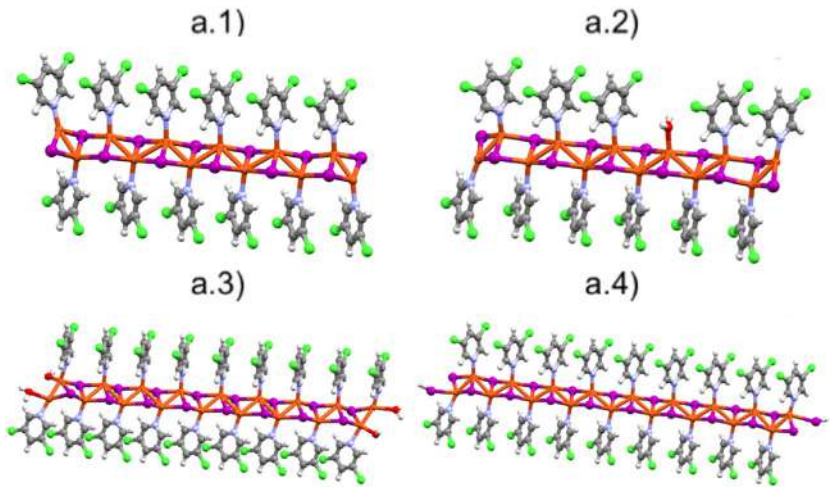

Fig. 15 Structures used for the theoretical calculation of the density of states as a function of the energy for: the pristine infinite chain case (a.1); an infinite defective chain with a lack of organic ligands (with a density of defects of 1/12) (a.2); 9-units defective chain fragments with two different terminating effects (a.3 and a.4). *Reprinted from Egea, J. C.; Gonzalez-Platas, J.; Rodriguez-Mendoza, U. R.; Martínez, J. I.; Pilar, O.; Fernandez, V.; Costa, R. D.; Fernandez.Cestay, J.; Zamora, F.; Amo-Ochoa, P.* J. Mater. Chem. C ***2020***, 8, *1448–1458 with permission, copyright 2020 Royal Society of Chemistry.*

structures consist of breaking a chain and leaving Cu(I) as the terminating atoms. In order to balance the charge, OH^- was considered as counter anion and H_2O groups were used to saturate the coordination environment. The second type of defect consists of breaking a chain leaving I^- as the terminating atoms and using H^+ to balance the charge. Finally, the third type of defect modeled on an infinite chain was the lack of an organic ligand (with a defect density of 1 ligand over 12 periodic units). Theoretical calculations predicted a red-shift in the emission properties due to the presence of the terminating Cu^+ and I^- defects, although not for the unlikely situation of lack of organic ligands. In short, the calculations foresee that the inclusion of punctual structural defects along the Cu_2I_2 double chain (in a 10% content, *i.e.*, Cu_2I_2 double chain breakage and presence of terminal iodine or OH substitution) produce the appearance of a defect state at around 0.2 eV below the Fermi energy within the mid-gap region and a band-gap reduction from 0.9 eV, for the pristine structure, to *ca.* 0.45–0.5 eV for the defective ones (Fig. 16).

This work highlights the effect of the atomic structural defects to define electronic properties in CPs.

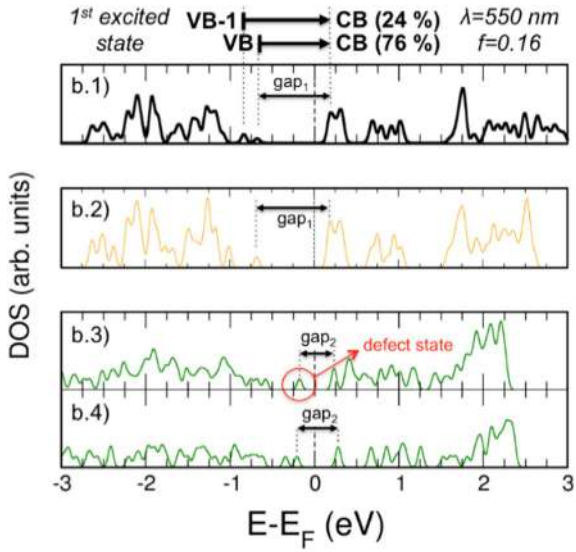

Fig. 16 Computed density of states (in arb. units) as a function of the energy (referred to the Fermi energy) for: the pristine infinite chain case (b.1); an infinite defective chain with a lack of organic ligands (with a density of defects of 1/12) (b.2); 9-units defective chain fragments with two different terminating effects (b.3 and b.4). Electronic states involved, photon wavelength, oscillator strength and weight of the contributing transitions are shown for the most pronounced low-lying optical excitation in the infinite pristine chain. *Reprinted from Egea, J. C.; Gonzalez-Platas, J.; Rodriguez-Mendoza, U. R.; Martínez, J. I.; Pilar, O.; Fernandez, V.; Costa, R. D.; Fernandez.Cestay, J.; Zamora, F.; Amo-Ochoa, P.* J. Mater. Chem. C ***2020***, 8, *1448–1458 with permission, copyright 2020 Royal Society of Chemistry.*

3. Tailoring the catalytic, adsorptive and conductive properties of metal-organic frameworks at the nanoscale

Metal-Organic Frameworks or MOFs are crystalline architectures containing nano-pores with rich chemistries, which are scalable and highly modular. MOF materials are composed of an inorganic part, which can be a cluster or a single metal cation, also called secondary building unit (SBU); and an organic part, denoted as linker, which is an organic coordinating ligand.[71]

SBU is a term described for the first time by Yaghi *et al.* in 1995 as the moiety including the metal cluster and the coordination sites of the linker.[72]

The primitive structure of the SBU plays a key factor in the MOF design, by conferring mechanical and chemical stability depending on the chemical nature of the metal and the organic linker.

On the other hand, the organic components of a MOF, the linkers, can possess different chemical natures, rigidity or flexibility, and points of extension. Typically, linkers employed in the synthesis of porous MOFs are barely rigid, composed of one or multiple phenyl rings. The points of extension, or coordinating groups, depend on the nature and the number of functional groups present in the organic linker, which can be ditopic (two points), tritopic, tetratopic, among others.[71]

Certainly, MOFs have marked a new era in the field of materials science, with more than 80,000 reported structures in the last 20 years, thanks to the versatility and tunability of these materials.[73] This synthetic and structural versatility results from the huge number of possible combinations between linkers of different nature and SBUs with different positions and number of extension points, resulting in different assembling or topologies (Fig. 17).[71,74]

Given their rich chemical and structural natures, MOFs are ideal porous platforms to be employed in applications, such as separation and storage of gases,[75,76] luminescence,[77] bio-imaging,[78] drug delivery[79] and heterogeneous catalysis,[80] as well as in energy and life technologies.[81] Alternatively, MOFs can be also employed as sacrificial templates, to produce high surface area and ordered nanostructured materials including carbon,[82] metal oxides,[83]

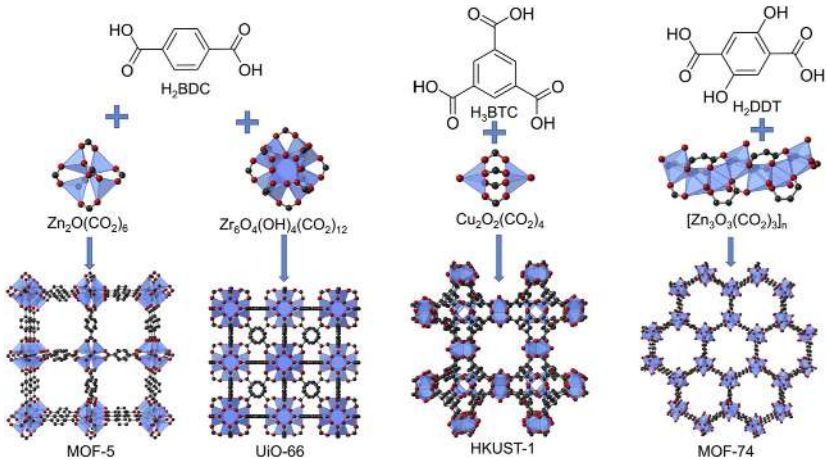

Fig. 17 Some representative examples of MOF materials. The combination of different organic linkers and inorganic SBUs results in MOFs with different porosity and topology.

metal oxide–carbon composites,[84] metallic nanoparticles–carbon composites,[85] nanoparticles or discrete molecular complexes introduced at MOFs[86,87] among others for electrochemical and catalytic applications.[88,89] These MOF-derived materials can potentially retain unique characteristics of the parent framework, such as controlled porosity, high specific surface areas and combinatorial chemistry.

One of the most fascinating features of MOFs is the possibility of modifying their chemistry and structures toward specific applications while retaining the architecture of the original framework. For this purpose, coupled with the advances in synthesis and functionalization of MOFs, "one-pot"methods as well as post-synthetic modifications (PSM) have drawn great attention as efficient and versatile methodologies to tune the properties of these materials (Scheme 1).

"One-pot" synthesis is the most direct approach to obtain MOFs containing mixed metals and/or organic linkers. Following this strategy, it is possible to incorporate a large number of different metal cations in the same SBU as well as different linkers, since the use of multiple precursors can be explored during the MOF synthesis.[90]

PSM methods rely on chemical modifications performed on the pristine MOF, after its preparation and activation. This strategy involves a target reactant (metal, linker, acidic or basic species) being diffused through the pores into the MOF internal surface, to react either with the ligand or the metal nodes without altering the topology of the parent MOF but tuning its original properties.[91] PSM has been employed not only to exchange different linkers[92] and metals[93] due to the reversible nature of coordination bonding, but also to add functional groups in the linkers using different reactions[94] or to incorporate compounds inside the pores of the MOF.[86]

One new horizon offered by MOFs is the controlled generation of defects in their structure, which opens up a new and fascinating field known as *defect engineering in MOFs*. Fischer and co-workers defined for the first time defects in MOFs as *sites that locally break the regular periodic arrangement of atoms or ions of the static crystalline parent framework because of missing or dislocated atoms or ions*.[7] However, the nature of a MOF defect might also go beyond this local definition, up to a long-range scale. When the MOF periodicity is retained at the long-range after the incorporation of defects (*e.g.,* incorporation of multiple metals within a common SBU), the structure of the defects can be assessed by crystallographic methods, in particular by applying powder neutron diffraction.[95] Regarding local defects, such as subtle structural distortions within the SBUs where the average MOF structure is not

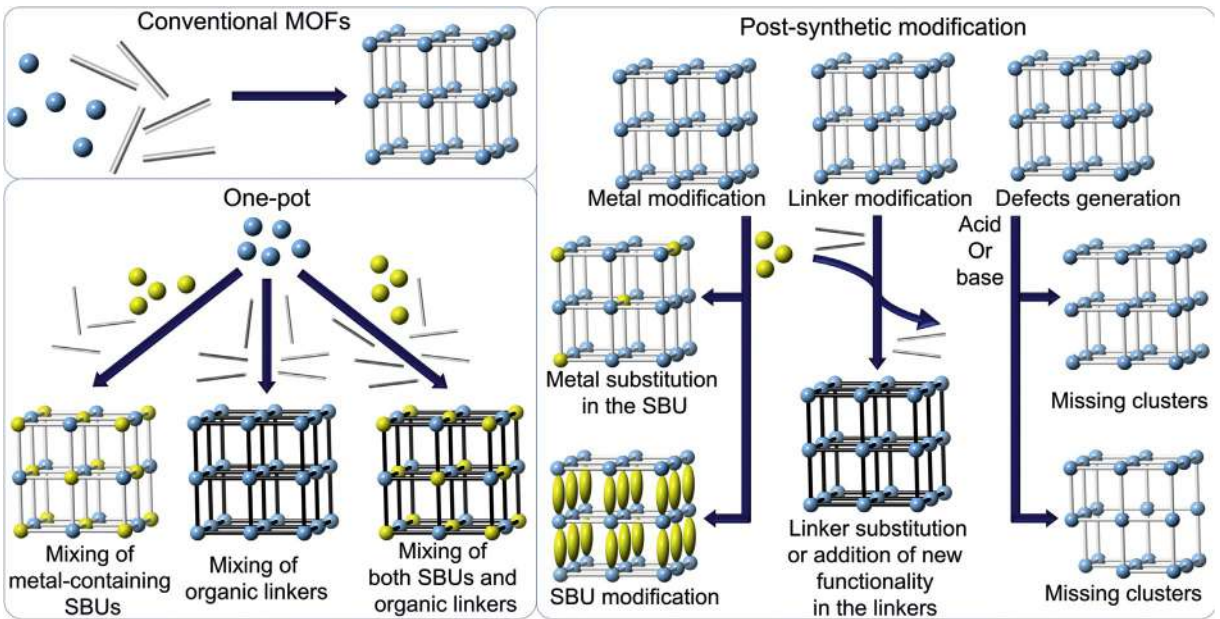

Scheme 1 Various strategies for introducing metals, linkers and/or defects into MOF structures.

compromised,[96] advanced synchrotron techniques such as Extended X-ray Absorption Fine Structure (EXAFS) and Pair Distribution Function (PDF) are crucial to better understand their structural nature. The characterization of defects can be additionally monitored by different techniques such as adsorption isotherms, thermal gravimetric analyses, microscopic and diffractometric techniques, among others.[97]

Defective-MOFs have attracted a great interest because they can be prepared by generating missing linkers or clusters within the structure, resulting in remarkable changes not only in adsorption and catalysis, but also in the addition of electrical and conductive properties.[98] In the following, it is discussed how the introduction of missing linker defects in nickel-based MOFs enhances both the CO_2 adsorption and the ionic conductivity properties with respect to pristine materials. Moreover, different strategies are shown for the modification of zirconia-based MOFs by the introduction of metal-oxo nano-clusters, acidic and basic sites and/or missing linker defects for catalytic applications. Finally, different strategies are presented for the development of multi-metal MOFs to be used as precursors of multi-metal oxides with electro-catalytic activity.

3.1 Generation of missing linker defects on nickel-based MOFs for CO_2 adsorption and ionic conductivity

As it was mentioned before, missing-linker defects can be introduced into crystalline MOF platforms by the application of post-synthetic treatments on pristine materials. In this context, it has been modified post-synthetically the isoreticular face-centered cubic (*fcu*) MOF series $[Ni_8(OH)_4(H_2O)_2(BDP\_X)_6]$ ($H_2BDP\_X = 1,4$-bis(pyrazol-4-yl) benzene-4-X with X = H (1), OH (2), NH_2 (3)), through the use of an ethanolic solution of KOH to yield $K[Ni_8(OH)_5(EtO)(BDP\_X)_{5.5}]$ (1@KOH, 3@KOH) and $K_3[Ni_8(OH)_3(EtO)(BDP\_O)_5]$ (2@KOH) (Fig. 18).[99]

The original network is based on octanuclear nickel (II) hydroxo cubic clusters, of formula $[Ni_8(OH)_4(H_2O)_2]^{+}_{12}$, connected by linear tetradentate bipyrazolate ligands as to generate a *fcu* MOF structure with well-defined cavities. Although the native MOF topology is maintained after the post-synthetic treatment, as can be deduced from the maintenance of the diffraction patterns (Fig. 19), it caused the introduction of both missing-linker defects and extra-framework cations as well as the deprotonation of coordinated water molecules.[99,100]

Particularly, after the chemical modification with KOH, the connectivity of the clusters decreased from 12 in the original frameworks 1–3 to 11 for the 1@KOH and 3@KOH systems and 10 for the 2@KOH material.

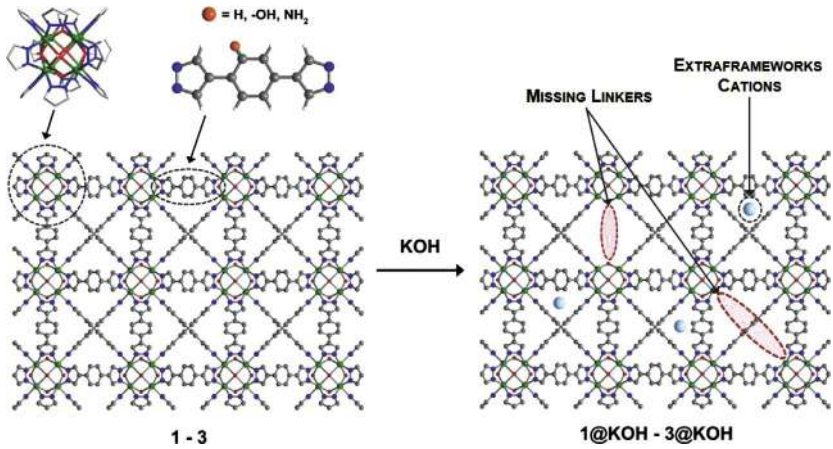

Fig. 18 Post-synthetic functionalization of the *fcu* framework $[Ni_8(OH)_4(H_2O)_2(BDP\_X)_6]$ systems (1, X = H; 2, X = OH; 3, X = NH_2) with KOH to yield the $K[Ni_8(OH)_5(EtO)(H_2O)_2(BDP\_X)_{5.5}]$ (1@KOH, 3@KOH) and $K_3[Ni_8(OH)_3(EtO)(H_2O)_6(BDP\_O)_5]$ (2@KOH) systems. *Reprinted with permission from López-Maya, E.; Montoro, C.; Colombo, V.; Barea, E.; Navarro, J. A. R.* Adv. Funct. Mater. ***2014,*** 24 *(39), 6130–6135 © 2014 John Wiley and Sons.*

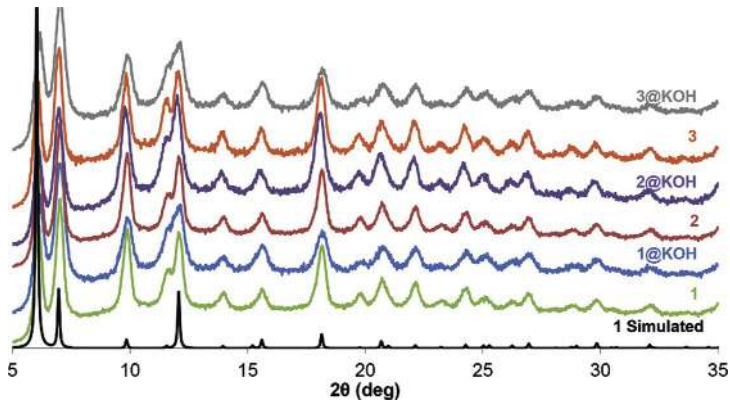

Fig. 19 Calculated XRPD pattern for 1 and experimental XRPD patterns for the isoreticular 1, 2, 3, 1@KOH, 2@KOH and 3@KOH materials. *Reprinted with permission from López-Maya, E.; Montoro, C.; Colombo, V.; Barea, E.; Navarro, J. A. R.* Adv. Funct. Mater. ***2014,*** 24 *(39), 6130–6135 © 2014 John Wiley and Sons.*

Indeed, this structural modification caused an increment of the accessibility to the porous structure and pore volume as can be deduced from the N_2 adsorption isotherms (Fig. 20), resulting in the occurrence of coordinately unsaturated metal centers that act as strong binding sites.

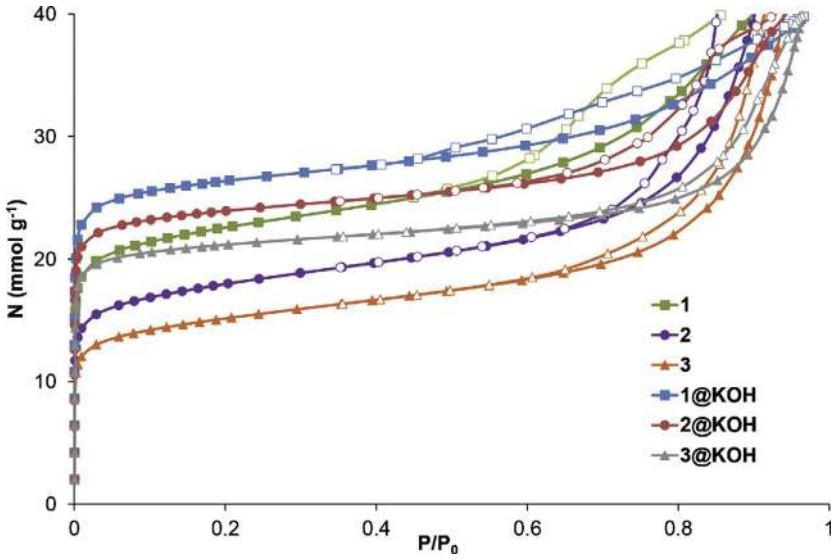

Fig. 20 Impact of framework functionalization on N_2 adsorption (77 K) for 1, 2, 3, 1@KOH, 2@KOH and 3@KOH. *Reprinted with permission from López-Maya, E.; Montoro, C.; Colombo, V.; Barea, E.; Navarro, J. A. R.* Adv. Funct. Mater. ***2014,*** 24 *(39), 6130–6135 © 2014 John Wiley and Sons.*

Apart from the generation of missing-linker defects and the formation of charge gradients due to the introduction of extra-framework cations, the post-synthetic treatment exhibited an enhancement of the basicity thanks to the deprotonation of coordinated water molecules from $[Ni_8(OH)_4(H_2O)_2]^{12+}$ to yield $[Ni_8(OH)_5(EtO)]^{10+}$ clusters. All these features were corroborated by elemental analysis (EA), thermogravimetric (TGA), inductively coupled plasma mass spectrometry (ICP-MS) and transmission electron microscopy (TEM) analyses.[99] Moreover, in the case of 2@KOH, the deprotonation of the hydroxo groups of the BDP_OH linkers originated from a larger fraction of missing linker defects and the formation of new phenolate nucleophilic sites, as deduced from its electronic spectra. Then, in a first approach, the effect of this post-synthetic treatment on the CO_2 capture properties of the materials was studied by static adsorption isotherms, pulse gas chromatographic experiments and breakthrough curve measurements. The results showed an enhancement on the CO_2 adsorption capacity of *ca.* 60% on passing from 1 to 1@KOH and of 100% on passing from 2 and 3 materials to 2@KOH and 3@KOH at $P = 0.14$ bar and 298 K (Fig. 21).

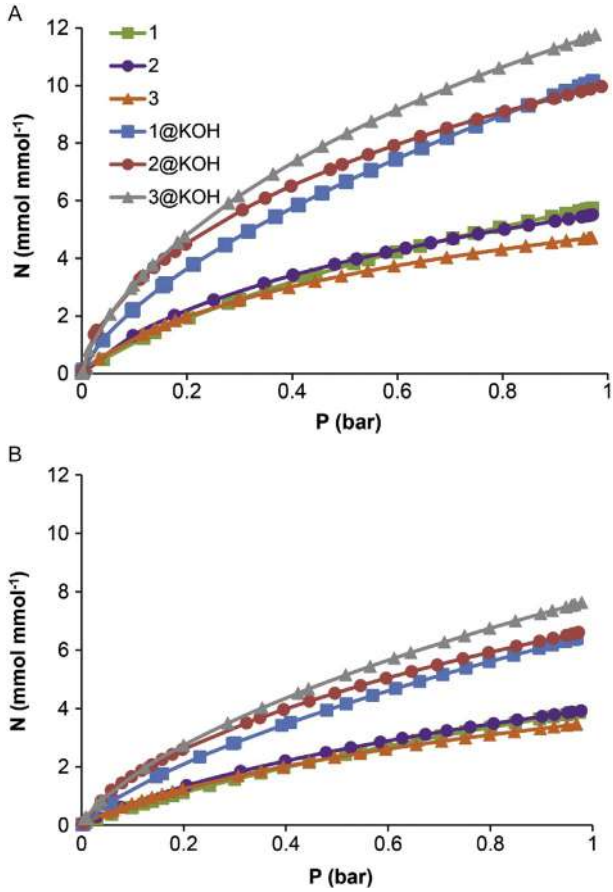

Fig. 21 Effect of framework functionalization on CO_2 adsorption at 273 K (A) and 298 K (B). The isotherms are expressed in mmol of adsorbate per formula unit of the materials in order to show the effect of framework functionalization on the CO_2 adsorption. *Reprinted with permission from López-Maya, E.; Montoro, C.; Colombo, V.; Barea, E.; Navarro, J. A. R.* Adv. Funct. Mater. ***2014,*** 24 *(39), 6130–6135 © 2014 John Wiley and Sons.*

On the other hand, the effect on the ionic conductivity properties of the modified materials was studied by electrochemical impedance spectroscopy (EIS) at different temperatures and relative humidities.[101] In this case, the ion mobility of hydroxide ions increases for the defective-MOFs with respect to their pristine materials, due to the occurrence of preferential pathways inside the clusters caused by the presence of the missing-linkers defects (Fig. 22). Specially, 2@KOH showed a hydroxide conductivity value of four orders of magnitude higher than the pristine material 2. Furthermore, the high

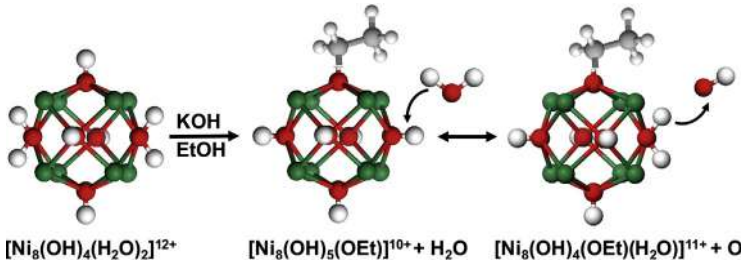

Fig. 22 Cluster deprotonation taking place during the conversion of 1–3 systems into 1@KOH-3@KOH materials and proposed proton transfer mechanism to explain the ion conductivity of the hydrated materials. *Reprinted with permission from Montoro, C.; Ocón, P.; Zamora, F.; Navarro, J. A. R.* Chem. Eur. J. ***2016,*** *22, 1646-1651 © 2016 John Wiley and Sons.*

basicity and hydrophilicity nature of 3@KOH eased a higher adsorption of hydration water molecules which provided a hydroxide ion conduction pathway facilitating a Grotthuss mechanism.

3.2 Modification of zirconia-based MOFs with catalytic groups

Metal-Organic Frameworks have also been thoroughly explored as nano-catalyst supports thanks to their exceptional chemistry and high surface area. Nano-catalyst incorporated into the MOF pores can be easily recycled and re-used several times in a heterogeneous manner, providing an interesting approach in catalysis. From metal nanoparticles of controlled sizes and shapes to discrete molecular complexes able to facilitate a wide range of chemical transformations, the variety of catalysts incorporated within porous MOF architectures is remarkable.[86,87] However, the interplay between the nano-catalyst and MOF and its role in the ultimate catalytic performance of the material is not fully understood yet. In this sense, research has focused on looking for possible answers to these unknowns through different approaches with satisfactory results as detailed below.

3.2.1 Deposition of catalytic metal-oxo nano-clusters within defective zirconia SBUs in NU-1000

NU-1000 is a large-pore zirconia-based MOF that has demonstrated to be a promising catalyst support.[102] In this porous architecture, the Zr^{IV}–O bonds within the $Zr_6(O)_8$ SBUs impart high chemical and thermal stability, thus allowing its use as catalyst for a wide range of chemical reactions while preserving the average structure without collapsing, and allowing the occurrence of local structural distortions.[96] In particular, the NU-1000 SBUs

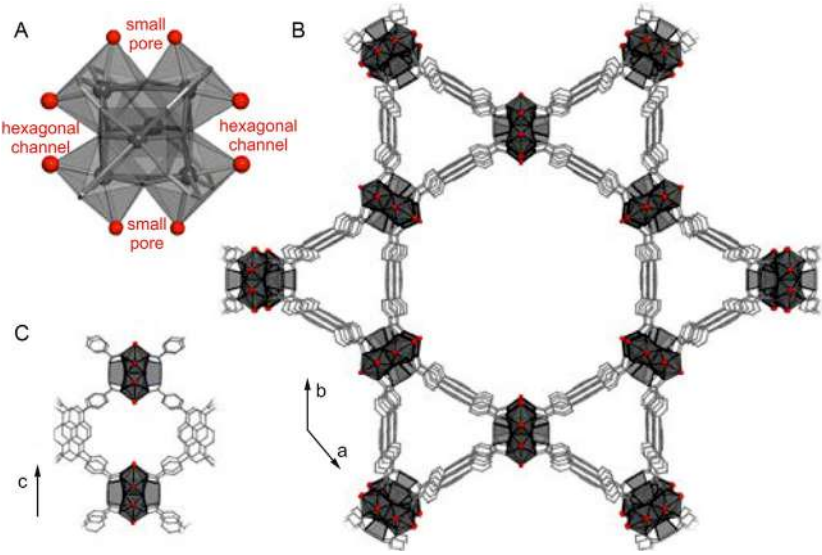

Fig. 23 Representation of the NU-1000 structure showing (A) the Zr_6-based nodes, (B) the hexagonal and triangular channels viewed perpendicular to the c-axis, and (C) the 8 Å pores viewed parallel to the *c*-axis. Hydroxyl groups, available for reaction with ALD reagents, are shown in red. *Reprinted with permission from Platero-Prats, A. E.; League, A. B.; Bernales, V.; Ye, J.; Gallington, L. C.; Vjunov, A.; Schweitzer, N. M.; Li, Z.; Zheng, J.; Mehdi, B. L.; Stevens, A. J.; Dohnalkova, A.; Balasubramanian, M.; Farha, O. K.; Hupp, J. T.; Browning, N. D.; Fulton, J. L.; Camaioni, D. M.; Lercher, J. A.; Truhlar, D. G.; Gagliardi, L.; Cramer, C. J.; Chapman, K. W.* J. Am. Chem. Soc. ***2017,*** 139 *(30), 10410–10418, copyright © 2017 American Chemical Society.*

were decorated by accessible $-OH_x$ groups $[Zr_6(\mu_3\text{-}O)_4(\mu_3\text{-}OH)_4(OH)_4(OH_2)_4]^{8+}$ pointing toward both the triangular pores and the hexagonal channels (Fig. 23), which can effectively bind metal-nano-catalysts using two post-synthesis modification methods: atomic-layer deposition (ALD In MOFs, AIM) and solvothermal deposition (Solvothermal deposition In MOFs, SIM). AIM is a two-step gas-phase modification process to incorporate well-defined metal-oxo clusters in MOFs, in which an organometallic reagent first reacts with the $-OH_x$ groups on the nodes. Subsequently, the remaining organic groups release upon exposition to moisture and regenerate the surface with fresh $-OH_x$ groups. On the other hand, the SIM method is based on the MOF treatment with a solution containing either a metal precursor or a target complex, that allows the coordination of the metal species to the $-OH_x$ groups accessible on the nodes. Taking into account this approach, it was demonstrated that the incorporation of nano-metal defects

within the NU-1000 nodes is a powerful approach to afford catalytically-active materials in chemical transformations relevant in energy.[103] Recently, the selective doping of the NU-1000 zirconia-SBUs with alkaline-metals to give defective-MOF materials active toward the degradation of nerve agents, has also been studied.[103]

AIM is also a powerful synthetic tool to decorate MOF clusters with nano-sized metal-oxo clusters of designer chemistries. Over the last years, this approach has been used to bind metal-oxo species with catalytic activity toward alkene dehydrogenation reactions on the nano-surface of defective NU-1000 nodes.[103] The defects in the $Zr_6(O)_8$ nodes in this MOF arise from the partial loss of labile water ligands binding to the zirconium(IV) centers, resulting in a more distorted local geometry of the cluster. Then, it was demonstrated that the defective-distorted $Zr_6(O)_8$ nodes are an excellent platform to stabilize catalytic metal nano-clusters *via* AIM-ing.[102]

The incorporation of NiO_xH_y species in NU-1000 resulted in a good heterogeneous catalyst for the conversion of ethylene to ethane,[104] after activation of the material at 200 °C in H_2. The Ni-decorated MOF revealed an unexpected structural feature, showing the formation of infinite hetero-bimetallic Ni(II)-Zr(IV)-oxo nanowires.[103] This peculiar structural feature found results from the selective location within the small triangular pores and bridging of the $Ni_4O_xH_y$ species to the $Zr_6(O)_8$ MOF nodes (Fig. 24).

Understanding the local structures of nano-materials is key to unrevealing the interplay of structure-activity in heterogeneous catalysis, in which localized interactions between reagents and surfaces must occur for a reaction to take place. To elucidate the local structural features of the catalytic NiO_xH_y species deposited within NU-1000, combined advanced synchrotron characterization and DFT modeling were applied. Pair Distribution Function (PDF) analyses of synchrotron X-ray total scattering and X-ray Absorption experiments at the Ni *K*-edge were performed under conditions relevant for reaction, revealing the formation of nano-sized Ni(II)-oxo clusters of 4-Ni atoms size with a local structure that resembles that of α-$Ni(OH)_2$ (Fig. 24A). DFT calculations corroborated the stability of the proposed structural model, further demonstrating the local geometry of the Ni_4-oxo clusters added.

Knowing the precise location of catalytic sites within a porous support, is critical to rationalize its ultimate properties. In the NU-1000 structure, there are two types of accessible pores where the Ni_4-clusters can potentially be deposited – either small triangular pores (*ca.* 8 Å) between two $Zr_6(O)_8$ MOF nodes or large hexagonal channels (*ca.* 30 Å). The location of the

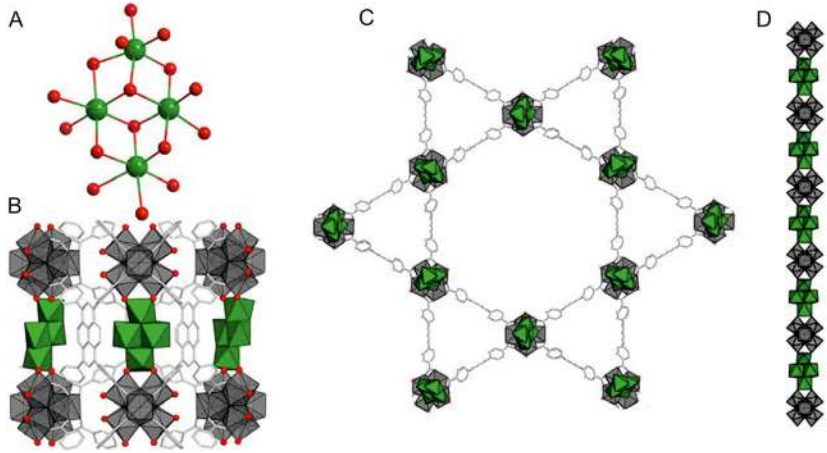

Fig. 24 (A) DFT-optimized $Ni_4O_xH_y$ cluster that best matches the experimental data. The distribution of related Ni_4-based clusters within NU-1000 from periodic density functional calculations viewed (B) parallel and (C) perpendicular to the c-axis. (D) Bimetallic metal oxide chains formed along the *c*-direction due to bridging of the Zr_6-based nodes by the Ni_4-based clusters [C: light gray, O: red, Ni: green, Zr: gray]. *Reprinted with permission from Platero-Prats, A. E.; League, A. B.; Bernales, V.; Ye, J.; Gallington, L. C.; Vjunov, A.; Schweitzer, N. M.; Li, Z.; Zheng, J.; Mehdi, B. L.; Stevens, A. J.; Dohnalkova, A.; Balasubramanian, M.; Farha, O. K.; Hupp, J. T.; Browning, N. D.; Fulton, J. L.; Camaioni, D. M.; Lercher, J. A.; Truhlar, D. G.; Gagliardi, L.; Cramer, C. J.; Chapman, K. W.* J. Am. Chem. Soc. ***2017,*** 139 *(30), 10410–10418, copyright © 2017 American Chemical Society.*

Ni-clusters within NU-1000 was determined by applying Difference Electron Density analyses of synchrotron X-ray powder diffraction data. The results showed the unexpected formation of well-defined hetero-bimetallic NiZr-oxo nanowires along the crystallographic *c*-axis, in which each Ni_4-cluster is bridging two adjacent defective $Zr_6(O)_8$ MOF nodes, providing a porous material containing catalytic defects with good performance for the hydrogenation of light alkenes.

An interesting alternative to chemically-modify MOF materials with nano-sized metal clusters is the SIM method. The incorporation of catalytic Co-oxo clusters within NU-1000 has been explored, being active for the oxidative dehydrogenation (ODH) of propane at low temperature.[105] It was shown that the activation in a flow of O_2 at 230 °C provided different catalytic cobalt sites depending on the method used. While the Co-AIM NU-1000 system gave the formation of nano-sized Co_4-clusters with a local structure that resembles that of spinel Co_3O_4, the Co-SIM modification

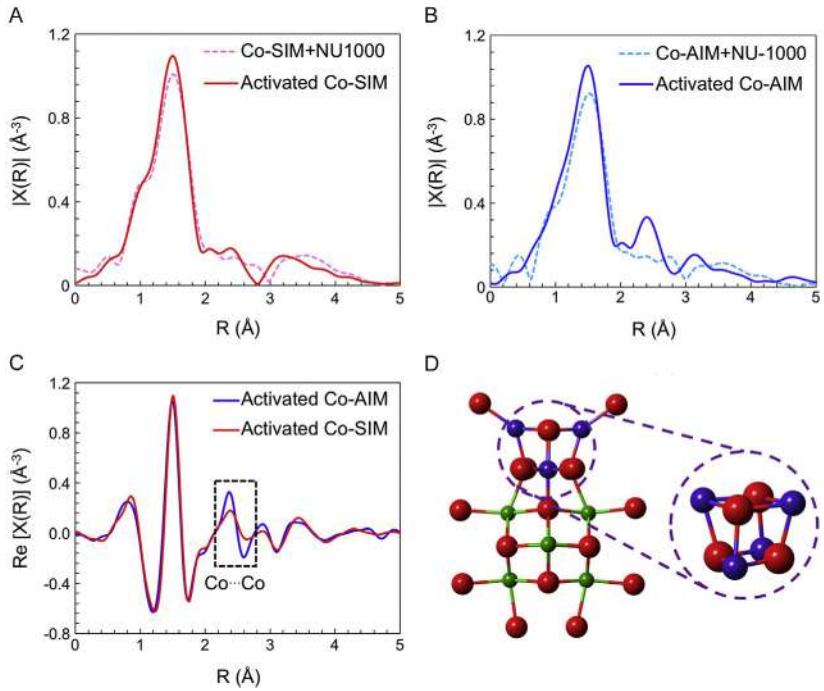

Fig. 25 (A and B) k^2-weighted magnitude of the Fourier transform of the EXAFS from $k = 3.0$ to 12.0 $Å^{-1}$ for Co-SIM + NU-1000 (A) and Co-AIM +NU-1000 (B) before and after activation in a flow of O_2 at 230 °C. (C) EXAFS spectra for activated Co-SIM + NU-1000 and Co-AIM + NU-1000 in the real part of *R*-space. (D) A proposed structural change of Co-AIM + NU-1000 upon activation. This tetranuclear cobalt cluster can be related to local structural features in spinel Co_3O_4. *Reprinted with permission from Li, Z.; Peters, A. W.; Bernales, V.; Ortuño, M. A.; Schweitzer, N. M.; Destefano, M. R.; Gallington, L. C.; Platero-Prats, A. E.; Chapman, K. W.; Cramer, C. J.; Gagliardi, L.; Hupp, J. T.; Farha, O. K.* ACS Cent. Sci. ***2017,*** 3 *(1), 31–38, copyright 2017 American Chemical Society.*

resulted in the formation of single tetrahedral Co-oxo sites (Fig. 25). The catalytic tests confirmed that the local structure of the catalytic cobalt defects play a crucial role, the Co-SIM clusters being the most active species for the transformation of propane into propene under oxidizing conditions. Combined DFT calculations with synchrotron XAS experiments under conditions relevant for catalyst activation were applied to elucidate the local structure of the cobalt catalytic sites in these NU-1000 systems.

3.2.2 Doping defective zirconia SBUs with acidic/basic species within porous MOF platforms

It is well-known that porous MOFs composed of zirconia-nodes are good Lewis acid catalysts for the hydrolytic degradation of toxic agents such as

chemical warfare agents (CWA).[106] Typically, these chemical transformations are performed using *N*-ethylmorpholine buffer solutions, hindering the catalyst deactivation by coordination of the degradation products to the zirconia nodes.[107] For this purpose, the incorporation of acidic, basic species and/or missing linker defects directly within the zirconia clusters has been studied for three archetypical mesoporous MOF materials (UiO-66,[108] NU-1000 and MOF-808[109]), through partial post-synthesis modification of the solids with different solutions.

Particularly, the enhancement of the phosphotriesterase catalytic activity was explored for the hydrolysis of P–F, P–O, and C–Cl bonds typically present in CWAs, using defective UiO-66 materials. UiO-66 ($[Zr_6O_4(OH)_4(bdc)_6]$ (bdc = benzene-1,4-dicarboxylate))[108] is a very robust zirconia-MOF where each Zr metal center is fully coordinated by 12 organic linkers to form a highly packed *fcu* structure featured by octahedral and tetrahedral cages of diameter 9 and 7 Å, respectively. In a first step, both defect-free UiO-66 and its missing-linker-defect analog $[Zr_6O_4(AcO)_6(bdc)_5]$[110] (AcO = acetate) were synthesized by using 2.1 mL of AcOH as modulator. Then, post-synthetic modification on both structures was carried out by introducing acidic Brønsted sites such as SO_4H^- groups to lead to $[Zr_6O_4(AcO)_4(bdc)_5(SO_4H)_2]$ material and by insertion of lithium alkoxides[111] such as LiOEt and Li*O*t*B*u to yield $[Zr_6O_6(bdc)_6(LiO\textit{t}Bu)_{0.3}]$, $[Zr_6O_8(bdc)_4(LiO\textit{t}Bu)_{0.3}]$ and $[Zr_6O_6(bdc)_6(LiOEt)_{0.25}]$ materials (Scheme 2).[112] It is worth highlighting that the original *fcu* topology of the UiO-66 is maintained after the chemical modification. As expected, the adsorption capacity of the defect-free pristine system decreased after the insertion of the different groups, while increased when starting from the defective MOF materials. Remarkably, the materials containing zirconia(IV)-nodes doped with Li*O*t*B*u showed the best catalytic performance toward degradation of CWAs.

Furthermore, the post-synthetic modification of NU-1000 and MOF-808 materials with methanolic solutions of magnesium methoxide has been also studied.[7] MOF-808 ($[Zr_6O_5(OH)_3(BTC)_2(HCOO)_5(H_2O)_2]$)[109] is a large-pore zirconia-MOF composed of tetrahedral cages of 4.8 Å diameter size, and a large adamant cage with an internal pore diameter of 18.4 Å. Interestingly, chemical modification of these materials with magnesium methoxide allowed the partial substitution of zirconia(IV)- by magnesium(II) ions within the MOF clusters, resulting in highly catalytically active MOFs for the degradation of toxic agents using unbuffered aqueous media at room temperature.

In order to better understand the local structural nature of the Mg(II)-doped zirconia nodes in these systems, Zr *K*-edge Extended X-ray

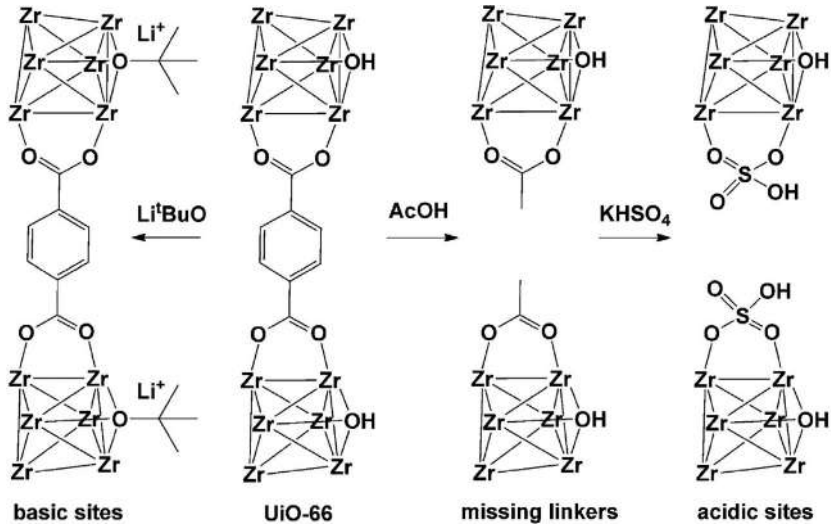

Scheme 2 Routes to improve the catalytic activity of $[Zr_6O_4(OH)_4\text{-}(bdc)_6]$ (UiO-66) by introduction of missing-linker defects and/or acidic and basic sites. *Reprinted with permission from López-Maya, E.; Montoro, C.; Rodríguez-Albelo, L. M.; Aznar Cervantes, S. D.; Lozano-Pérez, A. A.; Cenís, J. L.; Barea, E.; Navarro, J. A. R.* Angew. Chem. Int. Ed. ***2015,*** 54, *6790–6794 © 2015 John Wiley and Sons.*

Absorption Fine Structure (EXAFS) experiments were performed before and after treatment with the magnesium alkoxide. For the more active material, MOF-808, the EXAFS data indicated a significant decrease in the intensity of the $\chi(r)$-signal at $\sim$3.1 Å, which corresponds to the 3.54 Å Zr$\cdots$Zr distances within octahedral Zr-clusters (Fig. 26), evidencing the formation of local defects within the zirconia nodes after the incorporation of magnesium. The EXAFS data could be fitted using an octahedral $Mg(II)Zr(IV)_5$ cluster model, in agreement with chemical analyses, demonstrating the simultaneous occurrence of Mg$\cdots$Zr and Zr$\cdots$Zr distances at 3.34 and 3.56 Å, respectively. Moreover, the decrease in the signal centered at $\sim$1.6 Å, which is associated with Zr$-$O (formate) bond distances at 2.28 Å, associated with the partial loss (50%) of formate groups after magnesium doping.

The formation of this type of local chemical defects in MOF-808 was hypothesized to allow simultaneous increased basicity (increased nucleophilicity of OH^-/O^{2-} residues) and charge gradients in the $MgZr_5O_2(OH)_6$ heteronuclear clusters. This results in a significant synergistic effect allowing the degradation of the model nerve agent diisopropyl fluorophosphate by hydrolytic cleavage of polar P$-$X bonds (X$=$F, OR, SR).

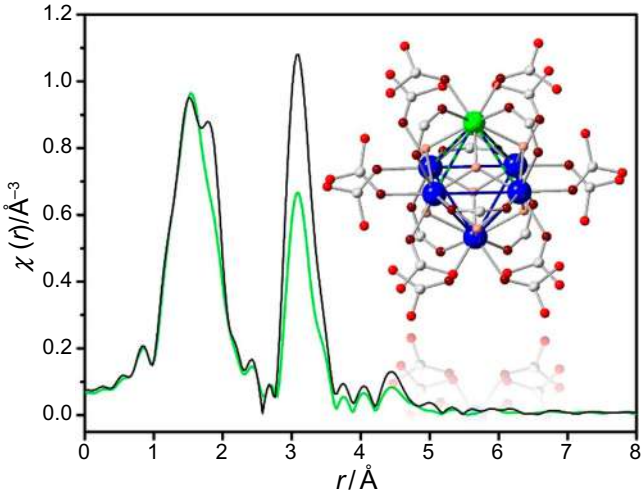

Fig. 26 k^2-weighted $\chi(r)$ Zr *K*-edge EXAFS data collected on pristine MOF-808 (black) and after modification with $Mg(MeO)_2$ on MOF-808@$Mg(MeO)_2$ (green). The inset shows the $MgZr_5O_2(OH)_6$ SBU model in the doped system. *Reprinted with permission from Gil-San-Millan, R.; López-Maya, E.; Platero-Prats, A. E.; Torres-Pérez, V.; Delgado, P.; Augustyniak, A. W.; Kim, M. K.; Lee, H. W.; Ryu, S. G.; Navarro, J. A. R.* J. Am. Chem. Soc. ***2019,*** 141 *(30), 11801–11805, copyright © 2019 American Chemical Society.*

3.3 Metal-cation arrangement control in SBU of MOFs and their translation to oxides electrocatalytically active

The use of MOF-derived advanced nanomaterials, obtained after the controlled calcination of the pristine MOF, has received a great interest because of their potential for electrochemical applications.[113,114] The incorporation of multiple metal elements into MOFs can be accomplished by following different synthetic approaches, which in turn determine how the various metal elements are arranged in the frameworks.[115] The three main synthetic methods to prepare MOFs containing more than one metal cation include: use of metalloligands (organic ligands with additional metal binding sites), post-synthetic metal exchange, or "one-pot" synthesis. However, the combination of multiple metal elements during the "one-pot" synthesis often leads to the appearance of competitive crystallization processes, rather than to the formation of the multi-metal MOFs. Indeed, in 2016 the factors that govern the incorporation of a second metal cation in the well-known MOF TMPF-88 were studied.[116]

TMPF-88 is composed of multiple zinc-clusters with different coordination modes and linked by 1,2,4-triazole and 4,4′-(hexafluoroisopropyliden)-bis(benzoic) acid organic ligands. Upon addition of different amounts of a

second metal cation (*i.e.*, cobalt(II)), the formation of competing phases was observed. Interestingly, both experimental and computational studies on the formation energy indicated that MOF phases that are thermodynamically favored when exclusively containing zinc in the SBU, do not allow the formation of the mixed Zn/Co MOF analog. Otherwise, MOFs whose formation is kinetically driven, can be obtained as mixed-metal forms. Based on these findings, it was recently demonstrated that it is possible to address the incorporation of various metal cations in the SBU of MOFs by taking advantage of kinetically-driven phases.[95] First, a known kinetically controlled phase, ZnPF-1, is selected as platform for the incorporation of different combinations of multiple metal elements (cobalt, manganese and calcium).

ZnPF-1 consists of the dicarboxylic ligand H_2hfipbb (4,4′-(hexafluoroisopropyliden)bis(benzoic) acid) as organic linker and a helical SBU with the tetrahedral zinc cations.[117] The resulting three-dimensional structure has square and hexagonal channels, running parallel to the *c* axis (Fig. 27A). This phase crystallizes in the hexagonal $P6_422$ space group [$a = 21.22(1)$ Å, $c = 7.710(5)$ Å]. Despite the extensive use of this organic linker to prepare different MOFs with various metal elements, thus far this MOF topology has only been reported with the use of zinc as metal cation.[117] The incorporation of different Zn:Mn:Co:Ca initial metal molar ratios, denoted molar codes, was investigated within the ZnPF-1 framework.[117] The combination of zinc and cobalt at different molar ratios resulted in the formation of the corresponding mixed-metal systems. The chemical composition of

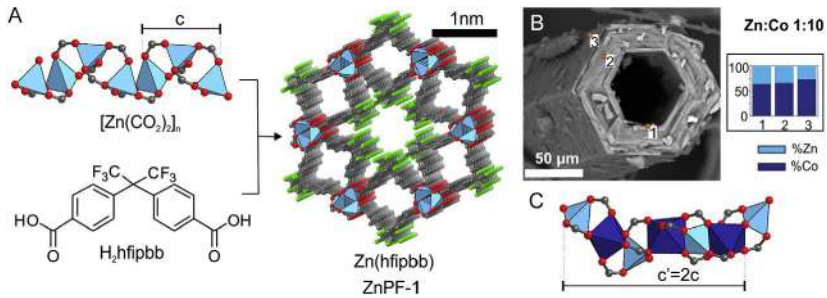

Fig. 27 (A) ZnPF-1 is formed by the combination of H_2hfipbb with a helical inorganic SBU where the zinc atoms are tetrahedrally coordinated. O, C, and F atoms are depicted as red, gray, and green balls, respectively, and pale blue tetrahedron represent zinc cations. (B) SEM image and EDS analysis of $Zn_{0.21}Co_{0.79}$(hfipbb). Metal atomic percentage was determined with the spectra recorded at the various points of the crystal indicated in the image. (C) The inorganic SBU might adapt to include octahedrally coordinated cations, which results in a unit cell transformation where the *c* parameter is doubled.

the bulk was determined by means of inductively coupled plasma (ICP) and elemental analysis. Through scanning electron microscopy (SEM) and energy-dispersive X-ray spectroscopy (EDS) analyses of the MOF crystals, it was observed that the amount of cobalt is larger in the external areas of the crystals than in the core (Fig. 27B). Single crystal X-ray diffraction studies showed that cobalt atoms present octahedral coordination environments depending on the initial Zn/Co molar ratio, resulting in a crystal symmetry change. Thus, the Zn:Co 1:2 M code sample was found to be isostructural to the original ZnPF-1, with the tetrahedral metal positions within the SBU occupied by both zinc and cobalt. Differently, the sample prepared with a Zn:Co 1:10 M code presented a unit cell with a doubled *c* parameter and $P6_522$ space group (Fig. 27C). This significant change in the *c* parameter arises from the splitting of the crystallographic metal sites within the SBUs, which are now composed of alternating tetrahedral and octahedral metal sites.

Due to the similar atomic number of zinc and cobalt, it was not possible to unequivocally determine their position in the MOF structure by X-ray diffraction. Therefore, neutron powder diffraction (NPD) experiments were carried out to determine the location of each metal element, as the scattering length of zinc and cobalt are different enough. Neutron thermos-diffraction experiments evidenced the occurrence of a phase transition for all Zn:Co samples between 140 and 80 K. Rietveld refinement of the NPD data collected at room temperature for the Zn:Co 1:2 sample indicated the presence of the ZnPF-1 phase, with only one tetrahedral metal site in the SBU occupied by either Co or Zn, with a ratio in agreement with chemical analyses. For the low-temperature data (50 K), a satisfactory refinement could not be achieved by considering only the transformed crystal cell. It was concluded that both phases are coexisting within the MOF crystals, as a result of the compositional variations. The best results were obtained considering a combination of the original ZnPF-1 phase (with tetrahedral alone in the SBUs) exclusively containing zinc, and the transformed phase (with the *c* parameter doubled and alternated tetrahedral and octahedral in the SBUs) containing zinc in the tetrahedral sites and cobalt in the octahedral sites. These results from NPD, along with the presence of compositional gradients in the crystals, indicated that this MOF was composed of an inner core with SBUs made of zinc atoms and an outer shell with SBUs made of alternating zinc and cobalt atoms (Fig. 28A). At room temperature, both atoms are in a tetrahedral environment, whereas by decreasing the temperature the cobalt atoms become octahedral, resulting in the unit cell change.

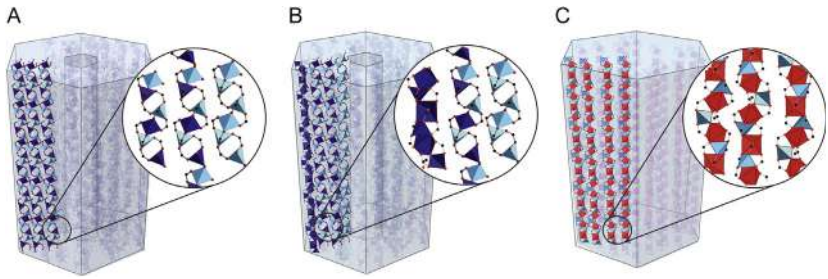

Fig. 28 Corresponding MOF crystals might include multiple SBUs mesoscopically arranged, or just a single one. (A) MOF crystal for the molar code Zn:Co 1:2, (B) Zn:Co 1:10 and (C) Zn:Mn 1:1.

In the case of the sample prepared from a Zn:Co 1:10 M ratio, the room temperature NPD pattern indicated the presence of both phases. Through a multiphase Rietveld refinement, the percentage of both phases was estimated to be 67 and 33 wt% for the original and transformed one, respectively. The original ZnPF-1 phase was refined to be composed of both zinc and cobalt. By decreasing the temperature down to 10 K, the majority of this phase is converted into the transformed phase with a double *c*. However, the 10 K NPD pattern showed also the presence of a residual portion of the original ZnPF-1 phase. Consequently, it was demonstrated that this MOF has three compositional domains[117]: a small core (no more than 5 wt% according to NPD Rietveld refinement) exclusively containing zinc, together with a shell where the SBUs are composed of zinc and cobalt cations. Within the first shell, whereas at room temperature both zinc and cobalt show tetrahedral environments, by decreasing the temperature cobalt becomes octahedral. Finally, in the outer shell (around 33 wt%), the SBUs are exclusively composed of cobalt cations with alternating tetrahedral and octahedral coordination environments (Fig. 28B).

Furthermore, when zinc is combined with manganese or calcium instead of cobalt, EDS analyses showed that there were no compositional gradients along the crystals. In this case, the SBUs are formed by alternating tetrahedral zinc and octahedral manganese/calcium cations according to single crystal X-ray and neutron diffraction analyses (Fig. 28C). Thus, zinc was found to be the structure-directing element in this system, being necessary to obtain the desired MOF SBU topology and always occupies the tetrahedral position in the SBUs. On the contrary, while cobalt can be located at both tetrahedral and octahedral sites, manganese and calcium were determined to be exclusively located in octahedral positions.

These differences in preferential coordination environments result in the ability to address the location of the metal cations in the inorganic SBUs of tri-and four-metallic systems composed of zinc, cobalt, manganese and/or calcium, by adjusting the initial molar ratios. Thus, it was shown that it is possible to harness the distribution of multiple metal-cations within the MOFs SBUs at both atomic and *meso* scales.

As a proof of concept, the electro-catalytic performance of multi-metal oxides derived from multi-metal MOFs in the oxygen reduction reaction (ORR) was evaluated.[118] The transference of the MOF chemical compositions to multi-metal oxides with novel and desired compositions was achieved by calcination. The resulting three- and four-metal-containing oxides showed spinel structures and exhibited excellent ORR activity, comparable to commercial Pt/C, with a high and long stability and methanol tolerance.

4. Conclusions and future perspectives

Although defect engineering of materials is a field of high relevance, allowing to gain crystal quality and specific physical and chemical properties, it remains very intricate, in particular for low dimensional defects present in low concentrations where the usual spectroscopic and diffractometric techniques do not provide information.

MMX are 1D-CP based on chains of dimetal units linked by halides. In particular those based on platinum-iodine $[Pt_2(dta)_4I_2]_n$ (dta = ditiocarboxylate) are excellent electrical conductors in bulk. They form different nanostructures, and even can be isolated as single chains, based on disassembly-reassembly processes between their two building blocks, $[Pt_2(dta)_4]$ and $[Pt_2(dta)_4I_2]$. The nanostructures so-formed are prone to the presence of defects. As most of the typical one-dimensional conductors, MMX are very sensitive even to a low density of structural defects, consequently they show a strong Anderson localization regime for long enough lengths. It has been shown that the electrical conductance measured in bulk MMX crystals is slightly higher than that in the nanostructures and fibers, pointing to a slightly lower density of defects in bulk as macroscopic crystals are grown close to thermodynamic equilibrium. Therefore, MMX nanostructures present more density of defects because their growth is dominated by kinetics (fast growth). However, MMX chains are one of the best molecular wire candidates even for long distances. We envision further work to optimize preparation routes to repair defects. Additionally, functionalization with different terminal

ligands enabling formation of more complex supramolecular structures will be an important step forward for molecular electronics.

Cu—I double chains grafted with different N-donor ligands such as pyridine, pyrazine or pyrimidine derivatives, is a family of 1D-CPs that shows interesting electronic properties, producing multifunctional materials merging emission and semi-conductivity. They are considered new stimuli-response materials because they present a very sensitive central Cu—I double chain. Hence, physical or/and chemical stimulus modify Cu—I distances and angles significantly, thus affecting their physical properties. Bottom-up methods based on fast precipitation have emerged as a suitable strategy for nano-structuring Cu—I double chain compounds. These novel nanostructures show either analogous physical properties to that found in the bulk or slight variations due to confinement effects. Importantly, Cu—I double chain nanostructures are useful to prepare a variety of composites with different matrices as ultra-thin films with thicknesses close to a few tens of nanometers. The thin-films retain the physical properties of the Cu—I double chains; therefore, they are a suitable alternative for the fabrication of new sensors.

Interestingly, the generation of specific defects in Cu—I double chains may significantly affect their electronic properties. Thus, by simple modification of the synthetic conditions it is possible to modulate the density of structural defects present in crystals of $[Cu(Cl_2\text{-py})I]_n$ (Cl_2-py = 3,5-dichloropyridine) with strong variations in the emission of the crystals so-produced. This is a very recent result in this research field that shows the relevance of defect engineering for the production of new materials based on in Cu—I double chains.

Finally, some of the examples in this chapter have been selected to illustrate the wide range of properties in MOF materials that can be tailored by *breaking* their native periodicity through synthesis. Defective-MOFs are adjustable materials, which can contain both local and long-range variations, not only in their chemistry but also in their structure, without compromising the average porous architecture. As we have shown, these defective materials often have enhanced catalytic, adsorptive, and conductive properties at the nanoscale, resulting in promising platforms for applications.

Defects in MOFs can be incorporated following different synthetic methodologies (either by 'one-pot' or post-synthesis methods, PSM), ranging from the generation of missing linkers or clusters, decoration with nano-species or multi-metal doping. The complex chemical and structural nature of the generated defects often requires the use of advanced characterization

techniques, including synchrotron X-rays and neutrons, in combination with computational studies. In particular, we envisage that the Pair Distribution Function (PDF) technique will become a definite probe to assess the atomistic structure of defects in MOFs.

Over the past years, defects are becoming key players in the field of MOFs, allowing materials with unprecedented and tunable properties. Rapid progress and advances in the area are likely to establish defective-MOFs as the next generation of functional coordination porous nanomaterials.

Acknowledgments

The authors thank financial support from the Spanish Ministerio de Economía y Competitividad (MAT2016-77608-C3-1-P, MAT2016-75883-C2-2-P), Spanish Ministerio de Ciencia, Innovación y Universidades (RTI2018-096138-A-I00), Regional Government of Madrid for a TALENTO grant (2017-T1/IND5148) and Universidad Autonoma de Madrid together with Regional Government of Madrid for a PRICIT project (MemCat-SI1/PJI/2019-00505). C.C.-B. acknowledges the European Social Funds and the Regional Government of Madrid for a postdoctoral contract (PEJD-2018-POST/IND-7909).

References

1. Rethwisch, D. G. In: *Fundamentals of Materials Science and Engineering*, Fifth ed.; Callister, W. D., Anderson, W., Eds.; John Wiley and Sons: New York, 2001; pp 102–122.
2. Fang, Z.; Bueken, B.; De Vos, D. E.; Fischer, R. A. *Angew. Chem. Int. Ed.* **2015**, *54*(25), 7234–7254.
3. Hernandez, W. Y.; Centeno, M. A.; Romero-Sarria, F.; Odriozola, J. A. *J. Phys. Chem. C* **2009**, *113*(14), 5629–5635.
4. Bispo, A. G., Jr.; Ceccato, D. A.; Lima, S. A. M.; Pires, A. M. *RCS Advances* **2017**, *7*(85), 53752–53762.
5. Byzynski, G.; Ribeiro, C.; Longo, E. *Int. J. Photoenergy* **2015**, 831930.
6. Qi, Y.; Xu, H.; Li, X.; Tu, B.; Pang, Q.; Lin, X.; Ning, E.; Li, Q. *Chem. Mater.* **2018**, *30*(15), 5478–5484.
7. Gil-San-Millan, R.; López-Maya, E.; Platero-Prats, A. E.; Torres-Pérez, V.; Delgado, P.; Augustyniak, A. W.; Kim, M. K.; Lee, H. W.; Ryu, S. G.; Navarro, J. A. R. *J. Am. Chem. Soc.* **2019**, *141*(30), 11801–11805.
8. Xia, Y. N.; Yang, P. D.; Sun, Y. G.; Wu, Y. Y.; Mayers, B.; Gates, B.; Yin, Y. D.; Kim, F.; Yan, Y. Q. *Adv. Mater.* **2003**, *15*(5), 353–389.
9. Ozin, G. A.; Arsenault, A. C. *Nanochemistry: A Chemical Approach to Nanomaterials*. RSC Publishing: Cambridge, 2005.
10. Kitagawa, S.; Noro, S. *Comprehensive Coordination Chemistry II*. Vol. 7. Elsevier: Amsterdam, 2004.
11. Constable, E. C. *Coord. Chem. Rev.* **2008**, *252*(8–9), 842–855.
12. Eddaoudi, M.; Kim, J.; Vodak, D.; Sudik, A.; Wachter, J.; O'Keeffe, M.; Yaghi, O. M. *Proc. Natl. Acad. U. S. A.* **2002**, *99*(8), 4900–4904.
13. Hosseini, M. W. *Chem. Commun.* **2005**, *47*, 5825–5829.
14. Janiak, C. *Dalton Trans* **2003**, *14*, 2781–2804.
15. Carne, A.; Carbonell, C.; Imaz, I.; Maspoch, D. *Chem. Soc. Rev.* **2011**, *40*(1), 291–305.

16. Mas-Balleste, R.; Gomez-Navarro, G.; Gomez-Herrero, J.; Zamora, F. *Nanoscale* **2011**, *3*, 20–30.
17. Mas-Balleste, R.; Gomez-Herrero, J.; Zamora, F. *Chem. Soc. Rev.* **2010**, *39*(11), 4220–4233.
18. Yuan, L.; Nerngchamnong, N.; Cao, L.; Hamoudi, H.; del Barco, E.; Roemer, M.; Sriramula, R. K.; Thompson, D.; Nijhuis, C. A. *Nat. Commun.* **2015**, *6*, 6324.
19. Ares, P.; Amo-Ochoa, P.; Soler, J. M.; Palacios, J. J.; Gomez-Herrero, J.; Zamora, F. *Adv. Mater.* **2018**, *30*(21), 1705645.
20. Hermosa, C.; Vicente Alvarez, J.; Azani, M.-R.; Gomez-Garcia, C. J.; Fritz, M.; Soler, J. M.; Gomez-Herrero, J.; Gomez-Navarro, C.; Zamora, F. *Nat. Commun.* **2013**, *4*, 1709.
21. Tuccitto, N.; Ferri, V.; Cavazzini, M.; Quici, S.; Zhavnerko, G.; Licciardello, A.; Rampi, M. A. *Nat. Mater.* **2009**, *8*(1), 41–46.
22. Welte, L.; Calzolari, A.; Di Felice, R.; Zamora, F.; Gomez-Herrero, J. *Nat. Nanotechnol.* **2010**, *5*(2), 110–115.
23. Calzolari, A.; Alexandre, S. S.; Zamora, F.; Di Felice, R. *J. Am. Chem. Soc.* **2008**, *130*(16), 5552–5562.
24. Gomez-Herrero, J.; Zamora, F. *Adv. Mater.* **2011**, *23*(44), 5311–5317.
25. Welte, L.; Garcia-Couceiro, U.; Castillo, O.; Olea, D.; Polop, C.; Guijarro, A.; Luque, A.; Gomez-Rodriguez, J. M.; Gomez-Herrero, J.; Zamora, F. *Adv. Mater.* **2009**, *21*(20), 2025–2028.
26. Gomez-Navarro, C.; de Pablo, P. J.; Gomez-Herrero, J.; Biel, B.; Garcia-Vidal, F. J.; Rubio, A.; Flores, F. *Nat. Mater.* **2005**, *4*(7), 534–539.
27. Armaroli, N.; Accorsi, G.; Cardinali, F.; Listorti, A. *Topics Curr. Chem.* **2007**, *280*, 69.
28. Zhu, H.-B.; Liang, L. *J. Coord. Chem.* **2015**, *68*(8), 1306–1316.
29. Song, Y.; Fan, R.; Wang, P.; Wang, X.; Gao, S.; Du, X.; Yang, Y.; Luan, T. *J. Mater. Chem. C* **2015**, *3*(24), 6249–6259.
30. Zhu, H.-B.; Yang, W.-N.; Shan, R.-Y. *J. Coord. Chem.* **2013**, *66*(3), 435–443.
31. Li, S.-L.; Zhang, R.; Hou, J.-J.; Zhang, X.-M. *Inorg. Chem. Commun.* **2013**, *32*, 12–17.
32. Safko, J. P.; Kuperstock, J. E.; McCullough, S. M.; Noviello, A. M.; Li, X.; Killarney, J. P.; Murphy, C.; Patterson, H. H.; Bayse, C. A.; Pike, R. D. *Dalton Trans.* **2012**, *41*(38), 11663–11674.
33. Prochowicz, D.; Justyniak, I.; Kornowicz, A.; Kaczorowski, T.; Kaszkur, Z.; Lewiński, J. *Chem. – Eur. J.* **2012**, *18*(24), 7367–7371.
34. Hou, Q.; Qu, X. J.; Jin, J.; Zhao, J. J.; Yu, J. H.; Xu, J. Q. *J. Cluster Sci.* **2011**, *22*(4), 715–722.
35. Hu, S.; Yu, F.-Y.; Yan, Y.; Hao, Z.-F.; Yu, L.; Tong, M.-L. *Inorg. Chem. Commun.* **2011**, *14*(5), 622–625.
36. Hao, Z.-M.; Wang, J.; Zhang, X.-M. *CrystEngComm* **2010**, *12*(4), 1103–1109.
37. Hassanein, K.; Conesa-Egea, J.; Delgado, S.; Castillo, O.; Benmansour, S.; Martinez, J. I.; Abellan, G.; Gomez-Garcia, C. J.; Zamora, F.; Amo-Ochoa, P. *Chem. – Eur. J.* **2015**, *21*(48), 17282–17292.
38. Ford, P. C.; Cariati, E.; Bourassa, J. *Chem. Rev.* **1999**, *99*(12), 3625–3648.
39. Slabbert, C.; Rademeyer, M. *Coord. Chem. Rev.* **2015**, *288*, 18–49.
40. Cariati, E.; Lucenti, E.; Botta, C.; Giovanella, U.; Marinotto, D.; Righetto, S. *Coord. Chem. Rev.* **2016**, *306*, 566–614.
41. Tsuge, K.; Chishina, Y.; Hashiguchi, H.; Sasaki, Y.; Kato, M.; Ishizaka, S.; Kitamura, N. *Coord. Chem. Rev.* **2016**, *306*(Part 2), 636–651.
42. Hardt, H. D.; Pierre, A. *Inorg. Chim. Acta* **1977**, *25*, L59–L60.
43. Benito, Q.; Le Goff, X. F.; Maron, S.; Fargues, A.; Garcia, A.; Martineau, C.; Taulelle, F.; Kahlal, S.; Gacoin, T.; Boilot, J. P.; Perruchas, S. *J. Am. Chem. Soc.* **2014**, *136*(32), 11311–11320.

44. Benito, Q.; Baptiste, B.; Polian, A.; Delbes, L.; Martinelli, L.; Gacoin, T.; Boilot, J. P.; Perruchas, S. *Inorg. Chem.* **2015**, *54*(20), 9821–9825.
45. Benito, Q.; Goff, X. F.; Nocton, G.; Fargues, A.; Garcia, A.; Berhault, A.; Kahlal, S.; Saillard, J. Y.; Martineau, C.; Trebosc, J.; Gacoin, T.; Boilot, J. P.; Perruchas, S. *Inorg. Chem.* **2015**, *54*(9), 4483–4494.
46. Aguirrechu-Comerón, A.; Hernández-Molina, R.; Rodríguez-Hernández, P.; Muñoz, A.; Rodríguez-Mendoza, U. R.; Lavín, V. C.; Angel, R. J.; Gonzalez-Platas, J. *Inorg. Chem.* **2016**, *55*(15), 7476–7484.
47. Cariati, E.; Bourassa, J. *Chem. Commun.* **1998**, *16*, 1623–1624.
48. Cariati, E.; Bu, X.; Ford, P. C. *Chem. Mater.* **2000**, *12*(11), 3385–3391.
49. Amo-Ochoa, P.; Hassanein, K.; Gomez-Garcia, C. J.; Benmansour, S.; Perles, J.; Castillo, O.; Martinez, J. I.; Ocon, P.; Zamora, F. *Chem. Commun.* **2015**, *51*(76), 14306–14309.
50. Hassanein, K.; Amo-Ochoa, P.; Gomez-Garcia, C. J.; Delgado, S.; Castillo, O.; Ocon, P.; Martinez, J. I.; Perles, J.; Zamora, F. *Inorg. Chem.* **2015**, *54*(22), 10738–10747.
51. Toivola, R.; Lai, P.-N.; Yang, J.; Jang, S.-H.; Jen, A. K. Y.; Flinn, B. D. *Comp. Sci. Tech.* **2017**, *139*, 74–82.
52. Li, Z. A.; Toivola, R.; Ding, F.; Yang, J.; Lai, P.-N.; Howie, T.; Georgeson, G.; Jang, S.-H.; Li, X.; Flinn, B. D.; Jen, A. K.-Y. *Adv. Mater.* **2016**, *28*(31), 6592–6597.
53. Killarney, J. P.; McKinnon, M.; Murphy, C.; Henline, K. M.; Wang, C.; Pike, R. D.; Patterson, H. H. *Inorg. Chem. Commun.* **2014**, *40*, 18–21.
54. Wang, F.; Wang, Y.-T.; Yu, H.; Chen, J.-X.; Gao, B.-B.; Lang, J.-P. *Inorg. Chem.* **2016**, *55*(18), 9417–9423.
55. Bouson, S.; Krittayavathananon, A.; Phattharasupakun, N.; Siwayaprahm, P.; Sawangphruk, M. *R. Soc. Open Sci.* **2017**, *4*(10), 170654.
56. Rodriguez-San-Miguel, D.; Amo-Ochoa, P.; Zamora, F. *Chem. Commun.* **2016**, *52*(22), 4113–4127.
57. Troyano, J.; Perles, J.; Amo-Ochoa, P.; Martínez, J. I.; Zamora, F.; Delgado, S. *CrystEngComm* **2014**, *16*(35), 8224–8231.
58. Mateo-Marti, E.; Welte, L.; Amo-Ochoa, P.; Sanz Miguel, P. J.; Gomez-Herrero, J.; Martin-Gago, J. A.; Zamora, F. *Chem. Commun.* **2008**, *8*, 945–947.
59. Amo-Ochoa, P.; Welte, L.; Gonzalez-Prieto, R.; Sanz Miguel, P. J.; Gomez-Garcia, C. J.; Mateo-Marti, E.; Delgado, S.; Gomez-Herrero, J.; Zamora, F. *Chem. Commun.* **2010**, *46*(19), 3262–3264.
60. Troyano, J.; Castillo, Ó.; Amo-Ochoa, P.; Fernández-Moreira, V.; Gómez-García, C. J.; Zamora, F.; Delgado, S. *J. Mater. Chem. C* **2016**, *4*(36), 8545–8551.
61. Conesa-Egea, J.; Gallardo-Martinez, J.; Delgado, S.; Martinez, J. I.; Gonzalez-Platas, J.; Fernandez-Moreira, V.; Rodriguez-Mendoza, U. R.; Ocon, P.; Zamora, F.; Amo-Ochoa, P. *Small* **2017**, 13(33), 1700965–1700976.
62. Conesa-Egea, J.; Nogal, N.; Martinez, J. I.; Fernandez-Moreira, V.; Rodriguez-Mendoza, U. R.; Gonzalez-Platas, J.; Gomez-Garcia, C. J.; Delgado, S.; Zamora, F.; Amo-Ochoa, P. *Chem. Sci.* **2018**, *9*(41), 8000–8010.
63. Denny, M. S., Jr.; Cohen, S. M. *Angew. Chem. Int. Ed.* **2015**, *54*(31), 9029–9032.
64. DeCoste, J. B.; Denny, M. S., Jr.; Peterson, G. W.; Mahle, J. J.; Cohen, S. M. *Chem. Sci.* **2016**, 7(4), 2711–2716.
65. Zhao, C. W.; Ma, J. P.; Liu, Q. K.; Wang, X. R.; Liu, Y.; Yang, J.; Yang, J. S.; Dong, Y. B. *Chem. Commun.* **2016**, *52*(30), 5238–5241.
66. Troyano, J.; Castillo, O.; Martinez, J. I.; Fernandez-Moreira, V.; Ballesteros, Y.; Maspoch, D.; Zamora, F.; Delgado, S. *Adv. Funct. Mater.* **2018**, *28*(5), 1704040.
67. Conesa-Egea, J.; Moreno-Vazquez, A.; Fernandez-Moreira, V.; Ballesteros, Y.; Castellanos, M.; Zamora, F.; Amo-Ochoa, P. *Polymers* **2019**, 11(6), 1047–1061.

68. Assefa, Z.; Omary, M. A.; McBurnett, B. G.; Mohamed, A. A.; Patterson, H. H.; Staples, R. J.; Fackler, J. P. *Inorg. Chem.* **2002**, *41*(24), 6274–6280.
69. Egea, J. C.; Gonzalez-Platas, J.; Rodriguez-Mendoza, U. R.; Martínez, J. I.; Pilar, O.; Fernandez, V.; Costa, R. D.; Fernandez-Cestay, J.; Zamora, F.; Amo-Ochoa, P. *J. Mater. Chem. C* **2020**, *8*, 1448–1458.
70. Li, J.-C.; Li, H.-X.; Li, H.-Y.; Gong, W.-J.; Lang, J.-P. *Cryst. Grow. Desig.* **2016**, *16*(3), 1617–1625.
71. Furukawa, H.; Cordova, K. E.; O'Keeffe, M.; Yaghi, O. M. *Science* **2013**, *341*(6149), 1230444–1230456.
72. Yaghi, O. M.; Li, H. *J. Am. Chem. Soc.* **1995**, *117*(41), 10401–10402.
73. Kalmutzki, M. J.; Hanikel, N.; Yaghi, O. M. *Sci. Adv* **2018**, *4,* eaat9180–eaat9196.
74. Bai, Y.; Dou, Y.; Xie, L. H.; Rutledge, W.; Li, J. R.; Zhou, H. C. *Chem. Soc. Rev.* **2016**, *45*, 2327–2367.
75. Eddaoudi, M.; Kim, J.; Rosi, N.; Vodak, D.; Wachter, J.; O'Keeffe, M.; Yaghi, O. M. *Science* **2002**, *295*(5554), 469–472.
76. Li, J. R.; Kuppler, R. J.; Zhou, H. C. *Chem. Soc. Rev.* **2009**, *38*, 1477–1504.
77. Cui, Y.; Yue, Y.; Qian, G.; Chen, B. *Chem. Rev.* **2012**, *112*(2), 1126–1162.
78. Della Rocca, J.; Liu, D.; Lin, W. *Acc. Chem. Res.* **2011**, *44*(10), 957–968.
79. Horcajada, P.; Gref, R.; Baati, T.; Allan, P. K.; Maurin, G.; Couvreur, P.; Férey, G.; Morris, R. E.; Serre, C. *Chem. Rev.* **2012**, *112*(2), 1232–1268.
80. Liu, J.; Chen, L.; Cui, H.; Zhang, J.; Zhang, L.; Su, C. Y. *Chem. Soc. Rev.* **2014**, *43*, 6011–6061.
81. Li, S. L.; Xu, Q. *Energy Environ. Sci.* **2013**, *6*, 1656–1683.
82. Hu, M.; Reboul, J.; Furukawa, S.; Radhakrishnan, L.; Zhang, Y.; Srinivasu, P.; Iwai, H.; Wang, H.; Nemoto, Y.; Suzuki, N.; Kitagawa, S.; Yamauchi, Y. *Chem. Commun.* **2011**, *47*, 8124–8126.
83. Cho, W.; Lee, Y. H.; Lee, H. J.; Oh, M. *Chem. Commun.* **2009**, 4756–4758.
84. Xia, W.; Zou, R.; An, L.; Xia, D.; Guo, S. *Energy Environ. Sci.* **2015**, *8*, 568–576.
85. Moon, H. R.; Lim, D. W.; Suh, M. P. *Chem. Soc. Rev.* **2013**, *42*, 1807–1824.
86. Rösler, C.; Fischer, R. A. *CrystEngComm* **2015**, *17*, 199–217.
87. Wu, C. D.; Zhao, M. *Adv. Mater.* **2017**, *29*(14), 1605446–1605467.
88. Farid, S.; Ren, S.; Hao, C. *Inorg. Chem. Commun.* **2018**, *94*, 57–74.
89. Zhao, Y.; Song, Z.; Li, X.; Sun, Q.; Cheng, N.; Lawes, S.; Sun, X. *Energ. Stor. Mater.* **2016**, *2*, 35–62.
90. D'Vries, R. F.; Álvarez-García, S.; Snejko, N.; Bausá, L. E.; Gutiérrez-Puebla, E.; De Andrés, A.; Monge, M. Á. *J. Mater. Chem. C* **2013**, *1*, 6316–6324.
91. Yin, Z.; Wan, S.; Yang, J.; Kurmoo, M.; Zeng, M. H. *Coord. Chem. Rev.* **2019**, *378*, 500–512.
92. Kim, M.; Cahill, J. F.; Fei, H.; Prather, K. A.; Cohen, S. M. *J. Am. Chem. Soc.* **2012**, *134*(43), 18082–18088.
93. Evans, J. D.; Sumby, C. J.; Doonan, C. J. *Chem. Soc. Rev.* **2014**, *43*, 5933–5951.
94. Cohen, S. *M.* Chem. Rev. **2012**, *112*(2), 970–1000.
95. Castillo-Blas, C.; De La Peña-O'Shea, V. A.; Puente-Orench, I.; De Paz, J. R.; Sáez-Puche, R.; Gutiérrez-Puebla, E.; Gándara, F.; Monge, Á. *Sci. Adv.* **2017**, *3*(7), e1700773–e1700783.
96. Platero-Prats, A. E.; Mavrandonakis, A.; Gallington, L. C.; Liu, Y.; Hupp, J. T.; Farha, O. K.; Cramer, C. J.; Chapman, K. W. *J. Am. Chem. Soc.* **2016**, *138*(12), 4178–4185.
97. Ren, J.; Ledwaba, M.; Musyoka, N. M.; Langmi, H. W.; Mathe, M.; Liao, S.; Pang, W. *Coord. Chem. Rev.* **2017**, *349*, 169–197.
98. Dissegna, S.; Epp, K.; Heinz, W. R.; Kieslich, G.; Fischer, R. A. *Adv. Mater.* **2018**, *30*(37), 1704501–1704524.

99. López-Maya, E.; Montoro, C.; Colombo, V.; Barea, E.; Navarro, J. A. R. *Adv. Funct. Mater.* **2014**, *24*(39), 6130–6135.
100. Padial, N. M.; Quartapelle Procopio, E.; Montoro, C.; López, E.; Oltra, J. E.; Colombo, V.; Maspero, A.; Masciocchi, N.; Galli, S.; Senkovska, I.; Kaskel, S.; Barea, E.; Navarro, J. A. R. *Angew. Chem. Int. Ed.* **2013**, *52*(32), 8290–8294.
101. Montoro, C.; Ocón, P.; Zamora, F.; Navarro, J. A. R. *Chem. – Eur. J.* **2016**, *22*, 1646–1651.
102. Mondloch, J. E.; Bury, W.; Fairen-Jimenez, D.; Kwon, S.; Demarco, E. J.; Weston, M. H.; Sarjeant, A. A.; Nguyen, S. T.; Stair, P. C.; Snurr, R. Q.; Farha, O. K.; Hupp, J. T. *J. Am. Chem. Soc.* **2013**, *135*(28), 10294–10297.
103. Platero-Prats, A. E.; League, A. B.; Bernales, V.; Ye, J.; Gallington, L. C.; Vjunov, A.; Schweitzer, N. M.; Li, Z.; Zheng, J.; Mehdi, B. L.; Stevens, A. J.; Dohnalkova, A.; Balasubramanian, M.; Farha, O. K.; Hupp, J. T.; Browning, N. D.; Fulton, J. L.; Camaioni, D. M.; Lercher, J. A.; Truhlar, D. G.; Gagliardi, L.; Cramer, C. J.; Chapman, K. W. *J. Am. Chem. Soc.* **2017**, *139*(30), 10410–10418.
104. Li, Z.; Schweitzer, N. M.; League, A. B.; Bernales, V.; Peters, A. W.; Getsoian, A. B.; Wang, T. C.; Miller, J. T.; Vjunov, A.; Fulton, J. L.; Lercher, J. A.; Cramer, C. J.; Gagliardi, L.; Hupp, J. T.; Farha, O. K. *J. Am. Chem. Soc.* **2016**, *138*(6), 1977–1982.
105. Li, Z.; Peters, A. W.; Bernales, V.; Ortuño, M. A.; Schweitzer, N. M.; Destefano, M. R.; Gallington, L. C.; Platero-Prats, A. E.; Chapman, K. W.; Cramer, C. J.; Gagliardi, L.; Hupp, J. T.; Farha, O. K. *ACS Cent. Sci.* **2017**, *3*(1), 31–38.
106. Mondloch, J. E.; Katz, M. J.; Isley, W. C.; Ghosh, P.; Liao, P.; Bury, W.; Wagner, G. W.; Hall, M. G.; Decoste, J. B.; Peterson, G. W.; Snurr, R. Q.; Cramer, C. J.; Hupp, J. T.; Farha, O. K. *Nat. Mater.* **2015**, *14*(5), 512–516.
107. De Koning, M. C.; Van Grol, M.; Breijaert, T. *Inorg. Chem.* **2017**, *56*(19), 11804–11809.
108. Hafizovic Cavka, J.; Jakobsen, S.; Olsbye, U.; Guillou, N.; Lamberti, C.; Bordiga, S.; Lillerud, K. P. *J. Am. Chem. Soc.* **2008**, *130*(42), 13850–13851.
109. Furukawa, H.; Gándara, F.; Zhang, Y. B.; Jiang, J.; Queen, W. L.; Hudson, M. R.; Yaghi, O. M. *J. Am. Chem. Soc.* **2014**, *136*(11), 4369–4381.
110. Wu, H.; Chua, Y. S.; Krungleviciute, V.; Tyagi, M.; Chen, P.; Yildirim, T.; Zhou, W. *J. Am. Chem. Soc.* **2013**, *135*(28), 10525–10532.
111. Ameloot, R.; Aubrey, M.; Wiers, B. M.; Gõmora-Figueroa, A. P.; Patel, S. N.; Balsara, N. P.; Long, J. R. *Chem. – Eur. J.* **2013**, *19*(18), 5533–5536.
112. López-Maya, E.; Montoro, C.; Rodríguez-Albelo, L. M.; Aznar Cervantes, S. D.; Lozano-Pérez, A. A.; Cenís, J. L.; Barea, E.; Navarro, J. A. R. *Angew. Chem. Int. Ed.* **2015**, *54*, 6790–6794.
113. Yu, L.; Wu, H. B.; Lou, X. W. D. *Acc. Chem.Res.* **2017**, *50*(2), 293–301.
114. Xia, W.; Mahmood, A.; Zou, R.; Xu, Q. *Energy Environ. Sci.* **2015**, *8*(7), 1837–1866.
115. Castillo-Blas, C.; Gándara, F. *Isr. J. Chem* **2018**, *58*(9–10), 1036–1043.
116. Castillo-Blas, C.; Snejko, N.; De La Peña-O'Shea, V. A.; Gallardo, J.; Gutiérrez-Puebla, E.; Monge, M. A.; Gándara, F. *Dalton Trans.* **2016**, *45*, 4327–4337.
117. Monge, A.; Snejko, N.; Gutiérrez-Puebla, E.; Medina, M.; Cascales, C.; Ruiz-Valero, C.; Iglesias, M.; Gómez-Lor, B. *Chem. Commun.* **2005**, 1291–1293.
118. Castillo-Blas, C.; López-Salas, N.; Gutiérrez, M. C.; Puente-Orench, I.; Gutiérrez-Puebla, E.; Ferrer, M. L.; Monge, M. Á.; Gándara, F. *J. Am. Chem. Soc.* **2019**, *141*(4), 1766–1774.

CHAPTER FOUR

Selected polyazole based coordination polymers displaying functional properties

Yann Garcia*

Institute of Condensed Matter and Nanosciences, Molecular Chemistry, Materials and Catalysis Division (IMCN/MOST), Universite catholique de Louvain, Louvain-La-Neuve, Belgium
*Corresponding author: e-mail address: yann.garcia@uclouvain.be

Contents

Abstract

In this account, we present recent on-going developments on the design and synthesis of transition metal (M(II) = Fe, Cu, Zn, Cd, Hg) coordination networks built from 1,2,4-triazole, tetrazole, benzimidazole or pyrazole building blocks. Special focus is placed on the use of a high energetic material made of a dissymmetric 1,2,4-triazole-tetrazole ligand, able to provide coordination polymers of alkali metals and alkaline earth metals, as well as salts. These materials, apart from their structural diversity and appeal, present some potential applications in gas or metallic storage, molecular electronics (spin cross-over), gas sensing, toxic metal sensing and capture, as well as in medicinal applications.

1. Introduction

Ligand molecules containing azole building blocks are widely used as organic connectors in supramolecular coordination chemistry,[1] as an alternative to classic pyridine and other nitrogen donor molecules.[2] Such molecules, which are often coordinated in multi-dentate fashion, have afforded a

Advances in Inorganic Chemistry
ISSN 0898-8838
https://doi.org/10.1016/bs.adioch.2020.04.001

variety of metal organic frameworks (MOFs) and coordination polymers (CPs) of different topologies. Such networks range from one dimensional (1D) CPs to two dimensional (2D) layered or three dimensional (3D) metal-azolate/azole networks (MANs).[3] Numerous functional properties were discovered with applications in gas storage,[4] catalysis,[5] chromatography,[6] optics,[7] magnetism,[8] health,[9] to name but a few. Among azole networks, those with 1,2,4-triazole or tetrazole building blocks coordinated to Fe(II) ions have attracted special interest because of their ligand field strength, which was found to be in the expected range for thermally induced spin crossover (SCO) observation.[10] For instance, the Fe(II) CP $[Fe(btzp)_3](ClO_4)_2$ (**1**) (***btzp*** = 1,4-bis (tetrazol-1-yl)butane, Scheme 1) discovered by van Koningsbruggen *et al.*[11] displayed on cooling a reversible SCO behavior, which was the first 1D chain for which the crystal structure was solved, in both low-spin (LS) and high-spin (HS) states. This linear chain allowed to introduce for the first time, the concept of elastic interactions cushioning (so called "airbag" effect) to explain the gradual character of its SCO behavior. In addition, it is considered as the first example of Light Induced Excited Spin State Trapping (LIESST) for a 1D chain, after green light irradiation at liquid helium temperatures.[11]

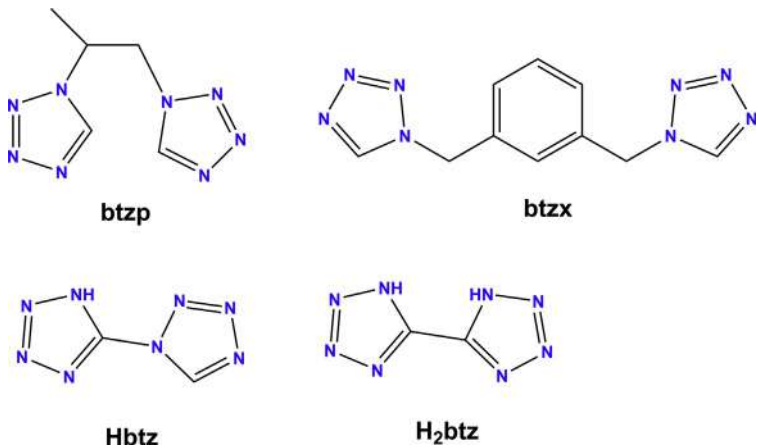

Scheme 1 Molecular structures of selected bis-tetrazole ligands.

Later a number of bis-tetrazole and tris-tetrazole CPs, with different dimensionalities, were investigated,[10,12] some being for instance studied for their gas storage properties, i.e., $[Fe(\mathbf{btzx})_3](ClO_4)_2$ (**2**) (***btzx*** = 1,4-bis (tetrazol-1-ylmethyl)benzene, Scheme 1).[13]

A noticeable interest has been devoted too to 1D Fe(II) chains with 4R-1,2,4-triazole ligands (R = substituent, Scheme 2), due to their synthetic modularity and high yield, allowing to derive structure-magnetic property relationships. Several chemical parameters were varied such as the nature of the R group on the 1,2,4-triazole unit, the counter anions (playing with their size, geometry, charge and volume) and solvent molecules, if any, allowing to discover a wide range of SCO behavior.[14] For instance, a linear relationship was established for the families $[Fe(hyetrz)_3](Anion)_2$ (**3**) (***hyetrz*** = 4–2′-hydroxy-ethyl-1,2,4-triazole),[15] and $[Fe(NH_2trz)_3](Anion)_2$ (**4**) (***NH₂trz*** = 4-amino-1,2,4-triazole),[16] involving the transition temperature observation and the volume of the inserted counter anion. The smaller the volume of the anion, the higher the transition temperature.[17] This has led to the discovery of SCO behavior

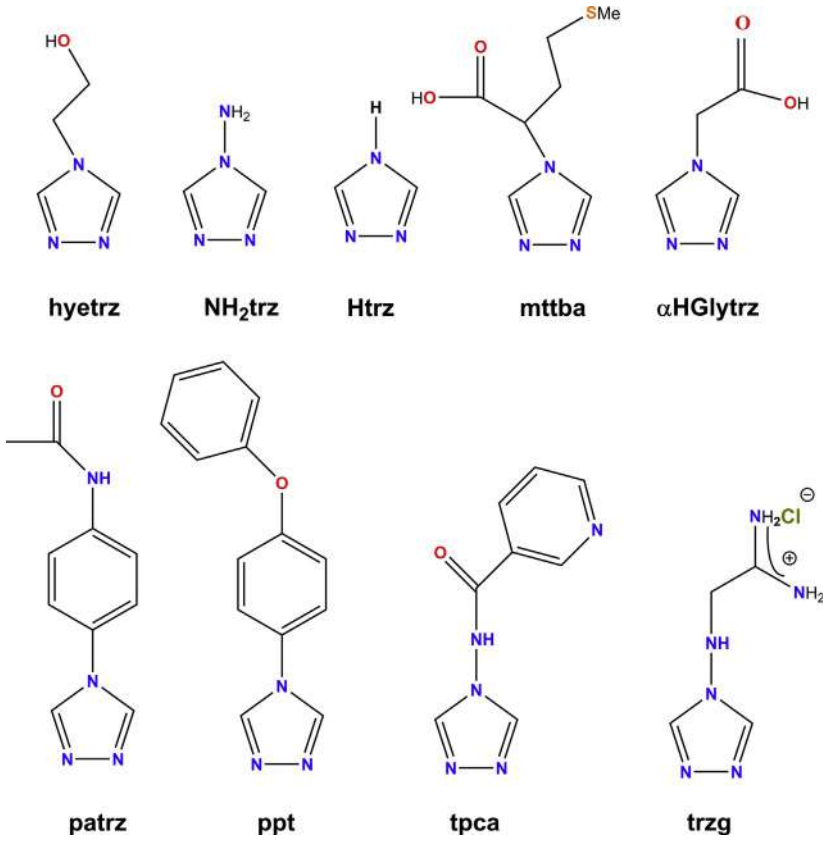

Scheme 2 Molecular structures of selected 4R-1,2,4-triazole molecules (R = substituent).

occurring around the room temperature region, with remarkable themochromic properties, e.g., for $[Fe(hyetrz)_3]I_2$•xsolv (**5**).[15] This material was shown to display, in addition to its thermochromism, weak pressure piezochromism properties allowing to derive a contact pressure optical sensor operating at room temperature. Applications in aeronautics and civil security were for instance proposed.[18] Numerous efforts were also devoted to nano-structuration of these 1D materials as nanoparticles or thin films,[19] while their implementation into spintronic devices has recently been investigated.[20] Hybrid materials including such 1D chains were also prepared, e.g., $[Fe(Htrz)trz]BF_4$ (**6**) (***Htrz*** = 4H-1,2,4-triazole, ***trz*** = 1,2,4-triazolato), embedded into the pores of MCM-41.[21] This material displays exceptional SCO characteristics near the room temperature region, with sharp spin transitions, a reproducible and large thermal hysteresis loop (35 K), as well as a contrasting color change. Last but not least, it does not contain any lattice solvent molecules, which are known to lead to non-reproducible spin transitions and fake hysteresis loops, when removed from the material by heating.

Apart for linear chains, whose polymerization relies on the bidentate mode of 4R-1,2,4-triazole, the design of a higher dimensionality network has involved the use of bis-1,2,4-triazole type ligands containing "long" flexible spacers, after the discovery of the first 2D SCO network, $[Fe(btr)_2(NCS)_2]$•H_2O (**7**) (***btr*** = 4,4′-bis-1,2,4-triazole),[22] and the first 3D SCO network $[Fe(btr)_3](ClO_4)_2$ (**8**).[23] The number of coordination networks with bis-1,2,4-triazole-derivatives remain, however, scarce.[10] This situation presumably depends on synthetic issues associated with the preparation of 4R-triazole precursors, which usually relies on the application of the Bayer's patent synthetic route, which is known to be moderately efficient in terms of yield and often involves unwanted chromatographic work ups.[24] As a result of the desire to efficiently produce 4R-triazole derivatives, and in particular the celebrated ***btr*** and ***btre*** (1,2-bis(1,2,4-triazol-4-yl)ethane) precursors in a large amount (Scheme 3) compared to the multi-step synthetic method from Bartlett and Humphrey,[25] we have revised a classic transamination reaction. This method has been extended to the synthesis of a wide range of 4R-1,2,4-triazole,[26] e.g., ***patrz*** = *N*-(4-(4*H*-1,2,4-triazol-4-yl)phenyl)acetamide (Scheme 2), an active intermediate in the "sumatriptan" drug. This methodology has been adopted by many groups to produce interesting CPs and MOFs.[27] In particular, we have prepared a new range of building blocks based on amino acids, which produced new azole CPs and MOFs.[28,29] In the present chapter, we present selected recent results in crystal engineering of CPs with azole based ligands with interesting properties.

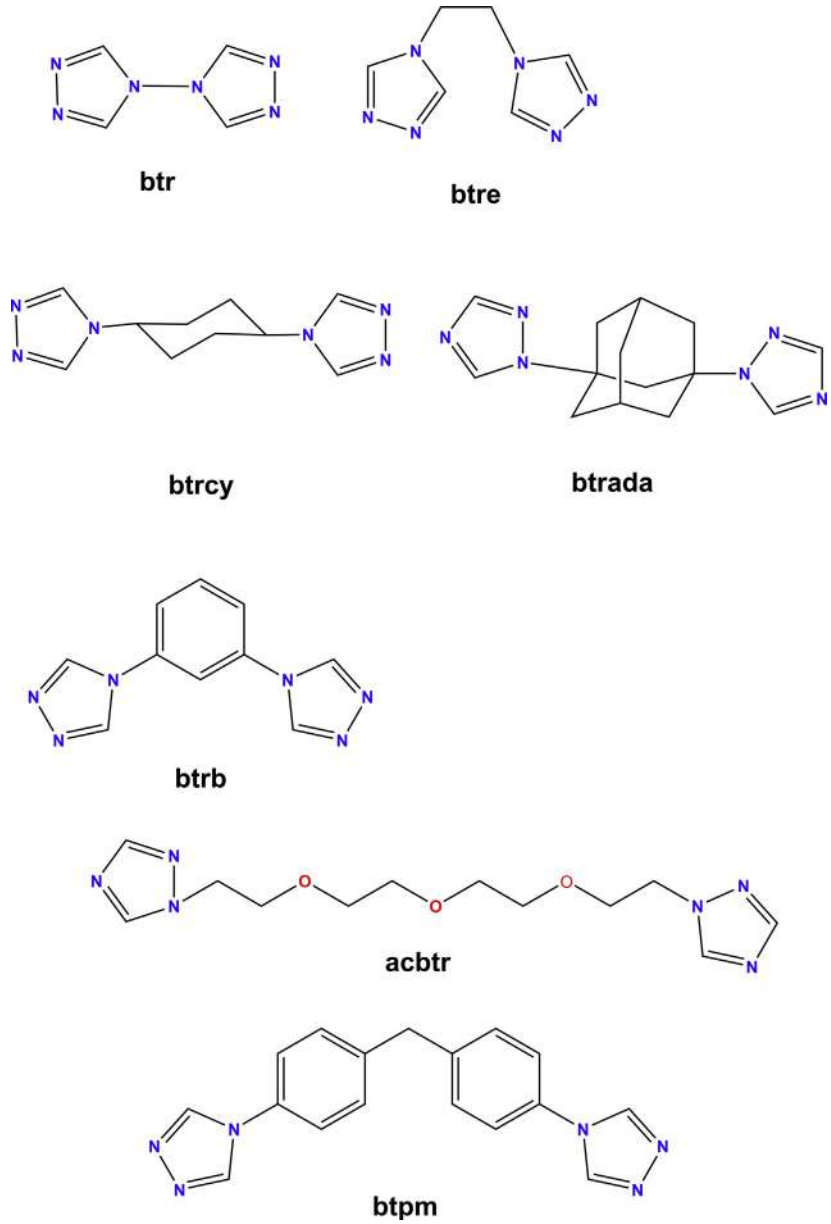

Scheme 3 Molecular structures of selected bis-1,2,4-triazole ligands.

2. Selected coordination networks for metal capture

Maintaining our efforts to produce CPs based on amino acid 1,2,4-triazole derivatives, which were reviewed in 2011,[29] Naik *et al*. have prepared a conformationally flexible triazole-carboxylic acid ligand derived from L-amino acid, namely 4H-1,2,4-triazol-4-yl-acetic acid (**αHGlytrz,** Scheme 2).[28a] Self-assembly of this small molecule in water with $CuSiF_6$ yielded a novel single-wall metal organic nanotube (SWMONT) crystallizing in the P31c space group (Fig. 1). This material of formula $\{[Cu_3(\mu_3\text{-}OH)(H_2O)_3(Glytrz)_3]\cdot SiF_6\cdot 8H_2O\cdot X\}$ (**9**) (where X = disordered lattice water molecules), is made of trinuclear Cu^{II} cluster units.[30] The originality of this material stems from its nano-tubular architecture, which is commonly available in single-walled carbon nanotubes (SWCNTs),[31] but herein prepared by a one-step synthesis using a simple and small organic precursor reacting to a common Cu(II) salt in water (Fig. 1). This material does not suffer any oxidation and could be prepared in diverse forms: (i) as single crystals which allowed to determine its crystal structure by X-ray diffraction. (ii) As powders, on a much larger scale, after checking that its formulation and crystal

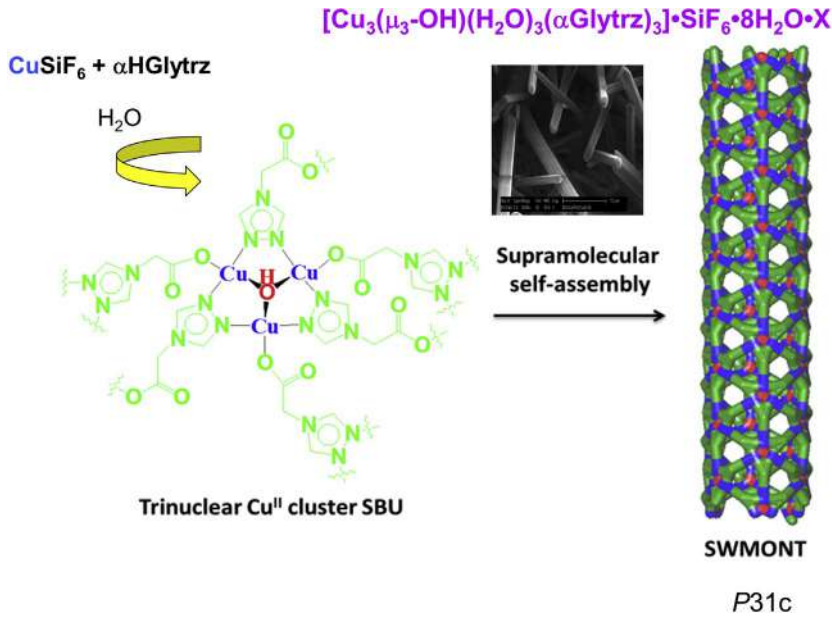

Fig. 1 Synthesis of **9**: a SWMONT obtained from 4H-1,2,4-triazol-4-yl-acetic acid (***αHGlytrz***).[30]

structure are preserved by powder X-ray diffraction. (iii) As thin layers by precipitation/deposition using an electrochemical method, to check its potential to be deposited on a large surface, which could be necessary in case this material would be used in a sensing device. This material, in addition to its unprecedented structure, features a pore size as large as zeolites,[32] thus offering potential, e.g., in gas storage.

Apart from gas storage, which is commonly encountered in MOFs, we have extended its storage properties to metals, in particular metallic mercury by applying Mercury intrusion porosimetry (MIP), a technique which is commonly used in the study of hierarchical porous solids, e.g., for catalytic applications.[33] Indeed, **9** was shown to store metallic mercury, after a moderate pressure treatment, contrary to previous examples (Fig. 2).

The need of a metallic mercury sensor is motivated by the ability of this inorganic element to compromise both respiratory and immune systems,[34a] and lead to neurological, heart and renal dysfunction when it comes into contact with a tissue in sufficient concentration,[34b] thus being considered as threat for public health environment. Interestingly, the chemical composition of **9** completely differs from MIL-53 (Cr), the first reported MOF with mercury storing properties,[35] thus opening a new field of investigation based on chemical design. This material could be used for instance as mercury sponge for household area safety issues, e.g., when children play with shining mercury marbles, coming from old thermometers or domestic lamps.[34a]

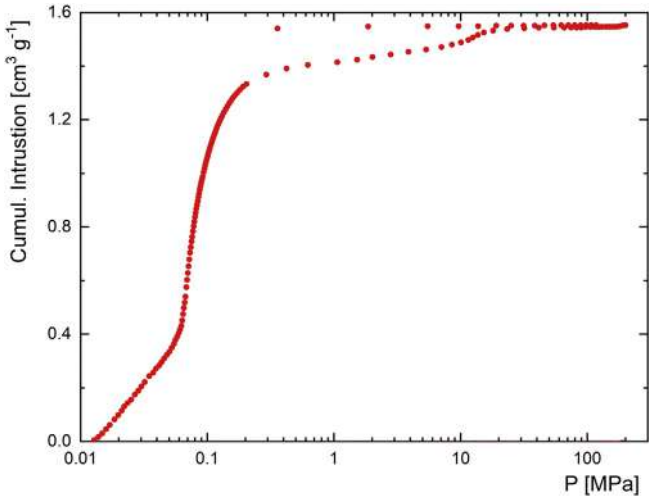

Fig. 2 Metallic mercury intrusion curve in SWMONT **9**.[30]

Apart from metallic mercury capture, Radi *et al*. recently designed a novel hybrid inorganic-organic material (**10**) made of modified silica on which a diamine Schiff base molecule able to capture Hg(II) was immobilized.[36] This hybrid material was prepared firstly by converting a diamine precursor, made of 4-aminophenol and picolinaldehyde in dry ethanol, using acetic acid as catalyst, on an alco-olate salt. This salt was subsequently reacted with a 3-glycidoxypropyltrimethoxysilan
e silylant agent, previously anchored on a silica surface in a heterogeneous manner to yield the target hybrid material (Fig. 3).

This material displayed good thermal stability as well as chemical stability in various acidic and buffer solutions (pH = 1–7). In addition to its porous properties, it presented a retention as high as 98(1) $mg.g^{-1}$ of Hg(II) after five cycles. More interestingly, regeneration was reproducible without destruction of the hybrid matrix by using 5–10 mL of 6 N HCl/g of support.[36] These characteristics offer new opportunities in water cleaning given the range of hybrid materials which could be prepared based on this technology, with interesting sensing properties not only concerning Hg(II) but also Cd(II), Cu(II), Zn(II), Pb(II) to name but a few.[37] In particular, selective properties of such hybrid materials towards a given metal was demonstrated. For instance, coordination of a metal ion (e.g., Cu(II)) was recently supported by a single X-ray diffraction study of a model Cu(II) dinuclear complex.[37b] Such hybrid materials have recently been applied to the cleaning of real water samples originating from two oriental Moroccan rivers: the *Ghiss*, who is known to drop into the *Al Hoceima Gulf*, and the *Touissit-bou-bekker* who is located near *Oujda*, with nearby mining activities recognized to bring enough polluting metals suitable for our investigations.

Pursuing our efforts to investigate the topology and emerging properties of new CPs with azole based ligands, Adarsh *et al*. could grow pale-green block shaped X-ray quality single crystals in reasonable yield (53%) of $[Cu(btzx)_2(MeOH)_2](NO_3)_2$ (**11**) by mixing, in methanol, $Cu(NO_3)_2 \cdot 3H_2O$ and ***btzx*** (Scheme 1) in a 1:2 and even in a 1:3 metal: ligand ratio.[38] The crystal structure of **11** reveals a coordination environment made of two ***btzx*** ligands and two MeOH solvent molecules with Cu-O = 2.2535(14) Å. The designed CuN_4O_2 units laid in a slightly distorted square bipyramidal geometry, with Cu-*N* = 2.0398(16) Å and Cu-*N* = 2.0659(17) Å. Such units are linked to form a 1D looped chain, crystallizing in the triclinic $P\bar{1}$ space group (Fig. 4). The intra metallic Cu⋯Cu distance is 10.238 Å. The polymeric chains recognize the nitrato counter anion via O-H⋯O

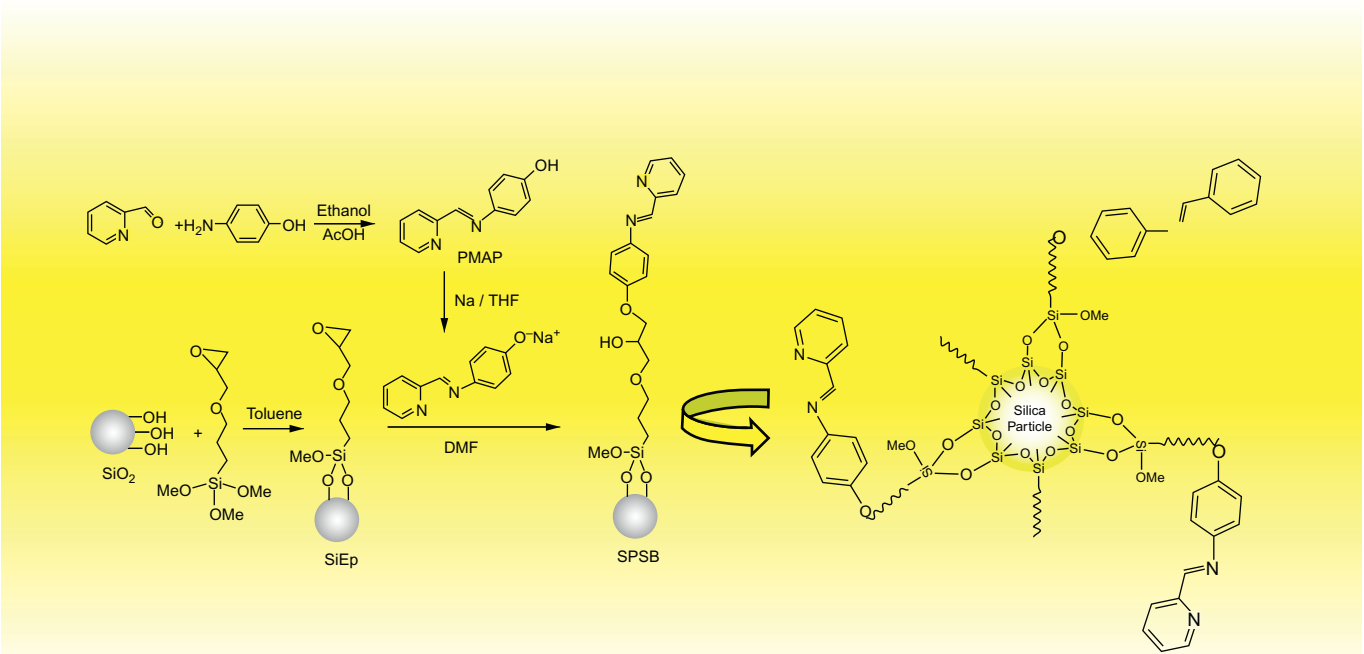

Fig. 3 Synthesis of **10**, a hybrid inorganic-organic silica material able to capture Hg(II).[36]

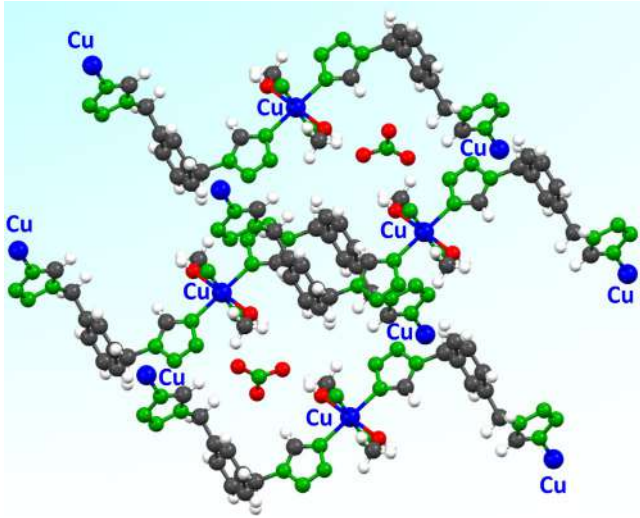

Fig. 4 View of the crystal structure of the 1D looped chain in **11** built from 1,4-bis(-tetrazol-1-ylmethyl)benzene (***btzx***).[38]

hydrogen bonding involving the metal bound methanol molecule [O···O = 2.696(5) Å; ∠O–H···O = 172.52°]. Such chains are packed on top of each other in a slightly off-set fashion sustained by various intermolecular interactions. Worthwhile to note is that the ***btzx*** ligand was previously used in iron(II) coordination chemistry to produce 1D chains.[39] These chains on cooling, displayed gradual SCO profiles due to the flexible and long ***btzx*** spacer between the active spin species, which inefficiently propagate elastic interactions associated with the spin state change. Nevertheless, these materials were found suitable to investigate the influence of gas storage on their SCO properties, in particular with $CO_{2(g)}$.[13]

With the idea of investigating the influence of the chair/boat conformation of cyclohexane on Cu(II) coordination chemistry, we have recently synthesized $[Cu(btrcy)_2(H_2O)_2](ClO_4)_2 \cdot \mathbf{G}$ (***btrcy*** = bis(1,2,4-triazole)-*trans*-cyclohexane; G = ***btrcy*** or 0), which is a 2D network presenting host-guest properties.[38a] Reaction of ***btrcy*** (Scheme 3) with $Cu(ClO_4)_2 \cdot 6H_2O$ in water in a 1:2 ratio afforded a blue precipitate of $[Cu(btrcy)_2(H_2O)_2](ClO_4)_2$ (**12**) which is a 2D network without any guest molecules inclusion. Extension to a 3D network was attempted by reacting $Cu(ClO_4)_2 \cdot 6H_2O$ with a third equivalent of ***btrcy*** in water, which also led to a blue precipitate. Recrystallization from a water/acetone medium provided shining blue colored single crystals after 1 week of slow

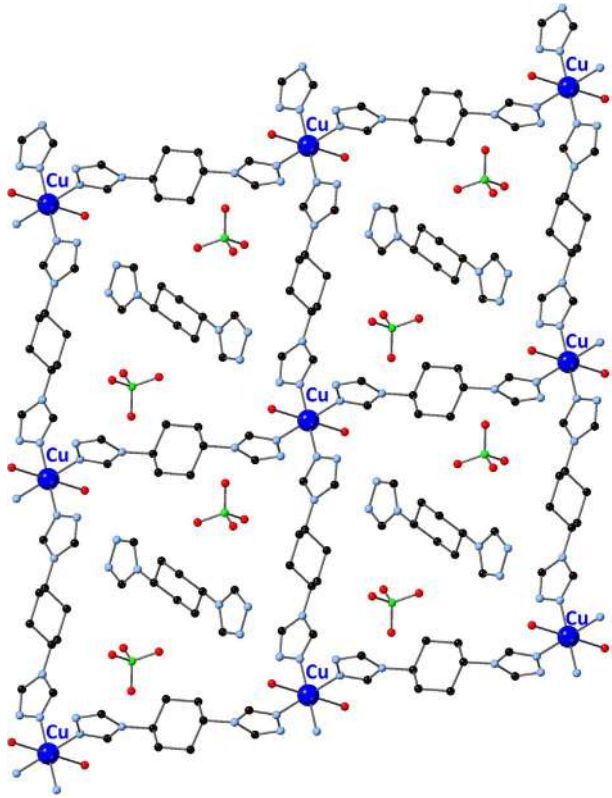

Fig. 5 Projection along the *a* axis of the 2D network **13** incorporating bis(1,2,4-triazole)-*trans*-cyclohexane (***btrcy***) molecules into its voids.[38a]

evaporation at room temperature, contrary to the previous experiment. The single-crystal X-ray diffraction data analysis revealed, however, a 2D-square grid crystallizing into the centrosymmetric triclinic space group $P\overline{1}$. The CP consists of ***btrcy*** connectors around Cu(II) modules coordinated to two water molecules and four ligands leading to CuN_4O_2 chromophores (Fig. 5). Such a Cu(II) coordination environment adopts a square bipyramid geometry, defined by only two Cu—N bond lengths (Cu–N4 = 2.014(2) Å and Cu–N1 = 2.035(2) Å) and one Cu—O bond length (Cu–O1 = 2.431(3) Å). The Cu(II) atoms are bridged by the ligands creating a polymeric 2D structure (Fig. 5). As a result, the shortest Cu ⋯ Cu distances do not bring into play copper atoms from the same layer. Channels are formed which can be considered as squared cavities with a surface of ca. 195 $Å^2$ and a volume equal to the volume of the crystallographic cell (1022 $Å^3$).

Coordination of Cu(II) to water molecules thus prevents the polymerization in the third dimension. Nevertheless, incorporation of three ***btrcy*** molecules was successful, but with an unexpected distribution compared to the target 3D $[Cu(btrcy)_3](ClO_4)_2$ network. Indeed, the formula of our new network is $[Cu(btrcy)_2(H_2O)_2](ClO_4)_2 \cdot btrcy$ (**13**) with a ***btrcy*** molecule no more acting as a ligand, but as a guest molecule trapped in the crystal lattice cavities. Indeed, one ***btrcy*** molecule and two perchlorate anions were encapsulated in these cavities (Fig. 5) supported by various H-bonding. The layers are linked to the guest molecules by H-bonding between the water molecules and the nitrogen atoms of the ligand and between the ligands and the perchlorate anions. The perchlorate anions are also involved in H-bonding with the ligand molecules with the same cavity. No relatively short distances are created between neighboring cavity contents. Therefore, the 2D-square grid architecture of **13** is further stabilized by ***btrcy*** molecules trapped as non-coordinated guest molecules in the crystal lattice, through hydrogen bonds involving the coordinated water molecules. Thus, this network is able to host large guest neutral molecules into its voids, a discovery which opens exciting perspectives for sensing guest molecular species which could be hosted into this network.

3. Spin crossover materials

Apart from bis-1,2,4-triazole chemistry, our group has recently focused on a reborn material made of Fe(II) nodes and the spider like tris-tetrazole ligand, ***N(entz)$_3$*** = tris[(tetrazole-1-yl)ethane]amine (Scheme 4).[40]

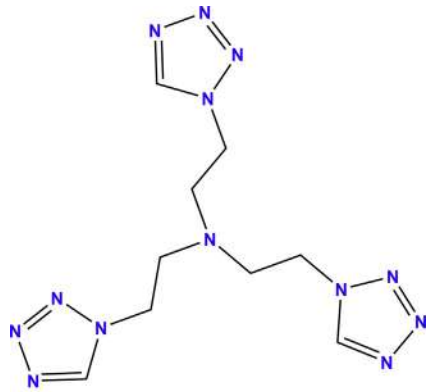

Scheme 4 Molecular structures of ***N(entz)$_3$*** and ***trz-tzH***.

This 2D material, $[Fe\{N(entz)_3\}_2](BF_4)_2$ (**14**) whose topology was first evidenced by Bronisz *et al.* during his PhD work,[41] represents the first spin transition grid built from a 1R-tetrazole ligand. It displays on cooling a sharp, hysteretic and complete SCO behavior with $T_C^{\downarrow} = 167$ K and $T_C^{\uparrow} = 176$ K. Reaction of ***N(entz)$_3$*** in acetonitrile with $[Fe(H_2O)_6](ClO_4)_2$ in 2:1 ratio lead to a clear solution, which after 1 week evaporation under darkness provided block shaped colorless crystals.[42] Single crystal X-ray diffraction analysis revealed 2D-corrugated sheets along the *b* axis, for $[Fe\{N(entz)_3\}_2](ClO_4)_2$ (**15**) crystallizing in the P-1 space group (Fig. 6). At 250 K, the Fe—N bong lengths were found to be 2.175–2.204 Å, which are typical for Fe(II) ions in the HS state. On cooling to 110 K, Fe-*N* = 1.992–1.998 Å, which is characteristic for Fe(II) LS ions.

Confirmation of a HS to LS transition was made by Mössbauer spectroscopy that revealed at room temperature, a quadrupole doublet with isomer

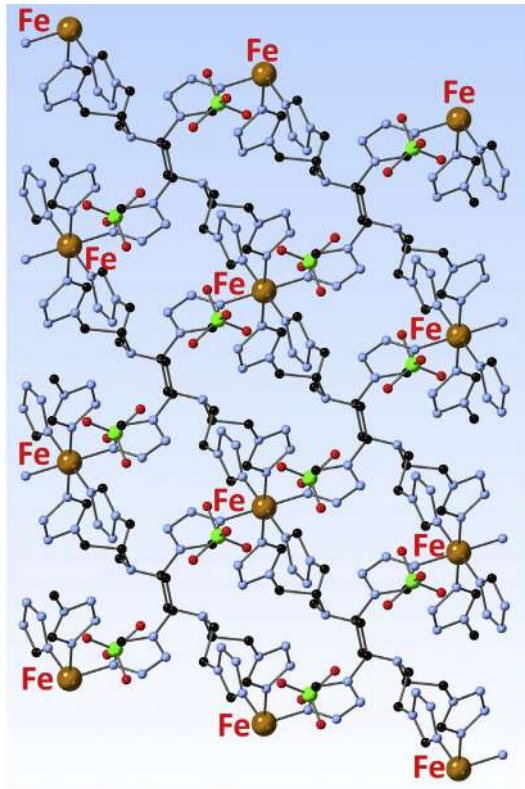

Fig. 6 View of the crystal structure of the 2D Fe(II) tris[(tetrazole-1-yl)ethane]amine (***N(entz)$_3$***) network (**15**) in the LS state, recorded at 110 K.[42]

shift $\delta^{HS} = 1.07(1)$ mm/s and quadrupole splitting $\Delta E_Q^{HS} = 1.46(1)$ mm/s typical of Fe(II) HS ions. Reduction of both isomer shifts and quadrupole splitting was observed at 78 K with $\delta^{LS} = 0.59(1)$ mm/s and $\Delta E_Q^{LS} = 0.21(1)$ mm/s, which are typical parameters for Fe(II) LS ions. Integration of the surface area of the Mössbauer spectra, assuming equal Debye Waller factors for HS and LS states, provided the temperature dependence evolution of the HS molar fraction. A steep, complete and hysteretic spin transition, shifted downwards compared to the BF_4^- derivative, with $T_C^{\downarrow} = 149$ K and $T_C^{\uparrow} = 170$ K, was observed (Fig. 7). This material displays in addition reversible thermochromism from white (room temperature) to violet (at liquid nitrogen temperature),[43] a feature which was preserved for the thin film obtained by drop casting an aqueous colloidal dispersion of flakes of this material into a poly(vinyl alcohol) matrix.[42]

Indeed, such appealing SCO properties combined to the 2D character of this material made it a candidate for a delamination study in view to ease its future implementation into spintronic devices, a field which has been recently reviewed.[44] Large size crystals were selected by Suarez-Garcia *et al.* and subsequently delaminated using an ultrasonic treatment followed by liquid-phase exfoliation using an orbital shaker. Centrifugation afforded stable colloidal suspensions of 2D flakes.[42]

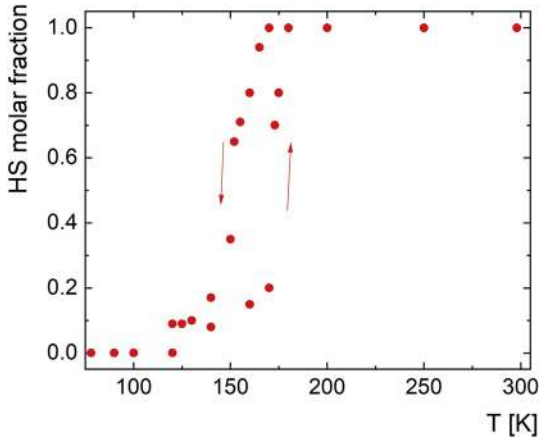

Fig. 7 Bistability domain as seen by the temperature dependence of the HS molar fraction for **15**.[43]

4. Crystal network design

Combing back to CPs design, the tetrafluoroborate anion has been used as template to precipitate/crystallize a number of cationic CPs and MOFs. It is known to be non-coordinating, with many reported examples, e.g., in Zn(II) complexes.[45–48] In addition, it is readily available in a number of metal salts and can be prepared easily from HBF_4 acid. It is preferred, along with the PF_6^- anion, to the perchlorate anion which is known to be potentially explosive.[49] The number of molecular complexes including coordinated BF_4 is rather weak due to the low coordination strength of metal-fluoro bonds, contrary to metal fluorides, e.g., $ZnF_2{\bullet}2H_2O$.[50] In particular, relatively few examples of Zn(II) complexes with coordinated BF_4^- anions have been reported. The list includes mononuclear complexes with monodentate coordination,[51–54] or μ_2 coordination,[55] as well as dinuclear complexes with mono coordination,[56–60] and μ_2 coordination,[61] a pentamer,[62] as well as an octamer.[63] This feature is interesting to block the propagation of a CP in the three space dimensions. Along this line, we have recently reported the first example of Zn(II) CP with a coordinated BF_4^- anion, which crystallized in a 1D coordination polymer.[64] Indeed, the reaction of $Zn(BF_4)_2 \cdot 6H_2O$ with acyclic cryptate-bis(1*H*-1,2,4-triazole) (***acbtr***) ligand (Scheme 3) in a 1:3 ratio in methanol yielded the 1D CP $Zn(acbtr)_2(BF_4)_2$, (**16**) which was crystallized in the monoclinic space group, *C*2/*m*.

The Zn(II) metal center sits in a slightly distorted octahedral geometry while the Zn(II) equatorial positions are occupied by the N atoms of the ligand. For **16**, Zn-*N* = 2.115(5) Å, which is longer than the bond lengths found in the dinuclear complex $[Zn_2(ptpp)_2]0.5EtOH$ (**17**) (***ptpp*** = (*E*)-2-({2-[3-(pyridin-2-yl)-1H-1,2,4-triazol-5-yl]phenylimino}methyl)phenol), or its polymorph, with Zn-*N* = 2.094 Å and 2.052 Å, respectively.[65,66] The Zn—N bond length is however shorter compared to the neutral trinuclear 1,2,4-triazole complex $[Zn_3(mttba)_6(H_2O)_6]$ (**18**) (***mttba*** = 4-(methylthio)-2-(4H-1,2,4-triazol-4-yl)butanoic acid, Scheme 2) with Zn-*N* = 2.159(4) Å and 2.145(4) Å.[67] The apical positions of Zn(II) are occupied with F atoms belonging to BF_4^- anions, with Zn-F = 2.178(7) Å. This bond length is in rather good agreement with the one of a dinuclear Zn(II) complex with Zn-F = 2.187 Å.[56] The ligand exhibits energetically less favorable *syn-syn* conformation around the aliphatic chain and keeps the 1,2,4-triazole rings *syn* to each other. Moreover the terminal 1,2,4-triazole rings coordinated to Zn(II) were oriented in a *syn* fashion resulting in an "W" shaped

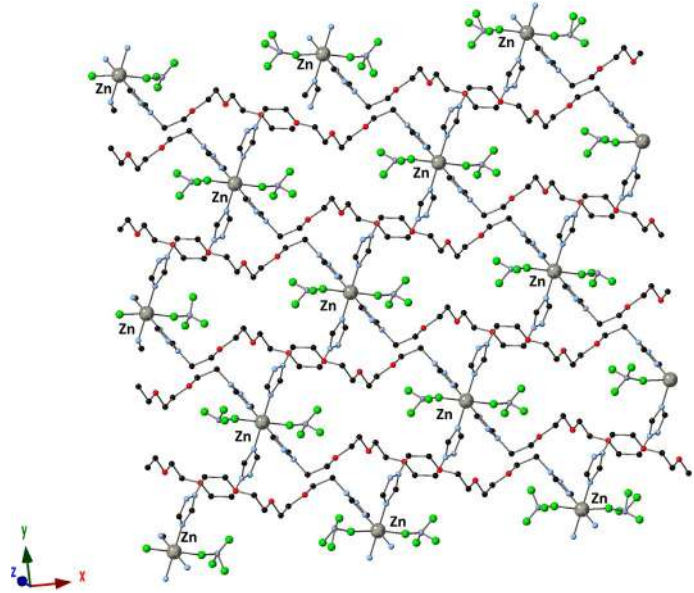

Fig. 8 Projection of the crystal structure of **16** showing 1D chains with the long acyclic cryptate-bis(1*H*-1,2,4-triazole) (***acbtr***) ligand.[64]

ligating topology. The conformational dependent "W" shaped ligating topology of the ligand, metal: ligand ratio (1:1), and coordination mode of the counter anion, leads to the formation of a 1D looped chain coordination polymer. C—H···F hydrogen bonding interaction was found in **16** involving the metal bound BF_4^- and C—H of the 1,2,4-triazole ring, which helped to stabilize the 1D looped CP chains (Fig. 8).

Reaction of ***acbtr*** with $Cu(NO_3)_2 \cdot 3H_2O$ in methanol led to the isostructural $Cu(acbtr)_2(NO_3)_2$ (**19**). The metal bound nitrate anion is connected to the C—H of a 1,2,4-triazole ring through a C—H···O interaction, which allows to consider this 1D looped chain as a 2D supramolecular polymer. Compound **19** represents a rare example of nitrato anion coordination in Cu(II) bis-triazole CPs. Few examples have been discovered including a 2D network, $[Cu(btr)_2(NO_3)_2] \cdot H_2O$ (**20**) and a 1D chain $[Cu_2(OH)(btrad)_2](NO_3)_3 \cdot 4H_2O$ (**21**) (***btrad*** = 1,3-bis(1,2,4-triazol-4-yl)-adamantane, Scheme 3) where nitrato anions are weakly coordinated with Cu-O = 2.747 Å,[68] and 2.768 Å,[69] respectively, contrary to **19** which shows a shorter distance with Cu-O = 2.447 Å. The situation differs for the 1D chain $[Cu(btrb)NO_3](NO_3) \cdot 2H_2O$ (**22**) with ***btrb*** = 1,3-di-(1,2,4-triazole-4-yl)

benzene, Scheme 3), where the nitrato anions μ_2-bridge the Cu(II) ions, with expected shorter Cu-O(NO_2) bond lengths of 2.3 Å.[70]

Sacrificial thermal treatment of molecular precursors is considered as a low energy consuming as well as straightforward method to produce metal oxides in powdered form, provided the molecular precursors are available in a decent amount, e.g., starting from polyaminocarboxylate metal complexes.[71] This method was only recently extended to CP and MOFs, e.g., to produce the β phase of CdO from the chain $[Cd_2(Glytrz)_2Cl_2]$ (**23**).[28a] Thermal treatment up to 537 °C of **16** and **19** afforded ZnO and CuO oxides, respectively.

Reaction of d^{10} transition metals (Zn(II), Cd(II) or Hg(II)) with flexible bent bis-1,2,4-triazole based ligands led to a set of CPs and mononuclear complexes of diverse topologies, which all display solid state blue luminescence at room temperature. Reaction of Zn(II) ions with ***btpm*** = bis(4-(1,2,4-triazol-4-yl)phenyl)methane (Scheme 3), a symmetric molecule prone to coordinate up to four metal centers to lead to multidimensional CPs, yielded a 1D chain $[ZnCl_2(btpm)]$ (**24**) (*P*–1) and a 2D square-grid $[Zn(btpm)_2(H_2O)](BF_4)_2{\cdot}2(btpm){\cdot}8H_2O$ (**25**) ($P2_12_12$). It is striking that such a diverse topology can be obtained while only modifying the reacting counter anion. Indeed, recrystallization from water of the precipitate obtained by the self-assembly of ***btpm*** with $ZnCl_2$ afforded the linear 1D CP (**24**) by repetition of $ZnCl_2$(btpm) units, with a bidentate bridging ***btpm*** spacer coordinating two tetrahedral Zn nodes, spaced out by 15.18(2) Å. Substitution of chloride by a weakly coordinating BF_4 anion resulted in the 2D CP (**25**). In **25**, ***btpm*** coordinates as in **24**, but four ligands are arranged around every Zn(II) cation, and a coordinated water molecule completes the coordination sphere. Given that a crystallographic twofold symmetry axis coincides with the $Zn-OH_2$ axis, the complex could be described as a distorted square pyramid, where the coordinated water molecule occupies the axial position. The distortion parameter τ_4 of 0.69, however, fits better with a trigonal-pyramidal geometry.[72] Working under hydrothermal conditions with $M(NO_3)_2$ (M = Zn, Cd) instead, led to the CP $[M_2(btpm)_3(H_2O)_4](NO_3)_4{\cdot}nH_2O$ (**26**) (M = Zn, $n = 1$ or M = Cd, $n = 3.5$),[73] whose crystal structure shows interpenetrating sheets with octahedral Zn nodes, confirming the influence of the synthetic conditions on the overall topology.

Reaction of a strongly coordinating anion, such as $CdCl_2$, under solvothermal conditions, resulted instead in a 1D chain, $[Cd_3Cl_6(btpm)_2]{\cdot}8H_2O$ (**27**) (*P*–1).[74] This compound only shows the μ_4-tetradentate coordination mode, and a bridging Cl anion. **27** forms a polymeric 1D chain

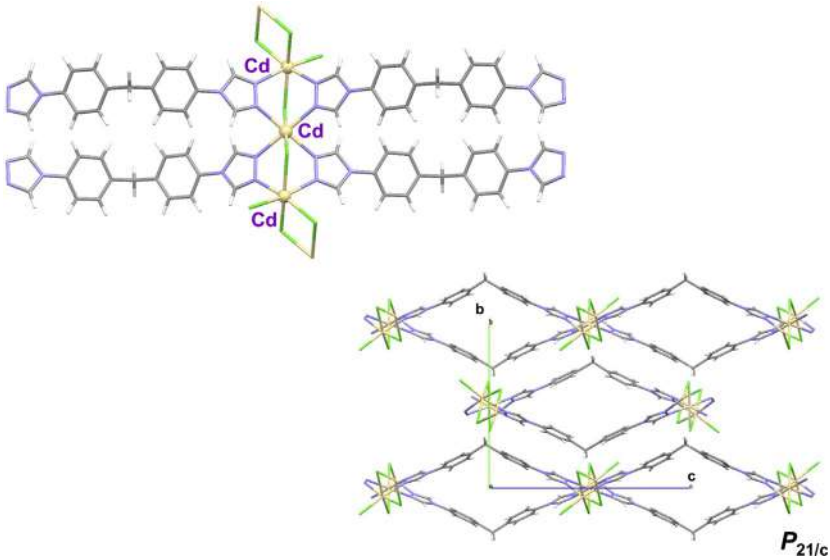

Fig. 9 View of the 2D bi waved polymer **27** built from bis(4-(1,2,4-triazol-4-yl)phenyl) methane (***btmp***).[74]

by repetition of linear tri-nuclear Cd units; the central Cd(II) ion is located on an inversion center and on either side it is coordinated by two bridging 1,2,4-triazole moieties and a bridging Cl atom, adopting a distorted octahedron. The terminal Cd(II) ions are also found in octahedral environments which are completed by three Cl atoms; two of these are bridging with a neighboring tri-nuclear unit, and one is a terminal Cl atom (Fig. 9).

Reaction with the newly designed ligand, ***ppt*** = 4-phenoxyphenyl-1,2,4-triazole (Scheme 2), afforded mononuclear complexes $[MCl_2(ppt)_2]$ (M = Zn, Hg) which crystallize in the *I2* (**28**) and *C2* (**29**) space groups, respectively. These were obtained following two crystallization methods, hydrothermal and slow diffusion, respectively. In each case, the metal ion is bound to one nitrogen atom belonging to two ppt ligands, as well as two chloride anions. A bivalent cationic 1D CP was, however, observed with Cd(II). $[Cd_2Cl_2(ppt)_4]CdCl_4 \cdot 4DMF$ (**30**) crystallizes in the *P-1* space group, with the inclusion of a non-coordinated $CdCl_4^{2-}$ anion which formed *in situ* (Fig. 10).

The use of the new bridging ligand, ***tpca*** = *N*-(1,2,4-triazol-4-yl)pyridine-3-carboxamide (Scheme 2) afforded two 1D chains of formula $[MCl_2(tpca)]$ (M = Zn (**31**) and Hg (**32**)) ($P2_1/c$) along with the 2D net, $[Cd(tpca)_2(H_2O)_2] \cdot 2H_2O$ (*C*2/c) (**33**).[74]

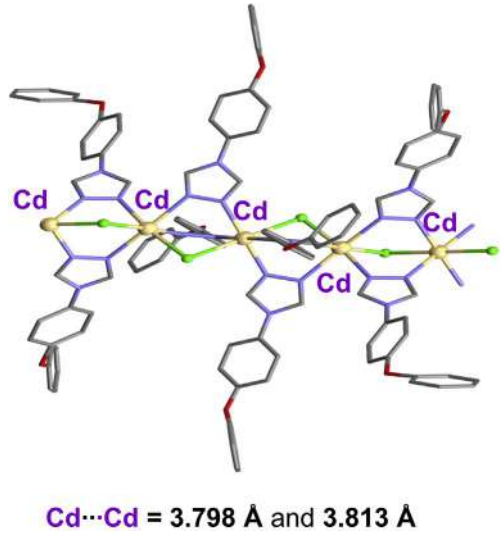

Fig. 10 View of the 1D chain **30** built from 4-phenoxyphenyl-1,2,4-triazole (***ppt***). $CdCl_4^{2-}$ anions were omitted for clarity.[74]

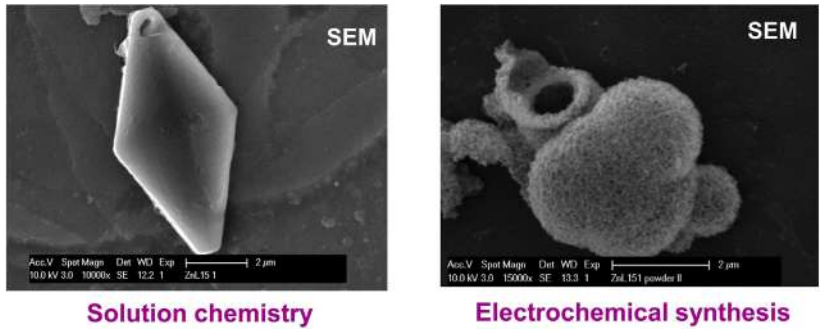

Fig. 11 Synthesis of single crystals (left) by solution chemistry or balls of coccolith morphology (right) by electrochemical synthesis of **25**.[74]

Electrochemical synthesis of such materials was demonstrated, e.g., on **25**, which constitutes a rare example of the successful application of this preparation method to CPs, a method which has been seldom applied to synthesize MOFs.[35,75] Hollow spherical clusters with micrometric dimensions were identified by scanning electron microscopy. Magnification shows hollow structures of ~1 μm diameter with potential porous properties (Fig. 11).[74] Interestingly, such spherical structuration was observed earlier on a bulk sample of $[Zn(trzg)_2Cl_2]Cl_2{\cdot}H_2O$ (**34**)

(***trzg*** = *N*-4*H*-1,2,4-triazol-4-yl-guanidine hydrochloride, Scheme 2), with porous balls of coccolith morphology with surface decorated sickle-shaped particles of ~100 nm thickness.[28a]

Pursuing our efforts in CPs synthesis, we have applied our revised trans-amination method,[26] to introduce a dissymmetric azole molecule, ***trz-tzH*** (5-(4H-1,2,4-triazol-yl)-2H-tetrazole, Scheme 4). This molecule with a high nitrogen content (~72%) can be compared to 5,5′-bistetrazole (***H_2btz***) and 1,5′-bistetrazole (***Hbtz)*** (Scheme 1).[76]

Such molecules can be considered as high energetic materials for low smoke pyrotechnics due to a combination of a fuel and a colorant in a single compound.[77] The synthesis of ***trz-tzH*** was done in one step from *N*,*N*′-dimethyl-formamide azine dihydrochloric acid in refluxing toluene overnight with 5-amino-tetrazole to lead to the target molecule in 70% yield.[26] Starting from *N*,*N*′-dimethyl-formamide azine in refluxing benzene afforded the target molecule in higher yield (79%).[78] Reaction of ***trz-tzH*** in water with M(OH) (M = Li, Na, K) yielded two alkali CPs. For instance, the crystal structure of [Li(trz-tz)H_2O] (**35**) reveals 1D chains of tetrahedrally coordinated Li^+ ion with two nitrogen atoms of the 1,2,4-triazole fragments belonging to two ***trz-tz*** anions and two water oxygen atoms (Fig. 12). The triazole fragments of the anionic ligands each coordinate two lithium cations in a bridging μ^2-*N*3,*N*4-coordination mode with the Li–N–N–Li torsion angle being 18.7(7)°. The bicyclic ligands are essentially planar, the dihedral

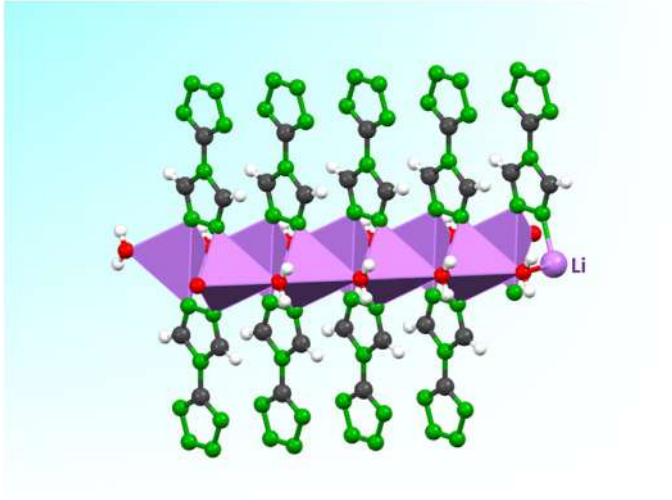

Fig. 12 View of the 1D chain **35** built from anionic ***trz-tz*** ligands.[79]

angle between triazole and tetrazole fragments being only 1.2(3)°. All ***trz-tz*** ligands are therefore coordinated almost orthogonally to the 1D chain axis (Fig. 12). The water molecules link two neighboring cations with a bridging μ^2-*O*-coordination mode. The Li—Li distances along and across the 1D chain are 3.434(15) and 3.535(16) Å, respectively, while the Li–O–Li and O–Li–O angles are equal to 117.9(6)°. Every 1D polymeric chain is connected to four neighboring chains through O–H···N hydrogen bonds, via a water molecule and *N*2 and *N*4 nitrogen atoms of the tetrazole cycles, thus forming a supramolecular network.[79]

Reaction of ***trz-tzH*** in water with $M(OH)_2$ (M = Mg, Ca) affords alkaline earth salts and a CP with M = Ba.[79] For the salt, $[Mg(H_2O)_6](trz\text{-}tz)_2$ (**36**), the magnesium ion is surrounded by six water molecules octahedrally coordinated while in $[Ca(H_2O)_8](trz\text{-}tz)_2$ (**37**) a square antiprism is formed with eight water molecules. In both structures, layers formed by the corresponding cationic parts $[Mg(H_2O)_6]^{2+}$ or $[Ca(H_2O)_8]^{2+}$, are separated by layers of anions ***trz-tz***. In **36**, the anions are, however, cross-packed whereas in $[Ca(H_2O)_8](trz\text{-}tz)_2$ they are packed parallel to each other (Fig. 13). Both structures contain an extensive hydrogen bonds network, which is also supported by the anions ***trz-tz***. The latter molecules are also stabilized by a number of $\pi\cdots\pi$ interactions.

The crystal structure of the CP $[Ba_2(trz\text{-}tz)_4(H_2O)_9]$ (**38**) comprises 1D polymeric chains, built from two different barium-containing building units. Both metal centers are nine-coordinated with the formation of mono-capped square anti-prismatic coordination polyhedra. The Ba(1) cation is coordinated by four nitrogen atoms originating from two *N*2-coordinated tetrazole and two μ^2-*N*1,*N*2-coordinated tri-azole rings,

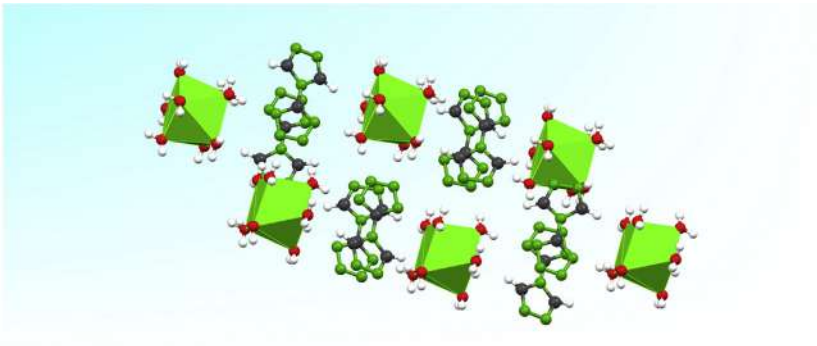

Fig. 13 View of mononuclear calcium units with ***trz-tz*** counteranions in **37**.[79]

corresponding to four different ***trz-tz*** anions. Two of these anionic ligands serve as bridging ligands between Ba(II) cations, connecting them through the triazole *N*1,*N*2-nitrogen atoms. The coordination environment of the Ba(1) cation is completed by two terminally coordinated and three μ^2-*O*-coordinated water molecules. The latter water molecules also participate in the coordination with Ba(2), which coordination environment is further completed by four terminal water molecules. Neighboring 1D chains are interpenetrated with each other and stabilized by a network of O–H···N hydrogen bonds as well as a number of $\pi\cdots\pi$ interactions, formed by the ***trz-tz*** heterocycles.

5. Sensing toxic industrial chemicals

There is currently a huge interest for "chemo-sensors" based on colorimetric sensor array (CSA) technology for the sensitive and selective detection of gas- and vapor-phase analytes. Such sensors are actively developed to reply to current needs of our society in terms of detection, particularly of toxic threats in food, air, surfaces, for medical diagnostics, and environmental monitoring. These sensor materials always incorporate a targeted set of chemically responsive colorants. Currently, coordination complexes are developed for colorimetric detection of metal-binding species, especially, toxic small molecules such as amines, covalent hydrides and alcohols. It mainly benefits from two contributions of metalo-colorants: (a) in well documented examples, analytes can directly coordinate to the metal center, causing significant changes to the d − d absorptions, and thus to the sensor color; (b) metal center can respond to redox reactions, thus provoking a sensor color change. Optical detection, in particular visible one, is the most demanded since it does not require sophisticated detection systems. Classic approaches consist of using irreversible color change due to metal or ligand oxidation. In this respect, iron sensors offer a large panel of possibilities due to their various spin and oxidation states. For instance, Fe(II) salts can oxidize in air from colorless to yellow/brown and can be used straightforwardly. More challenging are detectors which can offer different color sets depending on the probed analyte, as well as unlimited regeneration.

Reaction of $[Fe(H_2O)_6]A_2$ ($A = BF_4^-$, ClO_4^-) in water with ***trz-tzH*** at neutral pH afforded an air stable microcrystalline complex. Single crystal X-ray diffraction revealed a mononuclear Fe(II) neutral complex, $[Fe(trz\text{-}tz)_2(H_2O)_4]\cdot 4H_2O$ (**39**) which crystallizes in the P-1 space group (Fig. 14).[78]

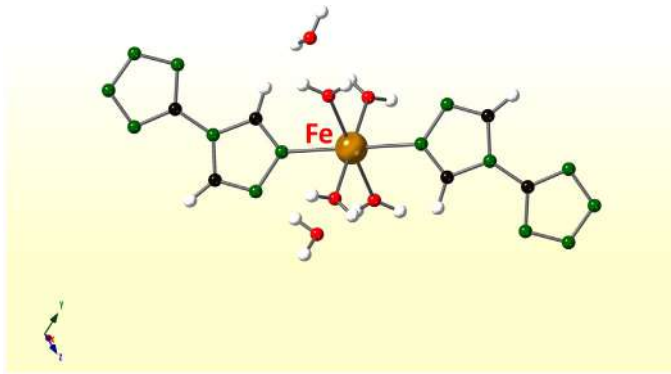

Fig. 14 View of the mononuclear iron(II) ***trz-tz*** complex **39**.[78]

In this molecule, two ***trz-tz*** ligands are bound through the N1 of the 1,2,4-triazole units to Fe(II), while four water molecules complete the octahedral coordination sphere. No counter anions are observed due to tetrazole deprotonation upon complexation, which balances the charge of the metal cation. The presence of coordinated water molecules in the coordination sphere sets a weak ligand field around the iron, which prevents any possibility of thermally induced spin switching. At room temperature, a large quadrupole doublet typical of the HS state, with $\delta = 1.17(2)$ mm/s and $\Delta E_Q = 3.18$ mm/s, is observed by ^{57}Fe Mössbauer spectroscopy. The HS state is also confirmed by X-ray diffraction with Fe-$N = 2.182(5)$ Å and Fe-O = 2.094(4) Å and 2.182(5) Å. Such material was screened for colorimetric sensing abilities for a wide spectrum of vapor-phase analytes (MeOH, EtOH) including toxic gases (HCl, HBr, hydrazine monohydrate, ammonia). Although pellet **39** possesses a single sensing unit without any other cross-reactive elements, it can capture information about analyte molecules in a distributed fashion that is encoded sufficiently to allow discrimination from other closely related chemical structures. In particular, the pink color detection (e.g., obtained with $MeOH_{(g)}$) was systematically associated to the emergence of $Fe^{II}N_6$ LS ions as shown by diffuse reflectance spectroscopy and ^{57}Fe Mössbauer spectroscopy.[78] Clear color differentiation among four different toxic industrial chemicals (TICs) and alcohols was demonstrated. Different TICs and alcohols were readily identified using a standard chemometric approach (hierarchical clustering analysis), with no misclassifications over 18 trials. ^{57}Fe Mössbauer spectroscopy was applied to investigate the driving spin state change of the analytes in this Fe-azole sensor material.[80] In particular, comparison was made before and after analyte

sensing. When the native hydrate sensor pellet **39** was in contact with $MeOH_{(l)}$, it turned instantly from white to pale pink. When the pellet was subjected to $MeOH_{(g)}$, it was transformed to the same pink color within 5 min, but took hours to be converted into dark pink until the material was saturated with $MeOH_{(g)}$. Remarkably, when MeOH was removed under vacuum at room temperature, the material did not return to its initial color and stayed pink. This MeOH removal was not associated with any spin state and iron coordination sphere modification as show by ^{57}Fe Mössbauer spectra recorded before and after pumping. Interestingly, this material turned back to white when exposed to water vapor or washed with water, with full iron site regeneration, as also shown by ^{57}Fe Mössbauer spectroscopy. **39** thus detects MeOH with a memory effect by visual, optical and magnetic feedback.[80] This material behaves much different from classic alcohols sensors, where control over the memory effect is unlikely because of the fake of analyte departure from the material. Indeed, after experiencing a color change due to guest molecule detection, the color is lost upon guest release. This situation holds for various Fe(II) spin crossover materials reported up to know.[81,82] Sensor **39** keeps, however, the color associated with alcohol detection, even after its full release from the material. Does size play a role for this coordination system regarding alcohol detection? Actually, the selectivity of detection decreases in the order MeOH > EtOH > i-PrOH > with increasing alcohol molecule size, and no color change was observed for higher size alcohol analogues (o-PrOH, BuOH, pentan-1-ol).[78] A weaker vapochromic behavior was indeed noticed when a pellet of **39** was exposed to EtOH vapors. Contrary to $MeOH_{(g)}$, the response time lasted much longer (2 days). Such a color change was only observed as a slight effect on the crystal surface of **39** when exposed to $EtOH_{(g)}$, presumably due to the lower available surface area.[78] Apart from alcohols, acid sensing was also studied, among other toxic chemicals. Although acetic, nitric, sulfuric and perchloric acids were not detected at all by this sensor, clear color changes to yellow and orange were observed for $HCl_{(g)}$ and $HBr_{(g)}$, respectively. Surprisingly no change was observed in the isomer shift, δ, deduced from Mössbauer spectra before and after gas uptake. This indicates that no change was provoked in the iron coordination sphere. Rather a protonation of tetrazole units leading to ***trz-tzH*** along with inclusion of halide anions is suggested. More surprising, is the Mössbauer spectrum after $NH_{3(g)}$ contact which shows the occurrence of iron(II) LS ions, with $\delta = 0.36(3)$ mm/s and $\Delta E_Q = 0.65(5)$ mm/s. Since NH_3 is known to set up a weak ligand field strength according to the spectrochemical series, as for

MeOH or EtOH, a similar mechanism valid for alcohol should also apply. This may imply reversible coordination of neighboring tetrazole ligands, a hypothesis currently under extensive investigation in our laboratory. This innovative approach opens up perspectives for the further development of iron materials as potential optical sensor arrays through colorimetric techniques, given the potential of molecules to be explored.[83]

6. Nanomedicine

Biomedical application of nanoscale materials for diagnosis and therapy is considered as a promising field of research where coordination chemistry could play a driving role. In particular, the design and synthesis of nanoscale CPs (NCPs) has become an intensive field of investigation.[84–87] The tune ability of supramolecular architectures through self-assembly processes of metallic ions with polydentate bridging ligands, has allowed to obtain a large set of nanoparticles with specific target properties, for instance for tumor immunotherapy.[88] Among bis-azole coordination networks, the use of bis-imidazole linkers allowed to produce a considerable amount of CPS and MOFs.[89] Recently, Adarsh *et al.* reviewed CPs built from 1,4-bis (imidazol-1-yl-methyl)benzene (***bimb***, Scheme 5).[90]

Despite the synthetic advances, challenging steps concern the design of surface functionalization of NCPs in order to improve their colloidal stability, biocompatibility and circulation time in blood, which are crucial for any optimized therapy. Within this frame, the group of Ruiz-Molina has made several advances, including the design of fluorescent dyes functionalized onto NPs in order to enable cellular uptake and monitoring. This applies for instance for dual fluorescent NCPs,[91] novel dual T_1/ T_2 NCPs as novel contrast agents for MRI in the treatment of brain tumor,[92] as well as Pt(IV) based NPCS,[93] to name but a few.

Surface decoration of NPs offer many advantages including the fine-tuning of solubility, biocompatibility and other properties such as, e.g., anti-oxidant and anti-bacterial properties. In particular, pyrazoles and benzimidazoles are present in many pharmaceuticals with a wide range of biological activities,[94–96] including potential activity against the proliferation of human tumor cells.[97] Benzimidazole complexes have been explored for their biological activity,[98] some having revealed relatively high antibacterial and antifungal properties.[99] For instance, zinc complexes, have been used, in addition to their antimicrobial activity, as anti-cancer agents for *in vitro* and *in vivo* studies, and have been shown to play an important role in the

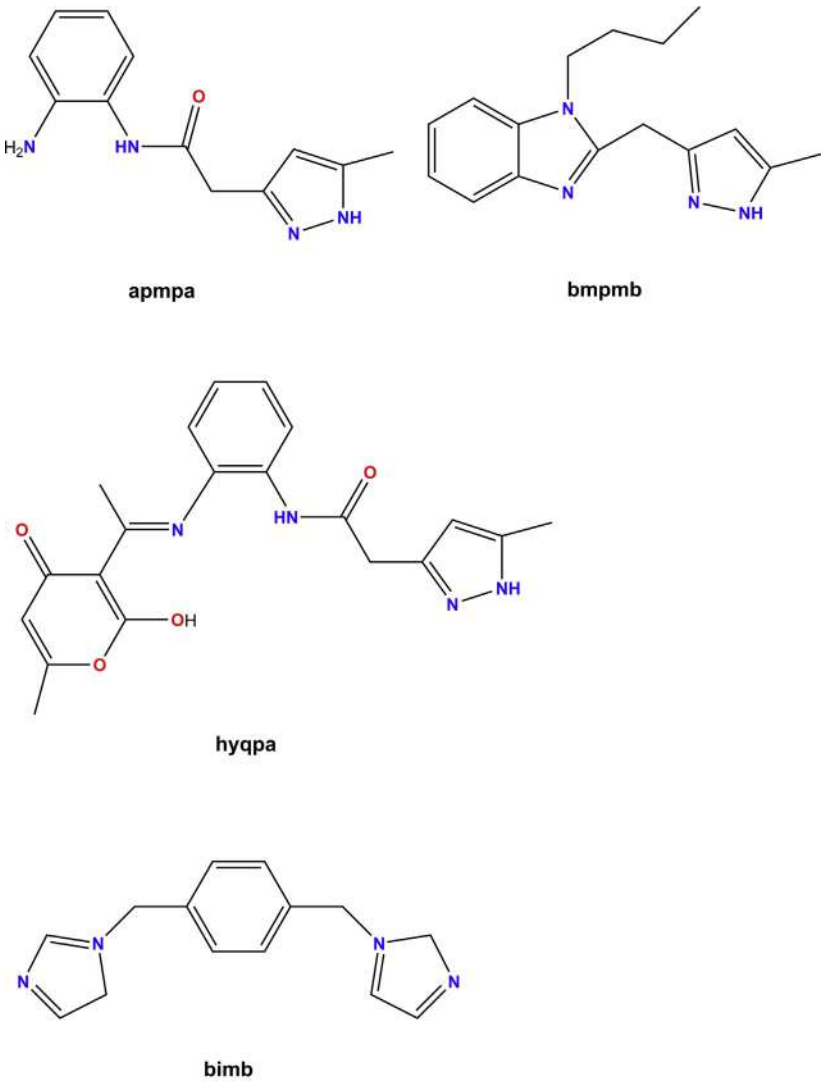

Scheme 5 Molecular structures of selected pyrazole and imidazole molecules.

chemotherapeutic process.[100] Other metal complexes have shown a significant cytotoxic activity, to name but a few.[101] Pyrazole derivatives are from their side known for their antimicrobial activities,[102] among many other properties. Along this line, Chkirate *et al.*[103] recently synthesized two mononuclear complexes $[Co(apmpa)_2(EtOH)_2]\cdot Cl_2$ (**40**) and $[Cu(hqpa)]\cdot H_2O$ (**41**), based on pyrazole-acetamide derivatives, namely *N*-(2-aminophenyl)-2-(5-methyl-1H-pyrazol-3-yl) acetamide (***apmpa***) and

(*E*)-*N*-(2-(1-(2-hydroxy-6-methyl-4-oxo-4H-pyran-3-yl)ethylideneamino) phenyl)-2-(5-methyl-1H-pyrazol-3-yl) acetamide (***hqpa***) (Scheme 5).

The crystal structures of **40** and **41** revealed 1D and 2D supramolecular architectures, respectively, via various hydrogen bonding interactions. Furthermore, the antioxidant activity of the ligands and their complexes were determined in vitro in different concentration ranges by 1,1-diphenyl-2-picrylhydrazyl (DPPH) and 2,2′-azino-bis(3-ethylbenzothiazoline-6-sulphonic acid (ABTS) radicals, and ferric reducing antioxidant power (FRAP) test. Significant antioxidant activity were recorded compared to literature references.[103]

Chkirate *et al.* extended their studies to pyrazole-benzimidazole derivatives by preparing three mononuclear coordination complexes of 1-butyl-2-((5-methyl-1H-pyrazol-3-yl)methyl)-1H-benzimidazole (***bmpmb***, Scheme 5) namely two pseudo-polymorphs $[Co(bmpmb)]Cl_2$ (**42**) and $[Co_2(bmpmb)_2]Cl_2{\cdot}H_2O$ (**43**) as well as $[Zn_2(bmpmb)_2]Cl_2$. Single crystals X-ray diffraction revealed that the presence of N—H···Cl and C—H···Cl hydrogen bonding in the crystal structure of $[M(bmpmb)]Cl_2$ (M = Co, Zn) assist the formation of a 2D hydrogen bonded sheet (M = Co) and an orthogonal packed (M = Zn) [2D sheet + a pair of 1D chain], leading to supramolecular structures. A combination of N—H···Cl, C—H···Cl, O—H···Cl, C—H···O interactions results, however, in a 2D corrugated hydrogen bonded sheet with inclusion of water molecules in **43**. Hirshfeld surface analysis confirmed the presence of various hydrogen bonding and π-stacking interactions, stabilizing the crystal structures.[104]

Noticeably, antibacterial activity against the strains of *Escherichia coli*, *Pseudomonas aeruginosa* and *Staphylocoque aureus* bacteria, was revealed for these complexes. In particular, a normalized minimum inhibitory concentration as low as 6.25 μg/mL s was recorded for **43**, even better than the antibiotic chloramphenicol.[104] This result correlates very well with its crystal structure determined by X-ray diffraction, which revealed a lattice included water molecule, which is one of the key factors for crystalline anti-bacterial properties. Indeed, crystalline materials having lattice included water molecules were reported to have more antibacterial activity, due to the hydrophilic attraction of the bacteria cell wall.[105]

7. Conclusions and future developments

In this contribution, we have shown selected examples of coordination networks including transition metals and azole building blocks. These materials display several potential applications, in gas or metallic

storage, molecular electronics, gas sensing, toxic metals sensing and capture, as well for medicinal applications. The development of nanoscale complexes, coordination polymers and metal-organic frameworks with azole based molecules is indeed flourishing and considered as an alternative to classic pyridine type networks to yield to diverse coordination networks with various topologies. Their suitable ligand field with Fe(II) along with their associated thermochromism observed for 1,2,4-triazole and tetrazole building blocks, make them often attractive to spin crossover developments toward nanodevices.[106] A number of other potential applications in various fields could also be proposed, be in opto-electronics, energy, public health and environmental issues. In particular, the biological properties of azole molecules constitute a potential functionality to explore within coordination networks, e.g., fungicide and pesticide properties known for 4R-1,2,4-triazole molecules.[24] This includes not only property testing but also the design of novel coordination networks including biomolecules and natural products. This development concerns metal-peptide networks,[107] as well as metal-biomolecule networks, e.g., with amino acids.[108] Despite the numerous derivatization possibilities offered by amino acids, due to the presence of several functional groups, their genuine chirality (except for glycine) and electronic asymmetry, can allow to introduce asymmetry in coordination network construction.[29] The synthesis of hybrid inorganic-organic materials containing azole based ligands, in particular in the form of nanoscale coordination polymers, is not to be neglected, given the unlimited potentialities offered by nanoparticles, opening a new world of investigation, particularly suitable in medicinal applications.[92]

Acknowledgments

Financial support from FNRS CDR 33694457 is gratefully acknowledged. We also acknowledge the input of all our collaborators cited in the reference section.

References

1. (a) Haasnoot, J. G. *Coord. Chem. Rev.* **2000**, *200–202*, 131–185; (b) Huang, Y.-Q.; Zhao, X.-Q.; Shi, W.; Liu, W.-Y.; Chen, Z.-L.; Cheng, P.; Liao, D.-Z.; Yan, S.-P. *Cryst. Growth Des.* **2008**, *8*, 3652–3660; (c) Deng, Y.; Liu, H.; Yu, B.; Yao, M. *Molecules* **2010**, *15*, 3478–3506; (d) Bai, S.-Q.; Young, D. J.; Andy Hor, T. S. *Chem. Asian J.* **2011**, *6*, 292; (e) Aromi, G.; Barrios, L. A.; Roubeau, O.; Gamez, P. *Coord. Chem. Rev.* **2011**, *255*, 485–546.
2. de Ruiter, G.; Lahav, M.; van der Boom, M. E. *Acc. Chem. Res.* **2014**, *47*, 3407–3416.
3. (a) Zhang, J.-P.; Zhang, Y.-B.; Lin, J.-B.; Chen, X.-M. *Chem. Rev.* **2012**, *112*, 1001; (b) Tăbăcaru, A.; Pettinari, C.; Galli, S. *Coord. Chem. Rev.* **2018**, *372*, 1–30.
4. Naik, A. D.; Dîrtu, M. M.; Leónard, A.; Tinant, B.; Marchand-Brynaert, J.; Su, B. L.; Garcia, Y. *Cryst. Growth Des.* **2010**, *10*, 1798–1807.

5. Lysenko, A. B.; Senchyk, G. A.; Domasevitch, K. V.; Hauser, J.; Fuhrmann, D.; Kobalz, M.; Krautscheid, H.; Neves, P.; Valente, A. A.; Goncalves, I. S. *Inorg. Chem.* **2015**, *54*, 8327–8338.
6. Meng, L.; Niu, Z.; Liang, C.; Dong, X.; Kang, L.; Li, G.; Li, C.; Han, Y.; Shi, Z.; Feng, S. *Chem. Eur. J.* **2018**, *24*, 13181–13187.
7. Wang, W.; Li, J.-L.; Jiang, C.; Hu, P.; Li, B.; Zhang, T.; Zhou, H.-C. *Chem. Commun.* **2018**, *54*, 13271–13274.
8. Boland, Y.; Tinant, B.; Safin, D. A.; Marchand-Brynaert, J.; Clerac, R.; Garcia, Y. *CrystEngComm* **2012**, *14*, 8153–8155.
9. Jafari, M.; Amani, V. *Sep. Sci. Plus* **2018**, *1*, 746–752.
10. Garcia, Y.; Adarsh, N. N.; Naik, A. D. *Chimia* **2013**, *67*, 411–418.
11. van Koningsbruggen, P. J.; Garcia, Y.; Kahn, O.; Fournès, L.; Kooijman, H.; Spek, A. L.; Haasnoot, J. G.; Moscovici, J.; Provost, K.; Michalowicz, A.; Renz, F.; Gütlich, P. *Inorg. Chem.* **2000**, *39*, 1891–1900.
12. (a) Garcia, Y.; Niel, V.; Munoz, M. C.; Real, J. A. *Top. Curr. Chem.* **2004**, *233*, 229–257; (b) Ksiazek, M.; Kusz, J.; Bialonska, A.; Bronisz, R.; Weselski, M. *Dalton Trans.* **2015**, *44*, 18563–18575; (c) Weselski, M.; Ksiazek, M.; Rokosz, D.; Dreczko, A.; Kusz, J.; Bronisz, R. *Chem. Commun.* **2018**, *54*, 3895–3898; (d) Ksiazek, M.; Weselski, M.; Ilczyszyn, M.; Kusz, J.; Bronisz, R. *Chem. Eur. J.* **2019**, *25*, 2250–2261; (e) Weselski, M.; Ksiazek, M.; Mess, P.; Kusz, J.; Bronisz, R. *Chem. Commun.* **2019**, *55*, 7033–7036.
13. Coronado, E.; Gimenez-Marques, M.; Mínguez Espallargas, G.; Rey, F.; Vitórica-Yrezábal, I. J. *J. Am. Chem. Soc.* **2013**, *135*, 15986–15989.
14. Roubeau, O. *Chem. Eur. J.* **2012**, *18*, 15230–15244.
15. Garcia, Y.; van Koningsbruggen, P. J.; Lapouyade, R.; Rabardel, L.; Kahn, O.; Wierczorek, M.; Bronisz, R.; Ciunik, Z.; Rudolf, M. F. *C. R. Acad. Sc. Paris Ser. IIc* **1998**, 523–532.
16. Lavrenova, L. G.; Shakirova, O. G.; Shvedenkov, Y. G.; Ikorskii, V. N.; Varnek, V. A.; Sheludyakova, L. A.; Larionov, S. V. *Koord. Khim.* **1999**, *25*, 208.
17. Dîrtu, M. M.; Rotaru, A.; Gillard, D.; Linares, J.; Codjovi, E.; Tinant, B.; Garcia, Y. *Inorg. Chem.* **2009**, *48*, 7838–7852.
18. Jureschi, C. M.; Linares, J.; Rotaru, A.; Ritti, M. H.; Parlier, M.; Dîrtu, M. M.; Wolff, M.; Garcia, Y. *Sensors* **2015**, *15*, 2388–2398.
19. Molnar, G.; Rat, S.; Salmon, L.; Nicolazzi, W.; Bousseksou, A. *Adv. Mater.* **2018**, *30*, 17003862.
20. Torres-Cavanillas, R.; Sanchis-Gual, R.; Dugay, J.; Coronado-Puchau, M.; Gimenez-Marques, M.; Coronado, E. *Adv. Mater.* **2019**, *31*, 1900039.
21. Zhao, T.; Cuignet, L.; Dîrtu, M. M.; Wolff, M.; Boldog, I.; Rotaru, A.; Garcia, Y.; Janiak, C. *J. Mater. Chem. C* **2015**, *3*, 7802–7812.
22. Vreugdenhil, W.; Van Diemen, J. H.; De Graaff, R. A. G.; Haasnoot, J. G.; Reedijk, J.; Van der Kraan, A. M.; Kahn, O.; Zarembowitch, J. *Polyhedron* **1990**, *9*, 2971–2979.
23. Garcia, Y.; Kahn, O.; Rabardel, L.; Chansou, B.; Salmon, L.; Tuchagues, J.-P. *Inorg. Chem.* **1999**, *38*, 4663–4670.
24. Bayer, H. O.; Cook, R. S.; Von Meyer, W. C. US Patent 382137628, 1974*Chem. Abstr.* **1972**, *76*, 113224.
25. Bartlett, R. K.; Humphrey, I. R. *J. Chem. Soc. C* **1967**, 1664.
26. Naik, A. D.; Marchand-Brynaert, J.; Garcia, Y. *Synthesis* **2008**, *1*, 149–154.
27. (a) Tahli, A.; MacLaren, J. K.; Boldog, I.; Janiak, C. *Inorg. Chim. Acta* **2011**, *374*, 506–513; (b) Gomez, V.; Lillo, V.; Escudero-Adan, E. C.; Martin, E.; Galan-Mascaros, J. R. *Dalton Trans.* **2013**, *42*, 6374–6380; (c) Kitchen, J. A.; Olguin, J.; Kulmaczewski, R.; White, N. G.; Milway, V. A.; Jameson, G. N. L.; Tallon, J. L.; Brooker, S. *Inorg. Chem.* **2013**, *52*, 11185–11199; (d) Chen, D.-M.; Ma, X.-Z.;

Zhang, X.-J.; Xu, N.; Cheng, P. *Inorg. Chem.* **2015**, *54*, 2976–2982; (e) Chen, D.-M.; Ma, J.-G.; Cheng, P. *Dalton Trans.* **2015**, *44*, 8926–8931; (f) Lin, J.-D.; Onet, C. I.; Schmitt, W. *Sci. Technol. Adv. Mater.* **2015**, *16*, 1–10; (g) Ye, Y.; Xiong, S.; Wu, X.; Zhang, L.; Li, Z.; Wang, L.; Ma, X.; Chen, Q.-H.; Zhang, Z.; Xiang, S. *Inorg. Chem.* **2016**, *55*, 292–299; (h) Chen, D.-M.; Tian, J.-Y.; Fang, S.-M.; Liu, C.-S. *CrystEngComm* **2016**, *18*, 2579–2584; (i) Chen, D.-M.; Tian, J.-Y.; Liu, C.-S. *Z. Anorg. Allg. Chem.* **2016**, *642*, 714–718; (j) Wang, L.; Ye, Y.; Li, Z.; Lin, Q.; Ouyang, J.; Liu, L.; Zhang, Z.; Xiang, S. *Cryst. Growth Des.* **2017**, *17*, 2081–2089; (k) Shao, M.; Li, M.-X.; Wang, Z.-X.; He, X.; Zhang, H.-H. *Cryst. Growth Des.* **2017**, *17*, 6281–6290; (l) Liu, M.; Yang, X.-F.; Zhu, H.-B.; Di, B.-S.; Zhao, Y. *Dalton Trans.* **2018**, *47*, 5245–5251; (m) Du, Y.; Su, H.; Fei, T.; Hu, B.; Zhang, J.; Li, S.; Pang, S.; Nie, F. *Cryst. Growth Des.* **2018**, *18*, 5896–5903.

28. (a) Naik, A. D.; Tinant, B.; Leonard, A.; Marchand-Brynaert, J.; Su, B. L.; Garcia, Y. *Cryst. Growth Des.* **2011**, *11*, 4034–4043; (b) Dîrtu, M. M.; Schmit, F.; Naik, A. D.; Rotaru, A.; Rusu, I.; Rackwitz, S.; Wolny, J. A.; Schünemann, V.; Garcia, Y. *Chem. Eur. J.* **2015**, *21*, 5843–5855; (c) Dîrtu, M. M.; Adarsh, N. N.; Naik, A. D.; Robeyns, K.; Garcia, Y. *New J. Chem.* **2016**, *40*, 9025–9029; (d) Dîrtu, M. M.; Naik, A. D.; Rotaru, A.; Spinu, L.; Poelman, D.; Garcia, Y. *Inorg. Chem.* **2016**, *55*, 4278–4295.
29. Naik, A. D.; Dîrtu, M. M.; Railliet, A. P.; Marchand-Brynaert, J.; Garcia, Y. *Polymer* **2011**, *3*, 1750.
30. Adarsh, N. N.; Dîrtu, M. M.; Naik, A. D.; Leonard, A. F.; Campagnol, N.; Robeyns, K.; Snauwaert, J.; Fransaer, J.; Su, B. L.; Garcia, Y. *Chem. Eur. J.* **2015**, *21*, 4300–4307.
31. Bati, A. S. R.; Yu, L.; Batmunkh, M.; Shapter, J. G. *Adv. Funct. Mater.* **2019**, *30*, 1902273.
32. Jiang, J.; Yu, J.; Corma, A. *Angew. Chem. Int. Ed.* **2010**, *49*, 3120–3145.
33. Su, B. L.; Garcia, Y. *Eur. J. Inorg. Chem.* **2019**, *27*, 3123–3125.
34. (a) Tezer, H.; Erkocoglu, M.; Kara, A.; Bayakci, B.; Düzova, A.; Teksam, O.; Aysun, S. *Eur. J. Pediatr.* **2011**, *170*, 397; (b) EPA *EPA Fact Sheet. EPA-823-F-01-011*. EPA, Office of Water: Washington, DC, 2001.
35. (a) Beurroies, I.; Boulhout, M.; Llewellyn, P. L.; Kuchta, B.; Ferey, G.; Serre, S.; Denoyel, R. *Angew. Chem. Int. Ed.* **2010**, *49*, 7526–7529; (b) Neimark, A. V.; Coudert, F. X.; Triguero, C.; Boutin, A.; Fuchs, A. H.; Beurroies, I.; Denoyel, R. *Langmuir* **2011**, *27*, 4734–4741.
36. Radi, S.; Toubi, Y.; Bacquet, M.; Degoutin, S.; Mabkhot, Y. N.; Garcia, Y. *RSC Adv.* **2016**, *6*, 34212.
37. (a) Radi, S.; Tighadouini, S.; Bacquet, M.; Degoutin, S.; Garcia, Y. *Anal. Methods* **2016**, *8*, 6923–6931; (b) El Massaoudi, M.; Radi, S.; Bacquet, M.; Degoutin, S.; Adarsh, N. N.; Robeyns, K.; Garcia, Y. *Inorg. Chem. Front.* **2017**, *4*, 1821; (c) Tighadouini, S.; Radi, S.; Anannaz, M.; Bacquet, M.; Degoutin, S.; Tillard, M.; Eddike, D.; Amhamdi, H.; Garcia, Y. *New J. Chem.* **2018**, *42*, 13229–13240; (d) El Massaoudi, M.; Radi, S.; Bacquet, M.; Degoutin, S.; Garcia, Y. *J. Environ. Chem. Eng.* **2018**, *6*, 5980–5989; (e) Tighadouini, S.; Radi, S.; Elidrissi, A.; Haboubi, K.; Bacquet, M.; Degoutin, S.; Zaghrioui, M.; Garcia, Y. *Beilstein J. Nanotechnol.* **2019**, *10*, 262–273; (f) Tighadouini, S.; Radi, S.; Ferbinteanu, M.; Garcia, Y. *ACS Omega* **2019**, *4*, 3954–3964; (g) Tighadouini, S.; Radi, S.; Elidrissi, A.; Zaghrioui, M.; Garcia, Y. *Eur. J. Inorg. Chem.* **2019**, *27*, 3180–3186; (h) Tighadouini, S.; Radi, S.; Garcia, Y. *Mol. Syst. Des. Eng.* **2020**, https://doi.org/10.1039/C9ME00140A.
38. (a) Adarsh, N. N.; Dîrtu, M. M.; Guionneau, P.; Devlin, E.; Sanakis, Y.; Howard, J. A. K.; Chattopadhyay, B.; Garcia, Y. *Eur. J. Inorg. Chem.* **2019**, *5*,

585–591; (b) Yang, Z.-J.; Ni, T.-J.; He, G.-J.; Huang, Q.-Q.; Yuan, Q.-T.; Zheng, W.-Q. *Asian J. Chem.* **2015**, *27*, 4103–4105.
39. Quesada, M.; Prins, F.; Bill, E.; Kooijman, H.; Gamez, P.; Roubeau, O.; Spek, A. L.; Haasnoot, J. G.; Reedijk, J. *Chem. Eur. J.* **2008**, *14*, 8486–8499.
40. Drabent, K.; Bronisz, R.; Ruldolf, M. F. *Conf. Proc. ICAME* **1995**, *50*, 7.
41. Bronisz, R.; PhD thesis, University of Wroclaw, Poland, 1999.
42. Suarez-Garcia, S.; Adarsh, N. N.; Molnar, G.; Bousseksou, A.; Garcia, Y.; Dîrtu, M. M.; Saiz-Poseu, J.; Robles, R.; Ordejon, P.; Ruiz-Molina, D. *ACS Appl. Nano Mater.* **2018**, *1*, 2662–2668.
43. Adarsh, N. N.; Dîrtu, M. M.; Rotaru, A.; Garcia, Y. *Hyperfine Interact.* **2017**, *238*, 60.
44. Coronado, E. *Nat. Rev. Mater.* **2020**, *5*, 87–104.
45. Zhang, L.; August, D.; Zhong, J.; Whitehead, G. F. S.; Vitorica-Yrezabal, I. J.; Leigh, D. A. *J. Am. Chem. Soc.* **2018**, *140*, 4982–4985.
46. Jin, C. M.; Zhu, Z.; Chen, Z. F.; Hu, Y. J.; Meng, X. G. *Cryst. Growth Des.* **2010**, *10*, 2054–2056.
47. Liu, X. G.; Wang, L. Y.; Zhu, X.; Li, B. L.; Zhang, Y. *Cryst. Growth Des.* **2009**, *9*, 3997–4005.
48. Soudry, H.; Desmarets, C.; Gontard, G.; Edgington, T.; Cooksy, A. L.; Amouri, H. *Dalton Trans.* **2017**, *46*, 10240–10245.
49. Robinson, W. R. *J. Chem. Ed.* **1985**, *62*, 1001.
50. Nierlich, M.; Charpin, P.; Herpin, P. *C. R. Acad. Sci.* **1973**, *276*, 1–3.
51. van Albada, G. A.; van der Horst, M. G.; Mutikainen, I.; Turpeinen, U.; Reedijk, J. *J. Chem. Cryst.* **2008**, *38*, 519–523.
52. Varonka, M. S.; Warren, T. H. *Inorg. Chem.* **2009**, *48*, 5605–5607.
53. Döring, A.; Flörke, U.; Hoffmann, A.; Jones, M. D.; Kuckling, D.; de Vasconcellos, J. M.; Herres-Pawlis, S. *Z. Anorg. Allg. Chem.* **2015**, *641*, 2147–2156.
54. Vantomme, G.; Jiang, S.; Lehn, J.-M. *J. Am. Chem. Soc.* **2014**, *136*, 9509–9518.
55. Żurowska, B.; Ślepokura, K.; Fabijanska, M.; Ochocki, J. *Inorg. Chim. Acta* **2013**, *407*, 19–24.
56. Tomat, E.; Cuesta, L.; Lynch, V. M.; Sessler, J. L. *Inorg. Chem.* **2007**, *46*, 6224–6226.
57. Mercer, D. J.; Loeb, S. J. *Dalton Trans.* **2011**, *40*, 6385–6387.
58. Hutchinson, D. J.; Hanton, L. R.; Moratti, S. C. *Inorg. Chem.* **2013**, *52*, 2716–2728.
59. Hutchinson, D. J.; Hanton, L. R.; Moratti, S. C. *Inorg. Chem.* **2011**, *50*, 7637–7649.
60. Gobeze, W. A.; Milway, V. A.; Moubaraki, B.; Murray, K. S.; Brooker, S. *Dalton Trans.* **2012**, *41*, 9708–9721.
61. Szymczak, N. K.; Berben, L. A.; Peters, J. C. *Chem. Commun.* **2009**, 6729.
62. Browne, C.; Ramsay, W. J.; Ronson, T. K.; Medley-Hallam, J.; Nitschke, J. R. *Angew. Chem. Int. Ed.* **2015**, *54*, 11122–11127.
63. Cao, X.-Y.; Harrowfield, J.; Nitschke, J.; Ramírez, J.; Stadler, A.-M.; Kyritsakas-Gruber, N.; Madalan, A.; Rissanen, K.; Russo, L.; Vaughan, G.; Lehn, J.-M. *Eur. J. Inorg. Chem.* **2007**, 2944–2965.
64. El Massaoudi, M.; Radi, S.; Salhi, A.; Mabkhot, Y. N.; Al Showiman, S. S.; Ghabbour, H. A.; Adarsh, N. N.; Garcia, Y. *New J. Chem.* **2018**, *42*, 11324–11333.
65. Baryshnikov, G.; Minaev, B.; Korop, A.; Minaeva, V.; Gusev, A. *Russ. J. Inorg. Chem.* **2013**, *58*, 928–934.
66. Minaeva, V.; Minaev, B.; Baryshnikov, G.; Kopylova, T.; Gadirov, R.; Eremina, N. *Russ. J. Gen. Chem.* **2011**, *81*, 2332–2344.
67. Naik, A. D.; Beck, J.; Dîrtu, M. M.; Bebrone, C.; Tinant, B.; Robeyns, K.; Marchand-Brynaert, J.; Garcia, Y. *Inorg. Chim. Acta* **2011**, *368*, 21–28.
68. Govor, E. V.; Lysenko, A. B.; Rusanov, E. B.; Chernega, A. N.; Krautscheid, H.; Domasevitch, K. V. *Z. Anorg. Allg. Chem.* **2010**, *636*, 209–217.

69. Senchyk, G. A.; Lysenko, A. B.; Rusanov, E. B.; Chernega, A. N.; Krautscheid, H.; Domasevitch, K. V. *Inorg. Chim. Acta* **2009**, *362*, 4439–4448.
70. Miao, S.; Ji, B.; Zhou, L. *Russ. J. Coord. Chem.* **2015**, *41*, 339–344.
71. Deligne, N.; Gonze, V.; Bayot, D.; Devillers, M. *Eur. J. Inorg. Chem.* **2008**, 896–902.
72. Yang, L.; Powell, D. R.; Houser, R. P. *Dalton Trans.* **2007**, 955–964.
73. Wang, N.; Chao Feng, Y.-C.; Shi, W.; Zhao, B.; Cheng, P.; Liao, D.-Z.; Yana, S.-P. *CrystEngComm* **2012**, *14*, 2769–2778.
74. Benaissa, H.; Wolff, M.; Robeyns, K.; Van Hecke, K.; Knör, G.; Campagnol, N.; Fransaer, J.; Garcia, Y. *Cryst. Growth Des.* **2019**, *19*, 5292–5307.
75. (a) Campagnol, N.; Souza, E. R.; De Vos, D. E.; Binnemans, K.; Fransaer, J. *Chem. Commun.* **2014**, *50*, 12545–12547; (b) Campagnol, N.; Van Assche, T. R. C.; Li, M.; Stappers, L.; Dinca, M.; Denayer, J. F. M.; Binnemans, K.; De Vos, D. E.; Fransaer, J. *J. Mater. Chem. A.* **2016**, *4*, 3914–3925; (c) Van Assche, T. R. C.; Campagnol, N.; Muselle, T.; Terryn, H.; Fransaer, J.; Denayer, J. F. M. *Microporous Mesoporous Mater.* **2016**, *224*, 302–310.
76. Fischer, N.; Iszak, D.; Klapötke, T. M.; Stierstorfer, J. *Chem. Eur. J.* **2013**, *19*, 8948.
77. Fischer, N.; Klapötke, T. M.; Peeters, K.; Rusan, M.; Stierstorfer, J. *Z. Anorg. Allg. Chem.* **2011**, *637*, 1693.
78. Naik, A. D.; Robeyns, K.; Meunier, C. F.; Leonard, A. F.; Rotaru, A.; Tinant, B.; Filinchuk, Y.; Su, B. L.; Garcia, Y. *Inorg. Chem.* **2014**, *53*, 1263–1265.
79. Safin, D. A.; Railliet, A. P.; Robeyns, K.; Mitoraj, M.; Kubisiak, P.; Sagan, F.; Garcia, Y. *New J. Chem.* **2017**, *41*, 6210.
80. Guo, Y.; Xue, S.; Dîrtu, M. M.; Garcia, Y. *J. Mater. Chem. C* **2018**, *6*, 3895–3900.
81. (a) Garcia, Y.; van Koningsbruggen, P. J.; Codjovi, E.; Lapouyade, R.; Kahn, O.; Rabardel, L. *J. Mater. Chem.* **1997**, *7*, 857–858; (b) van Koningsbruggen, P. J.; Garcia, Y.; Codjovi, E.; Lapouyade, R.; Kahn, O.; Fournès, L.; Rabardel, L. *J. Mater. Chem.* **1997**, *7*, 2069–2075.
82. Rodriguez-Jimenes, S.; Felthon, H. L. C.; Brooker, S. *Angew. Chem. Int. Ed.* **2016**, *55*, 15067–15071.
83. Wenger, O. S. *Chem. Rev.* **2013**, *113*, 3686–3733.
84. (a) Novio, F.; Simmchen, J.; Vázquez-Mera, N.; Amorín-Ferre, L.; Ruiz-Molina, D. *Coord. Chem. Rev.* **2013**, *257*, 2839–2847; (b) Della Rocca, J.; Liu, D.; Lin, W. *Acc. Chem. Res.* **2011**, *44*, 957–968.
85. Mu, J.; He, L.; Huang, P.; Chen, X. *Coord. Chem. Rev.* **2019**, *399*, 213039.
86. Lin, W. *Chem. Rev.* **2015**, *115*, 10407–10409.
87. He, C.; Liu, D.; Lin, W. *Chem. Rev.* **2015**, *115*, 11079–11108.
88. Zhao, H.; Xu, J.; Li, Y.; Guan, X.; Han, X.; Xu, Y.; Zhou, H.; Peng, R.; Wang, J.; Liu, Z. *ACS Nano* **2019**, *13*, 13127–13135.
89. (a) Deka, H.; Kumar, A.; Patra, S.; Awasthi, M. K.; Singh, S. K. *Dalton Trans.* **2020**, *49*, 757–763; (b) Solórzano, R.; Tort, O.; García-Pardo, J.; Escribà, T.; Lorenzo, J.; Arnedo, M.; Ruiz-Molina, D.; Alibes, R.; Busque, F.; Novio, F. *Biomater. Sci.* **2019**, *7*, 178–186; (c) Novio, F.; Lorenzo, J.; Nador, F.; Wnuk, K.; Ruiz-Molina, D. *Chem. Eur. J.* **2014**, *20*, 15443–15450; (d) Amorín-Ferre, L.; Busque, F.; Bourdelande, J. L.; Ruiz-Molina, D.; Hernando, J. *Chem. Eur. J.* **2013**, *19*, 17508–17516.
90. Adarsh, N. N.; Novio, F.; Ruiz-Molina, D. *Dalton Trans.* **2016**, *45*, 11233–11255.
91. Nador, F.; Wnuk, K.; García-Pardo, J.; Lorenzo, J.; Solorzano, R.; Ruiz-Molina, D.; Novio, F. *ChemNanoMat* **2018**, *4*, 183–193.
92. Suárez-García, S.; Arias-Ramos, N.; Frias, C.; Candiota, A. P.; Arús, C.; Lorenzo, J.; Ruiz-Molina, D.; Novio, F. *ACS Applied Materials Interf.* **2018**, *10*, 38819–38832.
93. Adarsh, N. N.; Frias, C.; Ponnoth Lohidakshan, T. M.; Lorenzo, J.; Novio, F.; Garcia-Pardo, J.; Ruiz-Molina, D. *Chem. Eng. J.* **2018**, *340*, 94–102.

94. Karrouchi, K.; Yousfi, E.; Sebbar, N. K.; Ramli, Y.; Taoufik, J.; Ouzidan, Y.; Ansar, M.; Mabkhot, Y. N.; Ghabbour, H. A.; Radi, S. *Int. J. Mol. Sci.* **2017**, *18*, 2215.
95. Karrouchi, K.; Radi, S.; Ramli, Y.; Taoufik, J.; Mabkhot, Y. N.; Al-aizari, F. A.; Ansar, M. *Molecules* **2018**, *23*, 134.
96. Pillai, R. R.; Karrouchi, K.; Fettach, S.; Armakovic, S.; Armakovic, S. J.; Brik, Y.; Taoufik, J.; Radi, S.; Faouzi, M. E.; Ansar, M. H. *J. Mol. Struct.* **2019**, *1177*, 47–54.
97. Reddy, T. S.; Kulhari, H.; Reddy, V. G.; Bansal, V.; Kamal, A.; Shukla, R. *Eur. J. Med. Chem.* **2015**, *101*, 790–805.
98. Devereux, M.; O'Shea, D.; O'Connor, H.; Grehan, H.; Connor, G.; McCann, M.; Rosair, G.; Lyng, F.; Kellett, A.; Walsh, M.; Egan, D.; Thati, B. *Polyhedron* **2007**, *26*, 4073–4084.
99. Bouchouit, M.; Said, M. E.; Kara Ali, M.; Bouacida, S.; Merazig, H.; Kacem, H.; Chaouche, H.; Chibani, A.; Zouchoune, B.; Belfaitah, A.; Bouraiou, A. *Polyhedron* **2016**, *119*, 248–259.
100. Tabassum, S.; Asim, A.; Arjmand, F.; Afzal, M.; Bagchi, V. *Eur. J. Med. Chem.* **2012**, *58*, 308–316.
101. Li, M. X.; Zhang, L. Z.; Chen, C. L.; Niu, J. Y.; Ji, B. S. *J. Inorg. Biochem.* **2012**, *106*, 117–125.
102. Dholakiya, P. P.; Patel, M. N. *Synth. React. Inorg. Met.-Org. Chem.* **2004**, *34*, 383–395.
103. Chkirate, K.; Fettach, S.; Karrouchi, K.; Sebbar, N. K.; El Essasi, M.; Mague, J. T.; Radi, S.; El Faouzi, A. M.; Adarsh, N. N.; Garcia, Y. *J. Inorg. Biochem.* **2019**, *191*, 21–28.
104. Chkirate, K.; Karrouchi, K.; Dege, N.; Sebbar, N. K.; Ejjoummany, A.; Radi, S.; Adarsh, N. N.; Talbaoui, A.; Ferbinteanu, M.; El Essasi, M.; Garcia, Y. *New J. Chem.* **2020**, *44*, 2210–2221.
105. Hu, S.; Mac, C.; Zhan, F.; Cao, Y.; Hu, P.; Zhen, Q. *Chem. Pap.* **2017**, *71*, 1323–1329.
106. Sawczak, M.; Jendrzejewski, R.; Maskowicz, D.; Garcia, Y.; Gosh, A. C.; Gazda, M.; Czechowski, J.; Śliwinski, G. *Eur. J. Inorg. Chem.* **2019**, *27*, 3249–3255.
107. Rabone, J.; Yue, Y. F.; Chong, S. Y.; Stylianou, K. C.; Bacsa, J.; Bradshaw, D.; Darling, G. R.; Berry, N. G.; Khimyak, Y. Z.; Ganin, A. Y.; Wiper, P.; Claridge, J. B.; Rosseinsky, M. J. *Science* **2010**, *329*, 1053–1057.
108. Joarder, B.; Chaudhari, A. K.; Nagarkar, S. S.; Manna, B.; Ghosh, S. K. *Chem. Eur. J.* **2013**, *19*, 11178–11183.

CHAPTER FIVE

Coordination compounds with siloxane/silane-containing ligands capable of self-assembly at nano/micro scale in solid state and in solution

Mirela-Fernanda Zaltariov, Maria Cazacu*

Department of Inorganic Polymers, "Petru Poni" Institute of Macromolecular Chemistry, Iasi, Romania
*Corresponding author: e-mail address: mcazacu@icmpp.ro

Contents

Abstract

The well-known particularities of the siloxane bond (dual character and flexibility) induce certain behaviors of the compounds in the structures in which it is found. Thus, carboxylic or azomethine ligands containing tetramethyldisiloxane spacers or trimethylsilane tails were prepared and used to build 0D, 1D, 2D or 3D metal complexes. Despite their great flexibility, in most cases their isolation in the crystalline state and structural characterization were successful. Due to the length of the ligands, even the simple discrete molecular coordination structures exceed one or a few nanometers,

Advances in Inorganic Chemistry, Volume 76
ISSN 0898-8838
https://doi.org/10.1016/bs.adioch.2020.03.003

whereas in the case of the 1D-3D structures the distances between the metal centers also often exceed such values, which may affect some properties especially their magnetic properties. The presence of highly hydrophobic dimethylsiloxane or trimethylsilane units in the structure along with relatively polar complexed metal units, give the complexes an amphiphilic character which affect their surface activity and the ability of micellar self-assembly depending on the polarity of the solvent. The formed aggregates can also be found in films generated by the rapid evaporation of the solvent. The flexibility of the siloxane or silane segment facilitates self-assembly by adopting the proper conformation in solution, depending on the concentration, but also in films in response to external stimuli (for example, optical or magnetic). In contrast, when using silane-centered polycarboxylic ligands, highly crystalline but insoluble structures are formed. These have different degrees of porosity, depending on the structure. Our own recent results in the development of such complexes and nanostructures are reviewed.

1. Coordination compounds in the "nano" context

Nanomaterials describe in principle chemical substances or materials "with any external dimension on the nanoscale (size range from approximately 1–100 nm) or having internal or surface structure on the nanoscale" often exhibit unique optical, electronic or mechanical properties.[1] Depending on whether they have all, two, one or no dimensions at the nanoscale, they are categorized as zero- (0D), one- (1D), two- (2D) or three-dimensional (3D), respectively.[2] Nanostructured materials include atomic clusters, layered (lamellar) films, filamentary structures, and bulk nanostructured materials.[3] Different from those formed in nature (e.g., volcanic ash, soot from forest fires) and incidental (e.g., welding, diesel engine by-products of combustion processes), engineered nanomaterials are intentionally produced and designed with physico-chemical properties for a specific purpose or function.[1] The nanomaterials have the advantage of a large surface/volume ratio, thus having a high contact surface, ideal for catalysis and sensors, and fundamental properties (optical, magnetic, electrical, thermal, biological or imaging) different from those of voluminous material with the same chemical composition.[4]

Classical nanomaterials are carbon and inorganic nanoparticles.[1,4] These materials may also find their way into more complex nanostructures and systems. Therefore, scientific marketing studies revealed the existence of four main classes of nanomaterials produced intentionally: carbon based materials (fullerenes, graphene flakes and single wall carbon nanotubes), metal based

materials (quantum dots, nanogold, nanosilver and metal oxides, such as titanium dioxide), dendrimers (nano-sized polymers built from branched units, thus having numerous chain ends, which can be tailored to perform specific chemical functions) and composites (which combine nanoparticles with other nanoparticles or with larger, bulk-type materials).[4,5] However, many other types of unconventional nanomaterials have been developed lately. Some of these are those based on *coordination compounds*.[4] Design and synthesis of coordination compounds, although it has long been a concern of the scientific world, is now attracting increasing interest. This is due to their unique tailorable properties and their applicative potential as functional materials in a wide range of domains.[6,7] Technological challenges stimulate continuous development of new approaches in the design and synthesis of coordination compounds with electronic, optical, electrochemical and magnetic properties, attractive for their nanoscale applications. The key to such developments is to understand the fundamental processes occurring in and around metal centers, as well as at the molecular interfaces. The structures of complexes can be either discrete molecular architectures with polyhedral or polygonal shapes, or infinite coordination polymers of metal ions with suitably chosen organic ligands.[8] As a particular class, coordination polymers (CPs), which appear as infinite chains (ICPs), amorphous or crystalline, are generally formed by an automatic supramolecular self-assembly process. This occurs between the metal ions or clusters, known as structural base units (SBUs), and connective ligands through coordination interactions leading to 1D, 2D or 3D architectures up to nanometer dimensions, depending on the functionality of the ligand and/or the nature of the metal ion.[7,9,10] By their organic-inorganic hybrid nature, these materials carry the properties of individual components as well as new ones induced by their coexistence.[11] Their molecular tune-ability allows them to be obtained as molecular nanomaterials in an infinite array of metal/metal cluster as SBUs and bridging ligands designed for specific applications.[12,13] By choosing appropriate reagents and working conditions, the coordination-driven self-assembly process allows quick access to mono-, bi- and polynuclear molecular or supramolecular structures of nanoscale dimensions.[14] Nanomaterials based on nitrogen- (porphyrin and phthalo-cyanine), oxygen- (β-diketones, carboxylates) or sulfur- (mainly thiophene and N,S heterocycles) containing ligands are already known.[15] Among the coordination polymers, special attention is given to the metal-organic frameworks (MOFs), an emerging new class of hybrid nanomaterials with promising features for a number of practical applications.[4] These define a research area, which is highly active

due to unprecedented structures, exciting topologies, and wide range of applications in optics, magnetism, catalysis, gas storage, sensing, electronics, photochemistry or biology.[11] More, CPs having self-assembled structures of nanometer dimensions, nano-CPs (NCPs), are attractive to investigate because their properties are controlled by the large number of molecules on the surface of the nanoparticle that are exposed to a different environment than the one inside the crystal.[9] The ability to simultaneously control the size, shape, composition and activity of nanomaterials continues to be a challenge.[16]

Regarding the size and morphology of the crystal in which these structures are packed, it should be reiterated that depending on them, compounds with the same composition may have different properties/behaviors. Two of the most important parameters that influence the final shape and size of a NCPs are the CPs structure, whose influence on the morphology of self-assembly is rather unpredictable, and the preparation method with its parameters (nature of solvent, concentration and ratio of reactants, the use or not of surfactants, the power of thermal, sonochemical or microwave irradiation, the reaction time, etc.) that has a direct influence on the morphology and size of the final particles.[9] In terms of the interaction with solvent, when this interaction is weak, in order to minimize the interfacial tension at the interface with the compound, the latter adopts a spherical morphology. When the crystalline lattice energy is superior to the particle/solvent interaction, crystalline morphology generally occurs, as in the case of particular MOFs that are highly ordered porous materials.[11] Organic ligands can exert interesting steric and electronic effects on the process of self-assembly of the coordination polymers. For example, aromatic spacers in ligands can act as acceptors or donors in hydrogen bonds, but also as sites for π-π stacking interactions with the formation of supramolecular structures when coordinating to metals.[6]

CPs are useful precursors/templates for the preparation of nanomaterials. Increasing interest and efforts to synthesize materials at the nanoscale have created the possibility to obtain such entities ranging from inorganic metal clusters to custom-built single molecules.[16] There are many methods for the preparation of nanomaterials, such as hydro- or solvothermal, ultrasound, and microwave-assisted, sol-gel, electrochemical, micro-emulsion, chemical vapor deposition, etc.[17,18] In addition, thermal decomposition of the NCPs has become a growing field for the preparation of metal oxides with improved properties for various applications.[7,9,10] NCPs can be used as precursors/templates for the preparation of certain nanomaterials with special

morphologies. This approach shows several advantages: simplicity of preparation without the need for special installations, a good correlation between the structures of the resulting products and the starting materials, allowing a good control over the composition, phases and products; the ability to manufacture on a large scale.[17] Thus, nanomaterials with different morphologies can be synthesized based on NCP precursors under appropriate experimental conditions.[7] Their suitability for the synthesis of nanomaterials and the assembly of nanostructures in ordered topographies of the surface make these materials both functional and operational—two crucial aspects of successful nanotechnology.[16] A disadvantage of this process would be the preparation of CP itself. The structure and interactions within the crystalline network (covalent, coordinative, hydrogen bonding and van der Waals forces) influence the solvent—CP electrostatic and dipolar field interactions, as well as, hydrophilic or hydrophobic interactions, giving rise to external forces that control system morphology.[17]

The vast majority of coordinating compounds are obtained with full organic ligands or ones containing nitrogen, phosphorus or sulfur.[19] Intense studies have been conducted to construct such polymeric network structures with spectacular topologies using rigid ligands, such as 4,4′-bipyridine, aromatic Schiff bases, or 2,4,6-tri(4-pyridyl)-1,3,5-triazine.[8] The use of flexible ligands with a number of degrees of freedom has been practically avoided due to the unpredictable nature of the resulting polymer structure. For such complexes to be potentially useful, it is essential that their structures can be adjusted predictably by variations in their building blocks. In this respect, the rational design of polymer coordination architectures using flexible ligands is still a challenge. On the other hand, when unusual, flexible bipyridyl ligands, able to adopt different conformations, was reacted with silver salts, it has been observed the formation of helices and other new-supramolecular architectures that are impossible to obtain geometrically with rigid linkers.[8]

2. Coordination compounds with siloxane/silane-containing ligands

Despite the fact that the siloxane linkage is present in a wide range of compounds and materials including those in nature, such as zeolites, periodically mesoporous organosilicates, polyhedral oligomeric silsesquioxanes (POSSs) and other porous materials, this motif is rarely found in the structure of coordination compounds including MOFs.[19] Ligands based on or

containing silicon are far fewer and much less than those containing siloxanes. Therefore, in recent years, our work has focused mainly on the development of such ligands containing siloxane or silane spacers or tails and derived metal complexes of interest for catalysis, magnetics, biology, materials science, nanoscience, reporting in the CCDC crystallographic database a large number of such structures.

2.1 Particularities of the diorgano-siloxane or silane motif

Organosiloxanes or silicones, compounds containing the basic motif of the type in Scheme 1, create an interface between pure inorganic silica and organic compounds.[20] Among the properties that make silicone derivatives distinguishable from most other materials are the high conformational flexibility and low surface energy that originate in the nature of the siloxane bond and the organic group (in general methyl) attached to the silicon atoms, respectively. The Si—O bond is formed by σ bonding of sp^3 hybridized electrons of silicon with the p electrons of oxygen and the additional interaction of the unpaired p electrons of the oxygen with the free 3d-orbitals of silicon via p_π-d_π conjugation, giving it a partial double bond character.[21,22] The substituents on the silicon atom can alter the ground state of the siloxane bond (bonding order) by induction, well evidenced by the values of physical constants, for example, IR and Raman frequencies of the Si—O—Si bond.[21–23] Electron-acceptor substitutes on the silicon atom that reduce the energy of 3d orbitals, or oxygen-bound metal atoms that increase its negative charge, cause an increase in the order of the bond, whereas the electron-donor substituents on silicon and electron-acceptor groups bound to the oxygen reduce the siloxane bond order.[21] Partial double bond character is reflected in the much higher value of the Si—O—Si binding angle compared to the angle of a single bond in an organic chain (e.g., 112° in the C—C backbone unit).[24] The equilibrium value for the Si—O—Si bond angle is around 145–160°. The energy required to deform this bond to 180° is very low (1.3 kJ/mol), whereas for deformation to lower values (toward 109°, which corresponds to sp^3 hybridization) much higher

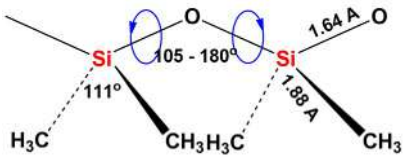

Scheme 1 The main bonding parameters in the dimethylsiloxane-based chain.[28]

energies are required.[25] The Si—O bond length of 1.64 Å also suggests an unusual binding situation, this being longer compared to 1.54 Å of C—C bond but shorter than the sum of the covalent radii of oxygen and silicon (r_{Si} =1.17 Å, r_O 0.66= Å),[24,26] also assigned to the partial double bond character. On the other hand, the difference between the electronegativity of the two atoms of the siloxane bond (1.8 for silicon and 3.5 for oxygen) results in a stronger bond having a polar, partial ionic (about 40%) character.[21,27] The length of the siloxane bond, as well as the high and flexible bonding angle, allow the rotation of the organic groups attached to the silicon atoms around the backbone axis, creating a shield that prevents the Si—O bond polarity manifestation and imposes its own character. The organic group attached to the silicon atoms in the siloxane compounds most commonly encountered as the sole or major substituent, is the methyl group known to be extremely nonpolar and hydrophobic. In this case, the intermolecular forces are almost the weakest possible (only those of the aliphatic fluorocarbon groups are lower).[29]

Another factor contributing to the high flexibility of the siloxane chain is the alternation of the unsubstituted oxygen bridge that reduces steric hindrance during conformational reorientation. That is why dimethylsiloxane chains show very low glass transition temperatures.[25] On the other hand, because the Si—C bond is long (from about 1.87 to about 1.90 Å) as compared with C—C (around 1.5 Å),[30] the presence of the silane motif in a ligand would allow greater conformational flexibility in metal coordination. The somewhat polar nature of this bond due to the difference of electronegativity between C and Si would have a positive impact on the ability of the materials to deposit gases.[31] The silane fragment can be encountered as a central element (spacer) or termination (tail) in the structure of a ligand. In the latter case, it appears as trimethylsilane unit, strongly hydrophobic due to the presence of three methyl groups, inducing specific properties.

2.2 Motivation for the interest in silicon-based ligands from the "nano" perspective

One of the manifestations of the low intermolecular forces in dimethylsiloxane-based compounds is the low surface energy (its liquid surface tension is 20.4 at 20 °C) at the highest molecular weight measured,[25,29] that gives silicones the ability to easily spread on the surface. But this is also the key factor that determines the phase separation and self-assembly of the compounds or materials in which silicone derivatives or even siloxane motifs are associated with any other organic and inorganic partners,[32] distinguishing

silicones from other materials. Longer siloxane bonding allows for easy change in conformation, giving flexibility to torsion and bending to the structure in which it is found.[27,32] On the other hand, due to the high hydrophobicity conferred by the methyl groups attached to the silicon atoms, the silicone compounds formed by attaching polar groups behave like surfactants.[33–39] Moreover, it is considered that the colloidal phenomena associated with the silicon element are a science of its own.[40] The ability of the silicones to self-assemble is the key to their functionality in making nanostructures.[32] Therefore, the capacity of the silicon-based materials for the formation of nano-aggregates and their utility in practical applications has been extensively studied.[41–45] Silicone chemistry offers a wide range of possibilities to engineer the molecules so that they are capable of forming phase domains or well-defined nano/microparticles particles. Siloxanes serve as the hydrophobic entity in surfactants that need to reduce the surface tension of water to a lower level than is possible with conventional surfactants. In addition, low surface tension recommends silicone derivatives for biomedical applications. It is suggested that they have minimal surface tension with aqueous protein solutions resulting in the lowest possible driving force for the protein.[25] New compounds can be developed, either by attaching functional groups to a siloxane skeleton, or by introducing siloxane moieties into other organic or inorganic compounds.

In this chapter, several cases of nanostructures based on coordination compounds with ligands containing siloxane or silane moieties obtained in our group over the last years are reviewed. These structures will be discussed not from the perspective of being part of some nanomaterials, but that of being themselves, as molecules, supramolecules or aggregates, on the nanoscale.[4]

3. Nano-sized coordination compounds of Schiff bases with siloxane spacer or silane tails

3.1 Mononuclear coordination compounds of Schiff bases with siloxane spacer

Schiff bases have played and still play an important role in the development of inorganic chemistry, being among the most commonly used ligands for metals to form complexes with different architectures. Binding to the metal occurs through nitrogen atom of azomethine group in chelating and bridging modes.[46–48] Schiff bases also serve as models for metal sites in metallo-proteins and enzymes.[49] In the literature there are reports on the

use of Schiff base complexes as components for the construction of nanomaterials, such as Fe(III) complexes of pendent Schiff base ligands (salten) used for stabilization and functionalization of gold nanoparticles,[50] Schiff base complexes encapsulated in hydrophobic silica channels having fluorescence, or in cavities of a zeolite having catalytic activity.[51,52]

A large research effort has been dedicated to complexes of Schiff bases with transitional metals. Of these, most were focused on complexes of Schiff bases of the salen- (N,N′-ethylenenebis(salicylaldimine)), salophen- (N,N′-*o*-phenylenebis(salicylaldimine)), and acacen- (N,N′-ethylenebis (acetylacetoneimine)) type, as simple or having attached extra functional groups or side chains, with variable length of the diamine spacer. A number of studies have been dedicated to the effect of the number of CH_2 groups between the imine groups (Scheme 2).[53,54] In ligands, because of the length of the N-$(CH_2)_n$-N bridge, the nitrogen and the phenolate atoms are mutually *cis*.[55] It has been found that in general, increasing the length of the spacer confers flexibility of the ligand allowing gradually the complex configuration to be changed, from *cis*-planar to *trans*-planar.[54] Data from studies on CuSalen complexes (n = 2, 3, 4, 6, 8, 10) show that the stereochemistry of copper complexes varies systematically from *cis*-planar (n = 2) to distorted tetrahedral (n = 3), the tetrahedral (n = 4), to distorted tetrahedral (n = 6), to *trans*-planar (n = 8).[54]

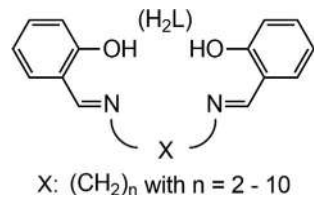

Scheme 2 Structure of the salen-type Schiff base with organic spacer.

On this basis, it is believed that the quadridentate complexes with long polymethylene spaced di-imines have an approximately tetrahedral geometry. Due to their size, the ligands are sufficiently flexible to allow this configuration to be achieved.[56] In addition, it has been found that with increasing aliphatic chain length, the lipophilicity of the complex increases, which results in increased cytotoxicity and cellular uptake rate, of interest when the targeted application is that of an antitumor drug.[57,58]

A series of complexes of transition metals coordinated in the N2O2 mode with Schiff bases of the salen-type derived from the single diamine with

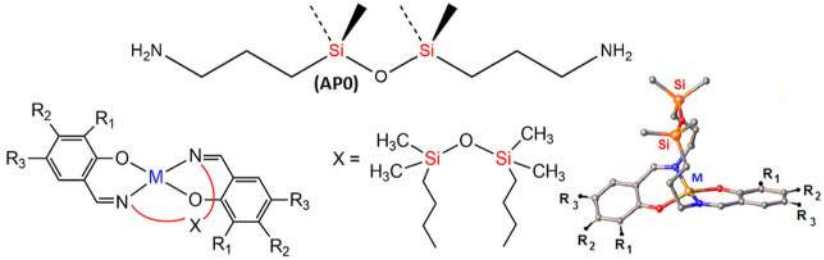

R1	R2	R3	M	Metal complex		R1	R2	R3	M	Metal complex	
						OCH_3	H	H	Cu	CuL^5	Ref.[63]
H	H	H	Cu	CuL^1	Ref.[59]	Br	H	Br	Cu	CuL^6	Ref.[59]
H	H	H	Zn	ZnL^1	Ref.[63]	Br	H	Br	Zn	ZnL^6	Ref.[60]
H	H	H	Zn	ZnL^1	Ref.[63]	Br	H	Br	Ni	NiL^6	Ref.[60]
H	OH	H	Cu	CuL^2	Ref.[59]	OH	H	H	Cu	CuL^7	-
H	H	Cl	Cu	CuL^3	Ref.[59]	H	H	NO_2	Cu	CuL^8	Ref.[59]
H	H	CH_3	Cu	CuL^4	Ref.[64]	*t*Bu	H	*t*Bu	Cu	CuL^9	Ref.[62]
H	H	CH3	Ni	NiL^4	Ref.[64]	*t*Bu	H	*t*Bu	Ni	NiL^9	Ref.[62]
H	H	CH3	Mn	MnL^4	Ref.[64]	*t*Bu	H	*t*Bu	Mn	MnL^9	Ref.[62]

Fig. 1 Coordination compounds of salen-type ligands containing tetramethyldisiloxane spacer; roughly overall dimensions of 12.7 × 6.3 Å.

siloxane spacer commercially available, 1,3-bis(3-propyl)tetramethyldisiloxane (**AP0**) (Fig. 1 top) with different salicylic aldehyde derivatives,[59–64] and not only,[65–67] were prepared (Fig. 1).

In these cases, the diamine spacer contains nine atoms. Due to the length and flexibility of the spacer, crystallization of ligands of this type was rarely achieved, viz. that derived from 1,3-bis(3-aminopropyl)tetramethyldisiloxane and pyrrol-2-carboxaldehyde, $\mathbf{L^{10}}$ (see below) with melting point 71 °C,[65] for which X-ray crystallography revealed a *cis* configuration and the presence of two intramolecular hydrogen bonds between the N—H groups and the imino nitrogen of the Schiff base. The other ligands were isolated in an oily state and characterized as such. However, in most cases the complexes were prepared in a single step with in situ formation of the ligands. Complexes of this type are generally nano-sized molecular compounds, with few exceptions, when supramolecular structures are formed through physical interactions (hydrogen bonds or π-π stacking), for example, $\mathbf{CuL^8}$,[34] $\mathbf{CuL^5}$,[63] or when other ligands and/or solvents are present in the coordination sphere as in $\mathbf{[CuL^2]\cdot[Cu(4\text{-}Me\text{-}Py)_4Cl]Cl\cdot 2H_2O}$.[59] Upon coordination of the doubly deprotonated tetradentate ligand $\mathbf{L^{2-}}$, two 6- and one 12-membered chelate rings are formed and the overall dimensions of the molecule often exceed 1 nm. In all compounds, the central metal atom is located in a tetrahedral, generally

slightly to moderately distorted, square-planar *trans*-N2O2 environment. The degree of tetrahedral distortion can be characterized by the τ_4 parameter ($\tau_4 = [360° - (\alpha + \beta)]/141°$, where α and β are the two largest θ angles at the M atom), introduced by Houser to describe the geometry of a four-coordinate metal complex, its value ranging from 1.00 for a perfectly tetrahedral geometry to zero for the perfect plane-square geometry.[68] The calculated values of this parameter for the synthesized complexes range from 0.142—**NiL^9**;[62] 0.16—**NiL^4**;[64] 0.15—**MnL^4**;[64] to 0.842—**ZnL^1**;[63] 0.46—**CuL^1**;[59] 0.387—**CuL^3**.[59] As the degree of distortion increases, the value of the siloxane angle slightly increases, e.g., from 159° in the case of **NiL^4**,[64] to 169° for **CuL^1**.[59] The variation of the siloxane bond angle in a relative wide range indicates a low degree of directionality of the Si—O bond and is proof of its partially ionic character.[62] Unlike all these, the compound **MnL^9** contains also in the coordination sphere an acetate ion as a bidentate chelating ligand. The Mn(III) ion exhibits a distorted axial-compressed octahedral geometry with an O4N2 donor set.[62] In all coordination compounds described, coordination at the central metal atom is ensured through the *trans*-N2O2 environment. In addition to the complexes shown in Fig. 1, the **NiL^{10}** complex was also obtained by template procedure based on 1,3-bis(3-aminopropyl)tetramethyldisiloxane, pyrrole-2-carbaldehyde and $NiCl_2$. The coordination compound having a central atom with a tetrahedrally distorted (τ_4 index of 0.263) square-planar environment, is isostructural with that found for the isolated ligand **L^{10}**, without significant modifications of the Si—O bond length (i.e., 1.619 Å in ligand and 1.617 Å in complex) and Si—O—Si angle (i.e., 160.7° in ligand and 161.7° in complex).[65]

3.2 Nano-structuration ability

Like diamines with a long, N-alkyl chain, 1,3-bis(3-aminopropyl)tetramethyldisiloxane may present surfactant properties.[57] These properties are further accentuated by converting 1,3-bis(propyl)tetramethyldisiloxane to bis-azomethine, when the dipole moment value increases, in dependence on the polarity of the carbonyl compound, from 0.794 D (**AP0**) to 1.389 D (**L^1**), 1.513 D (**L^9**) to 5.621 D (**L^8**), for example. This causes that both the ligands and, furthermore, the derived metal complexes have a somewhat amphiphilic character, consequently surface activity and the ability to self-assemble in solution depending on the polarity of the solvent. Thus, it has been found that such soluble coordination compounds reduce the surface tension of a solvent (for example, DMF, from 37.10 to 26.34 mN/m at

1.5 g/dL **CuL^9**) as its concentration increases. When the critical micellar concentration is reached (which in the case of the **CuL^1** complex, for example, was found to be 0.2 and 0.56 wt%), the compound assembles in aggregates from several hundred nanometers up to micrometers, as evidenced by dynamic light scattering (DLS).[34] It was found that the size of the aggregates in solution, estimated by DLS, depends on the polarity of the substituents from the aromatic nucleus and on the concentration. Thus, in DMF, at room temperature, at a concentration of 0.1 wt%, it was found that the size of the aggregates is smaller (average diameter = 6.808 nm) in the case of the **CuL^8** complex having strongly polar NO_2 substituents, than those formed under the same conditions by the **CuL^9** complex (average diameter = 42.406 nm) having strongly hydrophobic *tert*-butyl groups (Fig. 2 top). As expected, in all cases, the aggregate size increases with increasing concentration, to 55.243 nm at 1 wt% **CuL^8** and 148.651 nm at 4 wt% **CuL^1** (Fig. 2 down).

The analysis by small angle X-ray scattering (SAXS) indicates nanostructured models, which also change with increasing concentration, from disk-like to flat cylinder, for example, in the case of solutions of 1–7 wt% **CuL^1** in DMF. The aggregates, smaller in size than in the solution where they are in a swollen state, are found in a film in a thin layer remaining after the free evaporation of the solvent, as evidenced by transmission electron microscopy (TEM).[34] The obtained copper(II) complexes have been shown to be effective as catalyst precursors for the aerobic oxidation of benzyl alcohol to

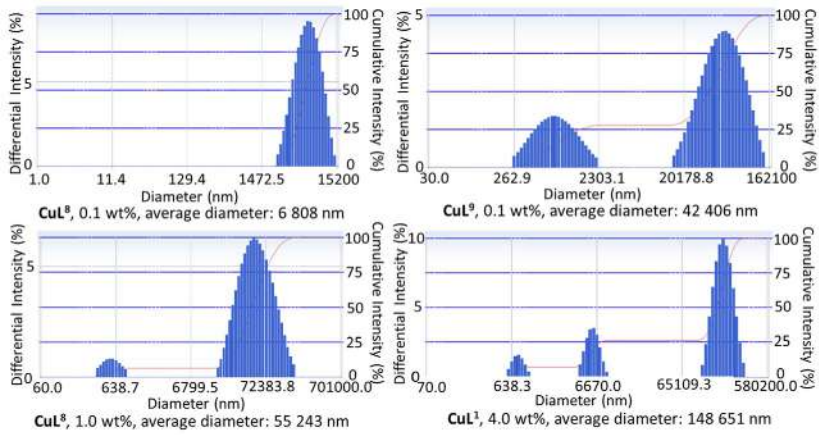

Fig. 2 DLS curves recorded for some copper complexes (**CuL^8**, **CuL^9**, **CuL^1**) as solutions in DMF with different concentrations, at room temperature.

benzaldehyde mediated by the TEMPO radical, reaching high yields in desired products, under mild and environmentally friendly conditions.[59] More suitable for this purpose proved to be especially those with electron-withdrawing substituents (chloro-, bromo-, and nitro- in **CuL^3**, **CuL^6**, **CuL^8**, respectively) to the aromatic ring. This can be explained by deepening the amphiphilic character of the complex, which favors more the self-assembly of the complex. In reactions being conducted in polar environment, the aggregates will logically expose the active (metal complexed unit) polar groups to the outside. In addition, as the DLS studies have shown, complexes with more polar substituents on the aromatic nucleus form smaller aggregates which give a larger catalyst contact surface available for reactants.

3.3 Polynuclear molecular complexes of Schiff base ligands with siloxane spacer or silane tails

Manganese(III) complexes of salen and salpn containing ancillary carboxylate ligands form often polymeric structures in the solid state.[69–71] Having at our disposal the Mn(III) complex, obtained with an acetate group in the coordination sphere (**MnL^9**, Fig. 1), such complex units were coupled through dicarboxylic acids to replace the acetate moiety, thus obtaining dinuclear structures.[72] Previously, the acetate group had been replaced with NCS to obtain a new high-spin d^4 roughly trigonal-bipyramidal manganese(III) complex with a salen-type ligand.[73] Dicarboxylic acids: fumaric (FA), benzene-1,4-dicarboxylic (BDCA) and biphenyl-4,4′-dicarboxylic (BPDCA) acid were used as bridging ligands (Fig. 3).

In the dinuclear structures obtained, the distances Mn⋯Mn are 8.736, 10.912, and 15.103 Å in **L^{9}Mn(OOCCH=CHCOO)MnL^9**, **L^{9}Mn(OOCC$_6$H$_4$COO)MnL^9**, and **L^{9}Mn(OOCC$_6$H$_4$C$_6$H$_4$COO)MnL^9**, respectively. Overall dimensions of the molecules are 8.841×23.769 Å, 8.152×25.839 Å and 8.975×29.902 Å, while the Si—O—Si angle values are 155°, 153° and 166°, respectively. The results of magnetic measurements and high-frequency and high-field electron paramagnetic resonance (HFEPR) suggest that magnetic exchange interactions may occur in di-Mn(III) systems over a relatively long distance (about 11 Å) similarly as in biological systems.[62]

In addition, azomethine ligands based on other carbonyl derivatives and/or another amine were obtained and characterized, but in general, for polynuclear metal complexes synthesis they were in situ generated in the reaction system by the template method (Fig. 4).

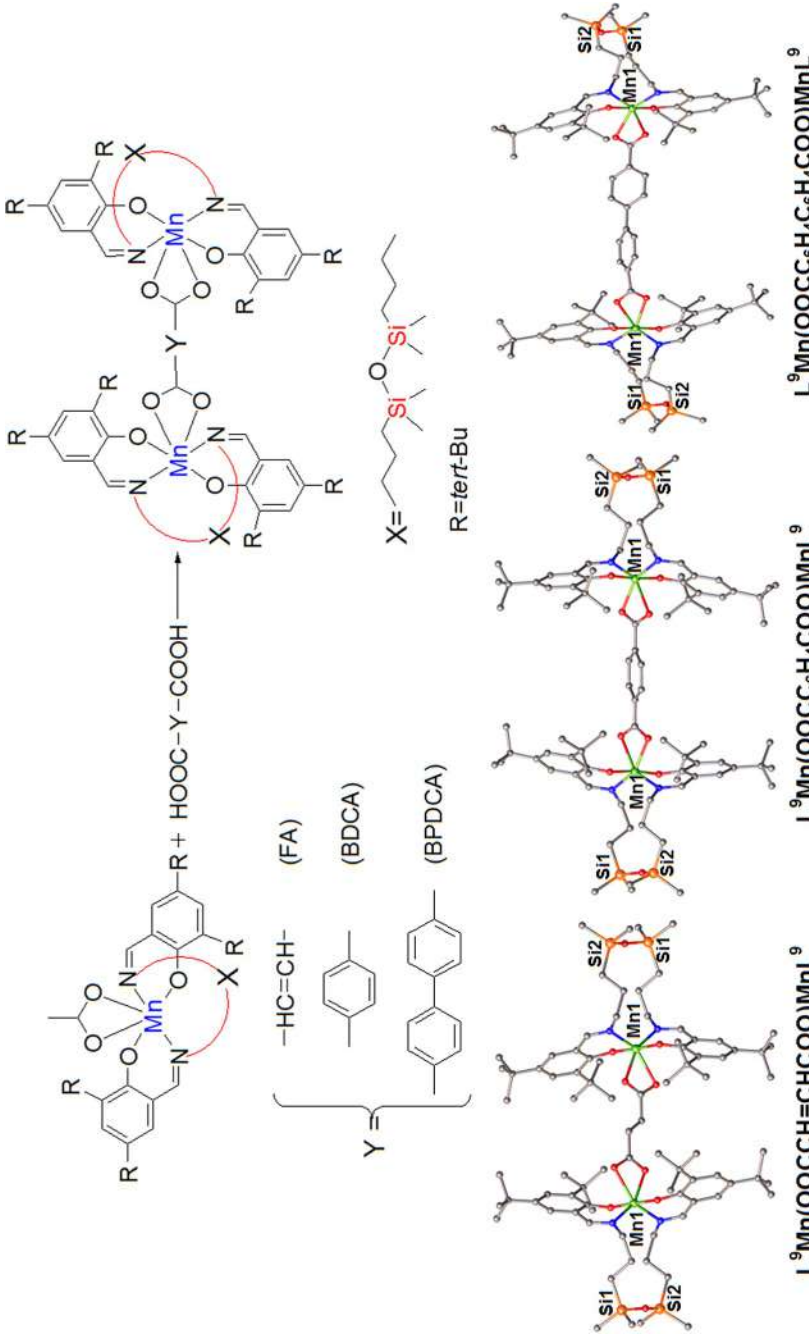

Fig. 3 Obtained dinuclear Mn(III) complexes spaced by organic segments with different flexibilities.[72]

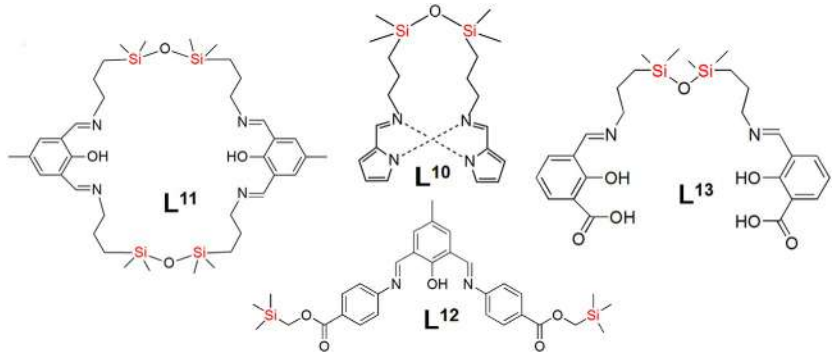

Fig. 4 Different Schiff base ligands containing siloxane spacers ($\mathbf{L^{10}}$, $\mathbf{L^{11}}$, $\mathbf{L^{13}}$) or trimethylsilyl tails ($\mathbf{L^{12}}$).[66,67,74,75]

Thus, the Schiff base ligand $\mathbf{L^{11}}$, derived from [2 + 2] condensation of 2,6-diformyl-4-methylphenol and 1,3-bis(3-aminopropyl)tetramethyldisiloxane, allowed to obtain μ-chlorido-bridged di-manganese(II) complexes, $\mathbf{[Mn_2Cl_2(H_2L^{11})(HL^{11})]Cl{\cdot}3H_2O}$ with Si-O-Si angle value ranging between 145–157°, while Si—O length is 1.590–1.666 Å; overall molecule dimensions are 16.7 × 17 Å (Fig. 5A). These complexes show an antiferromagnetic interaction between the two high-spin ($S = 5/2$, $g = 2$) manganese(II) ions through the μ-chlorido bridging ligands.[67] The complex proved to be suitable as catalyst or catalyst precursor for the oxidation of secondary alcohols to the respective ketones with *tert*-butyl hydroperoxide as oxidant under low-power microwave irradiation, at 80 °C and a moderate reaction time.[67]

The same ligand $\mathbf{L^{11}}$, when treated with $CuCl_2$, resulted in a tetranuclear copper(II) complex $\mathbf{[Cu_4(\mu_4\text{-}O)(L^{11})\text{-}Cl_4]}$ labeled as $\mathbf{CuL^{11}Cl}$, with overall molecule dimensions of 17.4 × 16.3 Å (Fig. 5B). The 1:2 condensation product of 2,6-diformyl-4-methylphenol with trimethylsilyl *p*-aminobenzoate ($\mathbf{L^{12}}$) forms with copper two different complexes, a tetranuclear complex with an open-chain, $\mathbf{[Cu_4(\mu_4\text{-}O)(L^{12})_2Cl_4]}$, labeled as $\mathbf{CuL^{12}Cl}$, with dimensions of 25.4 × 15.9 Å (Fig. 5C),[66] and a mononuclear complex, $\mathbf{CuL^{12}_2}$.[75] The central part of the $\mathbf{CuL^{11}Cl}$ and $\mathbf{CuL^{12}Cl}$ molecules consists of a tetranuclear $\{Cu_4\}$ core held together by a μ_4-oxido ligand. One doubly deprotonated macrocyclic ligand $\mathbf{(L^{11})^{2-}}$ in $\mathbf{CuL^{11}Cl}$, and two monodeprotonated ligands $\mathbf{(L^{12})^{-}}$ in $\mathbf{CuL^{12}Cl}$, are coordinated to the four copper(II) ions through four nitrogen atoms and two phenolato oxygen donors. In fact, they behave as bidentate chelating ligands for each of the four Cu(II) ions. The slightly distorted square-planar geometry of each metal center is completed by a chloride anion and the central μ_4-oxido ligand. In both

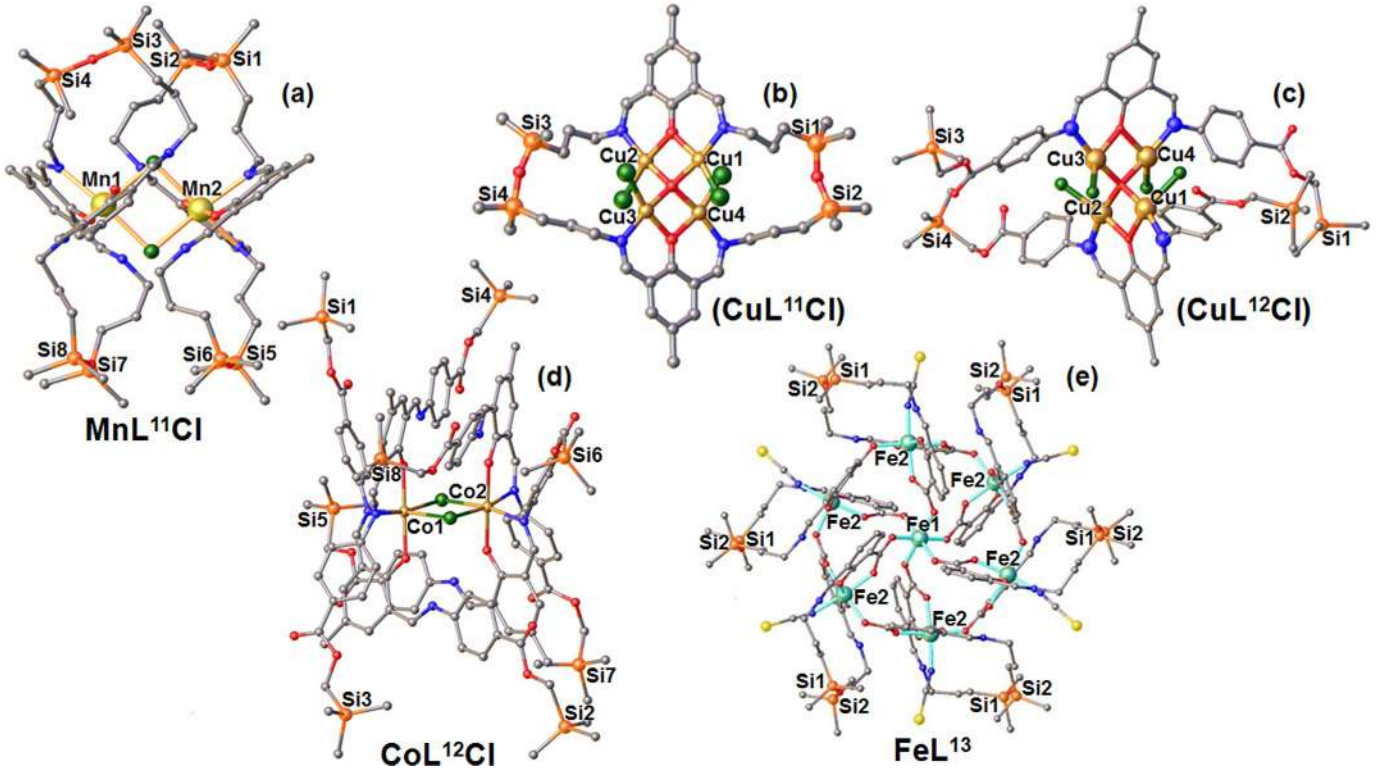

Fig. 5 Polynuclear coordination compounds obtained with ligands $\mathbf{L^{11}}$–$\mathbf{L^{13}}$ (see Fig. 3).[66,67,74,75]

CuL^{11}Cl and **CuL^{12}Cl**, the four copper ions of the {$Cu_4(\mu_4$-O)} core are located at the vertices of a distorted tetrahedron around the central μ_4-oxido ligand.[66] These coordination compounds also proved to be efficient as catalyst precursors for hydrocarboxylation of a variety of C5–C8 linear (*n*-pentane, *n*-hexane, *n*-heptane and *n*-octane) and cyclic (cyclopentane, cyclohexane, cycloheptane and cyclooctane) alkanes to give C6–C9 carboxylic acids with reasonable yields.[66]

The neutral units of mononuclear **CuL$_2^{12}$** resulted from coordination of two deprotonated bidentate **L^{12}** ligand molecules with Cu(II) ions in the N2O2 environment.[76] The molecular units of **[CuL$_2$]** are self-assembled with the adjacent units through bridging atoms O2 (Cu—O2 (2.94(1) Å)) and O6 (Cu—O6 (2.82(1) Å)) to form stepped polymeric chains via a center of inversion, giving Cu⋯Cu separations of 6.640(8) Å. The presence of strongly hydrophobic trimethylsilyl tails in the structure containing polar groups (imine, phenolate, ester) causes the self-assembly of these structures in micellar aggregates in solvents (for example, in hexane). These were evidenced both by DLS measurements in solution and by TEM on the film formed by rapidly leaving the solvent (Fig. 6).[76]

In situ preformed ligand **L^{12}** in a protic/aprotic solvent mixture, followed by addition of cobalt(II) chloride in the presence of a base, resulted in formation of the complex **[Co$_2$(μ-Cl)$_2$(HL^{12})$_4$][CoCl$_4$]·4.5CH$_3$CN** (**CoL^{12}Cl**) (Fig. 5D), with overall dimensions exceeding 1 nm (13.157 × 25.092 Å).[74] The crystal structure of the resulting complex consists of the **[Co$_2$Cl$_2$L$_4^{12}$]$^{2+}$** cation complex, **[CoCl$_4$]$^{2-}$** anion and solvate CH_3CN molecules. In the cation complex, the two Co atoms are linked through two μ-chlorido bridging ligands, according to a distance of Co—Co of 3.60 Å. Each cobalt ion has a *cis*-octahedral less distorted environment being coordinated by two bidentate Schiff bases and two chloride ligands (Fig. 5D). The magnetic measurements suggested the ferromagnetic interaction, which is released via two bridging coordinated chloride ions.[74] The ferromagnetic interactions between Co(II) ions was also evidenced by self-assembly of the Co(II) complex studied by magnetic force microscopy (MFM), where ordered self-organization in micelles was observed as shown in Fig. 7. The presence of magnetic centers in a flexible ligand-based structure allows the self-organization of the material deposited in the film under the action of the magnetic field of the cantilever (as can be seen in Fig. 7).

By complexing Fe(III) from $Fe(SCN)_3$ with a ligand in situ generated by the reaction between 3-formylsalicylic acid and 1,3-bis(3-aminopropyl)tetramethyldisiloxane (**L^{13}**), a {Fe}$_6$ wheel is formed, having hosted in the center a seventh iron(III) atom, **[Fe$_7$(H$_2$L^{13})$_6$(NCS)$_6$](ClO$_4$)$_3$·10H$_2$O**

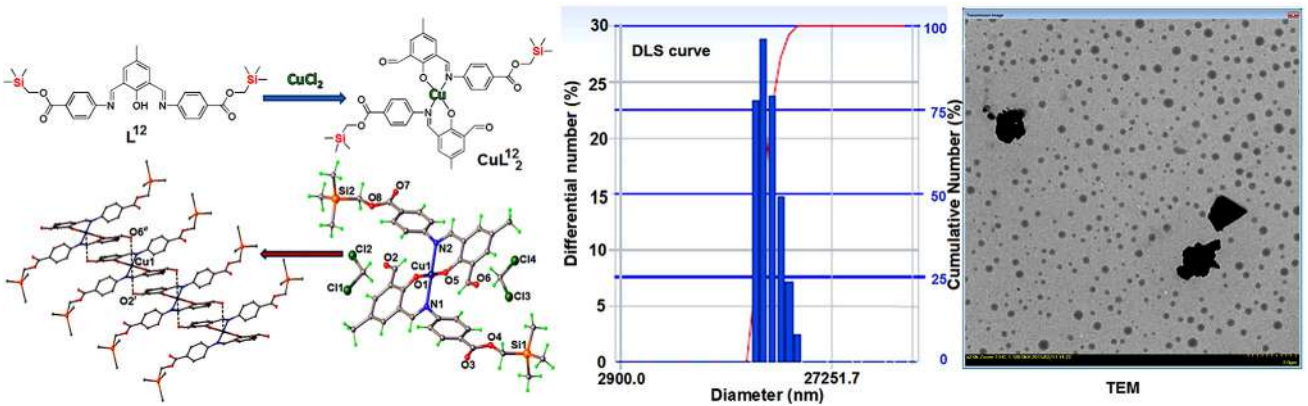

Fig. 6 Illustration of self-assembly of the $\mathbf{CuL_2^{12}}$ complex in crystal (left), in solution (middle) and in solution (right).[76]

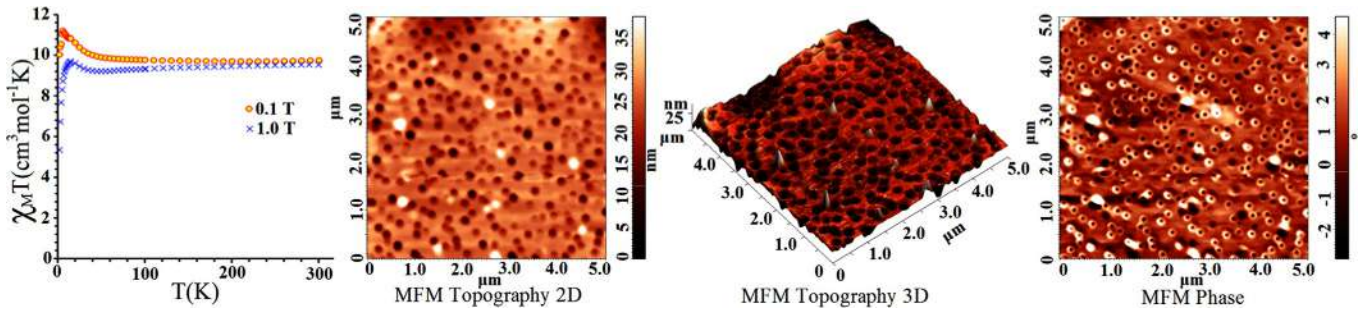

Fig. 7 Magnetic susceptibility data and magnetic force microscopy (MFM) images of **CoL^{12}Cl** complex.[74]

(Fig. 5E). Coordination is ensured by the COOH groups attached to the two formed aldimine fragments that remain protonated without participating in the coordination and separated by a long flexible aliphatic chain with a central tetramethyldisiloxane unit, in which Si—O—Si angle is 151°, while the —Si—O— bond length is 1.599 Å.[75] The overall dimensions of the molecule are 15.628 × 24.642 Å. Specific measurements indicate the presence of dominant antiferromagnetic interactions in the complex.

As we have shown in the case of Schiff base ligands, zero-dimensional, discrete molecular structures are obtained and only in some cases self-assembled by physical interactions in 1D or 2D architectures which have limited functionality as such. In order to achieve well-defined nanostructures, more functionality and extended control of chemical interactions are necessary. Polycarboxylic acids (aromatic or aliphatic), as well as ancillary ligands (imidazole, 4,4′-bipyridyl, 4,4′-azopyridine, 1,10-phenanthroline) and metal ions or clusters are the most common building blocks in the construction of metal-organic frameworks (MOFs) or coordination polymers with highly directional intermolecular interactions (metal-ligand and hydrogen bonds). The ability of polycarboxylic acids in coordination of metal ions allows the formation of different topologies: mono- and polynuclear 1D, 2D or 3D networks with regular pores of various sizes: 0.2–2 nm (microporous materials), 2–50 nm (mesoporous materials) and 50–1000 nm (macroporous materials) and predicted functions for gas storage, selective adsorption and separation, magnetism, luminescence. As it is known, the first MOF was constructed from tetrahedral zinc clusters $(Zn_4O)^{6+}$ bridged by 1,4-benzenedicarboxylate linker (MOF-5).[77] The linker can be easily replaced by different polycarboxylates leading to the IRMOF series with higher pore size (3.8–19.1 Å) and improved functionality, without altering the framework topology.

In our attempt to investigate the design and control of the self-assembly of MOFs with flexible or semi rigid (V-shaped) ligands, namely those containing siloxane and silane units, respectively, various complexes with interesting structures have been successfully isolated by template-directed synthesis and solvothermal procedure.

4. Metal complexes with siloxane-spaced or -supported polycarboxylate ligands

4.1 Amorphous metal-organic frameworks

4.1.1 Aluminum carboxylate

A less common dicarboxylic acid with siloxane spacer, 1,3-bis(carboxypropyl) tetramethyldisiloxane, $\mathbf{L}^{14}$, was used as a ligand having as a particularity the presence of the tetramethyldisiloxane moiety with high flexibility,

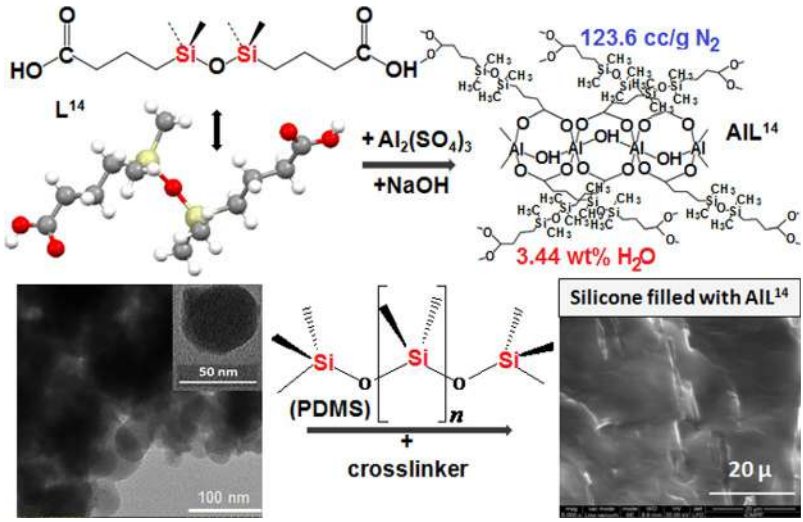

Fig. 8 Schematic illustration of the path from the dicarboxylic ligand with tetramethyldisiloxane spacer, **L^{14}**, to the coordination polymer **AIL^{14}** as nanoparticles and terminated with high transparent silicone nanocomposites.[78]

conferred by the siloxane linkage and hydrophobicity conferred by the methyl groups attached to the silicon atoms (Fig. 8). Also, the distance between the carboxylic groups is quite large, being made up of nine atoms. However, it could be isolated in the crystalline state and analyzed structurally by single crystal X-ray diffraction.[78] Instead, when used alone, this ligand in a reaction with aluminum sulfate in alkaline aqueous medium, by a protocol similar to that used for the synthesis of the commercial MOF Basolite A520,[79] led to an insoluble, amorphous, collapsed metal-organic network as roughly spherical particles of the order of tens of nanometers at most (Fig. 8).[78] The moisture sorption capacity of 3.44 wt% is about 15 times lower than the similar complex derived from fumaric acid and it does not undergo structural changes as a result of the repeated moisture sorption-desorption processes. Although the nitrogen sorption isotherms indicated low specific surface values (BET surface area 28.1 m^2/g; Langmuir surface area 36.4 m^2/g), which do not indicate a porous material, being a hydrophobic particulate one, it has proved to be highly dispersible and an effective reinforcing filler for silicone polymers (PDMS) due to their common nature.[78]

4.1.2 Copper carboxylates

Polycarboxylic compounds, which consist of cyclosiloxanes having attached at each silicon atom the highly hydrophobic methyl group and a carboxyl

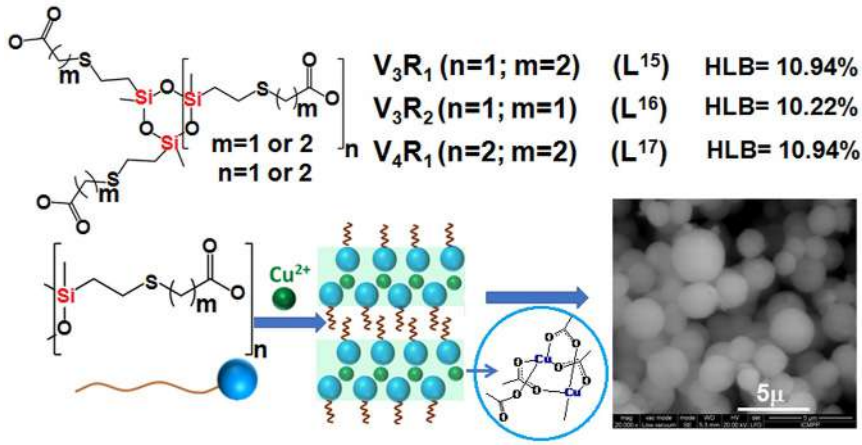

Fig. 9 Carboxy-functionalized methylcyclosiloxanes as amphiphilic ligands, $\mathbf{L^{15}}$–$\mathbf{L^{17}}$, and nano-sized metal complexes assembled on their bases.[80]

group coupled through thioether bridges, were prepared ($\mathbf{L^{15}}$–$\mathbf{L^{17}}$) (Fig. 9).[81] The coexistence in the structure of the highly polar carboxylic groups and highly hydrophobic methyl groups attached to the silicon atom confers an amphiphilic character on these ligands. As a result, at the concentration used, these are aggregated in solution, as evidenced by the in situ taken microscopy images and nanoparticle tracking analysis (NTA) technique. The values of the hydrophilic-lipophilic balance, calculated with the relation: HLB = (% by weight hydrophilic part)/5,[82,83] range between 10.22 and 10.94.[80] With the addition of copper acetate in such a system, copper ions are readily complexed within the ligand aggregates, concomitantly with self-assembly into particles with spherical morphology with dimensions of the order of several hundred nanometers up to over 1 μm (Fig. 9).[80]

Even though they are carboxylic acid coordination compounds, the complexes are quite hydrophobic (water vapor sorption capacity: $\mathbf{L^{15}Cu}$—4.22 wt%, $\mathbf{L^{16}Cu}$—5.65 wt%, $\mathbf{L^{17}Cu}$—3.02 wt%) due to the highly hydrophobic methyl groups attached to each silicon atom, which are exposed at the surface.[80] These compounds can be regarded as metallo-surfactants of interest for organic catalysis where they can react both with hydrophilic and hydrophobic substrates.[84–86] The tests performed indicate these copper complexes as an alternative to iron-based catalysts in Fenton reactions.[80]

4.2 Crystalline metal carboxylates

4.2.1 Siloxane-containing metal carboxylates

If the $\mathbf{L^{14}}$ carboxylic ligand alone formed amorphous structure with Al(III), as well as with other metal ions in our tests, crystalline structures resulted when the metal component was a preformed cluster or when a rigid co-ligand was used. Thus, the reaction product of $\mathbf{L^{14}}$ with in situ generated manganese salicylaldoximate complex was isolated in the crystalline state. The structural analysis showed an one-dimensional nano-sized coordination polymer consisting of hexa-manganese(III) salicylaldoxymate clusters, acting as SBUs, coupled by the double deprotonated $\mathbf{[L^{14}]^{2-}}$ anion, which behaves as a tetradentate linear linker (Fig. 10). According to crystallographic data, two $\{Mn_3(\mu_3\text{-}O)\}$ subunits are bridged by two oxygen atoms of the oxime ligand in the hexanuclear cluster. The Mn⋯Mn separation within the trinuclear subunits is 3.156(6)–3.252(6) Å, while the Mn⋯Mn length between trinuclear subunits is 3.391(6) Å. The Mn(III) ions within the trinuclear subunits are bridged by double deprotonated salicylaldoxime ligands, three water molecules and one protonated salicylaldoxime ligand in a monodentate coordination mode. The distance between the metal centers of two clusters connected by $\mathbf{L^{14}}$ is around 19 Å, while the diameter of the cluster is about 13 Å.[87]

The coexistence of SBUs and 1,3-bis(propyl)tetramethyldisiloxane sequences confers to the chain an amphiphilic character. The self-organization of the coordination polymer, in solution or in cast film, as either micelles or inverse micelles and vesicles depending on the solution concentration and solvent polarity, was demonstrated by multiple techniques: TEM, DLS, SAXS.[87] Thus, on the TEM images of the films obtained from DMF and $CHCl_3$ aggregates can be observed with dimensions slightly larger than 100 nm in both cases, but with cores having different optical densities in the two solvents (Fig. 10 down). DLS analysis in solution also reveals the presence of aggregates but larger (1–10 μm), because they are in a swollen state. SAXS investigations confirm the self-assembly of Mn(III) coordination polymer in a lamellar arrangement assigned to a particular ordering of the crystalline fragments in the vesicle wall. This behavior would be very useful for applications in catalysis and biology. The *ac* magnetic susceptibility registrations at low temperatures (2–5 K) confirmed a slow relaxation of magnetization depending on frequency, which is consistent with the single magnet molecule behavior. The magnetic interaction is essentially governed by the two antiferromagnetic interactions within the two triangles of the manganese cluster. As expected, the long aliphatic

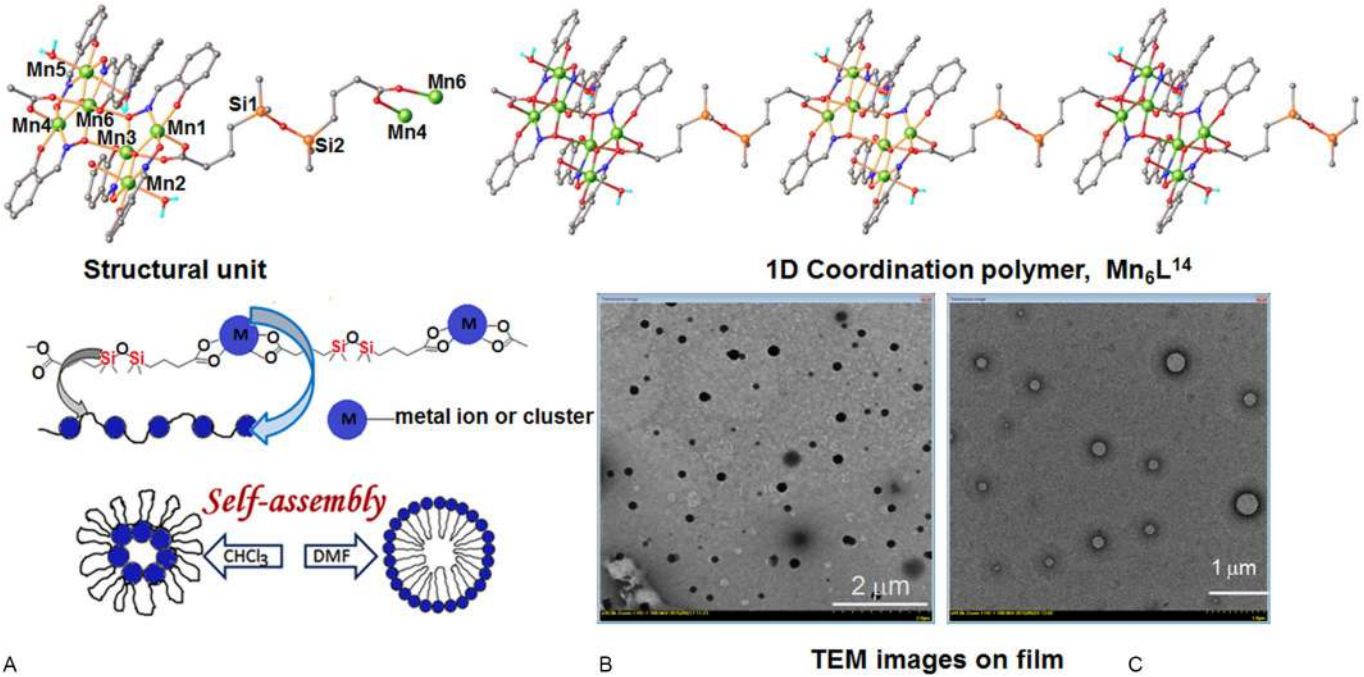

Fig. 10 1D Coordination polymer based on manganese and $\mathbf{L^{14}}$ ligand, $\mathbf{Mn_6L^{14}}$ (top); presumed mechanism for self-assembling polymer in solvents with different polarities (A) and TEM images of aggregates formed from DMF (B) and $CHCl_3$ (C) (down). *Adapted from Vlad, A.; Cazacu, M.; Zaltariov, M.F.; Bargan, A.; Shova, S.; Turta, C.* J. Mol. Struct. ***2014***, 1060 *(1), 94–101.*

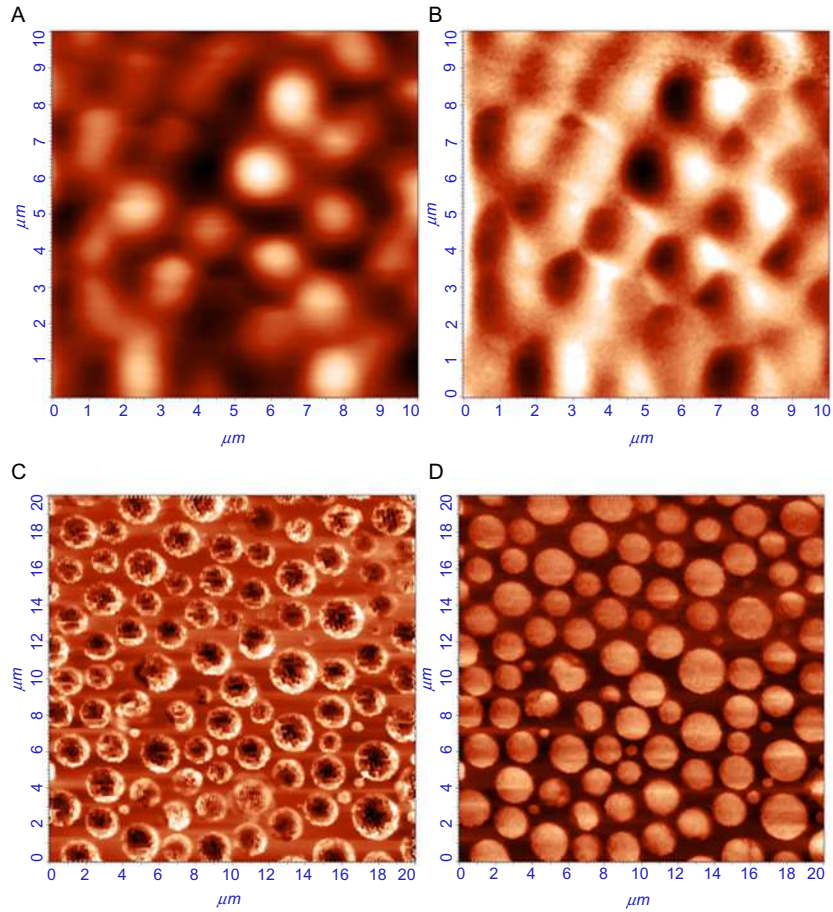

Fig. 11 Topographic (A,C) and phase (B,D) AFM (A,B) and MFM (C,D) images of the **Mn_6L^{14}** aggregates in film born from $CHCl_3$ solution.

siloxane spacer insures a good isolation of the SBUs.[87] The self-organization of the Mn(III) coordination polymer in magnetic field was studied by magnetic force microscopy (MFM) and the images confirmed its response by self-assembling in regular size and shape particles (Fig. 11A and B). Thus, the spherical aggregates, remained in film as a result of quick removal of solvent ($CHCl_3$), easily collapse when the film is scanned by MFM, as can be seen in Fig. 11C and D.

Also, the **L^{14}** ligand led to crystalline structures in the presence of rigid co-ligands, such as 4,4′-azopyridine (**APy**),[88,89] imidazole (**Im**),[89,90] 4,4′-bipyridyl (**BPy**) and 1,2-(4-bipyridyl)ethylene (**EBPy**).[91] Thus, crystalline

coordination polymers with different architectures, e.g., 1D with Zn(II),[89] or 2D with Co(II),[89] Zn(II),[88,91] and Cu(II),[90] were obtained. In all these structures, carboxylic acid acts either as a bidentate or tetradentate bridging ligand. Both *cis*-,[89,90] and *trans*-oide[87,89,90] conformations have been observed for the ligand $\mathbf{L^{14}}$ in these compounds, depending on the coordination geometry of the SBUs and H-bonding configuration.[87–90] The structures in which $\mathbf{L^{14}}$ is a co-ligand with **APy** for transition metals are built from dinuclear metal clusters as nodes interconnected by 1,3-bis (carboxypropyl)tetramethyldisiloxane dianions (one coordinating to the metal in bidentate and the other in bridging-bidentate mode) and 4,4′-azopyridine molecules (with weak π-π stacking interactions between aromatic rings) as spacers (Fig. 12). Heteronuclear structures of type **CoZnL^{14}Apy** (with Co/Zn ratio 1/1.5 or 1/3) were also prepared.

The metals in these structures have generally a strongly distorted octahedral environment [MN_2O_4].[88,89,92] M⋯M distance within the rigid chain is around 13.5 Å (Mn),[92] and 11.2 Å (Zn),[91] while along the $\mathbf{L^{14}}$ linker is 16.932 Å.[91]

In presence of 4,4′-bipyridyl (**BPy**), a 2D polymer, **{[Zn($\mathbf{L^{14}}$)(BPy)]·1.375$\mathbf{H_2O}$}$_n$**, **L^{14}BPyZn**, with the Zn atom tetrahedrally N2O2 coordinated by two monodentate carboxylate groups of the $\mathbf{L^{14}}$ ligand in a *trans*-oide conformation and two **BPy** ligands has also been obtained. The Zn⋯Zn distance separated by **BPy** and $\mathbf{L^{14}}$ is 11.220 and 16.932 Å, respectively.[91] When 1,2-(4-bipyridyl)ethylene (**EBPy**) was used as rigid co-ligand, the 2D extended structure **{[$\mathbf{Zn_2}$($\mathbf{L^{14}}$)$\mathbf{(Ac)_2}$(EBPy)^2]0.1.8$\mathbf{H_2O}$}$_n$**, **ZnL^{14}EBPy**, formed in which Zn has a strongly distorted N2O4 octahedral coordination with two **EBPy** ligands, two bidentate carboxylate groups provided by the acetate anion and $\mathbf{L^{14}}$ dianion in *trans*-oide conformation.[91] These networks showed very good catalytic activity in H_2O_2 decomposition and promising catalytic activity in the oxidation reactions of glucose and viscose. Similar hydrophobic MOFs, but based on Cu and Co, have been shown to be efficient and reusable catalysts for processes occurring in the aqueous environment, such as hydrogen peroxide breakdown in alkaline environment or Congo red photodecomposition.[93]

Imidazole was also used as co-ligand with $\mathbf{L^{14}}$ for the synthesis of coordination compounds with Cu,[90] or Zn.[89] X-ray diffraction analysis of the Cu complex formed, revealed the formation of an extended 2D network in which dinuclear copper(II) nodes are bridged by siloxane dicarboxylate ligands into a paddle-wheel unit, with Cu⋯Cu separation of 3.124(9) Å. The geometry around copper(II) is a five-coordinate distorted

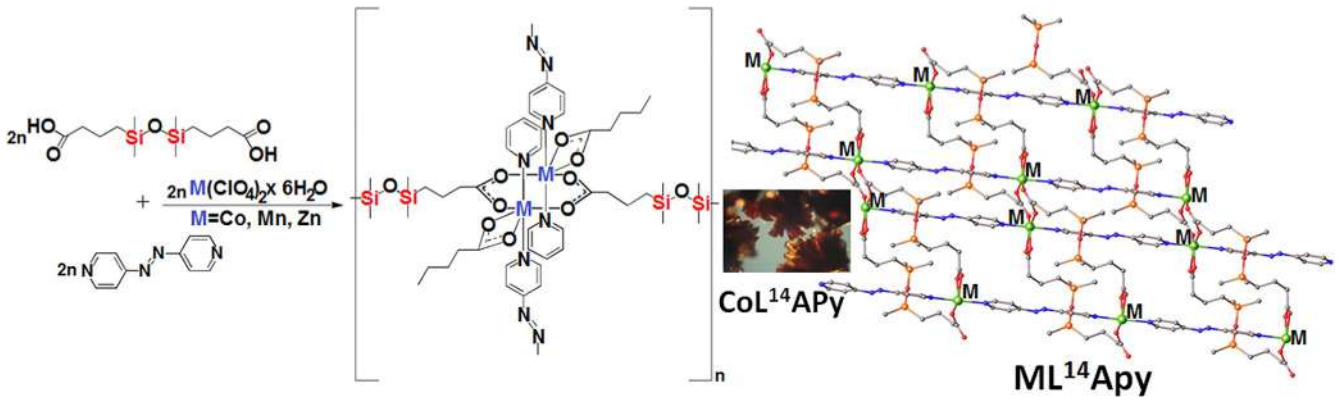

Fig. 12 General route leading to 2D covalent **ML^{14}APy** structure, with M═Co,[89] Zn,[88] or Mn (left);[92] two-dimensional coordination network formed (right); inset: the optical aspect of the crystal presented illustratively for **CoL^{14}APy**.[89]

square-pyramidal, the basal plane being occupied by two nitrogen atoms and two oxygen atoms. The carboxylate linker adopts a *cis*-oide conformation in stabilization of the crystalline network by coordination of copper(II) ions in a bidentate mode and H-bonds with the adjacent imidazole ligands, and a *trans*-oide conformation occupying the space between the 2D layers, leading to a high interconnected 3D network. Magnetic susceptibility analysis revealed an antiferromagnetic interaction between two Cu(II) paramagnetic centers within the nodes. It should also be mentioned that the H_2 and N_2 isotherms revealed very low sorption capacity, the obtained values at 1 atm being of 3.38 and 18.55 $cm^3\ g^{-1}$, respectively.[90] These are probably due to the incomplete removal of guest molecules or structural deformation during the thermal activation prior to N_2 and H_2 adsorption measurements, which have often been observed in coordination polymers (Fig. 13).[90]

Instead, in the case of Zn, the same ligand pair led to a hydrophobic (2.6 wt% moisture sorption at room temperature) 1D coordination polymer with tetrahedral coordinated zinc by three oxygen atoms from carboxylate groups and one nitrogen atom from imidazole as monodentate ligand.[89] One of the carboxylate groups coordinates in a bidentate bridging mode, while the second in a monodentate mode with the second oxygen atom involved as acceptor in intermolecular N—H···O hydrogen bond with imidazole leading to a 2D supramolecular structure. The ligand $\mathbf{L^{14}}$ is in the *cis* conformation and the Si—O—Si angle is 163°. The polymer shows a strong emission around 387 nm in the solid state upon 320 nm excitation being of interest in electroluminescent devices.[89]

All these structures show, besides melting and crystallization, also glass transitions assigned to highly flexible and hydrophobic tetramethyldisiloxane moieties within the polymeric structures. This transition occurs in general at low temperatures for a crystalline compound depending on the intermolecular forces manifested. So the values of these temperatures are generally lower for 1D (7 °C,[88] 14 °C[87]) structures than for 2D ones (76 °C,[89] 17.9 °C,[90] 23.02 °C,[88] 42.2 °C[91]). In general, these compounds behave as hydrophobic materials, the equilibrium moisture sorption capacity at 90% RH and room temperature, being 1.8 (**ZnL^{14}BPy**) and 2.5 (**ZnL^{14}EBPy**),[91] 1.50 (**CuL^{13}Im**),[90] or 2.6 wt% (**ZnL^{14}Im**).[89] In the case of the 1D hexamanganese complex with L^{14} (**Mn$_6$L^{14}**), due to the high contribution of the large aldoximate groups, the sorption capacity is rather high for a compound containing highly hydrophobic tetramethyldisiloxane moieties, i.e., 18.9 wt%.[87]

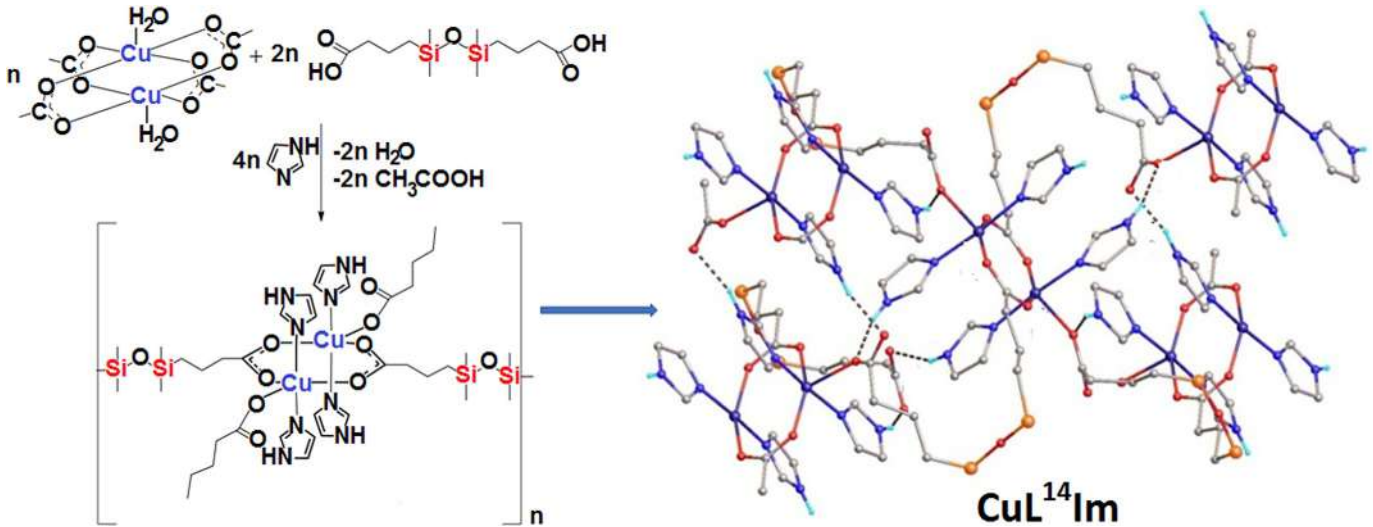

Fig. 13 Reaction leading to the formation of 2D **CuL^{14}Im** structure.[90]

The three main elements of such structures: the metal in a certain spin and oxidation state coordinated by the carboxylic groups, the high flexible and hydrophobic tetramethyldisiloxane extender and rigidity, as well as other particularities of the co-ligand, can confer these compounds magnetic, surface (self-assembly) or optical properties.[92] Thus, besides the ability to assemble in the crystal structure in 1D, 2D or 3D architectures, due to their amphiphilic character, these soluble coordination compounds have also the ability to self-assemble, both in solution and in film, forming more or less defined nanostructures, depending on the influence of other external factors. Thus, AFM images taken on the film of the 2D polymer **CoL^{14}APy** and **ZnCoL^{14}APy**, spin coated from a clear solution in the solvent mixture $CHCl_3$:THF:DMF, in volume ratio 1:1:1, reveal the self-assembly of the polymers in columnar aggregates having a size of the order of 100–200 nm (Fig. 14).

By irradiation with an UV laser (Xe—Cl excimers) beam at 308 nm and power density of 45 mJ/cm^2, the film based on the **MnL^{14}APy** complex is very quickly structured into hemispherical nanometer formations as a result of azopyridine photoisomerization (Fig. 15A and B). Structuring, but with a different pattern, also occurs under the action of a magnetic field when the film is investigated by MFM technique (Fig. 15C).[92]

This ability is of interest for their potential to orient other chemical species, such as biomolecules, or in catalysis.[94]

4.2.2 Silane-containing metal carboxylates

The carboxylic acids containing silane units can also be used as organic building units for metal-organic frameworks on the assumption that the

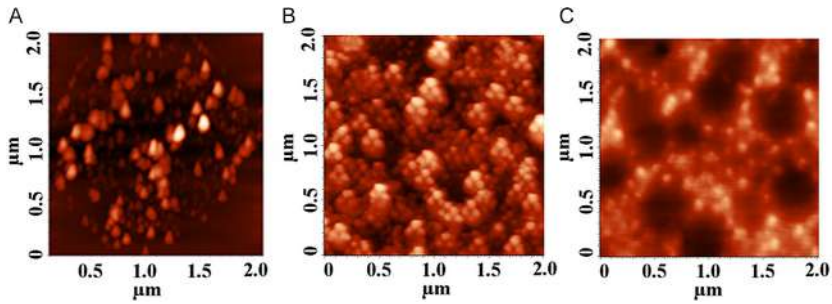

Fig. 14 Changing in structuration pattern in film (formed from $CHCl_3$:THF:DMF in volume ratio 1:1:1) of the heteronuclear **ML^{14}APy** 2D complexes in dependence of hetero-metal ratio: (A) Co; (B) Co/Zn = 1/1.5; (C) Co/Zn = 1/3 emphasized by AFM.

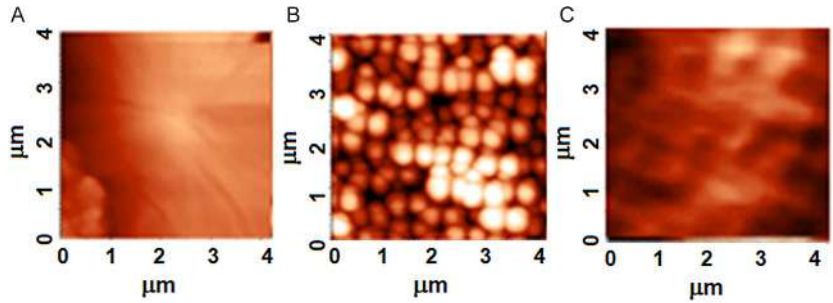

Fig. 15 AFM images of the **MnL^{14}APy** pristine (A) and UV-irradiated (B) film formed from methanol; (C) MFM image taken on pristine film.

presence of the relative flexible C—Si—C spacer, in their structures would facilitate the self-assembling in supramolecular architectures, decrease phase-transition temperatures, and, eventually, improve solubility. In addition, the phenyl rings can freely rotate around the C—Si—C single bond according to the small change in the coordination environment in order to minimize the steric hindrance.[95] The carboxylic acid groups can be partially or completely deprotonated, leading to various coordination modes; they can be involved in hydrogen bonds, both as an acceptor or as donor, while the aromatic ring can stabilize the crystal structure via π-π-stacking interactions. These structural properties are essential in the design of high dimensional frameworks.[96] There are a small number of publications in which silicon-containing carboxylic acids are used to prepare metal-organic frameworks, e.g., tetrakis-(4-carboxyphenyl)silane, di-(4-tolyl)-di-(4-carboxyphenyl)silane and (4-tolyl)-tris-(4-carboxyphenyl)silane, 5,5′-(dimethylsilanediyl)diisophthalic acid, 5,5′-[4,4′-(dimethylsilanediyl)bis(1,4-phenyl)bis-(ethine-1,2-diyl)]diisophthalic.[31,97–100] Different from these, the silicon-containing linker was prepared and used in bis-(*p*-carboxyphenyl)diphenylsilane, **L^{18}**, on the basis of which two manganese complexes, one pentanuclear and one trinuclear, **$Mn_5(L^{18})_4^{2-}(HCOO)_2(H_2O)_2(DMF)_4$**, **$Mn_5L^{18}$**, and **$[Mn_3(\mu\text{-}H_2O)(L^{18})_2^{1-}(L^{18})_2^{2-}(DMF)_2]\cdot 2DMF\cdot 12H_2O$**, **$Mn_3L^{18}$**, both as 2D coordination structures were obtained (Fig. 16).[101]

The formation of a nano-sized pentanuclear cluster is insured by the coordination of 10 carboxylate groups provided by four bis(*p*-carboxyphenyl)diphenylsilane and two formate ligands. While the latter act as bridging ligands, the dicarboxylic ligands play a dual role, holding together the metal ions of the SBU and bridging the SBU together. Crystal **Mn_3L^{18}** is built of trinuclear manganese(II) SBUs that are held

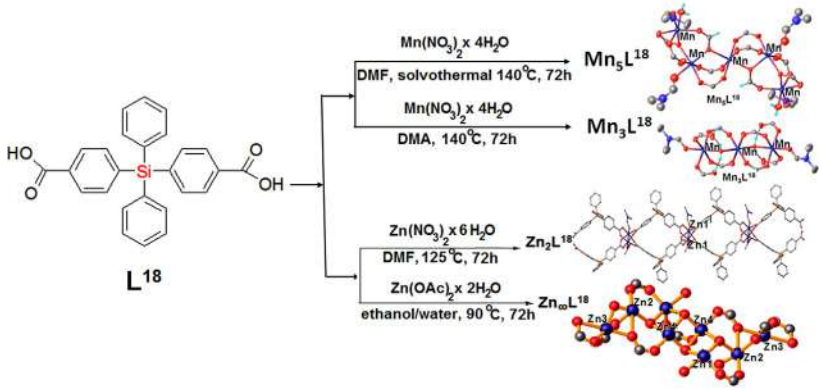

Fig. 16 Experimental pathways leading to: tri- and pentanuclear manganese(II), Mn_5L^{18} and Mn_3L^{18}, dinuclear zinc(II), Zn_2L^{18}, and infinite Zn(II) clusters, $Zn_\infty L^{18}$, as SBUs, self-assembled as MOFs by V-shaped silicon-containing dicarboxylates.[92,101]

together by $\mathbf{[L^{18}]^{2-}}$ and $\mathbf{[L^{18}]_2^{1-}}$ in a 2D (4,4) coordination polymer. The magnetic susceptibility measurements indicate antiferromagnetic interactions between paramagnetic manganese(II) centers modulated by the coordination mode of the carboxylate bridges. $\mathbf{Mn_5L^{18}}$ and $\mathbf{Mn_3L^{18}}$ contain large, bidirectional rectangular 8×9.2 Å^2 channels along the crystallographic *b* axes, comparable to MOF-5, where the 3D channel systems are of 8×12 Å.[77] These channels are filled with solvated water and DMF molecules in the case of $\mathbf{Mn_5L^{18}}$ (see below).[101] The solvent accessible surface values theoretically estimated on the basis of the crystallographic data for particular guest molecules (CO_2, H_2O, Ar, N_2), vary in the range 1.6% of unit cell volume for CO_2 (compound $\mathbf{Mn_5L^{18}}$) to 19.5% of unit cell volume for N_2 (compound $\mathbf{Mn_3L^{18}}$), whereas for water these values are 9.4% and 7.5% of unit cell volume in the case of the first and second compounds, respectively.

Following the same strategy, two zinc coordination polymers, $\mathbf{Zn_2L^{18}}$ and $\mathbf{Zn_\infty L^{18}}$, have been obtained under different solvothermal conditions (Fig. 16). The Zn(II)-coordination polymer $\mathbf{Zn_2L^{18}}$ is built up from deprotonated carboxylate linkers connected to the dinuclear Zn in a *syn-syn* bidentate coordination mode. The Zn⋯Zn separation is 2.941(2) Å, both Zn(II) ions being in a square-pyramidal environment assigned to the four oxygen atoms from carboxylate ligands with Zn—O length of 2.058 (5)–2.060(5) Å and to one oxygen atom from DMF molecules used as solvent with Zn—O distance of 1.989(5) Å. The self-assembly in the solid state occurred by parallel packing of 1D polymeric chains leading to the

formation of a 2D networks in which 4.9×11.3 Å^2 channels accommodate coordinated and solvated DMF guest molecules (Fig. 17). The channels are similar to those found in Zn-MOF-54 built with 2,5-dioxido-1,4,-benzene-dicarboxylate linker with 10.3×5.5 Å^2.[102] In the $\mathbf{Zn_\infty L^{18}}$ framework, the silicon linker extends in three dimensions by bridging the zinc(II) centers into infinite clusters as SBUs, the space between zinc(II) layers being occupied by diphenyl units attached to the silicon atom (Fig. 17). The geometry around a zinc(II) ion is a distorted trigonal bipyramid.

Dinuclear Ni(II) and Co(II) complexes were also prepared under solvothermal conditions by heating $\mathbf{L^{18}}$, 1,10-phenanthroline and metal acetates in a water/DMF mixture. Single-crystal X-ray structure analysis revealed that the Ni(II) complex adopts an extended 2D network composed from discrete dinuclear Ni(II) complexes connected in 1D supramolecular layers by two monodentate carboxylate groups, two nitrogen atoms from 1,10-phenanthroline and two water molecules in an octahedral environment (Fig. 18).

The Ni⋯Ni distance within the molecular unit is 13.4 Å. The structure is stabilized also by π-π stacking interactions between the parallel 1D chains leading to a very compact structure with no surface access for guest molecules. On the contrary, large cavities similar with those of $\mathbf{Mn_3L^{18}}$ are formed when Co(II) acetate is used as connector, the Co⋯Co distance being of 2.078(6) Å. Co adopts an octahedral geometry being coordinated by two nitrogen atoms from 1,10-phenanthroline, one carboxylate in bidentate bridging mode, two carboxylate groups in chelating bidentate mode and one water molecule (Fig. 18).

Pore expansion can be achieved by simply adjusting the structure of the carboxylate linker. Therefore, in addition to bis(*p*-carboxyphenyl)diphenylsilane ($\mathbf{L^{18}}$), another silane-based carboxylic acid, bis(3,4-dicarboxyphenyl) dimethylsilane ($\mathbf{L^{19}}$) was prepared and both were used to coordinate copper(II) in the presence of 1,10-phenanthroline as co-ligand (Fig. 19).[103]

The molecular structures of the two complexes formed resemble in principle. In both, the copper atom has a similar coordination polyhedra, a slightly distorted square-pyramidal N_4O coordination environment, both carboxylate ligands ($\mathbf{L^{18}}$ and $\mathbf{L^{19}}$) behave as monodentate ligands and participate in the coordination with half of the carboxylic groups, the other remaining protonated. Both complexes show 2D supramolecular architecture assembled via a complex network of O—H⋯O hydrogen bonds and π-π stacking interactions (Fig. 19). The solvent (water) accessible surface value, estimated by the technique available in Olex2,[104] reveals water

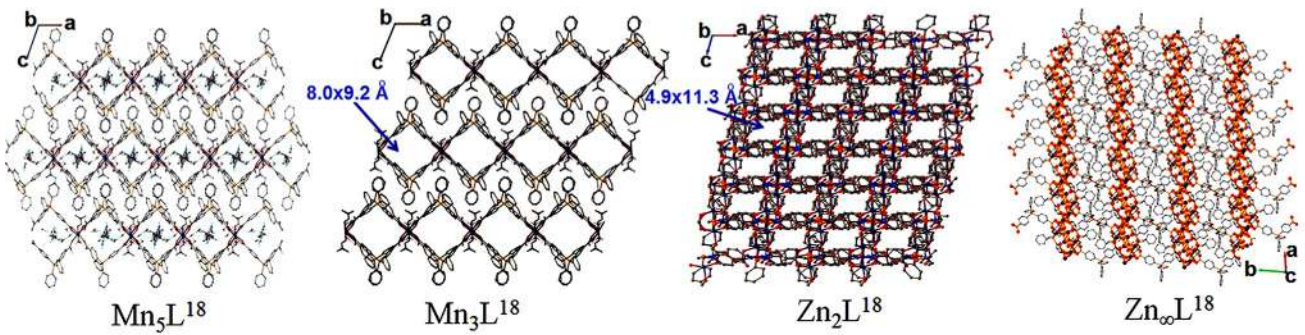

Fig. 17 3D coordination networks build on trinuclear- and pentanuclear manganese(II), dinuclear and infinite Zn(II) clusters and $\mathbf{L^{18}}$ ligand.

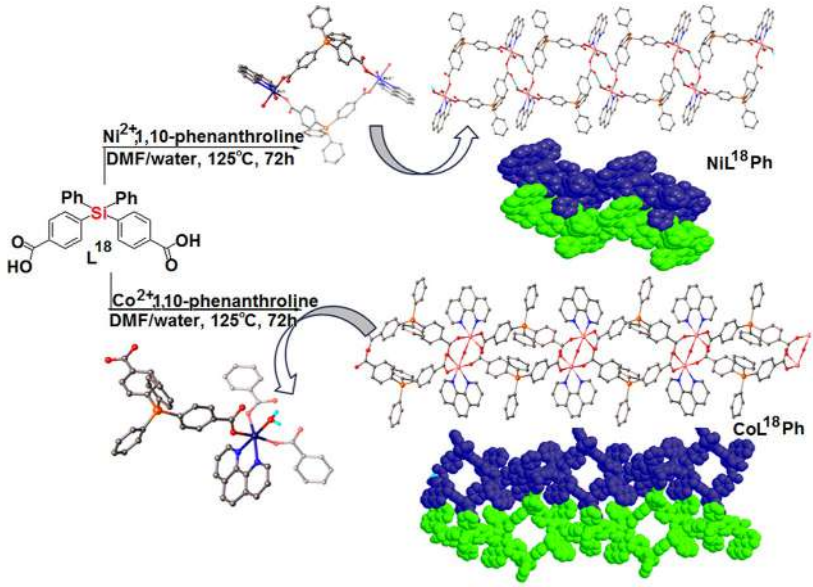

Fig. 18 Crystal structure and self-assembly in the solid state of Ni(II) and Co(II) complexes with **L[18]** and 1,10-phenanthroline co-ligands.

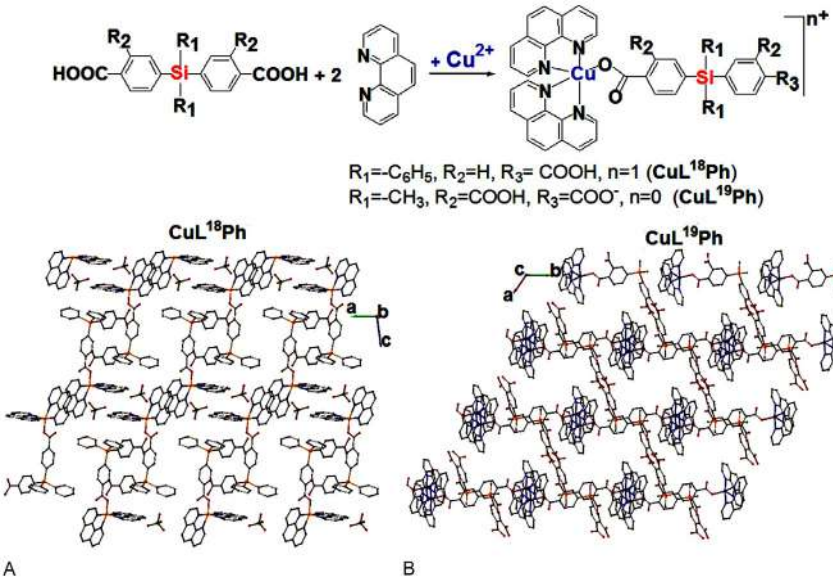

Fig. 19 The formation of copper complexes with phenantroline and di- and tetracarboxylic aromatic acids having silane spacer; view of the crystal structure packing: (A) complex **L[18]PhCu** along *a* axis; (B) complex **L[19]PhCu** along *c* axis.[103]

accessible volume of 493 Å (20.1%) and 834 Å (34.7%), respectively, for the two complexes. These relatively high values are justified by the presence of a large number of donor and proton acceptor groups in these structures. The results of magnetic measurements on these coordination compounds indicate the non-interaction of penta-coordinated copper paramagnetic centers (S = 1/2, g is 2.14 and 2.19).[103]

Another silane-centered polycarboxylic acid, tris(carboxyphenyl)phenyl silane ($\mathbf{L^{20}}$) was prepared and used alone to obtain 3D coordination networks with open channels in the presence of 3d and 4f block elements, under solvothermal conditions (Fig. 20).

X-ray structure of lanthanide MOFs revealed a unit cell containing one pentanuclear sub-unit with two eight-coordinated lanthanide(III) centers: Dy^{3+} or Eu^{3+}. The deprotonated tricarboxylate linker is coordinated in bidentate bridging and chelating modes leading to a separation between Eu(III) ions of 3.486(3) Å within the dinuclear centers. In Zn-MOF, X-ray diffraction studies revealed centro-symmetrical secondary building units formed by four Zn(II) ions bridged by four carboxylate groups and two μ_3-oxo atoms. The coordination environment of two Zinc(II) ions is described as a quite regular trigonal bipyramide, while other two Zinc(II) ions have a strong distorted tetrahedral coordination, as shown in Fig. 20. In the crystal, the carboxylate groups are connected through the benzene ring to the silicon atom which sits at the center of the nearly regular tetrahedron of the organic molecule. 3D extended structures resulted from self-assembly of unit cells in the crystal structure can be seen in Fig. 21.

The total solvent accessible volume calculated by tools available in the Olex2 program was estimated at 49.7% for $\mathbf{Zn_4L^{20}}$ and 68.4% for $\mathbf{Eu_2L^{20}}$, while in the case of $\mathbf{Dy_2L^{20}}$ the channels formed along the crystallographic axes accommodate water molecules. A comparison with the

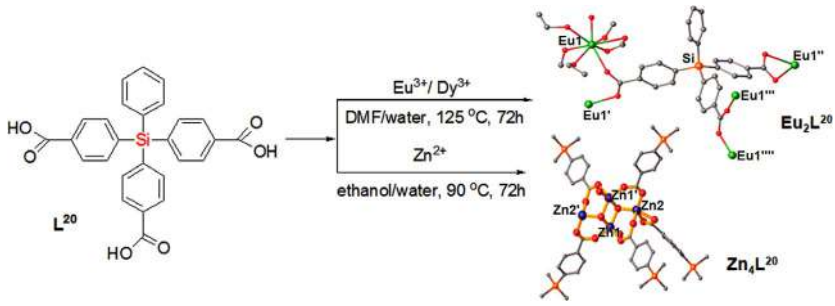

Fig. 20 Solvothermal procedures to obtain zinc(II) and lanthanide(III) MOFs.

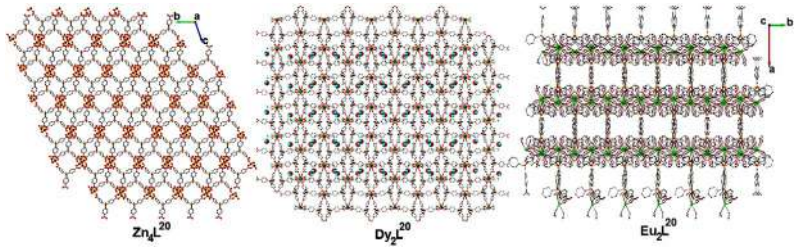

Fig. 21 Structural packing motif in Zn(II) and lanthanide(III) MOFs built with $\mathbf{L^{20}}$.

IRMOF series shows analogous values for IRMOF-5 (55.8%), the free volume being higher than the most open zeolites with 45–50%.[105]

In most cases, the properties of the crystalline structures based on silane-centered polycarboxylic acids with/without co-ligand (porosity, optical or catalytic, etc.) are investigated in the solid state, these being mostly insoluble.

5. Conclusions and future perspectives

Although used relatively rarely, organosiloxane/silane-spaced or silane-tailed ligands are valuable blocks for assembling metal coordination structures, at least from a few points of view. First of all, by their hybrid nature, such motifs constitute a bridge between the general organic part represented by the ligand and the inorganic component represented by the metal in coordination compounds. Then, the extremely high flexibility of the siloxane bond gives the ligand conformational freedom to adopt the most convenient position in the coordination sphere. The large length of the ligand, when it contains the tetramethyldisiloxane spacer, allows the formation of over nanometer-sized cyclic or linear structures. The hydrophobicity of the methylsiloxane moiety and the amphiphilic character of the resulting metal coordination compound allows the self-assembly in solution and in film in micellar structures of interest for catalysis, optics and biology.

Coordination compounds of Schiff base ligands containing siloxane spacer or silane tails were presented. Depending on the nature of the carbonyl component used in the Schiff basis synthesis, mononuclear compounds (mainly with salen-type ligands of salicylic aldehyde derivatives) or polynuclear derivatives with complex architectures were obtained in the case of ligands derived from 2,6-diformyl-4-methylphenol or 3-formylsalicylic acid having several coordination moieties. In addition, in the latter cases, metal salt anions are also often involved in coordination.

In the case of carboxylic ligands with tetramethyldisiloxane spacer, amorphous, hydrophobic structures with low specific surface area were obtained. When a rigid co-ligand was added, 1D or 2D, di- or poly-, homo- or heteronuclear crystalline structures were obtained. In addition to self-assembly in the solid state, these compounds, generally soluble, are capable of micellar self-assembly in solution and in film. The self-assembly pattern in the film, may be responsive to external stimuli such as optical or magnetic, depending on the structure. The use as ligands of silane-spaced polycarboxylic acids has led to 2D or 3D self-assembled structures, generally polynuclear. These crystalline structures, most of them insoluble, are useful as such, in solid state due to their optical, magnetic or porosity properties. However, their investigation is not complete and their properties have not yet been sufficiently validated, this being still in our attention.

Additionally, future prospects are on expanding the range of silicon-derived ligands and metal complexes with different architectures and nuclearities and assessing their suitability for emerging fields: catalysis, magnetics and spintronics, optics, biology and pharmaceutical, electronic, environmental protection, etc. The design and synthesis of the flexible metal-organic frameworks with the gate opening pressure is also intended to be further addressed.

Acknowledgment

This work was supported by a grant of Romanian Ministry of Research and Innovation, CNCS - UEFISCDI, project number PN-III-P4-ID-PCE-2016-0642, within PNCDI III, Contract 114/2017 (SiMOFs).

References

1. ISO/TS 80004–1:2015. https://www.iso.org/obp/ui/#iso:std:iso:ts:80004:-1:ed-2:v1:en.
2. *New Materials: Nanomaterials*. https://www.nanowerk.com/nanotechnology/introduction/introduction_to_nanotechnology_2.php.
3. Moriarty, P. *Reports Prog. Phys.* **2001**, *64*, 297–381.
4. Kharisov, B. I.; Kharissova, O. V.; Valdes, J. J. R.; Perez, V. M. J. *Synth. React. Inorg., Met.-Nano-Met. Chem.* **2010**, *40*(9), 640–650.
5. https://www.azonano.com/article.aspx?ArticleID=1872.
6. Hanifehpour, Y.; Saraei, N.; Asl, S. M.; Joo, S. W. *J. Inorg. Organomet. Polym. Mater.* **2012**, *22*(6), 1271–1278.
7. Rakibuddin, M.; Ananthakrishnan, R. *Appl. Surf. Sci.* 2016, *362*, 265–273.
8. Vallejos, J.; Brito, I.; Cárdenas, A.; Bolte, M.; Conejeros, S.; Alemany, P.; Llanos, J. *Polymer* **2016**, *8*(46), 1–16.
9. Masoomi, M. Y.; Morsali, A. *RSC Adv.* **2013**, *3*(42), 19191–19218.
10. Soltanian Fard, M. J.; Firoozadeh, A. *J. Sci. Islam. Repub. Iran* 2018, *29*(2), 113–119.
11. Zou, H.; Wang, L.; Zeng, C.; Gao, X.; Wang, Q.; Zhong, S. *Front. Mater. Sci.* **2018**, *12*(4), 327–347.

12. He, C.; Liu, D.; Lin, W. *Chem. Rev.* **2015**, *115*(19), 11079–11108.
13. Liu, D.; Huxford, R. C.; Lin, W. *Angew. Chem. Int. Ed.* **2011**, *50*(16), 3696–3700.
14. Olenyuk, B.; Whiteford, J. A.; Fechtenkötter, A.; Stang, P. J. *Nature* **1999**, *398*(6730), 796–799.
15. Kharisov, B. I. *Handbook of Less-Common Nanostructures*; CRC Press, 2012.
16. Okasha, R. M.; AL-Shaikh, N. E.; Aljohani, F. S.; Naqvi, A.; Ismail, E. H. *Int. J. Mol. Sci.* **2019**, 20(*3*), 743.
17. Masoomi, M. Y.; Morsali, A. *Coord. Chem. Rev.* **2012**, *256*(23–24), 2921–2943.
18. Iacob, M.; Racles, C.; Tugui, C.; Stiubianu, G.; Bele, A.; Sacarescu, L.; Timpu, D.; Cazacu, M. *Beilstein J. Nanotechnol.* **2016**, 7(1), 2074–2087.
19. Delmas, L. C.; Horton, P. N.; White, A. J. P.; Coles, S. J.; Lickiss, P. D.; Davies, R. P. *Chem. Commun.* **2017**, *53*(93), 12524–12527.
20. El-Kurd, H. M.; El-Nahhal, I. M.; El-Ashgar, N. M. *Phosphorus Sulfur Silicon Relat. Elem.* **2005**, *180*(7), 1657–1671.
21. Noll, W. *Chemistry and Technology of Silicones*; Academic Press Inc: New York, 1968
22. Voronkov, M. G.; Mileshkevich, V. P.; Yuzhelevskii, Y. A. *The Siloxane Bond: Physical Properties and Chemical Transformations*. Springer: New York, 1978.
23. Airey, W.; Glidewell, C.; Robiette, A. G.; Sheldrick, G. M. *J. Mol. Struct.* 1971, *8*, 413–422. and references herein.
24. Almenningen, A.; Bastiansen, O.; Ewing, V.; Hedberg, K.; Traetterberg, M. *Acta Chem. Scand.* **1963**, *17*, 2455–2460.
25. Owen, M. J. *Chim. Nouv.* 2005, *11*, 1–11. and references herein.
26. Mc. Grath, J. E.; Wany, L. F.; Mecham, J. B.; Ji, Q. *Polym. Prepr.* 1998, *39*(1), 455.
27. Cazacu, M. In: *Advances in Functional Heterochain Polymers*; Cazacu, M. Ed.; Nova Science Publishers: New York, 2008; pp 1–28. 288 pp.
28. Mojsiewicz-Pieńkowska, K.; Jamrógiewicz, M.; Szymkowska, K.; Krenczkowska, D. *Front. Pharmacol.* **2016**, *7*, 1–8.
29. Hillborg, H.; Tomczak, N.; Olàh, A.; Schönherr, H.; Vancso, G. J. *Langmuir* **2004**, *20*(3), 785–794.
30. Huheey, J.; Cottrell, K. *The Strengths of Chemical Bonds*. Butterworths: London, 1958.
31. Frahm, D.; Hoffmann, F.; Froeba, M. *CrystEngComm* **2013**, *15*, 9429–9436.
32. O'Lenick, A. J. In: *Cosmetic Nanotechnology*; Morgan, S. et al., Eds.; ACS Symposium Series. 961; American Chemical Society: Washington, DC, 2007, pp 165–175.
33. Racles, C. *Soft Mater.* **2010**, *8*(3), 263–273.
34. Soroceanu, A.; Cazacu, M.; Racles, C.; Stoica, I.; Sacarescu, L.; Varganici, C. D. *Soft Mater.* **2015**, *13*(2), 93–105.
35. Racles, C.; Cazacu, M.; Zaltariov, M.; Iacob, M.; Butnaru, M. *Phosphorus Sulfur Silicon Relat. Elem.* **2019**, *194*(10), 972–977.
36. Racles, C.; Cozan, V. *Soft Mater.* **2012**, *10*(4), 413–425.
37. Racles, C.; Alexandru, M.; Nistor, A.; Cazacu, M. *Rev. Roum. Chim.* **2011**, *56*(10 − 11), 941–946.
38. Racles, C.; Hamaide, T. *Macromol. Chem. Phys.* **2005**, *206*(17), 1757–1768.
39. Racles, C.; Hamaide, T.; Ioanid, A. *Appl. Organomet. Chem.* **2006**, *20*(4), 235–245.
40. Hauser, E. A. *Clays Clay Miner.* **1955**, *4*(1), 45–53.
41. Hill, R. M. *Curr. Opin. Colloid Interface Sci.* **1998**, *3*, 247–254.
42. Iwakiri, N.; Schlachter, I.; Feldmann-Krane, G. *Novel Surfactants*. Marcel Dekker, INC: New York; Basel, 1998
43. Hill, R. M. *Silicone Surfactants*. New York: Marcel Dekker, INC, 1999.
44. Hill, R. M. *Curr. Opin. Colloid Interface Sci.* **2002**, 7(5–6), 255–261.
45. Nishikawa, T.; Kaneko, Y.; Kadokawa, J. I. *Colloid Polym. Sci.* **2009**, *287*(5), 577–582.
46. Khalaji, A. D. In *Current Trends in X-Ray Crystallography*; Chandrasekaran, A. Ed.; InTech, 2011; pp 161–190. and references herein.

47. Pascu, M.; Clarkson, G. J.; Kariuki, B. M.; Hannon, M. J. *J. Chem. Soc. Dalton Trans.* 2006, *22*, 2635–2642.
48. Childs, L. J.; Pascu, M.; Clarke, A. J.; Alcock, N. W.; Hannon, M. J. *Chem. A Eur. J.* **2004**, *10*(17), 4291–4300.
49. Kilinçarslan, R.; Karabiyik, H.; Ulusoy, M.; Aygün, M.; Çetinkaya, B.; Büyükgüngör, O. *J. Coord. Chem.* **2006**, *59*(14), 1649–1656.
50. Mayer, C. R.; Cucchiaro, G.; Jullien, J.; Dumur, F.; Marrot, J.; Dumas, E.; Sécheresse, F. *Eur. J. Inorg. Chem.* 2008, *23*, 3614–3623.
51. Yin, W. *Faguang Xuebao* **2005**, *26*(3), 349–353.
52. Salavati-Niasari, M.; Sobhani, A. *J. Mol. Catal. A Chem.* **2008**, *285*(1–2), 58–67.
53. Vafazadeh, R.; Kashfi, M. *Bull. Korean Chem. Soc.* 2007, 28(7), 1227–1230. and references herein.
54. Nathan, L. C.; Koehne, J. E.; Gilmore, J. M.; Hannibal, K. A.; Dewhirst, W. E.; Mai, T. D. *Polyhedron* **2003**, *22*(6), 887–894.
55. Riley, P. E.; Pecoraro, V. L.; Raymond, K. N.; Carrano, C. J.; Bonadies, J. A. *Inorg. Chem.* **1986**, *25*(2), 154–160.
56. Weigold, H.; West, B. O. *J. Chem. Soc.* 1967, *1310*, 1310–1311.
57. Silva, H.; Barra, C. V.; Rocha, F. V.; Frézard, F.; Lopes, M. T. P.; Fontes, A. P. S. *J. Braz. Chem. Soc.* **2010**, *21*(10), 1961–1967.
58. Silva, H.; Valério Barra, C.; França da Costa, C.; de Almeida, M. V.; César, E. T.; Silveira, J. N.; Garnier-Suillerot, A.; Silva de Paula, F. C.; Pereira-Maia, E. C.; Fontes, A. P. S. *J. Inorg. Biochem.* **2008**, *102*(4), 767–772.
59. Soroceanu, A.; Cazacu, M.; Shova, S.; Turta, C.; Kožíšek, J.; Gall, M.; Breza, M.; Rapta, P.; Mac Leod, T. C. O.; Pombeiro, A. J. L.; Telser, J.; Dobrov, A. A.; Arion, V. B. *Eur. J. Inorg. Chem.* 2013, *9*, 1458–1474.
60. Soroceanu, A.; Cazacu, M.; Nistor, A.; Shova, S. *Rev. Roum. Chim.* **2013**, *58*, 209–216.
61. Zaltariov, M. F.; Cazacu, M.; Vornicu, N.; Shova, S.; Racles, C.; Balan, M.; Turta, C. *Supramol. Chem.* **2013**, *25*(8), 490–502.
62. Cazacu, M.; Shova, S.; Soroceanu, A.; Machata, P.; Bucinsky, L.; Breza, M.; Rapta, P.; Telser, J.; Krzystek, J.; Arion, V. B. *Inorg. Chem.* **2015**, *54*(12), 5691–5706.
63. Vlad, A.; Zaltariov, M. F.; Shova, S.; Cazacu, M.; Avadanei, M.; Soroceanu, A.; Samoila, P. *Polyhedron* **2016**, *115*, 76–85.
64. Vlad, A.; Avadanei, M.; Shova, S.; Cazacu, M.; Zaltariov, M. F. *Polyhedron* **2018**, *146*, 129–135.
65. Vlad, A.; Turta, C.; Cazacu, M.; Rusu, E.; Shova, S. *Eur. J. Inorg. Chem.* **2012**, *31*, 5078–5084.
66. Zaltariov, M.-F.; Alexandru, M.; Cazacu, M.; Shova, S.; Novitchi, G.; Train, C.; Dobrov, A.; Kirillova, M. V.; Alegria, E. C. B. A.; Pombeiro, A. J. L.; Arion, V. B. *Eur. J. Inorg. Chem.* **2014**, *2014*(29), 4946–4956.
67. Alexandru, M.; Cazacu, M.; Arvinte, A.; Shova, S.; Turta, C.; Simionescu, B. C.; Dobrov, A.; Alegria, E. C. B. A.; Martins, L. M. D. R. S.; Pombeiro, A. J. L.; Arion, V. B. *Eur. J. Inorg. Chem.* 2014, *1*, 120–131.
68. Yang, L.; Powell, D. R.; Houser, R. P. *Dalton Trans.* **2007**, *9*, 955–964.
69. Bonadies, J. A.; Kirk, M. L.; Lah, M. S.; Kessissoglou, D. P.; Hatfield, W. E.; Pecoraro, V. L. *Inorg. Chem.* **1989**, *28*(11), 2037–2044.
70. Zeini Jahromi, E.; Gailer, J. *Dalton Trans.* **2010**, *39*(2), 329–336.
71. Martinez, D.; Motevalli, M.; Watkinson, M. *Dalton Trans.* **2010**, *39*, 446–455.
72. Shova, S.; Vlad, A.; Cazacu, M.; Krzystek, J.; Ozarowski, A.; Malček, M.; Bucinsky, L.; Rapta, P.; Cano, J.; Telser, J.; Arion, V. B. *Dalton Trans.* **2019**, *48*(18), 5909–5922.

73. Shova, S.; Vlad, A.; Cazacu, M.; Krzystek, J.; Bucinsky, L.; Breza, M.; Darvasiova, D.; Rapta, P.; Cano, J.; Arion, V. B. *Dalton Trans.* **2017**, *46*(35), 11817–11829.
74. Zaltariov, M. F.; Cazacu, M.; Vlad, A.; Sacarescu, L.; Shova, S. *High Perform. Polym.* **2015**, *27*(5), 607–615.
75. Zaltariov, M. F.; Vieru, V.; Zalibera, M.; Cazacu, M.; Martins, N. M. R.; Martins, L. M. D. R. S.; Rapta, P.; Novitchi, G.; Shova, S.; Pombeiro, A. J. L.; Arion, V. B. *Eur. J. Inorg. Chem.* **2017**, *2017*(37), 4324–4332.
76. Shova, S.; Cazacu, M.; Novitchi, G.; Zoppellaro, G.; Train, C.; Arion, V. B. *Dalton Trans.* **2017**, *46*(6), 1789–1793.
77. Li, H.; Eddaoudi, M.; OKeeffe, M.; Yaghi, O. M. *Nature* **1999**, *402*, 276–279.
78. Cazacu, M.; Turcan-Trofin, G. O.; Vlad, A.; Bele, A.; Shova, S.; Nicolescu, A.; Bargan, A. *J. Appl. Polym. Sci.* **2019**, *136*(9), 47144.
79. Alvarez, E.; Guillou, N.; Martineau, C.; Bueken, B.; Vandevoorde, B.; Leguillouzer, C.; Fabry, P.; Nouar, F.; Taulelle, F.; Devos, D.; Chang, J. S.; Cho, K. H.; Ramsahye, N.; Devic, T.; Daturi, M.; Maurin, G.; Serre, C. *Angew. Chem. Int. Ed.* **2015**, *54*(12), 3664–3668.
80. Turcan-Trofin, G.-O.; Zaltariov, M.-F.; Iacob, M.; Tiron, V.; Branza, F.; Racles, C.; Cazacu, M. *Colloid. Surf. A Physicochem. Eng. Asp.* **2019**, *580*, 123756.
81. Turcan-Trofin, G. O.; Asandulesa, M.; Balan-Porcarasu, M.; Varganici, C. D.; Tiron, V.; Racles, C.; Cazacu, M. L. *J. Mol. Liq.* **2019**, *282*, 187–196.
82. Griffin, W. C. C. *J. Soc. Cosmet. Chem.* **1954**, *5*(4), 249–256.
83. Davies, J. T. In Proceedings of 2nd International Congress Surface Activity; 1957; pp 426–438.
84. Owen, T.; Butler, A. *Coord. Chem. Rev.* **2011**, *255*(7–8), 678–687.
85. Marín-García, M.; Benseny-Cases, N.; Camacho, M.; Perrie, Y.; Suades, J.; Barnadas-Rodríguez, R. *Dalton Trans.* **2018**, *47*(40), 14293–14303.
86. Racles, C.; Silion, M.; Iacob, M. *Colloid. Surf. A Physicochem. Eng. Asp.* **2014**, *462*, 9–17.
87. Zaltariov, M. F.; Cazacu, M.; Sacarescu, L.; Vlad, A.; Novitchi, G.; Train, C.; Shova, S.; Arion, V. B. *Macromolecules* **2016**, *49*(17), 6163–6172.
88. Vlad, A.; Cazacu, M.; Zaltariov, M. F.; Bargan, A.; Shova, S.; Turta, C. *J. Mol. Struct.* **2014**, *1060*(1), 94–101.
89. Vlad, A.; Cazacu, M.; Zaltariov, M. F.; Shova, S.; Turta, C.; Airinei, A. *Polymer* **2013**, *54*(1), 43–53.
90. Vlad, A.; Zaltariov, M. F.; Shova, S.; Novitchi, G.; Varganici, C. D.; Train, C.; Cazacu, M. *CrystEngComm* **2013**, *15*(26), 5368–5375.
91. Racles, C.; Shova, S.; Cazacu, M.; Timpu, D. *Polymer* **2013**, *54*(22), 6096–6104.
92. Cazacu, M.; Zaltariov, M. F. unpublished results.
93. Racles, C.; Zaltariov, M.-F.; Iacob, M.; Silion, M.; Avadanei, M.; Bargan, A. *Appl. Catal. B Environ.* **2017**, *205*, 78–92.
94. Grubbs, R. B. *J. Polym. Sci. A Polym. Chem.* **2005**, *43*(19), 4323–4336.
95. Wang, J.-J.; Cao, P.-X.; Gao, L.-J.; Fu, F.; Zhang, M.-L.; Ren, Y.-X.; Hou, X.-Y. *Chin. J. Struct. Chem.* 2011, *12*, 1787–1790.
96. Luo, Y.; Bernot, K.; Calvez, G.; Freslon, S.; Daiguebonne, C.; Guillou, O.; Kerbellec, N.; Roisnel, T. *CrystEngComm* **2013**, *15*(10), 1882–1896.
97. Lambert, J. B.; Liu, Z.; Liu, C. *Organometallics* **2008**, *27*, 1464–1469.
98. Liu, Z.; Stern, C. L.; Lambert, J. B. *Organometallics* **2009**, *28*, 84–93.
99. Davies, R. P.; Lickiss, P. D.; Robertson, K.; White, A. J. P. *CrystEngComm* **2012**, *14*, 758–760.
100. Wenzel, S. E.; Fischer, M.; Hoffmann, F.; Froeba, M. *Inorg. Chem.* **2009**, *48*, 6559–6565.

101. Vlad, A.; Zaltariov, M.-F.; Shova, S.; Novitchi, G.; Train, C.; Cazacu, M. *RSC Adv.* **2016**, *6*(44), 37412–37423.
102. Lu, W.; Wei, Z.; Gu, Z.-Y.; Liu, T.-F.; Park, J.; Park, J.; Tian, J.; Zhang, M.; Zhang, Q.; Gentle, T.; Bosch, M.; Zhou, H.-C. *Chem. Soc. Rev.* **2014**, *43*, 5561–5593.
103. Cazacu, M.; Vlad, A.; Zaltariov, M. F.; Shova, S.; Novitchi, G.; Train, C. *J. Organomet. Chem.* **2014**, *774*, 70–78.
104. Dolomanov, O. V.; Bourhis, L. J.; Gildea, R. J.; Howard, J. A. K.; Puschmann, H. *J. Appl. Crystallogr.* **2009**, *42*(2), 339–341.
105. The Chemistry of Nanostructured Materials, Ed. Peidong Yang, University of California, Berkeley, USA, World Scientific, 2003, pp. 261–290.

CHAPTER SIX

Nanoscale coordination compounds

Younes Hanifehpour[a,*], Babak Mirtamizdoust[b], Sang Woo Joo[c,*]
[a]Sayyed Jamaleddin Asadabadi University, Asadabad, Iran
[b]Department of Chemistry, Faculty of Science, University of Qom, Qom, Iran
[c]School of Mechanical Engineering, WCU Nano Research Center, Yeungnam University, Gyeongsan, South Korea
*Corresponding authors: e-mail address: younes.hanifehpour@gmail.com; swjoo@yu.ac.kr

Contents

Abstract

With the advent of new analytical technologies and a firm grasp on the fundamentals of chemical reactivity, the area of coordination-driven self-assembly has grown significantly over the last number of years. This field can be roughly divided into two subcategories: the solution and solid state based area of molecular architecture and the more materials-oriented discipline of coordination polymers and network solids. The former deals exclusively with single molecules that form in solution before crystallizing out, while the latter is focused on infinite systems in the solid state. Both hope to present chemists with large and well-defined, novel compounds that may have several potential applications and can be synthesized with relative ease and predictability. One of the most interesting and challenging fields is coordination polymers. Helping to link the black and white worlds of organic and inorganic chemistry, coordination polymers can simply be described as the bridging of coordinated metal centers with organic ligands resulting in supramolecular structures. In this section, we present an overview of methods for the preparation of coordination compounds and coordination polymers in two forms of bulk and nano. Here we summarize the effects of some factors such as structure and morphology of the products.

Advances in Inorganic Chemistry, Volume 76
ISSN 0898-8838
https://doi.org/10.1016/bs.adioch.2020.03.004

1. Introduction

The crystal engineering of inorganic–organic hybrid materials has become an increasingly popular field of research over the past few decades owing to the potential for the synthesis of technologically important compounds with tailored topologies. Metal-organic compounds, which consist of both an organic and inorganic components, have shown promise in a vast array of applications such as catalysis, gas storage, ion exchange, magnetic materials, optics, and separations.[1–6]

Among them, the design and synthesis of extended network materials has been an area of intense research over the past decade. Specifically, the porous nature of many of these materials makes them attractive for numerous applications.[7,8] Coordination compounds and coordination polymers can be designed through a node and linker. This method uses metal ions as nodes and organic molecules as linkers. The metal ion, with a preferred coordination number and geometry, in combination with divergent linker molecules, creates an extended network in one, two, or three dimensions. The interactions of the metal ion and the linker molecule vary widely and have included ionic, covalent, and coordinate interactions, as well as hydrogen bonding and π–π interactions. Often, the strengths of these interactions directly influence the overall stability of the resulting framework. Infinite coordination polymers have been the subject of much research for more than three decades. Having been studied for so long, a number of interesting applications have been discovered or postulated for such species. These include: molecular magnets, electrical conductivity and superconductivity, nonlinear optics, and ferroelectric materials.

In a direct way, the chemistry established with the coordination polymers has helped develop the coordination methodology that is prevalent in the larger, infinite supramolecular systems of today. These systems, which include such architectures, often attempt to mimic naturally occurring zeolites and provide materials with predictable pore sizes and functionality. The hopes are to create predesigned chemical environments for such phenomena as host-guest chemistry, anion-exchange, and catalysis.[9–12]

Along with the development of functional hybrid materials in recent years, synthesis, characterization and investigation of properties as well as applications of nanostructure materials, have been the subject of extensive research. This trend has found an even greater pace in the past few years.[13–15] These materials find very diverse potential applications including catalysis, magnetism, optics, sensors, biosensing, medical diagnostics, energy storage

and batteries, data storage and others.[16] There are many methods for the preparation of nanomaterials including hydrothermal or solvothermal methods, microwave-solvothermal synthesis, microwave synthesis, magnetic-field-assisted hydrothermal, sol–gel process, electrochemically induced sol–gel, microemulsion and reverse micelle/microemulsion, homogeneous precipitation method, cluster growth method, chemical vapor deposition, vapor–liquid–solid process, soft chemical method, electrophoretic deposition, electrochemical fabrication, chemical reduction method, electrolysis of metal salts, rapid expansion of supercritical solvents, photoreduction of metal ions, microwave plasma synthesis, sonochemical method and mechano-chemical processes.[16–40]

In this section, we reviewed some new coordination compounds (CC), coordination polymers (CP), nano coordination compounds (NCC), and nano coordination polymers (NCP).

2. General comment

2.1 Preparation of metal-organic coordination polymers

Metal-organic coordination polymers and porous metal-organic systems with regular-pore structure have attracted considerable attention in recent years for applications in gas storage, heterogeneous catalysis, selective guest adsorption, and sensing technologies. Several processes with the same starting reagents sometimes lead to different isomeric or polymorphic products.

Saturation methods allow crystal formation from a mixture of the different reagents. Molecular recognition permits the construction of products following pre-determined rules. This technique can be conducted using facile conditions:

- Crystals grow in saturated solutions, and ideal concentrations can be achieved by *slow evaporation* of the mother liquor
- Solubility increases with temperature, and crystals can appear during the *cooling* step, for which the speed of cooling and final temperature have to be controlled

Diffusion methods are preferred for obtaining single crystals that are suitable for X-ray diffraction analysis rather than non- or poly-crystalline products, especially if the products are poorly soluble. This method is based on gradually enhancing the contact of different species, which can be achieved by the following:

- Solvent *liquid diffusion,* where the components of the reaction are dissolved in appropriate immiscible solvents and crystal growth occurs at the interface

– *Slow diffusion of reactants,* which is similar to the previous method except that the reactants are each dissolved separately in one of the two solutions. Separation of the solutions can solve problems with the formation of layers or physical barriers. Instead of liquid solvents, gels are also used as diffusion and crystallization media in some cases, especially to slow down diffusion and to avoid precipitation of the bulk material.

Hydrothermal and solvothermal methods were originally used for the synthesis of zeolites but have been adopted for the formation of metal-organic coordination polymers. They exploit the self-assembly of products from soluble precursors. The temperature range is usually 120–260 °C inside a closed space (an autoclave) under autogenous pressure. Under these conditions, the reduced viscosity of water enhances the diffusion process and thus the extraction of solids and crystal growth from solution. The difference in solubility between organic and inorganic components in a solvent is often a barrier in the formation of single crystals. However, hydrothermal experiments can be a good approach since the solubility of starting materials can be increased. This crystallization technique is a non-equilibrium synthesis and may lead to metastable products. This can mainly be influenced by the cooling speed at the end of the reaction.

Microwave and ultrasonic methods have not been used as much for coordination polymer formation. They are also based on the improvement of solubility in order to improve the reaction or crystallization of involved species and products. These methods remain to be exploited more efficiently.

For lead(II) metal-organic coordination compounds, most of the syntheses are simple and straightforward in concept, but frequently present difficulties in execution. This results from the limited solubility of the desired species that are usefully crystalline. This has been overcome in many cases by making use of the temperature dependence of the solubility, which is generally common for lead(II) salts.

For less soluble species, suitable crystalline products have been accessed by methods where the reactants are placed in an appropriate solvent in separate arms of a sealed branched tube. The lower end of the tube contains the lead salt reactant, which is typically very insoluble. It is held in an oil bath at a relatively high temperature (around 60 °C), while the branch is at room temperature. Very frequently, crystalline material that is useful for X-ray studies is deposited in the branch, often only after an extended period. In most systems, the ligand in the branch held at room temperature is very readily soluble in the solvent, so the success of the procedure could also possibly depend on the slow rate of liquid phase diffusion.

2.1.1 Sonochemical methods in nanomaterial synthesis

Compared with traditional techniques, sonochemical methods are more convenient and easily controlled. Many nano-compound syntheses have been carried out using ultrasound, which result in high yields within a short reaction time. Ultrasound consists of high-frequency sound waves and are considered either destructive (20 kHz to 2 MHz) or nondestructive diagnostic ultrasound (5–10 MHz). Sonochemical applications require the high-energy waves of destructive ultrasound. When a liquid is irradiated with ultrasound, the sound waves locally compress and expand the liquid. The liquid follows the movements, but the distance between the molecules can become so large that cavitation bubbles are created, which increase in size over several compression and rarefaction cycles. When a bubble grows beyond a certain size, it becomes unstable and collapses. During the collapse, the liquid surrounding the bubble is strongly accelerated, and collisions between the molecules create hot spots with very high temperatures and pressures.

2.2 Lead(II) nano coordination compounds

2.2.1 Nano-peanuts lead(II) coordination polymer $[Pb(qcnh)(NO_3)_2]_n$

The reaction between 2-quinolincarbaldehyde nicotinohydrazide "qcnh" Schiff-base ligand and a solution of lead(II) nitrate led to the formation of the new lead(II) coordination compound $[Pb(qcnh)(NO_3)_2]_n$ (**1**). Nano structure of compound **1** was obtained by ultrasonic irradiation in a methanolic solution and single crystalline material was obtained using a heat gradient applied to a solution of the reagents. X-ray structure of complex **1** revealed the composition and stereochemistry of a fundamental building block, having a formula of $\{Pb(qcnh)(NO_3)_2\}$ (Fig. 1). These blocks are connected via non-covalent contacts originating from the qcnh and nitrato ligands into infinite 1D polymeric chain (Fig. 2). A view of the molecular structure of **1** together with atom numbering scheme is shown in Fig. 1.

The morphology of compound **1** prepared by the sonochemical method (Fig. 3) is very interesting. It is composed of peanuts-shape nanoparticles with diameter of about 50 nm.

2.2.2 Nano-flower lead(II) one-dimensional (1-D) coordination compound $\{[Pb(phen)(\mu\text{-}CH_3COO)][PF_6]\}_n$ (2) [phen = 1,10-phenanthroline]

The reaction between the "phen" ligand with a mixture of $Pb(CH_3COO)_2{\cdot}3H_2O$ and hexafluorophosphate led to the formation of

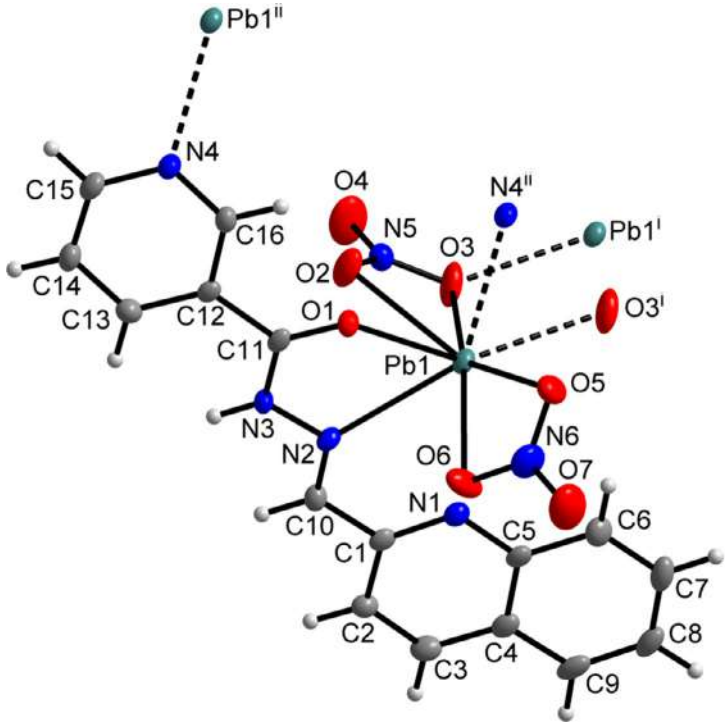

Fig. 1 A view of the molecular structure of $[Pb(Hqcn)(NO_3)_2]_n$ **1** with the atom numbering scheme, showing the coordination environment of the Pb(II) atom. Dashed lines indicate the coordination to the neighboring molecules, symmetry codes: (i) −x, −y, −z; (ii) −x, 1 − y, −z. The Pb(1)—N(1) bond (2.939(2)Å) is not shown for the clarity.[41]

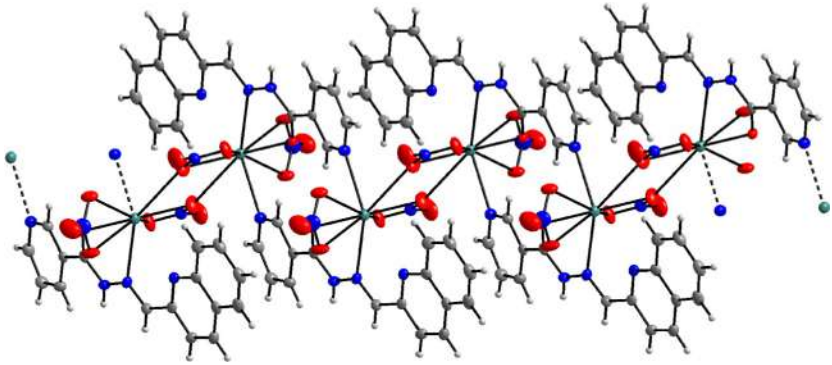

Fig. 2 A part of the crystal structure of **1**, showing the formation of 1D polymeric chains.

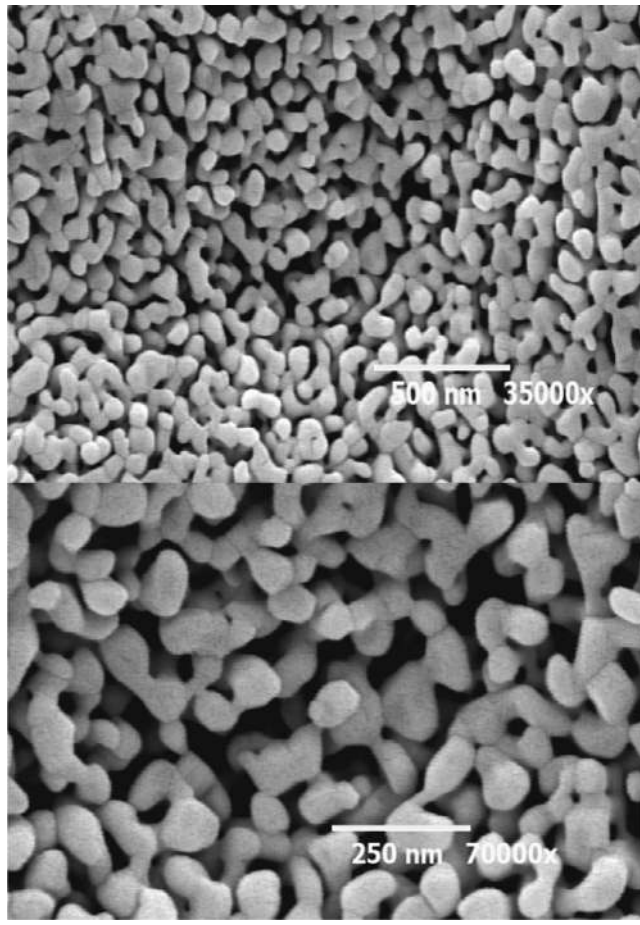

Fig. 3 SEM photographs of $[Pb(Hqcn)(NO_3)_2]_n$ (**1**) nano-groundnuts at different magnifications.[41]

the new lead(II) coordination compound $\{[Pb(phen)(\mu\text{-}CH_3COO)][PF_6]\}_n$ (**2**). Nano-flowers of compound **1** were obtained by ultrasonic irradiation in a methanolic solution, and single crystalline material was obtained using a heat gradient applied to a solution of the reagents.[42]

The X-ray structure of complex **2** revealed the composition and stereochemistry of a fundamental building block with a formula of $\{[Pb(phen)(\mu\text{-}CH_3COO)][PF_6]\}$. A view of the asymmetric molecular structure of **2**, together with a selected atom numbering scheme, is shown in Fig. 4. The lead (II) atoms are bridged by two acetate ions with a Pb ⋯ Pb distance of 4.220 Å. The complex takes the form of a one-dimensional polymer (Fig. 5).

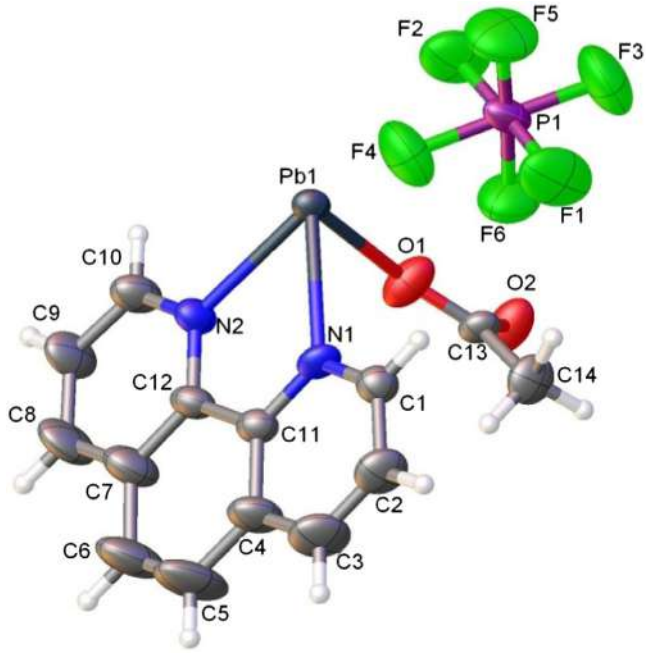

Fig. 4 Asymmetric molecular structure of $\{[Pb(phen)(\mu\text{-}CH_3COO)][PF_6]\}_n$ (**2**).

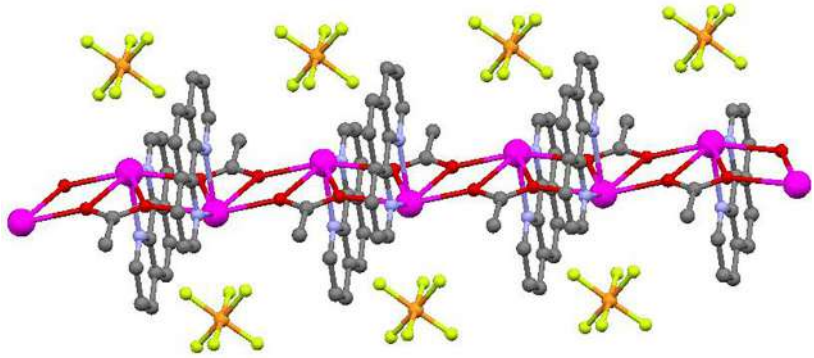

Fig. 5 Fragment of the coordination polymer showing the 1-D polymer **2**.

Fig. 6 shows the nano-flower that was observed by SEM. The morphology of compound **2,** prepared by the sonochemical method, is very interesting. It is composed of cross-sheets with thickness of about 40–50 nm.

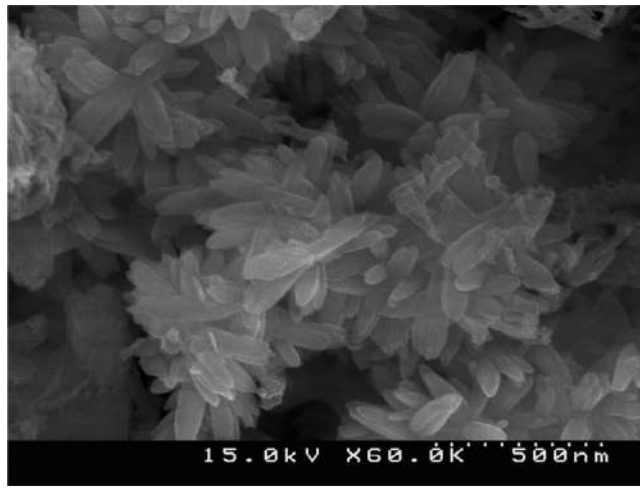

Fig. 6 SEM photographs of {[Pb(phen)(μ-CH_3COO)][PF_6]}$_n$ (**2**) nano-flowers.

2.2.3 Nano-cauliflower-shaped lead(II) metal-organic coordination polymer, [Pb(μ-2-pinh)N_3(H_2O)]$_n$ (3)

The reaction between the 2-pyridinecarbaldehyde isonicotinoylhydrazone (H-2-pinh) ligand with a solution of lead(II) acetate and sodium azide led to the formation of the new lead(II) coordination polymer, [Pb(μ-2-pinh)N_3(H_2O)]$_n$ (**3**). Nano-cauliflower shapes of compound **3** were obtained by applying ultrasound to a methanolic solution, and single crystalline material samples were obtained by applying a heat gradient to a solution of the reagents.

Single crystal X-ray structure determination reveals that **3** has the stoichiometry of [Pb(μ-2-pinh)N_3(H_2O)]$_n$. Fig. 7 shows the asymmetric unit and atom numbering scheme.

The data indicate that the lead atom is chelated by one oxygen and two nitrogen atoms of the 2-pinh ligand. It is also coordinated by the pyridyl-N4 atom of a neighboring molecule to generate a zigzag chain along the c-axis. Thus, the 2-pinh ligand is tetradentate. The lead atom is also coordinated by a water molecule and the N5 atom of a terminally bound azide. The water molecule and donor atoms from the 2-pinh ligands occupy an approximate plane with the azide N5 atom lying to one side. To the other side is a weakly connected N3 atom that is otherwise not involved in coordination such that the zigzag chains are linked into double chains (Fig. 8).[43]

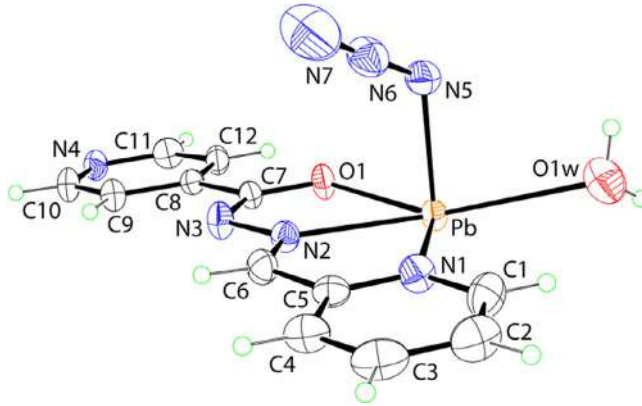

Fig. 7 Molecular structure of the asymmetric unit of $[Pb(\mu\text{-}2\text{-}pinh)N_3(H_2O)]_n$ with atom labeling.[43]

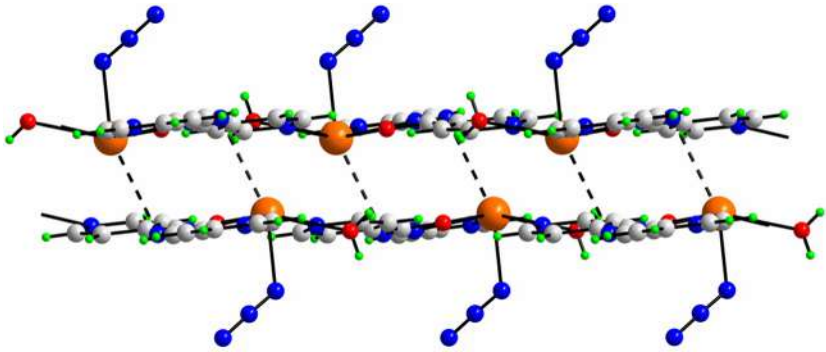

Fig. 8 Fragment of the coordination polymer showing the 1D zigzag polymeric chain. Association between chains related by twofold symmetry via Pb···N3 interactions.[43]

Compound **3** prepared by the sonochemical method shows interesting morphology comprising sheet-like structures with an approximate thickness of 30 nm (Fig. 9).

2.2.4 *Nanorods of a lead(II) 3D metal-organic coordination system $\{[Pb(\mu 2\text{-}NO_3)_4]\cdot(hmta)_2\cdot H_2O\}_n$ (4) (hmta = hexamethylenetetramine)*

The reaction between the hmta ligand with $Pb(NO_3)_2\cdot 3H_2O$ led to the formation of the new lead(II) 3D metal-organic coordination system $\{[Pb(\mu 2\text{-}NO_3)_4]\cdot(hmta)_2\cdot H_2O\}_n$ (**4**). Nanostructures of **4** were obtained unity

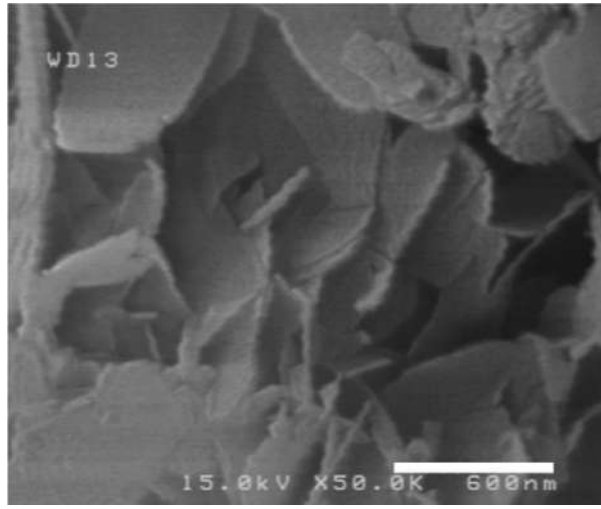

Fig. 9 SEM image of $[Pb(\mu\text{-}2\text{-pinh})N_3(H_2O)]_n$ (**3**) nano-cauliflower.[43]

ultrasound in a methanolic solution, and single crystal material was obtained using a heat gradient applied to a solution of the reagents.[44]

The X-ray structure of **4** revealed the composition and stereochemistry of a fundamental building block with a formula of $\{[Pb(\mu 2\text{-}NO_3)_4]\cdot(hmta)_2\cdot H_2O\}_n$ (Fig. 10). This building block crystallizes in an orthorhombic system with *Pmmn* space group and takes the form of a three-dimensional coordination polymer (Fig. 11).[44]

Fig. 12 shows the nan-orod structures that were observed by SEM. The formation mechanism of these structures needs to be investigated further. However, it may be a result of the supramolecular crystal structure of this compound; i.e., the packing of the structure on a molecular level might have influenced the morphology of the nanostructure of the compound.

2.2.5 Nano Pb(II) 1D metal-organic zigzag chain $[Pb(p\text{-}2\text{-einh})NO_2]_n$ (5) (p-2-einh = (1-(pyridin-2-yl)ethylidene)isonicotinohydrazide)

The reaction between the "Hp-2-einh" ligand with $Pb(CH_3COO)_2\cdot$and $NaNO_2$ led to the formation of the new lead(II) metal-organic polymer $[Pb(p\text{-}2\text{-einh})NO_2]_n$ (**5**). Nanostructures of compound **5** were obtained by ultrasonication in a methanolic solution, and the single crystalline sample was obtained using a heat gradient applied to a solution of the reagents.

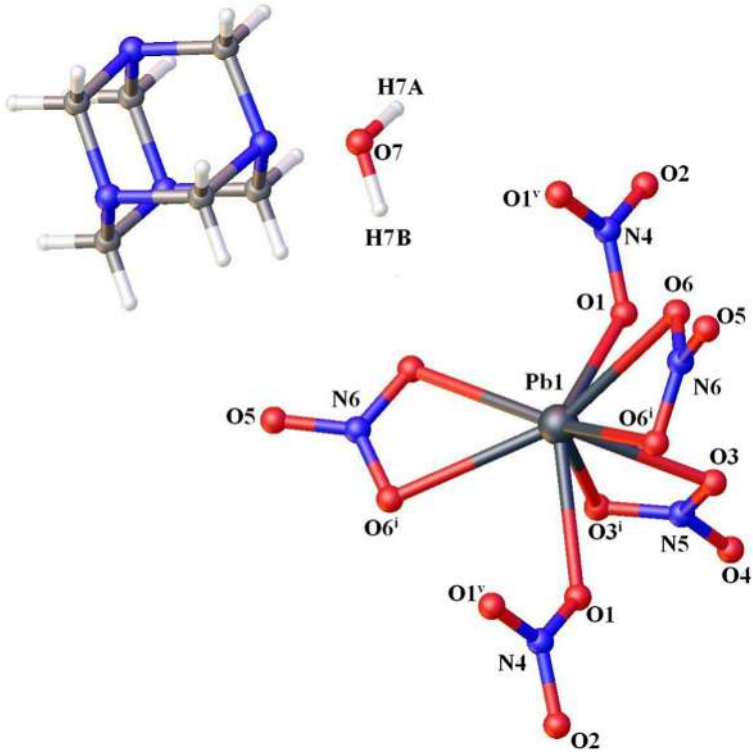

Fig. 10 Molecular Structure of $\{[Pb(\mu 2\text{-}NO_3)_4]\cdot(hmta)_2\cdot H_2O\}_n$ (**4**).[44]

Based on single crystal X-ray crystallography, the structure of [Pb(p-2-einh)NO_2]$_n$ (Fig. 13) crystallizes in the monoclinic system with space group $P2_1/n$, taking the form of a one-dimensional zigzag metal-organic polymer in the solid state (Fig. 14). A view of the asymmetrical unit structure of **5**, together with a selected atom numbering scheme, is shown in Fig. 13.[45]

Fig. 15 shows the nanostructures observed by scanning electron microscopy. Interestingly, the morphology of compound **5** prepared by the sonochemical method is composed of hexagonal nano-plates with thickness of 25–40 nm.[45]

The TEM image and SAED pattern of compound **5** confirm the hexagonal plate morphology and its crystallinity (Fig. 16).[45]

Further investigation is required to explain the mechanism of formation of these structures. However, the supramolecular structure of the compound may influence it. The morphology of the nanostructured compound can be affected by the packing of the structure on a molecular level (Fig. 17).[45]

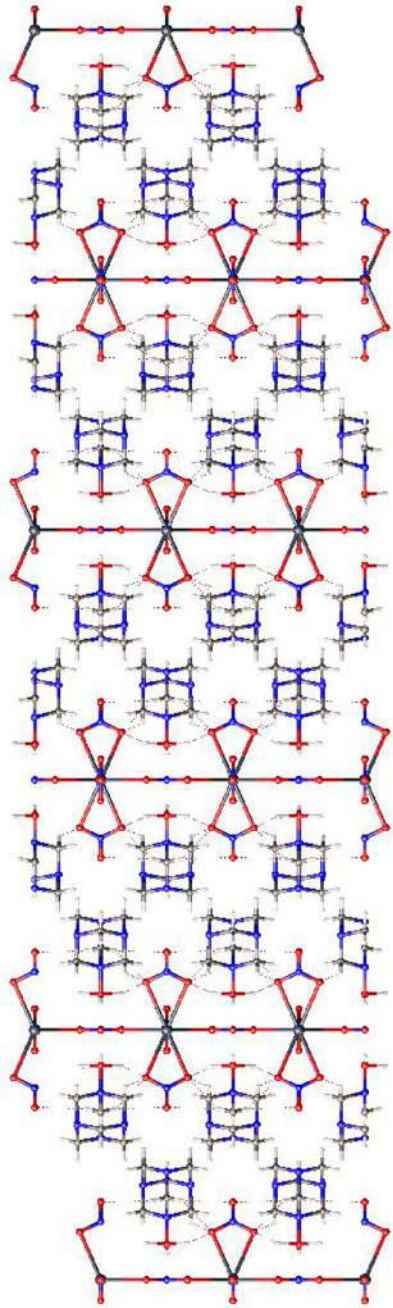

Fig. 11 Fragment of the coordination polymer showing the 3D arrangement in (**4**).[44]

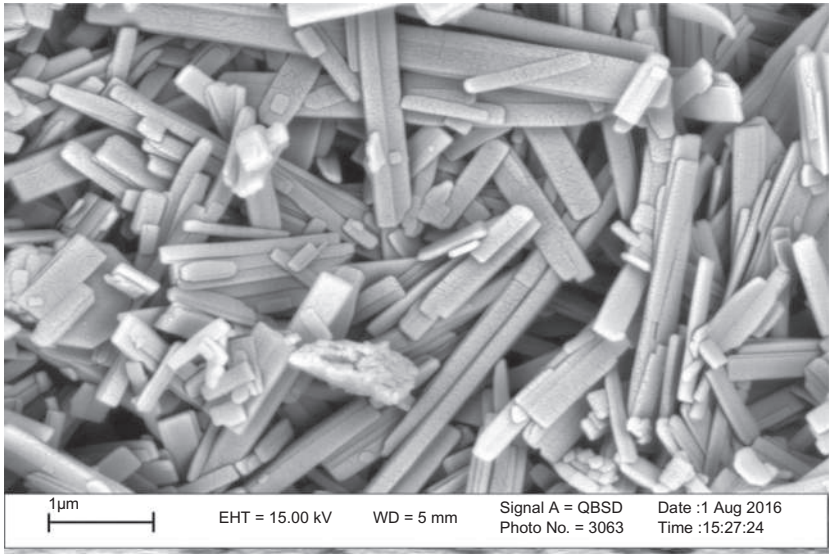

Fig. 12 SEM photographs of $\{[Pb(\mu 2\text{-}NO_3)_4]\cdot(hmta)_2\cdot H_2O\}_n$ (**4**) nanorods.[44]

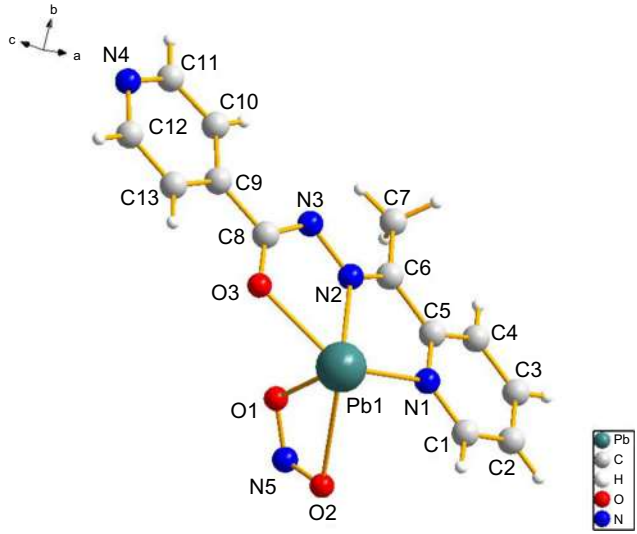

Fig. 13 Molecular asymmetrical unit of $[Pb(p\text{-}2\text{-}einh)NO_2]_n$ (**5**).

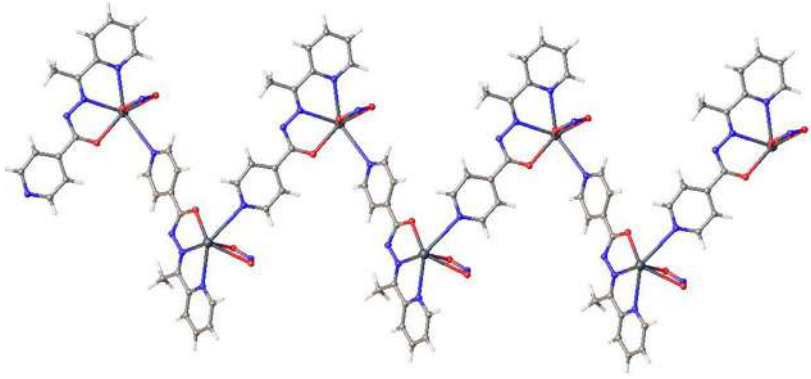

Fig. 14 Fragment of the coordination polymer showing the 1D zigzag metal-organic polymer.[45]

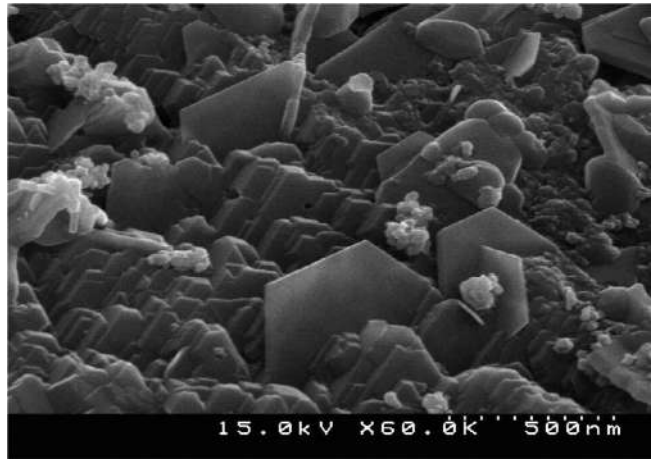

Fig. 15 SEM photographs of $[Pb(p\text{-}2\text{-}einh)NO_2]_n$ (**5**) nano structures.

2.2.6 Rod-shaped nanostructures of 1D lead(II) tri-nuclear coordination polymer $[Pb_3(tmph)_4(\mu\text{-}N_3)_5(\mu\text{-}NO_3)]_n$ (6)[46]

The reaction between the 3,4,7,8-tetramethyl-1,10-phenanthroline (tmph) ligand with a mixture of $Pb(NO_3)_2{\cdot}3H_2O$ and sodium azide led to the formation of the new lead(II) coordination compound $[Pb_3(tmph)_4(\mu\text{-}N_3)_5(\mu\text{-}NO_3)]$ (**6**). Nanorods of compound **6** were obtained by ultrasonic irradiation in a methanolic solution and single crystalline material was obtained using a heat gradient applied to a solution of the reagents.[46]

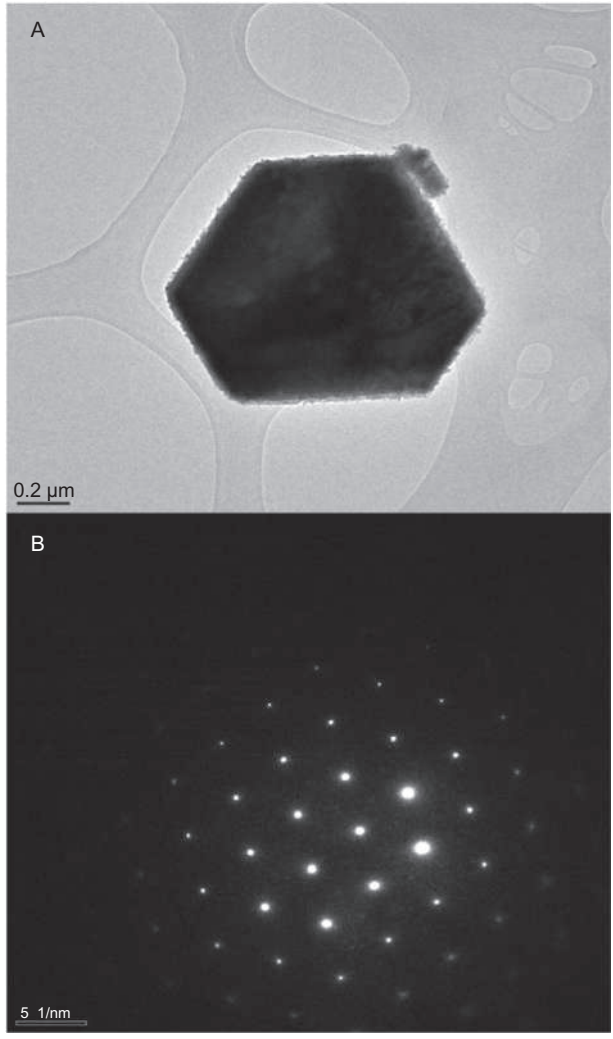

Fig. 16 TEM photographs of $[Pb(p\text{-}2\text{-}einh)NO_2]_n$ (**5**) nano-plates.[45]

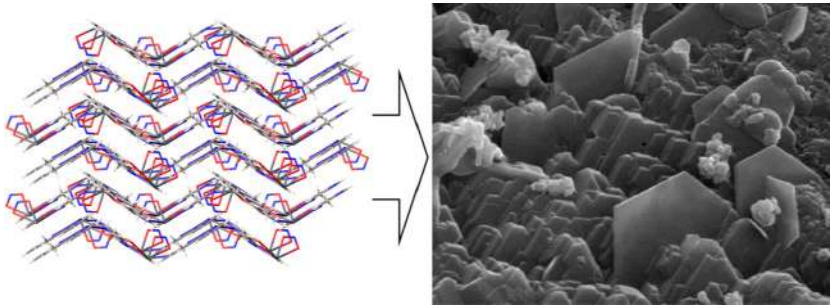

Fig. 17 Left: packing of the structure on a molecular level, Right: morphology of the nanostructure.

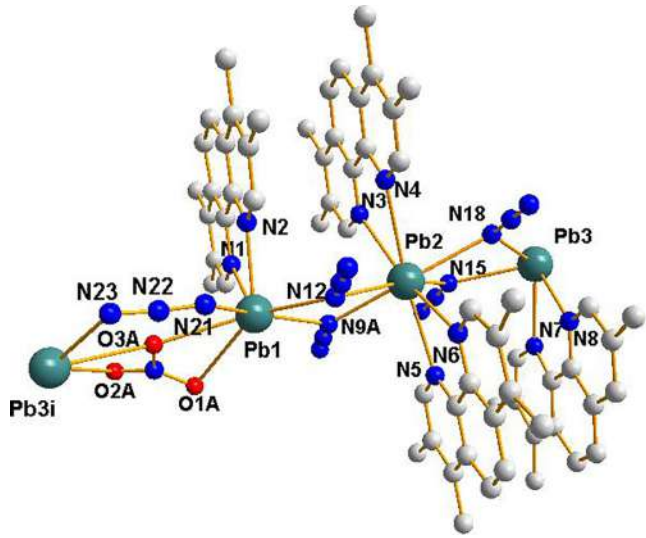

Fig. 18 Molecular structure of $[Pb_3(tmph)_4(\mu\text{-}N_3)_5(\mu\text{-}NO_3)]$ (6).

The determination of the structure of $[Pb_3(tmph)_4(\mu\text{-}N_3)_5(\mu\text{-}NO_3)]$ (**6**) (Fig. 18) showed that the complex crystallizes in the monoclinic system with space group $P_{2/1}$, taking the form of a one-dimensional polymer in the solid state (Fig. 19). A view of the molecular structure of **6** together with selected atom numbering scheme is shown in Fig. 18.

Fig. 20 shows the nanorods that were observed by scanning electron microscopy. The morphology of compound **6** prepared by the sonochemical method is very interesting. It is composed of cross-rods with thickness of about 55 nm (Fig. 20).

2.2.7 Nanostructures of a new coordination polymer with the ligands 1,10-phenanthroline (phen) and 4-aminobenzene sulfonic acid (4-abs), $[Pb(phen)_2(4\text{-}abs)_2]_n$ (7) [47]

The reaction of the 1,10-phenanthroline (phen) and 4-aminobenzene sulfonic acid (4-abs) ligands with a of Pb(II) acetate using two different routes provide crystalline materials of the general formula $[Pb(phen)_2(4\text{-}abs)_2]_n$ **(7)** (Fig. 21).

The determination of the structure of **7** by single crystal X-ray crystallography shows that the complex crystallizes in the orthorhombic system with space group P_{bna}, taking the form of a 1D polymer in the solid state (Fig. 22). A view of the molecular structure of **7** together with selected atom numbering scheme is shown in Fig. 21.

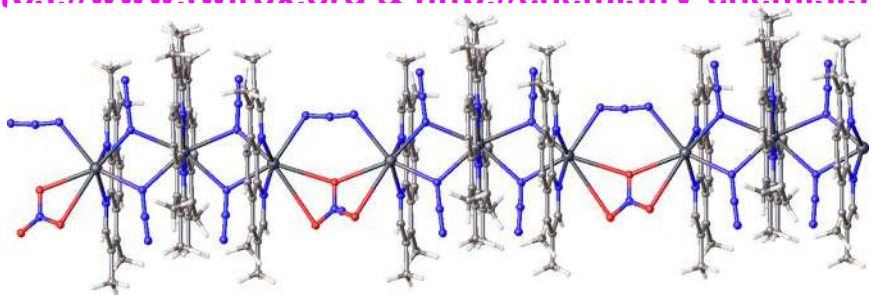

Fig. 19 Fragment of the coordination polymer showing the 1D polymer.[46]

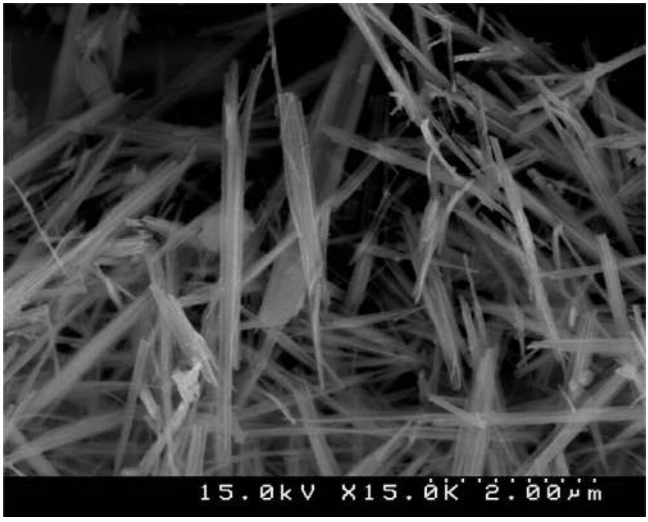

Fig. 20 SEM photographs of $[Pb_3(tmph)_4(\mu\text{-}N_3)_5(\mu\text{-}NO_3)]_n$ (**6**) nanorods.[46]

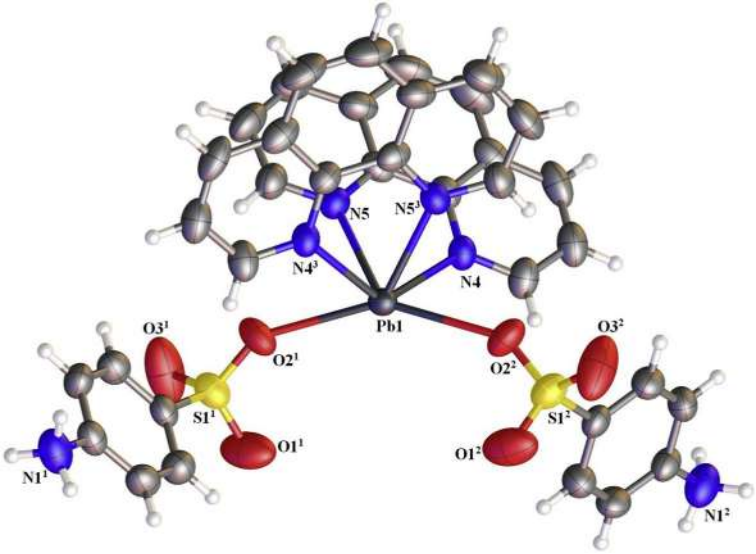

Fig. 21 The molecular structure of the asymmetric unit of $[Pb(phen)_2(4\text{-}abs)_2]$ (**7**).

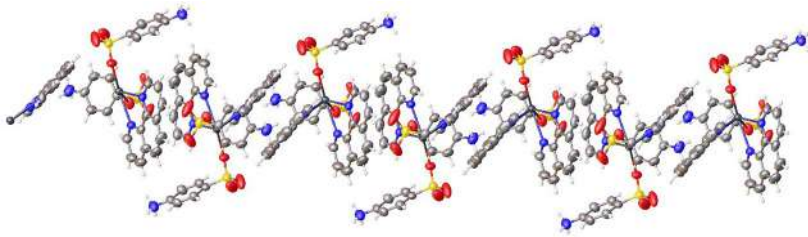

Fig. 22 Fragment of **11** showing the 1D polymer.[47]

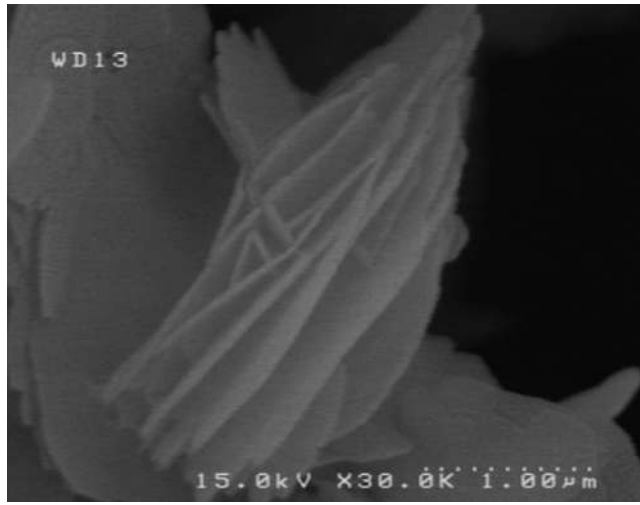

Fig. 23 SEM photographs of **11** nano-flowers.[47]

Fig. 23 shows the nano-layers that were observed by SEM. The morphology of **7** prepared sonochemically is very interesting. It is composed of cross-sheets with a thickness of ~32 nm that form a flower-like network. The packing of the structure on a molecular level might influence the morphology of the nanostructure of the compound (Fig. 24).

2.2.8 Neutral nanorod binuclear lead(II) azido coordination compound, $[Pb_2(tmph)_2(\mu\text{-}N_3)_2(CH_3COO)_2]$ (8) [tmph = 3,4,7,8-tetramethyl-1,10-phenanthroline][48]

The reaction between "tmph" ligand with a mixture of $Pb(CH_3COO)_2{\cdot}3H_2O$ and sodium azide led to the formation of the new lead(II) coordination compound $[Pb_2(tmph)_2(\mu\text{-}N_3)_2(CH_3COO)_2]$ (**8**). Nanorods of compound **8** were

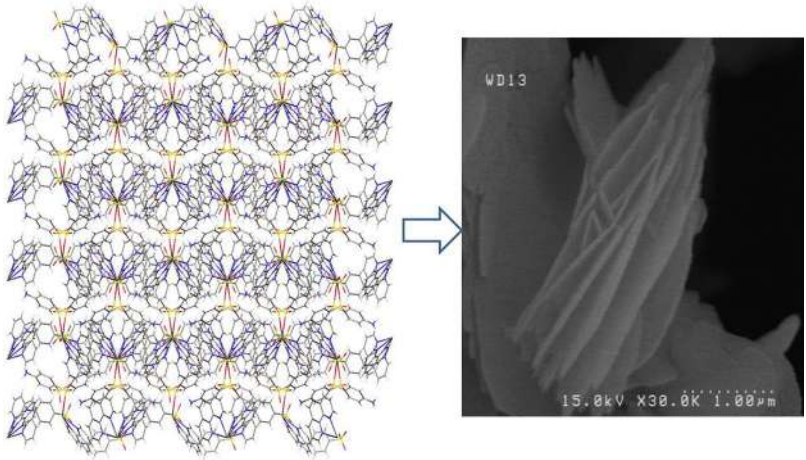

Fig. 24 Left: packing of the structure on a molecular level. Right: morphology of the nanostructure.

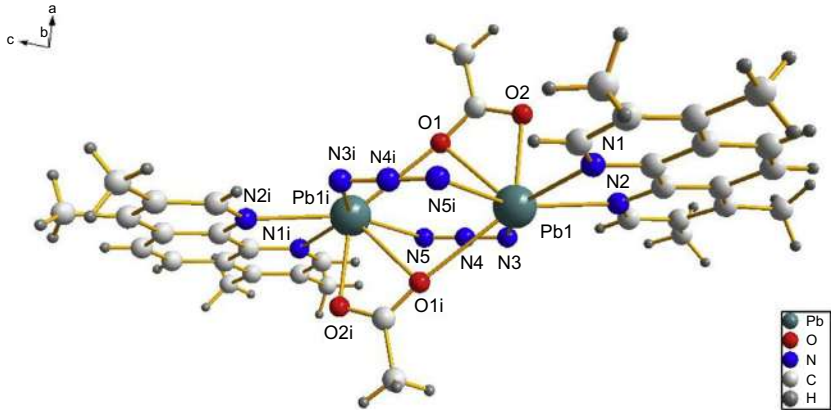

Fig. 25 Molecular structure of $[Pb_2(tmph)_2(\mu\text{-}N_3)_2(CH_3COO)_2]$ (**8**).[48]

obtained by ultrasonic irradiation in a methanolic solution and single crystalline material was obtained using a heat gradient applied to a solution of the reagents.

X-ray structure of complex **8** revealed the composition and stereochemistry of a fundamental building block, having a formula of $[Pb_2(tmph)_2(\mu\text{-}N_3)_2(CH_3COO)_2]$. A view of the molecular structure of **8** together with selected atom numbering scheme is shown in Fig. 25. The complex $[Pb_2(tmph)_2(\mu\text{-}N_3)_2(CH_3COO)_2]$ acts as a monomer unit in the 1D supramolecular chain (Fig. 26). The lead(II) atoms are bridged by two azide ions in a μ_2-1,3 fashion with a Pb⋯Pb distance of 4.302 Å.

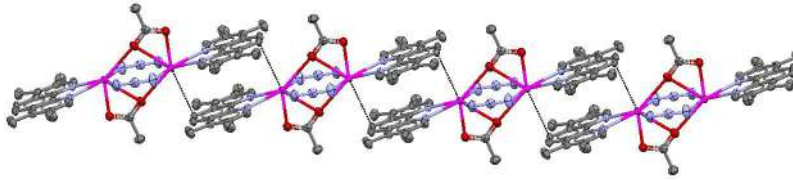

Fig. 26 Fragment of the supramolecular 1D polymer of $[Pb_2(tmph)_2(\mu\text{-}N_3)_2(CH_3COO)_2]_n$.

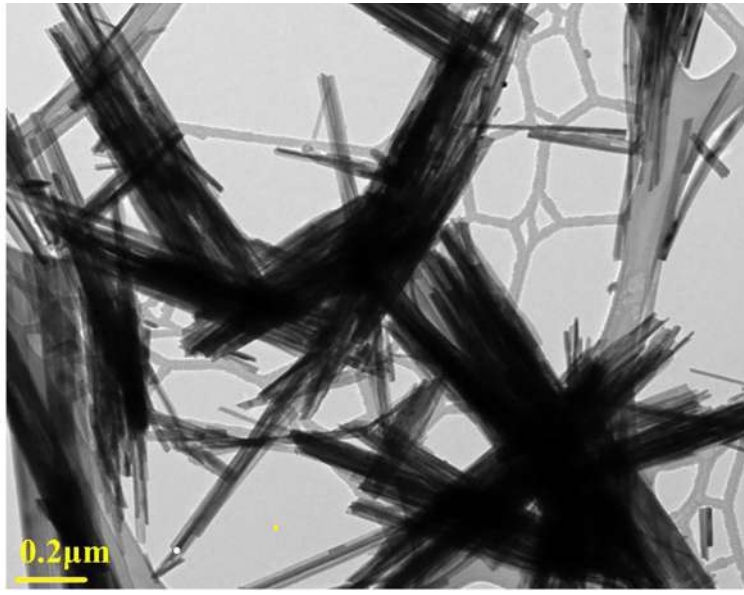

Fig. 27 TEM image of $[Pb_2(tmph)_2(\mu\text{-}N_3)_2(CH_3COO)_2]$ (**8**).[48]

There are two different types of non-covalent π–π stacking interactions between the parallel aromatic rings belonging to adjacent dimers. The interplanar distance of the "tmph" ligands are 3.38 and 3.61 Å, appreciably shorter than the normal π–π stacking. Consequently, the π–π stacking and Pb···C interactions also allow the $[Pb_2(tmph)_2(\mu\text{-}N_3)_2(CH_3COO)_2]$ (8) structure to form a 1D chains (Fig. 26).

Fig. 27 shows the nanorods that were observed by transmission electron microscopy. The morphology of compound **8** prepared by the sonochemical method is very interesting. It is composed of cross-rods with thickness of about 20–35 nm.

2.3 Some other metal coordination compounds

2.3.1 Bismuth(III) nano coordination polymer, $\{[Bi(pcih)(NO_3)_2]\cdot MeOH\}_n$ (9), ("pcih" is the abbreviations for 2-pyridinecarbaldehyde isonicotinoylhydrazoneate)[49]

Reaction between 2-pyridinecarbaldehyde isonicotinoylhydrazone ligand (Hpcih) with a solution of bismuth(III) nitrate led to the formation of the new bismuth(III) coordination polymer $\{[Bi(pcih)(NO_3)_2]\cdot MeOH\}_n$ (**9**). Nanorods of compound **9** were obtained by ultrasonic irradiation in a methanolic solution and single crystalline material was obtained using a heat gradient applied to a solution of the reagents (Fig. 28).

Determination of the structure of **9** by X-ray crystallography showed that the complex crystallizes in the monoclinic system with space group $P2_1/n$, taking the form of a zigzag one-dimensional polymer in the solid state (Fig. 29). A view of the crystal structure with atom numbering scheme is shown in Fig. 28.

The morphology of compound **9** prepared by the sonochemical method (Fig. 30) is very interesting. It is composed of rods structures with thickness of about 20–40 nm (Fig. 30).

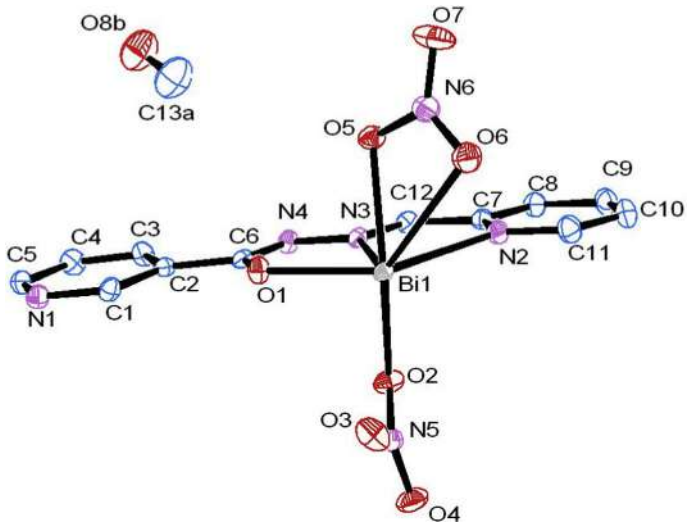

Fig. 28 The molecular structure of the asymmetric $\{[Bi(pcih)(NO_3)_2]\bullet MeOH\}_n$ unit.[49]

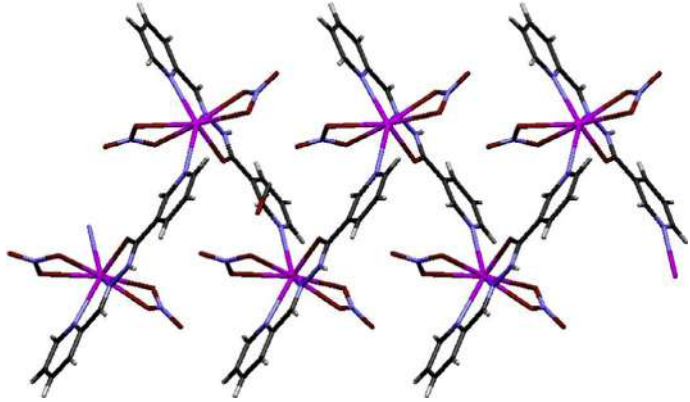

Fig. 29 Fragment of the coordination polymer showing the 1D zigzag polymer.[49]

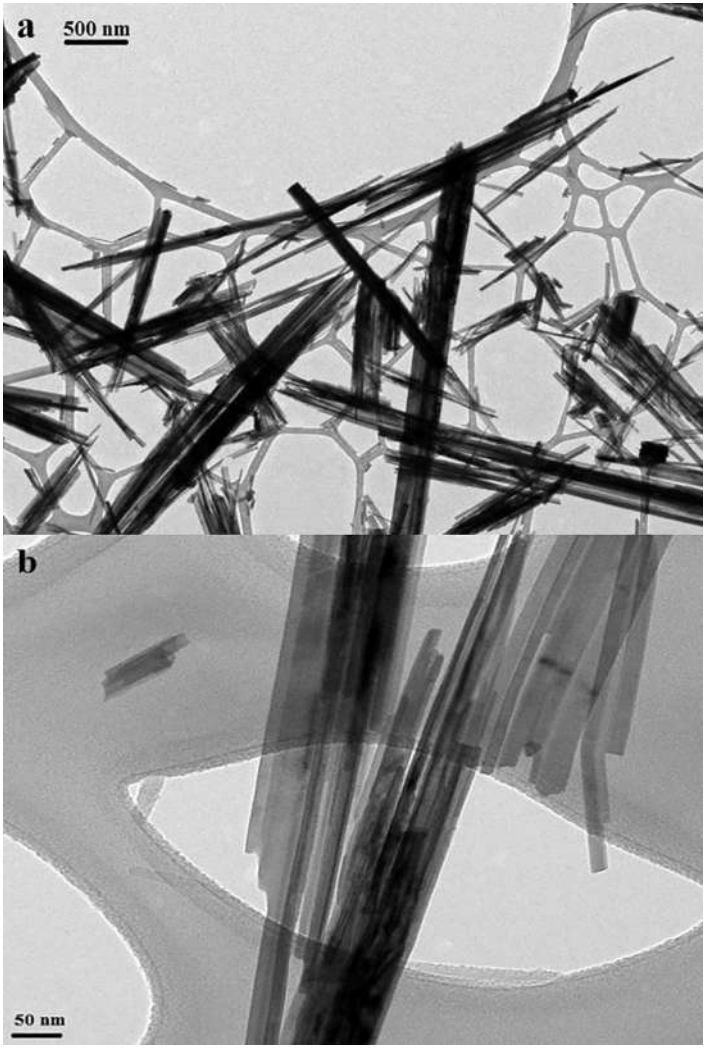

Fig. 30 TEM photographs of $\{[Bi(pcih)(NO_3)_2]\bullet MeOH\}_n$ (**9**) nanorods.

2.3.2 Flower-like cadmium(II) coordination compound, [cd(2,2′-bpy)(ftfa)$_2$]$_n$ (10), ("2,2′-bpy" and "ftfa" are the abbreviations for 2,2′-bipyridine and furoyltrifluoroacetonate) [50]

Reaction between furoyltrifluoroacetone (Hftfa) and 2,2′-bipyridine with a solution of cadmium(II) acetate led to the formation of the new cadmium(II) coordination compound [Cd(2,2′-bpy)(ftfa)$_2$]$_n$ (**10**). Flower-like crystals of compound **10** were obtained by ultrasonic irradiation in an ethanolic solution and single crystalline material was obtained using a heat gradient applied to a solution of the reagents. Structure determination at 100 K reveals that the complex **10** has the stoichiometry of [Cd(2,2′-bpy)(ftfa)$_2$]. A view of the crystal structure with atom numbering scheme is shown in Fig. 31.

With the presence of 2,2′-bipyridine ligands on each metal and furyl ring of the "ftfa" ligand, it is unsurprising that there are π–π interactions, given the importance of π–π stacking and C—H···π interactions apparent in the solid-state structures of numerous complexes of aza-aromatic ligands. The packing diagram of this complex (Fig. 32) exhibits self-assembled structural topologies via two different π–π stacking (face-to-face of furyl rings of "ftfa" ligands with distance of 3.371 Å, slipped face-to-face of 2,2′-bipyridines with distance of 3.402, and C3—H3···Cg(C22C23···C26N) with distance of 2.525 Å) appreciably shorter than the normal intermolecular interactions.[50]

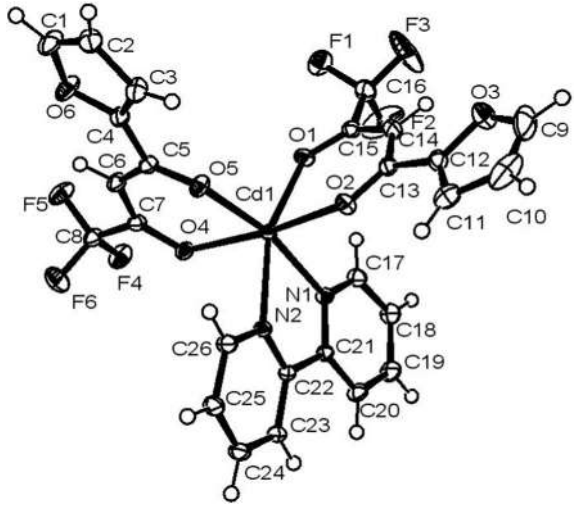

Fig. 31 Perspective view of the coordination environment of Cd atoms in **10**.[50]

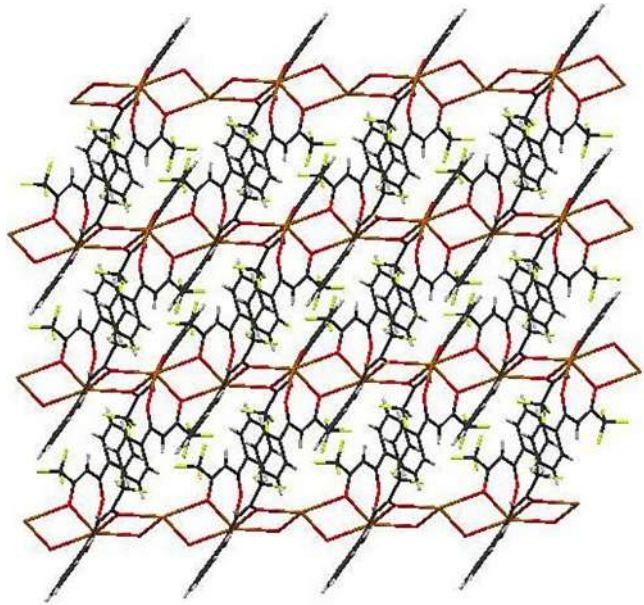

Fig. 32 The packing of **10** to form 3D supramolecular layers via intermolecular interactions.

The morphology of compound **10** prepared by the sonochemical method (Fig. 33) is composed of cross-sheets with thickness of about 40–200 nm, and they form a flower-like network (Fig. 32).

2.3.3 Nanostructures of cobalt(II) discrete coordination compound with the pyrazol (pzH) containing the terminal isothiocyanate anions, $[Co(pzH)_2(NCS)_2]$ (11)

The reaction between pyrazol (pzH) and cobalt(II) acetate and potassium thiocyanate using two different routes provided crystalline materials of the general formula $[Co(pzH)_2(NCS)_2]$ (**11**). Nanostructure of compound **11** was obtained by ultrasonic irradiation in a water/methanolic solution and single crystalline material was obtained using a heat gradient applied to a solution of the reagents.

X-ray structure of complex **11** revealed the composition and stereochemistry of a fundamental building block, having a formula of $[Co(pzH)_2(NCS)_2]$ (Fig. 34). The determination of the structure of $[Co(pzH)_2(NCS)_2]$, (**11**) showed that the complex crystallizes in the monoclinic system with space group *C2/c*, taking the form of a discrete coordination compound (DCC) in the solid state (Fig. 34).

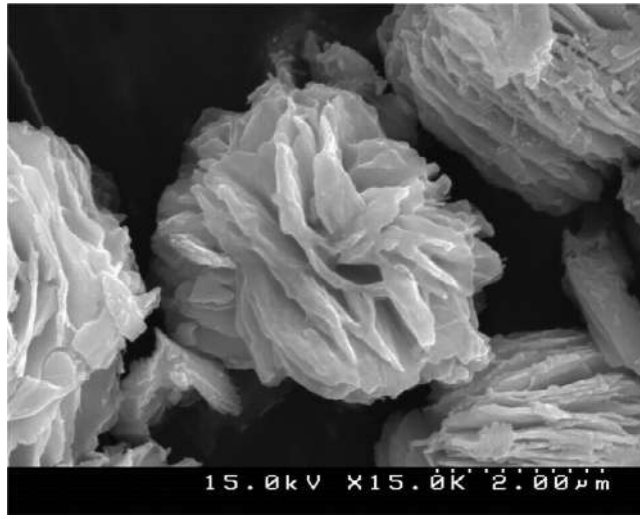

Fig. 33 SEM photographs of flower-like $[Cd(2,2'\text{-bpy})(ftfa)_2]_n$ (**10**).[50]

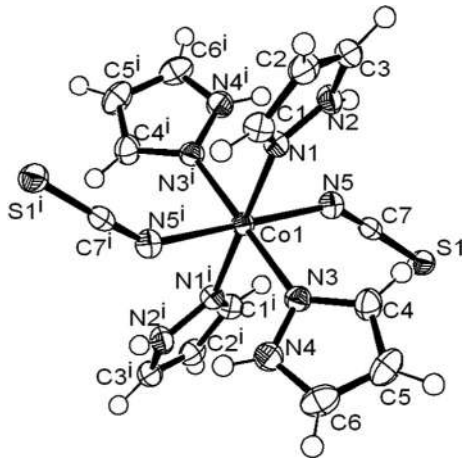

Fig. 34 Fragment of the discrete coordination compound (DCC) of **11**.[51]

There are several supramolecular interactions observed in the structure. There are N—H···S interactions, π···H—C interactions among the weak non-covalent contacts belonging to fragments of adjacent, distances values of these interactions that suggest relatively strong interactions within this class of weak non-covalent contacts. With expanding all the week supramolecular interactions, the discrete coordination compound interacts with neighbors and the structure extended to 3D supramolecular networks (Fig. 35).

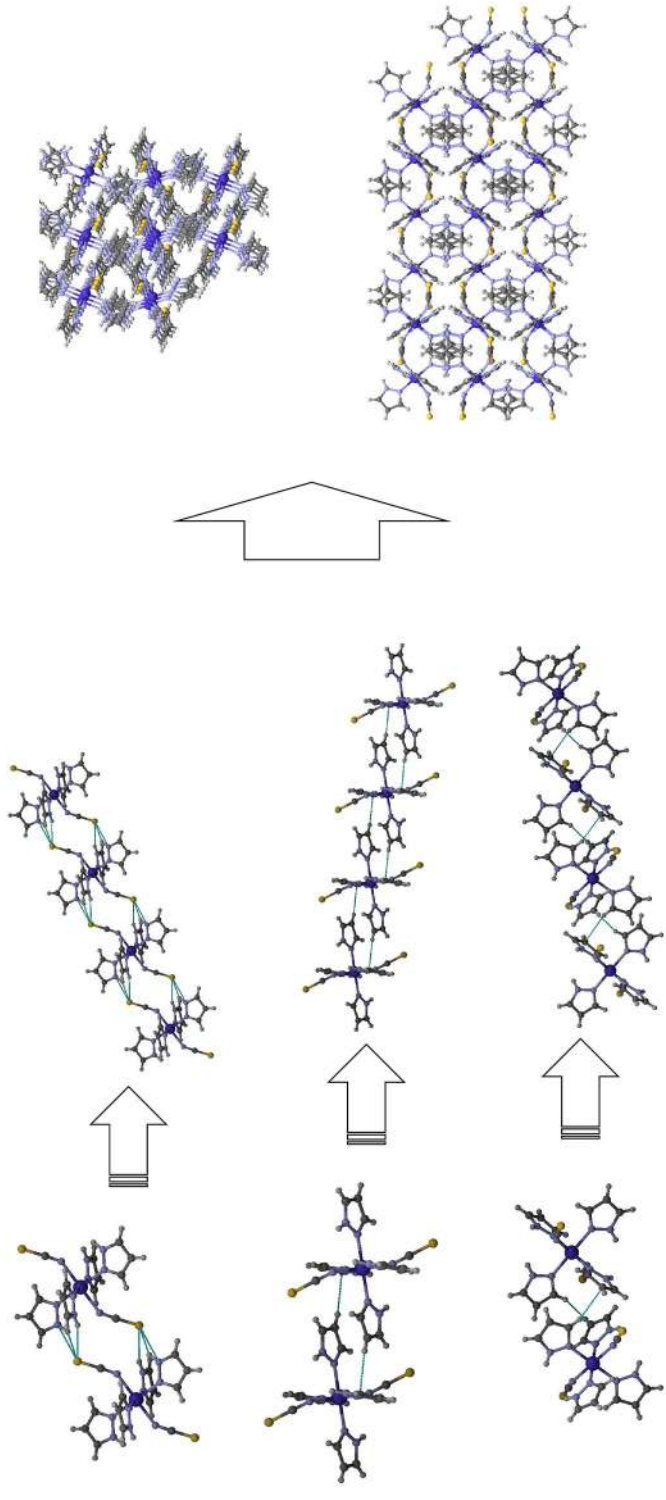

Fig. 35 From discrete coordination compound to supramolecular coordination networks via labile interactions.

The morphology of compound **11** prepared by the sonochemical method is very interesting. It is composed of flower sheets with thickness of about 15–40 nm (Fig. 36). The mechanism of formation of nano structures may be a result of the crystal structure of the compound which is, i.e., the packing of the structure on a molecular level might have influence on the morphology of the nanostructure of the compound.

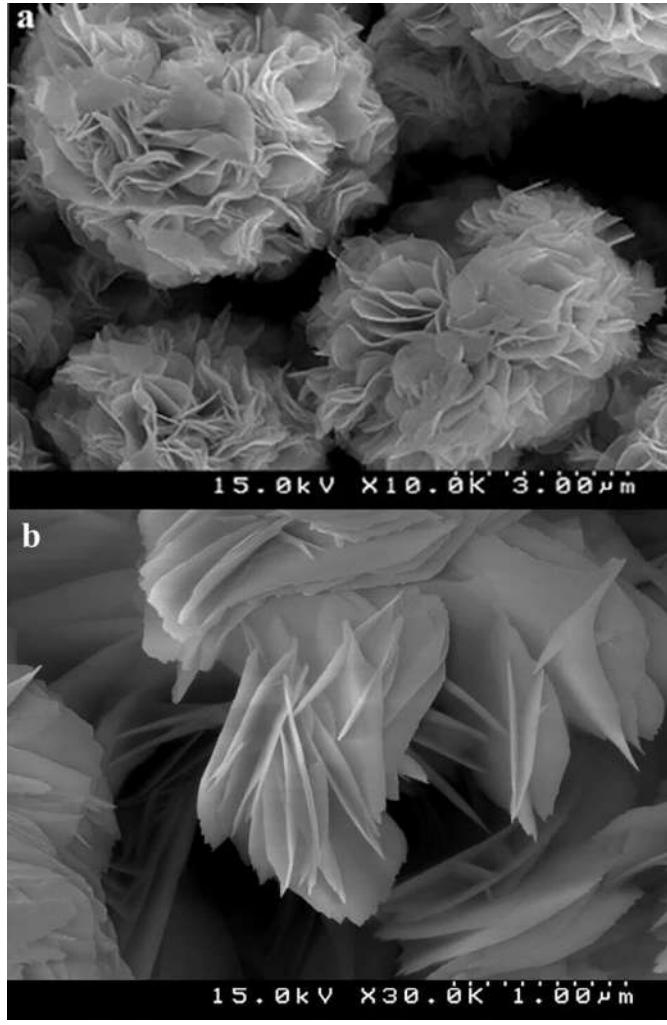

Fig. 36 SEM photograph of $[Co(pzH)_2(NCS)_2]$ (**11**) nano-flowers.[51]

2.3.4 Nanostructure of a zinc(II) organic-inorganic compound $[Zn(dapt)_2(ttfa)_2]$ (12) [dapt = 2,4-diamino-6-phenyl-1,3,5-triazine and ttfa = 2-thenoyltrifluoroacetonate][52]

The reaction between the 2,4-diamino-6-phenyl-1,3,5-triazine (dapt) and 2-thenoyltrifluoroacetone (ttfa) ligands with $Zn(CH_3COO)_2{\cdot}2H_2O$ led to the formation of the new zinc(II) coordination compound $[Zn(dapt)_2(ttfa)_2]$ (**12**). The nanostructured form of compound **12** was obtained by ultrasonic irradiation in a methanolic solution, and crystalline material was obtained using a heat gradient applied to a solution of the reagents.

The X-ray structure of complex **12** revealed the composition and stereochemistry of the fundamental building block as having a formula of $[Zn(dapt)_2(ttfa)_2]$ (**12**). The molecular structure of **12** and a selected atom numbering scheme are shown in Fig. 37.

Complex **12** has crystallographically-imposed centro-symmetry with the zinc atom at the center of a tetragonally elongated octahedron. The triazine ligands occupy the axial positions (Zn1–N1 = 2.3066(11) Å) and the chelating ttfa ligands the equatorial sites (Zn1–O1 = 2.0468(9) Å; Zn1–O2 = 2.0234(9) Å) resulting in a ZnN_2O_4 donor set. Fig. 38 also shows the intramolecular N—H ··· O hydrogen bonds which aid in establishing the orientation of the triazine ligand (Fig. 38).

Fig. 39 shows the nanostructure that was observed by SEM, and Fig. 40 shows the TEM image of the nanostructure. These structures may be a result of the crystal structure of a compound that is a supramolecular structure. The packing of the structure on a molecular level might have influenced the morphology of the nanostructure of the compound (Fig. 41).

2.3.5 Nanostructures of a new supramolecular coordination compound of divalent nickel with the pyrazol (pzH), $[Ni(pzH)_2(N_3)_2]$ (13)[53]

The reaction between pyrazol (pzH) and nickel (II) acetate and sodium azide using two different routes provided crystalline materials of the general formula $[Ni\ (pzH)_2(N_3)_2]$ (**13**). Nano structure of compound **13** were obtained by ultrasonic irradiation in a water/methanolic solution and single crystalline material was obtained using a heat gradient applied to a solution of the reagents.

The determination of the structure of $[Ni(pzH)_2(N_3)_2]$, (**13**) showed that the complex crystallizes in the monoclinic system with space group *C2/c*, taking the form of a discrete molecular architecture (DMA) in the solid state (Fig. 42).

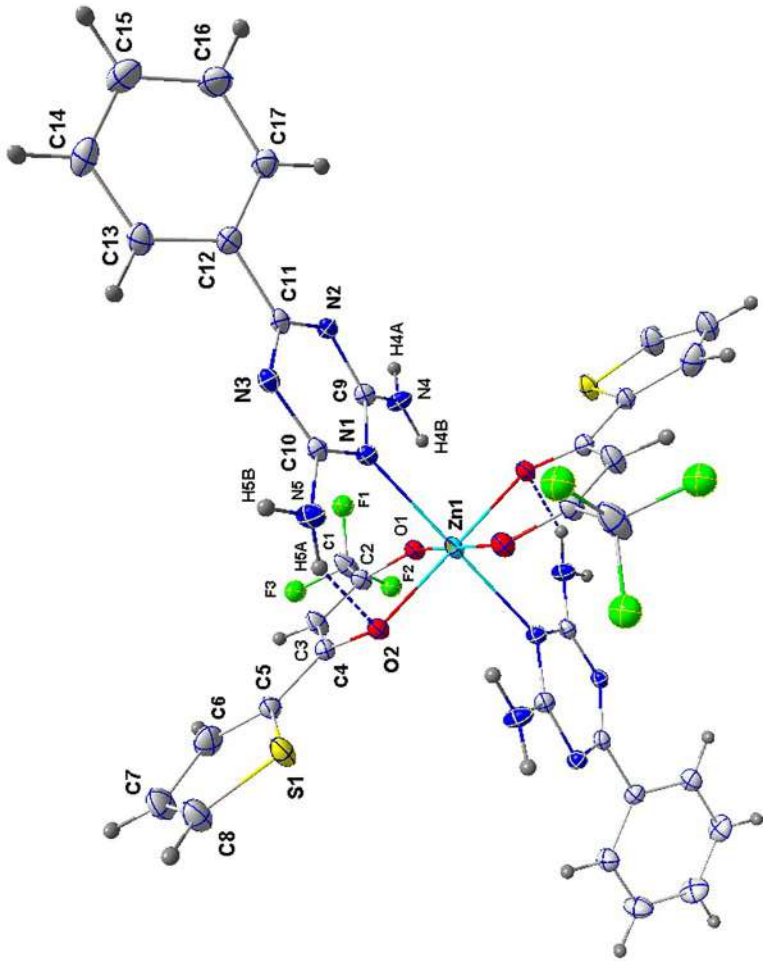

Fig. 37 Molecular structure of $[Zn(dapt)_2(ttfa)_2]$ (**12**). Unlabeled atoms are related to their labeled counterparts by the crystallographic center. Ellipsoids are drawn at the 50% probability level. The intramolecular N—H···O hydrogen bonds are shown as dotted lines.[52]

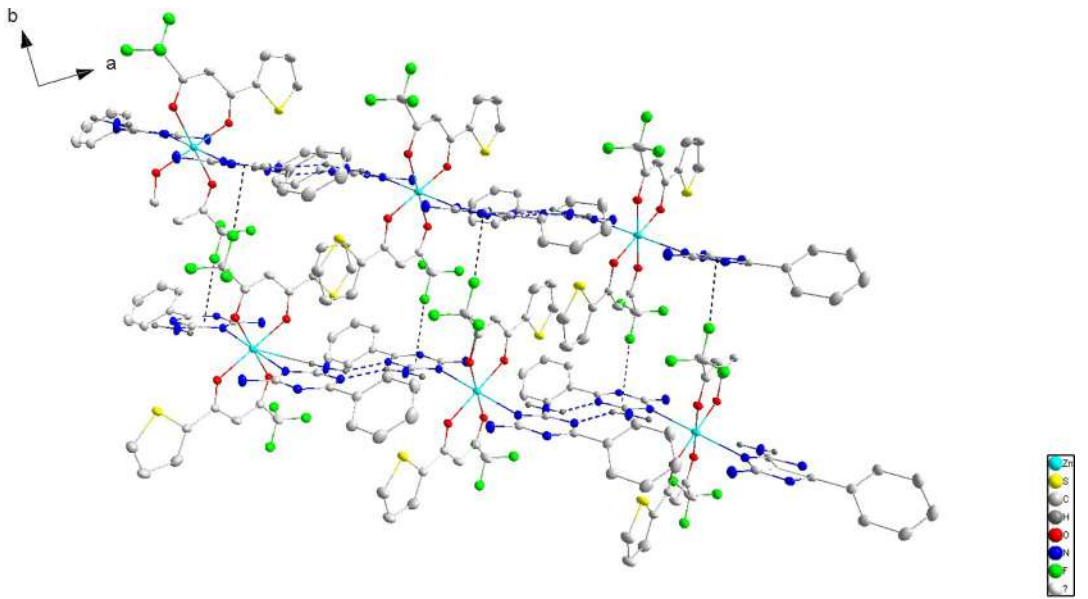

Fig. 38 Packing viewed down the *c*-axis. Intermolecular N—H⋯N hydrogen bonds are shown as blue dotted lines while intermolecular C—F⋯π interactions are shown by black dotted lines.

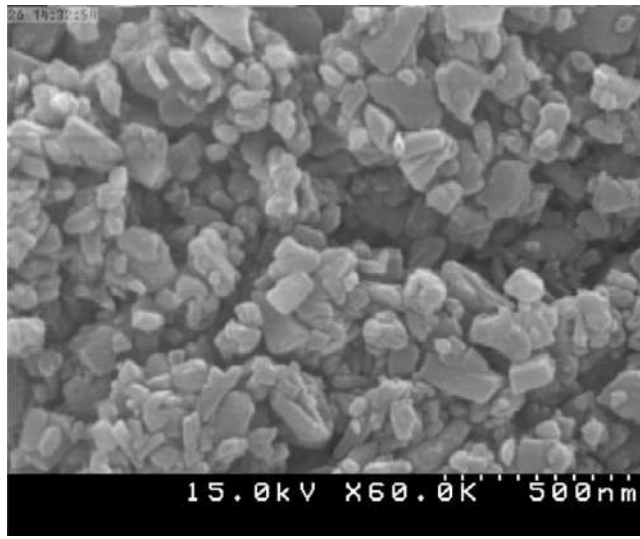

Fig. 39 SEM photographs of $[Zn(dapt)_2(ttfa)_2]$ (**12**) nanostructures.[52]

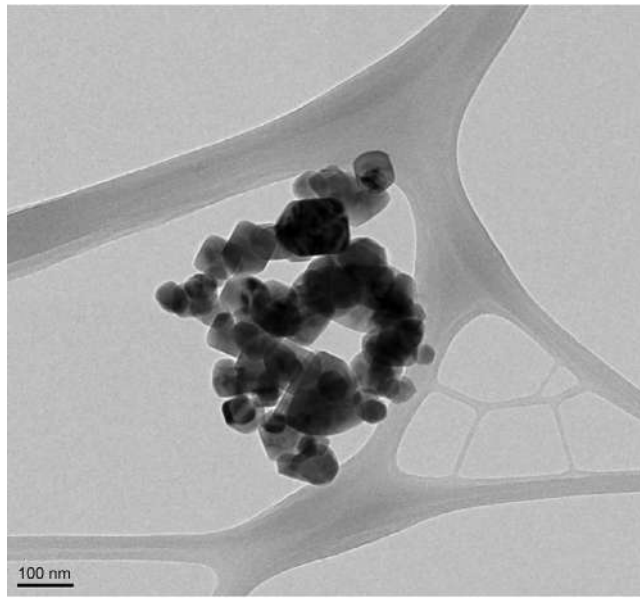

Fig. 40 TEM photographs of $[Zn(dapt)_2(ttfa)_2]$ (**12**) nanostructures.[52]

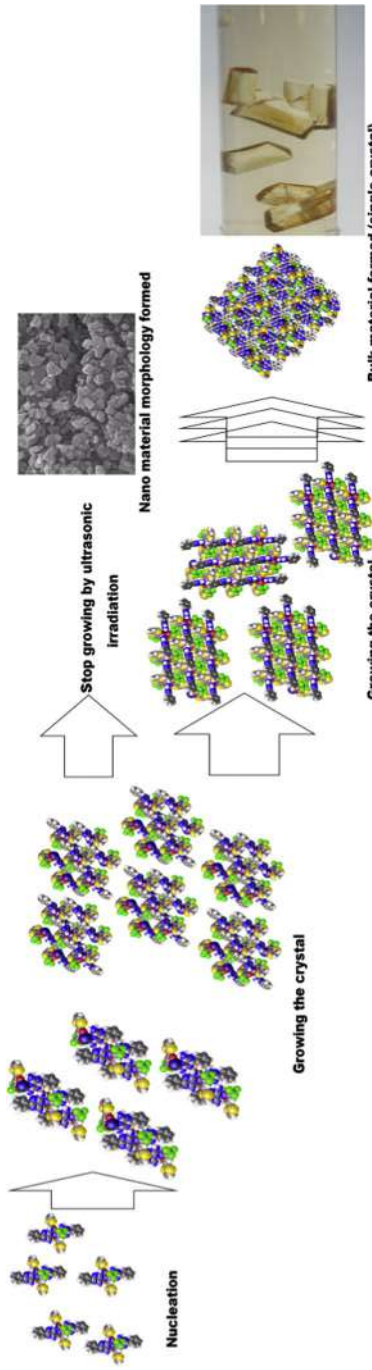

Fig. 41 Nanomaterials and bulk single crystal from initial nucleation to small objects.[52]

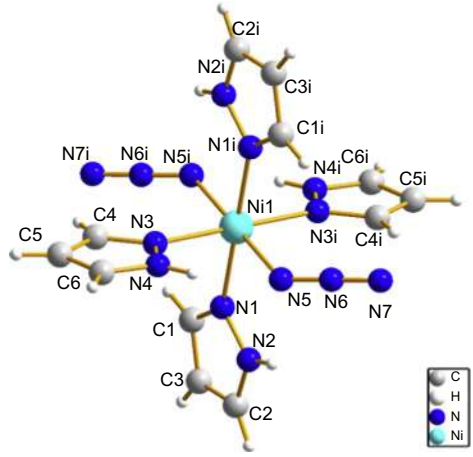

Fig. 42 Fragment of the discrete molecular (DMs) of **13**.[53]

There are several supramolecular interactions observed in structure **13**. There are N—H ⋯ N interactions, C—H ⋯ N and N—H ⋯ H—C interactions among the weak non-covalent contacts belonging to fragments of adjacent, distance values of these interactions that suggest relatively strong interactions within this class of weak non-covalent contacts. With expanding all the weak supramolecular interactions, the discrete molecular architecture interacts with neighbors and the structure extended to 3D supramolecular architecture (Fig. 43).

Nanostructure of compound **13** was obtained by ultrasonic irradiation in a water/methanolic solution as seen in Fig. 44. The mechanism of formation of nano structures may be a result of the crystal structure of the compound which is, i.e., the packing of the structure on a molecular level might have influenced the morphology of the nanostructure of the compound (Figs. 43 and 44).

2.3.6 Nickel(II) nano coordination complex, $\{[Ni(phen)_3](BF_4)_2{\cdot}H_2O\}_n$ (14) (phen = 1,10-phenamthroline)[54]

The reaction between the 1,10-phenamthroline (phen) ligand with $Ni(CH_3COO)_2$ and $NaBF_4$ led to the formation of the new nickel(II) supramolecular coordination polymer $\{[Ni(phen)_3](BF_4)_2{\cdot}H_2O\}_n$ (**14**). Nanostructures of compound **14** were obtained by ultrasonication in a methanolic solution, and the single crystal sample was obtained using a heat gradient applied to a solution of the reagents using the branched tube method.

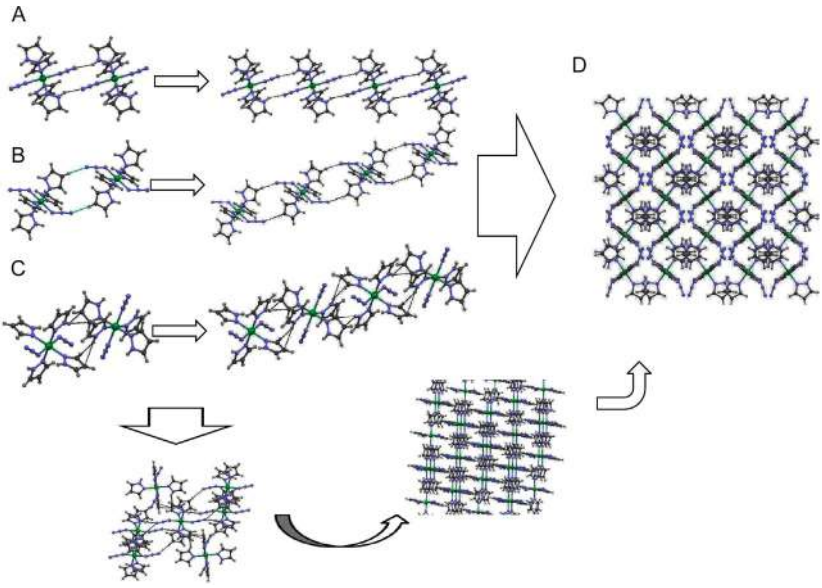

Fig. 43 From discrete molecular architecture to supramolecular coordination polymer via labile interactions.

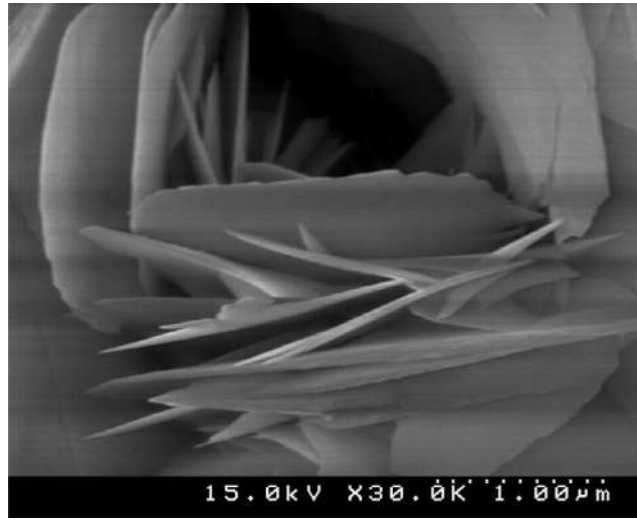

Fig. 44 SEM photograph of $[Ni(pzH)_2(N_3)_2]$ (**13**) nano structures.[53]

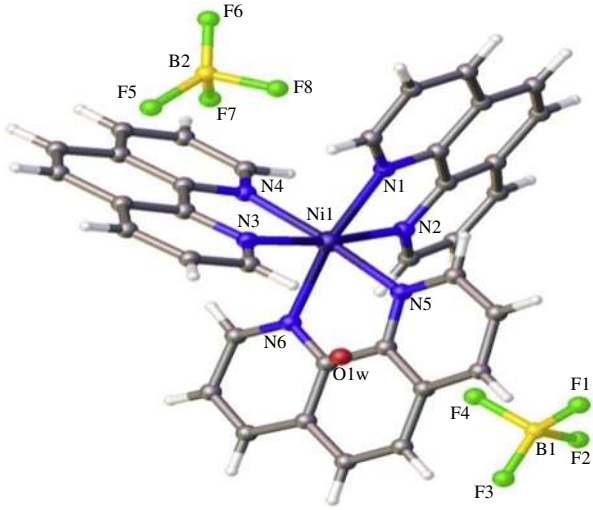

Fig. 45 Molecular structure of $\{[Ni(phen)_3](BF_4)_2 \cdot H_2O\}_n$ (**14**).[54]

Based on single crystal X-ray crystallography, the structure of $\{[Ni(phen)_3](BF_4)_2 \cdot H_2O\}_n$ crystallizes in a triclinic system with space group $P\bar{1}$ and takes the form of a discrete metal-organic polymer in the solid state. Fig. 45 shows a view of the asymmetrical unit structure of **14** with a selected atom numbering scheme.

The F⋯H—C and O⋯H—C interactions are usually classified as weak non-covalent bonding between adjacent atoms. However, the observed distance values for these interactions suggest relatively strong interaction between these atoms.

There are π–π stacking interactions in the structure between the parallel aromatic rings belonging to adjacent chains. The interplanar distance of the aromatic rings is 3.564 Å, which is noticeably shorter than the normal π–π stacking distance. As a consequence, the labile interactions also allow the discrete molecular architecture to interact with neighboring chains and for the structure to extend into a 3D supramolecular metal-organic coordination polymer (Fig. 46). Thus, the coordination sphere of nickel (II) ions in this complex may be controlled by labile and π–π stacking interactions.

Fig. 47 shows the nanostructures observed by SEM. Interestingly, compound **14** prepared by the sonochemical method (Fig. 47) showed nanorod morphology with diameter of 40–120 nm. The supramolecular structure of the compound may have an influence. The morphology of the nanostructured compound could be affected by the packing of the structure at a molecular level (Fig. 48).

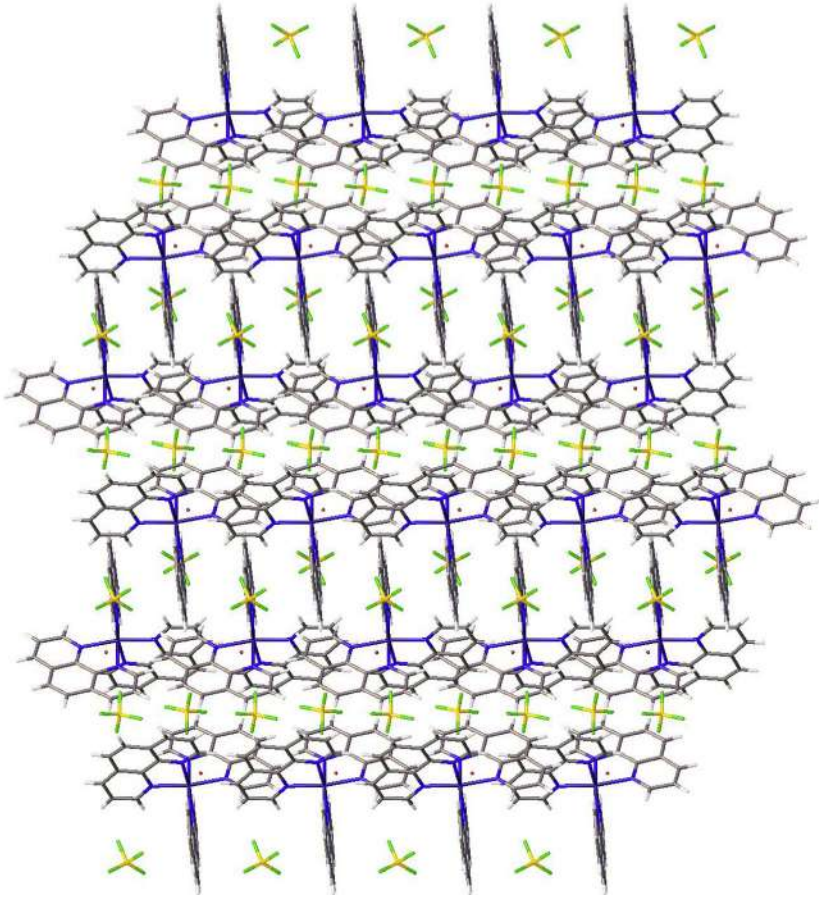

Fig. 46 From discrete architecture to supramolecular 3D polymer via labile interactions.

Fig. 47 SEM photographs of $\{[Ni(phen)_3](BF_4)_2 \cdot H_2O\}_n$ (**14**) nanorods.[54]

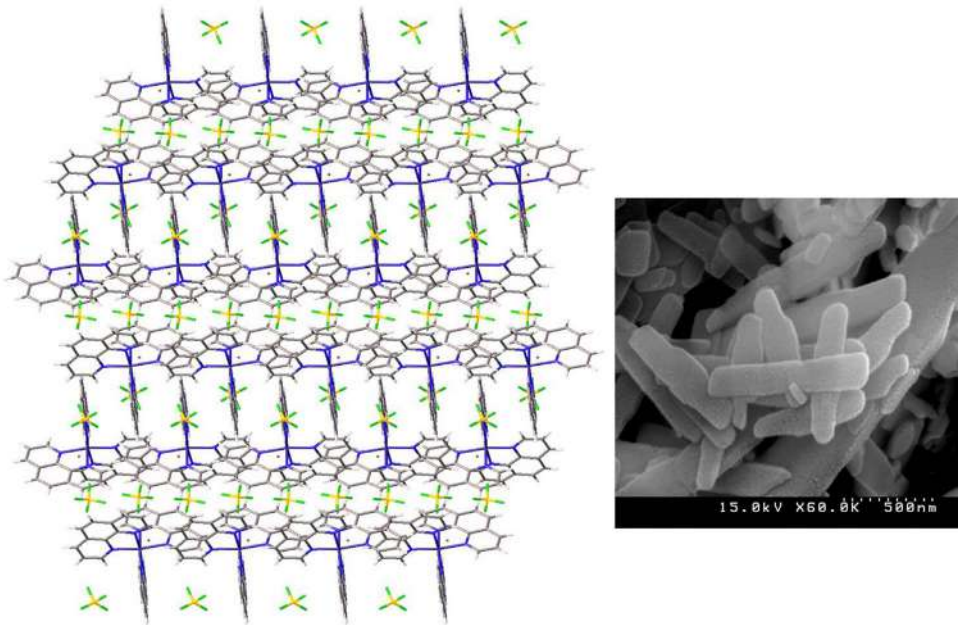

Fig. 48 Left: packing of the structure on a molecular level. Right: morphology of the nanostructure.

3. Conclusions and future perspectives

The design and synthesis of extended network materials has been an area of intense research over the past decade. In recent years, synthesis, characterization and investigation of properties as well as applications of nanostructure materials have been the subject of extensive research. These materials find very diverse potential applications including catalysis, magnetism, optics, sensors, biosensing, medical diagnostics, energy storage and batteries, data storage and others. There are many methods for the preparation of nanomaterials including hydrothermal or solvothermal methods, microwave-solvothermal synthesis, microwave synthesis, magnetic-field-assisted hydrothermal, sol–gel process, electrochemically induced sol–gel, microemulsion and reverse micelle/microemulsion, homogeneous precipitation method, cluster growth method, chemical vapor deposition, vapor–liquid–solid process, soft chemical method, electrophoretic deposition, electrochemical fabrication, chemical reduction method, electrolysis of metal salts, rapid expansion of supercritical solvents, photoreduction of metal ions, microwave plasma synthesis, sonochemical method and mechano-chemical process. The study of new structures of coordination polymers and nano coordination polymers are very interesting. There are relations between the structures at the molecular level and the morphology at the nano sized level. These structures may be a result of the crystal structure of a compound that is a supramolecular structure.

Most likely the mechanism of final morphology formation in nanomaterials depends on various intermediates controlled by inner and external forces during the formation process. Crystal structure and the interactions in metal-organic coordination compounds (MOCC) (such as covalence, coordination, hydrogen, and van der Waals forces) are inner forces affecting intermediates and solvent–MOCC interactions, electrostatic and dipolar fields as well as hydrophilic or hydrophobic interaction give rise to external forces controlling system morphology. Finally, finding the precise and clear-cut mechanisms for transformation of MOCCs to desired nanomaterials is the main challenge in this field. So, the future research should focus on description and explanation of nanomaterial formation mechanisms and finding rules that govern the relation between influential factors and final morphologies. This might be accomplished through purposeful utilization of various MOCPs with different compositions and structural varieties, i.e., 1D, 2D, 3D as well as porous and nonporous structures.

Acknowledgment

This work is funded by the grant NRF-2019R1A5A8080290 of the National Research Foundation of Korea.

References

1. Zapf, P. J.; Haushalter, R. C.; Zubieta, J. *Chem. Commun.* **1997**, *1*, 321–322.
2. Andruh, M.; Branzea, D. G.; Gheorghe, R.; Madalan, A. M. *CrystEngComm* **2009**, *11*, 2571–2584.
3. Zhang, H.; Wang, X.; Zhang, K.; Teo, B. K. *Coord. Chem. Rev.* **1999**, *183*, 157–195.
4. Allendorf, M. D.; Stavila, V. *CrystEngComm* **2015**, *17*, 229–246.
5. Zhang, H.; Wang, X.; Teo, B. K. *J. Am. Chem. Soc.* **1996**, *27*, 11813–11821.
6. Braga, D.; Grepioni, F. *Acc. Chem. Res.* **2000**, *19*, 601–608.
7. Wen, J.; Wilkes, G. L. *Chem. Mater.* **1996**, *14*, 1667–1681.
8. Sellergren, B. *TrAC, Trends Anal. Chem.* **1997**, *1*, 310–320.
9. Gütlich, P.; Garcia, Y.; Woike, T. *Coord. Chem. Rev.* **2001**, *219*, 839–879.
10. Campagna S, Puntoriero F, Nastasi F, Bergamini G, Balzani V. In Photochemistry and Photophysics of Coordination Compounds I 2007 (pp. 117-214). Springer, Berlin, Heidelberg.
11. Geary, W. J. *Coord. Chem. Rev.* **1971**, *1*, 81–122.
12. Jurisson, S.; Berning, D.; Jia, W.; Ma, D. *Chem. Rev.* **1993**, *93*, 1137–1156.
13. Rahman, M. M.; Jamal, A.; Khan, S. B.; Faisal, M. *Biosens. Bioelectron.* **2011**, *28*, 127–134.
14. Bai, J.; Xu, Z.; Zheng, Y.; Yin, H. *Mater. Lett.* **2006**, *60*, 1287–1290.
15. de Respinis, M.; De Temmerman, G.; Tanyeli, I.; van de Sanden, M. C.; Doerner, R. P.; Baldwin, M. J.; van de Krol, R. *ACS Appl. Mater. Interfaces* **2013**, *5*, 7621–7625.
16. Masoomi, M. Y.; Morsali, A. *Coord. Chem. Rev.* **2012**, *256*, 2921–2943 and references therein.
17. Mohammadikish, M. *CrystEngComm* **2014**, *16*, 8020–8026.
18. Ranjbar, M.; Nabitabar, M.; Çelik, Ö.; Yousefi, M. *J. Iran. Chem. Soc.* **2015**, *12*, 551–559.
19. Shirazi, F. S.; Akhbari, K. *Ultrason. Sonochem.* **2016**, *31*, 51–61.
20. Niu, H.; Chen, Q.; Ning, M.; Jia, Y.; Wang, X. *J. Phys. Chem. B* **2004**, *108*, 3996–3999.
21. Bucella, S.; Riello, P.; Scremin, B. F.; Calvelli, P.; Polloni, R.; Speghini, A.; Bettinelli, M. *Opt. Mater.* **2004**, *27*, 249–255.
22. De Santis, G.; Fabbrizzi, L.; Iacopino, D.; Pallavicini, P.; Perotti, A.; Poggi, A. *Inorg. Chem.* **1997**, *36*, 827–832.
23. Gorodetsky, B.; Samachetty, H. D.; Donkers, R. L.; Workentin, M. S.; Branda, N. R. *Angew. Chem. Int. Ed.* **2004**, *43*, 2812–2815.
24. Swiegers, G. F.; Malefetse, T. J. *Chem. Rev.* **2000**, *100*, 3483–3538.
25. Cheon, J.; Zink, J. I. *J. Am. Chem. Soc.* **1997**, *119*, 3838–3839.
26. Gao, F.; Luo, F.; Chen, X.; Yao, W.; Yin, J.; Yao, Z.; Wang, L. *Talanta* **2009**, *80*, 202–206.
27. Mohandes, F.; Salavati-Niasari, M. *Mater. Res. Bull.* **2013**, *48*, 3773–3782.
28. Qiu, X.; Li, L.; Sun, Y.; Kong, X. *Colloids Surf. A* **2016**, *506*, 670–677.
29. Dujardin, E.; Mann, S. *Adv. Mater.* **2004**, *16*, 1125–1129.
30. Yin, W.; Su, J.; Cao, M.; Ni, C.; Cloutier, S. G.; Huang, Z.; Ma, X.; Ren, L.; Hu, C.; Wei, B. *J. Phys. Chem. C* **2009**, *113*, 19493–19499.
31. Dick, K. A.; Deppert, K.; Mårtensson, T.; Mandl, B.; Samuelson, L.; Seifert, W. *Nano Lett.* **2005**, *5*, 761–764.

32. Fard, M. J.; Hayati, P.; Naraghi, H. S.; Tabeie, S. A. *Ultrason. Sonochem.* **2017**, *39*, 129–136.
33. Fard, M. J.; Hayati, P.; Firoozadeh, A.; Janczak, J. *Ultrason. Sonochem.* **2017**, *35*, 502–513.
34. Munteanu, C.; Caldararu, M.; Gingasu, D.; Feder, M.; Diamandescu, L.; Ionescu, N. I. *React. Kinet. Mech. Catal.* **2011**, *104*, 357–368.
35. Siegfried, M. J.; Choi, K. S. *Angew. Chem. Int. Ed.* **2005**, *44*, 3218–3223.
36. Asghar, N.; Mustafa, G.; Yasinzai, M.; Al-Soud, Y. A.; Lieberzeit, P. A.; Latif, U. *Appl. Biochem. Biotechnol.* **2019**, *189*, 1156–1166.
37. Kuznetsov, V. V.; Golyanin, K. E.; Ladygina, Y. S.; Pshenichkina, T. V.; Lyakhov, B. F.; Pokholok, K. V. *Russ. J. Electrochem.* **2015**, *51*, 748–757.
38. Liu, J.; Raveendran, P.; Shervani, Z.; Ikushima, Y.; Hakuta, Y. *Chem. Eur. J.* **2005**, *11*, 1854–1860.
39. Moradi, Z.; Akhbari, K.; Phuruangrat, A.; Costantino, F. *J. Mol. Struct.* **2017**, *1133*, 172–178.
40. Shahabadi, N.; Shiri, F.; Hadidi, S. *Nucleoside Nucleotides Nucleic Acids* **2018**, *37*, 147–168.
41. Mirtamizdoust, B.; Trávníček, Z.; Hanifehpour, Y.; Talemi, P.; Hammud, H.; Joo, S. W. *Ultrason. Sonochem.* **2017**, *34*, 255–261.
42. Hanifehpour, Y.; Mirtamizdoust, B.; Khomami, B.; Woo Joo, S. *Z Anorg. Allg. Chem.* **2015**, *641*, 2466–2472.
43. Mirtamizdoust, B.; Bieńko, D. C.; Hanifehpour, Y.; Tiekink, E. R.; Yilmaz, V. T.; Talemi, P.; Joo, S. W. *J. Inorg. Organomet. Polym. Mater.* **2016**, *26*, 819–828.
44. Mirtamizdoust, B.; Hanifehpour, Y.; Nazari, M.; Assoud, J.; Joo, S. W. *J. Inorg. Organomet. Polym. Mater.* **2017**, *27*, 827–834.
45. Hanifehpour, Y.; Zhou, T.; Mirtamizdoust, B.; Mostaanzadeh, H.; Joo, S. W. *J. Inorg. Organomet. Polym. Mater.* **2017**, *27*, 552–561.
46. Hanifehpour, Y.; Morsali, A.; Mirtamizdoust, B.; Joo, S. W. *J. Mol. Struct.* **2015**, *1079*, 67–73.
47. Mirtamizdoust, B.; Shaabani, B.; Joo, S. W.; Viterbo, D.; Croce, G.; Hanifehpour, Y. *J. Inorg. Organomet. Polym. Mater.* **2012**, *22*, 1397–1403.
48. Hanifehpour, Y.; Mirtamizdoust, B.; Morsali, A.; Joo, S. W. *Ultrason. Sonochem.* **2015**, *23*, 275–281.
49. Hanifehpour, Y.; Mirtamizdoust, B.; Hatami, M.; Khomami, B.; Joo, S. W. *J. Mol. Struct.* **2015**, *1091*, 43–48.
50. Hanifehpour, Y.; Mirtamizdoust, B.; Joo, S. W. *J. Inorg. Organomet. Polym. Mater.* **2012**, *22*, 549–553.
51. Hanifehpour, Y.; Soltani, B.; Mirtamizdoust, B.; Khomami, B.; Joo, S. W. *J. Inorg. Organomet. Polym. Mater.* **2016**, *26*, 335–343.
52. Mirtamizdoust, B.; Ghaedi, M.; Hanifehpour, Y.; Mague, J. T.; Joo, S. W. *Mater. Chem. Phys.* **2016**, *182*, 101–109.
53. Hanifehpour, Y.; Morsali, A.; Mirtamizdoust, B.; Joo, S. W.; Soltani, B. *Ultrason. Sonochem.* **2017**, *37*, 430–435.
54. Hanifehpour, Y.; Mirtamizdoust, B.; Wang, R.; Anbarteh, S.; Joo, S. W. *J. Inorg. Organomet. Polym. Mater.* **2017**, *27*, 1045–1052.

CHAPTER SEVEN

Nano-architectonics for coordination assemblies at interfacial media

Katsuhiko Ariga[a,b,*]

[a]WPI-MANA, National Institute for Materials Science, Tsukuba, Ibaraki, Japan
[b]Department of Advanced Materials Science, Graduate School of Frontier Sciences, The University of Tokyo, Kashiwa, Chiba, Japan
*Corresponding author: e-mail address: ARIGA.Katsuhiko@nims.go.jp

Contents

Abstract

As compared with self-assembly of lipids and surfactants, coordination-based assemblies are conducted through well-defined geometry to produce designable internal nano-structures of the assembled materials. Coordination would be a powerful tool in the nano-architectonics approach for functional materials. Another key term, interface, also has crucial roles in the nano-architectonics approaches. Interfacial environments provide anisotropic media for material associations. From the viewpoints of possible applications such as device usages and dominant contributions of surfaces in nano-sized objects, it is important to investigate fabrication and properties of the coordination assemblies at the interfacial media. In this chapter, fabrication and properties of metal complexes and coordination compounds are reviewed, focusing on their interfacial effects especially in interfacial thin films. Based on this background, some typical examples and recent examples in nano-architectonics for coordination assemblies at interfacial media are shortly introduced in this chapter. The introduced examples are categorized according to interfacial film types: (i) self-assembled monolayer (SAM) method; (ii) Langmuir-Blodgett (LB) technique; (iii) layer-by-layer (LbL) assembly; (iv) lipid bilayer membrane.

Advances in Inorganic Chemistry, Volume 76
ISSN 0898-8838
https://doi.org/10.1016/bs.adioch.2020.03.005

1. Introduction

Although novel methodologies based on information processing[1–4] and theories[5–9] have received much attention, research efforts for material production in organic syntheses,[10–15] polymer syntheses,[16–20] and inorganic material fabrication,[21–27] are continuously required for the development of functional materials. Increasing social demands for energy productions,[28–32] energy storages,[33–37] ecological strategies,[38–42] environmental problems,[43–47] sensing/detection,[48–51] devices,[52–55] and biomedical issues,[56–60] can be mostly solved with developments of functional materials. In addition to intrinsic functions of materials, fine tuning of their structures are often required for high efficiencies and high selectivity.[61–65] Control over nano-level structures within materials become more and more important in material sciences.

As a research field for nano-scale objects, nano-technology is well recognized. Research progress in nano-technology make us to observe and manipulate nanoscale objects such as atoms, molecules, and nanomaterials.[66–70] However, fabrication of large-size objects is not always scope of nano-technology. On the other hand, preparation of large-size objects on the micrometer-scale and even on the visible scale is often handled by other scientific disciplines such as supramolecular chemistry[71–74] and microfabrication.[75–77] Through combining these research fields, a new paradigm for rational preparation of functional materials with sufficient nano-level knowledge has to be established. This important task is taken by an emerging concept, nano-architectonics.[78,79]

The nano-architectonics concept in this meaning was initiated by Masakazu Aono[80] who proposed the nano-architectonics concept as methodology for construction of functional materials from non-units through fusion of research fields including nano-technology, organic chemistry, supramolecular chemistry, microfabrication, and biotechnology. In the nano-architectonics approach, functional materials are synthesized through selection and/or combination of various processes including atom/molecular manipulation, transformation by organic synthesis and catalysis, self-assembly and self-organization, field-induced assembly, microfabrication techniques, and bio-related processes (Fig. 1).[81,82] Unlike construction of objects on macroscopic scales, architectonics on the nanoscale has to take into account unavoidable fluctuations such as thermal fluctuations, statistical uncertainties, and quantum effects. Assemblies and constructions of nano-units have to be done under these

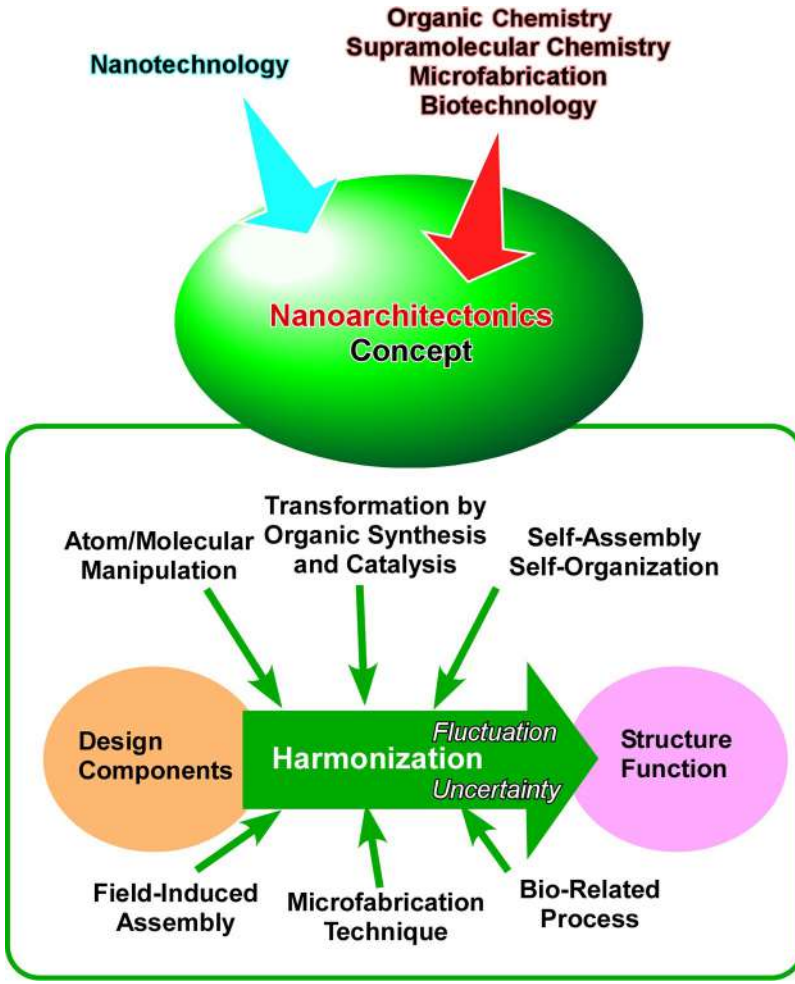

Fig. 1 Outline of the nano-architectonic approach where structures and functions are created through selection and/or combination of various processes including atom/molecular manipulation, transformation by organic synthesis and catalysis, self-assembly and self-organization, field-induced assembly, microfabrication techniques, and bio-related processes.

uncertainties.[83] Therefore, harmonization of various effects and processes is necessary rather than simple summation of the contributed effects.

These features and strategies can be common among many materials. The nano-architectonics concept has been recognized for many research targets including material production,[84,85] structural fabrication,[86,87] catalysts,[88,89] sensing,[90–92] energy applications,[93] environmental issues,[94]

device technology,[95,96] biological research,[97–99] and biomedical application.[100,101] Although many effects are included in various material systems for the nano-architectonics processes, the most important matter would be self-assembly/self-organization. Self-assembly is actually a key player in the nano-architectonics concept.[102] Therefore, developments in self-assembly research would have important influences in on-going evolution of the nano-architectonics concept. In addition to traditional and conventional self-assembly processes,[103–105] novel concepts in self-assembly such as supramolecular polymerization,[106,107] instructed assembly,[108] formation of discrete low-dimensional assemblies,[109] motional synchronization of assembling units,[110] and functional controls upon self-assemblies,[111–113] have been paid much attention in recent research approaches. Inclusion of these trends would promote their development and evolution.

In this chapter, two features are especially focused on for materials nano-architectonics. They are coordination interactions and interfacial environments. Self-assembly based on coordination has several advantages. As compared with self-assembly of lipids and surfactants, coordination-based assemblies are conducted through well-defined geometry to produce designable internal nanostructures of the assembled materials. As seen in metal-organic frame works (MOFs), porous coordination polymers (PCP), and the related nano-porous materials,[114–117] bulk materials integrated with well-defined nano-pore geometries can be synthesized by very simple processes, by mixing of well-selected organic ligands and metal ions. Therefore, coordination would be a powerful tool in the nano-architectonics approach for functional materials.

Another key term, interface, has crucial roles in the nano-architectonic approaches (Fig. 2).[118–120] Interfacial environments provide anisotropic media for material associations. At the liquid-solid interface, molecules dissolved in the solution often precipitate onto the solid surface with forming low-dimensional structures with oriented molecular organization. Similar features can be found in molecular self-assemblies at liquid-liquid interfaces. For example, the liquid-liquid interfacial precipitation method can create many types of fullerene assemblies based on drastic solubility changes of fullerene molecules at interfaces between good and poor solvents.[121] Liquid-liquid interfaces also provide opportunities for materials dissolved in different phases to encounter and form anisotropic thin film structures. Interfacial processes are related with various fabrication procedures of thin films such as self-assembled monolayer (SAM) method, Langmuir-Blodgett (LB) technique, and layer-by-layer (LbL) assembly.

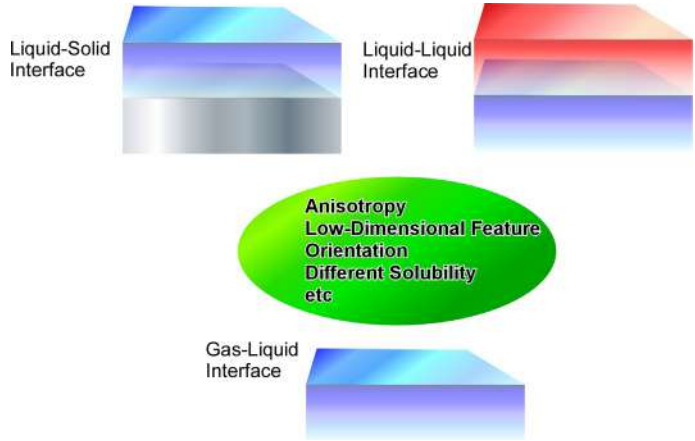

Fig. 2 Various types on interfacial media with their common features.

Based on this background, some typical examples and recent examples in nano-architectonics for coordination assemblies at interfacial media are shortly introduced in this chapter. The introduced examples are categorized according to the interfacial film types: (i) SAM; (ii) LB film; (iii) LbL assembly; (iv) lipid bilayer membrane.

2. General significance of research on coordination assemblies at interfacial media

Various properties of functional molecules and their aggregates, not limited to metal complexes, are often examined in solution systems or crystals.[122–125] In solution, molecules are dispersed by a certain-level of solvation, and influenced by intermolecular interaction from the other molecules are minimized. Properties close to the ideal state may be obtained by analyses of their solutions. In the case of crystals, conformation of molecules and complexes are fixed. Properties in sharp distributions without emotional disturbance can be evaluated. However, these properties might be different from those fixed at interfaces of such device surfaces. Functional molecules such as metal complexes in practical usages are often immobilized as a thin film on interfacial media such as electrodes.[126,127] Properties of functional molecules including coordination complexes in solution and at crystals might be far from those in working devices. We cannot avoid the high possibility that the complexes and molecules exhibit properties completely different from those known in solution and crystals.

Coordination assemblies placed at the interface may have a different energy state than in a bulk isotropic medium where structural factors such as orientation and organization would also affect their functions.

Interfaces are not so simple. There are many factors to alter properties of interfacial coordination assemblies from their isolated states. The interfaces are not only macroscopic visible-sized ones such as an electrode surface, but also an microscopic and nanoscopic interfaces such as a surface of a colloid particle or an inner pore surface of a nano-porous material.[128–130] In the case of bulk materials and macroscopic materials, the percentage of surfaces or interfaces are limited. However, nano-sized objects such as nanoparticles and ultrathin films have huge contributions from surfaces in their properties. As the material size or structural unit becomes nanometer-sized, the proportion of the material exposed to the interface increases dramatically. As a result, the physical properties and functions of the chemical species at the interface become dominant.

From the viewpoint of possible applications such as device usages and dominant contributions of surfaces in nano-sized objects, it is important to investigate the surface properties of the coordination assemblies at the interfacial media. In this chapter, fabrication and properties of metal complexes and coordination compounds are overviewed, focusing on their interfacial effects especially in interfacial thin films. Immobilization methods to immobilize coordination assemblies on the interface are not limited to simple adsorption. According to film types, SAM, LB, LbL, and lipid bilayer membrane, various nano-architectonic factors such as immobilization density, two-dimensional and three-dimensional arrangement, orientation, and anisotropy can be modulated. These characteristics are briefly described in this chapter with classification according to the interfacial film types.

3. Self-assembled monolayer (SAM)

Self-assembled monolayers (SAMs) are excellent strategies for strongly immobilizing functional groups or coordination complexes at the interfacial media such as electrodes (Fig. 3).[131–134] For example, functional species can be covalently immobilized onto various surfaces such as glasses and ITO (indium tin oxide) electrodes through reactions to form siloxane linkages (-O-Si-O-) between surface OH groups on the substrates and alkoxysilane ($-Si(OR)_3$, where R is methyl or ethyl) or chlorosilane ($SiCl_3$) groups of monolayer components. Another driving force to nano-architect stable

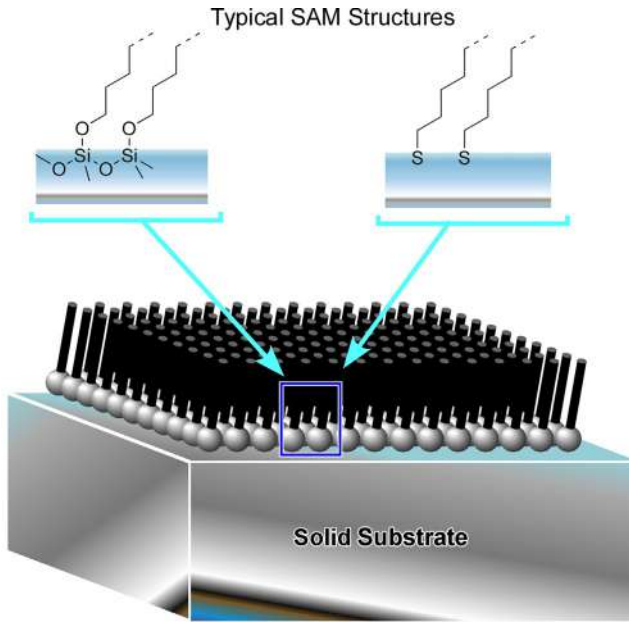

Fig. 3 Self-assembled monolayers (SAMs) with typical monolayer-forming species.

SAM structures is based on strong interaction between metal surfaces and thiol (-SH) and disulfide (-S-S-) groups of the monolayer components.

Not limited to typical alkyl-chain type SAM structures prepared with octadecyltrichlorosilane ($CH_3(CH_2)_{17}SiCl_3$) or dodecanethiol ($CH_3(CH_2)_{11}SH$), various functional molecules including coordination metal complexes attached with silane groups and/or thiol groups can be immobilized on the surfaces as SAM structures. For example, molecules having a specific shape can be precisely adsorbed and arranged as a monolayer on the surface. In some cases, the coordinating functional groups can be precisely attached to the substrate interface. As exemplified in Fig. 4, porphyrin ligands for their metal complex can be precisely embedded on metal surfaces.[135,136] Rotational motions are somewhat allowed between the central porphyrin ring and the phenyl substituents when the porphyrin ligands are in their reduced form. Conversion of the ligands into their oxidized form make the molecules much more inflexible because of double bond formation between the porphyrin ring and the phenyl substituents. Alteration of alkyl groups at phenyl substituents also controls opportunities of hydrogen bonding between hydroxyl groups in

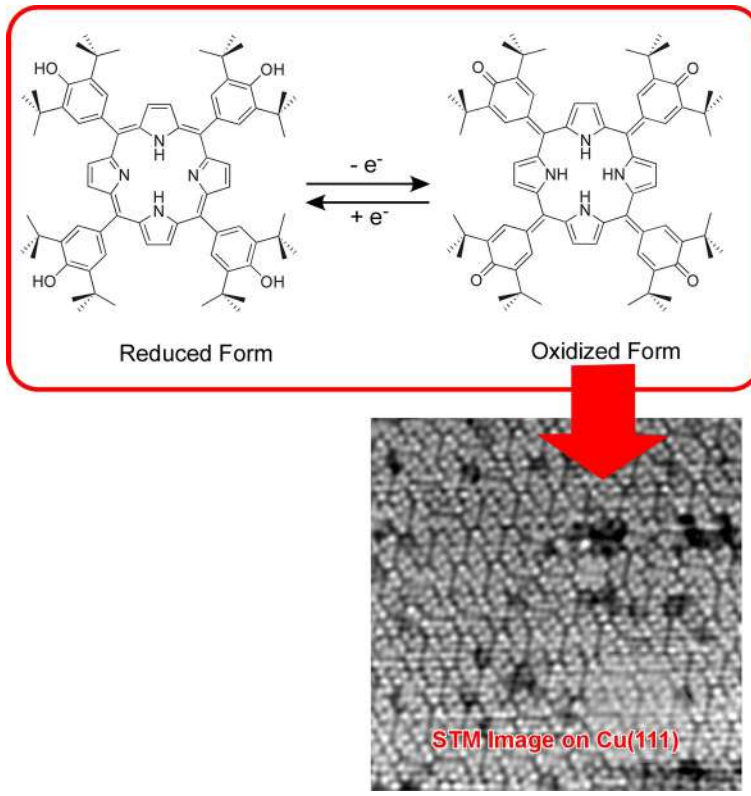

Fig. 4 An example of two-dimensional assembly of porphyrin-type ligand molecules.

their reduced form.[137] Molecular designs and their modifications can regulate two-dimensional arrangements for assemblies of the ligand units for coordination complexes.

Thermal control of the ligand arrangements were also demonstrated (Fig. 5). When these ligand molecules were immobilized on the Cu(111) surface at the sub-monolayer-level, upon vacuum evaporation at low temperatures, the hexagonal array was formed with well packed arrangements. As temperatures are increased, hexagonal phases formed at lower temperatures shifted into square arrangement. This example indicates that the two-dimensional arrangement of porphyrin ligand molecules can be precisely controlled on the surface of metals only by temperature control. These structures and their regulation would lead to molecularly (or even atomically) precise nano-architectonic regulation of coordination assemblies.

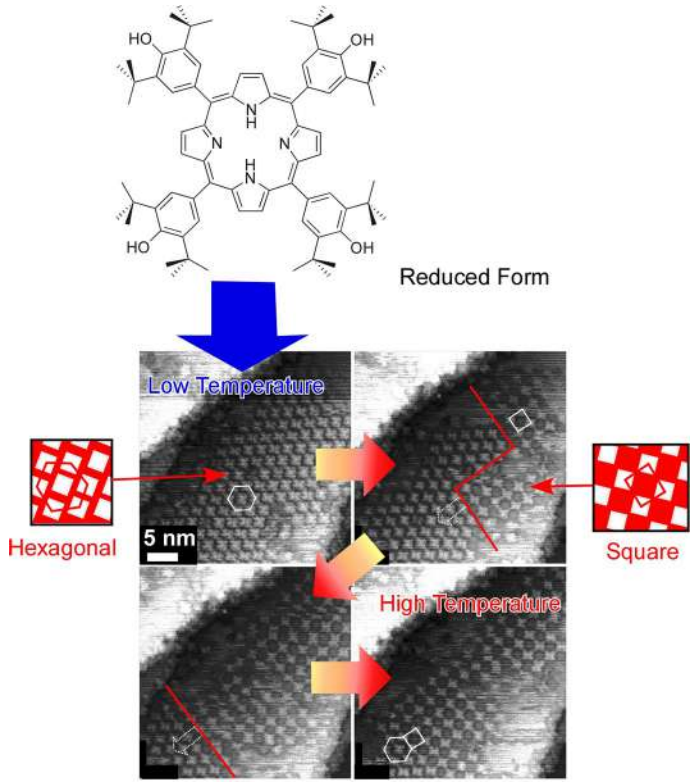

Fig. 5 Thermal control of two-dimensional ligand arrangements on the Cu(111) surface.

4. Langmuir-Blodgett (LB) film

The LB technique is based on formation of a monolayer of basically amphipathic molecules, such as surfactants and lipid molecules at the air-water interface (Fig. 6).[138–140] The formed monolayer is laterally compressed to a well-condensed monolayer film, which can be transferred onto a solid surface in layer-by-layer fashion. Langmuir monolayers have several interesting features.[141] Langmuir monolayers are thin film structures with monomolecular thickness placed at the boundary of two phases with totally different dielectric natures, air phase with low dielectric constant and water phase with high dielectric constant. Therefore, molecules and coordination complexes embedded within Langmuir monolayers often exhibit properties much different from those in bulk water. Another specific point of Langmuir monolayers is high anisotropy with motional freedoms.

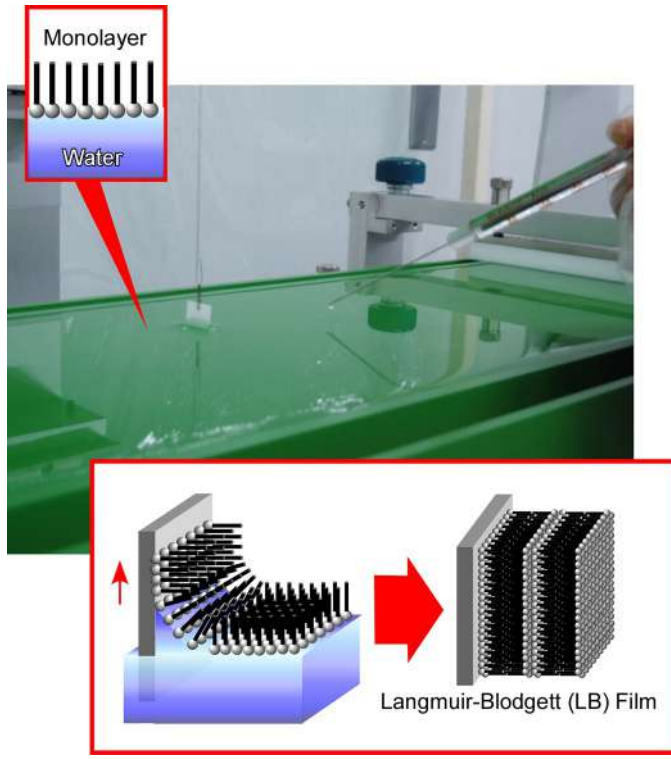

Fig. 6 Outline of Langmuir-Blodgett (LB) method.

In the lateral direction, Langmuir monolayer can be deformed (compression and expansion) in visible size. These macroscopic motions can be reflected to molecular motions and functions within the film of nano-sized thickness direction. Therefore, macroscopic mechanical motions and molecular-level functions can be connected in Langmuir systems.[142–144]

Because Langmuir monolayer systems provide opportunities of contacts between water-insoluble membrane components and aqueous molecules, they are often used for sensing and detection of aqueous biomolecules such as amino acids, peptides, saccharides, nucleobases, and nucleic acids by monolayers of well-designed molecular receptors (Fig. 7).[145,146] The air-water interface is also medium suitable for coordination assembly, where the coordination complex can be formed between a water-insoluble ligand in the monolayer phase and aqueous metal ions. Syntheses of two-dimensional coordination networks and MOF structures have been explored.[147,148]

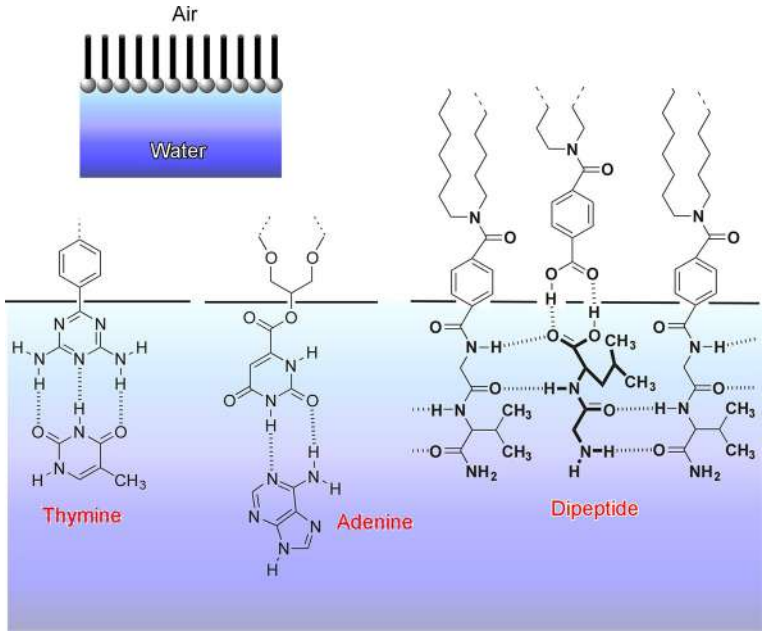

Fig. 7 Examples of biomolecular recognition at the air-water interface.

Talham and coworkers demonstrated the preparation of two-dimensional coordination networks at the air-water interface (Fig. 8).[149] The coordination network structures were prepared through coordination between an amphiphilic pentacyanoferrate complex in the monolayer phase and Ni^{2+} ions from the aqueous phase. Formation of two-dimensional iron-nickel cyanide-bridged network structures were confirmed by various analytical methods including X-ray photoelectron spectroscopy, FT-IR spectroscopy, SQUID magnetometry, X-ray absorption fine structure, and grazing incidence synchrotron X-ray diffraction. Preparation of two-dimensional MOF structures was reported by Makiura et al. (Fig. 9).[150] Multilayer structures of MOF structures were also nano-architected through repeated transfer of the monolayer MOF onto a solid substrate with incorporation of metal-coordinated pyridine molecules. With these structure motifs, a highly ordered and interdigitated MOF sheets can be formed.

Formation of two-dimensional structures by specific reaction, interaction, and coordination, depends highly on molecular interaction capabilities at interfacial media. Such interaction with molecules and ions largely depends on the dielectric environment of the medium. Several interactions such as coordination, electrostatic interaction, and hydrogen bonding are

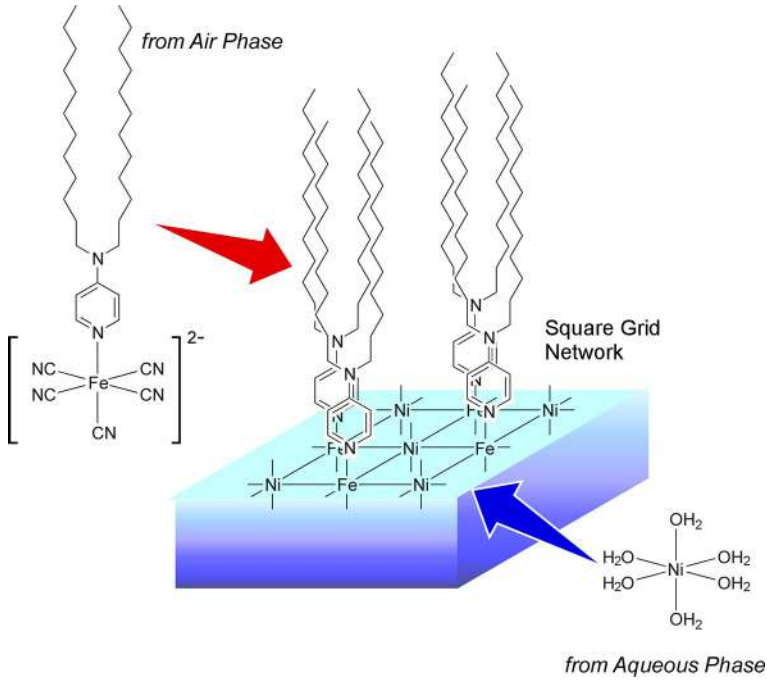

Fig. 8 Two-dimensional iron-nickel cyanide-bridged network structure at the air-water interface prepared through coordination between an amphiphilic pentacyanoferrate complex in the monolayer phase and Ni^{2+} ions from the aqueous phase.

governed with uneven distributions of electronic status such as charged states. In the aqueous phase, stabilization of charged species by hydration significantly decreases efficiencies of such interaction. On the other hand, at the interface with the low dielectric phase, molecular interaction often increases dramatically (Fig. 10)[151] compared to molecular dispersions in water. Theoretical consideration based on quantum chemical calculations, confirmed that the dielectric environment of the vicinity medium can also have significant influences to interactions of molecules embedded at the interfacial media.[152,153]

It is possible to control the optical properties of the metal coordination complex at interfacial boundaries between totally different dielectric media. As shown in Fig. 11, a new concept, so-called submarine emission, has been recently demonstrated by faint positional controls of the coordination complex at the air-water interface.[154] In this case, double-decker platinum complexes are laid as a monomolecular film on the air-water interface. Compression of the monolayer of the double-decker platinum

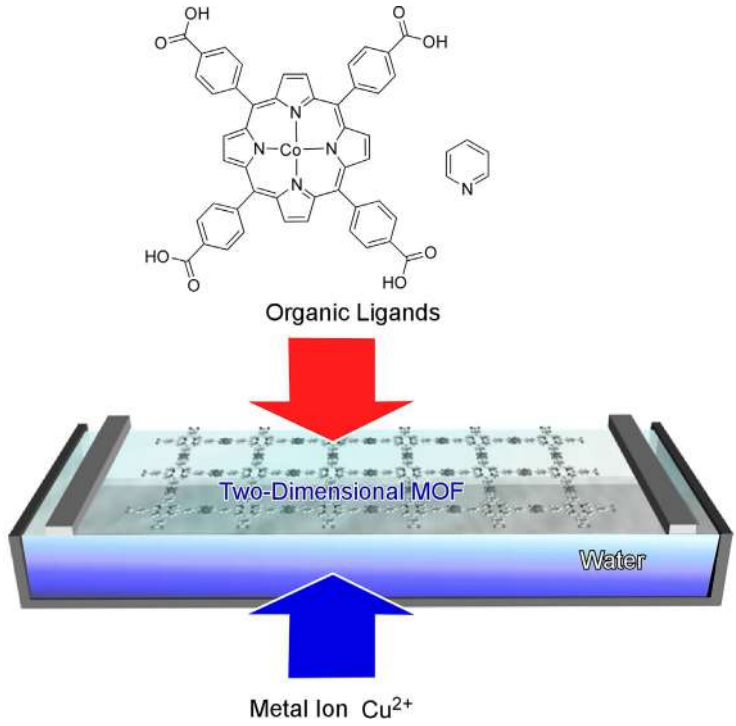

Fig. 9 Preparation of two-dimensional MOF structures at the air-water interface.

complex changes positions of the complexes at the air-water interface accompanied with drastic changes of luminescence emission. Due to the high sensitivity of emission properties on the dielectric nature of surrounding media, floating up of the double-decker platinum complex from the water to the air phase induces a significant increase of luminescence emission. This is called submarine light emission because it emits light when floating on water.

Another characteristic of the Langmuir monolayer, the connection of macroscopic mechanical motions and molecular functions, can be used for operation of molecular machines tuning the molecular receptor structures at the air-water interface.[155] In the case depicted in Fig. 12, monolayer assemblies of molecular receptor, Li^+ complex of cholesterol-armed cyclononane, are laterally compressed at the air-water interface.[156] Mechanical compression induces fine mechanical tuning of the receptor conformations for optimized molecular recognition. By gradually changing the compression state of the monolayers, selective discrimination of uracil

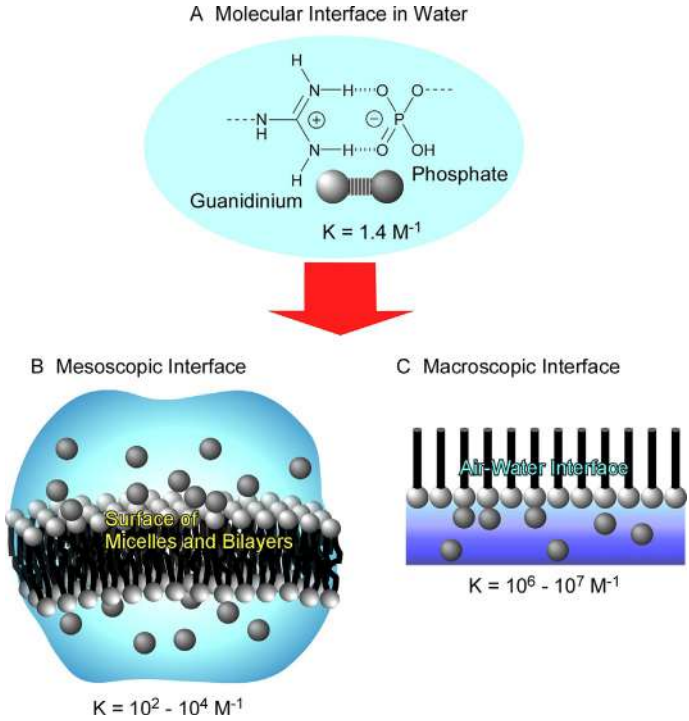

Fig. 10 Binging constant between guanidinium and phosphate with electrostatic hydrogen bonding capability at various interfacial media.

from thymine derivatives was optimized to have about 75 times difference of binding constants between these similar nucleic acid bases, which cannot be discriminated by DNA or RNA.

Because suitable monolayer components in the LB technique usually have lipid-like balanced amphiphilic nature of the hydrophobic part and the hydrophilic part, some coordination metal complexes themselves might not be well used for the LB method. However, application of many coordination complexes to the LB systems becomes possible by mixing them into an appropriate monolayer matrix. As shown in Fig. 13, vitamin B_{12} Co-complex derivatives are successfully incorporated into the matrix of dialkylorganosilane-type monomolecular film at the air-water interface.[157–159] The latter matrix monolayer forms a stable network through formation of siloxane linkages upon reaction of the tri-ethoxysilane group under acidic conditions, which maintains the monolayer structure

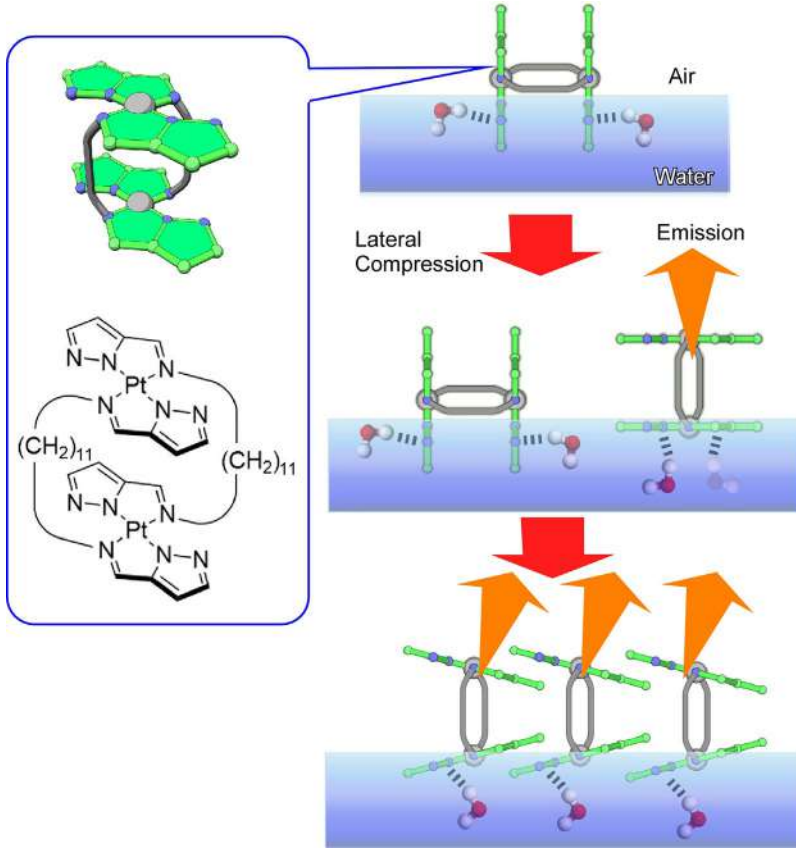

Fig. 11 Submarine emission by weak positional control of the coordination complex at the air-water interface.

even with incorporation of bulky vitamin B_{12} derivatives. The formed monolayers can be transferred to the surface of an ITO electrode and further immobilized through the remaining silanol groups with the surface. Cyclic voltammetry measurements confirmed the electrochemical properties derived from vitamin B_{12} derivatives.

Interfacial medium for the LB method, i.e., the air-water interface, provides environments for contact of components with different solubility to water with enhanced interaction efficiencies. It can be also a place for the association of the organic ligand and the metal ion, creating various coordination assemblies such as two-dimensional coordination polymers and MOF materials.

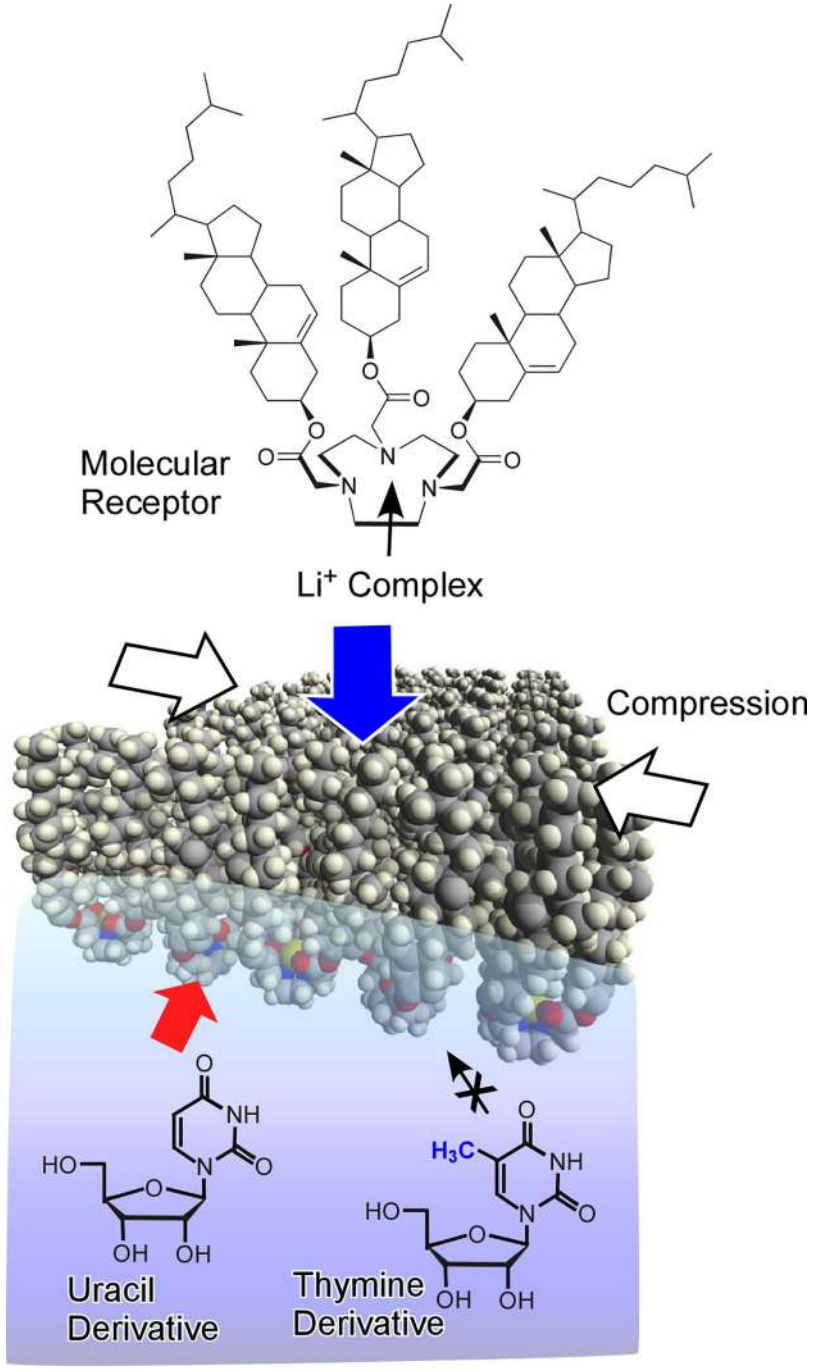

Fig. 12 Selective binding between the uracil and thymine derivatives by monolayer assemblies of the molecular receptor, Li^+ complex of cholesterol-armed cyclononane.

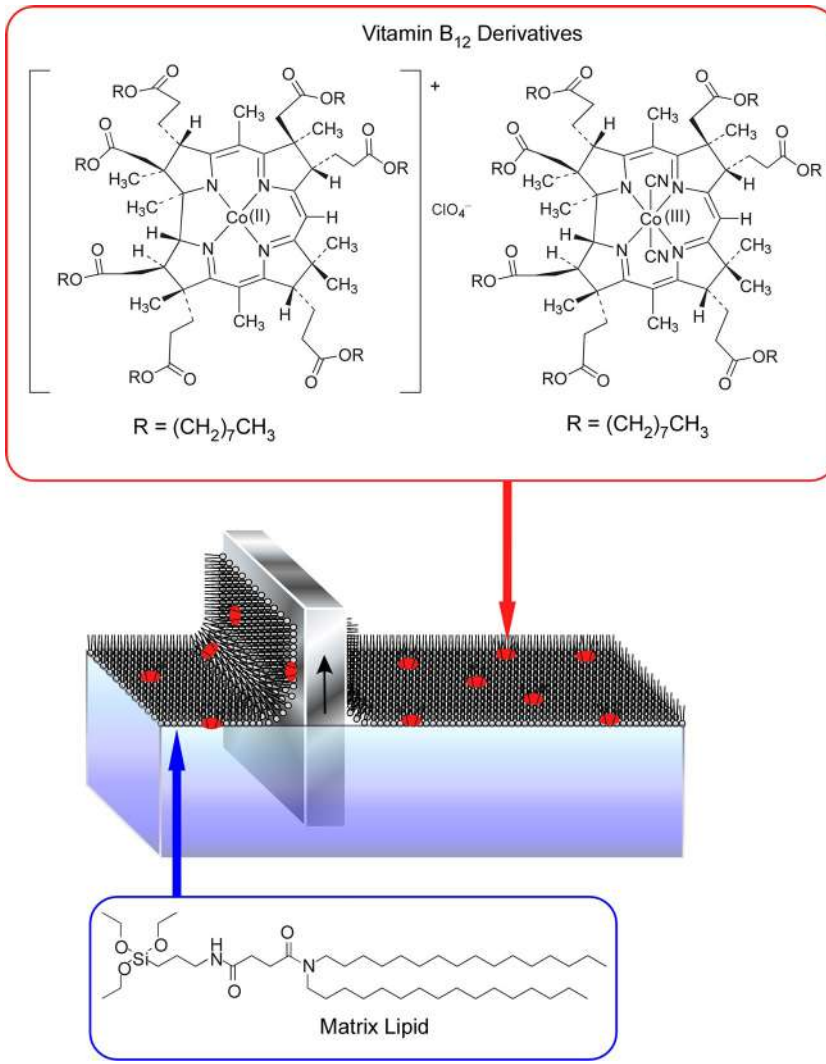

Fig. 13 Vitamin B_{12} Co-complex derivatives incorporated into the matrix of dialkylorganosilane-type mono-molecular film at the air-water interface.

5. Layer-by-layer (LbL) assembly

As a nano-architectonics technique for multilayer structures for a wider range of substances, a layer-by-layer (LbL) assembly is well recognized.[160–162] A typical layer-by-layer method uses electrostatic interaction

as a driving force (Fig. 14). When a solid substrate having a negative charge is immersed in an aqueous solution of a polyelectrolyte having a positive charge, adsorption of positive polyelectrolyte is induced due to electrostatic interaction. Interestingly, the adsorption occurs not only in neutralization but also in excess, and finally reaches charge re-saturation accompanied

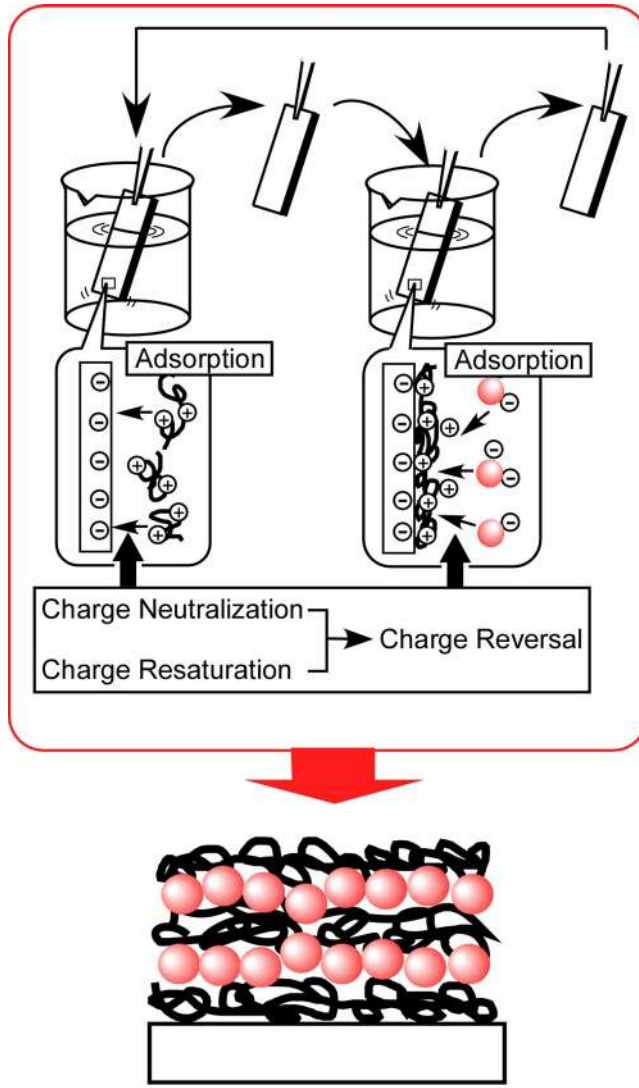

Fig. 14 A typical layer-by-layer (LbL) assembly with electrostatic interaction as a driving force.

by inversion of the surface charge. At this stage, the surface of the films on the solid substrate becomes positive. Further immersion of the substrate with the film into another aqueous solution of a nanoparticle with a negative charge, efficiently induces adsorption of the latter negative nanoparticles with surface charge reversion to negative. This general rule of surface charges in the LbL process enables us to architect multilayer films with desirable thickness and sequences.

One of the pronounced advantages of the LbL assembly is its huge versatility.[163,164] Driving forces for the LbL assembly are not limited to electrostatic interaction. Various interactions including coordination, hydrogen bonding, charge transfer interaction, bio-specific recognition, supramolecular inclusion, sol-gel reaction, and stereo-complex formation can be used for the LbL assembly. This high freedom in assembling mechanisms leads to a wide range of applicability in the component materials including polyelectrolytes, biomolecules such as proteins and DNA, colloid particles, quantum substances, supermolecules, molecular aggregates, and coordination complexes, Assembling processes for the LbL assembly can be done very easily only using beakers and tweezers, while advanced techniques to use automatic machines, spin-coating, and spray coatings have been also proposed.

As mentioned above, coordination interactions are recognized as useful driving forces for the LbL assembly. Mallouk and co-workers used complex formation between phosphoric acid and zirconium ions for the logical assembly of layer-by-layer structures (Fig. 15).[165,166] They initiated this strategy in a very early stage in the history of the LbL assembly, which was carried out historically parallel to the electrostatic LbL assembly by Decher and co-workers.[167,168] The LbL method proposed by Mallouk and co-workers is named as Molecular Beaker Epitaxy to represent the simple nature of this technique.[169] In their method, the SAM structure of a phosphonate-functionalized thiol compound was first anchored on a gold surface. Onto the modified surface, zirconium ions and 1,2-ethanediylbis (phosphonic acid) were adsorbed in layer-by-layer manner. Successful preparation of multilayered structures were confirmed with various analytical methods including X-ray photoelectron spectroscopy, ellipsometry, and electrochemical measurements. It was said that the prepared multi-layered films would have a higher order than the conventional electrostatic LbL films.

Coordination-based LbL assembly have been done by many researchers. For example, Hatzor et al. fabricated multi-layered metal coordination

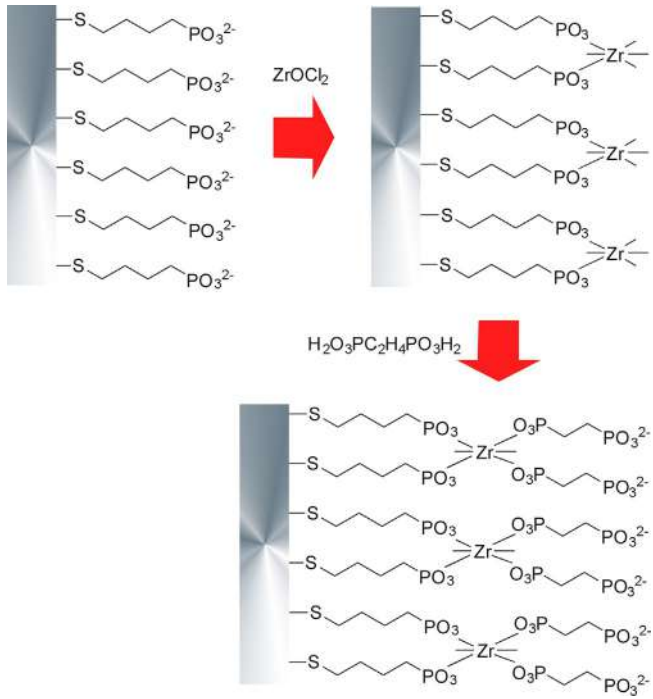

Fig. 15 LbL assembly based on complex-formation between phosphoric acid and zirconium ions.

assemblies using bishydroxamate and phosphonate.[170] These ligands can strongly interact with tetravalent ions such as zirconium. In this case, bishydroxamate groups were immobilized onto a gold surface, first through interaction between disulfide and gold. Ligand molecules with bishydroxamate groups at both ends were assembled in layer-by-layer fashion through interaction with the zirconium ion. Introduction of phosphate layers are possible because both bishydroxamate and phosphonate interact strongly with zirconium ions. These two kinds of ligands have different sensitivity to addition of acids. Therefore, selective peeling of layers becomes possible under selected acidic conditions.

Fabrication of LbL assemblies consist of rigid-rod chromophores connected by terminal pyridine moieties to palladium centers on a siloxane-based template SAM layer was reported by Van der Boom and co-workers (Fig. 16).[171] This LbL assembly was done on the photo-patterned surfaces. Controllability in lateral and vertical directions as well as high freedom of

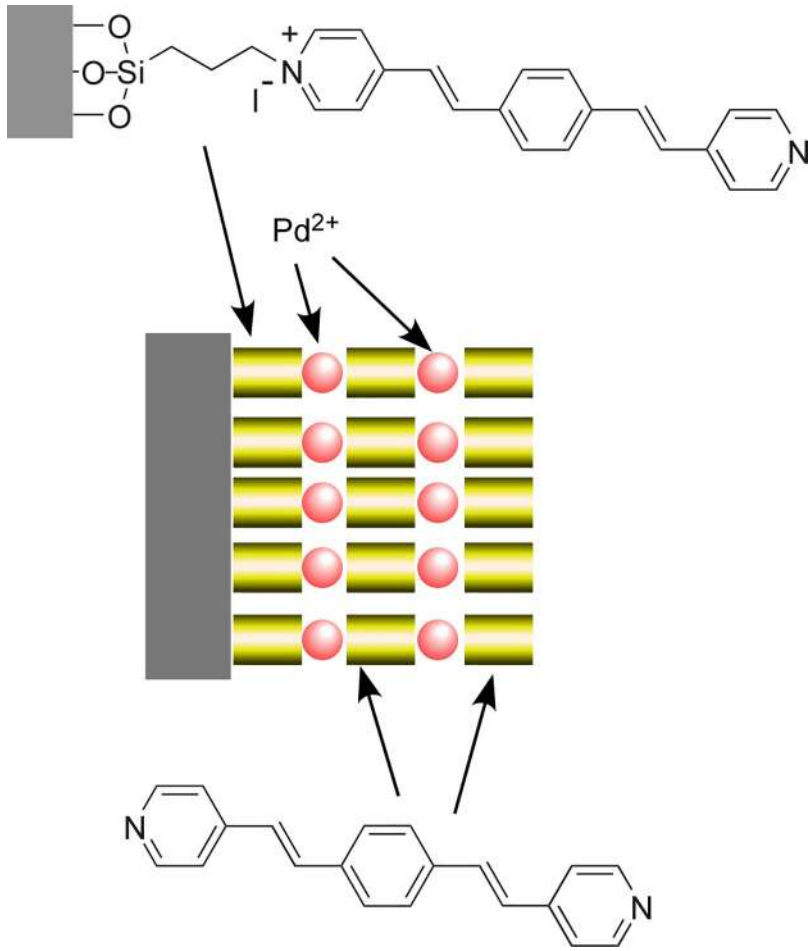

Fig. 16 LbL assemblies consist of rigid-rod chromophores connected by terminal pyridine moieties to palladium centers on a siloxane-based template SAM layer.

chromophore ligands, would be a powerful nano-architectonic strategy to fabricate stable custom-designed three-dimensional layered materials.

Yamauchi and colleagues succeeded in fabricating an LbL thin film in which a coordination polymer and graphene oxide were alternately stacked by a one-pot process.[172] In this process, a lamellar crystal structure is formed by depositing a thin film structure of a coordination polymer comprising nickel and cyano groups on the surface of the graphene oxide nanosheet. The formed LbL structure shows very good electrochemical catalytic activity and high durability against oxygen reduction reaction.

6. Lipid bilayer membrane

Interfacial assemblies are not limited to those on the solid surface. Mesoscopic interfaces formed by lipid bilayer membranes provide mesoscopic-size interfacial environments dispersed in water. Spherical assemblies based on lipid bilayer structures, liposomes and vesicles, have been aggressively used as cell membrane mimics and/or artificial cells.[173–176] These membranes are often used for imitating natural cell functions by immobilizing various functional units including coordination complexes.

In the assembled system on a lipid bilayer membrane, the dynamic change of the metal coordination function can mimic to signal transduction of a biological system (Fig. 17).[177–180] An artificial receptor molecule and a natural enzyme (lactate dehydrogenase, LDH) are immobilized on a lipid bilayer. Two events, coordination of Cu^{2+} to the receptor site and inhibition of enzyme activity by Cu^{2+}, can be balanced depending on addition of external signals. Enzymatic activity of LDH is inhibited by Cu^{2+} that can be entrapped by the artificial receptor. Addition of aldehyde-type signal molecules to the system induces formation of Schiff's base between the aldehyde-type signal and the amine-type receptor. The resulting

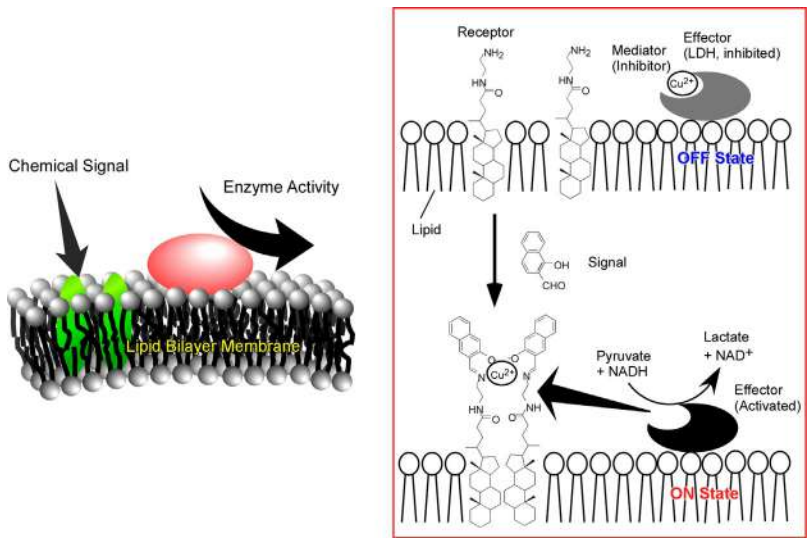

Fig. 17 Mimic of a signal transduction system based on coordination of Cu^{2+} to the receptor site and inhibition of enzyme (lactate dehydrogenase, LDH) activity by Cu^{2+} on lipid bilayer membrane.

Schiff's base structure form coordination with Cu^{2+} and removal of Cu^{2+} from the solution can switch on LDH activity.

Photo-sensitive features can be introduced to this artificial signal transduction systems using an azobenzene-type artificial receptor (Fig. 18). Although the Schiff's base structure formed upon reaction of aldehyde, the chemical signal has the capability of binding to Cu^{2+}, photo-isomerization from trans to cis isomer of the azobenzene moiety significantly suppress binding with Cu^{2+}. As a result, the activity of the enzyme LDH is activated only with appropriate combination of a chemical signal and photo-signal. The demonstrated system with combined regulation of metal ion coordination and enzyme activity can be regarded as an AND-type logic gate. While the system is considered to mimic the signal

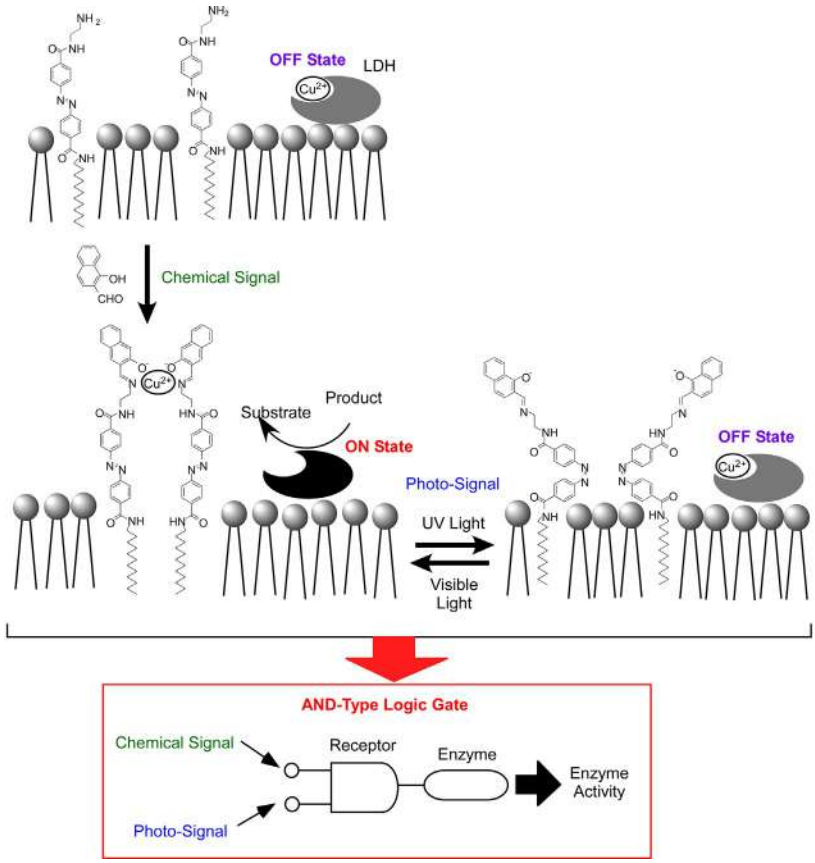

Fig. 18 An AND-type logic gate of artificial signal transduction systems with chemical signal and photo-signal.

transduction system of living organisms, it enables complex information conversion by combining coordination and enzyme inhibition. This nano-architectonic strategy can be connected even with a more advanced concept, molecular computation.

7. Summary and future perspective

In this chapter, the methods for assembling and immobilizing functional molecules including metal complexes at interfaces using various thin film structures, self-assembled monolayers (SAM), Langmuir-Blodgett (LB) films, layer-by-layer (LbL), and lipid bilayer membranes, are outlined. Although the most advanced designs of metal complexes themselves are not completely included in these examples, the basic concept introduced here can be widely applied to various kind of coordination complexes. Especially, nano-architectonic efforts for functional coordination complexes using thin films, surface and interface structures would lead to possibilities of applications including devices and biomedical usages. In addition to their advanced functional features of coordination complexes, some features such as biocompatibility[181] and wet system conjugations[182] would open ways for practical applications.

Acknowledgments

This study was partially supported by the JSPS KAKENHI Grant JP16H06518 (Coordination Asymmetry), and CREST JST Grant JPMJCR1665.

References

1. Zhao, R.; Yan, R.; Chen, Z.; Mao, K.; Wang, P.; Gao, R. X. *Mech. Sys. Sig. Proc.* **2019**, *115*, 213–237.
2. Sumita, M.; Tamura, R.; Homma, K.; Kaneta, C.; Tsuda, K. *Bull. Chem. Soc. Jpn.* **2019**, *92*, 1100–1106.
3. Rajkomar, A.; Dean, J.; Kohane, I. N. *Engl. J. Med.* **2019**, *380*, 1347–1358.
4. Gubaev, K.; Podryabinkin, E. V.; Hart, G. L. W.; Shapeev, A. V. *Comp. Mater. Sci.* **2019**, *156*, 148–156.
5. Saitow, M.; Dutta, A. K.; Neese, F. *Bull. Chem. Soc. Jpn.* **2019**, *92*, 170–174.
6. Hosoya, H. *Bull. Chem. Soc. Jpn.* **2019**, *92*, 205–215.
7. Zhang, S.; Guo, S.; Chen, Z.; Wang, Y.; Gao, H.; Gomez-Herrero, J.; Ares, P.; Zamora, F.; Zhu, Z.; Zeng, H. *Chem. Soc. Rev.* **2018**, *47*, 982–1021.
8. Ozaki, Y. *Bull. Chem. Soc. Jpn.* **2019**, *92*, 629–654.
9. Matubayasi, N. *Bull. Chem. Soc. Jpn.* **2019**, *92*, 1910–1927.
10. Povie, G.; Segawa, Y.; Nishihara, T.; Miyauchi, Y.; Itami, K. *Science* **2017**, *356*, 172–175.
11. Morisaki, Y.; Chujo, Y. *Bull. Chem. Soc. Jpn.* **2019**, *92*, 265–274.
12. Hirai, M.; Tanaka, N.; Sakai, M.; Yamaguchi, S. *Chem. Rev.* **2019**, *119*, 8291–8331.

13. Ohkuma, T.; Kurono, N.; Arai, N. *Bull. Chem. Soc. Jpn.* **2019**, *92*, 475–504.
14. Sun, Z.; Ikemoto, K.; Fukunaga, T. M.; Koretsune, T.; Arita, R.; Sato, S.; Isobe, H. *Science* **2019**, *363*, 151–154.
15. Kawamura, S.; Sodeoka, M. *Bull. Chem. Soc. Jpn.* **2019**, *92*, 1245–1262.
16. Kuwabara, J.; Kanbara, T. *Bull. Chem. Soc. Jpn.* **2019**, *92*, 152–161.
17. Ma, P.; Hu, F.; Wang, J.; Niu, J. *Coord. Chem. Rev.* **2019**, *378*, 281–309.
18. Takata, T. *Bull. Chem. Soc. Jpn.* **2019**, *92*, 409–426.
19. Corrigan, N.; Yeow, J.; Judzewitsch, P.; Xu, J.; Boyer, C. *Angew. Chem. Int. Ed.* **2019**, *58*, 5170–5189.
20. Akagi, K. *Bull. Chem. Soc. Jpn.* **2019**, *92*, 1509–1655.
21. Matsuba, K.; Wang, C.; Saruwatari, K.; Uesusuki, Y.; Akatsuka, K.; Osada, M.; Ebina, Y.; Ma, R.; Sasaki, T. *Sci. Adv.* **2017**, *3, e1700414.*
22. Wang, X.-B.; Jiang, X.-F.; Bando, Y. *Bull. Chem. Soc. Jpn.* **2019**, *92*, 245–263.
23. Niihori, Y.; Yoshida, K.; Hossain, S.; Kurashige, W.; Negishi, Y. *Bull. Chem. Soc. Jpn.* **2019**, *92*, 664–695.
24. Kang, H.; Buchman, J. T.; Rodriguez, R. S.; Ring, H. L.; He, J.; Bantz, K. C.; Haynes, C. L. *Chem. Rev.* **2019**, *119*, 664–699.
25. Imaoka, T.; Yamamoto, K. *Bull. Chem. Soc. Jpn.* **2019**, *92*, 941–948.
26. Ouyang, T.; Ye, Y.-Q.; Wu, C.-Y.; Xiao, K.; Liu, Z.-Q. *Angew. Chem. Int. Ed.* **2019**, *58*, 4923–4928.
27. Kageyama, H.; Yajima, T.; Tsujimoto, Y.; Yamamoto, T.; Tassel, C.; Kobayashi, Y. *Bull. Chem. Soc. Jpn.* **2019**, *92*, 1349–1357.
28. Guo, D.; Shibuya, R.; Akiba, C.; Saji, S.; Kondo, T.; Nakamura, J. *Science* **2016**, *351*, 361–365.
29. Maeda, K.; Mallouk, T. E. *Bull. Chem. Soc. Jpn.* **2019**, *92*, 38–54.
30. Jiang, Q.; Zhao, Y.; Zhang, X.; Yang, X.; Chen, Y.; Chu, Z.; Ye, Q.; Li, X.; Yin, Z.; You, J. *Nat. Photon.* **2019**, *13*, 460–466.
31. Roy, N.; Suzuki, N.; Terashima, C.; Fujishima, A. *Bull. Chem. Soc. Jpn.* **2019**, *92*, 178–192.
32. Fujigaya, T. *Bull. Chem. Soc. Jpn.* **2019**, *92*, 400–408.
33. He, J.; Hartmann, G.; Lee, M.; Hwang, G. S.; Chen, Y.; Manthiram, A. *Energy Environ. Sci.* **2019**, *12*, 344–350.
34. Rao, C. N. R.; Pramoda, K. *Bull. Chem. Soc. Jpn.* **2019**, *92*, 441–468.
35. Ohno, H.; Yoshizawa-Fujita, M.; Kohno, Y. *Bull. Chem. Soc. Jpn.* **2019**, *92*, 852–868.
36. Ma, Y.; Hou, C.; Zhang, H.; Zhang, Q.; Liu, H.; Wu, S.; Guo, Z. *Electrochim. Acta* **2019**, *315*, 114–123.
37. Sengottaiyan, C.; Jayavel, R.; Shrestha, R. G.; Subramani, T.; Maji, S.; Kim, J. H.; Hill, J. P.; Ariga, K.; Shrestha, L. K. *Bull. Chem. Soc. Jpn.* **2019**, *92*, 521–528.
38. Kobayashi, H.; Fukuoka, A. *Bull. Chem. Soc. Jpn.* **2018**, *91*, 29–43.
39. Zhao, H.; Cheng, Y.; Lv, H.; Ji, G.; Du, Y. *Carbon* **2019**, *142*, 245–253.
40. Glotov, A.; Stavitskaya, A.; Chudakov, Y.; Ivanov, E.; Huang, W.; Vinokurov, V.; Zolotukhina, A.; Maximov, A.; Karakhanov, E.; Lvov, Y. *Bull. Chem. Soc. Jpn.* **2019**, *92*, 61–69.
41. Destek, M. A.; Sarkodie, S. *Sci. Total Environ.* **2019**, *650*, 2483–2489.
42. Chen, Z.; Huang, T.; Feng, Y.; Hu, W.; Mao, F.; Zhang, C.; Liu, Y.; Fu, Z. *Bull. Chem. Soc. Jpn.* **2019**, *92*, 1824–1833.
43. Ma, X. E.; Lou, Y.; Chen, J. *Bull. Chem. Soc. Jpn.* **2018**, *91*, 515–522.
44. Gao, Q.; Xu, J.; Bu, X.-H. *Coord. Chem. Rev.* **2019**, *378*, 17–31.
45. Yang, Z.; Asoh, T.-A.; Uyama, H. *Bull. Chem. Soc. Jpn.* **2019**, *92*, 1453–1461.
46. He, C.; Cheng, J.; Zhang, X.; Douthwaite, M.; Pattisson, S.; Hao, Z. *Chem. Rev.* **2019**, *119*, 4471–4568.

47. Jawdat, F. H.; Lin, J.; Dou, S. X.; Park, M.-S.; Nattestad, A.; Kim, J. H. *Bull. Chem. Soc. Jpn.* **2019**, *92*, 2012–2018.
48. Lu, Y.; Biswas, M. C.; Guo, Z.; Jeon, J.-W.; Wujcik, E. K. *Biosens. Bioelectron.* **2019**, *123*, 167–177.
49. Sai-Anand, G.; Sivanesan, A.; Benzigar, M. R.; Singh, G.; Gopalan, A. I.; Baskar, A. V.; Ilbeygi, H.; Ramadass, K.; Kambala, V.; Vinu, A. *Bull. Chem. Soc. Jpn.* **2019**, *92*, 216–244.
50. Kim, J.; Campbell, A. S.; de Avila, B. E. F.; Wang, J. *Nat. Biotechnol.* **2019**, *37*, 389–406.
51. Rodlamul, P.; Tamura, S.; Imanaka, N. *Bull. Chem. Soc. Jpn.* **2019**, *92*, 585–591.
52. Yang, Y.; Gao, W. *Chem. Soc. Rev.* **2019**, *48*, 1465–1491.
53. Kitamori, T. *Bull. Chem. Soc. Jpn.* **2019**, *92*, 469–473.
54. Yamashita, Y.; Tsurumi, J.; Ohno, M.; Fujimoto, R.; Kumagai, S.; Kurosawa, T.; Okamoto, T.; Takeya, J.; Watanabe, S. *Nature* **2019**, *572*, 634–638.
55. Watanabe, Y.; Sasabe, H.; Kido, J. *Bull. Chem. Soc. Jpn.* **2019**, *92*, 716–728.
56. Li, B. L.; Setyawati, M. I.; Chen, L.; Xie, J.; Ariga, K.; Lim, C.-T.; Garaj, S.; Leong, D. T. *ACS Appl. Mater. Interfaces* **2017**, *9*, 15286–15296.
57. Kumar, J.; Liz-Marzan, L. M. *Bull. Chem. Soc. Jpn.* **2019**, *92*, 30–37.
58. Kobayashi, J.; Okano, T. *Bull. Chem. Soc. Jpn.* **2019**, *92*, 817–824.
59. Li, J.; Pu, K. *Chem. Soc. Rev.* **2019**, *48*, 38–71.
60. Tanaka, M.; Kobayashi, S.; Murakami, D.; Aratsu, F.; Kashiwazaki, A.; Hoshiba, T.; Fukushima, K. *Bull. Chem. Soc. Jpn.* **2019**, *92*, 2043–2057.
61. Che, X.; Li, Y.; Qu, Y.; Forrest, S. R. *Nat. Energy* **2018**, *3*, 422–427.
62. Fujita, K. *Bull. Chem. Soc. Jpn.* **2019**, *92*, 344–351.
63. Yamanaka, N.; Hara, T.; Ichikuni, N.; Shimazu, S. *Bull. Chem. Soc. Jpn.* **2019**, *92*, 811–816.
64. Yuan, J.; Zhang, Y.; Zhou, L.; Zhang, G.; Yip, H.-L.; Lau, T.-K.; Lu, X.; Zhu, C.; Peng, H.; Johnson, P. A.; Leclerc, M.; Cao, Y.; Ulanski, J.; Li, Y. *Joule* **2019**, *3*, 1140–1151.
65. Ozaki, M.; Nakaike, Y.; Shimazaki, A.; Jung, M.; Maruyama, N.; Yakumaru, S.; Rafieh, A. I.; Ekanayake, P.; Saito, T.; Shimakawa, Y.; Sasamori, T.; Murata, Y.; Murdey, R.; Wakamiya, A. *Bull. Chem. Soc. Jpn.* **2019**, *92*, 1972–1979.
66. Agawa, H.; Okamoto, T.; Isobe, T.; Nakajima, A.; Matsushita, S. *Bull. Chem. Soc. Jpn.* **2018**, *91*, 405–409.
67. Liu, S.; Zhou, X.; Zhang, H.; Ou, H.; Lam, J. W. Y.; Liu, Y.; Shi, L.; Ding, D.; Tang, B. Z. *J. Am. Chem. Soc.* **2019**, *141*, 5359–5368.
68. Pileni, M. P. *Bull. Chem. Soc. Jpn.* **2019**, *92*, 312–329.
69. Zhu, C.; Espulgar, W. V.; Yoo, W.; Koyama, S.; Dou, X.; Kumanogoh, A.; Tamiya, E.; Takamatsu, H.; Saito, M. *Bull. Chem. Soc. Jpn.* **2019**, *92*, 1834–1839.
70. Kawai, S.; Krejči, O.; Nishiuchi, T.; Sahara, K.; Kodama, T.; Pawlak, R.; Meyer, E.; Kubo, T.; Adam, S.; Foster, A. S. *Sci. Adv.* **2020**, *6*, eaay8913. https://doi.org/10.1126/sciadv.aay8913.
71. Dai, D.; Li, Z.; Yang, J.; Wang, C.; Wu, J.-R.; Wang, Y.; Zhang, D.; Yang, Y.-W. *J. Am. Chem. Soc.* **2019**, *141*, 4756–4763.
72. Kameta, N.; Ding, W. *Bull. Chem. Soc. Jpn.* **2019**, *92*, 1053–1059.
73. Mako, T. L.; Racicot, J. M.; Levine, M. *Chem. Rev.* **2019**, *119*, 322–477.
74. Toyota, S.; Yamamoto, Y.; Wakamatsu, K.; Tsurumaki, E.; Munoz-Castro, A. *Bull. Chem. Soc. Jpn.* **2019**, *92*, 1721–1728.
75. Wang, S.; Xu, J.; Wang, W.; Wang, G.-J. N.; Rastak, R.; Molina-Lopez, F.; Chung, J. W.; Niu, S.; Feig, V. R.; Lopez, J.; Lei, T.; Kwon, S.-K.; Kim, Y.; Foudeh, A. M.; Ehrlich, A.; Gasperini, A.; Yun, Y.; Murmann, B.; Tok, J. B.-H.; Bao, Z. *Nature* **2018**, *555*, 83–88.

76. Li, M.-T.; Liu, M.; Yu, Y.-H.; Li, A.-W.; Sun, H.-B. *Bull. Chem. Soc. Jpn.* **2019**, *92*, 283–289.
77. Chen, C.-Y.; Wang, C.-M.; Liao, W.-S. *Bull. Chem. Soc. Jpn.* **2019**, *92*, 600–607.
78. Ariga, K.; Ji, Q.; Nakanishi, W.; Hill, J. P.; Aono, M. *Mater. Horiz.* **2015**, *2*, 406–413.
79. Ariga, K.; Yamauchi, Y. *Chem. Asian J.* **2020**, *15*, 718–728. https://doi.org/10.1002/asia.202000106R1.
80. Ariga, K.; Ji, Q.; Hill, J. P.; Bando, Y.; Aono, M. *NPG Asia Mater.* **2012**, *4*, *e17*.
81. Ariga, K.; Li, M.; Richards, G. J.; Hill, J. P. *J. Nanosci. Nanotechnol.* **2011**, *11*, 1–13.
82. Ariga, K.; Li, J.; Fei, J.; Ji, Q.; Hill, J. P. *Adv. Mater.* **2016**, *28*, 1251–1286.
83. Aono, M.; Ariga, K. *Adv. Mater.* **2016**, *28*, 989–992.
84. Ariga, K.; Malgras, V.; Ji, Q.; Zakaria, M. B.; Yamauchi, Y. *Coord. Chem. Rev.* **2016**, *320*, 139–152.
85. Ariga, K.; Mori, T.; Kitao, T.; Uemura, T. *Adv. Mater.* **2020**. https://doi.org/10.1002/adma.201905657. (in press).
86. Ramanathan, M.; Shrestha, L. K.; Mori, T.; Ji, Q.; Hill, J. P.; Ariga, K. *Phys. Chem. Chem. Phys.* **2013**, *15*, 10580–10611.
87. Komiyama, M.; Mori, T.; Ariga, K. *Bull. Chem. Soc. Jpn.* **2018**, *91*, 1075–1111.
88. Abe, H.; Liu, J.; Ariga, K. *Mater. Today* **2016**, *19*, 12–18.
89. Komiyama, M.; Ariga, K. *Mol. Catal.* **2019**, *475*, 110492.
90. Ishihara, S.; Labuta, J.; Van Rossom, W.; Ishikawa, D.; Minami, K.; Hill, J. P.; Ariga, K. *Phys. Chem. Chem. Phys.* **2014**, *16*, 9713–9746.
91. Ariga, K.; Makita, T.; Ito, M.; Mori, T.; Watanabe, S.; Takeya, J. *Beilstein J. Nanotechnol.* **2019**, *10*, 2014–2030.
92. Liu, J.; Zhou, H.; Yang, W.; Ariga, K. *Acc. Chem. Res.* **2020**, *53*, 644–653. https://doi.org/10.1021/acs.accounts.9b00612.
93. Kim, J.; Kim, J. H.; Ariga, K. *Joule* **2017**, *1*, 739–768.
94. Ariga, K.; Ishihara, S.; Abe, H.; Li, M.; Hill, J. P. *J. Mater. Chem.* **2012**, *22*, 2369–2377.
95. Ariga, K.; Watanabe, S.; Mori, T.; Takeya, J. *NPG Asia Mater.* **2018**, *10*, 90–106.
96. Ariga, K.; Ito, M.; Mori, T.; Watanabe, S.; Takeya, J. *Nano Today* **2019**, *28*, 100762.
97. Ariga, K.; Leong, D. T.; Mori, T. *Adv. Funct. Mater.* **2018**, *28*, 1702905.
98. Zhao, L.; Zou, Q.; Yan, X. *Bull. Chem. Soc. Jpn.* **2019**, *92*, 70–79.
99. Liang, X.; Li, L.; Tang, J.; Komiyama, M.; Ariga, K. *Bull. Chem. Soc. Jpn.* **2020**, *93*, 581–603. https://doi.org/10.1246/bcsj.20200012.
100. Ariga, K.; Ji, Q.; Mori, T.; Naito, M.; Yamauchi, Y.; Abe, H.; Hill, J. P. *Chem. Soc. Rev.* **2013**, *42*, 6322–6345.
101. Nakanishi, W.; Minami, K.; Shrestha, L. K.; Ji, Q.; Hill, J. P.; Ariga, K. *Nano Today* **2014**, *9*, 378–394.
102. Ariga, K.; Nishikawa, M.; Mori, T.; Takeya, J.; Shrestha, L. K.; Hill, J. P. *Sci. Technol. Adv. Mater.* **2019**, *20*, 51–95.
103. Ariga, K.; Hill, J. P.; Lee, M. V.; Vinu, A.; Charvet, R.; Acharya, S. *Sci. Technol. Adv. Mater.* **2008**, *9, 014109.*
104. Roy, B.; Govindaraju, T. *Bull. Chem. Soc. Jpn.* **2019**, *92*, 1883–1901.
105. Hasegawa, M.; Masahiko, I. *Bull. Chem. Soc. Jpn.* **2020**, *93*, 154–162.
106. Yonamine, Y.; Cervantes-Salguero, K.; Minami, K.; Kawamata, I.; Nakanishi, W.; Hill, J. P.; Murata, S.; Ariga, K. *Phys. Chem. Chem. Phys.* **2016**, *18*, 12576–12581.
107. Dhiman, S.; George, S. J. *Bull. Chem. Soc. Jpn.* **2018**, *91*, 687–699.
108. He, H.; Xu, B. *Bull. Chem. Soc. Jpn.* **2018**, *91*, 900–906.
109. Shimizu, T. *Bull. Chem. Soc. Jpn.* **2018**, *91*, 623–668.
110. Seki, T. *Bull. Chem. Soc. Jpn.* **2018**, *91*, 1026–1057.
111. Hu, Q.; Li, H.; Wang, L.; Gu, H.; Fan, C. *Chem. Rev.* **2019**, *119*, 6459–6506.
112. Fukunaga, K.; Tsutsumi, H.; Mihara, H. *Bull. Chem. Soc. Jpn.* **2019**, *92*, 391–399.
113. Shimizu, T.; Ding, W.; Kameta, N. *Chem. Rev.* **2020**, *120*, 2347–2407.

114. Lustig, W.; Mukherjee, S.; Rudd, N. D.; Desai, A. V.; Li, J.; Ghosh, S. K. *Chem. Soc. Rev.* **2017**, *46*, 3242–3285.
115. Azhar, A.; Li, Y.; Cai, Z.; Zakaria, M. B.; Masud, M. K.; Hossain, M. S. A.; Kim, J.; Zhang, W.; Na, J.; Yamauchi, Y.; Hu, M. *Bull. Chem. Soc. Jpn.* **2019**, *92*, 875–904.
116. Xiao, J.-D.; Jiang, H.-L. *Acc. Chem. Res.* **2019**, *52*, 356–366.
117. Chi, V. N.; Chiang, W.-H.; Wu, K. C.-W. *Bull. Chem. Soc. Jpn.* **2019**, *92*, 1430–1435.
118. Ariga, K.; Lee, M. V.; Mori, T.; Yu, X.-Y.; Hill, J. P. *Adv. Colloid Interface Sci.* **2010**, *154*, 20–29.
119. Ariga, K. *ChemNanoMat* **2016**, *2*, 333–343.
120. Ariga, K.; Ishii, M.; Mori, T. *Curr. Opin. Colloid Interface Sci.* **2019**, *44*, 1–13.
121. Shrestha, L. K.; Ji, Q.; Mori, T.; Miyazawa, K.; Yamauchi, Y.; Hill, J. P.; Ariga, K. *Chem. Asian J.* **2013**, *8*, 1662–1679.
122. Eckhardt, K.; Bon, V.; Getzschmann, J.; Grothe, J.; Wisser, F. M.; Kaskel, S. *Chem. Commun.* **2016**, *52*, 3058–3060.
123. Waclawek, S.; Lutze, H. V.; Grubel, K.; Padil, V. V. T.; Cernik, M.; Dionysiou, D. D. *Chem. Eng. J.* **2017**, *330*, 44–62.
124. Mizuno, A.; Shuku, Y.; Awaga, K. *Bull. Chem. Soc. Jpn.* **2019**, *92*, 1068–1093.
125. Narita, M.; Teraoka, T.; Murafuji, T.; Shiota, Y.; Yoshizawa, K.; Mori, S.; Uno, H.; Kanegawa, S.; Sato, O.; Goto, K.; Tani, F. *Bull. Chem. Soc. Jpn.* **2019**, *92*, 1867–1873.
126. Schreier, M.; Luo, J.; Gao, P.; Moehl, T.; Mayer, M. T.; Gratzel, M. J. *Am. Chem. Soc.* **2016**, *138*, 1938–1946.
127. Furusawa, H.; Ichimura, Y.; Harada, S.; Uematsu, M.; Xue, S.; Nagamine, K.; Tokito, S. *Bull. Chem. Soc. Jpn.* **2018**, *91*, 1020–1025.
128. Shrestha, L. K.; Shrestha, R. G.; Yamauchi, Y.; Hill, J. P.; Nishimura, T.; Miyazawa, K.; Kawai, T.; Okada, S.; Wakabayashi, K.; Ariga, K. *Angew. Chem. Int. Ed.* **2015**, *54*, 951–955.
129. Xia, B. Y.; Yan, Y.; Li, N.; Wu, H.-B.; Lou, X. W.; Wang, X. *Nat. Energy* **2016**, *1*, 15006.
130. Ohata, Y.; Kouchi, T.; Sugaya, T.; Kamebuchi, H.; Tadokoro, M. *Bull. Chem. Soc. Jpn.* **2019**, *92*, 655–660.
131. Zuo, L.; Chen, Q.; De Marco, N.; Hsieh, Y.-T.; Chen, H.; Sun, P.; Chang, S.-Y.; Zhao, H.; Dong, S.; Yang, Y. *Nano Lett.* **2017**, *17*, 269–275.
132. Casalini, S.; Bortolotti, C. A.; Leonardi, F.; Biscarini, F. *Chem. Soc. Rev.* **2017**, *46*, 40–71.
133. Kise, R.; Fukumi, A.; Shioya, N.; Shimoaka, T.; Sonoyama, M.; Amii, H.; Takagi, T.; Kanamori, T.; Eda, K.; Hasegawa, T. *Bull. Chem. Soc. Jpn.* **2019**, *92*, 785–789.
134. Akiyama, T. *Bull. Chem. Soc. Jpn.* **2019**, *92*, 1181–1199.
135. Hill, J. P.; Wakayama, Y.; Schmitt, W.; Tsuruoka, T.; Nakanishi, T.; Zandler, M. L.; McCarty, A. L.; D'Souza, F.; Milgrom, L. R.; Ariga, K. *Chem. Commun.* **2006**, 2320–2322.
136. Hill, J. P.; Wakayama, Y.; Ariga, K. *Phys. Chem. Chem. Phys.* **2006**, *8*, 5034–5037.
137. Hill, J. P.; Wakayama, Y.; Akada, M.; Ariga, K. *J. Phys. Chem. C* **2007**, *111*, 16174–16180.
138. Ariga, K.; Yamauchi, Y.; Mori, T.; Hill, J. P. *Adv. Mater.* **2013**, *25*, 6477–6512.
139. Liu, X.; Riess, J. G.; Krafft, M. P. *Bull. Chem. Soc. Jpn.* **2018**, *91*, 846–857.
140. Yunoki, T.; Kimura, Y.; Fujimori, A. *Bull. Chem. Soc. Jpn.* **2019**, *92*, 1662–1671.
141. Ariga, K.; Mori, T.; Li, J. *Langmuir* **2019**, *35*, 3585–3599.
142. Ariga, K.; Mori, T.; Hill, J. P. *Adv. Mater.* **2012**, *24*, 158–176.
143. Ariga, K.; Mori, T.; Ishihara, S.; Kawakami, K.; Hill, J. P. *Chem. Mater.* **2014**, *26*, 519–532.
144. Ariga, K.; Mori, T.; Nakanishi, W. *Chem. Asian J.* **2018**, *13*, 1266–1278.
145. Ariga, K.; Kunitake, T. *Acc. Chem. Res.* **1998**, *31*, 371–378.

146. Ariga, K.; Ito, H.; Hill, J. P.; Tsukube, H. *Chem. Soc. Rev.* **2012**, *41*, 5800–5835.
147. Sakamoto, R.; Takada, K.; Sun, X.; Pal, T.; Tsukamoto, T.; Phua, E. J. H.; Rapakousiou, A.; Hoshiko, K.; Nishihara, H. *Coord. Chem. Rev.* **2016**, *320*, 118–128.
148. Ariga, K.; Matsumoto, M.; Mori, T.; Shrestha, L. K. *Beilstein J. Nanotechnol.* **2019**, *10*, 1559–1587.
149. Culp, J. T.; Park, J.-H.; Stratakis, D.; Meisel, M. W.; Talham, D. R. *J. Am. Chem. Soc.* **2002**, *124*, 10083–10090.
150. Makiura, R.; Motoyama, S.; Umemura, Y.; Yamanaka, H.; Sakata, O.; Kitagawa, H. *Nat. Mater.* **2010**, *9*, 565–571.
151. Onda, M.; Yoshihara, K.; Koyano, H.; Ariga, K.; Kunitake, T. *J. Am. Chem. Soc.* **1996**, *118*, 8524–8530.
152. Sakurai, M.; Tamagawa, H.; Inoue, Y.; Ariga, K.; Kunitake, T. *J. Phys. Chem. B* **1997**, *101*, 4810–4816.
153. Tamagawa, H.; Sakurai, M.; Inoue, Y.; Ariga, K.; Kunitake, T. *J. Phys. Chem. B* **1997**, *101*, 4817–4825.
154. Adachi, J.; Mori, T.; Inoue, R.; Naito, M.; Le, N. H.-T.; Kawamorita, S.; Hill, J. P.; Naota, T.; Ariga, K. *Chem. Asian J.* **2020**, *15*, 406–414.
155. Ariga, K.; Minami, K.; Ebara, M.; Nakanishi, J. *Polym. J.* **2016**, *48*, 371–389.
156. Mori, T.; Okamoto, K.; Endo, H.; Hill, J. P.; Shinoda, S.; Matsukura, M.; Tsukube, H.; Suzuki, Y.; Kanekiyo, Y.; Ariga, K. *J. Am. Chem. Soc.* **2010**, *132*, 12868–12870.
157. Ariga, K.; Tanaka, K.; Katagiri, K.; Kikuchi, J.-I.; Ohshima, E.; Hisaeda, Y. *Colloid Surf. A* **2000**, *169*, 47–58.
158. Ariga, K.; Tanaka, K.; Katagiri, K.; Kikuchi, J.; Shimakoshi, H.; Ohshima, E.; Hisaeda, Y. *Phys. Chem. Chem. Phys.* **2001**, *3*, 3442–3446.
159. Shimakoshi, H.; Nakazato, A.; Tokunaga, M.; Katagiri, K.; Ariga, K.; Kikuchi, J.; Hisaeda, Y. *Dalton Trans.* **2003**, 2308–2312.
160. Ariga, K.; Yamauchi, Y.; Rydzek, G.; Ji, Q.; Yonamine, Y.; Wu, K. C.-W.; Hill, J. P. *Chem. Lett.* **2014**, *43*, 36–68.
161. Rodrigues, V. C.; Moraes, M. L.; Soares, J. C.; Soares, A. C.; Sanfelice, R.; Deffune, E.; Oliveira, O. N., Jr. *Bull. Chem. Soc. Jpn.* **2018**, *91*, 891–896.
162. Ariga, K.; Ahn, E.; Park, M.; Kim, B.-S. *Chem. Asian J.* **2019**, *14*, 2553–2566.
163. Ariga, K.; Hill, J. P.; Ji, Q. *Phys. Chem. Chem. Phys.* **2007**, *9*, 2319–2340.
164. Rydzek, G.; Ji, Q.; Li, M.; Schaaf, P.; Hill, J. P.; Boulmedais, F.; Ariga, K. *Nano Today* **2015**, *10*, 138–167.
165. Lee, H.; Kepley, L. J.; Hong, H.-G.; Mallouk, T. E. *J. Am. Chem. Soc.* **1988**, *110*, 618–620.
166. Hong, H.-G.; Mallouk, T. E. *Langmuir* **1991**, *7*, 2362–2369.
167. Decher, G.; Hong, J. D. *Maktomol. Chim. Macromol. Symp.* **1991**, *46*, 321–327.
168. Decher, G. *Science* **1997**, *277*, 1232–1237.
169. Keller, S. W.; Kim, H.-N.; Mallouk, T. E. *J. Am. Chem. Soc.* **1994**, *116*, 8817–8818.
170. Hatzor, A.; Moav, T.; Cohen, H.; Matlis, S.; Libman, J.; Vaskevich, A.; Shanzer, A.; Rubinstein, I. *J. Am. Chem. Soc.* **1998**, *120*, 13469–13477.
171. Altman, M.; Shukla, A. D.; Zubkov, T.; Evmeneko, G.; Dutta, P.; van der Boom, M. E. *J. Am. Chem. Soc.* **2006**, *128*, 7374–7382.
172. Zakaria, M. B.; Li, C.; Ji, Q.; Jiang, B.; Tominaka, S.; Ide, Y.; Hill, J. P.; Ariga, K.; Yamauchi, Y. *Angew. Chem. Int. Ed.* **2016**, *55*, 8428–8430.
173. Yang, Y.; Wang, J.; Shigematsu, H.; Xu, W.; Shih, W. M.; Rothman, J. E.; Lin, C. *Nat. Chem.* **2016**, *8*, 476–483.
174. Bulbake, U.; Doppalapudi, S.; Kommineni, N.; Khan, W. *Pharmaceutics* **2017**, *9*, 12.
175. Rodrigues, V. C.; Moraes, M. L.; Soares, J. C.; Souza, A. L.; Soares, A. C.; Oliveira, O. N., Jr.; Goncalves, D. *Bull. Chem. Soc. Jpn.* **2019**, *92*, 847–851.

176. Jackman, J. A.; Ferhan, A. R.; Cho, N.-J. *Bull. Chem. Soc. Jpn.* **2019**, *92*, 1404–1412.
177. Kikuchi, J.; Ariga, K.; Miyazaki, T.; Ikeda, K. *Chem. Lett.* **1999**, 253–254.
178. Kikuchi, J.; Ariga, K.; Ikeda, K. *Chem. Commun.* **1999**, 547–548.
179. Kikuchi, J.; Ariga, K.; Sasaki, Y.; Ikeda, K. *J. Mol. Catal. B-Enzym.* **2001**, *11*, 977–984.
180. Fukuda, K.; Sasaki, Y.; Ariga, K.; Kikuchi, J. *J. Mol. Catal. B-Enzym.* **2001**, *11*, 971–976.
181. Stauss, S.; Honma, I. *Bull. Chem. Soc. Jpn.* **2018**, *91*, 492–505.
182. Nishizawa, M. *Bull. Chem. Soc. Jpn.* **2018**, *91*, 1141–1149.

CHAPTER EIGHT

Mussel inspired self-healing materials: Coordination chemistry of polyphenols

Henrik Birkedal*, Yaqing Chen
Department of Chemistry & iNANO, Aarhus University, Aarhus, Denmark
*Corresponding author: e-mail address: hbirkedal@chem.au.dk

Contents

Abstract

Coordination bonds are most often reversible. Using them to crosslink polymers into for example hydrogels can therefore be expected to result in reversible crosslinks, which in turn provides self-healing properties. Polyphenols such as the catechol group of the special amino acid DOPA (L-3,4-dihydroxyphenylalanine), which is used in mussel byssal threads to form a self-healing coating and for adhesion, are excellent coordinators of hard metal ions like iron(III). We will discuss the use of polyphenols and metal crosslinking to form self-healing hydrogels. We also treat less specific effects of metal ions on hydrogel gel mechanical properties by describing Hofmeister effects of cations on hydrogel rheological properties.

Advances in Inorganic Chemistry, Volume 76
ISSN 0898-8838
https://doi.org/10.1016/bs.adioch.2020.03.006

1. Introduction

Crosslinking of polymers can result in a wide range of advanced materials such as coatings and hydrogels. A multitude of crosslinking mechanisms has been proposed.[1] There is a special interest in materials with the ability to self-heal.[2–5] To this end, reversible crosslinks are needed, i.e., chemical interactions that can reform following damage. Coordination bonds between ligands and metals are especially promising in this regard due to their reversible nature and the potential that coordination bonds can reform very rapidly and without external energy. Coordination chemistry based crosslinking is widespread in many biological systems[6] and self-healing involving metal ions has been observed in several biological systems including bone[7] and mussel byssus threads.[8,9] Especially mussel byssus threads have proven to be an immense source of inspiration in bioinspired materials design, to a large degree due to the fact that this system is one of the best understood advanced, multicomponent biological material.[10–12] The key chemical motif of mussel byssus thread—essential for both self-healing, covalent crosslinking and underwater adhesion—is the special polyphenolic amino acid DOPA (L-3,4-dihydroxyphenylalanine), Fig. 1.[10,13,14] The mussel byssus has a complex architecture with DOPA playing important roles in many aspects of the thread.[10–12,15,16] The byssus is formed in the mussel foot, Fig. 1, by injection molding in a process that is becoming increasingly understood even if some details are still missing.[10,11,17,18] The byssus is in

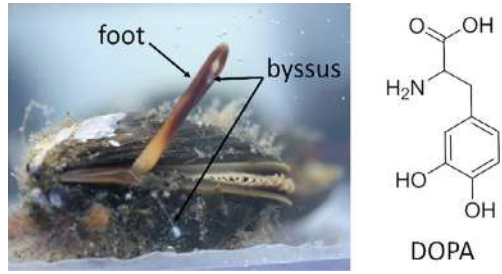

Fig. 1 The blue mussel byssus is a bundle of threads made by injection molding of proteins into a mold made by the mussel foot organ that is caught in the action of making a new byssus thread in this photo. The pH increases dramatically upon release from the acidic conditions in foot cavity to seawater. The amino acid DOPA (L-3,4-dihydroxyphenylalanine) is a key ingredient in the mussel foot proteins and a central component in mussel inspired materials, including self-healing ones based on coordination chemistry.

many species covered by a granular coating that is quite hard, yet very deformable.[9] Using resonance Raman spectro-microscopy, it was shown that the granules contain iron-DOPA tris-complexes that were proposed to be involved in shape-restoration after large deformations.[8]

The catechol moiety of DOPA enables multiple chemical interactions and reactivities[19] as will be discussed in Section 2; with proper control over its functionality it is a versatile and extremely powerful functionality that has rendered it possible to design a multitude of materials. Polyphenols, such as DOPA, are excellent ligands for hard metal ions like for example Fe(III). In this chapter, we will describe our recent advances on developing self-healing hydrogel materials based on polyphenols that we and others have used in conjunction with coordination chemistry to make advanced materials.[20–24]

It should be stressed that other types of coordination chemistry are used for crosslinking in biological systems, especially histidine coordination with zinc or copper. This occurs both in the central part (see below) of mussel byssus threads[25] but also in the jaws of marine polychaete worms. The intertidal bristle worm, *Nereis* sp., has two impressive pincer jaws made from histidine rich proteins crosslinked by zinc coordination chemistry so that the local stiffness is governed by the zinc-induced protein crosslinking.[26–28] The predatory blood-red *Glycera* marine worm has needle sharp jaws that both harbor a copper biomineral (atacamite) and copper coordination-based cross linking of proteins.[26,29,30] These interactions can also be harnessed for self-healing materials design, as recently reviewed by the Harrington group.[25]

2. Catechol chemistry

Polyphenols like the catechol functionality of DOPA have a very rich chemical reactivity.[19–24] Scheme 1 summarizes this reactivity. In the following section, we will refer to the reactions in Scheme 1 by placing the referring letter in parentheses. The catechol itself is involved in equilibria with oxidized forms, semi-quinone (b) and quinone (a); above pH about 8 in air, the conversion to quinone is spontaneous and rapid. The catechol reacts with hard metal ions like iron(III) to form coordination complexes (c) in pH dependent equilibria compounding mono-, bis- and tris-complexes with higher-order catechol coordination at increased pH. Complexes can also be formed with boron (d). The metal coordination is responsible for adhesion to metal surfaces (f).[13] The catechol can also participate in π-π stacking (f), cation-π interactions (e), and hydrogen bonds (h). The quinone is quite

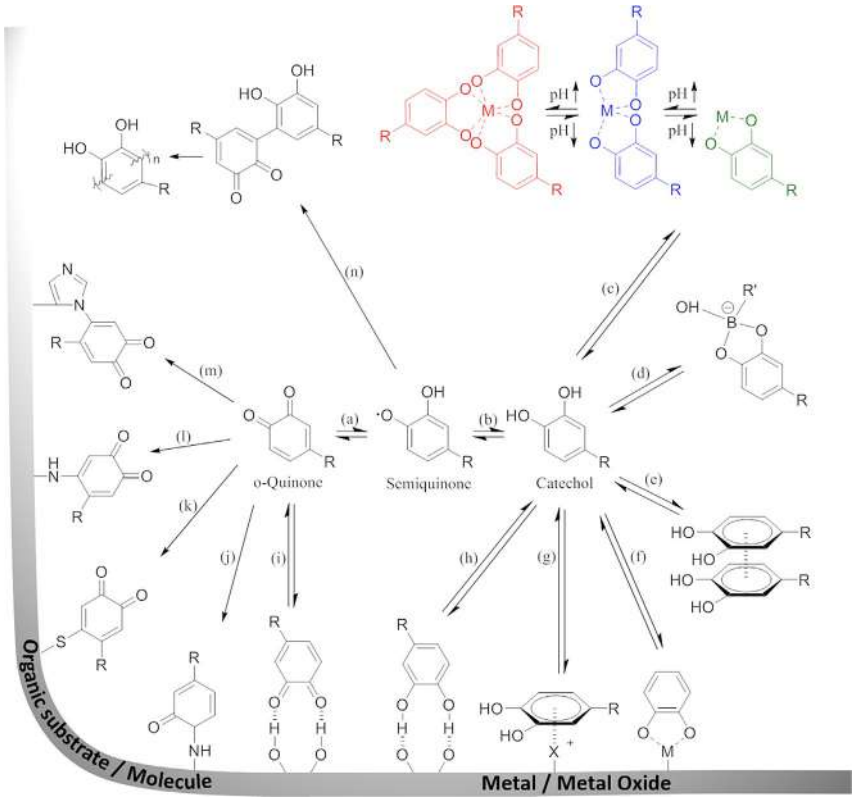

Scheme 1 Summary of the diverse reactivity of catechols. Redrawn with modifications from a figure in Andersen et al.[20] For details, see text.

reactive. It can form hydrogen bonds to surfaces (i) but will typically undergo covalent bond formation if suitable reagents are present. These include amines (j, l) and sulfhydryls (k), but also imidazoles (m) and other catechols (n). This reactivity of the quinone form has on its own given birth to a broad range of materials.[10,19,22,23,31] Herein, our focus will be on the reversible metal coordination bonds (c).[20,21]

3. Self-healing hydrogels based on polyphenols

The first example of coordination-chemistry based hydrogels using polyphenol ligands was by Holten-Andersen et al.[32] The hydrogel was based on a 4-armed PEG (polyethylene glycol) polymer functionalized by boc-protected DOPA, PEG-(*N*-boc-DOPA)$_4$. This molecule was conveniently

made from a central 4-arm PEG functionalized with amines to which *N*-boc-DOPA was coupled using carbodiimide chemistry. The low solubility of Fe(III) in aqueous solution at ambient pH was circumvented by forming mono-complexes at low pH and then increasing pH to the desired level by addition of base. The coordination equilibria were followed using UV-VIS (ultraviolet-visible) spectroscopy exploiting the fact that the mono-, bis- and tris-catecholato iron complexes are green, blue and red, respectively. Mono-complexes dominated up to a pH of 5.5, bis-complexes in the pH range 5.5–9, and tris complexes above pH 9. The complex formation could also be followed by resonance Raman spectroscopy, which is facilitated by the large resonance enhancement of the Raman bands involving metal-ligand vibrations. The concept of initiating complexation at low pH and then driving increased coordination by addition of base emulates the proposed processing of mussel byssi, i.e., a pH change from acidic to basic conditions upon release of the nascent thread from the mussel foot cavity to sea water. The pH increase resulted in a drastic change in the physical behavior. At low pH, the polymer chains remained isolated and the solution was a liquid. Upon increasing pH, the formation of bis- and tris-complexes resulted in increased polymer crosslinking. This gave first a very viscous liquid at pH about 8 and at higher pH, an elastic moldable solid. Thus coordination chemical crosslinking drove a phase change from liquid to solid.

The drastic change in physical properties upon increased coordination crosslinking could be followed by oscillatory rheology. Liquids and solids have very different responses to mechanical load: an ideal liquid has a purely viscous response, where all added mechanical energy is dissipated, whereas an ideal solid will respond elastically following Hook's law. Viscoelastic materials, like hydrogels and byssus threads, will behave somewhere in between depending on the time scale of the chemical interactions binding the material together. Shearing a sample between two plates at varying frequency or amplitude will therefore sample the relative contributions of elastic, storage modulus, G', and dissipative, loss modulus, G'', behavior. A material is a gel, if the elastic modulus exceeds the loss modulus, i.e., $G' > G''$. Oscillatory rheology on the PEG-(*N*-boc-DOPA)$_4$ iron quantified the qualitative observations: liquid behavior at low pH and solid-like behavior at high pH. The obtained storage modulus was significant suggesting that the coordination bonds achieved strengths approaching the lower end of covalent bonds. The rheological behavior of such systems was since systematically explored to reveal how ligand and metal choice can govern the crosslinking dynamics.[33] The gels were also self-healing in

contrast to gels formed by covalent bonds. Covalent gels can be formed easily by oxidizing the catechol to the reactive quinone form using sodium periodate, $NaIO_4$. Such gels were brittle whereas the iron-coordination chemistry based gels regained structural integrity rapidly across the damaged interface.

3.1 Magnetic gels: Incorporating magnetic nanoparticles

Instead of iron-ion crosslinking, nanoparticles can also be used as crosslinkers to form nanoparticle-functionalized gels: the catechol functionalized four arm PEG in the form of PEG-$(dopamine)_4$ (4cPEG) formed the basis of hydrogels containing magnetic nanoparticles to result in magnetically responsive hydrogels with altered rheological properties compared to the iron-ion crosslinked gels.[34] First the authors prepared iron oxide nanoparticles that were stabilized by a linear PEG functionalized at one end by a carboxylate group. Adding 4cPEG to solution containing more than 1 vol% of the iron oxide nanoparticles gave gels by exchange of the surface stabilizing molecules on the nanoparticles by the 4cPEG at pH ~ 4–5 and a temperature of 50 °C. The relaxation behavior of the hydrogels was studied by frequency sweeps in rheology. Analysis of the data afforded effective relaxation spectra that were compared to the behavior observed in covalent gels formed by oxidative crosslinking with sodium periodate and with iron-ion crosslinked gels. The relaxation spectra of the covalent gels displayed little scale dependence whereas that of ion-linked gels had strongly time-dependent crosslinking dynamics. The nanoparticle gels were intermediate between the covalent and ion-crosslinked gels. Contrary to covalent gels, they retained self-healing properties. These gels were interesting not only because they revealed new aspects of the complex rheological properties of these hydrogels but also because of their magnetic properties obtained from the nano-scale coordination chemistry between the polymers and iron oxide nanoparticles.

Magnetic hydrogels were obtained in a similar approach using catechol functionalized chitosan (see also Section 3.3). The gels were formed by reaction of the catechol functionalized chitosan polymer (0.5 wt%) in 15% acetic acid with 1 mL of 0.1 or 1 equivalent of nanoparticles to catechol. The mechanical properties of the resulting nanocomposite were analyzed by nano-indentation. Incorporation of the nanoparticles gave stiffer hydrogels. The hydrogels retained the superparamagnetic magnetic response of the nanoparticles and macroscopic hydrogel pieces could be attracted to a magnet.[35]

The same concept of catechol binding to iron oxide nanoparticles was used to make ultra-light-weight iron oxide/carbon frameworks.[36] The frameworks only had a density of 4 mg cm^{-3} and were made by sintering polyurethane sponges grafted with polyacrylic acid that had been dipped in ferric iron solutions. The resulting magnetic frameworks were coated by nitrocatechol-functionalized chitosan. Interestingly, the coating process resulting in self-healing ultra-light-weight frameworks presumably by interaction between the iron oxide nanoparticles and the catechol bearing biopolymer.[36]

3.2 Closer to biology: Amine rich polymers

We then designed polymer models incorporating more of the chemical moieties of the mussel byssus thread.[37,38] The mussel foot proteins (MFPs) are rich in lysine and DOPA.[10,11] We hypothesized that employing an amine rich polymer in hydrogel design would lead to a change in pH behavior, because the polymer itself becomes pH responsive and has reduced electrostatic self-repulsion as the pH reaches and exceeds the pK_a of the amine groups on the polymer. We first synthesized *g*-DOPA-polyallylamine, Scheme 2, with a grafting density of 9.5% using polyallylamine with a M_W (molecular weight) of 120–200 kg/mol.[38] We used DOPA to ensure that the total number of free amines remained unchanged so that the polymer charge remained constant. We then formed hydrogels by forming coordination bonds with iron(III). As in the case of PEG-(*N*-boc-DOPA)$_4$, complexation was easily controlled by pH. The mono-, bis- and tris-complexes were found by UV-VIS spectroscopy to dominate below pH 5, pH 5–10.8 and above pH 10.8, respectively, as illustrated in Fig. 2A. The minor variation in the pH ranges for each complex resulted from changes in the polymer environment. At the lowest pH values, below about 2.5, the mono-complexes were not fully formed, reflected in a

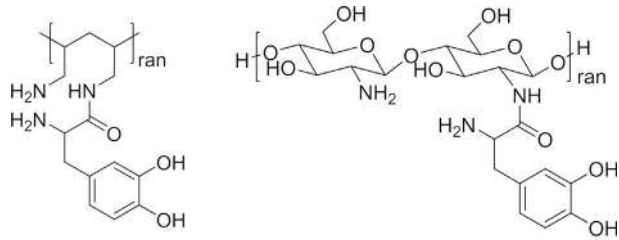

Scheme 2 DOPA-grafted amine rich polymers: *g*-DOPA-polyallylamine and *g*-DOPA-chitosan.

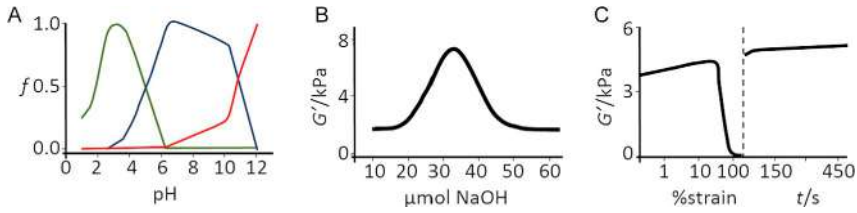

Fig. 2 Coordination chemistry and self-healing behavior of *g*-DOPA-polyallylamine crosslinked with Fe(III). (A) Speciation determined by UV-VIS spectroscopy. Green, blue, red show the fraction of mono-, bis-, and tris-catecholato-iron(III) complexes as a function of pH, respectively. (B) Shear storage modulus as a function of pH given as the amount of base added. The maximum in the curve occurs at pH 9.3 while the left and right hand side of the plot are pH 4 and 12, respectively. (C) Self-healing behavior probed by oscillatory rheology for a gel at pH 9. The sample was subjected to increasing shear strain at a frequency of 1 s^{-1}. After the maximum applied strain, indicated by the vertical dashed line, the healing was monitored at 1% strain, 1 s^{-1} frequency. The stiffness recovered almost fully within the time resolution of the experiment. Data redrawn from results originally presented by Krogsgaard et al.[38]

mono-complex fraction below 1 in Fig. 2A. This was explained as resulting from coordination inhibition between the highly charged polymer and the highly charged iron(III) ion below the pH generated by the free iron(III) ion.

We made gels with a DOPA:Fe molar ratio of 3:1. At a polymer weight fraction of 15 wt% (150 g/L), the storage moduli were in the kPa range. Upon addition of base to the acidic starting solution, the storage modulus rose sharply, Fig. 2B, reflecting the increased crosslinking induced by the shift from mono- to bis- to tris-complexes. Above pH 9.3, the storage modulus started decline with pH in spite of increased coordination chemical crosslinking. At this pH value, the polyallylamine polymer is half-way to charge neutrality and the free unfunctionalized polymer was found to undergo a structural transition from an extended to a more compact structure as revealed by small angle X-ray scattering. The gels had excellent self-healing properties as illustrated in Fig. 2C. In this oscillatory rheology experiment, the sample was subjected to increasing strain at a constant frequency. Above a threshold strain, the gel lost its storage modulus and was purely dissipative reflecting that the crosslinks holding the gel together had been broken. After deforming to 100% strain, the strain was returned to 1% strain and the storage modulus was followed. The storage modulus was essentially fully recovered within the time resolution of the measurement, Fig. 2C, reflecting the very rapid reformation of cohesive coordination crosslinks.

3.2.1 Changing metal ions—Gel strength and catechol oxidation

Polyphenols coordinate many metal ions very well. Based on the gel formation mechanism described above, one would expect that changing the coordination chemistry by changing the metal from iron to metals with different metal-catechol binding constants should afford self-healing hydrogels with different maximum storage moduli depending on the choice of metal. We therefore synthesized hydrogels with Al(III), Ga(III) or In(III) chlorides as the metal source with the rationale that going down group III should result in progressive less cross-linked gels due to the lower propensity of the metal to form catechol complexes.[37] This was indeed observed; the maximum storage modulus fell from Al(III) (18.5 kPa) over Ga(III) (13 kPa) to In(III) (12 kPa) whereas the pH of maximum crosslinking was almost unchanged at pH 8.8, 8.1 and 8.5, respectively. Secondly, these metals are not redox active unlike Fe(III) that in some cases can oxidize catechols even under moderate acidic conditions.[39] Thus we showed that solutions of *g*-DOPA-polyallylamine remained colorless at pH 12 as long as oxygen was kept away; simple purging with nitrogen gas was sufficient to ensure this. In the presence of oxygen, catechol oxidation could be rescued under basic conditions using ascorbic acid as antioxidant.

An additional advantage of using these main group metals to form gels is their lack of electrons in *d*-valence orbitals meaning that their catecholato-complexes are uncolored in stark contrast to the deep, almost black, color of the corresponding Fe(III) tris-coordination complex hydrogels. Characterizing the degree of catechol coordination—mono, bis, or tris—is in turn challenging for these systems since there are, e.g., no facile UV-VIS spectral signatures. Therefore, we used gallium EXAFS spectroscopy. The analysis was complicated by the fact that sensitivity to the second coordination sphere is needed because the first coordination sphere is oxygen with almost constant bond distance at all pH as the complexes at low pH are mixed catecholato/aqua complexes:

$$M(OH_2)_4cat \underset{\leftarrow}{\rightarrow} M(OH_2)_2cat_2 \underset{\leftarrow}{\rightarrow} Mcat_3,$$

where cat represents the catechol. This means that the dominant contribution to the EXAFS signal coming from the first coordination sphere almost does not change with pH. Nevertheless, changes in the radial distance distribution reflecting the carbon atoms from bis and tris complexes could be detected, which is consistent with the expected coordination chemistry based crosslinking mechanism.

3.2.2 Changing the backbone polymer

To further explore the impact of the polymer design on the pH dependent properties of the self-healing hydrogels, we synthesized *g*-DOPA-chitosan, Scheme 2. Chitosan is derived from the biopolymer chitin, which is highly ordered and difficult to work with. As shown by other authors, notably the Lee group, grafting chitosan with DOPA drastically improves solubility and process-ability of chitosan to make it a versatile and very useful material.[31,40] The amine group on chitosan has a significantly lower pK_a value than that of polyallylamine, about 6.7 rather than ca. 9.5. As a consequence, we observed a shift to lower pH values in the maximum storage modulus in hydrogels formed from *g*-DOPA-chitosan with a grafting ratio of 3.3% crosslinked by Fe(III) in a 3:1 DOPA:Fe(III) ratio.

3.3 Crabs and mussels: Double network and double crosslinked hydrogels based on chitosan and catechol chemistry

Hydrogels are formed by crosslinked chemical networks. Having two types of crosslinks results in double crosslink hydrogels (DC). Such hydrogels display altered rheological properties due to the presence of crosslinks at two different time scales as illustrated elegantly for coordination chemical crosslinks by Holten-Andersen and coworkers.[33,41] It has been proposed that hydrogel toughness can be improved by having two interpenetrating hydrogel networks, that is to form double network (DN) hydrogels.[42] For optimal properties, one network should be highly crosslinked with stiff crosslinks, while the other network should be loosely crosslinked and in consequence soft and ductile. Thus the first network provides high stiffness while the second affords energy dissipation and therefore toughness. DN hydrogels have provided promising mechanical properties.[43–45] Introducing self-healing crosslinks in the first network via adamantane/cyclodextrine host-guest chemistry improved hysteresis properties during the first loading cycle, which has otherwise been a problem.[46] This work also showed that some level of covalent crosslinks between the two networks can improve the mechanical performance.

We wished to obtain tough hydrogels that at the same time were stiff and could be made by injection.[47] To this end we explored the *g*-DOPA-chitosan described above, here with a grafting density of 5.1%. The hydrogel design is illustrated in Fig. 3. Chitosan can be covalently crosslinked by the reagent genipin. Thereby, DC hydrogels were simply formed by mixing iron, *g*-DOPA-chitosan and genipin. Adding genipin

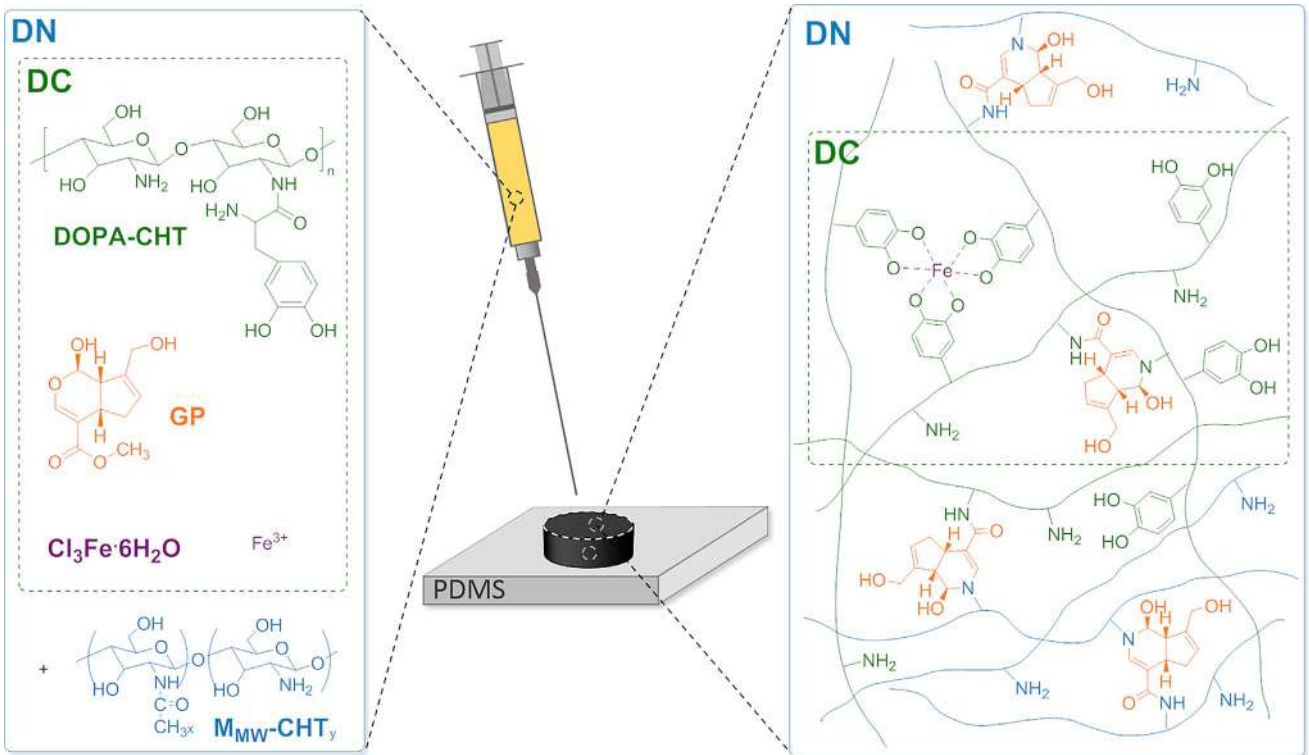

Fig. 3 Tough double crosslink (DC) and double network (DN) hydrogels. The DC hydrogel is based on *g*-DOPA-chitosan crosslinked by Fe(III) coordination chemistry and genipin covalent crosslinks. Further addition of another chitosan (M_{MW}-CHT in blue) afforded DN hydrogels with superior properties.[47]

Table 1 Mechanical properties of chitosan based hydrogels crosslinked with genipin (GP) and/or through Fe(III) coordination crosslinks, see also Fig. 3.

Hydrogel	*E*/kPa	ε/percent	Strength/MPa
Single covalent network, GP crosslinked	16.6	48	~0.1
Single coordination network, Fe(III) crosslinked *g*-DOPA-chitosan	1.6	≤90%	0.9
Double crosslink hydrogel	28.5	≤90%	1.1
Double network hydrogel	49.6	≤90%	2.5

Data measured at 37 °C.[47]

to chitosan alone affords covalently crosslinked hydrogels. Therefore, we synthesized DN hydrogels by adding an additional higher molecular weight, but not DOPA functionalized, chitosan, to the *g*-DOPA-chitosan solution. Hydrogels pucks were formed by injection into PDMS molds (Fig. 3).

The mechanical properties of the gels were compared in compression and the results are summarized in Table 1. The covalent genipin crosslinked gel was stiff and brittle while the coordination chemistry crosslinked gel was ductile, had much higher compressibility and almost an order of magnitude higher compressive strength. The double crosslinked gel combined the features of both: high stiffness, high compressibility and strength. However, replacing just 10% of the *g*-DOPA-chitosan with medium molecular weight chitosan (M_{MW}-CHT, Fig. 3) gave drastically improved properties: while retaining compressibility, the stiffness increased 1.74-fold and the strength more than doubled (Table 1) proving that the DN hydrogel indeed had superior properties.

The differences in mechanical properties were further explored in cyclic compressibility tests where the gels were cyclically compressed to 50% and back. The behaviors of the gels were very different. DN gels recovered their shape fully while the single network gels did not. Additionally, mechanical measurements (displacement, load curves) showed that DN gels had an opened hysteresis loop reflecting a significant dissipation mechanism and toughness introduced by the DN design. Self-healing was demonstrated by cutting gels with a blade; full recovery was observed for the DN hydrogels within 5 min.

The DN hydrogels thus formed showed promising capabilities for potential biomedical applications. Hydrogels could be made injectable by a double syringe design where one syringe contained the chitosans and genipin while the other contained Fe(III). The fast formation (on a second time scale) of coordination crosslinks meant that injection of the solutions into spaces or molds quickly set into DN hydrogels. The biocompatibility of the gels was tested on 1 d old hydrogels on which ATDC5 cells were seeded. After 7 d incubation, the cell viability was investigated. It was higher for DN hydrogels (91%) than single network hydrogels or coordination chemistry only hydrogels (about 88%).

The DN hydrogels thus combined injectability, high toughness, self-healing and good biocompatibility processes and indicate that such hydrogels may become useful in applications requiring high toughness, including possibly even biomedical ones.

3.4 Deconstructed hydrogel design: Self-healing hydrogels from supramolecular interactions between polyphenol-metal coordination polymers and polyallylamine

The hydrogels discussed above result from coordination chemical crosslinking of polymers to formed crosslinked polymer networks. Evidently, other chemical interactions, for example supramolecular ones, can form hydrogels as in protein folding driving networks known from gelatin. We hypothesized that it should also be possible to form hydrogels by having two polymers interact supra-molecularly where one of the polymers was formed by crosslinking polyphenols into coordination polymers in situ. To this end, we required multivalent polyphenol bearing molecules. Tannic acid is one such molecule, Scheme 3. Tannic acid is a multivalent polyphenol, where pyrogallol groups decorate a central sugar group in a manner akin to dendrimers. Like catechols, pyrogallol groups can undergo coordination chemistry and/or oxidative coupling reactions, Scheme 3. Tannic acid and analogous molecules are known from plants and were first suggested by Messersmith and coworkers to be useful in coating formation akin to the use of dopamine.[48] It was then proposed by Caruso and coworkers that one can form coordination chemical shells using a variety of metal ions that bind tannic acid into shells on sacrificial templates.[49,50]

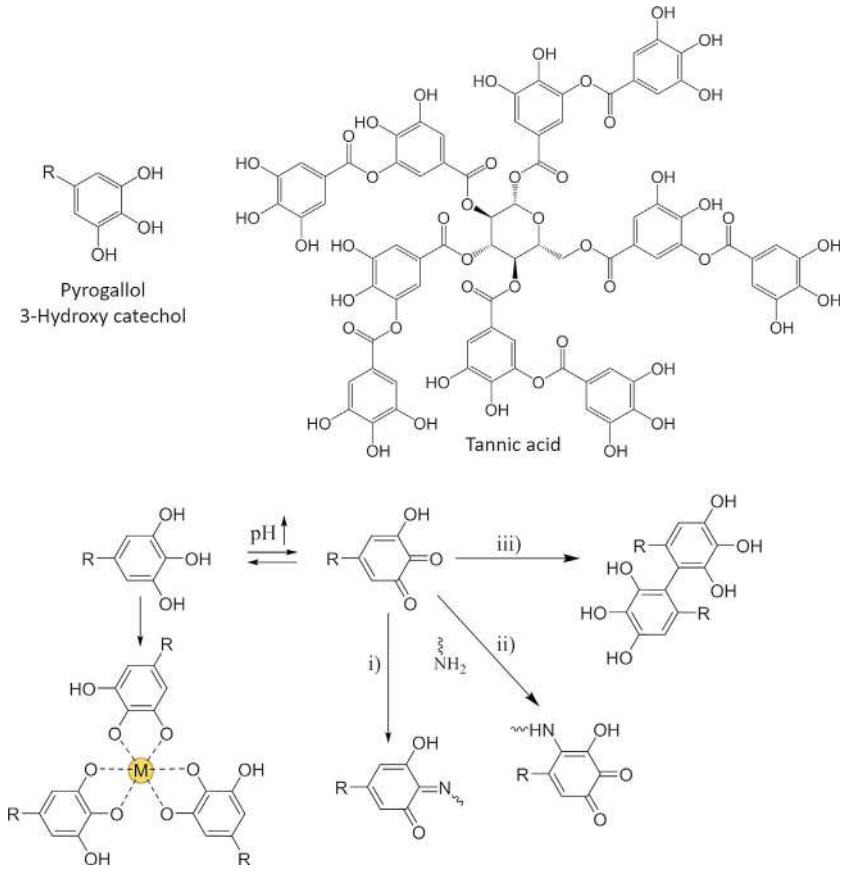

Scheme 3 Pyrogallol groups are very useful polyphenols, for example, in the form of tannic acid. Like catechols (Scheme 1) pyrogallols can form coordination bonds (here, only a tris complex is shown) and undergo oxidative crosslinking, most notably with amines as used in the text.

We instead made coordination polymers of tannic acid with Fe(III) or Al(III) that formed supramolecular hydrogels with polyallylamine in a simple one pot reaction.[51] Hydrogels were formed by the following way: Dissolving 2.2 mg tannic acid and 19.9 mg polyallylamine hydrochloride (120–200 kDa M_W) in 75 μL demineralized H_2O gave a solution of pH 1.5. We then added 25 μL 0.0865 M $FeCl_3$ (aq) to afford a pyrogallol to Fe(III) molar ratio of 3:1. Upon mixing this immediately gave a very dark green/blue colored solution. Adjusting the pH to the desired value by addition of 50 μL NaOH gave the final hydrogel. When the base contacted the polymer solution, the color locally became dark red immediately reflecting

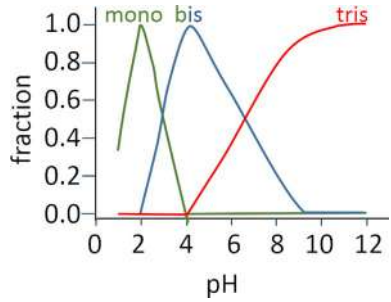

Fig. 4 Sketch of speciation of iron coordination by tannic acid in a mixture of tannic acid, Fe(III) and polyallylamine as determined by UV-VIS spectroscopy of dilute solutions at a pyrogallol to iron molar ratio of 3:1.

tris-complex formation. Mechanical mixing for 1 min gave homogeneous hydrogels with a final tannic acid and polyallylamine concentration of 14.7 and 133 mg/mL, respectively. We investigated the pH dependence of iron coordination by tannic acid in dilute hydrogel solutions by fitting spectral models to UV-VIS spectra. The results are shown in Fig. 4. A significant shift toward lower pH values are observed in the mono-bis and bis-tris equilibria. This is an important advantage of using pyrogallols and other more acidic polyphenols over simple catechols as the one on DOPA.

Based on the coordination equilibria, mono complexes dominate below pH 3. Indeed below this pH, a green liquid was observed. Above however, hydrogels were obtained. The storage modulus obtained from oscillatory rheology is shown in Fig. 5. The storage modulus increased with pH until pH around 4 after which it was constant until pH 8 above which it increased again. We rationalized this behavior as follows: below pH 8 the gels result from supramolecular interactions between coordination polymers of Fe(III) and tannic acid. Below pH 4, these are less stiff since the coordination polymers are not fully formed due to the large fraction of mono-coordination. In the bis/tris-regime from pH 4 upward, the hydrogel storage modulus is independent of pH because the supramolecular interactions do not change with pH. Above pH 8, however, covalent crosslinking sets in giving networks consisting of coordination polymers covalently crosslinked to the polyallylamine, Fig. 5B.

Support for this idea came from a combination of experiments. First, the need for all three components was explored in inversion tests of gel formation at pH 8. Gels formed instantly when all three components were present,

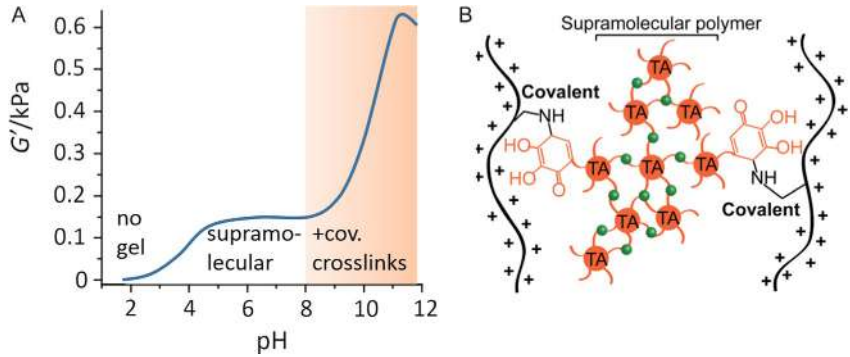

Fig. 5 Hydrogels formed by a one pot reaction between tannic acid, Fe(III) and polyallylamine are dominated by supramolecular interactions below pH 8 and by a combination of covalent crosslinks and coordination polymers formed by pyrogallol groups of tannic acid and iron above pH 8. Panel (B) shows a hypothetical structure of the high pH hydrogel.

but vials with only tannic acid and polyallylamine, tannic acid and iron, or polyallylamine and iron all remained liquid. After 15 h, the latter two remained liquid. The vial with tannic acid and polyallylamine had a dark coating on the air water interface and partial gel formation that we ascribe to oxidative crosslinking between the two components at the air water interface; this type of interaction has been explored by others in slightly different systems to form films that could self-repair while in contact with the liquid from which they formed.[52] The vial containing all three components remained a hydrogel. Secondly, gel formation could be reversed in competitive binding assays with EDTA (ethylenediaminetetraacetate) at pH 6 but not at 9 or 12, illustrating the covalent ramification above pH 8. Thirdly, small angle X-ray scattering revealed nanostructural signatures that differed from those in pure polyallylamine or in Fe(III)/tannic acid solutions. As pH increased, the SAXS data indicated that larger nanostructures formed consistent with the crosslinking mechanisms proposed above. The hydrogels obtained by this facile route were self-healing at pH 6, 9 and 12 as evidenced by rheology. In qualitative experiments at pH 8, gel pieces cut by a spatula were found to have self-healing properties: when the two pieces were brought back together, the interface rapidly gained strength allowing lifting/straining the gel without damage. Hydrogels formed also with poly-L-lysine instead of polyallylamine or Al(III) instead of Fe(III), further illustrating the concept.

Interestingly, Rahim et al. recently reported that gels could be obtained directly by reaction of tannic acid with Ti(IV) in organic solvents or water.[53] This provided a facile route to hydrogels or organogels that could be functionalized by nanoparticles, other metal ions or graphene oxide. These gels only formed with Ti(IV) (and Zr(IV)) and not with Fe(III).

In our tannic acid, polyallylamine, M(III) system, however, another interesting phenomenon was observed.[51] At high concentrations (15-fold that of the hydrogel formation procedure presented above) and low pH, a sticky and viscous fluid was obtained. It easily attached to various surfaces, for example spatula or glass. It was extremely shear thinable, i.e., it underwent immense plastic deformation when subject to load. This allowed pulling meter long threads from it. This could be achieved by pulling threads onto a motor-driven spindle. It was only possible to draw long threads when all three components where present; either Fe(III) or Al(III) could be used. The thread thickness depended on the pulling speed as expected for the strongly non-Newtonian behavior of the liquid. The thread diameter increased exponentially with pulling speed from 39 to 280 μm at pulling speed from 10 to 25 rounds per minute.

The wet threads were highly plastically deformable. Dried threads were remarkably strong with a tensile strength of 3.8 MPa, about 1% of that of cotton, which is remarkable considering that it is held together purely by supramolecular interactions. The dried threads were highly swell-able and gained 15%–25% in mass within 20 min at 45% relative humidity. This suggested that they could be used as vapor sensitive "locks": containers could be sealed by applying the tacky liquid and letting it dry. Upon swelling by addition of water, the seals broke unlocking the containers. This behavior was quantified at 90% humidity where the tensile strength of previously dried gels exposed to the high humidity dropped almost a factor of two to 2 MPa. We hypothesized that this swelling-induced thread weakening might be rescued in part if the network could be fortified by covalent cross-links. This was achieved by exposing threads to ammonia gas. This did not change significantly the tensile strength of dry threads, but the drop in strength at high humidity was cut in half: ammonia exposed threads had a tensile strength of 3 MPa at high humidity. These highly non-Newtonian liquids are remarkable. They are stable over a long time; they flow even if they contain extremely high concentrations of active reagents (0.22 g/mL tannic acid and 1.99 g/mL polyallylamine), over twice the mass of water in the "solution."

The hydrogel synthesis discussed in this section is very easy. Indeed, we currently use it in freshman laboratory exercises at Aarhus University to introduce students to supramolecular chemistry, coordination chemistry, self-healing materials and hydrogels. In these exercises, the students study gel formation by inversion tests, follow coordination and oxidation by UV-VIS spectroscopy and study the self-healing properties of the hydrogels quantitatively by oscillatory rheology.

3.5 Double crosslinked hydrogels that retain self-healing by combination of oxidation resistant and oxidation labile polyphenols

The hydrogels discussed thus far are based on catechols that can both undergo coordination and oxidative crosslinking (Scheme 1). These have been very successful, but there is a risk that slow oxidation impairs the coordination crosslinking and thereby the self-healing properties. Therefore, it would be beneficial to employ polyphenol ligands that are less sensitive to oxidation. Catechols with electron-withdrawing substituents such as –Cl, $–NO_2$, –CN, $–CF_3$ (Scheme 4) are hard to oxidize compared to pure catechol, whereas the opposite holds for catechols with electron-donating substituents such as –OMe and –Me.[54,55] Thus, chloro- and nitro-catechols have been employed in bioinspired materials with the added benefit, respectively, of antibacterial properties and the ability to break down the network by light induced cleavage of the nitro-catechol from the polymer.[56,57]

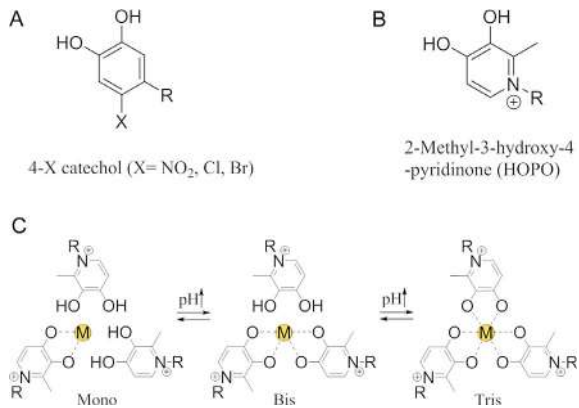

Scheme 4 Oxidation resistant catechol analogues. (A) Electron withdrawing substituents reduce the propensity to oxidation. (B) Changing the ring structure to a pyridinone achieves the same effect. (C) pH dependent chelation equilibria of 3-hydroxy-4-pyridinone.

Oxidation can also be prevented by use of alternate ring structures as proposed by Menyo et al. who used a chelating HOPO functionality instead of DOPA (the structure of HOPO, 3-hydroxy-4-pyridinone, is shown in Scheme 4B).[58] HOPO is less prone to oxidation than DOPA because electron density is withdrawn from the ring by inductive and resonance effects. This dramatically lowers the phenolic pK_a values (HOPO: $pK_{a1} = 3.6$, $pK_{a2} = 9.9$, DOPA: $pK_{a1} = 9.1$, $pK_{a2} = 14$).[58] HOPO retains high affinity toward hard metal ions such as Fe^{III} and Al^{III}, meaning that it is a very good replacement for DOPA in hydrogel design.[59]

We synthesized a HOPO analogue functionalized by a carboxylic acid, cHOPO, 1-(2′-carboxyethyl)-2-methyl-3-hydroxy-4(1H)-pyridinone, to allow facile coupling to e.g. polyallylamine.[60] cHOPO was synthesized from maltol inspired by the synthesis of 1-carboxymethyl-3-hydroxy-2-methyl-4-pyridinone described by Mawani et al. and Zhang et al.[61,62] We then made *g*-cHOPO-polyallylamine using standard EDC/NHS coupling chemistry on to polyallylamine (MW 120–200 kDa) giving a cHOPO grafting density of 7%.

We determined the pK_a of the catechol analogue by UV-VIS titration using the pH dependent integrated absorption signals. The resulting titration curves are shown in Fig. 6. For pure cHOPO the first pK_a was 3.52 and the second was 9.89. Upon conjugation to polyallylamine, these values changed significantly. The first pK_a shifted almost a full pH unit to 2.60 while the second shifted to 9.65 and broadened significantly (Fig. 6). We ascribe the shift in the first pK_a to the change in environment upon conjugation

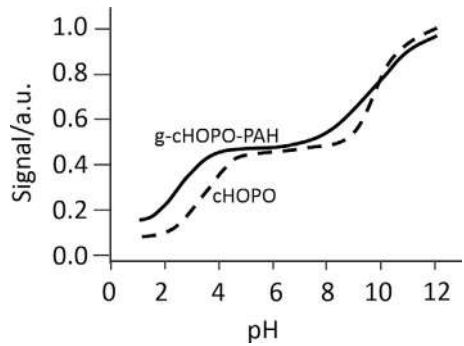

Fig. 6 UV-VIS titration of cHOPO (dashed line) and *g*-cHOPO-polyallylamine (*g*-cHOPO-PAH, full line). Note the shift in the first pK_a and the broader transition in *g*-cHOPO-polyallylamine around pH 9. *Redrawn from data in Andersen, A.; Krogsgaard, M.; Birkedal, H.* Biomacromolecules ***2018***, 19, *1402–1409.*

to polyallylamine, where the molecule changes from having a carboxylic acid substituent to being linked via an amide bond to the polyamine environment of polyallylamine, i.e., from $-CH_2CH_2COOH$ to $-CH_2CH_2CONH$-polymer. The second pK_a shifts less, but the transition broadens significantly from an apparent width of 2.9 pH units to one of 5.5 pH units. We ascribe this to overlap with the pK_a of the amines of the polymer backbone, which means that the local electronic environment of the HOPO rings changes significantly with pH in this pH range.

The iron complexes were strongly colored, purple at low pH and orange at high pH and the absorption spectra of the Fe(III) complexes with cHOPO shifted from about 450 nm to around 550 nm as the pH increased from 1 to 11. The mono-complex is thus purple while the tris-complex is orange. Upon grafting to polyallylamine, the absorption peaks start to red shift at significantly lower pH than for free cHOPO, around pH 3 rather than 7. This indicates that the onset of the bis-complex formation shifts to much lower pH values for *g*-cHOPO-polyallylamine than for free cHOPO, most likely due to a combination of the lower pK_a but possibly also to the spatial proximity of cHOPOs bound to the same polymer molecule. Thus polymer conjugation shifts the formation of higher-order complexes (bis- and tris-complexes) to lower pH, which is a significant advantage for hydrogel formation and reflects that the coordination and crosslinking properties of these ligands can be altered by substituents several carbons away from the hetero-aromatic ring.

We formed self-healing hydrogels with Al(III) to circumvent the strongly colored Fe(III)-cHOPO complexes. Hydrogel formation was reversible at all pH values as evidenced by competitive binding experiments with EDTA. Additionally, we conducted UV-VIS absorption experiments of solutions of iron complexes mixed at pH 1 and then subjected for 5 min to pH 12, after which the pH was returned to pH 1. The absorption spectra reversed completely for *g*-HOPO-polyallylamine while persistent changes reflecting oxidation at high pH were observed for *g*-DOPA-polyallylamine. The concept of fully reversible gel formation was thus established. The hydrogels were self-healing at all pH values as shown for oscillatory rheology on Al(III) hydrogels. Qualitative macroscopic tests, where gel pieces were cut in half and placed in contact to heal, confirmed the rheological data: the gel pieces healed within minutes and could be lifted and strained with a spatula without breaking.

The hydrogel mechanics were investigated by oscillatory rheology as summarized in Fig. 7A. In keeping with the pH dependence of the

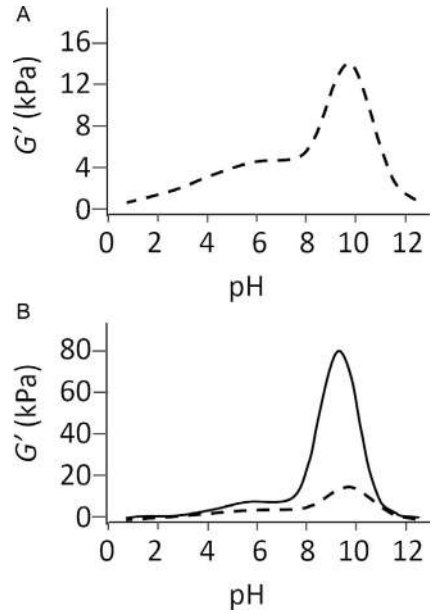

Fig. 7 Storage modulus of hydrogels of Al(III) and *g*-cHOPO-polyallylamine as a function of pH. (A) Pure Al(III)—*g*-cHOPO-polyallylamine hydrogel. (B) Comparison of pure Al(III)—*g*-cHOPO-polyallylamine hydrogel with ones where 1 mol% tannic acid was added for additional pH dependent oxidative crosslinking. *Redrawn from data in Andersen, A.; Krogsgaard, M.; Birkedal, H.* Biomacromolecules ***2018***, 19, *1402–1409.*

coordination complex equilibria and the general hydrogel formation mechanism of these polyallylamine backbone polymer hydrogels, the storage modulus increases until pH 9 where a maximum storage modulus of about 15 kPa was obtained. The hydrogel formed already at pH ~4, which is about 3 pH units lower than in the corresponding DOPA based hydrogel due to the shift in cHOPO-metal stoichiometric changes to lower pH values. This lowering of the pH onset of significant gel crosslinking is a significant additional advantage of the cHOPO-hydrogels over the corresponding DOPA ones.

We hypothesized that combining in a controllable manner the effects of coordination and covalent crosslinks would afford detailed control over hydrogel stiffness while retaining self-healing at all pH values and all times. We achieved this by forming DC hydrogels: the Al(III) *g*-cHOPO-polyallylamine hydrogels were reinforced in a dial-in manner by covalent crosslinks through addition of tannic acid that was also used in the one pot hydrogel formation system described in the preceding section.

This worked very well. Storage moduli as a function of pH of purely coordination crosslinked gels are compared to ones with 1 mol% tannic acid, corresponding to 5 mol% pyrogallol groups per amine monomer, in Fig. 7B. At low pH, before oxidative crosslinking can set in, the two curves are similar. However above pH of about 8 where oxidative crosslinking becomes important, the storage modulus increased drastically and reached a maximum stiffness 5.5 times larger than without tannic acid at pH 9, proving that the DC hydrogels combine the two crosslinking mechanisms. Between pH 4 and 7, the tannic acid system has somewhat higher storage modulus than the pure coordination system. We suggest this is caused by the larger proportion of metal binding ligands in the tannic acid containing system, which provides additional crosslinking in this bis-complex dominant regime.

The self-healing properties of the hydrogels were retained both as determined by macroscopic qualitative tests and by rheology at pH 3, 6, 9 and 12. Competitive binding by EDTA showed that hydrogel formation no longer was reversible as expected for the added covalent crosslinking. Next we investigated the dependence of the storage modulus on the concentration of added tannic acid. The storage modulus at pH 9 increased exponentially with tannic acid concentration until about 2 mol% tannic acid where a storage modulus of no less than 434 kPa was reached in comparison to the 15 kPa for pure coordination chemistry hydrogel. Above this tannic acid concentration, the hydrogels became syneretic, i.e., they excluded water due to the high degree of covalent crosslinking and the stiffness no longer increased in the same manner. Nevertheless, the results clearly demonstrated that the hydrogel stiffness could be dialed-in at will through control of the concentration of added tannic acid.

We further harnessed the reversible Al(III) gelation of *g*-cHOPO-polyallylamine to study the plasmonic sensing with chiral plasmonic gold nanostructures.[63] Chiral gold nano-hooks were made by hole-mask colloidal lithography and could be lifted out. The nano-hooks were only a few hundred nanometers in diameter with a complex curving 3D structure generating the chiral hook-shape. The chirality of the nano-hooks gave them strong circular dichroism. The nano-hooks were incorporated into Al(III) *g*-cHOPO-polyallylamine hydrogels. The CD (circular dichroism) signature of the nano-hooks remained easily measureable. The wavelength of the CD spectral signatures depended on polymer concentration. This made it possible to follow the water uptake into the hydrogel during swelling experiments by following the change in the CD spectra over time.[63]

This illustrates the versatility of these hydrogels that we expect can find widespread used in many nanoscience scenarios.

4. Specific ion effects in hydrogels: Impact on gel strength and a platform for chemical gardens

In the preceding sections, we have discussed how coordination chemistry can be used to form and control hydrogel mechanics. However, metal ions can also impact hydrogels through specific ion or Hofmeister effects.[64–66] For example, changing anions added to ethylene glycol-functionalized poly-isocyanide based hydrogels, drastically influences the thermal behavior of the gels.[67] There have only been a few studies of such effects based on cations and we therefore explored how metal chloride salts of mono- and divalent metal ions impact rheological properties of gelatin hydrogels.[68] We observed that gelatin gels were weakened upon addition of in particular divalent metal chlorides and to a lesser degree by monovalent metal chlorides. We quantitatively investigated rheological behavior of gelatin gels to which various quantities of Na^+, K^+, Rb^+, Cs^+, Mg^{2+}, Ca^{2+}, Mn^{2+}, Zn^{2+}, Sr^{2+}, and Ba^{2+}. Gels with Cu^{2+} were observed to be very significantly softened, but quantitative rheological measurements were not possible due to partial reduction of copper in the rheometer. Gels were melted at 55 °C and the temperature then reduced to 25 °C. We measured the time to gelation and measured the magnitude of the gel complex modulus ($G^* = G' + iG''$, i.e., the sum of the storage and loss moduli) after 500 min gelation time. Additionally, we measured the gel melting time. Addition of cationic chlorides reduced the gel modulus, increased the gelation time and reduced the melting temperature. The effects were drastic for divalent cations but less so for monovalent ions as illustrated in Fig. 8 for the ions with largest and smallest effects. The impact of the ions followed the orders $Cs^+ > Rb^+ > K^+ > Na^+$ for the monovalent and $Ba^{2+} > Sr^{2+}/Ca^{2+} > Zn^{2+} > Mn^{2+} > Mg^{2+}$ for the divalent ions, which is consistent with the chaotropic Hofmeister series.[69] The effects were drastic, for example the melting point (Fig. 8) dropped by over 5 K at a $BaCl_2$ ionic strength of 1 M corresponding to a $BaCl_2$ concentration of 0.33 M. Likewise, large increases were observed in the gelation time from ~8 min to over half an hour for 1 M ionic strength $BaCl_2$. The behavior of the investigated properties were found to follow the power law behavior

$$T_m(I) = T_m^0 - k_T I^x, \quad x \geq 1,$$

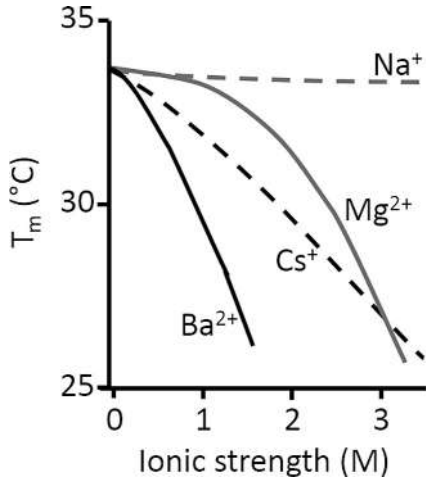

Fig. 8 Melting temperature of gelatin gels to which metal ions were added as a function of the ionic strength of the added salts. Dashed lines indicate the envelope of responses for monovalent ions, while full lines do so for the divalent earth alkali metal ions. *Figure redrawn from data reported in Andersen, A.; Ibsen, C. J. S.; Birkedal, H.* J. Phys. Chem. B ***2018***, 122, *10062–10067*.

for the melting point where I is the ionic strength, T_m^0 is the melting temperature at zero added salt, x and k_T are adjustable coefficients. A similar behavior was observed for $\log|G^*|$ while the gelation time followed

$$\log\left(t_{\text{gel}}(I)\right) = \log\left(t_{\text{gel}}^0\right) + k_{t\text{gel}} I^x, \quad x \geq 1.$$

Fitting these expressions to the data showed that the pre-factors, k_T, $k_{t\text{gel}}$, and $k_{|G^*|}$, depended linearly on the ionic radius cubed (r_{ion}^3) that was used as a proxy for ion size and hence polarizability. The linear relationship differed for monovalent and divalent cations. This showed that the Hofmeister effects on gelatin gels depend on ion size in an ionic charge dependent manner. Fourier transform infrared spectroscopy in attenuated total reflection mode as a function of added KCl, $MgCl_2$ or $CaCl_2$ indicated that the gelatin chains were increasingly denatured, corresponding to a decrease in the fraction of helical collagen, upon addition of cations and that this effect was larger for ions with larger impact on gel rheology.

We used the metal-laden gelatin gels as one component in crystallization experiments as part of our broader work on bioinspired crystallization and the controlled formation of nano-crystalline materials through nanoscale coordination chemistry.[70–80] By adding a volume of solution containing

phosphate or carbonate at high pH on top of the gel, the scene was set for inter-diffusion crystallization processes. The result was the formation of chemical gardens.[81] Chemical gardens are tubular (typically) structures formed by instabilities in a membrane between two liquids/phases. Classically, metal salts are placed in water glass (sodium silicate) and tubes grow in a tree like fashion from the membrane formed by initial dissolution of the metal salts.[82] Chemical gardens are a subset of a larger set of reaction-diffusion or self-organized reaction systems that are gaining increasing interest.[82–85] In our incarnation, the cations are placed in the gelatin gel while the anion source for forming crystals are placed in a solution in which the gel is placed, Fig. 9A. After a brief time, a mineralized slightly swollen interface

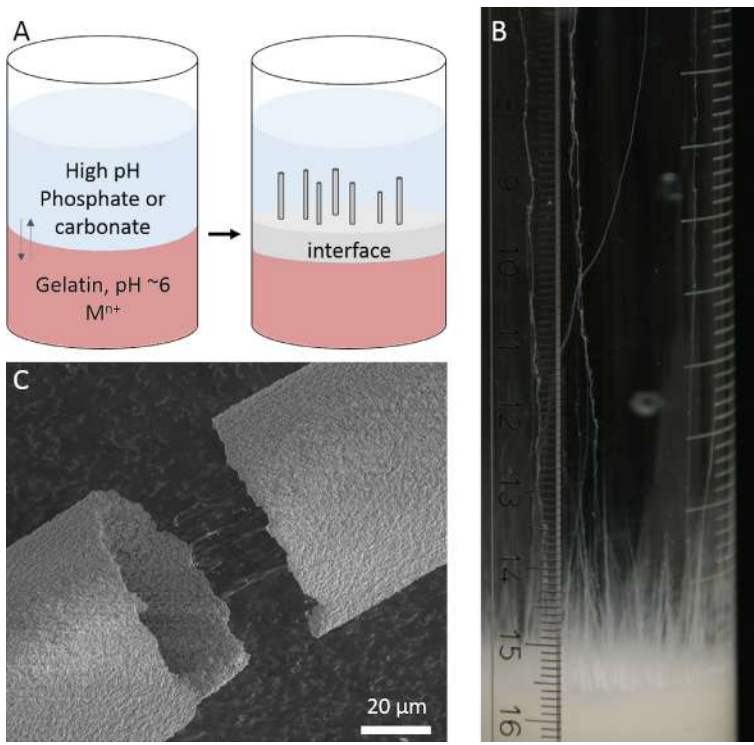

Fig. 9 Chemical gardens formed by placing an anion source on top of a metal-ion laden gelatin gel.[81] (A) Sketch of the process. A carbonate or phosphate solution was placed on top of a gelatin gel containing metal chloride salts. The interface between gel and liquid mineralized to form a membrane and tubes formed by jetting from defects in this membrane. (B) Example of tubes (optical photograph). The scale is indicated by the rule (cm-scale) to the left. The tubes are for gels containing $SrCl_2$ layered with Na_3PO_4 solution. (C) SEM image of tube extracted from the growth solution for gels containing a 50:50 mix of $CaCl_2$ and $SrCl_2$ overlain by K_3PO_4 solution.

between the solution and gel was formed.[81] Many cm long tubes then grew by jetting of metal ion carrying liquid from the gel into the high pH anion containing liquid followed by precipitation of minerals at the liquid/liquid interface, Fig. 9A and B. The system was found to be quite general. We investigated solutions containing carbonate or phosphate with either sodium or potassium as counter ions. The cations spanned Ca^{2+}, Sr^{2+}, Ba^{2+}, Cu^{2+} and Zn^{2+}. We formed apatite phases for calcium, strontium and barium accompanied by mixed sodium/strontium or sodium/barium salts when Na_3PO_4 was used as the anion source. For zinc and copper, chloro-hydroxides or carbonate-hydroxides (malachite) were formed. The observed minerals are summarized in Table 2 and are seen to follow the propensity of the different metals to form carbonate and phosphate minerals. Similar behavior was observed for calcium-laden agar gels in phosphate solutions.[86] The crystals that form the tube walls were in general very small and in many cases nano-crystalline. For the case of $SrCl_2$-laden gelatin overlaid by sodium phosphate solution gave tubes with a complex wall structure that consisted of a main wall about 10 μm thick, which was further decorated by large Hopper-like needle shaped crystals. The main wall consisted of two layers, a ball layer formed of ball-shaped aggregates of nanocrystals of sodium-substituted strontium apatite and a needle layer containing a few

Table 2 Mineral phases of tubes formed in the chemical garden systems shown in Fig. 9 as a function of which cations were in the gelatin gel phase and which anions were placed in the liquid phase placed on top of the gelatin gel.

Cation\Anion	Na_2CO_3	Na_3PO_4
$CaCl_2$	Vaterite, calcite ($CaCO_3$ polymorphs)	Apatite ($Ca_{10}(PO_4)_6(OH)_2$)
$SrCl_2$	Strontanite ($SrCO_3$)	Sr-apatite ($Sr_{10}(PO_4)_6(OH)_2$), Nastrophite ($NaSr(PO_4)\cdot 9H_2O$)
$BaCl_2$	Witherite ($BaCO_3$)	Ba-apatite ($Ba_{10}(PO_4)_6(OH)_2$)
$CuCl_2$	Atacamite ($Cu_2Cl(OH)_3$), Malachite ($Cu_2CO_3(OH)_2$)	
$ZnCl_2$	Simonkolleite ($Zn_5(OH)_8Cl_3\cdot H_2O$), "$Zn_2NaCl_4 \pm H_2O$"	Simonkolleite ($Zn_5(OH)_8Cl_3\cdot H_2O$), amorphous
$CuCl_2/ZnCl_2$ 50:50	Atacamite ($Cu_2Cl(OH)_3$)	

μm long needles about 50 nm wide. For the calcium chloride/sodium phosphate system, the wall was formed of needle shaped apatite nanocrystals and displayed significant nanocrystal size broadening in X-ray powder diffraction. Indeed, size broadening was observed in almost all cases indicating that the rapid nucleation at the liquid/liquid interface during tube formation generally favored nanocrystal formation.

The gelatin based system was later expanded upon by others with the aim of making potential biomaterials.[87,88] The weakening of the gelatin gel by the metal ions could be large enough to preclude formation of the membrane needed for chemical garden formation. With $CuCl_2$ for example, the gel was extremely soft. Instead of chemical gardens, beautiful 3D precipitation patterns formed in the gel, most likely driven by a mixture of convection and precipitation while the surface of the gel was decorated by malachite balls.[81]

5. Conclusions

In this chapter we have discussed how metal coordination chemistry can be engineered into hydrogel designs to afford self-healing materials. We harnessed the coordination of hard metal ions by polyphenols—mussel inspired materials—to form reversible crosslinks. By tailoring the polyphenol chemistry, detailed control over hydrogel properties were obtained. We stressed that metal ions also can play other roles as illustrated by the Hofmeister type weakening of gelatin hydrogels by mono- and divalent metal ions, which was further harnessed as a platform for the formation of chemical gardens in a diffusion-reaction self-organized system.

The self-healing materials, formed by coordination chemistry of hard metal ions like Fe(III) with polyphenols such as catechols or pyrogallols, were shown to be very versatile. Indeed, hydrogels were formed either by conjugating these groups covalently to polymer back bones or through in situ formation of coordination polymers by the multivalent polyphenol tannic acid. By using pH responsive polymers, just as in the blue mussel byssus, additional pH responsiveness was introduced. Both polyallylamine and the chitosan derived from the biopolymer chitin were employed. Introducing double crosslinked or double network hydrogels into this chemistry afforded independent control over storage moduli and self-healing properties. Gels based on magnetic nanoparticles added functionality and altered mechanical properties. The chemistry of polyphenols is rich and in our view an excellent tool for the synthesis of advanced self-healing materials and indeed nano-materials with a multitude of advanced properties.

Acknowledgments

We acknowledge financial support from the Lundbeck Foundation, grant number R180-2014-3468, and the Chinese Scholarship Council. Affiliation with the Center for Integrated Materials Research (iMAT) at Aarhus University is gratefully acknowledged.

References

1. Tillet, G.; Boutevin, B.; Ameduri, B. *Prog. Polym. Sci.* **2011**, *36*(2), 191–217.
2. Taylor, D. L. In Het Panhuis, M. *Adv. Mater.* **2016**, *28*(41), 9060–9093.
3. Diesendruck, C. E.; Sottos, N. R.; Moore, J. S.; White, S. R. *Angew. Chem. Int. Ed.* **2015**, *54*, 10428–10447.
4. Wei, Z.; Yang, J. H.; Zhou, J.; Xu, F.; Zrinyi, M.; Dussault, P. H.; Osada, Y.; Chen, Y. M. *Chem. Soc. Rev.* **2014**, *43*, 8114–8131.
5. Hager, M. D.; Greil, P.; Leyens, C.; van der Zwaag, S.; Schubert, U. S. *Adv. Mater.* **2010**, *22*, 5424–5430.
6. Degtyar, E.; Harrington, M. J.; Politi, Y.; Fratzl, P. *Angew. Chem. Int. Ed.* **2014**, *53*, 12026–12044.
7. Fantner, G. E.; Hassenkam, T.; Kindt, J. H.; Weaver, J. C.; Birkedal, H.; Pechenik, L.; Cutroni, J. A.; Cidade, G. A. G.; Stucky, G. D.; Morse, D. E.; Hansma, P. K. *Nat. Mater.* **2005**, *4*(8), 612–616.
8. Harrington, M. J.; Masic, A.; Holten-Andersen, N.; Waite, J. H.; Fratzl, P. *Science* **2010**, *328*, 216–220.
9. Holten-Andersen, N.; Fantner, G. E.; Hohlbauch, S.; Waite, J. H.; Zok, F. W. *Nat. Mater.* **2007**, *6*, 669–672.
10. Lee, B. P.; Messersmith, P. B.; Israelachvili, J. N.; Waite, J. H. *Annu. Rev. Mater. Res.* **2011**, *41*, 99–132.
11. Rubin, D. J.; Miserez, A.; Waite, J. H. *Adv. Insect Phys.* **2010**, *38*, 75–133.
12. Waite, J. H.; Holten-Andersen, N.; Jewhurst, S. A.; Sun, C. J. *J. Adhesion* **2005**, *81*, 297–317.
13. Lee, H.; Scherer, N. F.; Messersmith, P. B. *PNAS* **2006**, *103*, 12999–13003.
14. Li, Y.; Wen, J.; Qin, M.; Cao, Y.; Ma, H.; Wang, W. *ACS Biomater. Sci. Eng.* **2017**, *3*(6), 979–989.
15. Waite, J. H.; Lichtenegger, H. C.; Stucky, G. D.; Hansma, P. *Biochemistry* **2004**, *43*, 7653–7662.
16. Waite, J. H. *Biol. Rev.* **1983**, *58*, 209–231.
17. Petrone, L.; Kumar, A.; Sutanto, C. N.; Patil, N. J.; Kannan, S.; Palaniappan, A.; Amini, S.; Zappone, B.; Verma, C.; Miserez, A. *Nat. Commun.* **2015**, *6*, 8737.
18. Priemel, T.; Degtyar, E.; Dean, M. N.; Harrington, M. J. *Nat. Commun.* **2017**, *8*, 14539.
19. Yang, J.; Cohen Stuart, M. A.; Kamperman, M. *Chem. Soc. Rev.* **2014**, *43*, 8271–8298.
20. Andersen, A.; Chen, Y.; Birkedal, H. *Biomimetics* **2019**, *4*(2), 30.
21. Krogsgaard, M.; Nue, V.; Birkedal, H. *Chem. Eur. J.* **2016**, *22*, 844–857.
22. Saiz-Poseu, J.; Mancebo-Aracil, J.; Nador, F.; Busqué, F.; Ruiz-Molina, D. *Angew. Chem. Int. Ed. Engl.* **2019**, *58*(3), 696–714.
23. Sedó, J.; Saiz-Poseu, J.; Busqué, F.; Ruiz-Molina, D. *Adv. Mater.* **2013**, *25*, 653–701.
24. Rahim, M. A.; Kristufek, S. L.; Pan, S.; Richardson, J. J.; Caruso, F. *Angew. Chem. Int. Ed.* **2019**, *58*(7), 1904–1927.
25. Zechel, S.; Hager, M. D.; Priemel, T.; Harrington, M. J. *Biomimetics* **2019**, *4*, 20.
26. Lichtenegger, H. C.; Birkedal, H.; Waite, J. H.; Sigel, A.; Sigel, H.; Sigel, R. K. O., Eds.; *Metal Ions in Life Sciences*; Vol. 4;Springer, 2008; pp 295–325.
27. Birkedal, H.; Khan, R. K.; Slack, N.; Broomell, C.; Lichtenegger, H. C.; Zok, F.; Stucky, G. D.; Waite, J. H. *ChemBioChem* **2006**, 7(9), 1392–1399.

28. Lichtenegger, H. C.; Schoberl, T.; Ruokolainen, J. T.; Cross, J. O.; Heald, S. M.; Birkedal, H.; Waite, J. H.; Stucky, G. D. *Proc. Natl. Acad. Sci. U. S. A.* **2003**, *100*(16), 9144–9149.
29. Lichtenegger, H. C.; Birkedal, H.; Casa, D. M.; Cross, J. O.; Heald, S. M.; Waite, J. H.; Stucky, G. D. *Chem. Mater.* **2005**, *17*(11), 2927–2931.
30. Lichtenegger, H. C.; Schöberl, T.; Bartl, M. H.; Waite, H.; Stucky, G. D. *Science* **2002**, *298*, 389–392.
31. Ryu, J. H.; Hong, S.; Lee, H. *Acta Biomater.* **2015**, *27*, 101–115.
32. Holten-Andersen, N.; Harrington, M. J.; Birkedal, H.; Lee, B. P.; Messersmith, P. B.; Lee, K. Y. C.; Waite, J. H. *PNAS* **2011**, *108*(7), 2651–2655.
33. Grindy, S. C.; Learsch, R.; Mozhdehi, D.; Cheng, J.; Barrett, D. G.; Guan, Z.; Messersmith, P. B.; Holten-Andersen, N. *Nat. Mater.* **2015**, *14*(12), 1210–1216.
34. Li, Q.; Barrett, D. G.; Messersmith, P. B.; Holten-Andersen, N. *ACS Nano* **2016**, *10*(1), 1317–1324.
35. Zvarec, O.; Purushotham, S.; Masic, A.; Ramanujan, R. V.; Miserez, A. *Langmuir* **2013**, *29*(34), 10899–10906.
36. Chen, N.; Pan, Q. *ACS Sustainable Chem. Eng.* **2017**, *5*(9), 7905–7911.
37. Krogsgaard, M.; Hansen, M. R.; Birkedal, H. *J. Mater. Chem. B* **2014**, *2*, 8292–8297.
38. Krogsgaard, M.; Behrens, M. A.; Pedersen, J. S.; Birkedal, H. *Biomacromolecules* **2013**, *14*(2), 297–301.
39. Fullenkamp, D. E.; Barrett, D. G.; Miller, D. R.; Kurutz, J. W.; Messersmith, P. B. *RSC Adv.* **2014**, *4*, 25127–25134.
40. Shin, M.; Park, S.-G.; Oh, B.-C.; Kim, K.; Jo, S.; Lee, M. S.; Oh, S. S.; Hong, S.-H.; Shin, E.-C.; Kim, K.-S.; Kang, S.-W.; Lee, H. *Nat. Mater.* **2017**, *16*(1), 147–152.
41. Mozhdehi, D.; Neal, J. A.; Grindy, S. C.; Cordeau, Y.; Ayala, S.; Holten-Andersen, N.; Guan, Z. *Macromolecules* **2016**, *49*(17), 6310–6321.
42. Gong, J. P.; Katsuyama, Y.; Kurokawa, T.; Osada, Y. *Adv. Mater.* **2003**, *15*(14), 1155–1158.
43. Gong, J. P. *Soft Matter* **2010**, *6*(12), 2583.
44. Haque, M. A.; Kurokawa, T.; Gong, J. P. *Polymer* **2012**, *53*(9), 1805–1822.
45. Costa, A. M. S.; Mano, J. F. *Eur. Polym. J.* **2015**, *72*, 344–364.
46. Rodell, C. B.; Dusaj, N. N.; Highley, C. B.; Burdick, J. A. *Adv. Mater.* **2016**, *28*(38), 8419–8424.
47. Azevedo, S.; Costa, A. M. S.; Andersen, A.; Choi, I. S.; Birkedal, H.; Mano, J. F. *Adv. Mater.* **2017**, *29*(28), 1700759.
48. Sileika, T. S.; Barrett, D. G.; Zhang, R.; Lau, K. H. A.; Messersmith, P. B. *Angew. Chem. Int. Ed.* **2013**, *52*, 10766–10770.
49. Guo, J.; Ping, Y.; Ejima, H.; Alt, K.; Meissner, M.; Richardson, J. J.; Yan, Y.; Peter, K.; von Elverfeldt, D.; Hagemeyer, C. E.; Caruso, F. *Angew. Chem. Int. Ed.* **2014**, *53*, 5546–5551.
50. Ejima, H.; Richardson, J. J.; Liang, K.; Best, J. P.; van Koeverden, M. P.; Such, G. K.; Cui, J.; Caruso, F. *Science* **2013**, *341*, 154–157.
51. Krogsgaard, M.; Andersen, A.; Birkedal, H. *Chem. Commun.* **2014**, *50*, 13278–13281.
52. Hong, S.; Schaber, C. F.; Dening, K.; Appel, E.; Gorb, S. N.; Lee, H. *Adv. Mater.* **2014**, *26*(45), 7581–7587.
53. Rahim, M. A.; Björnmalm, M.; Suma, T.; Faria, M.; Ju, Y.; Kempe, K.; Müllner, M.; Ejima, H.; Stickland, A. D.; Caruso, F. *Angew. Chem. Int. Ed.* **2016**, *55*(44), 13803–13807.
54. Ramsden, C. A.; Riley, P. A. *ARKIVOC* **2010**, 248–254.
55. Garcia-Fernandez, L.; Cui, J. X.; Serrano, C.; Shafiq, Z.; Gropeanu, R. A.; San Miguel, V.; Ramos, J. I.; Wang, M.; Auernhammer, G. K.; Ritz, S.; Golriz, A. A.; Berger, R.; Wagner, M.; del Campo, A. *Adv. Mater.* **2013**, *25*(4), 529–533.
56. Shafiq, Z.; Cui, J.; Pastor-Pérez, L.; San Miguel, V.; Gropeanu, R. A.; Serrano, C.; del Campo, A. *Angew. Chem. Int. Ed.* **2012**, *51*, 4332–4335.

57. García-Fernández, L.; Cui, J.; Serrano, C.; Shafiq, Z.; Gropeanu, R. A.; San Miguel, V.; Ramos, J. I.; Wang, M.; Auernhammer, G. K.; Ritz, S.; Golriz, A. A.; Berger, R.; Wagner, M.; del Campo, A. *Adv. Mater.* **2012**, *25*, 529–533.
58. Menyo, M. S.; Hawker, C. J.; Waite, J. H. *Soft Matter* **2013**, *9*(43), 10314–10323.
59. Dobbin, P. S.; Hider, R. C.; Hall, A. D.; Taylor, P. D.; Sarpong, P.; Porter, J. B.; Xiao, G.; van der Helm, D. *J. Med. Chem.* **1993**, *36*(17), 2448–2458.
60. Andersen, A.; Krogsgaard, M.; Birkedal, H. *Biomacromolecules* **2018**, *19*, 1402–1409.
61. Mawani, Y.; Cawthray, J. F.; Chang, S.; Sachs-Barrable, K.; Weekes, D. M.; Wasan, K. M.; Orvig, C. *Dalton Trans.* **2013**, *42*(17), 5999–6011.
62. Zhang, Z.; Rettig, S. J.; Orvig, C. *Can. J. Chem.* **1992**, *70*(763).
63. Klös, G.; Andersen, A.; Miola, M.; Birkedal, H.; Sutherland, D. S. *Nano Res.* **2019**, *12*(7), 1635–1642.
64. Lo Nostro, P.; Ninham, B. W. *Chem. Rev.* **2012**, *112*, 2286–2322.
65. Ninham, B. W.; Lo Nostro, P. *Molecular Forces and Self Assembly in Colloid, Nano Sciences and Biology*. Cambridge University Press: Cambridge, 2010.
66. Gibb, B. C. *Nat. Chem.* **2019**, *11*(11), 963–965.
67. Jaspers, M.; Rowan, A. E.; Kouwer, P. H. J. *Adv. Funct. Mater.* **2015**, *25*(41), 6503–6510.
68. Andersen, A.; Ibsen, C. J. S.; Birkedal, H. *J. Phys. Chem. B* **2018**, *122*, 10062–10067.
69. Cacace, M. G.; Landau, E. M.; Ramsden, J. J. *Q. Rev. Biophys.* **1997**, *30*(3), 241–277.
70. Jensen, A. C. S.; Birkedal, H.; Bertinetti, L. *Phys. Chem. Chem. Phys.* **2019**, *21*(24), 13230–13233.
71. Ibsen, C. J. S.; Leemreize, H.; Mikladal, B. F.; Skovgaard, J.; Bremholm, M.; Eltzholtz, J. R.; Iversen, B. B.; Birkedal, H. *Cryst. Growth Des.* **2018**, *18*(11), 6723–6728.
72. Ibsen, C. J. S.; Birkedal, H. *Minerals* **2018**, *8*, 65.
73. Huynh, T. P.; Pedersen, C.; Wittig, N. K.; Birkedal, H. *Cryst. Growth Des.* **2018**, *18*, 1951–1955.
74. Ibsen, C. J. S.; Gebauer, D.; Birkedal, H. *Chem. Mater.* **2016**, *28*, 8550–8555.
75. Ibsen, C. J. S.; Chernyshov, D.; Birkedal, H. *Chem. Eur. J.* **2016**, *22*, 12347–12357.
76. Jensen, A. C. S.; Hinge, M.; Birkedal, H. *Cryst. Eng. Commun.* **2015**, *17*, 6940–6946.
77. Jensen, A. C. S.; Ibsen, C. J. S.; Birkedal, H. *Cryst. Growth Des.* **2014**, *14*, 6343–6349.
78. Tseng, Y.-H.; Birkbak, M. E.; Birkedal, H. *Cryst. Growth Des.* **2013**, *13*, 4213–4219.
79. Ibsen, C. J. S.; Birkedal, H. *J. Appl. Crystallogr.* **2012**, *45*, 976–981.
80. Ibsen, C. J. S.; Birkedal, H. *Nanoscale* **2010**, *2*(11), 2478–2486.
81. Ibsen, C. J. S.; Mikladal, B. F.; Jensen, U. B.; Birkedal, H. *Chem. Eur. J.* **2014**, *20*, 16112–16120.
82. Barge, L. M.; Cardoso, S. S. S.; Cartwright, J. H. E.; Cooper, G. J. T.; Cronin, L.; De Wit, A.; Doloboff, I. J.; Escribano, B.; Goldstein, R. E.; Haudin, F.; Jones, D. E. H.; Mackay, A. L.; Maselko, J.; Pagano, J. J.; Pantaleone, J.; Russell, M. J.; Sainz-Díaz, C. I.; Steinbock, O.; Stone, D. A.; Tanimoto, Y.; Thomas, N. L. *Chem. Rev.* **2015**, *115*, 8652–8703.
83. De, S.; Klajn, R. *Adv. Mater.* **2018**, *30, e1706750.*
84. Cera, L.; Schalley, C. A. *Adv. Mater.* **2018**, *30, e1707029.*
85. Epstein, I. R.; Xu, B. *Nat. Nanotechnol.* **2016**, *11*(4), 312–319.
86. Kamiya, K.; Yoko, T.; Tanaka, K.; Fujiyama, Y. *J. Mater. Sci.* **1989**, *24*(3), 827–832.
87. Hughes, E. A. B.; Williams, R. L.; Cox, S. C.; Grover, L. M. *Langmuir* **2017**, *33*(8), 2059–2067.
88. Hughes, E. A. B.; Chipara, M.; Hall, T. J.; Williams, R. L.; Grover, L. M. *Biomater. Sci.* **2020**,

Index

Note: Page numbers followed by "*f*" indicate figures, "*t*" indicate tables, and "*s*" indicate schemes.

D

E

F

M

N

O

P

U

Z

Index

Note: Page numbers followed by "*f*" indicate figures, "*t*" indicate tables, and "*s*" indicate schemes.

D

E

F

M

N

O

P

U

Z

Serial Editor
Rudi van Eldik
University of Erlangen–Nuremberg, Germany
Jagiellonian University, Krakow, Poland
N. Copernicus University, Torun, Poland

ELSEVIER

ACADEMIC PRESS
An imprint of Elsevier
elsevier.com/books-and-journals

ISBN 978-0-12-820252-4
9 780128 202524